



GREAT LAKES COASTAL WETLAND RESPONSE TO CLIMATE CHANGE

using the coastal wetland response
model (CWRM)



Government
of Canada

Gouvernement
du Canada

Canada

Cat. No.: CW66-778/2-2022E-PDF
ISBN: 978-0-660-43794-1
EC22022

Unless otherwise specified, you may not reproduce materials in this publication, in whole or in part, for the purposes of commercial redistribution without prior written permission from Environment and Climate Change Canada's copyright administrator. To obtain permission to reproduce Government of Canada materials for commercial purposes, apply for Crown Copyright Clearance by contacting:

Environment and Climate Change Canada
Public Inquiries Centre
12th Floor, Fontaine Building
200 Sacré-Coeur Boulevard
Gatineau QC K1A 0H3
Telephone: 819-938-3860
Toll Free: 1-800-668-6767 (in Canada only)
Email: enviroinfo@ec.gc.ca

Cover photo: © Gettyimages

© His Majesty the King in Right of Canada, represented by the Minister of Environment and Climate Change, 2022

Aussi disponible en français

Recommended Citation:

Environment and Climate Change Canada. (2022). Great Lakes coastal wetland response to climate change using the CWRM (Coastal Wetland Response Model). Great Lakes Protection Initiative (2017-2022). Sévigny, C., Thériault, D., Maranda, A., Gosselin, R., Roy, M., Hogue-Hugron, S., Fortin, N., Bachand, M. and Morin, J. 537 p.

RESEARCH TEAM

Environment and Climate Change Canada – Meteorological Service of Canada –
Hydrodynamic and Ecohydraulic Section

Research

Marianne Bachand, Ph.D.

Olivier Champoux, M.Sc.

Mouna Doghri, Ph.D.

Nicolas Fortin, B.Sc.

Patrice Fortin, B.Sc.

Rémi Gosselin, Ph.D., Eng.

Guillaume Guénard, Ph.D.

Sandrine Hogue-Hugron, M.Sc.

Antoine Maranda, M. ATDR

Jean Morin, Ph.D.

Mathieu Roy, Ph.D.

Caroline Sevigny, Ph.D.

Dominic Thériault, M.Sc.

Management

Marianne Bachand, Ph.D.

Olivier Champoux, M.Sc.

Jean Morin, Ph.D.

Mathieu Roy, Ph.D.

Chief Section

Jean Morin, Ph.D.

PREFACE

This report has been peer reviewed. The following are the general comments of the reviewers.

General comments from Bill Werick, reviewer

I was really impressed with the care that was taken in each segment, the self-critical review of datasets and the careful grooming that followed, the masks, all anticipating and resolving questions before they could be asked. The degree of difficulty was high with the serial dependence of the forecasts. If you had come to me before and said you wanted to predict vulnerability cell by cell I would have said it likely couldn't be done. Random Forest must have helped.

Not just a project success, this is the payoff for the last 20 years of creating and sustaining a cutting edge modeling center.

Kudos to Dr. Morin.

General comments from Todd Redder (LimnoTech), reviewer

Thank you for the opportunity to provide this review. The CWRM effort is a very impressive "landmark" modeling effort, and we found it very interesting to read through the documentation of the various technical aspects of the effort. Congratulations again to you and the rest of your team!

ACKNOWLEDGEMENTS

This Program is supported by the Great Lakes Protection Initiative (GLPI) of Environment and Climate Change Canada. Through this initiative, the Government of Canada takes action to address the most significant environmental challenges affecting Great Lakes water quality and ecosystem health by delivering on Canada's commitments under the Canada-United States Great Lakes Water Quality Agreement.

The Hydrodynamic and Ecohydraulic Section wants to acknowledge the support that it received from the other branches of ECCC involved in this project (CWS, RDGO, WLSL and NHS-BWIU), more specifically: Patrick Rivers, Pauline Quesnelle, Morgan Hrynyk, Daniel Rokitnicki Wojnik, Frank Seglenieks, Greg Mayne, Greg Grabbas, Wendy Leger, Sean Backus, André Temgoua & Jason Duffe.

We also want to thank for their input Drs. Claude Lavoie, Janice Gilbert and Ouranos.

EXECUTIVE SUMMARY

Great Lakes coastal wetlands are strongly influenced by their physical environment, particularly by water-level fluctuations that incorporate the effect of large-scale synoptic systems controlling climate (i.e. surface air temperature, precipitation, evaporation, winds, etc). Water levels are therefore frequently described as the primary driver of changes of wetland structure, composition, and distribution, with annual, seasonal, and sub-seasonal fluctuations maintaining wetland vegetation biodiversity and habitat extent. Wetland ecosystems are hence highly vulnerable to the anticipated global warming, as altered lake hydrology can have a significant impact on their ecology. Adverse effects of climate change, which may result in habitat and/or biodiversity loss or increased anthropogenic stressors and expansion of invasive plant species, may lead to a dramatic deterioration of their conservation and functional values.

In 2017, Environment and Climate Change Canada (ECCC) announced the Great Lakes Protection Initiative (GLPI; 2017-2022), which contains a study to confront the impacts of climate change entitled 'Assessing and Enhancing the Resilience of Great Lakes Coastal Wetlands'. This study supports the 2012 Great Lakes Water Quality Agreement (GLWQA) and the 2014 Canada Ontario Agreement (COA), on Great Lakes Water Quality and Ecosystem Health in their focus on conserving productive wetland ecosystems and resilient populations of native species. It was built on three central objectives: (1) to assess the vulnerability of coastal wetlands; (2) to recommend adaptation strategies, measures, and actions to enhance their resilience; and (3) to engage, share information, and build consensus on priorities with partners, stakeholders, and rights holders.

Scientists and technical experts from four branches of ECCC, under the direction of the Strategic Policy Branch's Regional Director General, conducted the GLPI work. The other branches involved are the National Hydrological Service (NHS), Canadian Wildlife Service (CWS) and the Wildlife and Landscape Science Directorate (WLSA). Some of the key elements of this project were to determine the character, magnitude and rate of climate change to which wetlands are likely to be exposed, as well as the degree to which wetland distribution and composition will be affected, which form the basis of the vulnerability assessment. To address these aspects, the Hydrodynamic and Ecohydraulic Section of the NHS modelled the succession of wetland class distribution (submerged aquatic vegetation, emergent marshes, wet meadows, and swamps) and two invasive plant expansions under climate scenarios for the period 2070 to 2099. Four main objectives were pursued to meet the study priorities:

1. Develop two-dimensional lake models (hydrodynamic and wave models) to simulate physical conditions near coastal wetlands;
2. Collect, transform and integrate geo- and time-referenced environmental data (topography and plant distribution) on selected wetlands;
3. Build two-dimensional predictive models of wetland classes and invasive plant distribution;
4. Estimate the changes in wetland composition and the potential of expansion for two invasive plants expected under the projected climate by the end of the current century.

The sensitivity of Great Lakes coastal wetlands to global warming was assessed using a Coastal Wetland Response Model (CWRM), which predicts the spatiotemporal succession of large wetland classes based on hydrodynamic and waves time series. The CWRM, which simulates physical (water depth and waves) and environmental (vegetation distribution) conditions, was adapted to twenty wetland sites along the Canadian Great Lakes coastline. The model links large-scale dynamics (i.e., those that define the Great Lakes climate and hydrodynamics) to small-scale processes that explain changes in wetland class distribution through changes in physical conditions.

To project wetland class distribution, downscaled CMIP5 Atmosphere-Ocean General Circulation Models (AOGCMS) forced by a scenario of moderate anthropogenic CO₂ emissions (i.e. Representative Concentration Pathway 4.5) were used. These models project a mean increase in annual surface air temperature of 3.3°C in the Midwest and Great Lakes region (Byun and Hamlet, 2018), although large variability affects the different climate projections in the CMIP5 ensemble. These models represent possible future climates from which water levels and waves can be generated, providing time series covering the recent past (1980 to 2009, baseline) and future (2070 to 2099) periods. A subset of two CMIP5 AOGCMSs was selected to delineate the range of anticipated changes in lake levels: the lower- and upper-bounds scenarios. The Boundary Water Issues Section of the NHS estimated projected mean lake levels using the components net basin supply approach.

The CWRM is composed of a 10 m grid adapted for coastal wetlands that are directly influenced by lake hydrology. It integrates relevant local topography information extracted from high-resolution digital elevation models (DEMs) generated from corrected LIDAR-derived and bathymetric datasets. These digital representations of the bare ground (bare earth) topographic surface have an average error of 16 cm (ranging from 10 cm to 27 cm), providing accurate elevation in the terrestrial and lacustrine portions of wetlands. Nearshore-dynamics (water levels and waves) were extracted from several lake models (hydrodynamic and waves) built to

characterize the physical environment of coastal ecosystems on an annual, seasonal, and sub-seasonal (or daily) basis, and projected onto the CWRM grids. Two distinct modelling approaches were used to simulate lake surface dynamics, allowing for an accurate two-dimensional representation of the physics of both the deep (Ontario and Huron) and shallow lakes (St. Clair and Erie). Physical variables responsible for changes in wetland class distribution are estimated on a quarter-monthly time step to predict annual wetland classes and invasive plant expansion. These variables include a description of the short- and long-term fluctuations that shape the structure of wetland ecosystems, accounting for the effect of the episodic and periodic events that modulate lake levels.

For the restricted set of climate scenarios used, the results show that mean lake levels are expected to change under global warming, with a minor to moderate decrease for the period 2070 to 2099 relative to baseline under the lower-bound scenario and a significant increase under the upper-bound scenario. Lake Ontario, including the Upper St. Lawrence River, will likely be the most affected lake, with a net increase in the mean level of up to ~0.70 m, which is 2.5 times its natural variability observed between 1980 and 2009. The interannual variability in levels is also projected to increase by more than 25% by the end of the century in the Lower Great Lakes, including the Lower Detroit River. Again, the change in the year-to-year variation is particularly pronounced in Lake Ontario and the Upper St. Lawrence River, with a relative increase of 88% to 94%. No significant change in interannual variability was projected for Lakes St. Clair and Huron.

Consequently, wetland sites are expected to show an overall increase in their mean annual strictly flooded area by 2099. This increase primarily affects sites on Lake Ontario (and Upper St. Lawrence), where the relative difference ranges from 6% to 34%, as well as drowned river mouths, which show a high upper-bound projection relative to basin-scale values. The transition zone, where sub-seasonal wet/dry cycles occur, is also projected to expand by 2070 to 2099 in Lakes Ontario wetlands, as well as in riverine systems of Lake Erie, and some sites in Lake Huron. Conversely, this zone is projected to decrease significantly in connecting channel sites. In Lake St. Clair, the interannual variability of the strictly flooded area and transition zone are both projected to decrease, with changes ranging from -80 to -90%. The wetlands of Lake St. Clair will likely experience more stable physical conditions in the later decades of the century and, therefore, a less dynamic environment that heightens the risk of habitat loss.

In general, an increase in mean lake levels forces an upland migration of wetland classes, but it will likely result in more frequent declines in wetland area in modelled sites. This decrease is

primarily due to land use types preventing landward migration (i.e. agricultural land and urban zones), especially at the more anthropized southern sites. Lakes Erie and St. Clair sites could be among the most affected, with projected changes ranging from significant increases to significant decreases (29% to -55%) of total wetland area according to the lower- and upper-bound scenarios, respectively. Emergent marshes are likely to be the more abundant classes in Lake Erie by 2099 owing to their high ability to move landward or lakeward in response to changes in mean lake levels. In Lake Ontario, the submerged aquatic vegetation will likely increase with higher water levels and emergent marshes will migrate to higher elevations replacing wet meadows and swamps. This will likely result in an 8% to 10% total increase in wetland area, which is somewhat opposite to what is projected in Lake Erie and the Huron-Erie Corridor. Increase in submerged aquatic vegetation and landward migration of wetlands are also expected to occur in some sites of Lake Huron, which will likely offset the loss of wetland area under the upper-bound projection. However, changes in this lake will range from a moderate increase in wetland area, mainly swamps, to an overall decrease in total wetland area depending on the scenario. Overall, the upper-bound scenario projects a decrease in the relative abundance of all wetland classes with few exceptions, which could affect wetland biodiversity and functionality.

With respect to future expansion of the invasive species cattail (*Typha*) and common reed (*Phragmites*), a scenario of rising levels in Lake Ontario, including the Upper St. Lawrence River, will likely favour both invasive species. *Phragmites* expansion could even be a threat for wetlands where the species is not yet established. In Lake Erie, all projections indicate conditions favorable to high cattail abundance by the end of the century, as well as significant *Phragmites* expansion. Climate change will likely trigger common reed growth in this lake, especially if the mean lake levels decline. A similar conclusion can be drawn for most sites of the Huron-Erie Corridor under the lower-bound scenario, with the exception of Johnston Bay Wetlands at the mouth of St. Clair River. However, a large increase in the levels of Lake St. Clair by 2099 will likely reduce the expansion of both species, as wetlands will be largely inundated, creating unsuitable conditions for *Typha* and *Phragmites*. Most sites in Lake Huron are currently marginally affected by invasive species. Based on invasive species modelling, this situation is not expected to be exacerbated or worsened by projected changes in lake levels.

Finally, it is worth mentioning that many assumptions and simplifications were employed to make the modeling of the various physical and ecological processes incorporated in the CWRM possible. As a result, some key elements, such as coastal erosion, sediment transport, nutrient loading, ice conditions, chemical exposure, and water clarity, were not considered in this study

due to their complexity or the effort that would have been required to model them. Other elements, such as land use and site topography, were instead fixed, limiting the scope of the results should any of these aspects change in the future. Nevertheless, similar assumptions are unavoidable in modelling and allow the conclusions of the study to be limited to the conditions explored, which are primarily focused on the impacts of a change in mean level on the composition and distribution of wetland classes. Lastly, this study is restricted to 20 wetlands dispersed along the Canadian shores of the Great Lakes, with the exception of Lake Superior that was removed from the work due to time and computational constraints. It would be appropriate to include sites along the U.S. and Lake Superior coasts in the CWRM to provide a more comprehensive view of the potential impacts of climate change on wetlands in the Great Lakes basin.

TABLE OF CONTENTS

Research Team.....	3
Preface	4
Acknowledgements	5
Executive Summary.....	6
Table of Contents.....	11
List of Figures.....	17
List of Tables.....	41
1. Introduction.....	47
1.1. Background.....	47
1.2. Objectives.....	49
1.3. Scope of study	50
1.3.1. Study sites.....	50
1.3.2. Expected changes.....	51
1.3.3. Modelling approach	55
1.3.4. Presentation of results.....	59
2. Climate Modelling.....	61
2.1. Introduction.....	61
2.2. Atmospheric models.....	61
2.2.1. Atmosphere-Ocean General Circulation Models.....	61
2.2.2. Representative Concentration Pathways.....	62
2.2.3. Selected AOGCMs: Upper- and lower-bound scenarios.....	63
2.2.4. Hydrodynamic forcing: Scenarios outputs.....	66
2.3. Winds.....	66
2.3.1. Reference datasets.....	66

2.3.2.	Post-processing.....	78
2.4.	Projected changes: 2070-2099.....	83
2.4.1.	Future changes in wind speed.....	83
3.	Great Lakes Physical Modelling.....	92
3.1.	Introduction.....	92
3.2.	Physical processes in the Great Lakes	92
3.2.1.	Surface motions.....	93
3.2.2.	Water levels: Interannual variability, long- and short-term variations.....	97
3.2.3.	Two-Dimensional hydrodynamic modelling.....	108
3.2.4.	Surface gravity waves.....	110
3.3.	Mean lake level modelling	122
3.3.1.	Component Net Basin Supply and projections	123
3.3.2.	Projected time series	124
3.4.	Hydrodynamic modelling	128
3.4.1.	Numerical solver.....	128
3.4.2.	Two-dimensional modelling and assumptions.....	128
3.4.3.	Modelling approaches: Complex vs. scenario-based	132
3.4.4.	Summary table: lake-specific approaches and water level uncertainties.....	144
3.5.	Lake models	146
3.5.1.	Upper St. Lawrence River	146
3.5.2.	Lake Ontario.....	149
3.5.3.	Lake Erie.....	153
3.5.4.	Lake St. Clair.....	178
3.5.5.	Lake Huron.....	183
3.6.	Wave modelling	189
3.6.1.	Spectral wave models: WWIII and SWAN.....	189

3.6.2.	Modelling approaches: Time-varying and scenario-based methods.....	198
3.6.3.	Validation: Historical period, 1980–2010.....	203
3.7.	Physical variables for wetland modelling.....	212
3.7.1.	Wavelet analysis.....	212
3.7.2.	Water-level fluctuations.....	214
3.7.3.	Waves.....	225
3.8.	Projected changes.....	230
3.8.1.	Lake dynamics: Long and short-term fluctuations, waves climate.....	230
3.8.2.	Site-scale dynamics.....	235
3.8.3.	Summary.....	245
4.	Selected Sites.....	246
4.1.	Site description.....	251
4.1.1.	St. Lawrence River.....	251
4.1.2.	Lake Ontario.....	251
4.1.3.	Lake Erie.....	255
4.1.4.	Huron – Erie Corridor.....	259
4.1.5.	Lake Huron.....	262
4.2.	Area of Interest (AOI).....	268
4.3.	Masked areas.....	270
4.3.1.	Masks related to physical variable.....	270
4.3.2.	Masks related to land use.....	273
5.	High-Resolution Digital Elevation Models of Coastal Wetlands.....	278
5.1.	Introduction.....	278
5.1.1.	Definitions and key concepts:.....	278
5.2.	Methods.....	280
5.2.1.	Coordinates reference systems.....	280

5.2.2.	Topographic datasets	281
5.2.3.	Bathymetry datasets.....	294
5.2.4.	DEM creation and interpolation methods.....	298
5.2.5.	DEMs filtering.....	300
5.2.6.	Extraction of elevation values on CWRM grid	302
5.2.7.	Primary terrain attributes.....	303
5.3.	Results.....	305
5.3.1.	DEMs accuracy assessment.....	305
5.3.2.	Primary terrain attributes.....	311
5.4.	Summary.....	311
6.	Great Lakes Coastal Wetland Modelling.....	314
6.1.	Vegetation modelling.....	314
6.1.1.	Wetland succession modelling.....	315
6.1.2.	Wetland class datasets.....	316
6.1.3.	Clustering analysis.....	321
6.1.4.	Supervised machine learning model: Random Forest	324
6.1.5.	Selection of the explanatory variables	325
6.1.6.	Wetland succession algorithm.....	326
6.1.7.	Variable importance for each wetland class.....	332
6.1.8.	Wetland model calibration and validation.....	342
6.2.	Invasive species modelling.....	349
6.2.1.	Cattail (<i>Typha</i>).....	350
6.2.2.	Common reed (<i>Phragmites australis</i>).....	365
6.2.3.	Models calibration and validation.....	380
6.3.	Results.....	395
6.3.1.	Wetland succession modelling.....	395

6.3.2.	Invasive species modelling	411
7.	Conclusion.....	434
7.1.	Summary of methods	435
7.1.1.	Physical modelling.....	435
7.1.2.	Digital Elevation Model	435
7.1.3.	Wetland class succession modelling	436
7.2.	Summary of results and discussion.....	437
7.2.1.	Climate scenarios: Lower and upper-bound projections	437
7.2.2.	Changes in physical variables and vegetation	437
7.2.3.	Lakes modelling: Long- and short-term fluctuations.....	443
7.2.4.	Wetland modelling.....	444
7.2.5.	Invasive species modelling	444
7.3.	Model limitations	445
7.3.1.	Climate modelling limitations.....	445
7.3.2.	Physical modelling limitations.....	446
7.3.3.	DEM limitations	447
7.3.4.	Vegetation modelling	448
7.3.5.	Implications	449
7.4.	Key findings.....	449
7.5.	Future developments.....	451
8.	Appendixes	453
	APPENDIX A: Ground-truth points, LIDAR and bathymetry datasets used for each site DEM	453
	APPENDIX B: List of multispectral images used for DEM correction.....	454
	APPENDIX C: Statistical model terms for DEM correction.....	455
	APPENDIX D: ASPRS Standard Lidar Point Classes.....	456

APPENDIX E: Species frequency by water body	457
APPENDIX F: Observed species.....	460
9. References.....	483
Section 1: Introduction	483
Section 2: Climate Modelling.....	485
Section 3: Great Lakes Physical Modelling.....	492
Section 4: Selected Sites	511
Section 5: High-Resolution Digital Elevation Models of Coastal Wetlands.....	516
Section 6: Great Lakes Coastal Wetland Modelling.....	521

LIST OF FIGURES

Figure 1: Generalized framework for Great Lakes and coastal vulnerability assessment.....	49
Figure 2: Geographical location of the 20 selected sites.	51
Figure 3: CWRM type integrated analysis applications	52
Figure 4: Schematic representation of the modelling framework used to produce expected wetland classes for each year of the modelling periods.	55
Figure 5: Coastal Wetland Response Model (CWRM) workflow.	57
Figure 6: Global fossil-fuel emission under different emission scenarios with projected global warming by 2100 relative to pre-industrial levels. From Hausfather and Peters (2020).	63
Figure 7: Inter-model variability of changes in temperature and precipitation for RCP8.5, for horizon 2080. The AOGMs included in the first subset of scenarios used to select the lower and upper bounds are identified by a circular symbol, whereas excluded ones are represented by a diamond. CanESM2 and GFLD-ESM2M are identified in blue and yellow, respectively. The inner circle identifies the mean range of expected changes in the CMPI5 ensemble, while the outer circle identifies the maximum projected changes. Modified from Byun and Hamlet (2018).....	64
Figure 8: The land-sea mask of the Great Lakes of the Climex and CFSR datasets. The black colour represents the grid cells where the surface land fraction is zero (open-lake area). The inset (left panel) shows Climex' North American domain.....	68
Figure 9: Location of monitoring stations in the Great Lakes region (including buoys). In green, coastal (nearshore) stations, and in blue, open lake (offshore) stations.....	69
Figure 10: (a) Land-sea mask of Climex (left) and CFSR (right) datasets with the position of the Rock of Ages station, in Lake Superior (white star). (b) Climatology of the 16 sectors wind rose for observed near-surface winds (left panel) during March, April and May (MAM) at Rock of Ages station, for the period 1980-2010. Idem for Climex (middle panel) and CFSR (right panel) datasets.....	73
Figure 11: (a) Land-sea mask of Climex (left) and CFSR (right) datasets with the position of the South Georgian Bay buoy, in Lake Huron (white star). (b) Climatology of the 16 sectors wind rose for observed near-surface winds (left panel) during June, July and August (JJA) at South	

Georgian Bay station, for the period 1980-2010. Idem for Climex (middle panel) and CFSR (right panel) datasets.....	73
Figure 12: Heat maps comparing the performance of Climex and CFSR for wind speed (left panels) and direction (right panels) anomalies distribution based on the Kuiper metric for each Great Lake, for the period 1980-2010. (a) For all coastal and offshore stations, and (b) for offshore (open-lake) stations only. A negative value indicates that Climex outperforms CFSR (better skill).....	75
Figure 13: Heat maps comparing the performance of Climex (left panels) and CFSR (right panels) for climatological mean wind speeds based on the RV metric for each Great Lake, for the period 1980-2010. (a) For all coastal and offshore stations, and (b) for offshore (open-lake) stations only. A positive RV value indicates a good performance (or skill).	76
Figure 14: Wind speed climatology for the Western Island station, in the southeastern part of Georgian Bay (Lake Huron, offshore station), for the period 1980–2010. The climatology is given for each day-of-year (doy). The shaded area specifies the first and third quartiles of the observed distribution.	77
Figure 15: The Great Lakes domain for debiased wind scenarios (coloured areas).	79
Figure 16: Maps of the mean wind speed during 1980-2013 for July in: a) the Climex run (reference product); and b) the raw SIM01 run (cf. Table 1)). Maps of corresponding biases (r_{rank} relative to the reference product r_{rank}) considering: c) the raw SIM01 run; d) the univariate debiased time series (unshuffled uas and unshuffled vas); e) the debiased time series using uas as the master variable (vas is shuffled); and f) the debiased time series using vas as the master variable (vas is shuffled). The violet-to-green colorbar corresponds to direct wind speed values in panels a) and b), whereas the red-to-blue colorbar corresponds to biases in the four other panels (after Grenier and Music, 2020).....	81
Figure 17: (a) Zonal wind (uas) lag-1 auto-correlation (Spearman) coefficients for a specific grid tile (“middle” of Lake Huron) for simulation SIM03 (cf. Table 1). For each month-of-the-year, four distributions of coefficients are shown: for the reference product (Climex, in grey), for the raw simulation (red), for adjusted simulation without shuffling (blue) and for the adjusted simulation with shuffling (orange). Each distribution is made of 34 values, one for each year of the calibration period (1980-2013). For any distribution, the box plot shows the minimum and maximum values (coloured vertical thin line) as well as the 25th and 75th percentiles (coloured central box) and the median (black horizontal line). Dashed vertical lines are	

between-month separators (for better visual appreciation only), whereas dashed horizontal lines are the zero lines (no auto-correlation). (b) SIM03 was 3-hourly time series for the first month of the calibration period (January 1980). The raw simulation is presented in red, the adjusted simulation without shuffling in blue, and the adjusted simulation with the supplementary shuffling procedure in orange. Numbers presented in the legend box are the respective lag-1 auto-correlation (Spearman) coefficients. The concerned grid tile is located in the middle of Lake Huron (after Grenier and Music, 2020). 82

Figure 18: Left panels: Climate reference map for annual mean wind speed for the period 1980–2009 obtained from the reference product (Climex, cf. Section 2.3). The violin plot shows biases in grid points close to in-situ stations located near Lakes Ontario and Erie, and Mean gives the mean observed wind speed in stations. Right panels: The upper and lower bound of the projected change in annual mean wind speed for the period 2070–2099. Results are provided for the Lower Great Lakes. 90

Figure 19: Idem as Figure 18, but for the Upper Great Lakes..... 91

Figure 20: Steady wind set-up (in m) for a wind stress of 1.0 Pa in Lake Erie. Left panel: longitudinal response. Right panel: transverse response. After Hamblin (1987)..... 94

Figure 21: First gravitational normal mode for Lake Ontario, with one amphidromic point (black dot). The dashed lines indicated the relative amplitude of the free surface height, and the plain lines, the phase lag. For a nominal period of ~5h, a phase of 90° corresponds to a lag of 1.25h. After Rao & Schwab, 1976. 95

Figure 22: Observed average annual lake levels for the period 1918–2020. From the NOAA Great Lakes Environmental Research Laboratory (GLERL) Dashboard (https://www.glerl.noaa.gov/data/dashboard/data/levels/1918_PRES/)..... 98

Figure 23: Recorded water levels in 2017 at station Toledo, Lake Erie. The top panel gives the water level as recorded (in blue), as well as the long-term, seasonal trend (in green). The bottom panels explicit the anomalies, i.e. the low- (red; periods > 2 days) and high- (purple; periods < 2 days) frequency components extracted from the recorded signal. Details are given in the text. 99

Figure 24: The low-frequency water level anomalies (top panel) recorded at station Toledo (Lake Erie), in 2017. The anomalies observed between June and September are shown in the middle panel (green line), as well as zonal wind component along the main axis of the lake,

up (black line). The bottom panel highlights set-ups events of amplitude > 5 cm (black dots) detected from anomalies (blue line) and computed wind stress (green line). 100

Figure 25: (a) The spectral coherence computed from low frequency anomalies and zonal winds recorded in station Toledo, in 2017 (cf. Figure 24). The black, horizontal line gives the 95% confidence level for coherence amplitude significance. (b) Coherence amplitude map for a variable principal axis, i.e. the angle of rotation of the coordinate system used to compute the zonal component of the wind, up . The angle refers to a counter-clockwise rotation of the coordinate system by an angle of $90 - \theta$, with θ the wind vector azimuth (i.e. the direction towards which the wind is blowing). 101

Figure 26: The amplitude of the wind set-ups detected at Cleveland (a) and Toledo (b), in Lake Erie, between 1980 and 2010, versus the magnitude of the winds responsible for the water level rise/fall (i.e. the maxima observed in the low-frequency anomalies). The dot color indicates the months in which the events were observed, while the black lines describe the linear (a, and b, left panel) or cubic (b, right panel) relation between set-ups and wind speeds. Gray dots are outliers, i.e. events that do not follow the linear trends in (a) and (b). For Toledo (b), all detected events, regardless of the month, are shown in the left panel, while only events detected during the fall and winter seasons are kept in the right panel. 105

Figure 27: Monthly wind set-ups and surface seiches amplitude statistics for two Lake Erie stations, Toledo (a) and Erieau (b). From top to bottom: distribution of monthly wind speed observed during maximum (purple) and mean (brown) set-up events, at nearshore stations; distribution of monthly mean (red) or maximum (green) set-up amplitude; and mean and standard deviation of the log-normal distribution of daily range values for the period 1980–2010. The amplitude of the oscillation can be estimated as twice the daily variation. 107

Figure 28: Top panel: Definition of wave parameters. Adapted from <https://opentextbc.ca/geology/chapter/17-1-waves/>. Bottom panel: Generation of surface waves. Adapted from Garrison (2012)..... 111

Figure 29: Wave transformation from deep water to the shoreline, and orbital motion of the water particles under the waves. The table in the upper right corner gives the relative importance of the various processes affecting the wave evolution. Adapted from <https://opentextbc.ca/geology/chapter/17-1-waves/> and Battjes (1994). 113

Figure 30: Data recorded at buoy 45132, in Lake Erie (Central Basin), for the period 2002–2010. (a) The long-term Weibull distribution of significant wave heights, for wave parameters

recorded under westerly winds (red), or other wind directions (blue). Each black dot gives the binned observations for the 2002–2010 distributions, while the straight lines show the best-fit candidate distributions (maximum likelihood). (b) The joint distribution of significant wave height, HS , and peak wave period, Tp . Observations were classified by local wind direction: westerly winds (SW–NW; red lines), or others (gray lines). The dashed black line gives the wave steepness, HS/L , 1:40. The inset on the right shows the probability distribution of wave height. 117

Figure 31: Wind roses for winds observed between April–November at buoys 45139 (Niagara Basin) and 45135 (Rochester Basin) in Lake Ontario, for the period 1980–2010. The winds were extracted from the homogenized dataset (cf. Section 2.3.1). 120

Figure 32: The joint distribution of significant wave height and wind speed for buoy 45132, in Lake Erie (Central Basin). The insets at the right and top show the respective probability distributions. Observations were classified by local wind direction: westerly winds (SW–NW; red lines), or others (gray lines)..... 121

Figure 33: The projected past and future mean levels for Lakes Ontario (upper panels) and Erie (lower panels). The two selected AOGCM-RCMs are highlighted in each graph, with dashed lines for CanESM2 (or SIM01 and SIM02 for RCP4.5 and 8.5, respectively), and solid lines for GFLD-ESM2M (or SIM03 and SIM04 for RCP4.5 and 8.5, respectively). The grey lines provide the results obtained from other CMPI5 AOGCMs included in the NA-CORDEX project, while the black lines give the observed historical time series. One of the Lake Ontario time series illustrates doubtful results obtained under the regulation rules for the high emission scenario (RCP8.5). . Note: the GFLD-ESM2M time series is missing for Lake Ontario, since this scenario was removed from the study due to unrealistic projections. Details are given in the text..... 125

Figure 34: Idem as Figure 33, but for Lakes St. Clair (top panels) and Michigan-Huron (bottom panels)..... 126

Figure 35: 2D Quadratic element and its interconnection with adjacent cells..... 129

Figure 36: External forces on a 2D mesh cell 130

Figure 37: The surface Ekman layer generated by a wind stress (adapted from Cushman-Roisin and Beckers (2011))..... 131

Figure 38: Illustration of the effect of limiting depth on the wind setup in a 2D model 132

<i>Figure 39: Complex physics approach, using unsteady simulations.</i>	134
Figure 40: The solution space, with its several mean lake level and wind classes.	136
Figure 41: Empirical distribution of observed wind speed during identified wind set-ups in Kingston, Lake Ontario. Wind values refer to observations recorded offshore, at the Prince Edward buoy (in blue; cf. Section 2.3.1), or values extracted from the regionally averaged Climex series (in orange). Solid line gives the estimated PDF, while empirical is provided by the shaded boxes. The left panel shows results obtained from 2days-filetered time series, while the right panel, from unfiltered series. Details are given in the text.	137
Figure 42: The conceptual ellipses used by Harris and Cook (2014) to define the joint PDF of wind speed and direction. Details given in the text.....	139
Figure 43: Example of a regionally averaged wind time series (upper right panel), along with the clustering results obtained for the presented 2D spatial wind distribution (upper left panel). The clusters, shown as ellipses in the u, v space, display shaded colors that refer to their frequency (or weight) in the mixture model. Filtered and un-filtered time series are also presented.....	141
Figure 44: The bilinear interpolation process. Details given in the text.....	142
Figure 45: Bathymetry of the Upper St. Lawrence River and boundary conditions used for the modelling.	147
Figure 46: Modelled water levels obtained for the RMA2 model and the calibrated USLR model. The x-axis gives the distance from the mouth of the Niagara River, representing water levels along an axis that follows the course of the Upper St. Lawrence.....	148
Figure 47: Mesh details (upper panel) and bathymetry (lower panel) used for the Lake Ontario model. Boundary conditions are also defined.	150
Figure 48: Observed (grey dots) and modelled (orange dots) wind-driven set-ups at Kingston, Lake Ontario. The black and red lines show the linear regression obtained from the detected events, i.e. the relationship between event amplitude and wind speed for the zonal (left panel) and meridional (right panel) wind components.....	151
Figure 49: Upper panel: Observed (blue) and modelled (green) seasonal water level fluctuations for year 1990 at Kingston, in Lake Ontario. Lower panel: Idem, but for the short-term fluctuations, which include only the set-up events for the 2days-filtered time series (orange	

and red). The grey line gives the full detailed series of observed short-term disturbances, including surface seiches (which are not modelled) and set-ups. 152

Figure 50: The mesh (top) and the bathymetry (bottom) of the Lake Erie hydrodynamic model. Insets show details of the lake's inlet (Detroit River) and outlet (Niagara River)..... 154

Figure 51: The Manning's coefficient in the lake, and in the Detroit and Niagara Rivers..... 155

Figure 52: Top panel: Discharge simulated (orange) and observed (red) in 2013, at Fort Erie station (Niagara River). Bottom panel: relative error (%) between the simulated and observed discharge (blue), and relative mean error (black line) computed for the period April–November 2013. The relative error ranges from 86–107 % according to the 2.5 and 97.5 centiles, for this specific year. 156

Figure 53: Top panel: Water level observed time series at Buffalo (black dots) and Fort Erie (green line), at the mouth of the Niagara River. The reconstructed Fort Erie time series, estimated using a Gradient Boosting regression algorithm, is shown by the red dots. Bottom panel: Absolute bias calculated from the estimated and observed water level time series at Fort Erie. 157

Figure 54: The Lake Erie watershed, with details of some of its secondary and tertiary watersheds, and the location of one hydrometric (gauging) station (adapted from <https://www2.erie.gov/environment/index.php?q=lake-erie-watershed-protection-alliance> and ECCO-OMECC, 2018). 158

Figure 55: Simulated water levels obtained for Fairport, between May–September 2013, obtained using various evaporation and precipitation datasets: CaPA, the Canadian Precipitation Analysis, MSWEP, the Multi-Source Weighted-Ensemble Precipitation, and LLTM-1D, the Large Lakes Thermodynamics Model, and Climex. 162

Figure 56: Examples of results obtained from step 3 of the data assimilation process for (left) westerly winds, and (right) northerly winds. Top panels: The wind pattern extracted from the forcing database at initialization time T (black arrows) opposed to closest wind pattern extracted from the historical database at time t' (red arrows). Bottom panels: The lake's slope "observed" at time T opposed to the lake's slope "estimated" based on water level records extracted from the historical database, at time t' . Details given in the text. 167

Figure 57: Bias distributions calculated from the observed and simulated (historical) monthly water level series (1980–2010) for each Lake Erie station, starting with the westernmost station, Toledo (upper left corner), and sorted by longitude..... 170

Figure 58: Monthly bias distributions for wind set-ups amplitude and wind speed at Toledo, for the period 1980-2010. The bar plots give the errors as estimated from (1) all identified individual events (referred to as mean, clear colors), and (2) the maximum monthly values only (referred to as max, dark colors). Wind speed refers to the magnitude of the wind that generated the events in the simulated and observed time series. The observed winds were extracted from the homogenized observational dataset, while the simulated winds were extracted from Climex, at Toledo location (cf. Section 2.3). Only distributions with a minimum of ten values have been retained. 176

Figure 59: Upper panel: monthly bias distributions for hourly (green) and lowpass-filtered (red) time series at Kingsville, for the period 1980–2010. Lower panel: snapshot of the observed (black) and simulated (red) hourly time series at Kingsville for late April, early May 2016. 177

Figure 60: Upper panel: monthly bias distributions for hourly (green) and lowpass-filtered (red) time series at Toledo, for the period 1980–2010. Lower panel: snapshot of the observed (black) and simulated (red) hourly time series at Toledo for late May, early June 2015... 178

Figure 61: Details of the bathymetry (left panel) and Manning’ coefficients (right panel) used in the Huron-Erie Corridor model..... 179

Figure 62: The computational grid used for the Huron-Erie Corridor model, with details in vicinity of the St. Clair Delta and the mouth of the Detroit River..... 180

Figure 63: Monthly mean water level errors (RMSE) at several gauging stations, for the period 1980–2018. Errors are broken down by month. 181

Figure 64: Idem as Figure 63, but for discharge values at Port Huron (St. Clair River) and Fort Wayne (Detroit River)..... 183

Figure 65: Mesh details (upper panels) and bathymetry (lower panel) used for the Lake Huron model. Boundary conditions are also defined. 185

Figure 66: Observed (grey dots) and modelled (orange dots) wind-driven set-ups at Collingwood, Georgian Bay. The black and red lines show the linear regression obtained from the detected

events, i.e. the relationship between event amplitude and wind speed for the zonal (left panel) and meridional (right panel) wind components.....	186
Figure 67: Upper panel: Observed (blue) and modelled (green) seasonal water level fluctuations for year 1990 at Collingwood, in Georgian Bay Lower panel: Idem, but for the short-term fluctuations, which include only the set-up events for the 2days-filtered time series (orange and red). The grey line gives the full detailed series of observed short-term disturbances, including surface seiches (which are not modelled) and set-ups.	188
Figure 68: Top panel: Comparison of the most popular numerical wave models, the processes involved and their application (adapted from Roelvink, 2011). Bottom panel: Summary of physical processes in commonly used wave models. Green boxes indicate processes exclusively related to shoreline dynamics.....	191
Figure 69: Schematic of the steps required to build and set-up a wave model (adapted from https://texample.net/tikz/examples/swan-wave-model/).....	192
Figure 70: Nesting approach for wave modelling. Details are given in the text.	194
Figure 71: The nested SWAN grids for the Lynde Creek marshes (5LCM, Lake Ontario). The shaded colors show the bathymetry, relative to IGLD85, generated for the finer computational grid, which has a resolution of 20 m and extends over the terrestrial area of the site. Dry cells are removed from the calculation and updated at each forcing time step (i.e., 1 hour), based on water level fluctuations. Uncolored areas are masked cells.....	195
Figure 72: Schematic illustration of the scenario-based approach to wave modelling (Lake Ontario). The selection of the standing wave scenario at a specific time step is performed in two steps. First, the selection of the closest hydrodynamic forcing, which depends on the wind speed and direction observed at time t in the filtered and regionally averaged wind time series (first half of the diagram). Second, the selection of the closest wave scenario, which is based on the wind speed and direction observed at time t in the regionally averaged unfiltered wind time series (second half of the diagram).....	200
Figure 73: Time series (left panels) and Q-Q plots (rights panel) of observed and simulated significant wave heights at buoys 45132 (a) and 45142 (b), in Lake Erie.....	207
Figure 74: Time series (left panels) and Q-Q plots (rights panel) of observed and simulated significant wave heights at buoys 45135 (a) and 45139 (b), in Lake Ontario.....	209

Figure 75: Schematic of wavelet analysis, with the concepts of translation, dilation and convolution. The wavelet is represented by the black sinusoid..... 213

Figure 76: Example of a water-depth time series extracted from the simulated data, for a given grid cell, with the wet/dry cycle detection scheme. The vertical black lines in the middle graph indicate the time index where the water depth changes from $h > 0$ to $h < 0$, indicating a change in cell state (from wet to dry or inversely)..... 217

Figure 77: Post-processing technique used to analyze hydrodynamic data: (a) time series of water depth at a point, with detection of dry/wet cycles (black vertical lines); (b) scalogram; (c) physical variables extracted from the event analysis, i.e. total cycle duration (blue), average cycle period (red), and number of cycles included in an event (separate bars in the graph); (d) scale-averaged wavelet power..... 219

Figure 78: Example of results for Long Point Wetland, Lake Erie: the average period (top panel) and the percentage of time a grid cell is subject to water level fluctuations (dry/wet cycles; bottom panel). Results are presented for a given quarter-month..... 222

Figure 79: Same as Figure 77, but for a grid cell located in the Rondeau Bay wetland in Lake Erie. Left panels: results obtained from non-stationary scenarios. Right panels: results obtained from stationary scenarios (i.e., the scenario-based approach)..... 224

Figure 80: Upper panel: extracted near-bottom wave orbital velocity for a randomly selected grid cell in the Long Point Wetland, Lake Erie, for the year 2013. Lower panel: near-bottom wave orbital velocity histogram and associated distributions, i.e., Weibull mixture model (blue), simple Weibull distribution (orange), simple Weibull distribution fitted for low-wave climate (green), and simple Weibull distribution fitted for high-wave climate (red)..... 227

Figure 81: Example of results from the highest 95th percentile in the Rondeau Bay wetland (Lake Erie). The area exposed to wave activity at the tip of the peninsula is characterized by high 95th percentile values (i.e., strong waves climate). This area is occupied by long sandy beaches, which is expected when physical conditions are highly unfavorable for submerged aquatic vegetation. 228

Figure 82: Range of relative changes from baseline projected by the lower and upper bound scenarios for some of the key physical variables. Shaded colors indicate the sign of changes (positive in orange, and negative in green), as well as the level of significance of each projections. The black lines make the projected range explicit, based on the significant

values. This figure should be read as a clustered bar chart with overlapping bars, where the lengths represent actual values rather than proportional ones.	236
Figure 83: Left panels: Climate reference map for mean annual partially flooded area, which gives the % of time a grid cell is subjected to fluctuating water level during the growing season, for the period 1980–2009 in Airport Creek Marshes, Lake Ontario. Right panels: The upper and lower bound of the projected change for this variable by 2070–2099 relative to baseline.	239
Figure 84: Example of changes in mean water depth across the transition zone for Lynde Creek Marshes, in Lake Ontario, for past and future periods (left panels), as well as projected changes in the maximum scale-averaged wavelet power (right panel). Black shaded areas in all maps indicated zones that remain strictly dry during the 30-year periods.....	242
Figure 85: Left panel: Climate reference map for mean annual cycle duration for the period 1980–2009 in Rondeau Bay Wetlands, Lake Erie. Right panels: The upper and lower bounds of projected change for this variable by 2070–2099 relative to baseline. Duration gives the total number of days during the growing season that a grid cell is subject to sub-seasonal water level fluctuations.....	244
Figure 86: Hydrogeomorphic classification of Great Lakes coastal wetlands (Albert et al., 2005).	248
Figure 87: Relative surface area of each hydrogeomorphic system in: (a) the St. Marys River; (b) Lake Huron; (c) the Huron-Erie Corridor; (d) Lake Erie; (e) Lake Ontario and (f) The St. Lawrence River as quantified through the GLCWI (Ingram et al. 2004).	250
Figure 88: Hill Island East, Thousand Islands National Park, Ontario. Photo Credit: Canadian Wildlife Service – Ontario Region, Environment and Climate Change Canada, August 2002	251
Figure 89: Airport Creek Marsh, Desoronto, Ontario. Photo Credit: Canadian Wildlife Service – Ontario Region, Environment and Climate Change Canada, August 2019.	252
Figure 90: South Bay, Milford, Ontario. Photo Credit: Canadian Wildlife Service – Ontario Region, Environment and Climate Change Canada, September 2016.	253
Figure 91: Lynde Shores Conservation Area, Whitby, Ontario.....	254
Figure 92: Jordan Harbour, Jordan Station, Ontario. Photo Credit: Canadian Wildlife Service – Ontario Region, Environment and Climate Change Canada, September 2016.	255

Figure 93: Byng Island, Dunnville, Ontario. Photo Credit: Grand River Conservation Authority, 2010.....	256
Figure 94: Selkirk Provincial Park, Selkirk, Ontario. Photo Credit: Canadian Wildlife Service – Ontario Region, Environment and Climate Change Canada, July 2019.....	256
Figure 95: Bouck’s Pond, Long Point National Wildlife Area, Ontario. Photo Credit: Canadian Wildlife Service – Ontario Region, Environment and Climate Change Canada, November 2018.....	257
Figure 96: Rondeau Provincial Park, Ontario. Photo Credit: Ontario Parks, August 2010.....	258
Figure 97: Fox Creek Marsh, Harrow, Ontario. Photo Credit: Canadian Wildlife Service – Ontario Region, Environment and Climate Change Canada, July 2019.	259
Figure 98: Detroit River Marshes, LaSalle, Ontario. Photo Credit: Canadian Wildlife Service – Ontario Region, Environment and Climate Change Canada, July 2012.....	260
Figure 99: St. Clair National Wildlife Area – St. Clair Unit, Pain Court, Ontario. Photo Credit: Canadian Wildlife Service – Ontario Region, Environment and Climate Change Canada, September 2017.....	261
Figure 100: Johnston Bay/ St. Anne Marsh, Walpole Island First Nation, Ontario. Photo Credit: Canadian Wildlife Service – Ontario Region, Environment and Canada, June 2019.	262
Figure 101: Bruce Power Nuclear Plant, Tiverton, Ontario. Photo Credit: Bruce Power, 2019.	263
Figure 102: Hay Bay, Fathom Five National Marine Park. Photo Credit: Southwestern Ontario Orthoimagery Project (SWOOP), Ontario Ministry of Natural Resources and Forestry, 2015.	263
Figure 103: Hog Bay, Midland, Ontario. Photo Credit: South Central Ontario Orthoimagery Project (SWOOP), Ontario Ministry of Natural Resources and Forestry, 2013.....	264
Figure 104: Treasure Bay, Beausoleil Island, Georgian Bay. Photo Credit: BC2 Groupe, July 2018.....	265
Figure 105: Frances Point, Franklin Island, Ontario. Photo Credit: Canadian Wildlife Service – Ontario Region, Environment and Climate Change Canada, May 2019.....	266
Figure 106: Whiskey Harbour, Wiikwemkoong Unceded Territory. Photo Credit: Canadian Wildlife Service – Ontario Region, Environment and Climate Change Canada, May 2018.	266

Figure 107: Anderson Creek, Desbarats, Ontario. Photo Credit: Canadian Wildlife Service – Ontario Region, Environment and Climate Change Canada, July 2015.....	267
Figure 108: Part of the mask (in red) applied on water portions of Rondeau Bay’s (10RBY) area of interest where bathymetry datasets (bright green) are not available.	271
Figure 109: Part of the mask (in red) applied on Fox Creek (11FCK) area of interest, based on a 20 m buffer applied on each side of watercourses and on waterbodies disconnected to the lake (yellow hashed) that also appear on satellite’s imagery.	271
Figure 110: In Rondeau Bay (10RBY), dyke and pump system regulates water level near agricultural lands.	272
Figure 111: In Lake St-Clair (13LSC), water level on agricultural lands (left side) is maintained artificially low compared to the lake’s level (right side).	272
Figure 112: In Detroit River Marsh (12DRM), upland area from the road is mostly anthropogenic. Therefore, it was assumed that the road would act as a dyke and areas upland have been masked (yellow).	273
Figure 113: Mask related to land use in Rondeau Bay (10RBY) site, determined from a combination of ELC and SOLRIS 3.0 datasets.	275
Figure 114: Mask related to land use for Hay Bay (16HBW) site, delineated manually.....	276
Figure 115: Difference between Digital Surface Model and Digital Terrain Model.	279
Figure 116: Errors obtained by comparing minimum-bin gridding LIDAR derived DEM values and ground-truth values at 11 different resolutions for the Anderson Creek (23ACK) site. On the right-end, errors obtained with the average bin gridding at 2 m resolution.	285
Figure 117: Example of the correction model outputs for Lynde Creek Marsh (5LCM). The red shaded box gives the resolution with the lowest RMSE, while values of the nine terms involved are listed in the lower table.....	287
Figure 118: Workflow for applying the correction model on the raw LIDAR-derived DEM.....	288
Figure 119: For sites covered by LEAP dataset, point classification is not reliable to identify laser pulses that hit water surface. Here, points in pink are classified as water (class 9) and green, as ground (class 2). On the right, satellite image of the same sector.....	289

Figure 120: DEM generated with five different techniques on a portion of Anderson Creek (23ACK). A) LMT B) GCP C) PGF D) KGF E) MBG. F) Satellite image of the sector with ground truth points in green. (Z=10x) 290

Figure 121: Error values obtained when comparing elevation values from 6 LIDAR-derived DEMs and ground-truth points for Long Point Wetlands (9LPW). Corrected DEM is on the right end and is identified as LMT (LEAN modified technique)..... 291

Figure 122: Pictures taken in South Bay Marsh (3SBM) showing the swampy and muddy nature of the terrain, which can leads to errors of several centimeters when measuring ground truth elevations..... 293

Figure 123: Different bathymetry datasets used for 10RBY DEM. Blue: bathymetric LIDAR dataset; Yellow: echosounder dataset from BC2; Purple: echosounder dataset from Fisheries and Oceans Canada; Red: Bathymetry grid from NOAA; White: Area of interest boundaries. 295

Figure 124: A) DEM of Baie du Doré (15BDD) generated with echo-sounder dataset for the water portion of the lake; RMSE=0.57m; B) DEM of Baie du Doré (15BDD) generated with bathymetric LIDAR dataset for the water portion of the lake; RMSE=0.87m; (Z=10x). 296

Figure 125: Elevation difference between echosounder points and bathymetric LIDAR points that are within a 0.5 (A), 1m (B), 1.5m (C) and 2m (D) radius from each other. In this case, 0.28m was subtracted from bathymetric LIDAR elevation values. 297

Figure 126: Bathymetric LIDAR elevation shifts ensure seamless DEMs in transitions zones between two different bathymetric datasets (circled in red). A) DEM generated without elevation shift and B) DEM generated with elevation shift at 5LCM (Z=10x). 298

Figure 127: With distance-based weight interpolation (A) query point's value would be the average of the 3 surrounding known values (14.33) over-representing the dense values (16 and 18), while area-based interpolation (B) would give a lower value (12.96). Source: (Lucas G., 2011) 299

Figure 128: A) 19TBY DEM created with echosounder dataset interpolated with Natural Neighbour technique. B) Treasure Bay's DEM created with echosounder dataset interpolated by Ordinary Kriging. C) Treasure Bay echosounder dataset. D) Spherical variogram. 300

Figure 129: Fox Creek's DEM (11FCK) before filters were applied (outlier values appear in red). 301

Figure 130: Lynde Creek Marsh’s DEM: A) With no filter applied; B) With ROTO filter applied; C) with ROTO and Gaussian filters applied..... 302

Figure 131: Baie du Doré’s (15BDD) 2 m resolution DEM elevation values are transferred on the 10 x 10m CWRM grid. 303

Figure 132: Clock-type grid cell numbering scheme..... 304

Figure 133: Distribution of DEM’s elevation error for the 19 study sites. Most sites have a distribution centered on 0 (red line). Only sites where the LIDAR correction method was less effective (2ACM, 6JSM) still have a positive elevation bias (curve shift to the right). 309

Figure 134: Error distribution between Government of Ontario DEMs and ground truth points for the 9 study sites. All sites show positive elevation bias (curve shifts to the right) which is typical of uncorrected LIDAR-derived DEMs..... 310

Figure 135: Residual elevation error in Baie du Doré DEM (15BDD) don’t show any spatial distribution pattern. (Errors in m, final DEM elevation minus ground-truth point values). . 311

Figure 136: Typical sequence of coastal wetland classes observed on a gradient of elevation (IJC.org, url: http://www.ijc.org/loslr/en/background/w_wetlans.php) 315

Figure 137: Coastal Wetland Response Model (CWRM) Framework. Blue squares are for data, grey ellipses are data operation (i.e. sampling, geospatial operation) and other colored ellipses are modelling operations. 316

Figure 138: Wetland succession algorithm scheme. Green arrow signifies a transition towards a drier class, whereas red arrow signifies a transition towards a wetter class. The red square corresponds to the re-initialization of the wetland following a disturbance. Each wetland class has their respective tile numbers and the proposed conditions for transition are presented along the transition arrows. 331

Figure 139: Variables importance by wetland classes (left) and global variable importance (right) for the Hill Island East random forest model. 334

Figure 140: Physical variables distribution by wetland class for the Hill Island East vegetation dataset. Orange line corresponds to the median while green dashed line corresponds to the mean..... 335

Figure 141: Variables importance by wetland classes (left) and global variable importance (right) for the Lake Ontario random forest model. 335

Figure 142: Physical variables distribution by wetland class for the Lake Ontario vegetation dataset. Orange line corresponds to the median while green dashed line corresponds to the mean..... 336

Figure 143: Variables importance by wetland classes (left) and global variable importance (right) for the Lake Erie random forest model. 336

Figure 144: Physical variables distribution by wetland class for the Lake Erie vegetation dataset. Orange line corresponds to the median while green dashed line corresponds to the mean. 337

Figure 145: Variables importance by wetland classes (left) and global variable importance (right) for the Grand River Mouth random forest model..... 337

Figure 146: Physical variables distribution by wetland class for the Grand River Mouth vegetation dataset. Orange line corresponds to the median while green dashed line corresponds to the mean..... 338

Figure 147: Variables importance by wetland classes (left) and global variable importance (right) for the Detroit River Mouth random forest model. 339

Figure 148: Physical variables distribution by wetland class for the Detroit River Marsh vegetation dataset. Orange line corresponds to the median while green dashed line corresponds to the mean..... 339

Figure 149: Variables importance by wetland classes (left) and global variable importance (right) for the Lake St. Clair random forest model. 340

Figure 150: Physical variables distribution by wetland class for the Lake St. Clair vegetation dataset. Orange line corresponds to the median while green dashed line corresponds to the mean..... 340

Figure 151: Variables importance by wetland classes (left) and global variable importance (right) for the Lake Huron random forest model. 341

Figure 152: Physical variables distribution by wetland class for the Lake Huron vegetation dataset. Orange line corresponds to the median while green dashed line corresponds to the mean. 341

Figure 153: Wetland model prediction using the observed water levels time series (1980-2018) at Airport Creek Marsh (2ACM) in 2008 (upper) and observed wetland classes by ELC (lower)

for the same year. ELC wetland classes were converted to match with CWRM wetland classes.....	347
Figure 154: Wetland model prediction using the observed water levels time series (1980-2018) at South Bay Marsh (3SBM) in 2008 (left) and observed wetland classes by ELC (right) for the same year. ELC wetland classes were converted to match with CWRM wetland classes.	347
Figure 155: Wetland model prediction using the observed water levels time series (1980-2018) at Long Point (9LPW) in 2010 (upper) and observed wetland classes by ELC (lower) for the same year. ELC wetland classes were converted to match with CWRM wetland classes.	348
Figure 156: Wetland model prediction using the observed water levels time series (1980-2018) at Rondeau Bay (10RBY) in 2010 (upper) and observed wetland classes by ELC (lower) for the same year. ELC wetland classes were converted to match with CWRM wetland classes.	348
Figure 157: Independent variables relative importance of the cattail suitable habitat model. ..	355
Figure 158: Boxplot distribution of the environmental variables of the cattail suitable habitat model dataset. Orange line corresponds to median, whereas green dashed line corresponds to mean.....	356
Figure 159: Typha Population Growth model conceptual scheme representing the different stages (white boxes) and the mechanisms (grey ellipses) that cause the change of stage from one year to another.....	358
Figure 160: Typha germination probability as a function of the water level variation between the preceding year and the current germination period.....	359
Figure 161: Typha germination probability as a function of the water depth during the germination period of the current year.....	360
Figure 162: Typha seedling survival probability in function of the water depth during the current growing season.....	361
Figure 163: Typha litter accumulation probability as a function of the water depth during the current growing season.....	362

Figure 164: Typha vegetative propagation probability in function of the water depth during the current growing season.	363
Figure 165: Typha vegetative propagation probability in function of the water level fluctuations between the preceding and current growing seasons.	364
Figure 166: Independent variables relative importance of the Phragmites suitable habitat model.	371
Figure 167: Boxplot distribution of the environmental variables of the Phragmites suitable habitat model dataset. Orange line correspond to median, whereas green dashed line corresponds to mean.....	372
Figure 168: Phragmites population growth model scheme.	373
Figure 169: Germination probability according to the water level variation between the preceding year and the current germination period.....	374
Figure 170: Germination probability according to the water depth during the germination period.	374
Figure 171: Seedling survival probability according the mean water depth during the current growing season.....	376
Figure 172: Seedling survival probability according to the number of consecutive flooded quarter-months.....	376
Figure 173: Establishment rate increase according to the distance between the neighbors and the pollinator.....	377
Figure 174: Vegetative propagation probability according to the mean water depth during the growing season.....	379
Figure 175: Vegetative propagation probability according to the slope with the neighboring points.	379
Figure 176: Predicted area (line) for Phragmites and Typha and observed area (point) for both species (Phragmites: red, Typha: orange) in Thoroughfare, Long Point (9LPW). Results produced using observed water level time series (black dash-dotted line).....	385
Figure 177: Invasive species model prediction using the observed water levels time series (1980-2018) at Thoroughfare, Long Point (9LPW) in 1985 (left) and observed wetland classes by	

WTT (right) for the same year. WTT wetland classes were converted to match with CWRM wetland classes.....	385
Figure 178: Invasive species model prediction using the observed water levels time series (1980-2018) at Thoroughfare, Long Point (9LPW) in 2015 (left) and observed wetland classes by ELC (right) for the same year. ELC wetland classes were converted to match with CWRM wetland classes. ELC Typha class corresponds to “shallow marsh” class.	386
Figure 179: Predicted area (line) for Phragmites and Typha and observed area (point) for both species (Phragmites: red, Typha: orange) in Airport Creek Marsh (2ACM). Results produced using observed water level time series (black dash-dotted line).	387
Figure 180: Invasive species model prediction using the observed water levels time series (1980-2018) at Airport Creek Marsh (2ACM) in 2008 (lower) and observed wetland classes by ELC (upper) for the same year. ELC wetland classes were converted to match with CWRM wetland classes. ELC Typha class corresponds to “shallow marsh” class.	387
Figure 181: Predicted area (line) for Phragmites and Typha and observed area (point) for both species (Phragmites: red, Typha: orange) in South Bay Marsh (3SBM). Results produced using observed water level time series (black dash-dotted line).	388
Figure 182: Invasive species model prediction using the observed water levels time series (1980-2018) at South Bay Marsh (3SBM) in 1986 (left) and observed wetland classes by WTT (right) for the same year. WTT wetland classes were converted to match with CWRM wetland classes.....	389
Figure 183: Invasive species model prediction using the observed water levels time series (1980-2018) at South Bay Marsh (3SBM) in 1999 (left) and observed wetland classes by WTT (right) for the same year. WTT wetland classes were converted to match with CWRM wetland classes.....	389
Figure 184: Invasive species model prediction using the observed water levels time series (1980-2018) at South Bay Marsh (3SBM) in 2008 (left) and observed wetland classes by ELC (right) for the same year. ELC wetland classes were converted to match with CWRM wetland classes. ELC Typha class corresponds to “shallow marsh” class.	390
Figure 185: Predicted area (line) for Phragmites and Typha and observed area (point) for both species (Phragmites: red, Typha: orange) in Rondeau Bay (10RBY). Results produced using observed water level time series (black dash-dotted line).	391

Figure 186: Invasive species model prediction using the observed water levels time series (1980-2018) at Rondeau Bay (10RBY) in **2010** (left) and observed wetland classes by ELC (right) for the same year. ELC wetland classes were converted to match with CWRM classes. ELC Typha class corresponds to “shallow marsh” class. Phragmites prediction data was provided by Ontario Ministry of Natural Resources and Forestry (OMNRF, 2010)..... 391

Figure 187: Predicted area (line) for Phragmites and Typha and observed area (point) for both species (Phragmites: red, Typha: orange) in Lynde Creek (5LCM). Results produced using observed water level time series (black dash-dotted line). 392

Figure 188: Invasive species model prediction using the observed water levels time series (1980-2018) at Lynde Creek (5LCM) in **1986** (left) and observed wetland classes by WTT (right) for the same year. WTT wetland classes were converted to match with CWRM wetland classes. 393

Figure 189: Invasive species model prediction using the observed water levels time series (1980-2018) at Lynde Creek (5LCM) in **2001** (left) and observed wetland classes by WTT (right) for the same year. WTT wetland classes were converted to match with CWRM wetland classes. 393

Figure 190: Invasive species model prediction using the observed water levels time series (1980-2018) at Lynde Creek (5LCM) in **2008** (left) and observed wetland classes by ELC (right) for the same year. ELC wetland classes were converted to match with CWRM wetland classes. ELC Typha class corresponds to “shallow marsh” class. Results and discussio 394

Figure 191: Range of relative projected change in wetland area (%) between recent past and future periods for all study sites, with changes defined as the difference in a nnuual distributions between the future (2070–2099) and the recent past (1980–2009). Acronyms are defined in Table 60..... 397

Figure 192: A) State of reference of wetland class area, as a proportion of total site area (%) in the recent past period (historic). Annotations on top of the bars represents the absolute area of the wetland class in hectares. Total wetland area (WETLAND) sums all classes, except OW and UPL.B) Variation (%) between the recent past and future periods for each wetland class for the lower-bound simulation and C) upper-bound simulation in Lake Ontario..... 400

Figure 193: Changes in wetland class distribution between recent past and simulated future with the upper-bound scenario (red: loss, green: Gain, Black: Urban areas unsuitable to wetland

establishment) at Lynde Creek (5LCM), Lake Ontario. Left: Upland migration of EM. Middle: Loss of SW. Right: Google Satellite imagery.	401
Figure 194: A) State of reference of wetland class area, as a proportion of total site area (%) in the recent past period (historic). Annotations on top of the bars represents the absolute area of the wetland class in hectares. SS and TS classes were summed into a single SW class. Total wetland area (WETLAND) sums all classes, except OW and UPL.B) Variation (%) between the recent past and future periods for each wetland class for the lower-bound simulation and C) upper-bound simulation in Lake Erie.	403
Figure 195: Changes in wetland class distribution between recent past and future with the upper-bound scenario (red: loss, green: Gain) at Rondeau Bay (10RBY), Lake Erie. Left: Upland migration of EM. Middle: Loss of SS. Right: Google Satellite imagery.	404
Figure 196: A) State of reference of wetland class area, as a proportion of total site area (%) in the recent past period (historic). Annotations on top of the bars represents the absolute area of the wetland class in hectares. Total wetland area (WETLAND) sums all classes, except OW and UPL.B) Variation (%) between the recent past and future periods for each wetland class for the lower-bound simulation and C) upper-bound simulation in Lake St. Clair – Detroit River.	406
Figure 197: Changes in wetland class distribution between recent past and future with the upper-bound scenario (red: loss, green: Gain, Black: Urban areas unsuitable to wetland establishment or where the physical variables could not be calculated) at Detroit River Marsh 12DRM. Left: Landward migration of SAV. Middle: EM habitat loss. Right: Google Satellite imagery.	406
Figure 198: Changes in wetland class distribution between recent past and future with the upper-bound scenario (red: loss, green: Gain, Black: Urban areas unsuitable to wetland establishment or where the physical variables could not be calculated) at Johnston Bay (14SAM). Left: Landward migration of SAV. Middle: EM habitat loss. Right: Google Satellite imagery.	407
Figure 199: A) State of reference of wetland class area, as a proportion of total site area (%) in the recent past period (historic). Annotations on top of the bars represents the absolute area of the wetland class in hectares. Total wetland area (WETLAND) sums all classes, except OW and UPL.B) Variation (%) between the recent past and future periods for each wetland class for the lower-bound simulation and C) upper-bound simulation in Lake Huron.	409

Figure 200: Changes in wetland class distribution between recent past and future with the upper-bound scenario (blue: loss, red: Gain, Black: Urban areas unsuitable to wetland establishment or where physical variables were unavailable) at Treasure Bay (19TBY). Up Left: EM landward migration, up right: WM landward migration, down left: SW landward migration, down right: Google Satellite imagery..... 410

Figure 201: Range of relative changes of two invasive species habitat (%), between the recent past and the future periods, based on the lower-bound and upper-bound scenarios. Shaded colors indicate the scenarios (lower bound in teal, and upper bound in orange), as well as the level of significance of each scenarios (significant for $p < 5\%$). The black lines make the projected range explicit, based on the significant values. Statistically significant differences between recent past and future periods are calculated using Mann-Whitney U statistical test ($\alpha = 0.05$)..... 414

Figure 202: Range of Carrying capacity/Wetland area ratio projected by the lower and upper bound scenarios for Phragmites (left) and Typha (right) population growth models. Shaded colors indicate the scenarios (lower bound in teal, and upper bound in orange). The black lines indicate the range of projected change (difference between both scenarios). 415

Figure 203: Projected water levels during the growing season for the lower and upper bound climate change scenarios in Lake Ontario (LKO)..... 417

Figure 204: Phragmites (left) and Typha (right) evolution and logistic growth model in Hill Island East (1HIE) for lower (blue) and upper (orange) bound simulations. 418

Figure 205: Phragmites (left) and Typha (right) evolution and logistic growth model in Airport Creek Marsh (2ACM) for lower (blue) and upper (orange) bound simulations..... 418

Figure 206: Phragmites (left) and Typha (right) evolution and logistic growth model in South Bay Marsh (3SBM) for lower (blue) and upper (orange) bound simulations. 419

Figure 207: Phragmites (left) and Typha (right) evolution and logistic growth model in Lyndee Creek Marsh (5LCM) for lower (blue) and upper (orange) bound simulations. 419

Figure 208: Phragmites (left) and Typha (right) evolution and logistic growth model in Jordan Station (6JSM) for lower (blue) and upper (orange) bound simulations..... 420

Figure 209: Projected water levels during the growing season for the lower and upper bound climate change scenarios in Lake Erie (LKE)..... 421

Figure 210: Phragmites (left) and Typha (right) evolution and logistic growth model in Grand River Mouth (7GRM) for lower (blue) and upper (orange) bound simulations.....	422
Figure 211: Phragmites (left) and Typha (right) evolution and logistic growth model in Selkirk Provincial Park (8SPP) for lower (blue) and upper (orange) bound simulations.	422
Figure 212: Phragmites (left) and Typha (right) evolution and logistic growth model in Long Point (9LPW) for lower (blue) and upper (orange) bound simulations.....	423
Figure 213: Phragmites (left) and Typha (right) evolution and logistic growth model Rondeau Bay (10RBY) for lower (blue) and upper (orange) bound simulations.	423
Figure 214: Phragmites (left) and Typha (right) evolution and logistic growth model in Fox Creek (11FCK) for lower (blue) and upper (orange) bound simulations.	424
Figure 215: Invasive species (Phragmites: red, Typha: orange) spatial distribution at Rondeau Bay (10RBY) in 2099 under the lower (left) and upper (right) bound scenario.....	424
Figure 216: Projected water levels during the growing season for the lower and upper bound climate change scenarios in Lake St. Clair(LSC).....	425
Figure 217: Phragmites (left) and Typha (right) evolution and logistic growth model in Detroit River Marsh (12DRM) for lower (blue) and upper (orange) bound simulations.....	426
Figure 218: Phragmites (left) and Typha (right) evolution and logistic growth model in Lake St. Clair(13LSC) for lower (blue) and upper (orange) bound simulations.	426
Figure 219: Phragmites (left) and Typha (right) evolution and logistic growth model in Johnston Bay (14SAM) for lower (blue) and upper (orange) bound simulations.....	427
Figure 220: Invasive species (Phragmites: red, Typha: orange) spatial distribution at Detroit River Marsh (12DRM) in 2098 under the lower (left) and upper (right) bound scenario.	427
Figure 221: Invasive species (Phragmites: red, Typha: orange) spatial distribution at Johnston Bay (14SAM) in 2098 under the lower (left) and upper (right) bound scenario.	428
Figure 222: Projected water levels during the growing season for the lower and upper bound climate change scenarios in Lake Huron (LKH).....	429
Figure 223: Phragmites (left) and Typha (right) evolution and logistic growth model in Baie du Doré (15BDD) for lower (blue) and upper (orange) bound simulations.	430
Figure 224: Phragmites (left) and Typha (right) evolution and logistic growth model in Hay Bay (16HBW) for lower (blue) and upper (orange) bound simulations.	430

Figure 225: Phragmites (left) and Typha (right) evolution and logistic growth model in Hog Bay (18HGW) for lower (blue) and upper (orange) bound simulations..... 431

Figure 226: Phragmites (left) and Typha (right) evolution and logistic growth model in Treasure Bay (19TBY) for lower (blue) and upper (orange) bound simulations..... 431

Figure 227: Phragmites (left) and Typha (right) evolution and logistic growth model in Whiskey Harbor (22WHW) for lower (blue) and upper (orange) bound simulations..... 432

Figure 228: Phragmites (left) and Typha (right) evolution and logistic growth model in Anderson Creek (23ACK) for lower (blue) and upper (orange) bound simulations..... 432

Figure 229: Phragmites (left) and Typha (right) evolution and logistic growth model in Frances Point (27FPT) for lower (blue) and upper (orange) bound simulations..... 433

LIST OF TABLES

- Table 1: Driving AOGCMs and Representative Concentration Pathways (RCP) of the selected climatic scenarios, with their scenario code. 65
- Table 2: Mean wind speed biases, $X_{lon, lat} - Obs(lon, lat)$, over each of the Great Lakes for the selected reference products, Climex and CFSR. Biases were estimated for low ($< 3.3 \text{ ms}^{-1}$), moderate ($3.3\text{-}10.7 \text{ ms}^{-1}$) and high ($> 10.7 \text{ ms}^{-1}$) wind intensity, according to the Beaufort scale. Statistics were calculated considering all nearshore and offshore stations (left columns), and all over-lake stations only (right columns). 70
- Table 3: Reference conditions and projected changes for near-surface winds. The changes in means and standard deviations are provided, with missing values (or dash, –) when the statistical tests did not satisfy the 10% significance level (i.e. U-test for the mean and Levene’ test for the variability). Shaded colours indicate relative changes that reach at least 5 or 25% and reveal clear climate change signal, i.e. when both scenarios agree on the sign of the projected changes (positive, in orange, or negative, in green)..... 86
- Table 4: Published seiche oscillation modes (in hours) for the five Great Lakes. After data compiled by Trebitz (2006). 96
- Table 5: Statistics of the observed wind set-ups and surface seiches for 17 stations in the Great Lakes Basin, for the period 1980 – 2010. The mean amplitude of the maximum set-ups is given (left columns), as well as the mean amplitude of the free surface oscillations, i.e. half the mean of the log-normal distribution of daily-range values (right columns). The monthly range provides the minimum and maximum monthly means, while annual values provide the annual mean of the distribution, with first and third quantile in brackets. All values are in centimetres. Details are given in the text. 102
- Table 6: Wave statistics for Lakes Erie and Ontario, for the period 1980–2010. Data were classified according to local winds observed at the time of recording, i.e. north (NW–NE), east (NE–SE), south (SE–SW), or west (SW–NW) winds. The blue lines indicated wind direction associated with major wave events for each of the lake sub-basins. Columns indicate: water depth at buoy locations; lake sub-basins in which the wave buoy is moored; period or record; percentage of data available during the period of record; percentage of data recorded under calm conditions ($HS < 0.05 \text{ m}$); the wind direction; the percentage of occurrence of a specific wind direction in the dataset; the mean (and variance) of the

significant wave height (based on the best-fit Weibull distribution); the 99 th percentile of the wave height distribution (and the absolute maximum value); and the median peak wave period (with the 2.5 th and 97.5 th percentiles).....	117
Table 7: Summary table for the different lake models.	145
Table 8: Calibration results for the USLR model.....	149
Table 9: The errors (RMSE) obtained for the long- and short-term fluctuations in Lake Ontario, according to the calibrated model.....	152
Table 10: Lake Erie secondary watersheds, their major tributary, including tributaries used as boundary conditions in the hydrodynamic model (indicated by a star, *), their associated gauging station, as well as the drainage (in km ²) area and percentage of the gauged area.	160
Table 11: Summary of hydrodynamic and atmospheric forcing datasets used for the historical period (1980–2018; observations), and recent past and future periods (1980–2010, 2070–2100; climatic projections).	164
Table 12: Mean bias (with first and third quartiles) and RMSE calculated from the observed and simulated water level series (1980–2010), and detailed for monthly variations (seasonal water level), wind set-ups event, and surface seiches.....	171
Table 13: Amplitude skill score rules for water level anomalies.	174
Table 14: Statistics and amplitude skill scores for set-ups events (left) and surface seiches (right) in Lake Erie, for the reference period (1980–2010).....	175
Table 15: Water level errors obtained for different sections of the Huron-Erie Corridor for years 1980–2018, according to two different periods. The first (Mar 15 th to Nov 15 th) includes late spring, when ice conditions can be observed in the St. Clair and Detroit Rivers.....	182
Table 16: The errors (RMSE) obtained for the long- and short-term fluctuations in Lake Huron, according to the calibrated model.....	187
Table 17: Characteristics of the computational grids and numerical schemes used for WW3 and SWAN models. Acronyms refer to wetland sites.....	197
Table 18: Wind classes used for the scenario-based modelling approach.	202
Table 19: Summarized validation statistics of WW3 wave models data relative to in-situ measurements in Lakes Erie and Ontario. Statistics for winds (wind speed at 10 m),	

significant wave height, and wave period are presented at buoy locations, along with detailed statistics broken in wind directions for Lake Ontario. Statistics include bias, root-mean-square error (RMSE), Mean Absolute Percentage Error (MAPE), scatter index (SI, and index of agreement (IOA). *HS* Weibull refers to the mean of the best-fitted Weibull distribution, while *HS95*, to waves in the upper range of the distribution (> 95th quantile)..... 204

Table 20: Growing seasons in quarter-months. * For Lake Erie, hydrodynamic modelling was initiated prior to the definition of the growing season and limited to the beginning of April to the end of October. This period was retained. 216

Table 21: The physical variables selected to aggregate the hydrodynamic data. 218

Table 22: The physical variables selected to aggregate the wave data. 229

Table 23: Projected changes in lakes dynamics for the period 2070-2099. Results are presented for change in means and interannual variability, described here by the standard deviation. Changes are provided with missing values (or dash, –) when statistical tests did not meet the 10% significance level (i.e. U-test for the mean and Levene' test for the variance). Shaded colors indicate relative changes that reach at least 5 or 25% and reveal a clear signal of change, i.e. when the two scenarios agree on the sign of the projected changes (positive, in orange, or negative, in green). Grey boxes indicate no data. 232

Table 24: Idem as Table 23, but for some of the physical variables developed for wetland modelling: strictly flooded area, defined as the % of the site kept flooded during the growing season; cycle period, which is the mean period of dry/wet cycles detected in the transition zone (ignoring zero values); maximum scale-averaged wavelet power, defined as the mean annual maximum values observed in the quarter-months; the cycle duration, defined as the total time (in days) that a grid cells is subject to fluctuating water levels during the growing season; near bottom wave orbital velocity; and partially flooded area, defined as the % of sites included in the transition zone, where dry/wet cycle are observed. Details are given in the text. 233

Table 25: Hydrogeomorphology (HGM) and land tenure for twenty Great Lakes coastal wetlands assessed. ¹ - Refers to a wetland managed by a provincial conservation authority. 249

Table 26: Historical high and low water levels per lake (based on monthly averaged values): 268

Table 27: CWRM Areas of Interest..... 269

Table 28: ELC classes present in the AOIs and considered not suitable for wetland (please refer to Ontario Ministry of Natural Resources and Forestry, 2019b for description of each class).	274
Table 29: SOLRIS land use classes present in the AOIs and considered not suitable for wetland (please refer to Ontario Ministry of Natural Resources and Forestry (2019a) for description of each class).....	275
Table 30: Area of interest (AOI) for the twenty Great Lakes Coastal Wetland sites and their respective masked areas (physical modelling and land use masks. Non-masked AOI area is the resulting AOI after applying physical modelling and land use masks.	277
Table 31: Study sites and the associated horizontal coordinate reference systems.	280
Table 32: Conversion values between different vertical datum and Lake low water datum for each study site.....	281
Table 33: Root mean square errors (in meter) between ground-truth points and DEMs generated with 6 different techniques.	292
Table 34: Comparison of RMSE values from DEMs created with LEAN modified technique (LMT) and five other ground filtering techniques.	293
Table 35: Accuracy assessment of the final DEMs.	306
Table 36: Accuracy assessment of Government of Ontario DEMs.	307
Table 37: Accuracy assessment of imagery derived DEM.....	308
Table 38: Description of the datasets used to calibrate and validate the wetland models.....	319
Table 39: Wetland classification dataset used in the study and the respective survey years for each sites.....	320
Table 40: Regrouping of species with rare frequencies or with interest prior to clustering analysis. WET group includes FACW and OBL. DRY group includes FACU and UPL, see Reed (1997, 1988) for more definitions on the wetness index.	322
Table 41: Description of the wetland classes modelled in the CWRM.....	323
Table 42: Validation metrics for Hill Island (1HIE) wetland community model.	343
Table 43: Validation metrics for Lake Ontario wetland community model.	344
Table 44: Validation metrics for Grand River Mouth (7GRM) wetland community model.	344

Table 45: Validation metrics for Lake Erie wetland community model.....	345
Table 46: Calibration and validation metrics for the Detroit river marsh (12DRM) wetland community model.....	345
Table 47: Calibration and validation metrics for the Lake Saint Clair (13LSC and 14SAM) wetland community model.....	346
Table 48: Calibration and validation metrics for the Lake Huron wetland community model...	346
Table 49: Cattail hydrological and topographical habitat requirements according to the life stages of the species.....	352
Table 50: Description of the vegetation dataset used to calibrate the cattail suitable habitat models composed of presence and absence of various sources (Wetland Trends through Time, Ecological Land Classification and GLPI vegetation surveys).	354
Table 51: Probability of vegetative propagation in the different wetland classes.	364
Table 52: Effects of environmental conditions on the different <i>Phragmites australis</i> life stages.	368
Table 53: Description of the vegetation datasets used to calibrate the <i>Phragmites</i> suitable habitat model composed of presence and absence of various sources (Wetland Trends through Time, Ecological Land Classification and GLPI quadrats surveys).	370
Table 54: Germination probability in function of the wetland class predicted by the wetland model and the cattail models.....	375
Table 55: Vegetative propagation probability according to the wetland class of the neighbor point	380
Table 56: Validation metrics for the <i>Typha</i> suitable habitat model OOB validation.	381
Table 57: Validation metrics for the <i>Phragmites</i> suitable habitat model OOB validation.	381
Table 58: Sites and data used to calibrate and validate Population Growth Models for <i>Typha</i> and <i>Phragmites</i>	383
Table 59: Difference in median water level between recent past (1980-2009) and future (2070-2099) periods for the lower and upper bound climate simulations.	396
Table 60: Range of relative projected change in wetland area (%) in the future period (2070-2100) relative to the recent past period (1980-2009) for the lower-bound and upper-bound	

simulations. USL: Upper St. Laurence, LKO: Lake Ontario, LSC: Lake St. Clair – Detroit River, LKH: Lake Huron. Red indicates significative decrease, green indicates significative increase and black indicates insignificant change in wetland area between the recent past and future periods. Statistical analysis were done using a Mann-Whitney U statistical test ($\alpha=0.05$)..... 396

Table 61: Coefficient of variation difference between the recent past and future periods of the lower- and upper-bound scenario for the different wetland classes in Upper St. Lawrence and Lake Ontario sites. Difference in variance between the recent past and future periods that are statistically significant according to a Brown-Forsythe test ($\alpha=0.05$) are in bold. 401

Table 62: Coefficient of variation difference between the recent past and future periods of the lower- and upper-bound scenario for the different wetland classes in Lake Erie sites. Difference in variance between the recent past and future periods that are statistically significant according to a Brown-Forsythe test ($\alpha=0.05$) are in bold..... 404

Table 63: Coefficient of variation difference between the recent past and future periods of the lower- and upper-bound scenario for the different wetland classes in Huron-Erie Corridor sites. Difference in variance between the recent past and future periods that are statistically significant according to a Brown-Forsythe test ($\alpha=0.05$) are in bold..... 407

Table 64: Coefficient of variation difference between the recent past and future periods of the lower- and upper-bound scenario for the different wetland classes in Lake Huron sites. Difference in variance between the recent past and future periods that are statistically significant according to a Brown-Forsythe test ($\alpha=0.05$) are in bold..... 410

1. INTRODUCTION

1.1. Background

The Laurentian Great Lakes are an important freshwater resource that accounts for almost 20% of the world's surface freshwater and provides drinking water to more than 35 million North Americans (ECCC & EPA, 2021). This basin supports multi-billion dollars per year of economic activities, and its ecosystem sustains over 4 000 living species with approximately 2 695 coastal wetlands (>2 ha) covering 216 545 hectares (ECCC & US. EPA, 2021). These valuable habitats promote an impressive biodiversity (Brazner *et al.*, 2001) and ensure many ecological services (Sierszen *et al.*, 2011) such as critical habitat for most of Great Lakes fish species (Wei *et al.*, 2004).

Coastal wetlands are particularly vulnerable to climate change given their location at the dynamic land-water interface, and because their structure, composition and distribution are highly dependent on air and water temperature, variation in water levels, and wave intensity (Acerman *et al.*, 2009; Mortsch *et al.*, 2006). The potential impacts of global warming on wetland health are broad as chemical and physical processes (e.g., coastal erosion, thermal habitat, chemical reactions), as well as wetland ecology, are likely to be affected. Therefore, the projected changes in wetlands are worrying, especially since a significant deterioration of their extent and biodiversity can be anticipated, as well as an alteration of their functions and ability to maintain critical ecosystem services. The effects may be even worse considering the existing anthropogenic stresses (e.g. Host *et al.*, 2019) and the threat of invasive species that wetlands currently face.

The 2012 Great Lakes Water Quality Agreement (GLWQA) and the 2014 Canada Ontario Agreement (COA) on Great Lakes Water Quality and Ecosystem Health recognize the impacts of climate change as an issue of concern. This reflects the recognition by national, provincial, state and local governments, Indigenous Peoples, and key interest groups and stakeholders that climate change impacts are already being observed and documented throughout the Great Lakes Basin. There is growing consensus that further changes are expected and that imminent actions are needed to understand and address ecosystem vulnerabilities, and to identify required adaptation options.

In 2017, Environment and Climate Change Canada (ECCC) announced the Great Lakes Protection Initiative (GLPI; 2017-2022), which contains a study to confront the impacts of climate

change entitled *‘Assessing and Enhancing the Resilience of Great Lakes Coastal Wetlands’*. This study supports the GLWQA and COA in their focus on conserving productive wetland ecosystems and resilient populations of native species, and it was built on three central objectives:

1. Assess the vulnerability of coastal wetlands and determine how they are likely to respond to future climate conditions;
2. Recommend adaptation strategies, adaptive measures, and actions to enhance the resilience of coastal wetlands to climate change impacts; and
3. Engage, share information, and build consensus on priorities with partners, stakeholders, and rights holders.

In order to answer these specific points, the GLPI project was structured around an integrated framework for assessing vulnerability to climate change (Figure 1). This approach combines findings from the literature, field surveys, georeferenced data, and modelling to operationalize the theoretical components used to determine the degree to which wetlands are susceptible to, and unable to cope with, adverse effects of climate change. Vulnerability assessment seeks to describe the character, magnitude and rate of change to which a system is **exposed**, its **sensitivity**, and its **adaptive capacity** (IPCC). **Exposure** defines the degree of climate stress, and it is determined, in this case, by key climate variables, including the variability in lake levels to which coastal wetlands may be exposed during the 21st century. **Sensitivity** examines the degree to which wetlands distribution and composition are likely to be affected by projected climate change. The magnitude of the expected response, which strictly depends on exposure and sensitivity, yields the **potential impacts** or potential response, which can encompass a wide range of effects. By combining this potential response with an assessment of the inherent capacity for wetlands to cope and persist through disturbance (i.e. **adaptive capacity**), it is then possible to determine how and where coastal wetlands and species are vulnerable to climate change.

This report summarizes the effort of ECCC-NHS Hydrodynamic and Ecohydraulic Section dedicated to analyzing the exposure and sensitivity of the coastal wetlands under a range of climate change scenarios.

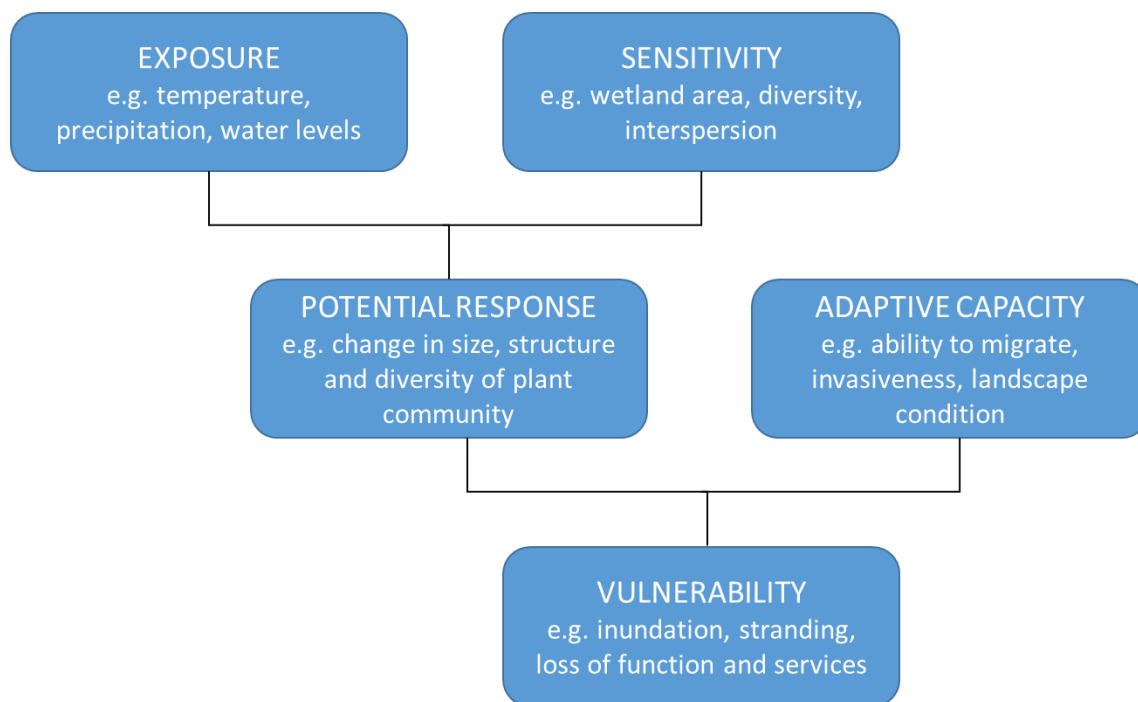


Figure 1: Generalized framework for Great Lakes and coastal vulnerability assessment.

1.2. Objectives

To evaluate the wetland exposure and sensitivity to climate change, a Coastal Wetland Response Model (CWRM) was built and used to predict the spatial and temporal succession of wetland communities. CWRM is a two-dimensional (2D), integrated habitat-modelling platform developed by ECCC-NHS Hydrodynamic and Ecohydraulic Section to assess the response of coastal wetlands to changes in water levels. In the GLPI study project, this model projects the area, structure and distribution of wetland classes and invasive species at 20 selected sites across the Great Lakes under past and future physical conditions.

The work described in this report can be divided in four main objectives:

1. Develop 2D lake models (hydrodynamic and wave) to simulate physical conditions near coastal wetlands in the recent past (1980–2009) and future (2070–2099) under two distinguished climate scenarios;
2. Gather, transform and integrate geo- and time-referenced information on selected wetlands;
3. Build 2D predictive models of wetland classes and invasive plant distribution;
4. Estimate the changes in wetland composition in response to the projected climate by the end of the current century.

The analyses produced by the CWRM are part of a joint effort by several ECCC sections that have been working towards the overall goals of the GLPI. For instance, the selected future climate simulations are based on work conducted by ECCC-NHS Boundary Water Issues Unit, which simulated a range of future Great Lakes water levels under a variety of climate scenarios (Seglenieks and Temgoua, 2022). The results extracted from the CWRM in turn supplied key information to the National Wildlife Service (CWS), which had to analyze the potential impacts of climate change and, hence, helped determine how and where coastal wetlands are likely to respond.

1.3. Scope of study

1.3.1. Study sites

For this project, 20 coastal wetland sites were selected in the Canadian Great Lakes along the Canadian shoreline of lakes Huron, St. Clair, Erie, and Ontario, and along the shores of two connecting channels: the Detroit River in the Huron-Erie Corridor and the upstream portion of the Upper St. Lawrence River (Figure 2). Lake Superior, which was originally included in the study, is not represented in this project effort. Time and computational constraints made its modeling unrealistic for the project timeframe. This lake was therefore removed from the work and retained for future investigations

Figure 2 shows the geographic location of these wetlands and provides the names and acronyms used throughout this report. The CWRM approach focused on Areas Of Interest (here after referred to as AOI) that cover the terrestrial and lacustrine surroundings of selected wetlands, totaling 124 220 hectares. A complete description of the site and area of interest characteristics is provided in Section 4.

While wetland modelling produces results at the site scale, physical modelling must simulate the full range of spatial scales involved in the physical processes that modulate water depth and wave exposure. Therefore, the simulations performed provide not only a physical description at the wetland scale, but also at the lake scale, which implies a considerable amount of data and processing capacities.

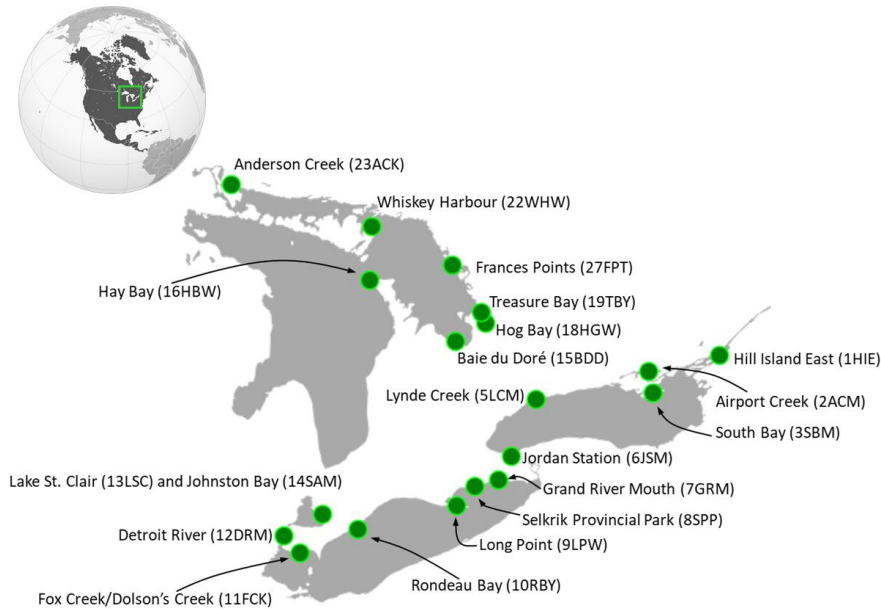


Figure 2: Geographical location of the 20 selected sites.

1.3.2. Expected changes

CWRM is an adapted version of ECCC Hydrodynamic and Ecohydraulic Section's two-dimensional Integrated Ecosystem Response Model (here after referred to as IERM2D) originally developed for the International Lake Ontario–St. Lawrence River Study (LOSLR; Talbot *et al.*, 2006). Since then, this modelling approach has been adopted in numerous studies led by NHS to assess the potential impacts of changes in hydrological regime (Figure 3). Historically, IERM2D has been used to compare the state of the system obtained under reference and alternative conditions to reflect the possible impacts of fluctuating flows and water levels on various environmental and socio-economic factors. For example, alternative conditions may include changes in flow regime resulting from new regulation rules or the implementation of flood mitigation measures.

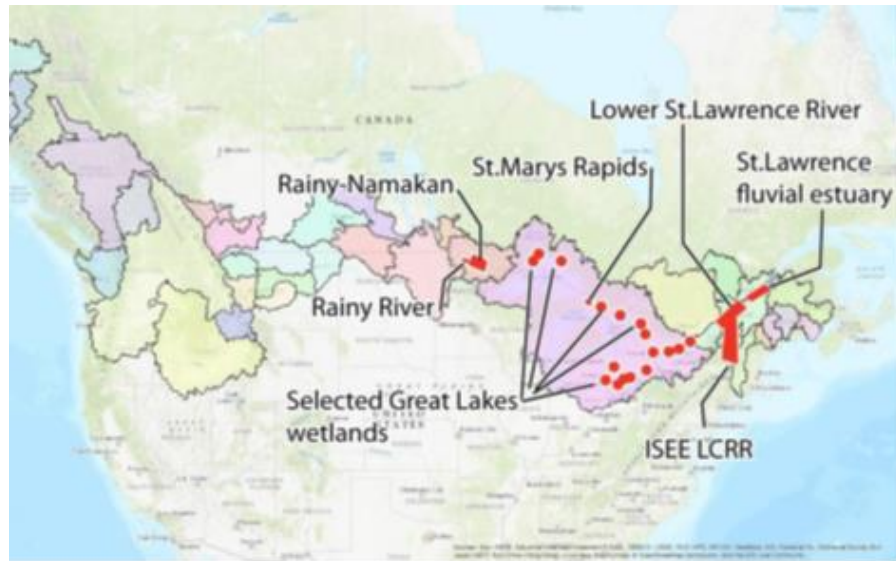


Figure 3: CWRM type integrated analysis applications

The novelty of CWRM lies in the use of climate scenarios that provide future projections of the state of the system rather than alternatives that seek to reproduce only changes in past conditions. Thus, modelling must take into account the particularities of climate change science, especially with respect to the interpretation of projected changes, in order to communicate valuable and credible information.

1.3.2.1. Possible future climates

Since 2011, the Coupled Model Intercomparison Project Phase 5 experiment (CMIP5; Taylor *et al.* 2012) provided climate projections for climate assessment studies. This project includes a set of Atmosphere-Ocean General Circulation Models (AOGCMS) that were coupled to anthropogenic CO₂ emissions scenarios, described using Representative Concentration Pathway (referred to as RCP), which provide an ensemble of possible future climates.

Given the computational effort needed to produce all of the physical variables required by the CWRM, two dynamically downscaled AOGCMS were selected to delineate a range of possible futures:

1. CanESM2 (Canadian Earth System Model), representing the low-risk (lower-bound) scenario;
2. GFLD-ESM2M (NOAA' Geophysical Fluid Dynamics Laboratory Earth System Model), accounting for a high-risk (upper-bound) scenario.

Both models were driven by a medium emission scenario that projects a pathway for stabilization by the end of the century, i.e. RCP 4.5, which results in a decrease in emissions around 2040 and a warming of 2.5°C above pre-industrial levels by 2100. The low-risk simulation (CanESM2) projects moderate change in future air temperature and precipitation rates, resulting in lower projections of mean lake levels relative to historically observed long-term averages, whereas the higher-risk simulation (GFLD-ESM2M) projects a smaller change in air temperature and a moderate change in precipitation rates, which results in a significant increase in future mean lake levels.

1.3.2.2. Climate change signal

Owing to the natural variability of the system, a clear climate change signal must be extracted from climate data averaged over relatively long periods. Focusing on short-term trends, or even annual values, could lead to observations that are the opposite of the expected global climate trend. To facilitate results comparison and study coordination, climate centers around the world use a standard 30-year timeframe to characterize long-term climatic conditions, which is endorsed by the World Meteorological Organization (WMO; Charron, 2016). Since this study aims to evaluate changes initiated by global warming, the results presented are extracted from 30-year time series. Furthermore, it is important to note that even the best models do not reproduce the exact succession or timing of meteorological events due to the chaotic nature of the climate system, which remains difficult to model. Instead, models tend to reproduce the main statistical properties of the observed records, such as mean, variance, interannual variability, and seasonality, and are therefore used to provide a representation of expected changes in these properties given the current state of knowledge. Because they are mathematical representations of climate, the models are generally biased and cannot be used as is in opposition to observed historical values. The climate change signal is rather determined by comparing results obtained from projections produced for the recent past and the future via a given model, and over comparable periods. This method, known as the delta method, eliminates model-specific parametrization biases while retaining the climate change signal, which quantifies the changes projected by a given simulation.

1.3.2.3. Modelling periods

Since the current project aims to describe the evolution of Great Lakes coastal wetlands under projected climate change scenarios, several modelling periods were used to create the necessary output sets. The final CWRM product takes the form of a wetland classes map that gives the most

likely spatial distribution of wetland classes in a given year (Figure 4), based on the physical conditions encountered during past growing seasons. Because the wetland models required calibration and validation to ensure correct prediction of ecohydraulic processes, two types of periods were employed: the historical period and the projected periods. While the former refers to the recent past period, spanning from 1980 to 2018, the latter is strictly dedicated to climate analysis, and is therefore used to provide the projected state of the wetlands under a changing climate.

More explicitly, the simulated periods are:

1. Historical Period (1980–2018) used for wetland model calibration and validation. For this purpose, water levels and waves were simulated with observed data and available historical datasets to provide accurate numerical representation of past physical conditions. The resulting wetland distribution through the time series gives the reference state of the system, i.e. the historical conditions under which changes in distribution of wetland classes are observed and measured. As the climate modelling was performed over a 30-year window, the reference state is determined based only on the first 30 years of the historical time series (1980–2009). The Historical Period is not used to evaluate the impact of climate change scenarios on wetlands distribution. This is done by comparing the two following periods.
2. Recent Past Period (1980–2009) is the projected past state of the system, determined based on climate change scenarios, which generally follow the observed trends and means under the Historical Period without reproducing them entirely. These scenarios were obtained under a greenhouse gas emission scenario that seeks to replicate the global warming of the recent past. Since projected emissions begin in 2005 in the climate scenarios used for this project, the 30-year period is defined, in this case, as the recent past encompasses the first years of the projected emission trend (Figure 4). The recent past time series is used strictly as a basis of comparison (i.e. baseline), to quantify the expected changes and trends for the current century.
3. Future Period (2070–2099) gives the projected state of the system in the last decades of the century (often referred to as “Horizon 2085”). These 30-year time series are therefore simulated using climate scenarios generated under up-to-date greenhouse gas emission scenarios, which estimated the rate of harmful gas emissions from 2005 to 2100. These series defined the “possible futures” expected under a changing climate. Again, they are strictly used to quantify expected changes and trends for the current century, in combination with results obtained from the recent past period.

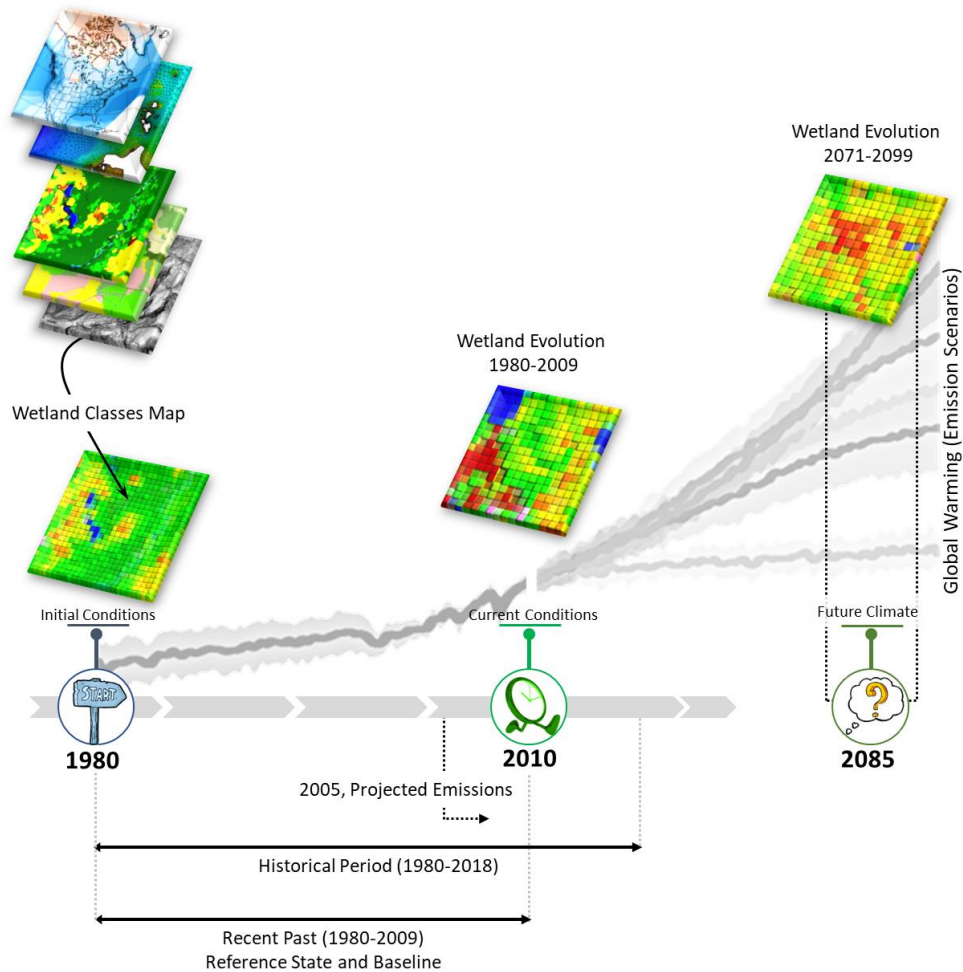


Figure 4: Schematic representation of the modelling framework used to produce expected wetland classes for each year of the modelling periods.

1.3.2.4. CWRM Grid

All layers of information integrated in the CWRM are transposed, via various interpolation methods, on a regular 10m x 10m grid that covers the 20 AOI, creating a unique geo- and time-referenced database with more than 14 million nodes. As a result, all the relevant information to predict yearly wetland classes and invasive plants distribution are available at each node of the grid, for each time step. Being geo- and time-referenced, all the information from CWRM can be easily imported into any GIS software for visualization or further analyses. Finally, results can be spatially integrated, for a rapid analysis of a specific region or the entire study area.

1.3.3. Modelling approach

Coastal wetlands are highly responsive and dynamic ecosystems (Keddy and Reznicek, 1986) that adapt to current and past natural physical factors to which they are exposed, with their plant

communities well conditioned to the unstable and unpredictable conditions (and processes) that characterize the nearshore zone. In the Great Lakes, wetlands are particularly acclimatized to large-lake hydrology and disturbances that play out over multiple temporal and spatial scales. These variable hydrological conditions largely control the location, extent, productivity, and diversity of these ecosystems, and thus can be considered the primary drivers of change (Mortsch, 1998). Level fluctuations experienced by a wetland indirectly incorporate the effect of precipitation, evaporation, and topography, which are essential components of their distribution. They also reflect the climate variability, including extreme weather events and episodic storms, as well as longer-term variations that modulate lake levels over years and decades. Therefore, to determine how coastal wetlands change over time, it is essential to identify the disturbance regime that defines shoreline dynamics, keeping in mind the different scales of the system (Kenough, 1990): local (i.e. site-specific) or short-term; lake-wide or annual; and regional or long-term (greater than a year). While short-term disturbances primarily affect organisms with daily or short lifespan, long-term disturbances can influence perennial plant communities and cause shifts in species distribution and population trends (Kenough *et al.*, 1999). In an effort to replicate Great Lakes coastal wetland vegetation zones and their hydrological gradient from deep aquatic habitat to dry terrestrial areas, two major questions must be answered:

1. What is the time scale and magnitude of natural disturbances within the wetland, which take the form of water depth variations and wave exposure (e.g. Wilcox and Nichols, 2008; Uzarski, 2009)?
2. How do plants move along the hydrological gradient in response to environmental disturbances, with migration of wetland classes that follows their inherent dispersal capabilities (e.g. Gathman *et al.*, 2005)?

These questions are the basis of the modelling approach taken for this project, which seeks to identify and characterize the physical processes and conditions that modulate Great Lakes nearshore dynamics and how these physical factors shape coastal wetlands across a range of possible climates. This effort was accomplished using the CWRM, which is a two-dimensional habitat modelling platform that relies on a collection of georeferenced layers to evaluate the effect of hydrodynamic time series on plants. This model was used to predict the evolution of 20 selected wetland sites under a changing climate. It offers a comprehensive description of expected changes in wetland and invasive plant distribution by the end of the century based on scenarios that provide assessment of regional climate change due to greenhouse effects.

The following subsections give a description of the CWRM, as well as the workflow used to integrate the various components into the modelling architecture. Each component of this scheme is extensively detailed in a separate section, creating the structure of this document (Figure 5).

1.3.3.1. Coastal Wetland Response Model (CWRM) Framework

The CWRM integrates two main modelling components, which are used to define the physical (water depth and waves) and ecological (plants and topography) conditions spatially over various time steps for specific wetland sites over the Great Lakes. Thus, it is possible to link large-scale dynamics, defining the general climate and lake-wide dynamics, to small-scale ecosystem processes, which relate changing physical factors to changing wetland composition. Figure 5 gives an overview of the CWRM.

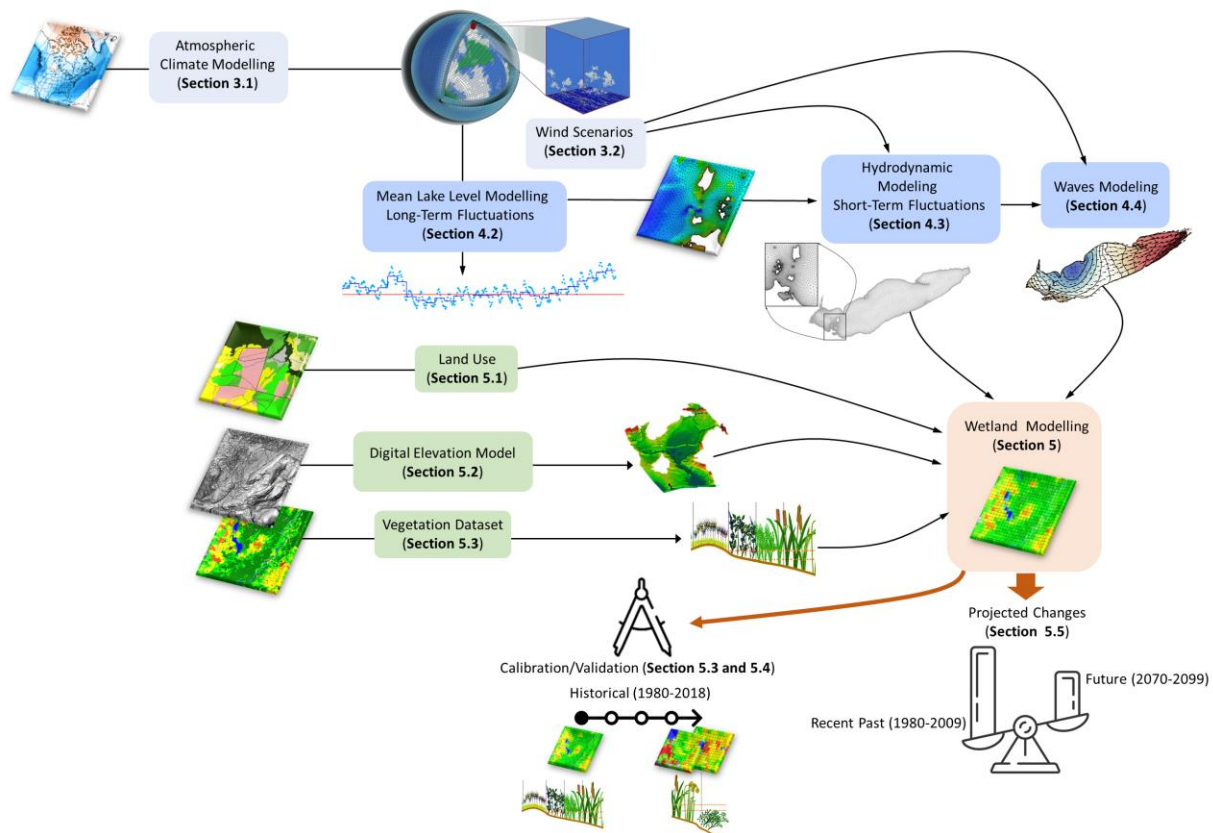


Figure 5: Coastal Wetland Response Model (CWRM) workflow.

1.3.3.1.1. Atmospheric modelling

Atmospheric modelling is used to define the climate to which ecosystems are exposed and hence, the climate variables that modulate the natural water-level regime on a seasonal, annual and

multi-year basis. Because Great Lakes levels are the integrated sum of water inputs and losses from the system, they are directly linked to the weather patterns that control the precipitation and the evaporation, as well as the frequency and duration of storm events. When working with scenarios, the integration of this information is essential to provide the “climate exposure” that will determine basin- and lake-scale dynamics. All information related to this aspect of the CWRM is provided in Section 2, which also includes a detailed description of the wind scenarios used. Although winds are primarily related to short-term water level fluctuations and have no incidence on the overall lake and basin water balance, they are included in the atmospheric components of the CWRM as they are extracted from atmospheric models.

1.3.3.1.2 Lakes modelling

Lake modelling is used to quantify the physical processes and conditions that drive lake dynamics on different time and space scales. This physically based modelling provides an accurate description of the various temporal scales that characterize water-level fluctuations. It describes well interannual and seasonal water levels change over years or decades, but also short-term disturbances related to processes operating on timescales of days (wind-driven fluctuations), hours (surface seiches) and minutes (waves). The different spatial scales of the system are also managed by this modeling component using models that translate observed changes in hydrology, flow, and winds to the shoreline dynamics that directly influence wetlands. A detailed description of the different physical models used in the CWRM is provided in Section 3, along with definitions of the physical variables employed to inform the ecological modelling, which is the final modelling component of the CWRM.

1.3.3.1.3 Ecological modelling

Ecological modelling integrates the ecological aspects that control the spatial distribution and composition of wetlands, including landform, land uses, and wetland classes. It has two major components. The first is the Digital Elevation Model (DEM), a precise representation of the topographic bare ground surface within the wetland boundaries. It is a three-dimensional digital representation used in combination with physical outputs to provide changes in water depth (and other physical variables) at fine spatial resolution. It also helps define some of the key terrain attributes, such as slope and profile curvature, which influence wetland classes and species distribution. A full description of the methodology behind the creation of high-resolution DEMs is provided in Section 5. The second major component of ecological modelling is wetland models. These models predict the wetland class that should occur at a specific location based on the

physical variables extracted from the lake modelling. They rely on historically observed physical and biological conditions to elucidate the relationship between these two important ecosystem dimensions and allow for a numerical representation of wetland eco-hydrological processes. These complex models provide successional processes and spatial distribution of wetland classes, as well as the presence and extent of two invasive species (Phragmites and Typha) at each site from the recent past to the end of the century according to various climate scenarios. Sections 6.1 and 6.2 present this topic. Other aspects of ecological modelling, such as land use and vegetation data, are also discussed in Section 4.

1.3.4. Presentation of results

All input variables that are processed to predict annual wetland classes and invasive species distribution are available at each grid node of the CWRM, for each quarter-month of the recent past (1980–2009) and future periods (2070–2099). Thus, for each variable, it is possible to generate time series and distribution maps at different time and space scales, or to create animations from sequential images. While such products are useful to reflect the spatiotemporal components of CWRM modelling approach, they should not be used to represent expected changes in a future climate. As mentioned in Section 1.3.2., climate scenario outputs should not be interpreted as a representation of reality at a specific point in time, but rather should be analyzed based on long-term trends.

Therefore, in the scope of CWRM study, modelling results are expressed via the lower- and upper-bounds of projected changes as determined based on the 30-year periods. These bounds give, for each variable, the possible range of changes expected by the end of the century under the RCP 4.5 emission scenario for a limited set of climate scenarios. These results are available for each of the 14 million CWRM grid nodes, allowing a fine representation of expected changes in the spatial distribution of properties, whether physical or ecological, as well as the range of variations projected by the selected AOGCMs at the basin- and local-scales.

This report summarizes the effort of NHS to analyze, with the CWRM approach, the exposure and sensitivity of coastal wetlands to various physical variables under a range of different future climates. The report is divided into sections that describe the different modelling components needed to achieve this task. Each of the modelling components are presented with full methodology, results and discussion, starting from the broader climate models (atmospheric and winds), to lake models (hydrodynamic and waves) and ending with finer scale ecological models

(wetland classes and invasive plants). Overall summary, conclusion and key findings integrating all modelling components can be found at the end of the report.

2. CLIMATE MODELLING

Author: Caroline Sévigny, Ph.D.

2.1. Introduction

Since changes in wetland ecosystems are primarily driven by changes in their physical environments, the CWRM framework incorporates climate exposure that is linked to large-scale atmospheric systems. This exposure is used to determine how shifts in global weather conditions may influence the total amount of water entering or leaving the Great Lakes system and, hence, the resulting changes in lake levels. In modelling, climate is usually defined with a set of atmospheric scenarios that are intended to replicate conditions experienced in the past, as well as future changes expected from global warming. For the current study, these climate scenarios are used to (1) project changes in mean lake levels, which respond to changes in large-scale weather patterns, and (2) provide wind datasets needed to simulate short-term fluctuations in water levels, which are important features of lake and nearshore wetland dynamics. Because winds are mainly determined by the synoptic atmospheric circulation, appropriate forcing is required to transpose this influence at the basin scale, as well as to the temporal scale of daily and sub-daily processes they influence. This section offers a short review of the fundamental concepts related to climate modelling, along with a description of the climate models selected for this project (Section 2.2) and a general overview of the work achieved to generate the wind scenarios (Section 2.3).

2.2. Atmospheric models

2.2.1. Atmosphere-Ocean General Circulation Models

Expected changes in wetlands between the recent past to the end of the century are projected using climatic scenarios, which predict the climate system response to various forcings. Since 2011, the Coupled Model Intercomparison Project Phase 5 experiment (CMIP5; Taylor *et al.* 2012) provided a set of climatic projections produced with up-to-date high-resolution, coupled Atmosphere-Ocean models, called Atmosphere-Ocean General Circulation Models (or AOGCMs, also referred to as GCMs)¹. These Earth system models, which have a horizontal

¹ The Coupled Model Intercomparison Project Phase 6 experiment was completed in 2021, in parallel to the Intergovernmental Panel on Climate Change (IPCC) Sixth Assessment Report (AR6).

resolution of hundreds of kilometers, include a representation of all large-scale physical processes (atmosphere, ocean, land and sea ice) and, in some cases, various biogeochemical cycles (carbon cycle, dynamic vegetation, ozone, etc.; Flato 2011). AOGCMs simulate observed climatic conditions from the early modern industrial period to the recent past (1850-2005), as well as expected future atmospheric conditions (2006-2100) for an ensemble of projected anthropogenic greenhouse gas and aerosol emissions. For the CMPI5 project, the range of possible emissions and concentrations was captured by scenarios of radiative forcing, which seek to encompass the range of future projections predicted by scientific literature. These scenarios give possible carbon emissions (e.g. low, moderate, and high), but did not include explicit socioeconomic pathways as would be the case with the use of Shared Socioeconomic Pathways (SSPs) that would provide a broader description of feedback between climate change and key factors (e.g. economy, technologies, public policies). These forcing scenarios are therefore called Representative Concentration Pathway (referred to as RCPs).

2.2.2. Representative Concentration Pathways

The RCPs not only provide the time series of emissions and concentrations of harmful gases, but also the trajectory² followed over time to reach a specific long-term concentration level (van Vuuren, 2011). They describe a set of possible developments and a range of futures for the evolution of atmospheric composition. These scenarios are identified by their radiative forcing peak expected by the end of the century, relative to pre-industrial conditions (in Wm^{-2}), which expresses the (net) energy gain from solar irradiance per square metre of surface per second. Three categories of RCPs are used to force the AOGCMs: a low forcing level (RCP2.6), medium stabilization scenarios (RCP4.5 and RCP6), and a very high baseline emission scenario (RCP8.5). RCP 4.5 and 8.5, the most commonly used scenarios, were selected to estimate the evolution of wetlands over time under a changing climate. While the former involves policy scenarios that project an initial increase in total CO₂ equivalent greenhouse gas emission followed by a decrease around 2040 through mitigation (stabilization without overshoot pathway to 4.5 Wm^{-2} at stabilization after 2100), the latter is a no-climate policy scenario that projects a steady increase in emissions (rising radiative forcing pathway leading to 8.5 Wm^{-2}). RCP8.5 is often referred to as the “business as usual” scenario, and its projection is found to be within 1% of the total cumulative CO₂ emissions observed for 2005 to 2020 (Friedlingstein *et al.*, 2019). In

² Without any explicit assumption relating to population or economic development.

terms of increase in global average near-surface air temperature, RCP4.5 projects warming of 2.5°C above pre-industrial levels in 2100, whereas RCP8.5 projects 5 °C, which is beyond the 3 °C of warming that current policies suggest (Ho *et al.*, 2019; Figure 6). This RCP was selected to highlight the possible impact of climate change on wetlands in the absence of any mitigation scenario, as well as to provide a comparative view of expected projections. However, and as will be explained in Section 3.3, the results obtained for this high emission scenario were considered unrealistic and were therefore set aside for this project.

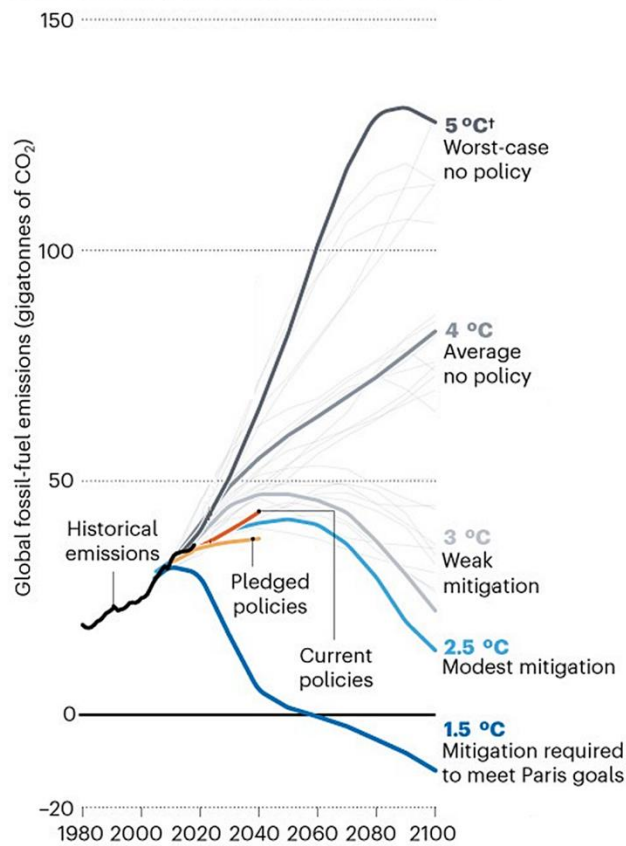


Figure 6: Global fossil-fuel emission under different emission scenarios with projected global warming by 2100 relative to pre-industrial levels. From Hausfather and Peters (2020).

2.2.3. Selected AOGCMs: Upper- and lower-bound scenarios

Given the computational effort required to produce all physical variables needed for the CWRM, only a few climate models were selected to project changes in wetlands. Each AOGCM of the CMIP5 experiment yields a possible climate future that lies, for a given driving RCP, within a wide range of conditions. To account for this uncertainty in climate change projections, it is desirable

to choose models that can delineate the span of possible futures: low-risk (lower-bound) and high-risk (upper-bound) scenarios.

Byun and Hamlet (2018) tested the performance of the CMIP5 ensemble over the Midwest and Great Lakes region, according to its ability to simulate historical climate. They ranked the 31 (downscaled) AOGCMs³ based on a performance metric that quantifies model skill in terms of historical climatology (1950-2005) and extreme temperature and precipitation events. Scenarios in the upper half of this ranking were identified as the first subset for the selection of low- and high-risk AOGCMs used in this project. The models included in this subgroup project a wide variability of annual temperature and precipitation changes over the Great Lakes domain for the 2080 horizon (2070-2100; Figure 7). Changes in annual surface air temperature over the domain relative to 1970-2000 range on average from 3.31 °C and 6.45 °C according to RCP4.5 and 8.5, respectively, but significant variations are observed between models. To capture as much variability as possible, a first AOGCM included in the inner range of change of the CMIP5 subset was selected, CanESM2, and a second in the outer range, GFLD-ESM2M. GFLD-ESM2M is in the lower percentiles in terms of projected air temperature change (Figure 7).

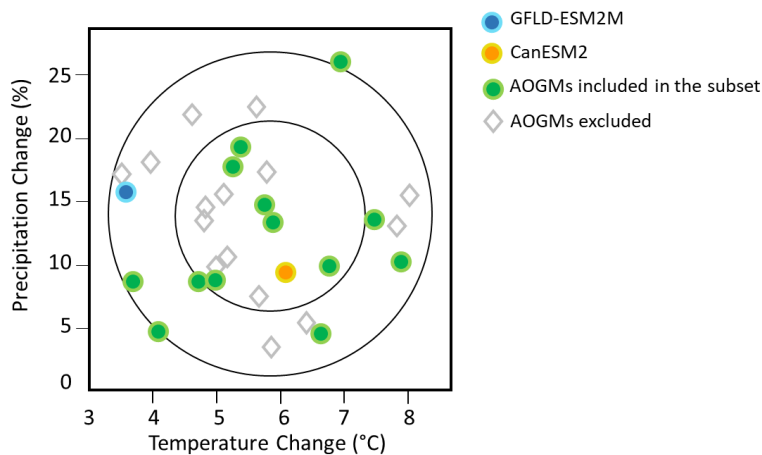


Figure 7: Inter-model variability of changes in temperature and precipitation for RCP8.5, for horizon 2080. The AOGMs included in the first subset of scenarios used to select the lower and upper bounds are identified by a circular symbol, whereas excluded ones are represented by a diamond. CanESM2 and GFLD-ESM2M are identified in blue and yellow, respectively. The inner circle identifies the mean range of expected changes in the CMIP5 ensemble, while the outer circle identifies the maximum projected changes. Modified from Byun and Hamlet (2018).

³ A Hybrid Delta approach was used by Buyn and Hamlet (2018) to downscale the AOGCMs projections and remove the bias.

2.2.3.1. Regional climate models

Downscaled outputs must be used to force hydrodynamic models, as the horizontal resolution of typical AOGCMs is too coarse to resolve sub-grid physical processes that affect climate at a local scale (e.g. smaller scale convective storms). Most AOGCMs do not even include any representation of inland water bodies such as large lakes (Briley *et al.*, 2021), which can strongly modify the structure and transport properties of the atmospheric boundary layer.

To support impact assessment studies over North America, the Coordinated Regional Climate Downscaling Experiment for North America (NA-CORDEX; Mearns *et al.* 2017) produced downscaled regional climate projections of 8 AOGCMs of the CMIP5 ensemble (see <https://na-cordex.org/briefing-document>), including CanESM2 and GFLD-ESM2M. The NA-CORDEX climate simulations are derived using nested Regional Climate Models (referred to as RCMs) with a horizontal resolution of 10 to 50 km. These RCMs admit richer spatial and temporal details and improvement over AOGCM simulations that may be important over complex land surfaces (Lucas-Picher *et al.* 2012), especially over large lakes (Weiss and Sousounis, 1999).

Table 1: Driving AOGCMs and Representative Concentration Pathways (RCP) of the selected climatic scenarios, with their scenario code.

Emission Scenarios	Driving AOGCMs	Scenario Codes
RCP 4.5	CanESM2	SIM01
	GFLD-ESM2M	SIM03
RCP 8.5	CanESM2	SIM02
	GFLD-ESM2M	SIM04

The Canadian Regional Climate Model version 5 (referred to as CRCM5; Martynov *et al.* 2013; Separovic *et al.* 2013), developed by the ESCER Centre (Centre pour l'Étude et la Simulation du Climat à l'Échelle Régionale, Université de Montréal) in collaboration with Environment and Climate Change Canada, was selected to downscale the CanESM2 and GFLD-ESM2M outputs to a grid of ~25 km of resolution that covers the Great Lakes Basin (Table 1). According to Mailhot *et al.* (2019), these two sets of AOGCM-RCMs are found to satisfactorily reproduce the annual cycle of the Great Lakes net basin supply as estimated by the Large Lake Statistical Water Balance Model⁴ (L2SWBM; Gronewold *et al.* 2016) for the period 1970-2000.

⁴ L2SWBM combines measurement-based estimates with models while closing the Laurentian Great Lakes water balance.

2.2.4. Hydrodynamic forcing: Scenarios outputs

The sets of AOGCM-RCMs provide several physical output variables: precipitation, near-surface temperature, total runoff, surface runoff, surface air pressure, surface downwelling short- and long-wave radiation, near-surface winds, etc. Most of these variables were used to calculate quarter-monthly mean water levels and outflows in the Great Lakes Basin for the baseline and future periods⁵. For the simulation-based projections, these data provide climate forcing for the Great Lakes hydrodynamic models by implying a net change in water supply. By doing so, the water levels time-series produced by the hydrodynamic models include the combined effect of over-lake precipitation, over-lake evaporation and runoff for each of the driving scenarios. More details regarding these quarter-monthly mean water-level time-series are given in Section 3.3.

2.3. Winds

While the seasonal variation of Great Lakes water levels is obtained through hydrodynamic forcing, lake response to atmospheric conditions requires the use of gridded wind datasets. The wind inputs must therefore be sufficiently accurate to describe the small-scale atmospheric disturbances affecting each lake, which range in size from 311 to 563 km (at their largest horizontal dimension), and their smallest basins (North Channel of Lake Huron and Georgian Bay, e.g.). Waves modelling also requires high spatial and temporal forcing (3-hour time step, or less) to account for the strong non-stationarity of the wave field, as well as to ensure better consistency between observed and simulated wave climate (Moeini *et al.*, 2010; Rusu *et al.*, 2009; Schaeffer *et al.* 2011). The choice of a gridded wind dataset is hence crucial, and intensive work has been undertaken to characterize the pros and cons of available options. The reference product was intended to be used to (1) force historical (observation-based) simulations, and (2) post-process wind scenarios extracted from the sets of AOGCM-RCMs, which were employed to create projections (hydrodynamic and waves).

2.3.1. Reference datasets

Two preselected gridded datasets were included in the analysis of the reference product: an atmospheric reanalysis, the Climate Forecast System Reanalysis (referred to as CFSR; Saha *et al.*, 2010), and a recent-past climate simulation generated as part of the Climate Change and

⁵ The simulated mean water level of Lake Ontario takes into account the current regulation Plan 2014 that determines outflows at Cornwall, in the Upper St. Lawrence River. No change was applied to this plan to generate the future projections.

Hydrological Extremes experiments (referred to as Climex; Leduc *et al.*, 2019). At the beginning of the GLPI project, the 10 km North American Precipitation and Land Surface Reanalysis Based on the Global Environmental Multiscale Atmospheric Model (GEMR; Gasset *et al.*, 2021) was only available for the 2000s, and was therefore not considered as a possible product.

2.3.1.1. Preselected products

The Climate Forecast System Reanalysis, produced by NCEP (National Centers for Environmental Prediction), is a global reanalysis dataset created by a coupled model of atmosphere, land surface, ocean and sea ice. This dataset is generated with a sequential data assimilation scheme, under which ground observations are combined with model outputs to adjust the simulation trajectory (Fletcher, 2017). Prior estimates are therefore constrained by sea-surface temperature, sea-ice concentration, snow depth and precipitation, but the wind fields are pure forecast and contain no influence or forcing from assimilated observations except in their initialization. CFSR offers hourly data with a horizontal resolution of approximately 38 km. The accuracy of this reanalysis product increases over time, as more observational data become available (Saha *et al.*, 2010).

The Climex experiment is a large ensemble of regional climate simulations at high spatial resolution, i.e. approximately 12 km, designed to support impact studies. The simulations, which cover the northeastern part of North America, were created with the CRCM5 model forced by 50 CanESM2 climate change scenarios (RCP8.5) over the period 1950-2099. One additional run was performed with the European Centre for Medium-Range Weather Forecasts Interim Reanalysis (ERA-Interim), offering a downscaling product of the initial 80 km dataset (Dee *et al.*, 2011). This reanalysis simulation spans the historical period, from 1973 to 2013, with outputs archived every 3 hours. ERA-Interim provides boundary conditions for atmospheric pressure, horizontal wind, temperature and specific humidity to CRCM5 every 6 hours, and spectral nudging is applied to the large-scale winds at each time step. This technique constrains the regional climate model, which then reproduces the development of the large-scale atmospheric dynamics (from the boundary conditions), while allowing the development of regional-scale details (Schaaf *et al.* 2017; Riette and Caya 2002).

Figure 8 shows the land-sea mask of each preselected product.

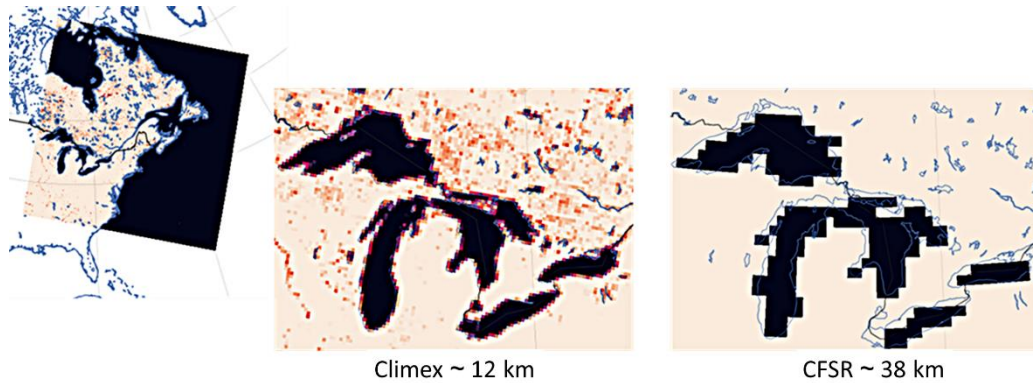


Figure 8: The land-sea mask of the Great Lakes of the Climex and CFSR datasets. The black colour represents the grid cells where the surface land fraction is zero (open-lake area). The inset (left panel) shows Climex' North American domain.

2.3.1.2. Comparison of preselected datasets with observations

To test the ability of each preselected product to reproduce the recent past wind climate over the Great Lakes region, wind speed and direction extracted from the gridded datasets were compared with grounded observations. These observations were drawn from the Integrated Surface Database (ISD; Smith *et al.* 2011) of the NOAA's National Climate Data Center (NCDC; <https://gis.ncdc.noaa.gov/maps/ncei/cdo/hourly>), which provides standardized in-situ global hourly data of surface variables. Over lake observations were also collected from the National Data Buoy Center (NBDC, <https://www.ndbc.noaa.gov/>), a marine buoys network that includes observations for the Great Lakes. Canadian buoys are owned and operated by ECCO, while those in the U.S. are mainly operated by the NBDC and the Great Lakes Environmental Research Laboratory (GLERL), and, to a lesser extent, private owners. Overall, 106 stations were included in the analysis, 26 of them providing open lake conditions (Figure 9). The reference period used for the analysis ranges from 1980 to 2010.

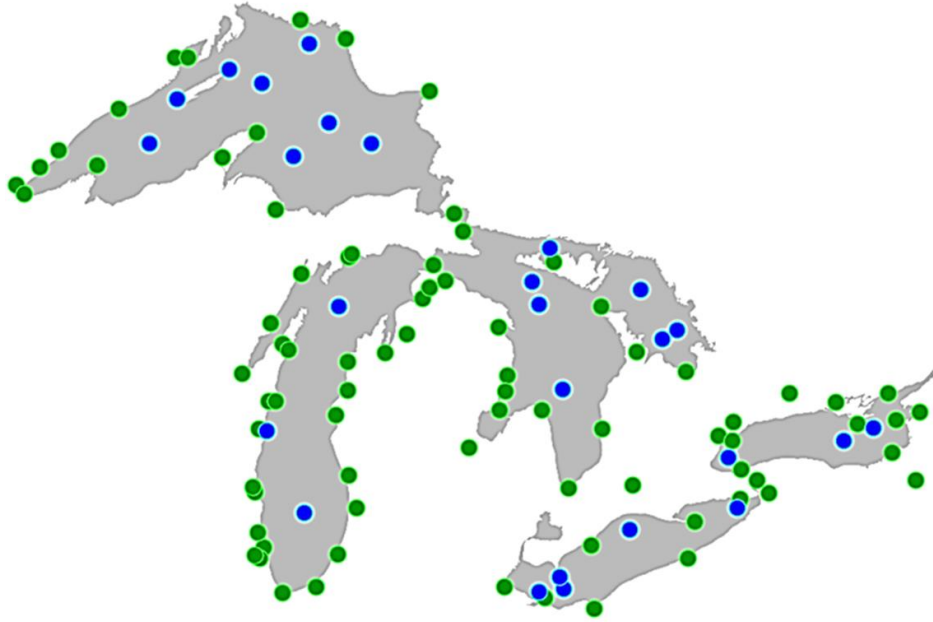


Figure 9: Location of monitoring stations in the Great Lakes region (including buoys). In green, coastal (nearshore) stations, and in blue, open lake (offshore) stations.

2.3.1.2.1. Pre-processing of the observations

Since the recorded wind data are subject to error, the observations were first processed to:

1. Correct for the anemometer height when known. Although standard wind speed and direction measurements are made at 10 m, stations used in the past may have varying anemometer heights that affect the records: the wind speed profile is usually assumed semi-logarithmic in the atmospheric boundary layer. Since selected stations are located in the nearshore area of the Great Lakes or in open water, the correction applied follow the classical 1/7 power law and the formulation of Large and Pond (1981), respectively. The latter introduces a modification of the drag coefficient under moderate and strong wind conditions for offshore measurements. These corrections ensure equivalent winds at 10 m height in all locations.
2. Correct for surface wave distortion. The anemometer height of the buoys is typically between 3 and 5 m above the water surface. The marine wind profile is known to be distorted from its logarithmic form due to the instability of the atmosphere-lake boundary layer and surface waves (Deardorff, 1968; Large and Crawford., 1995), which are accounted for by the Large and Pond (1981) correction. However, wave distortion, which can increase wind stress by more than 40% in strong wind conditions, is neglected, introducing an important bias in offshore wind measurements. Buoy observations were therefore corrected according to Large, Morzel & Crawford (1995).
3. Correct for heterogeneities. Human intervention at measurement stations (e.g. changes in instrumentation, station relocation, introduction of different observing practices) and changes in the local environment (e.g. urbanization) may induce sharp or gradual changes in time series, as well as gaps and missing data. When comparing long-term in-situ

atmospheric climate data, it is therefore important to identify inhomogeneities and adjust the observed time series to compensate for the biases they produce. All 10 m wind equivalent observations, including offshore measurements (once corrected), were therefore processed with the Climatol R package (<http://www.climatol.eu/>, WMO Commission for Climatology), which provides functions for quality control, homogenization, and missing data infilling. Daily averaged wind speed observations were first homogenized, and then a correction was applied to the sub-daily wind components (zonal and meridional).

2.3.1.3. Climatological means and anomalies distribution

Time series of wind speed and direction were extracted from gridded products for each selected station in the Great Lakes Basin, with time series produced as a weighted sum of the four closest grid cells based on station locations. Several characteristics of in situ observations were analyzed to determine the capability of the datasets to reproduce the observed climatological means, in terms of both annual variability and spatial pattern, and the distribution of anomalies. Anomaly distributions are useful for comparing multiple datasets because of their higher spatial correlation over a specific region (Hansen and Sato, 2016) compared to the absolute mean, which can vary significantly over short scales. The temporal characteristics of the anomalies over a large area can therefore be extracted from a limited number of stations. For a specific location, (lon, lat) , anomalies are defined as:

$$X'(lon, lat, t) = X(lon, lat, t) - \bar{X}(lon, lat) \quad 2.1$$

with \bar{X} , the mean value over the reference period at this specific location, and X , the local wind value at each time t .

Table 2 summarizes the regional climatological mean wind speed biases over the area for four specific ranges of wind intensity, i.e. the low ($<3.3 \text{ ms}^{-1}$), moderate ($3.3 - 10.7 \text{ ms}^{-1}$), and high ($> 10.7 \text{ ms}^{-1}$) wind conditions that were defined based on the Beaufort scale (respectively 0-2, 3-5, and > 5 ; WMO 2018). The so-called over-lake statistics refer to stations located in open water conditions, such as buoys or stations installed on isolated offshore islands. The bias is here calculated as $\langle X(lon, lat) - Obs(lon, lat) \rangle$, i.e. the regional mean of the difference between gridded values, X , and observations, Obs .

Table 2: Mean wind speed biases, $\langle X(lon, lat) - Obs(lon, lat) \rangle$, over each of the Great Lakes for the selected reference products, Climex and CFSR. Biases were estimated for low ($< 3.3 \text{ ms}^{-1}$), moderate ($3.3-10.7 \text{ ms}^{-1}$) and

high ($> 10.7 \text{ ms}^{-1}$) wind intensity, according to the Beaufort scale. Statistics were calculated considering all nearshore and offshore stations (left columns), and all over-lake stations only (right columns).

	ALL STATIONS		OVER-LAKE STATIONS	
	BIAS (ms^{-1})		BIAS (ms^{-1})	
	Climex	CFSR	Climex	CFSR
<u>Low intensity, $< 3.3 \text{ ms}^{-1}$ (2.2 ms^{-1} / 182°)</u>				
Ontario	1.1 (8.8 ; 2.0)	1.1 (1.0 ; 1.3)	2.0 (2.0 ; 2.3)	0.7 (0.7 ; 1.0)
Erie	1.9 (0.8 ; 2.0)	0.7 (0.5 ; 1.0)	2.2 (2.0 ; 2.5)	0.9 (0.6 ; 1.2)
Huron	2.0 (1.4 ; 2.8)	1.6 (1.2 ; 2.0)	3.0 (2.5 ; 3.1)	1.9 (1.8 ; 2.1)
Michigan	1.1 (0.7 ; 1.5)	1.6 (1.2 ; 1.8)	2.1 (2.0 ; 2.1)	1.4 (1.2 ; 1.5)
Superior	1.3 (0.7 ; 2.0)	1.3 (1.0 ; 1.5)	2.0 (1.9 ; 2.1)	1.3 (1.1 ; 1.4)
<u>Moderate intensity, 3.3-10.7 ms^{-1} (5.8 ms^{-1} / 196°)</u>				
Ontario	-0.4 (-0.9 ; 0.1)	0.1 (-0.6 ; 0.3)	0.1 (0.0 ; 0.3)	-0.8 (-1.1 ; -0.6)
Erie	0.2 (-0.7 ; 0.7)	-0.8 (-1.0 ; -0.3)	0.7 (0.3 ; 0.9)	-0.9 (-1.1 ; -0.4)
Huron	0.4 (-0.1 ; 0.9)	0.1 (-0.8 ; 0.4)	0.6 (0.4 ; 0.9)	0.1 (-0.5 ; 0.3)
Michigan	-0.1 (-0.8 ; 0.4)	0.9 (0.3 ; 1.2)	0.4 (0.4 ; 0.5)	0.6 (0.3 ; 0.6)
Superior	-0.6 (-0.8 ; 0.4)	0.0 (-0.4 ; 0.7)	0.1 (0.1 ; 0.9)	-0.1 (-0.3 ; 0.6)
<u>High intensity, $>10.7 \text{ ms}^{-1}$ (12.6 ms^{-1} / 214°)</u>				
Ontario	-3.4 (-4.0 ; 2.1)	-2.1 (-3.0 ; -1.9)	-1.9 (-2.4 ; -1.6)	-3.4 (-4.0 ; -2.6)
Erie	-2.1 (-3.2 ; -1.4)	-2.8 (-3.4 ; -2.3)	-0.8 (-1.6 ; 0.1)	-2.7 (-3.1 ; -2.3)
Huron	-2.1 (-2.6 ; -1.4)	-2.1 (-3.2 ; -1.3)	-0.7 (-2.6 ; -0.4)	-1.2 (-2.4 ; -1.2)
Michigan	-2.8 (-4.3 ; -2.1)	-1.5 (-2.3 ; -0.6)	-2.4 (-2.4 ; -2.0)	-1.6 (-1.9 ; -1.3)
Superior	-2.9 (-4.1 ; -1.8)	-2.1 (-2.9 ; -1.3)	-1.8 (-2.4 ; -1.5)	-2.2 (-2.6 ; -1.5)

Climex and CFSR datasets show similar behaviour in terms of wind speed, that is a slight overestimate of light winds and an underestimate of higher winds. The gridded products therefore smooth out the regional surface wind intensities, which can affect the performance of the hydrodynamic and waves simulations in their representation of set-ups and high wave events, as observed in larger oceanic systems (Dullart *et al.*, 2020). While the relative biases of CFSR and Climex surface winds are quite similar for wind speeds higher than 12.6 ms^{-1} over the Great Lakes Basin, i.e. -15% and -16% respectively, Climex displays small improvements over the lakes, at buoy and offshore stations. The relative bias decreases to -11%, compared to -17% for CFSR, revealing that Climex is generally in better agreement with open-lake observations (except for Lake Michigan). In terms of wind direction, both products show positive bias (not shown), as

expected for a representation of the wind direction that favours a clockwise rotation in the Northern Hemisphere (Carvalho, 2019).

A closer look at the station climatology provides a better understanding of the dataset performance. Wind roses are particularly useful for this purpose, as they provide a visual description of wind intensity in each geographical direction, and thus more easily explain the biases associated with the Great Lakes numerical representation. Figure 10 and Figure 11 display wind roses for the Rock of Ages station, located at the western end of Isle Royale (Lake Superior), and South Georgian Bay station, a buoy moored in the southwestern part of Georgian Bay. In the first case (Rock of Ages, Figure 10), spring winds (March, April and May) show a dominant northeasterly component, which is consistent with winds coming from the Thunder Bay area with unobstructed fetch⁶ of about 70 km. This NNE wind component can be seen in the Climex data, whose horizontal description (12 km) is fine enough to resolve the bay, but mostly absent from CFSR, which only roughly describes the northern coast of Lake Superior (Figure 10a). A similar artefact due to the lake configuration is observed in the climatology of South Georgian Bay (Figure 11). At this station, CFSR data show a predominance of southwesterly winds in summer (June, July and August) that are not observed in in-situ measurements, except for a general persistence of westerly winds, between SW and NW. Again, Climex shows better agreement with observations, which can be attributed to the finer resolution of the Bruce Peninsula (Figure 11a) that separates Georgian Bay from Lake Huron and limits the wind fetch from this large body of water.

⁶ [Def.] The distance traveled by wind across open water.

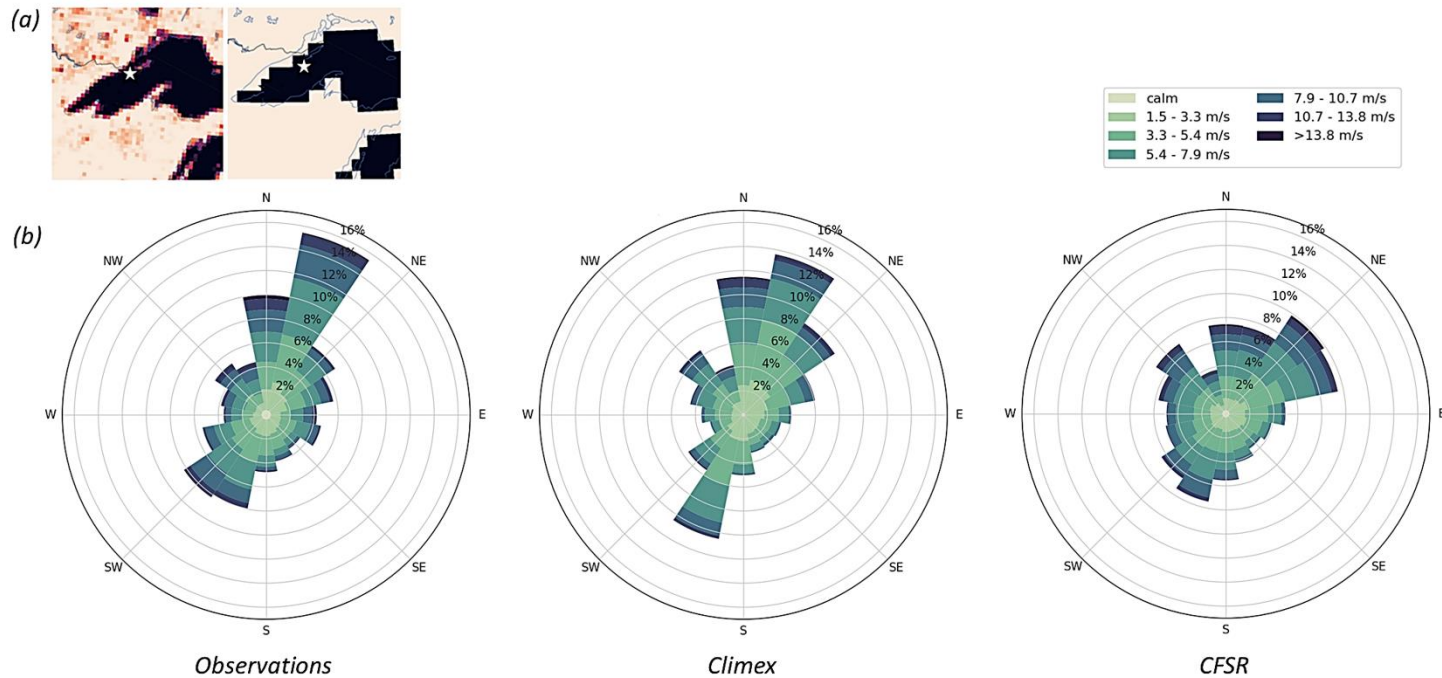


Figure 10: (a) Land-sea mask of Climex (left) and CFSR (right) datasets with the position of the Rock of Ages station, in Lake Superior (white star). (b) Climatology of the 16 sectors wind rose for observed near-surface winds (left panel) during March, April and May (MAM) at Rock of Ages station, for the period 1980-2010. Idem for Climex (middle panel) and CFSR (right panel) datasets.

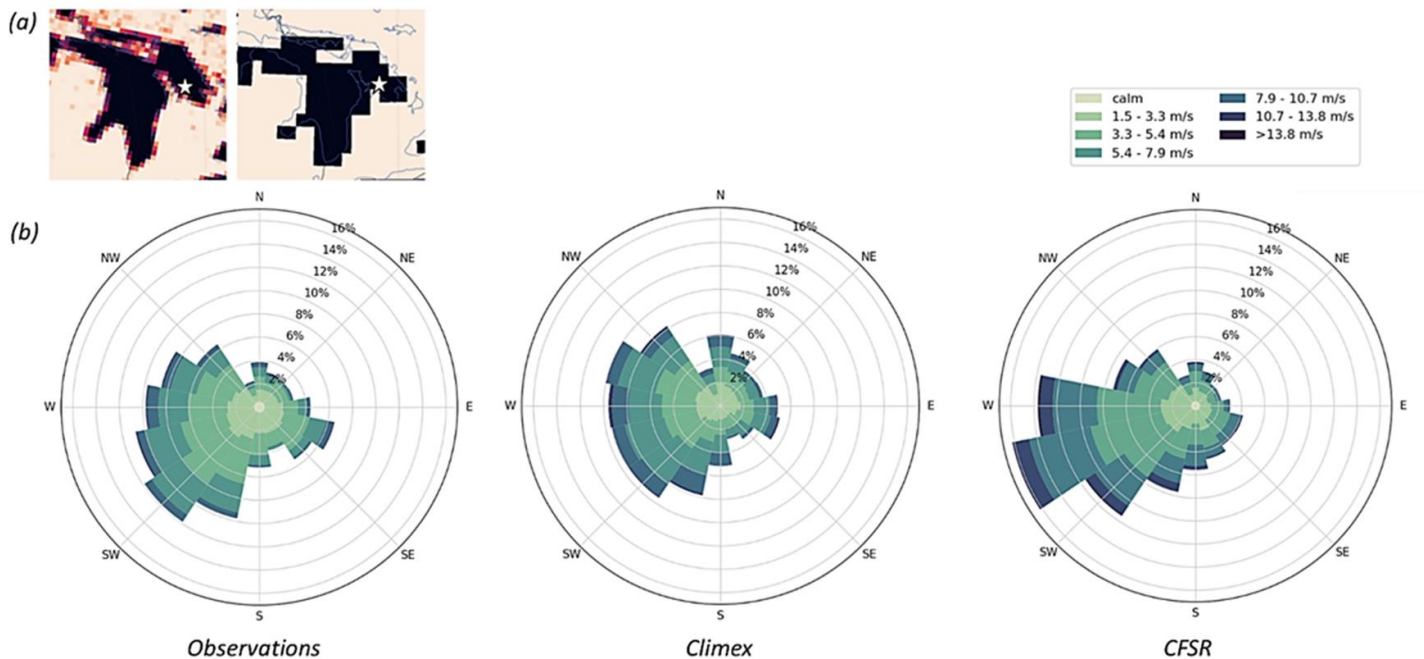


Figure 11: (a) Land-sea mask of Climex (left) and CFSR (right) datasets with the position of the South Georgian Bay buoy, in Lake Huron (white star). (b) Climatology of the 16 sectors wind rose for observed near-surface winds (left panel) during March, April and May (MAM) at South Georgian Bay buoy, for the period 1980-2010. Idem for Climex (middle panel) and CFSR (right panel) datasets.

panel) during June, July and August (JJA) at South Georgian Bay station, for the period 1980-2010. Idem for Climex (middle panel) and CFSR (right panel) datasets.

To provide a summary of the performance of Climex and CFSR for the Great Lakes region, the wind speed and direction anomaly distributions of the two datasets were compared with observations via two score metrics: the Kuiper goodness-of-fit metric (Kuiper 1960) and the Perkins metric (Perkins *et al.* 2007). The Kuiper metric is used to compare two sample distributions by measuring the distance between their respective cumulative empirical distribution function, and is defined as:

$$D_k = \max_{-\infty < x < \infty} [ECDF_k(x) - ECDF_{obs}(x)] + \max_{-\infty < x < \infty} [ECDF_{obs}(x) - ECDF_k(x)] \quad 2.2$$

with $ECDF_k$ and $ECDF_{obs}$, the cumulative empirical distribution function of dataset k and recorded datasets, respectively. A D_k value of zero refers to a perfect match between the two distributions, while a value of one indicates no overlap. Instead, the Perkins metric uses the empirical probability distribution function, EPDF, to characterize the similarity between distributions:

$$1 - PSS_k = 1 - \sum_{x=1}^n \min(EPDF_k(x), EPDF_{obs}(x)) \quad 2.3$$

with n , the number of x bins used to calculate the normalized histograms, and $EPDF_k$ and $EPDF_{obs}$, the density of the normalized histograms at bin x . The EPDFs were evaluated over fixed bin sizes of 0.1 ms^{-1} and 5° for wind speed and direction respectively. A $1 - PSS_k$ score of 0 indicates perfect overlap and inversely for a score of 1, as for Kuiper metric.

Figure 12 shows the difference in Kuiper score for the five Great Lakes and each season, including the period from April to November, which covers most of the growing season used in the modelling (cf. Section 3.7.2.2). The difference was calculated as $D_{Climex} - D_{CFSR}$ for ease in interpretation, a negative result being representative of a better performance of the Climex dataset. Scores were computed on all stations (Figure 12a), as well as on open-lake stations only (Figure 12b) to highlight the capability of both products to reproduce wind climate anomalies in open-lake conditions, conditions critical to lake dynamics modelling. As can be seen (Figure 12, left panels), the simulation-based wind speeds outperform the reanalysis winds for all seasons except spring (MAM) for lakes Erie, Michigan and Ontario when the full set of stations is considered. Climex's performance remains superior for Lakes Ontario and Erie, the two smallest lakes modelled, when the analysis is restricted to the over-lake stations. Overall, both products

are effective in simulating the anomalies distribution, with a score generally less than 0.2 (all stations) or 0.25 (over-lake stations), excluding the winter months for which few observations are available (buoys are generally removed for the winter to avoid ice conditions). For wind direction (Figure 12, right panels), CFSR is overall better, except for the summer months (JJA) and the period covering the growing season (April-November) for Lakes Erie and Ontario. Similar results for wind speed and direction were obtained for the Perkins metric (not shown).

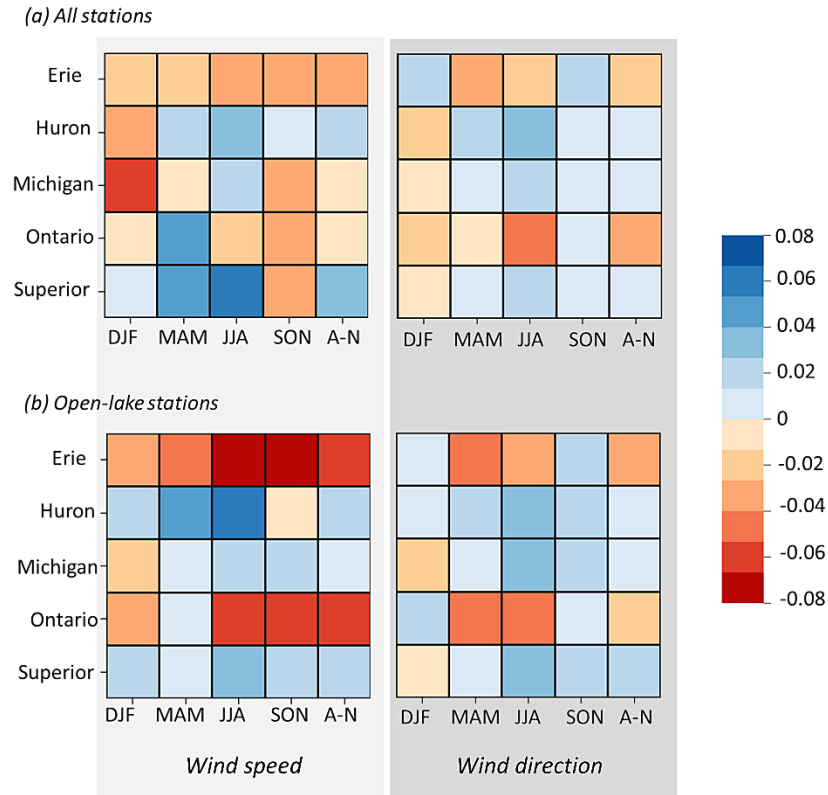


Figure 12: Heat maps comparing the performance of Climex and CFSR for wind speed (left panels) and direction (right panels) anomalies distribution based on the Kuiper metric for each Great Lake, for the period 1980-2010. (a) For all coastal and offshore stations, and (b) for offshore (open-lake) stations only. A negative value indicates that Climex outperforms CFSR (better skill).

Finally, the climatological spatial pattern was assessed using the Reduction of Variance (RV) metric, which compares the mean square error (MSE) between the mean of a dataset and the spatial variance of the observed climatological mean for a specific region (or lake):

$$RV_k = 1 - \frac{MSE(k, Obs)}{s_{obs}^2} = 1 - \frac{\sum_{i=1}^N (\bar{Y}_{ki} - \overline{Obs}_i)^2}{\sum_{i=1}^N (\overline{Obs}_i - \langle \overline{Obs} \rangle)^2} \quad 2.4$$

with \bar{Y}_{ki} and $\overline{\text{Obs}_i}$, the climatological mean of dataset k and recorded data for station i , $\langle \overline{\text{Obs}} \rangle$, the spatial mean over the lake, and N , the number of stations. For a positive RV_k , the MSE value of the dataset is smaller than the observed spatial variance.

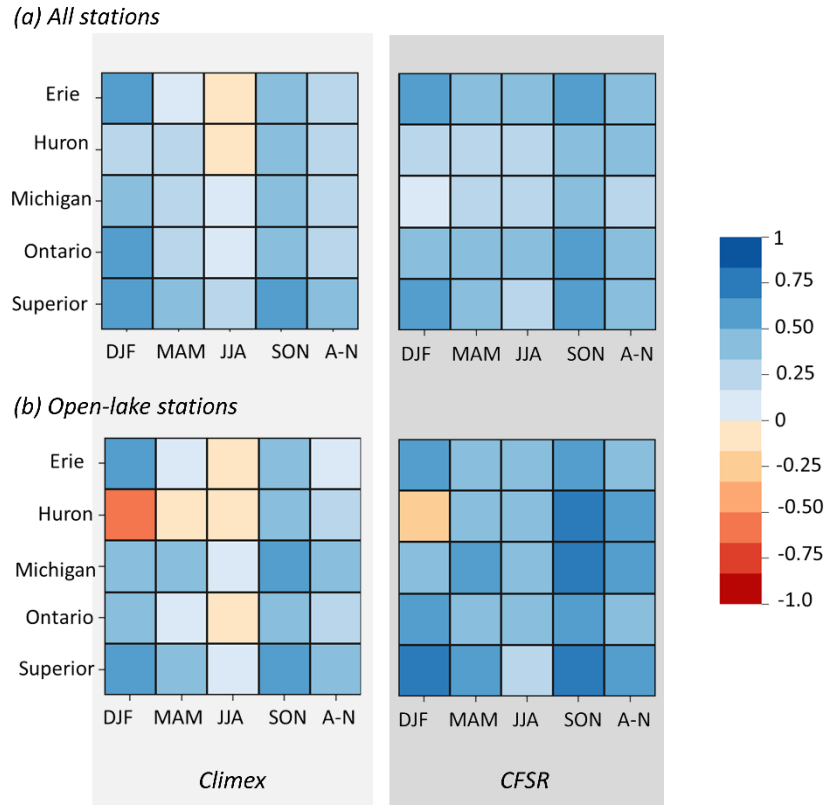


Figure 13: Heat maps comparing the performance of Climex (left panels) and CFSR (right panels) for climatological mean wind speeds based on the RV metric for each Great Lake, for the period 1980-2010. (a) For all coastal and offshore stations, and (b) for offshore (open-lake) stations only. A positive RV value indicates a good performance (or skill).

In general, both Climex and CFSR show good performance in reproducing climatological means (wind speed, Figure 13, and direction, not shown), for inland (Figure 13a) or over-lake stations (Figure 13b). Only Lake Huron shows negative RV values, and this is with the Climex simulation, for most seasons (DJF, MAM, and JJA). This lake appears more problematic for the simulation-based product, both for the anomalies distribution and the mean. However, and similarly to other lakes, the wind speeds and directions extracted from this dataset are generally within the first and third quartiles of the observed climatological distributions for most sites (e.g., Figure 14, Western Island in the southeastern part of Georgian Bay), which is desirable for a reference product.

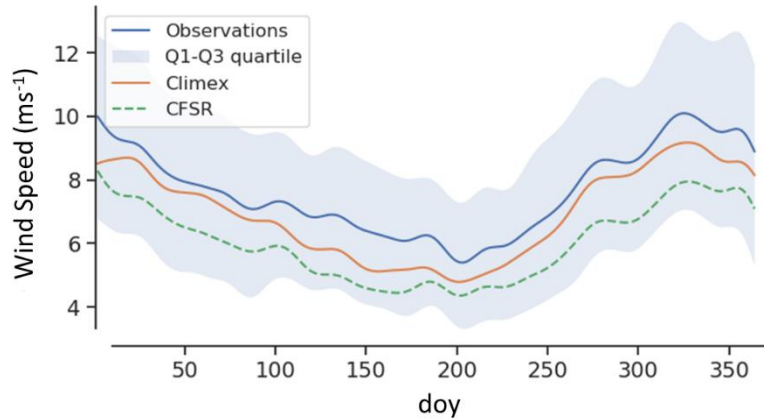


Figure 14: Wind speed climatology for the Western Island station, in the southeastern part of Georgian Bay (Lake Huron, offshore station), for the period 1980–2010. The climatology is given for each day-of-year (doy). The shaded area specifies the first and third quartiles of the observed distribution.

In summary, both products display similar behaviour in terms of wind speeds and directions in the Great Lakes Basin: overestimation of light winds, underestimation of strong winds, and a positive bias in wind direction, consistent with a clockwise rotation of atmospheric systems in the Northern Hemisphere. However, Climex shows a smaller bias at open-lake stations for winds $> 10.7 \text{ ms}^{-1}$, which may help to correctly represent set-ups and high wave events. According to Kuiper and Perkins metrics, the simulation-based product performs better than the reanalysis in its representation of the anomalies distribution, particularly at open-lake stations of Lakes Erie and Ontario, which are the two smallest lakes modelled. As the GLPI project focus on Lakes Ontario, Erie and Huron, this observed benefit to the lower lakes becomes important. The good performance of Climex datasets on smaller lakes may be a direct result of the grid resolution ($\sim 12 \text{ km}$), which allows for better representation of the lakes, their shorelines, and their connecting bays and channels. As illustrated by the wind roses (Figure 10 and Figure 11), the grid resolution may alter the wind climate in specific areas of the Great Lakes, where the coastline displays complex features that are not well defined by a horizontal scale of $\sim 38 \text{ km}$. The realism of the Great Lakes in the gridded product thus becomes a decision criterion as it can likely improve the quality of subsequent modelling. The main limitation of Climex is the lack of any form of data assimilation, which could correct for model discrepancy. However, this design specificity does not translate into an overall inferior performance to CFSR when simulation data are compared to grounded observations. For these reasons, Climex was considered the most adequate reference product, and was therefore used to simulate the historical period.

2.3.2. Post-processing

Climatic scenarios produced by AOGCM-RCMs are generally biased, i.e. all climate variables provided by them show differences between the modelled and observed historical climatology. Bias-correction techniques are therefore used to adjust the scenarios and correct their inaccuracies based on a reference product that covers the recent past period. The “10-m wind” components extracted from the selected driving scenarios (c.f. Section 2.2.3) were debiased using the chosen reference product, Climex, over the period 1980-2013. The debiasing technique utilized is a sophisticated quantile mapping algorithm, which contains an optional bivariate shuffling procedure that, when activated, forces the simulations to adopt the local inter-component rank correlation coefficients of the reference product (Vrac, 2018; Guo *et al.*, 2019). While the first post-processing step involves a standard univariate (single-variable) debiasing scheme, the second allows for bias adjustment of two variables simultaneously, which is based on the inter-variable statistical dependencies. This multivariate technique was tested on the zonal, u_{as} , and meridional, v_{as} , near-surface wind components. Since wind is a vector field, debiasing u_{as} and v_{as} separately can lead to a bias in wind direction, as univariate debiasing does not account for the existing dependencies between these two components. Although there is no risk of physical inconsistency related to bias adjustment when the time steps are taken separately, as the two components can take any value without being linked by a mathematical relationship, multivariate debiasing can potentially introduce biases in the daily sequence.

The objective of this section is to present the debiasing technique adopted for the winds extracted from the selected AOGCM-RCM scenarios. A more detailed description of this work can be found in Grenier and Music (2020).

2.3.2.1. Multivariate debiasing

The debiasing technique was applied to the data extracted from the driving scenarios (c.f. Table 1) in a domain that encompasses the Great Lakes and their surrounding lands (Figure 15). While the spatial resolution of the RCM outputs is approximately 25 km, the climate change simulations were first interpolated, using a cubic procedure, to a 12 km resolution grid that fits the Climex reference product. The temporal resolution of the wind scenarios is 3 hours, similar to the Climex series, and the calibration and future periods cover the years 1980-2013 and 2067-2100 respectively.

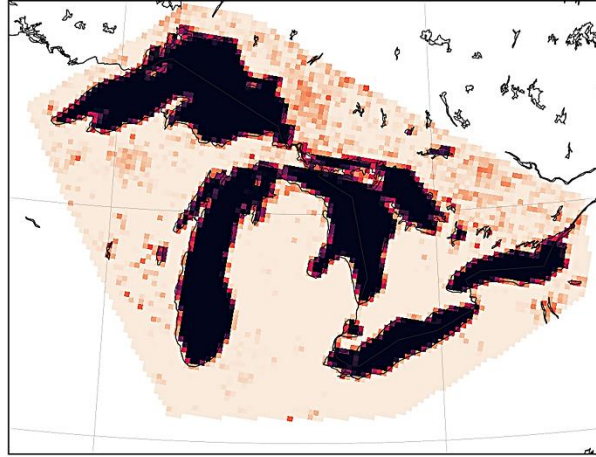


Figure 15: The Great Lakes domain for debiased wind scenarios (coloured areas).

As stated previously, the post-processing technique used is a two-step approach:

1. A univariate step. This step refers to the standard univariate debiasing, which is based on the commonly used quantile mapping technique (Agbazo and Grenier, 2019). In quantile mapping (QM), a transfer function is applied to adjust the distribution of modelled climatic variables to match its corresponding reference distribution. Each time step of the day is treated as an independent daily index and each day-of-year (DOY), considered separately. The transfer function was designed with a 31-day moving window, centered on a DOY, to avoid climatological discontinuities between two successive months. While the adjustment is strictly applied to the residuals (i.e. deviations from the trend), the long-term trend extracted from the modelled data was added once the univariate step completed to preserve simulated trends.
2. A shuffling step. This optional step is introduced before the trend adjustment on the residuals. Although this shuffling is inspired by Vrac *et al.* (2018), it was adapted to introduce additional univariate considerations (i.e. trend preservation and moving window). The multivariate debiasing first considers a master variable and a slave variable⁷, both being the residuals of the wind components once QM applied. The shuffling of the slave variable, e.g. v_{as} (u_{as} being the master variable), is performed so that the master-slave Spearman rank-order correlation coefficient (or r_{rank} ⁸) of the scenario replicates the master-slave r_{rank} of the reference product for a specific DOY.

⁷ The reader should note that the master/slave terminology had been adopted at the moment of writing the preliminary report and producing most of the figures (March-April 2020), only by analogy with some traditional descriptions in electronics theory, in informatics and in other scientific fields (e.g.: Bugg, D.V., 1991, Electronics. Circuits, Amplifiers and Gates. Institute of Physics Publishing). In no manner this choice of terminology was intended to emphasize any historical or societal events. Eventually, such terminology could be replaced, and subsequent work based on the current report could rather adopt the unshuffled/shuffled terminology.

⁸ The Spearman rank-order correlation coefficient measures the strength and direction of the monotonic relationship between two variables.

Debiasing was performed once with v_{as} as a slave variable, once with u_{as} . Three sets of debiased outputs were thus produced: unshuffled u_{as} (master) and shuffled v_{as} (slave; bivariate), unshuffled v_{as} (master) and shuffled u_{as} (slave; bivariate), and unshuffled u_{as} et v_{as} (univariate).

2.3.2.2. Overview of results

Several statistical analyses were conducted on the debiased simulations to evaluate the performance of the bias adjustment technique. They demonstrated that debiasing does what was *a priori* expected: adoption of the properties of the reference product distribution, preservation of the long-term simulated trends, and debiasing of the local inter-component correlation coefficients when the shuffling procedure was activated. The results also indicated that shuffling does not generally improve the debiasing wind speed compared to univariate technique alone: no additional bias adjustment on the monthly mean value of the zonal and meridional near-surface winds was observed (Figure 16). The univariate QM already shows a good correction on the mean values and most of the scenarios have a relatively small initial bias. The impact of debiasing on wind direction has not been investigated.

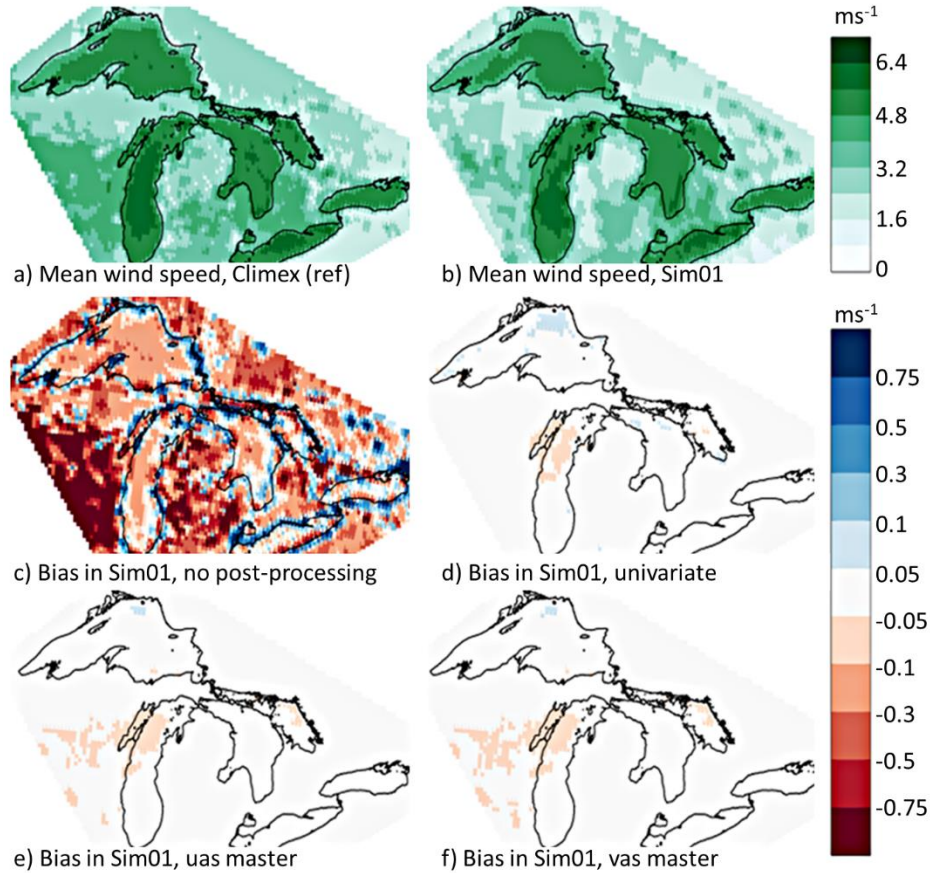


Figure 16: Maps of the mean wind speed during 1980-2013 for July in: a) the Climex run (reference product); and b) the raw SIM01 run (cf. Table 1)). Maps of corresponding biases (rank relative to the reference product rank) considering: c) the raw SIM01 run; d) the univariate debiased time series (unshuffled v_{as} and unshuffled u_{as}); e) the debiased time series using u_{as} as the master variable (v_{as} is shuffled); and f) the debiased time series using v_{as} as the master variable (u_{as} is shuffled). The violet-to-green colorbar corresponds to direct wind speed values in panels a) and b), whereas the red-to-blue colorbar corresponds to biases in the four other panels (after Grenier and Music, 2020).

A detailed inspection of the results further showed that the shuffling removes much of the interannual variability of the shuffled (slave) variable, as well as lag-1 auto-correlation of the shuffled components and wind speed (Figure 17a). Debiasing values of the slave variable are exchanged between years, and no parallel procedure was used to preserve the temporal sequences (Figure 17b), which also leads to a loss of spatial correlation (not shown). Both of these consequences are problematic for the intended use of the debiased simulations, namely atmospheric forcing of physical models. With a change in the daily sequence and spatial pattern, the realism of the wind forcing is not guaranteed: the wind set-ups are a direct result of the action of the wind on the lake surface, and therefore strongly depend on the duration of the events, as well as on the atmospheric systems trajectories. Finally, any long-term changes in correlation coefficients projected by the climate simulations are not retained in the bivariate scenarios. For

any application period (here 1980-2013 and 2067-2100), the climatic scenarios are forced to adopt the correlation coefficients of the reference product. Some information regarding the change in wind climate between baseline and future periods may therefore be lost.

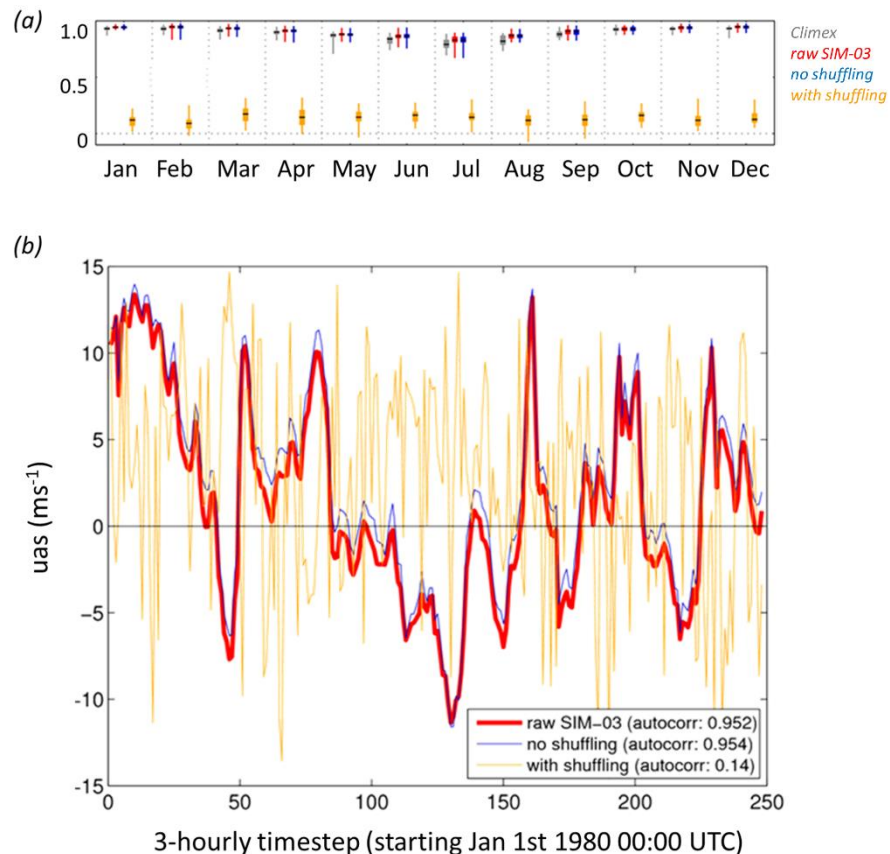


Figure 17: (a) Zonal wind (uas) lag-1 auto-correlation (Spearman) coefficients for a specific grid tile (“middle” of Lake Huron) for simulation SIM03 (cf. Table 1). For each month-of-the-year, four distributions of coefficients are shown: for the reference product (Climex, in grey), for the raw simulation (red), for adjusted simulation without shuffling (blue) and for the adjusted simulation with shuffling (orange). Each distribution is made of 34 values, one for each year of the calibration period (1980-2013). For any distribution, the box plot shows the minimum and maximum values (coloured vertical thin line) as well as the 25th and 75th percentiles (coloured central box) and the median (black horizontal line). Dashed vertical lines are between-month separators (for better visual appreciation only), whereas dashed horizontal lines are the zero lines (no auto-correlation). (b) SIM03 uas 3-hourly time series for the first month of the calibration period (January 1980). The raw simulation is presented in red, the adjusted simulation without shuffling in blue, and the adjusted simulation with the supplementary shuffling procedure in orange. Numbers presented in the legend box are the respective lag-1 auto-correlation (Spearman) coefficients. The concerned grid tile is located in the middle of Lake Huron (after Grenier and Music, 2020).

Although the multivariate shuffling procedure is the most promoted technique in the current literature, alternative approaches that use successive conditional univariate applications (e.g. Piani and Haeter, 2012) and principal component transformations (e.g. Hnilica *et al.*, 2017) also exist. Since these alternatives were not tested, it is difficult to determine the actual improvements

of multivariate debiasing for wind speed and, ultimately, wind direction over the more conventional treatments. Since the objective of the bias adjustment method here is to provide corrected wind inputs for the physical models, the use of the bivariate wind scenarios is not recommended due to the deterioration of the auto-correlation coefficients. Therefore, for the project, simple univariate wind scenarios were used.

2.4. Projected changes: 2070-2099

Projected changes in over-lake, near-surface winds were assessed using debiased wind scenarios, with changes defined as the difference in annual distributions between the future period (2070–2099) and reference (1980–2009) periods. As the wind climate experienced by the lakes and its Interannual Variability (hereafter referred to as IV) may be impacted, both the difference in the mean and standard deviation of daily wind speeds were estimated.

The year-to-year variability of low-level winds over the Great Lakes is thought to have some links to synoptic-scale weather systems, such as the Southern Oscillation (i.e. SO) that brings lower mean wind speeds and more frequent lulls during El Niño events (or positive El Niño-Southern Oscillation or ENSO; Li *et al.*, 2010). According to the 1979–2008 climatology (Li *et al.*, 2010), the location of the Great Lakes relative to the typical atmospheric circulation pattern over North America (i.e. the polar jet-stream position; Shabbar *et al.*, 1997) would also play an important role in the development of these variations. Nevertheless, the response to different phases of ENSO (positive or negative) is not directly opposed, and interactions between several modes, including North Atlantic Oscillation and Pacific–North American teleconnection pattern, also drive variability (Schoof and Pryor, 2014).

2.4.1. Future changes in wind speed

Table 2 presents the changes in annual mean “10-m wind speed” calculated for the daily average and daily maximum distributions, the latter being representative of the extreme gusts that blow over the lakes. Only the climate simulations performed under the RCP4.5 emission scenario were analyzed, i.e. SIM01 and SIM03 (cf. Table 1), as only these scenarios were used to project wetland distribution in the future (cf. Section 3.3). To quantify the significance of the estimated future changes for each individual climate scenario, the significance confidence level was evaluated using statistical tests.

2.4.1.1. Tests of significance and autocorrelation

To ensure robustness of the projected changes, the U-test was applied to determine whether the recent past and future distributions obtained for a climatic parameter differ or, in other words, whether the climate change signal is significant. This test, also known as the Mann-Whitney-Wilcoxon test (Wilcoxon, 1945; Mann and Withney, 1947; Pettitt and Siskind, 1981), assesses if the rank of the data samples is altered between the past and future climate, resulting in a positive or negative climate change. To test the hypothesis of change, the two samples are combined into a single order sample and ranks are assigned to each value without regard to the underlying populations. The test statistic is then evaluated as the sum of the ranks assigned to the samples in one specific population relative to the other. If the sum is too small (or too large), there is an indication that populations differ, and the null hypothesis of no difference between populations can be rejected (at a predetermined significance level, here 10%, which corresponds to a p value of 0.10).

For the current purpose, the 30 years contributing to each period are compared, using mean annual values. The U-test is nonparametric and especially dedicated to right-skewed distributions, which is the case for wind speed (e.g. Jung and Schindler, 2019), and it is commonly used in climatic studies to compare means (e.g. Rodionov, 2005).

2.4.1.1.1. Lag-1 Autocorrelation

The U-test assumes that the data are statistically independent within each sample, which requires testing for serial dependence. The existence of positive autocorrelation in time series increase the number of unjustified shift detections (Wang, 2008), i.e. significant differences are found more frequently than expected while there may not actually be any. The structure of serial correlation can be adequately described by the lag-1 autocorrelation coefficient (Cunderlik and Burn, 2004). Although strong lag-1 autocorrelation is very uncommon in mean annual climate model outputs (Decremer *et al.*, 2014), and it is a standard procedure to relax this assumption for annual climatic series (Costa and Soares, 2009), serial dependence was tested.

The lag-1 autocorrelation coefficient is the correlation between the first $N - 1$ observations of the time series X_t , with $t = 1, 2, 3 \dots, N - 1$, and the following X_{t+1} observations:

$$\rho_1 = \frac{\sum_{t=1}^{N-1} (X_t - \bar{X}) (X_{t+1} - \bar{X})}{\sum_{t=1}^N (X_t - \bar{X})^2} \quad 2.5$$

where upper bar denotes simple average. Serial dependence is tested for significance at the 10% level according to the probability limits of the two-tailed test as defined for an independent series:

$$\rho_1(90\%) = \frac{-1 \pm 1.697 \times (N - 2)^{1/2}}{N - 1} \quad 2.6$$

Serial correlation is assumed when ρ_1 lies outside the confidence interval. Each 30-year time series was tested for the autocorrelation before the Mann-Whitney-Wilcoxon test was applied. None revealed statistical serial dependence at lag-1.

2.4.1.1.2 Equality of variance

The significance of the difference between the past and future interannual variability was tested with the modified Levene's test (Levene, 1960; e.g. Ahmed *et al.*, 2013; Ozturk *et al.*, 2015), which is a non-parametric test used to determine whether the variances of two sample populations are equal. This method considers the distance between the sample values and their population median rather than the mean, which provides robustness when the underlying data have a skewed distribution.

To perform Levene's test, the time series of size N is divided into k subgroups, with N_i the sample size of the i th subgroup ($i = 1, 2, \dots, k$), and the test statistic is defined as:

$$W = \frac{(N - k) \sum_{i=1}^k N_i (\bar{Z}_i - \bar{Z})^2}{(k - 1) \sum_{i=1}^k \sum_{j=1}^{N_i} (Z_{ij} - \bar{Z}_i)^2} \quad 2.7$$

and

$$Z_{ij} = |X_{ij} - \bar{X}_i| \quad 2.8$$

where \bar{X}_i is the median of the i th subgroup, \bar{Z}_i are the group means of the Z_{ij} , and \bar{Z} is the overall mean of the Z_{ij} . The Levene's test rejects the null hypothesis that the variances are equal if $W > F_{(\alpha, k-1, N-k)}$, the critical value of the F distribution with $k - 1$ degrees of freedom at a α significance level (here 10%). In addition, to obtain unbiased estimate of the IV, the linear trend was removed from the time series before calculating the STD for a given 30-year period (Räsänen, 2002).

Results are presented in Table 3, with missing values (or dash, –) when the statistical tests did not satisfy the 10% significance level. Shaded colours indicate relative changes that reach at least 5 or 25% and reveal clear climate change signal, i.e. when both scenarios agree on the sign of the projected changes (positive, in orange, or negative, in green; Mastrandrea *et al.*, 2011).

2.4.1.2. Annual mean near-surface wind speed

The data in Table 3 show projected changes averaged over all grid points located in open-lake conditions, i.e. excluding land areas. Results were broken down by seasons and by annual mean.

Based on data compiled for the baseline period (1980–2009), annual mean wind speed values range from 6.3 to 6.8 ms⁻¹ depending on the lake, with strongest winds observed in fall and winter, where mean daily maximum can reach ~10 ms⁻¹. The interannual variability ranges from 0.2 to 0.4 ms⁻¹, with lower year-to-year variation in summer due to weaker overall wind speeds observed between June and August, when the region is influenced by high-pressure systems. Conversely, greater IV is observed in winter during period of stronger winds, when the wind climate is more sensitive to the changes in synoptic-scale weather systems (Eichenlaub, 1978).

Table 3: Reference conditions and projected changes for near-surface winds. The changes in means and standard deviations are provided, with missing values (or dash, –) when the statistical tests did not satisfy the 10% significance level (i.e. U-test for the mean and Levene' test for the variability). Shaded colours indicate relative changes that reach

at least 5 or 25% and reveal clear climate change signal, i.e. when both scenarios agree on the sign of the projected changes (positive, in orange, or negative, in green).

Near-Surface Wind Speed						
Annual Mean Daily 10 m Wind Speed (ms ⁻¹)			Annual Mean Daily Maximum 10 m Wind Speed (ms ⁻¹)			
	Reference	Projected Changes		Reference	Projected Changes	
	Mean (STD)	Mean	STD	Mean (STD)	Mean	STD
DJF						
Ontario	7.58 (0.38)	-0.23 ; -		10.16 (0.54)	-0.44 ; -	
Erie	7.74 (0.43)	-0.21 ; -		10.26 (0.55)	-0.39 ; -	
Michigan-Huron	7.85 (0.35)	-0.18 ; -		10.35 (0.48)	-0.36 ; -	
Superior	7.44 (0.32)	-0.15 ; 0.22		9.85 (0.42)	-0.30 ; -	
MAM						
Ontario	5.73 (0.28)			8.03 (0.40)	-0.19 ; -	
Erie	6.33 (0.30)			8.71 (0.38)	-0.20 ; -	
Michigan-Huron	6.39 (0.26)			8.77 (0.34)	-0.18 ; -	(-0.17 ; -)
Superior	5.94 (0.27)			8.29 (0.33)		
JJA						
Ontario	4.83 (0.21)	-0.18 ; -		7.02 (0.28)	-0.20 ; -	
Erie	5.40 (0.19)	-0.23 ; -	(- ; 0.07)	7.73 (0.23)	-0.26 ; -	
Michigan-Huron	5.43 (0.19)	-0.18 ; -		7.80 (0.25)	-0.17 ; -	
Superior	5.08 (0.23)			7.37 (0.29)		
SON						
Ontario	6.87 (0.33)	-0.29 ; 0.15		9.21 (0.44)	-0.34 ; 0.23	(- ; 0.12)
Erie	7.19 (0.31)	-0.39 ; 0.16	(- ; 0.12)	9.49 (0.39)	-0.48 ; 0.22	(- ; 0.11)
Michigan-Huron	7.64 (0.30)	-0.27 ; 0.13	(- ; 0.09)	10.08 (0.44)	-0.28 ; 0.23	(- ; 0.10)*
Superior	7.58 (0.32)	-0.13 ; 0.15		10.06 (0.42)	- ; 0.22	
Annual						
Ontario	6.25 (0.16)	-0.20 ; 0.05		8.60 (0.21)	-0.29 ; 0.07	(- ; 0.03)
Erie	6.66 (0.17)	-0.24 ; 0.06	(- ; 0.08)	9.04 (0.22)	-0.33 ; -	(- ; 0.10)
Michigan-Huron	6.82 (0.15)	-0.18 ; 0.07		9.24 (0.21)	-0.24 ; 0.09	(- ; 0.01)
Superior	6.50 (0.16)	-0.11 ; 0.10	(-0.07 ; -)	8.88 (0.21)	-0.14 ; 0.11	(-0.07 ; -)

<u>Negative Changes</u>		<u>Positive Changes</u>	
>5%	>25%	>5%	>25%

For all lakes, the annual climate change signal remains unclear for mean daily and mean daily maximum wind speed values, with difference in means ranging from (-0.24, 0.10) ms⁻¹ and (-0.33, 0.11) ms⁻¹ respectively. With the exception of Lake Superior, which exhibits similar absolute differences for both bound scenarios, the projected decrease in near -surface wind speeds is more

pronounced but stays less than 5% in relative difference. This ambiguity in projection is likely driven by the fall winds (i.e. SON), which have a large uncertainty in the sign of the expected changes by the end of the century, with mean annual values that are highly variable. Instead, there is a significant decrease in winter and summer wind speeds for all lakes, excluding Lake Superior, as well as a decrease in extreme wind climate in all months except fall.

This decline in the magnitude of mean and strong near-surface wind speeds is consistent with the results reported for CMPI5 AOGCMs over a large part of the United States by Jung and Schindler (2019), under RCP8.5 forcing, and across the Northern Hemisphere (NH) midlatitudes by Karnauskas *et al.* (2018), under RCP4.5 and RCP8.5 scenarios. The values listed in Table 3 indicate negative changes that are around -2%, which is within the range predicted by Breslow and Sailor (2002) for the US continental, where a reduction in wind speeds of 1.4 to 4.5% is expected over the century. A decrease in annual maximum wind speed in 2074–2100 relative to 1979–2005 was also reported over much of the United States (Kumar *et al.*, 2015), in agreement with current data for all seasons except fall. Nevertheless, the literature reveals the existence of a large discrepancy between the predictions of models for the US (Solaun and Cerda, 2019), particularly among the different RCMs of the NA-CORDEX project (Chen, 2020). Clear conclusions are therefore difficult to draw from the current set of scenarios.

2.4.1.3. Interannual Variability (IV)

The IV of mean annual daily maximum wind speeds, as measured by standard deviations calculated from 30-year annual means, is likely to increase over the 2070–2099 period relative to baseline conditions for most lakes, with changes up to 64% in Lake Erie (0.10 ms^{-1}). Only Lake Superior shows a decrease in the year-to-year variation, with a negative change of up to 34% (29%) of the standard deviation projected for average (strong) conditions. This variability in wind speeds is primarily observed in fall (i.e. SON), when projected changes in wind speeds are highly variable according to the AOGCMs. Based on climatology (1950–2005; Schoof and Pryor, 2014), this season is characterized by a predominantly negative ENSO phase (La Niña conditions), which is associated with significantly stronger 10-m wind speeds over most of the US. Although further investigations should be conducted to describe the role of large-synoptic systems on the projected wind climate, current results suggest that the increased wind IV may be associated with the increased variability in large-scale circulation features projected by AOGCMs (e.g. Klink, 2007; Schoof and Pryor, 2014).

2.4.1.4. Change in spatial distribution

Figure 18 and Figure 19 show the spatial distribution of changes in mean annual daily wind speeds on the Lower and Upper Great Lakes, respectively, as well as the reference condition for the 1980–2009 period.

As observed in the baseline conditions (left panels of Figure 18 and Figure 19), high wind speed gradient is detected between land and open-lake areas, with winds $> 7 \text{ ms}^{-1}$ over lake points. The decrease in wind intensity projected by the lower bound of changes mainly affects the surface of lakes, with a variation that ranges between $(-0.26, -0.08) \text{ ms}^{-1}$, $(-0.27, -0.16) \text{ ms}^{-1}$, $(-0.24, -0.11) \text{ ms}^{-1}$ and $(-0.16, -0.03) \text{ ms}^{-1}$ in Lakes Ontario, Erie, Michigan-Huron and Superior, respectively (2.5th and 97.5th centiles). Lower values are less predominant in Lake Superior, where wind intensity is expected to decrease by less than 2% on average by the end of the century based on the lower-bound value. The climate signal for this lake is unclear, with projected changes ranging from -2% to 2%. Lake Superior remains the region in the Great Lakes where the greatest uncertainty in future wind climate can be expected, as shown in Figure 19. Similar conclusions regarding the spatial distribution of changes can be drawn for extreme winds and interannual variability (not shown).

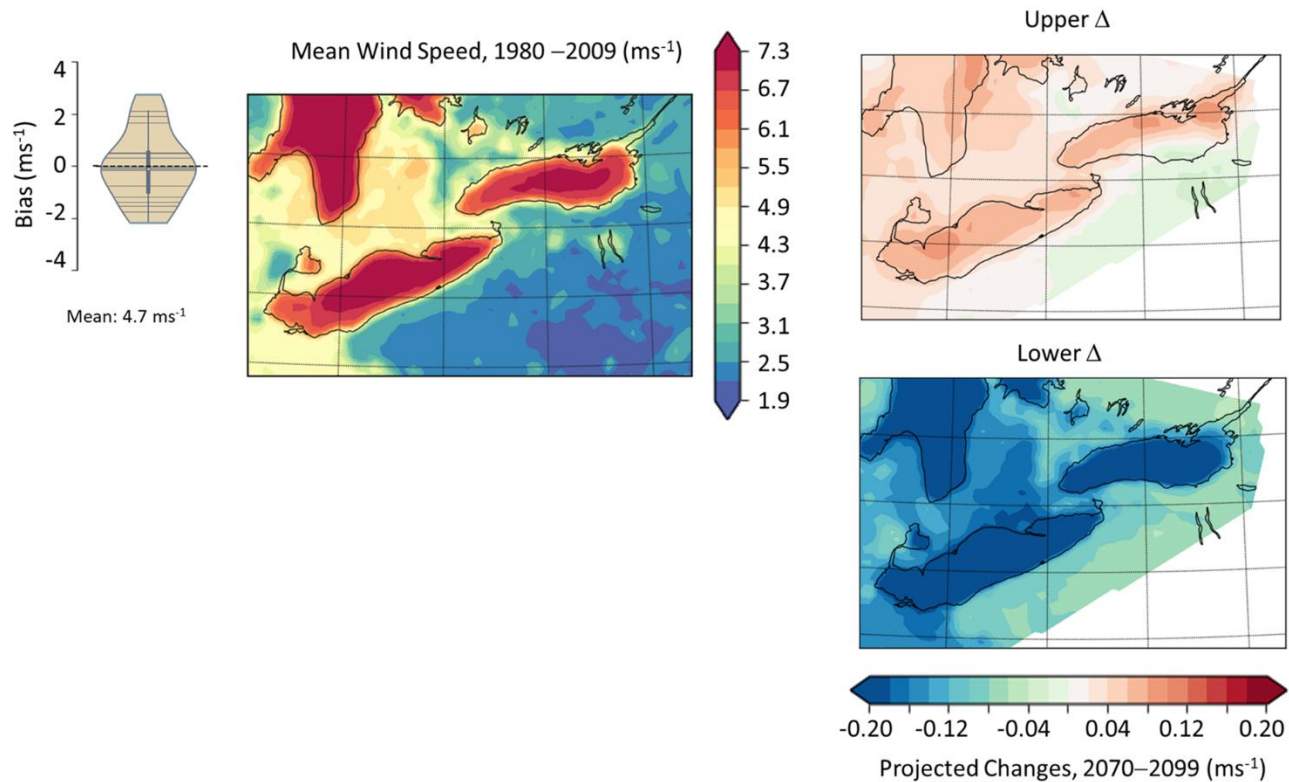


Figure 18: Left panels: Climate reference map for annual mean wind speed for the period 1980–2009 obtained from the reference product (Climex, cf. Section 2.3). The violin plot shows biases in grid points close to in-situ stations located near Lakes Ontario and Erie, and Mean gives the mean observed wind speed in stations. Right panels: The upper and lower bound of the projected change in annual mean wind speed for the period 2070–2099. Results are provided for the Lower Great Lakes.

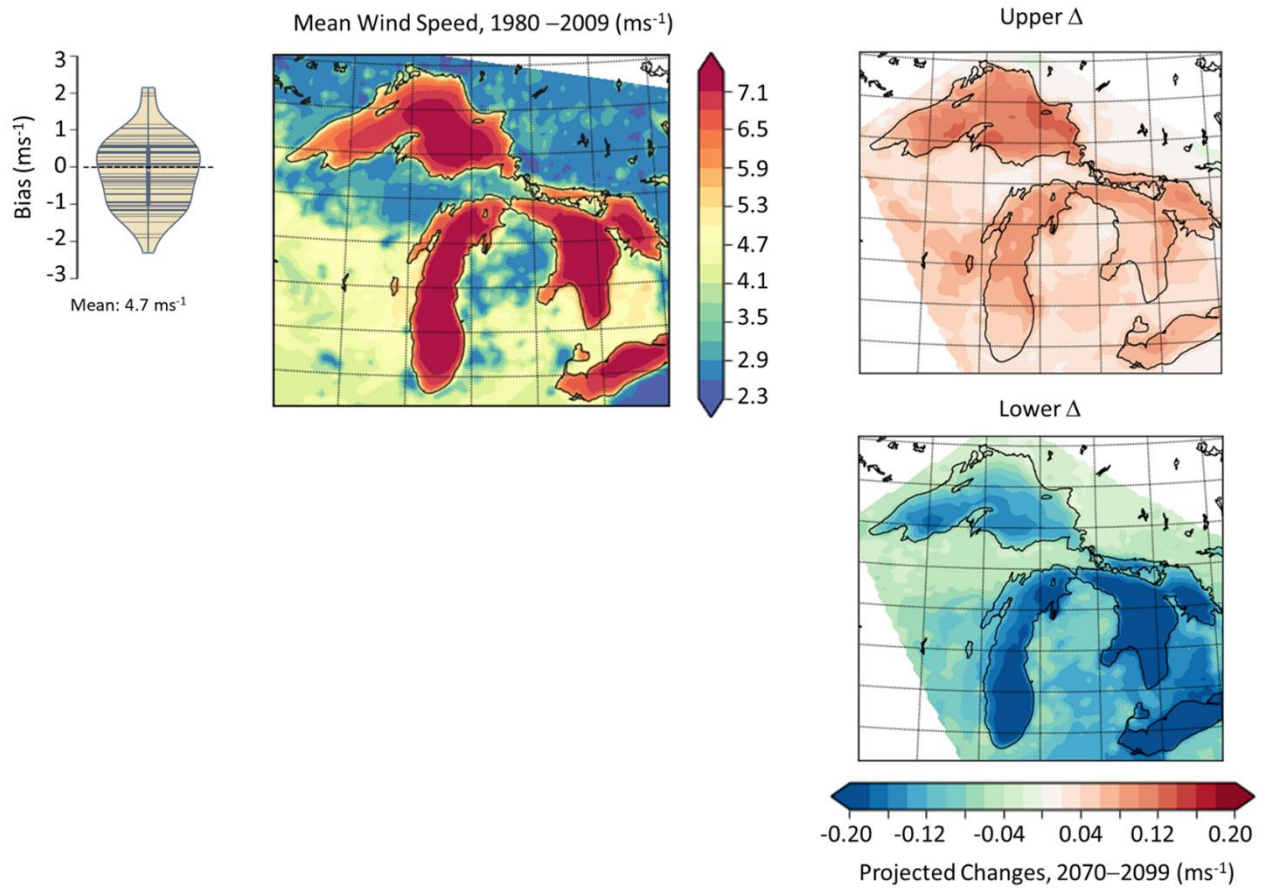


Figure 19: Idem as Figure 18, but for the Upper Great Lakes.

3. GREAT LAKES PHYSICAL MODELLING

Authors: Caroline Sévigny, Ph.D.; Rémi Gosselin, Ph.D.; Jean Morin, Ph.D.

3.1. Introduction

Lake modelling is used to inform wetland models on the spatial and temporal scales that characterize water level fluctuations on shorelines, where plants thrive. In this modelling approach, water levels are defined as the primary drivers of change for wetland distribution and species composition, as they integrate changes in environmental conditions, such as precipitation, evaporation, or air temperature (e.g.), which can trigger shifts in ecosystems. Because several aspects of lake dynamics are considered in this approach, this chapter is divided into sections that provide a detailed description of the physical processes observed in the Great Lakes (Section 3.2) and how they were parametrized in the CWRM framework (Sections 3.3 to 3.7). The modelling encompasses the observed annual and inter-annual variations in water levels at the basin (or lake) scale, as well as any fluctuations that modulate dry and wet cycles at local scales, over a period of days or less, which influence plant growth and survival. Thus, Sections 3.3 to 3.6 give a wide overview of the approach adopted to model changes in mean lake level (Section 3.3) and how this information is used to provide valuable knowledge regarding changes in short-term water level fluctuations and waves at the wetland scale (Sections 3.4 and 3.7). This includes the modelling approaches chosen to generate hydrodynamic and waves simulations, as well as the physical variables extracted from these simulations to instruct wetland models on nearshore dynamics. The final subsection (Section 3.8) is devoted to a broader description of the expected changes for the 2070–2099 period under the atmospheric scenarios used to create water level projections, which provide insights into possible future climate-related changes in the Great Lakes Basin in terms of physical variables.

3.2. Physical processes in the Great Lakes

The Great Lakes systems are dominated by their coastal nature. In this sense, they are often described as inland seas, since they share common physical processes with coastal oceans and are large enough to be influenced by the Earth rotation. Nevertheless, the Great Lakes remain closed basins, which strongly constrains the motion and gives rise to physical dynamics specific to large enclosed water bodies, namely the propagation of long, standing waves. The objective of this section is to describe the main physical processes that influence the water level fluctuations

in the Great Lakes and the approximations underlying the two-dimensional hydrodynamic modelling.

3.2.1. Surface motions

Horizontal motions in the Great Lakes are governed by an equilibrium between external forcing, Coriolis force and density gradients. When the focus is on the displacement of the free surface under forced motion, away from the lateral boundaries, bottom friction can be neglected. The Coriolis force is also much smaller than the frictional forces acting on the lake surface, the ratio between the two being inversely proportional to the square of the depth. In mid-latitudes, the Coriolis number, f , is about 10^{-4}s^{-1} , which induces a correction of the mean horizontal surface motions of scale larger than 100–200 km (which is reduced to a few kilometers for internal motions).

3.2.1.1. Wind set-ups and storm surges

A persistent, steady wind acting on a lake will generate a force on the surface well-mixed layer that is proportional to the frictional stress:

$$\tau = \rho_{air}u^2C_D \quad 3.1$$

which depends on the square of the wind speed, u , the drag coefficient, $C_D \sim 1 \times 10^{-3}$, and the air density at the lake-atmosphere interface, ρ_{air} . Since the water is constrained within the basin by the boundary conditions, a slope is created at the lake surface that is in equilibrium with the applied force at the ends of the lake. This generates a tilt that describes a decrease in water level along the upwind end of the lake and an increase (or set-up) along the downwind end (Figure 20). Under stable stratification, the surface layer moves freely over the subsurface waters, with stratification suppressing the transfer of the wind energy below the thermocline⁹. Onshore transport generated by the winds is therefore restricted to the upper layer, which is known as the Ekman transport.

⁹ When wind blows across a stratified lake, an opposing motion is created in the subsurface waters to compensate for the density gradient generated by the tilt of the thermocline (following initial surface waters displacement; Stevens and Lawrence, 1997). As nearshore waters are generally well mixed, this balancing transport occurs primarily in deeper basins.

A spontaneous change in atmospheric pressure can also generate a change in the surface slope. While the effect of wind is generally an order of magnitude greater than the pressure effect in coastal waters (typically 0–20 m) and in shallow lakes (e.g. Lake Erie), both effects are of equal importance in deeper parts of the lakes, where the depth exceeds 100 m. However, and apart from resonance effects¹⁰ (i.e. meteotsunamis; Donn, 1952, and Bechle *et al.*, 2016), the effect of the pressure gradient cannot exceed the water barometer, i.e., 10 cm of water for each 10 hPa of pressure. Typical large amplitude events (or storm surges) over the Great Lakes are associated with strong disturbances travelling from southwest to northeast, comparable in size to the lakes, so that the disturbance speed is just right to excite a wave of speed $(gh)^{1/2}$ in water of depth h , with g the gravitational force.



Figure 20: Steady wind set-up (in m) for a wind stress of 1.0 Pa in Lake Erie. Left panel: longitudinal response. Right panel: transverse response. After Hamblin (1987).

While the Great Lakes tend to be stratified in late summer (except for Western Lake Erie and Lake St. Clair), with a distinct thermocline in the upper 30 m (Rao and Schwab, 1976), they are predominantly unstratified during the winter-time, when cooling at the surface forces convective overturning motions. The absence of stratification and the higher wind speeds observed in late fall and winter generate large set-ups as the wind energy penetrates deeper into the water column and sets in motion a greater volume of water. According to Oort and Taylor (1969), the Great Lakes are characterized by a 2-day storm cycle, which is consistent with the typical mid-latitude cyclone passage period (2–4 days; Trigo *et al.* 1999). Since large lakes take several days to fully adapt to atmospheric forcing, and transit from one steady condition to another, the observed state

¹⁰ Resonance occurs when the dominant frequencies of the external forcing match the eigen frequencies of the basin.

of motion is the sum of previous wind events and the response to current ones. Only rare, large events occurring after a long period of calm can therefore be directly related to a specific wind episode.

3.2.1.2. Surface seiches and tides

Once the wind stress at the origin of the set-up stops, the relaxation of the lake surface generates a number of propagating disturbances or wave-like modes called *seiches*. These forced oscillatory motions are basin-scale barotropic standing waves with spatial patterns and periods dependent on basin geometry, water depth, and oscillatory resonance (Wilson, 1972). They can be visualized as constructive reflection of long, free-surface gravitational waves in a closed canal: when the waves are reflected at each end of the canal, only the waves whose incoming and outgoing components are in phase survive. Exclusively discrete values of wavelengths and (eigen) frequencies occur, while the amplitude of the oscillation varies in space, with zero-surface displacement at the nodes (called amphidromic points) and maximum amplitude at antinodes (Figure 21). While the frequencies and modal structure of the seiches are independent of the exciting force, their magnitude exhibits stochastic temporal variations depending on fetch, winds, barometric pressure, and time since the initial set-up. The restoring force of the seiches is provided by the gravity, which seeks to return the fluid surface to its equilibrium state.

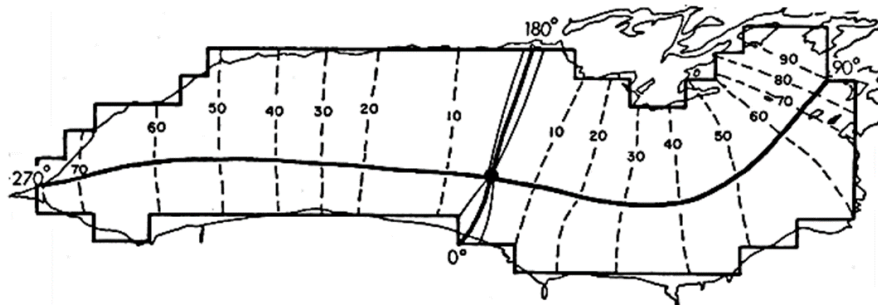


Figure 21: First gravitational normal mode for Lake Ontario, with one amphidromic point (black dot). The dashed lines indicated the relative amplitude of the free surface height, and the plain lines, the phase lag. For a nominal period of $\sim 5h$, a phase of 90° corresponds to a lag of $1.25h$. After Rao & Schwab, 1976.

In the Great Lakes, the free gravitational, barotropic waves are dominated by Poincaré and Kelvin modes, with frequency less or greater than f respectively. In narrow, deep lakes¹¹, rotation has a negligible effect on the period of the modes (Rao & Schwab, 1976) and the main disturbances are mainly longitudinal: pure transverse oscillations are only apparent for higher modes (Table 4).

¹¹ Lakes with mean depth h for which the Rossby radius of deformation, \sqrt{gh}/f , is much larger than their breadth.

The Earth rotation produces a cross-basin oscillation that lags behind the longitudinal motion, creating a counter-clockwise rotation of the disturbance around the amphidromic points (Figure 21). The relative importance of surface seiches thus varies within the basin and their maximum amplitude is not reached simultaneously from one point of the coast to another following a single wave disturbance. As for wind set-ups, several long-standing waves generated by distinct events may travel through the lake, generating complex constructive or destructive interferences. The free surface disturbances last several inertial periods, i.e. $1/f$, even days (Wilson, 1972; Csanady, 1968), before fading due to bottom frictional effects and stratification when internal gravitational motions are present (Cushman-Roisin *et al.*, 2005). Their amplitude decays at a rate of 50% per cycle (Bolsenga and Herdendorf, 1993), which reduces their detectability over time. Table 4 gives the period of the main seiche oscillation modes for the five Great Lakes. The fundamental mode, which is the mode with the lowest frequency or longest period, is usually the main disturbance that explains the amplitude of observed surface seiches in the major Great Lakes' basins.

Table 4: Published seiche oscillation modes (in hours) for the five Great Lakes. After data compiled by Trebitz (2006).

Mode	Ontario	Erie	Huron	Michigan	Superior
L1	4.9–5.1	14.1–14.4	6.5–6.7	8.8–9.12	7.8–7.9
L2	2.9–3.2	8.9–9.1	4.6–5.3	5.0–5.3	4.5–4.8
L3	2.3–2.4	5.7–5.9	3.5–3.8	3.5–3.8	3.6–3.8
L4		4.1–4.2	2.9–3.2	2.9–3.2	3.2–3.4
L5		3.6–3.7	2.3–2.5	2.3–2.5	2.9–3.0
L6		3.0			2.2–2.6
L7		2.5			
L8		2.2			
T1				2.2	

The Great Lakes have complex shorelines, with multiple small adjoining bays, gulfs, inlets, and harbours. The main-basin oscillations are affected by, and drive oscillations in, these small extents of water. These zeroth-mode oscillations, also known as Helmholtz modes (Rabinovich, 2009), are characterized by nodes near the entrance of the partially enclosed water bodies and peak amplitude toward their ends. These specific modes, which are similar to the fundamental tone of an acoustic resonator, may be imperceptible in the main basin when the attached bay is small relative to the lake. Green Bay in Lake Michigan (Rao *et al.*, 1976), Georgian and Saginaw Bays, and North Channel in Lake Huron (Schwab and Rao, 1977; Suzuki *et al.*, 1995), as well as Frenchman's Bay in Lake Ontario (Hlevca *et al.*, 2015), display similar oscillation signatures.

Trebitz *et al.* (2006) conducted a thorough examination of the detectable frequency components in measured water levels for the five Great Lakes, at each of the gauging stations located on the Canadian and US shores. Their analysis reveals perceptible non-tidal spectral peaks that correspond to the published seiche oscillation modes (with exception of the peak below a 2h frequency, which remain undetectable with hourly data). The seiche signature is generally strong in Lakes Erie and Superior at most stations, but generally weak in Lakes Huron, Michigan and Ontario.

Although not as significant as in larger seas, astronomic tidal motions (mainly diurnal and semidiurnal) are also present in the Great Lakes, with amplitude of only few centimetres. As their importance is much less than other long-term or short-term physical processes that modulate the water levels, the Great Lakes are generally considered non-tidal.

3.2.2. Water levels: Interannual variability, long- and short-term variations

Over the past decades, Great Lakes mean water level has shown major interannual variations related to weather-scale processes and potential climatic connections, which are responsible for long-term precipitation and evaporation patterns, as well as stage-dependent outflow (Hanrahan *et al.*, 2010; Watras *et al.*, 2014; Assani *et al.*, 2016; Ghanbari *et al.*, 2008; Fu and Steinschneider, 2019). Since the beginning of the official period of records in 1918, Great Lakes experienced extremely low levels in the late 1920s and the mid-1960s and extremely high levels in the 1970s and 1980s. Historic highs have been reached in recent years, however, with historic highs observed in 2017 and 2019 (Lakes Ontario, Erie, St. Clair and Superior) and 2020 (Lakes Michigan and Huron), following the increasing trend seen in the basin since 2013 (<https://www.lre.usace.army.mil/Missions/Great-Lakes-Information/>). Over the past 100 years, annual mean water levels have varied by up to 2 m on the lakes below Superior, with cycles of several years (near- decadal oscillation; Figure 22).

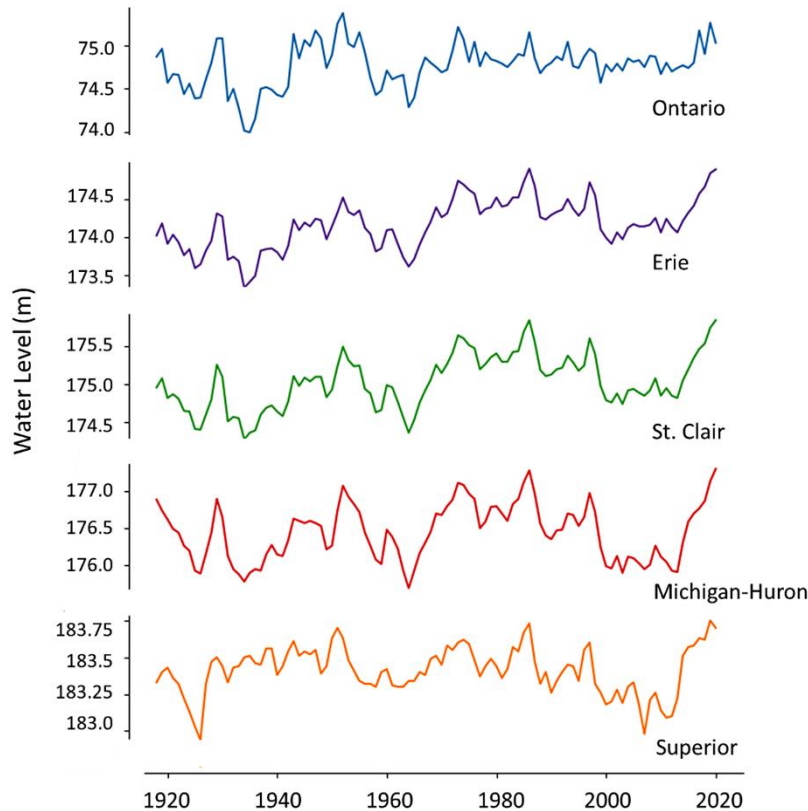


Figure 22: Observed average annual lake levels for the period 1918–2020. From the NOAA Great Lakes Environmental Research Laboratory (GLERL) Dashboard (https://www.glerl.noaa.gov/data/dashboard/data/levels/1918_PRES/).

3.2.2.1. Observed water levels: High- or low-frequency components

On an annual basis, water level fluctuations in the Great Lakes exhibit long- and short-term variations that are related to physical processes unique to these large, enclosed water bodies. The long-term, annual and seasonal variation of the free-surface elevation is primarily controlled by the net basin supply, which is the balance between basin runoff to the lake, over-lake precipitation, over-lake evaporation, and inter-basin inflow and outflow from connecting channels (or inter-basin diversion). Any change in the water storage explains the variations experienced by the lake over a year, which typically range from 20 to 40 cm, with the maximum level being reached in July–September and the minimum at the end of winter, in February–March (<https://glisa.umich.edu/>). This monthly and seasonal variation can be highlighted in the recorded water levels using a low-pass filter (Butterworth), which allows the extraction of long fluctuations of a 30-day period or more. The top panel of Figure 23 shows the result of this filtering for the Lake Erie water level time series, with the green line indicating the seasonal cycle (i.e. trend extracted by using a low-pass filter).

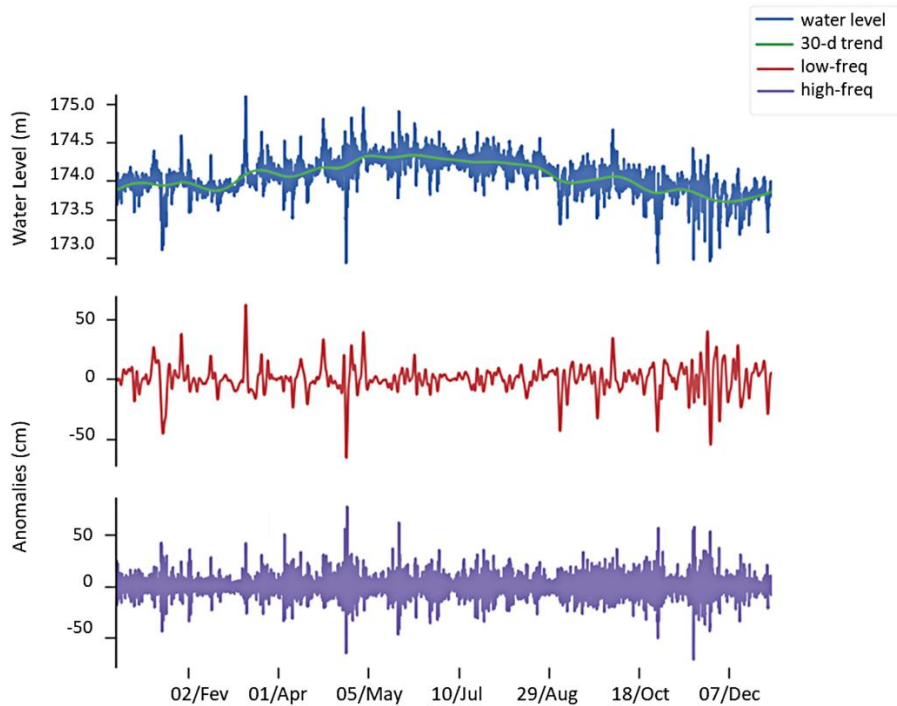


Figure 23: Recorded water levels in 2017 at station Toledo, Lake Erie. The top panel gives the water level as recorded (in blue), as well as the long-term, seasonal trend (in green). The bottom panels explicit the anomalies, i.e. the low- (red; periods > 2 days) and high- (purple; periods < 2 days) frequency components extracted from the recorded signal. Details are given in the text.

Once the seasonal cycle is removed from observed water levels (i.e. subtracting the seasonal cycle from the original time series), the remaining anomalies reveal variations that are characteristic of the Great Lakes hydrodynamics and can result in amplitude of up to a meter. These episodic and periodic events can be classified into two specific categories according to the temporal scale of their main features:

1. Fluctuations of period > 2 days: The low-frequency components of the anomalies are generated by the atmospheric forcing, i.e. winds or atmospheric pressure changes that generate set-ups and storm surges. The characteristic period of these anomalies is longer than two days, which is consistent with the typical period of midlatitude storms (Figure 23, middle panel).
2. Fluctuations of period < 2 days: The high-frequency components of the anomalies include all events with a period of less than two days, which generate the shortest detectable variations in water level records. Several events can be listed in this category, such as tides, surface seiches, waves, and any local disturbance that can modulate the observed water levels. However, since time series are generally recorded on a temporal scale of several minutes and filtered to a period of 1 hour to remove any undesirable noise, waves and short-term disturbances are not present in the water level time series (Figure 23, lower panel).

The close correlation between atmospheric events and low-frequency anomalies are revealed by the spectral signature of the observed wind speeds and water levels at a specific location. Examples are given in Figure 24 for data recorded at station Toledo, in Lake Erie, between June and September 2017 (Figure 24, top panel inset). As shown in the middle panel of Figure 24, the wind speed observed at the meteorological station (black line, positive axis pointing downward in Figure 24) is well in phase with the low-frequency water level anomalies (green line), i.e. spectral components with periodicity greater than two days. Abrupt changes in wind intensity and direction can initiate local water level fluctuations, but are unlikely to transfer sufficient energy to the surface mixed layer to establish a basin-scale motion. Only large, synoptic-scale atmospheric systems that cross the Great Lakes area and generate strong wind speed are prone to trigger a set-up. Smaller atmospheric disturbances, smaller in scale than the lake, are observed as “noise” or interference superimposed on the basic anomalies pattern (Harris, 1953).

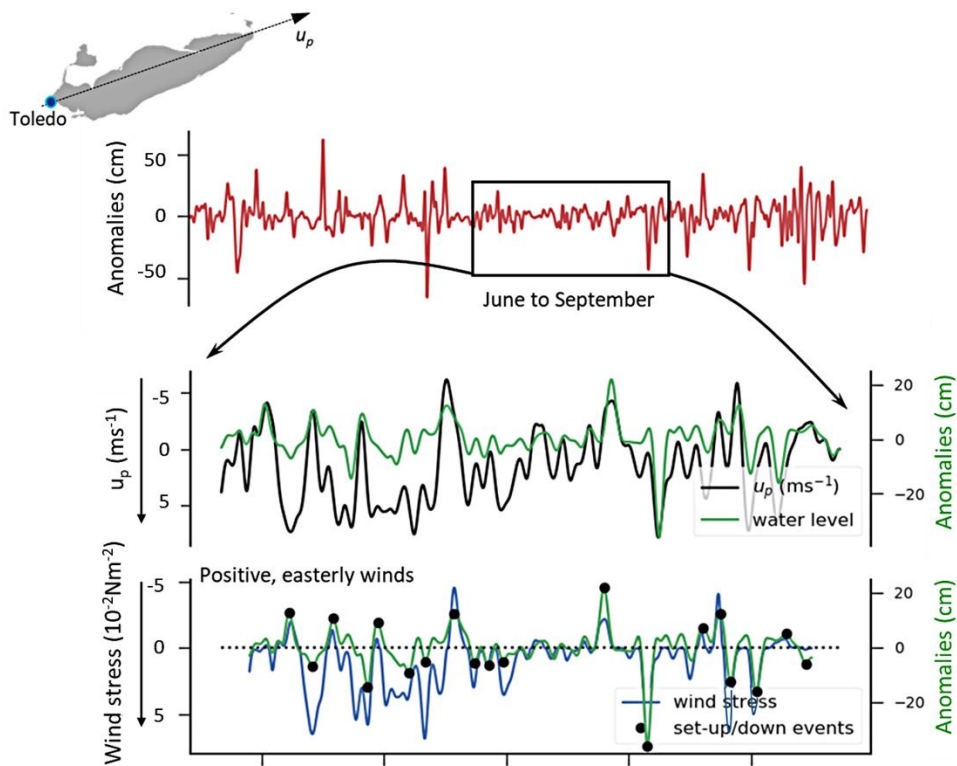


Figure 24: The low-frequency water level anomalies (top panel) recorded at station Toledo (Lake Erie), in 2017. The anomalies observed between June and September are shown in the middle panel (green line), as well as zonal wind component along the main axis of the lake, u_p (black line). The bottom panel highlights set-ups events of amplitude > 5 cm (black dots) detected from anomalies (blue line) and computed wind stress (green line).

The wind speed in Figure 24 refers to the magnitude of the zonal wind component along the main axis of the lake, u_p (i.e. along an axis that joins the western and eastern ends of the lake; image at top of Figure 24), which better describes the winds blowing across the lake in the direction of maximum fetch. A positive u_p is observed under easterly winds. In such conditions, the wind stress, $\tau = \rho_{air} u_p^2 C_D$, acting on the lake surface generates a decrease in water levels at the western end of the lake, which is detected at station Toledo (i.e. negative anomalies)¹². The spectral coherence derived from in-situ time series displays statistically significant amplitude for periodic components with a period of two days or more (frequency of 0.5 day⁻¹; Figure 25), attesting to the intrinsic temporal scale of the lake response to wind forcing. Inspection of the choice of the principal axis used to calculate the zonal wind component shows an increase in coherence amplitude for a rotation of the coordinate system of $\sim 18.6^\circ$ (winds blowing to 71.4° ; inset Figure 25b), close to the rotation angle of the axis that joins the two ends of the lake (18.2°).

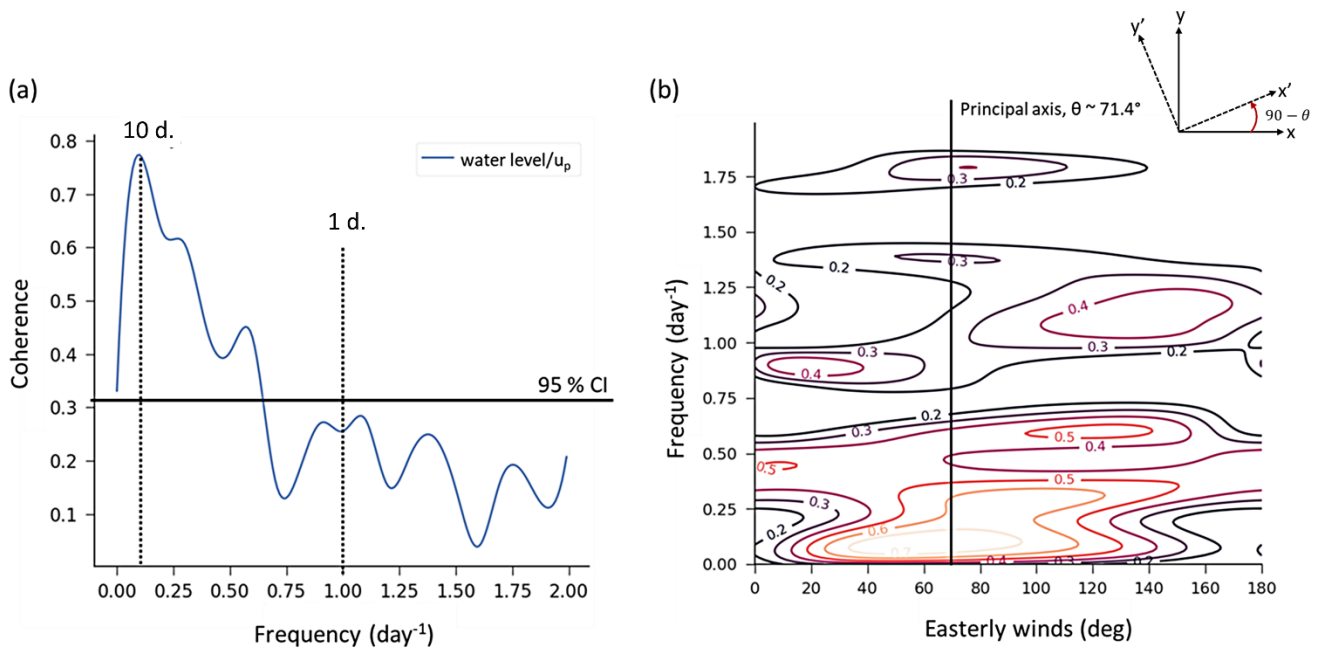


Figure 25: (a) The spectral coherence computed from low frequency anomalies and zonal winds recorded in station Toledo, in 2017 (cf. Figure 24). The black, horizontal line gives the 95% confidence level for coherence amplitude significance. (b) Coherence amplitude map for a variable principal axis, i.e. the angle of rotation of the coordinate system used to compute the zonal component of the wind, u_p . The angle refers to a counter-clockwise rotation of the coordinate system by an angle of $90 - \theta$, with θ the wind vector azimuth (i.e. the direction towards which the wind is blowing).

¹² Conversely, an increase in water levels at the eastern end of the lake generates positive anomalies at station Toledo.

Since winds and low-frequency anomalies are well correlated, wind set-up events can be detected in the time series of all stations in the Great Lakes Basin. A set-up is identified at a gauging location if the winds recorded at a nearby weather station show an increase (decrease) that is in phase with the fluctuations observed in the low-frequency water level anomalies. To do so, a low-pass Butterworth filter is applied to the observed time series to remove periodic components with a period of two days or less (i.e. high-frequency anomalies). Since phase-lag (or time-lag) is observed at periods of significant coherence amplitude, the maximum time allowed between the detected winds/anomaly maxima is 24 hours. A short analysis was conducted on several gauging stations in Lakes Ontario, Erie, and Huron to quantify the characteristic set-up amplitude for the reference period, i.e. 1980 – 2010. The results are summarized in Table 5 (left columns), with detailed statistics of the monthly range and annual maximum amplitude of the events identified in the 30-year period. The maximum was chosen rather than mean since it is these occasional, but significant, events that carry enough energy to initiate significant surface seiches (discussed below). Georgian Bay and the North Channel of Lake Huron (referred to as NC in Table 5) were considered separately as several complex oscillation modes exist in these connected bays.

Table 5: Statistics of the observed wind set-ups and surface seiches for 17 stations in the Great Lakes Basin, for the period 1980 – 2010. The mean amplitude of the maximum set-ups is given (left columns), as well as the mean amplitude of the free surface oscillations, i.e. half the mean of the log-normal distribution of daily-range values (right columns). The monthly range provides the minimum and maximum monthly means, while annual values prove the

annual mean of the distribution, with first and third quantile in brackets. All values are in centimetres. Details are given in the text.



	Maximum Set-Ups		Surface Seiches	
	Monthly Range (cm)	Annual (cm)	Monthly Range (cm)	Annual (cm)
Lake Ontario				
Toronto	2.3 – 6.6	4.3 (2.7 ; 5.5)	2.6 – 3.6	3.1 (2.8 ; 3.4)
Cobourg	1.7 – 4.1	3.0 (2.0 ; 3.8)	2.4 – 3.3	2.9 (1.8 ; 4.5)
Kingston	2.1 – 7.6	4.9 (2.8 ; 6.4)	2.4 – 3.8	3.1 (2.6 ; 3.5)
Rochester	1.8 – 3.5	3.0 (2.2 ; 3.7)	2.4 – 5.8	2.7 (2.4 ; 3.7)
Lake Erie				
Toledo	16.1 – 41.9	26.6 (13.8 ; 35.5)	11.2 – 16.1	12.9 (11.4 ; 14.2)
Erieau	2.5 – 9.0	5.1 (2.6 ; 6.8)	3.6 – 5.2	4.2 (3.7 ; 4.6)
Buffalo	10.9 – 47.0	27.0 (12.2 ; 36.6)	9.0 – 15.0	11.1 (9.3 ; 12.3)
Cleveland	3.8 – 11.9	8.0 (4.4 ; 10.6)	4.6 – 6.4	5.2 (4.5 ; 5.7)
Huron-Erie Corridor				
Amherstburg	6.0 – 17.6	12.1 (6.6 ; 15.9)	4.8 – 6.7	5.6 (5.0 ; 6.1)
Lake St. Clair Shores	2.9 – 7.5	5.3 (1.1 ; 6.7)	0.8 – 2.2	1.8 (0.6 ; 2.1)
Lake Huron				
Essexville	12.0 – 23.0	19.3 (12.4 ; 22.5)	5.2 – 7.4	6.7 (6.1 ; 7.3)
Mackinaw City	3.3 – 9.1	5.7 (3.9 ; 7.1)	4.2 – 5.1	4.6 (4.2 ; 4.8)
Tobermory	4.7 – 11.9	8.3 (5.6 ; 10.0)	1.7 – 2.3	2.0 (1.8 ; 2.2)
Fort Gratiot	6.9 – 17.8	13.0 (8.3 ; 16.6)	5.7 – 7.0	6.3 (5.7 ; 6.7)
Georgian Bay and North Channel				
Thessalon (NC)	4.0 – 10.2	6.9 (4.5 ; 8.5)	3.2 – 4.8	4.0 (3.5 ; 4.3)
Parry Sound	7.9 – 23.3	13.4 (8.6 ; 15.4)	2.9 – 5.2	3.9 (3.3 ; 4.4)
Collingwood	5.8 – 18.7	12.9 (7.9 ; 15.6)	3.2 – 5.4	4.5 (4.0 ; 5.0)

As expected, the maximum set-up amplitude is observed at the ends of the lake major axis, with the largest events recorded in Lake Erie (up to 27 cm), the shallowest lake. Mackinaw City, which is the northern end of Lake Huron, is the exception. The fetch in the Straits of Mackinac, which connects the northern portion of Lakes Huron and Michigan, is limited and unfavourable to the development of water level disturbance (Donn, 1959; Mason *et al.*, 2018). Essexville (Saginaw

Bay) and Parry Sound, located at the end of semi-enclosed shallow bays in Lake Huron, show major events, with anomalies of up to 19 and 13 cm, respectively. The dynamics of these small bays are highly complex and respond to local winds (Saylor and Danek, 1977) as well as lake motion, which acts as an additional forcing term for the set-up (in addition to the wind stress and atmospheric pressure gradient; Harris, 1953). Although there is evidence of transverse (north-south) displacement of surface waters in Lakes Ontario and Erie (i.e. at stations Cleveland and Rochester), the corresponding rise (or fall) in water level is rather small, especially in Lake Erie. An interesting observation is the detection of set-up events in the Detroit River, at station Amherstburg (Huron-Erie Corridor). Water level rises (or declines) in this connecting channel are correlated with westerly (easterly) winds: the set-ups generated in Lake Erie are thus felt beyond the mouth of the river, which creates a dynamic that is reminiscent of maritime channels. This signal is no longer perceptible in Lake St. Clair, which is itself subject to the effect of wind stress, with typical events of 5.3 cm.

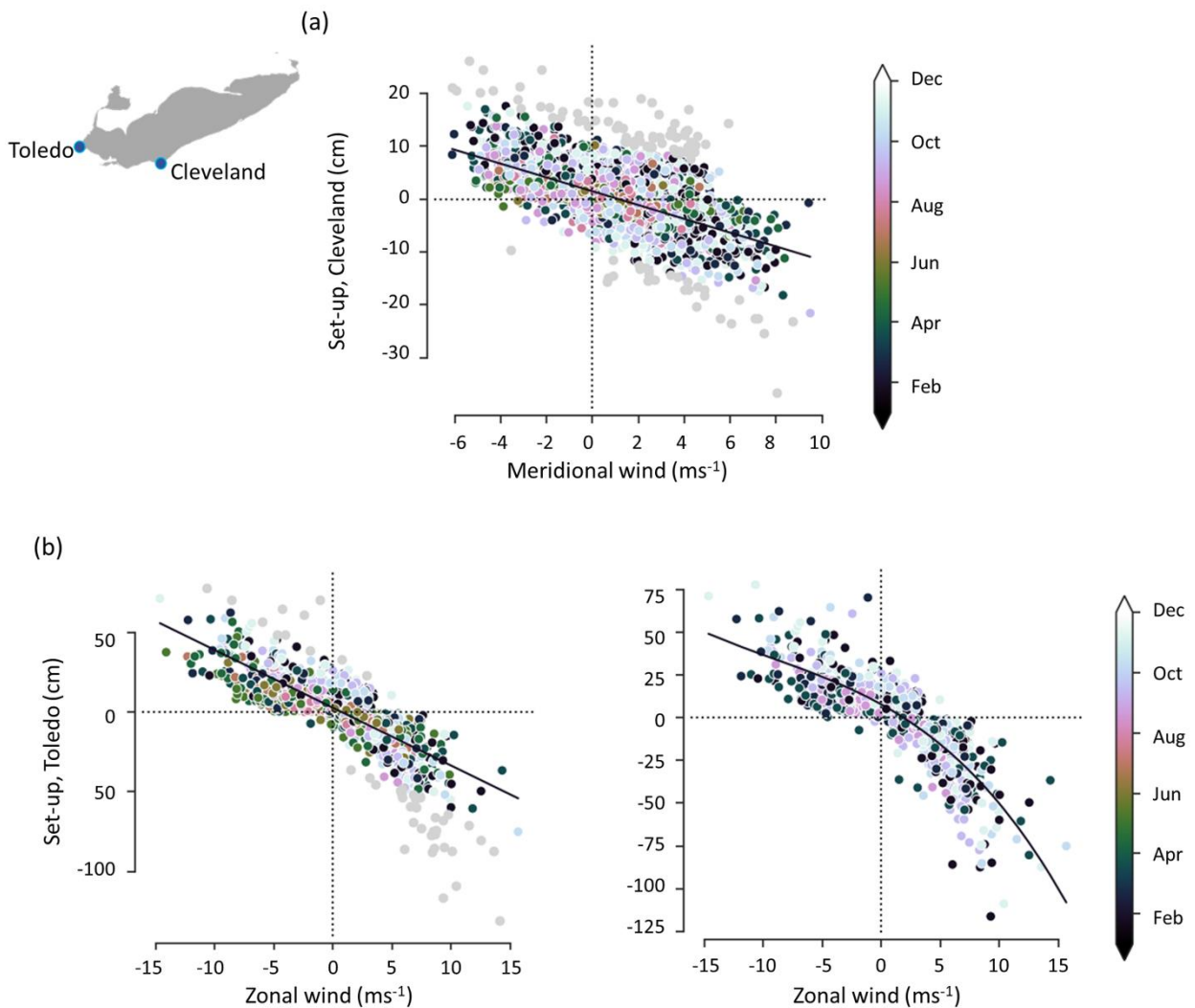


Figure 26: The amplitude of the wind set-ups detected at Cleveland (a) and Toledo (b), in Lake Erie, between 1980 and 2010, versus the magnitude of the winds responsible for the water level rise/fall (i.e. the maxima observed in the low-frequency anomalies). The dot color indicates the months in which the events were observed, while the black lines describe the linear (a, and b, left panel) or cubic (b, right panel) relation between set-ups and wind speeds. Gray dots are outliers, i.e. events that do not follow the linear trends in (a) and (b). For Toledo (b), all detected events, regardless of the month, are shown in the left panel, while only events detected during the fall and winter seasons are kept in the right panel.

At most stations, a linear correlation can be observed between the zonal (or meridional for stations Cleveland and Rochester) wind component and the low-frequency anomalies, which is obvious for stations showing the largest events (e.g. Toledo; Figure 26). For Lake Erie stations, the correlation between wind and set-up deviates from its linear trend when recorded wind speeds rise above 10 ms⁻¹. The anomalies amplitude then exhibits an exponential (or quadratic) behaviour, which is especially noticeable during the fall (September–November) and winter

seasons (December, January, and February; Figure 26b, right panel) when strongest winds occur (Zhong *et al.*, 2010). Figure 27 shows the monthly change in set-up amplitude for two stations of Lake Erie. The more intense the winds (Figure 27, top panels), the deeper the frictional force (or wind stress) acting on the lake, creating a deep upper Ekman layer in which forced motions are constrained. Typical values of Ekman depth (or depth of frictional influence) in mid-latitude range from 50 to 100 m for wind speed of 10 and 20 ms^{-1} when the stratification is weak or absent (Pond and Pickard, 1983). Strong winds set in motion a deeper portion of the surface waters, resulting in large wind set-ups, such as those observed in December at the Toledo station (Figure 26 and Figure 27; with maximum events of ~ 1 m). Severe and long-lasting storms can also generate a deepening of the well-mixed surface layer, allowing greater penetration of wind energy into upper layers¹³. When the lake is shallow, as is the case for Lake Erie, the entire water column can be moved under extreme wind conditions. The lake then acts as a single-layer system, which may explain the behaviour observed when nearshore winds reach a nominal speed $> 10 \text{ ms}^{-1}$ (Figure 26b).

¹³ As stated by Monismith (1985), it is the relative magnitude of mixed-layer acceleration induced by the wind stress and deceleration due to the developing baroclinic pressure gradient (internal modes of motion) that determines the fluid motion.

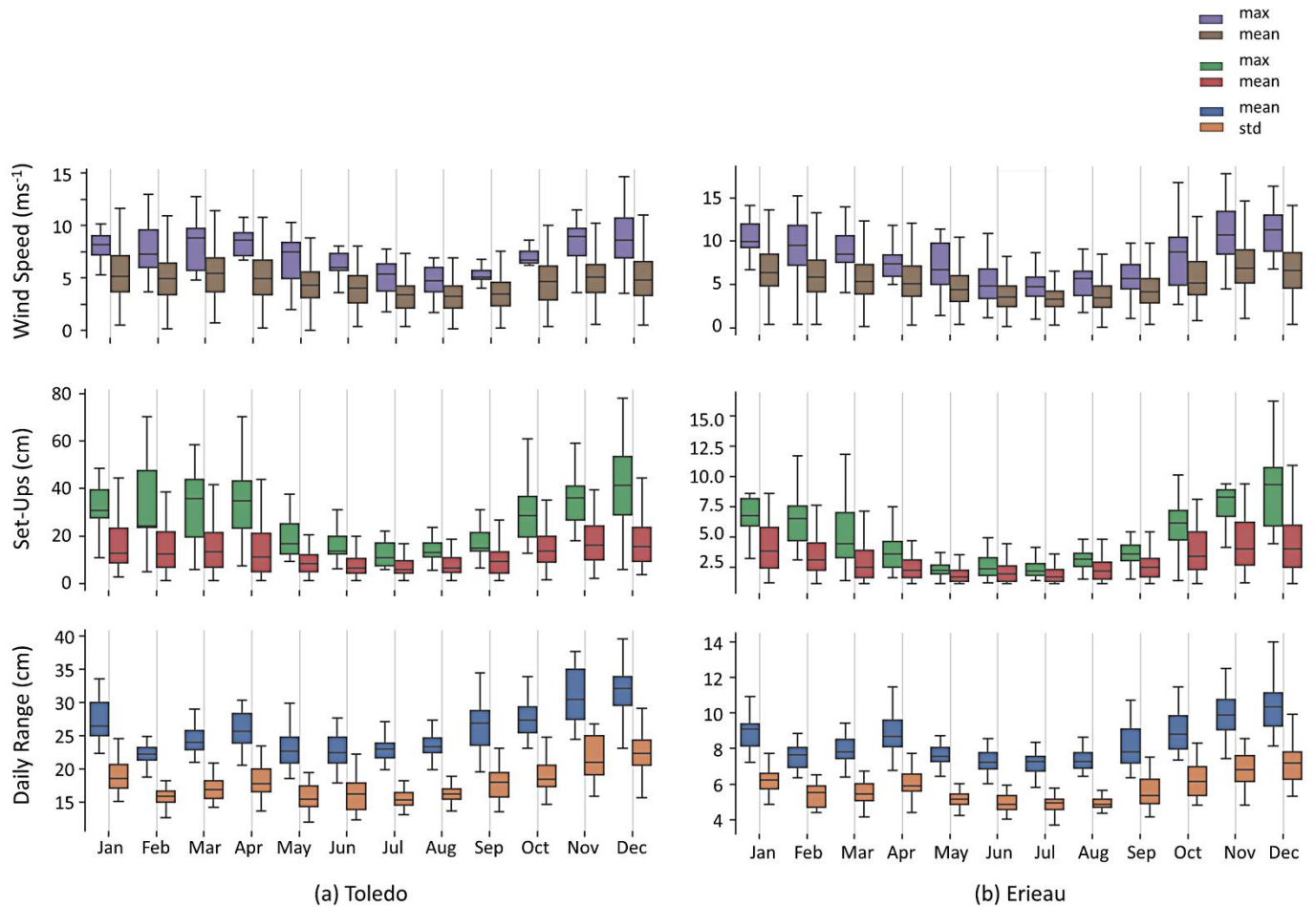


Figure 27: Monthly wind set-ups and surface seiches amplitude statistics for two Lake Erie stations, Toledo (a) and Erieau (b). From top to bottom: distribution of monthly wind speed observed during maximum (purple) and mean (brown) set-up events, at nearshore stations; distribution of monthly mean (red) or maximum (green) set-up amplitude; and mean and standard deviation of the log-normal distribution of daily range values for the period 1980–2010. The amplitude of the oscillation can be estimated as twice the daily variation.

Since the high-frequency anomalies observed in the recorded time series are primarily related to surface seiches, an analysis similar to that conducted for the set-up events can be used to quantify the importance of these free surface oscillations. In this case, a high-pass Butterworth filter is applied to in-situ water levels to extract all fluctuations with periods less than two days. Because basin-scale oscillations are not directly initiated by winds and may last several days after the initial surface water displacement, it is impossible to isolate single events. An approach similar to that used by Trebitz (2006) was therefore adopted, i.e. estimating the daily range fluctuations of high-frequency anomalies, defined as the difference between the maximum and minimum value on any given day. As the daily anomalies range distribution follows a right-skewed, log-normal shape (with few large anomalies related to major events), the mean and the standard deviation of the

log-n distribution for each day-of-year were estimated for the time series ranging from 1980–2010. Table 5 and Figure 27 show the results obtained, with the seiches amplitude, estimated as half the mean daily range, reported in Table 5 instead of the daily range statistics for ease of comparison.

As illustrated in Table 5, the amplitude of free surface oscillations in the Great Lake Basin is consistent with the amplitude of the observed set-ups: the largest surface seiches are predominantly detected at the head of the lakes and in shallow coastal embayments. While the former can be explained by the spatial pattern of the dominant seiches mode (e.g. Figure 21), the latter is due to harbour mode, which acts as a Helmholtz harmonic resonator that amplifies the basin-wide oscillations. Lake Erie shows the most striking empirical evidence of free-surface oscillations, with a mean surface seiche amplitude of up to 16 cm, resulting in a daily water level change of over 30 cm. Again, fall and winter are the more active seasons, but with a slight decrease in magnitude of high-frequency anomalies in February and March during the peak ice cover period (Wang *et al.*, 2012; Farhadzadeh, 2017; Figure 27). The lake's ice cover promotes turbulent friction at the ice-water interface that dissipates the kinetic energy carried by the long-period waves and dampens oscillations (and modifies seiche periods; Zyryanov, 2011). As for the wind set-ups, typical Lake Erie seiches (period of ~14 h) are detectable in the Detroit River (Amherstburg; Table 5), with an amplitude of 5.6 cm. Lake St. Clair, which acts as a damper for oscillations coming from the St. Clair (Lake Huron) and Detroit Rivers (Lake Erie; Jackson, 2016), reveals only small oscillations that remain less than 2 cm (Table 5).

Finally, the water level fluctuation associated with the anomalies is the sum of wind set-up and surface seiches, resulting in an overall daily variation of up to ~16, 80, and 40 cm in Lakes Ontario, Erie, and Huron, respectively (excluding Saginaw Bay and Parry Sound). In contrast to the seasonal variation in lakes, which induces a fluctuation of 20 to 40 cm on average, these combining effects can have major influence on wetland dynamics, especially for wetlands located in the lower reach of tributaries that are mainly affected by major changes in lake level (called freshwater estuaries; Brant and Herdendorf, 1972; Herdendorf, 1987).

3.2.3. Two-Dimensional hydrodynamic modelling

The Great Lakes hydrodynamics behavior is primarily three-dimensional, with basin-scale processes influenced by stratification as observed in coastal oceans. The lakes' thermal structure, however, is highly variable by time of the year, ranging from nearly well-mixed waters in winter

(November–April) to progressively stratified waters in summer (May–October). While vertical gradients are negligible in winter, and the circulation is almost entirely wind-driven, several density layers can form in summer and favour baroclinic processes. The dominant processes also differ between nearshore areas, defined as the region between the wave-breaking zone and the open lake, and deep, central basins. In the former, frictional forces are the main physical components of motion, and wind is the primary driving force. This shallow area tends to be well-mixed due to wind action (and frequent upwelling or downwelling events along the coasts), which rarely displays long-term persistence and generates a highly transient coastal state. In the latter, pressure gradients and Earth rotation (i.e. Coriolis force) are important, and several complex processes can emerge following initial movement of surface waters and persist over several days (e.g. internal seiches, gyres circulation). The distance between the nearshore and offshore dynamics depends on wind stress and bathymetry (Csanady, 1981) and is typically on the order of 3 to 5 km (Rao and Schwab, 2007).

When focusing on water level fluctuations, without attempting to detail general circulation patterns and vertical transport, the primary concern is on active processes in the surface well-mixed layer. While wind stress moves the surface waters on a time scale of hours to days, stratification counteracts any displacement at the thermocline depth, and the surface layer can be considered as moving freely. Wind set-ups and surface seiches can hence be modelled using a single-layer, homogeneous model, reducing the modelling approach to a two-dimensional problem (neglecting the vertical dimension). The interference that develops at the base of the well-mixed layer by differential motion of the lower waters (i.e. internal seiches; Cushman-Roisin *et al.*, 2005) is considered negligible, although it may influence the damping of long-standing, surface oscillations to some extent¹⁴. The deepening of the surface mixed layer under sustained and intense winds that promote mixing of denser water below the thermocline is also neglected. The surface layer depth is kept equal to the water column depth (except in the special case of scenario-based modelling, c.f. Section 3.4.2.3): atmospheric forcing acts from the surface to the bottom in nearshore and offshore areas, and water displacement is obtained by considering vertically integrated quantities. While this assumption is reasonable to a first approximation in shallow lakes such as St. Clair (which averages ~3 m in depth, respectively), it becomes unreliable for deeper lakes during periods of strong stratification. A similar two-dimensional, vertically integrated approach has been used in the past to model surface seiches (and wind set-ups) in large lakes,

¹⁴ Primary damping of surface seiches is due to frictional effects between the water mass and the lake bed.

e.g. Zacharias and Ferentinos (1997; Lake Trichonis, Greece), Cueva *et al.* (2019; Lake Chapala, Mexico), and Roberts *et al.* (2019; Lake Tahoe, USA).

3.2.4. Surface gravity waves

A wind acting upon the water surface generates several classes of waves with a typical period of less than one minute. Under small atmospheric pressure fluctuations and wind friction, the surface is first disrupted by small ripples called *capillary waves* for which surface tension is the main restoring force. Their periods are shorter than 1/4 s and wavelengths, less than 10 cm. As soon as the wind has a stronger effect on the water, which depends on the wind speed and surface roughness, wavelets covering a wide range of wavelengths are produced (from 0.1–1500 m in deep water). The latter have a period of more than 1/4 s and their prime restoring force is gravity, which is why they are called *gravity waves*. When generated by local wind, these waves have an irregular, short-crested form, creating a sea state often referred to as *wind sea* (Figure 28). Once they leave their generation zone, the waves take on a regular, long-crested shape, forming the *swell* that can be encountered in the ocean. Swells are fast-travelling waves that disperse across the basin with little attenuation (Kantha, 2006).

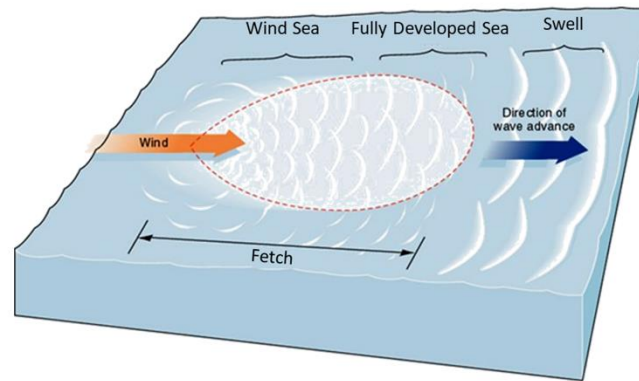
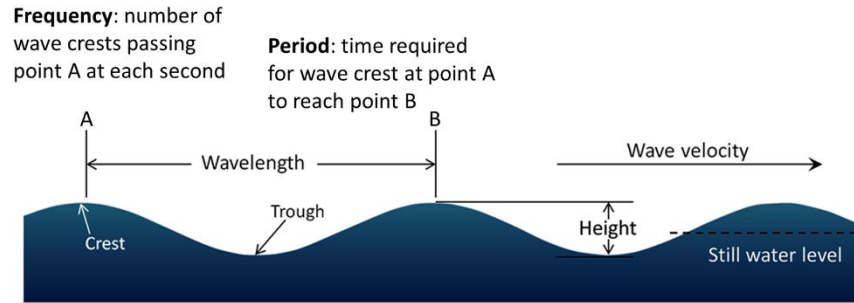


Figure 28: Top panel: Definition of wave parameters. Adapted from <https://opentextbc.ca/geology/chapter/17-1-waves/>. Bottom panel: Generation of surface waves. Adapted from Garrison (2012).

The Great Lakes are semi-enclosed basins with relatively shallow depth compared to the oceans. The wave dynamics of these large inland lakes are therefore slightly different from that generally observed in coastal areas. First, the fetch¹⁵ size and propagation distance are limited, which significantly constrains the development of lower frequencies (or long periods) and give a prominent role to short waves. The Great Lakes are thus characterized by a wind-sea-dominated wave climate, with moderate swell contributions (Hands, 2018), and wave periods that rarely exceed 10 s (Thompson, 1980). Under similar conditions, waves grow quite rapidly, forming what is known as *young sea state* where waves remain underdeveloped (except in light winds). Second, the average wind stress experienced by lakes is higher than that typically observed in oceans, which is a direct consequence of the (young) wave state (Donelan, 1982; Boyce, 1989): the longest waves in an undeveloped sea are much steeper than their fully developed counterparts, which increases the roughness of the wind sea. The wave spectrum, which describes how the variance in lake-surface elevation is distributed over the frequencies of the

¹⁵ In open-sea conditions, wave generation is limited by the extent of the atmospheric disturbances, which determine the fetch length.

waves that create the surface fluctuations (Holthuijsen, 2010), hence shows an enhanced peak amplitude at higher frequencies than the commonly used spectral form. The energy transfer between wind and sea can account for a significant fraction of the total stress at the spectral peak (Donelan, 1990). Finally, because shallow water areas occupy an important portion of the Great Lakes, wave dynamics are significantly affected by the depth-induced (surf-)breaking mechanism that becomes dominant over all other processes in the surf zone (as opposed to white-capping, which primarily affects wave dynamics in deep water; Mao *et al.*, 2016). The monthly variation in lake levels in the system may be a non-negligible factor for the dissipation in nearshore areas (water depths 10–20 m), i.e. in the surf and swash zones where waves break, and water rushes over the land.

3.2.4.1. Wave transformation: From offshore to nearshore

Waves undergo several transformations as they travel from the deep-water areas to the nearshore zone, where water depth comes into play, altering the properties of the waves and ultimately causing them to collapse. The transition between the two occurs when the water depth, D , is roughly less than half the wavelength, L , which is the distance between two successive crests (Figure 28). By following the displacement of a wave generated in open sea to its final stage, i.e. breakers dissipating their energy on the shoreline, three main zones can be defined (Figure 29):

1. Deep-water ($D > L/2$): In deep-water, waves travel without being affected by the bottom. Their propagation speed depends only on the wavelength (or frequency), which is why these waves are called *dispersive*. Waves with longer wavelengths move at a higher speed than shorter ones, creating more regular wave field with low frequencies in the lead and high frequencies in the trailing edge. Wave dynamics are dominated by wind generation, wave-wave interactions, and white-capping, which is the process describing the wave breaking in deep water. On average, the dissipative effect of white-capping on waves is rather weak.
2. Shallow water ($D < L/20$): As the water depth decreases, the interaction between the waves and the bottom becomes important. In very shallow water, the propagation speed is no longer frequency dependent and the waves are said to be *non-dispersive*. Instead, they travel at a speed that is related to water depth: the shallower the water, the slower the wave speed. Since the period of the waves remains constant, the wavelength decreases with depth and wave height increases to maintain the total amount of energy¹⁶ flux carried by the wave field: this is the shoaling effect (also referred to as *energy bunching*). Active processes in this area also include bottom friction, which involves wave

¹⁶ The wave energy is proportional to the square of the wave height

energy dissipation, and refraction, which is a change in wave direction due to depth or current.

3. **Surf and swash zone** ($H/L > 1/7$): As the water depth decreases further, the waves become unstable and break. The limit is reached when the wave steepness, defined as the ratio of wave height to wavelength, becomes greater than $1/7$ (or when the wave height reaches roughly 80% of the water depth; Dally, 2019). Depth-induced breaking is the dominant process in the surf zone, although wind also affects breaking, causing waves to spill sooner or later, and leading to compression or widening of the surf zone (Douglass, 1990). As the waves approach the shoreline, they collapse to form the characteristic uprush and downrush in the swash zone, which depends on the prevailing wave conditions in the surf zones (and the underlying beach). Wave reflection, which causes wave energy to bounce back (e.g. from a barrier), can also interfere with incoming waves and play a role in nearshore wave dynamics.

The table in the upper right corner of Figure 29 provides an overview of the relative importance of the various processes affecting wave evolution in deep and shallow water (after Battjes, 1994).

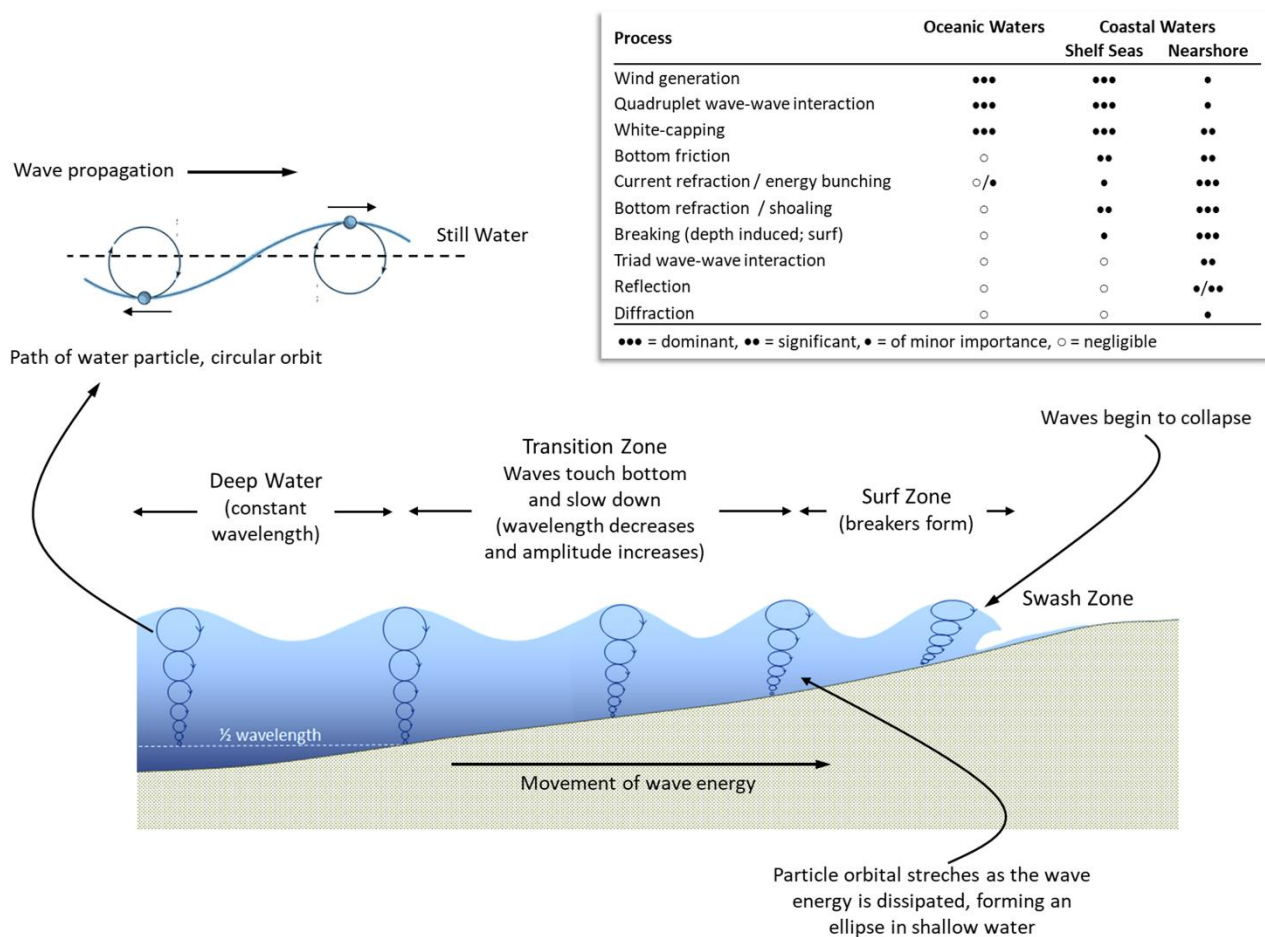


Figure 29: Wave transformation from deep water to the shoreline, and orbital motion of the water particles under the waves. The table in the upper right corner gives the relative importance of the various processes affecting the wave evolution. Adapted from <https://opentextbc.ca/geology/chapter/17-1-waves/> and Battjes (1994).

3.2.4.2. Bottom orbital velocity

Waves are said to *feel the bottom* when the water depth is less than half their wavelength. This expression refers to the displacement induced by the surface gravity waves in the water column, which can be perceptible within this depth limit.

A water particle entrained by a long-crested, harmonic wave propagating in the x-direction experiences a motion with zero velocity in the y-direction. The motion draws a closed, circular or elliptical orbit, and the particle travels along this path at a speed called the *orbital velocity* (Figure 29, upper left corner). The velocity at the wave crest is always oriented in the down-wave direction of propagation and inversely in the trough, with faster motion below the wave crest, causing a small horizontal drift for any object carried by the wave. In deep water, the wave-induced velocities decrease exponentially with the distance to the surface and can be observed down to a maximum depth of about half the wavelength (below the still water surface; Figure 29). At the surface, the motion follows a circle whose radius is equal to the wave amplitude, while negligible water movement due to waves is perceivable at depth $L/2$. As the waves approach the shoreline and move into shallower water ($D < L/2$), the motion describes ellipses growing that flatten toward the bottom, and the frictional interaction of waves with the seabed stretches the orbits as wave energy is dissipated, slowing the motion at the bottom of the wave. In very shallow water, the ellipses maintain their horizontal length through the water column. When the waves break, the remaining wave motion becomes a chaotic surf until the water spreads onto the beach as swash, dissipating the residual energy. Orbital velocities decrease with decreasing water depth in the surf zone as a response to decreasing wave height and wave collapse (Raubenheimer *et al.*, 2002).

3.2.4.3. Wave energy and wetlands

Wetland plants can hardly establish in a high wave environment, as the shear stress generated by the waves destroy plant tissues, in addition to causing severe erosion and sediment transport that disrupt the habitat. Only a few emergent plants, primarily bulrushes or spike rushes (*Eleocharis spp.*), can survive in an active wave climate. Such plants can migrate into the underlying bed or extend sidewise due to their strong rooting system, and their annual evolution allows them to exploit new habitats. However, this vegetation is restricted to a narrow offshore fringe, outside the influence of extreme waves that characterize the physical lake environment of open shoreline wetlands, large open embayments, or even deltas.

Given that the Great Lakes region is exposed to intense and consistent storms with complex evolution patterns, the wave climate is dominated by rapidly changing wind fields and intense wind gradients that can have a pronounced effect on a site's plant diversity, depending on its exposure. Waves are therefore an important physical attribute of wetland types (Albert *et al.*, 2005), and wave exposure is commonly used in modelling to assess wetlands extent and communities shaping (e.g. Angradi *et al.*, 2013; Weller and Chow-Fraser, 2019). Wave energy can also be used as a surrogate for the substrate when the latter is not considered in modelling. Sand and bare rock are primarily found in erosive coastal environments subject to substantial wave action, outside of the usual extent of submerged aquatics and free-floating plants that are more commonly associated with silty and clay soils (Johnston *et al.*, 2007). In order to incorporate this physical factor into the wetland models, the near-bottom orbital velocity, u_{bot} , is used to quantify the wave-generated shear stress (Jonsson and Carlsen, 1976). This velocity is a common output of nearshore wave models.

Finally, it is worth noting that wave dissipation over vegetation canopies is related not only to wave characteristics, but also to plant density, stiffness, and submergence (Anderson and Smith, 2014). Wave attenuation increases with the first two factors and decreases with the latter. Under certain circumstances, living, mixed marshes are able to withstand large wave force without substantial erosion, increasing the resilience of wetlands to changing wave climate (Möller *et al.*, 2014). Wave energy shapes the vegetation cover, and the vegetation cover controls the wave energy along the coastline: it is a two-way process.

3.2.4.4. Wave Climate: 1980–2010

To characterize the wave climate in the Great Lakes Basin for the period 1980–2010, historical measurements collected by the NDBC were used, which come from wave buoys operated by the NOAA and ECCO, among others. These buoys have been in operation since the early 1980s and are mainly located offshore in the deep-water areas of lakes, far from coastal zones where the wave characteristics are altered by nearshore processes. Wave data are recorded during the open-water season, generally from April to December, as the buoys are decommissioned in wintertime due to ice cover. Since surface waves modelling efforts were restricted to the lower lakes, i.e. Lakes Ontario and Erie, only the latter will be discussed in the following paragraphs.

The climatology of surface waves is analyzed through long-term statistics, considering stationary conditions of the wave field, i.e. the significant wave height or peak wave period estimated from short time series (with the duration of 15 or 30 minutes) at each 1-hour interval. The significant

wave height, H_S , is calculated as the average of the highest one third of the wave heights during the 15–30 minute sampling period, and it is related to the mean wave energy, \bar{E} :

$$H_S \approx H_{m0} \equiv 4 \sqrt{\bar{E}/(g\rho)} \quad 3.2$$

with H_{m0} , the energy-based significant wave height, calculated from the wave spectrum (Holthuijsen, 2010). The peak wave period, T_p , is the period with the maximum wave energy. These wave parameters are measured by an accelerometer mounted on a vertically stabilized frame in the buoy. All buoys in the NDBC network also report wind speed and direction at 3–5 m above the lake surface.

The long-term significant wave height distribution can be fit by a three-parameter Weibull probability distribution, which defines the probability of non-exceedance of each observed value:

$$Pr\{\underline{H_S} \leq H_S\} = \begin{cases} 1 - \exp\left[-\left(\frac{H_S - \alpha}{\beta}\right)^\gamma\right] & \text{for } H_S > \gamma \\ 0 & \text{for } H_S \leq \gamma \end{cases} \quad 3.3$$

The parameters α , β and γ are the location, scale, and shape of the distribution, respectively. Wave climate can therefore be determined based on the best-fit distribution, which gives estimates of the mean and variance of the significant wave height, as well as the maximum expected wave height, defined here as the 99th percentile of the distribution, H_{S99} . The Figure 30a shows the best-fit Weibull distribution for wave data collected by the buoy located in the Central Basin of Lake Erie, 45132 (Port Stanley), for the period 2002–2010. Significant wave heights were classified based on the observed wind direction at the station, depending on whether the winds came from the north (NW–NE), east (NE–SE), south (SE–SW), or west (SW–NW). Since the Great Lakes are dominated by wind-sea, the wave climate should be highly correlated to the local winds, resulting in distinct wave characteristics under dominant wind patterns, if any. In Figure 30a, the westerlies were isolated from the observed values to highlight the influence of prevailing winds on the waves generated in the Central Basin.

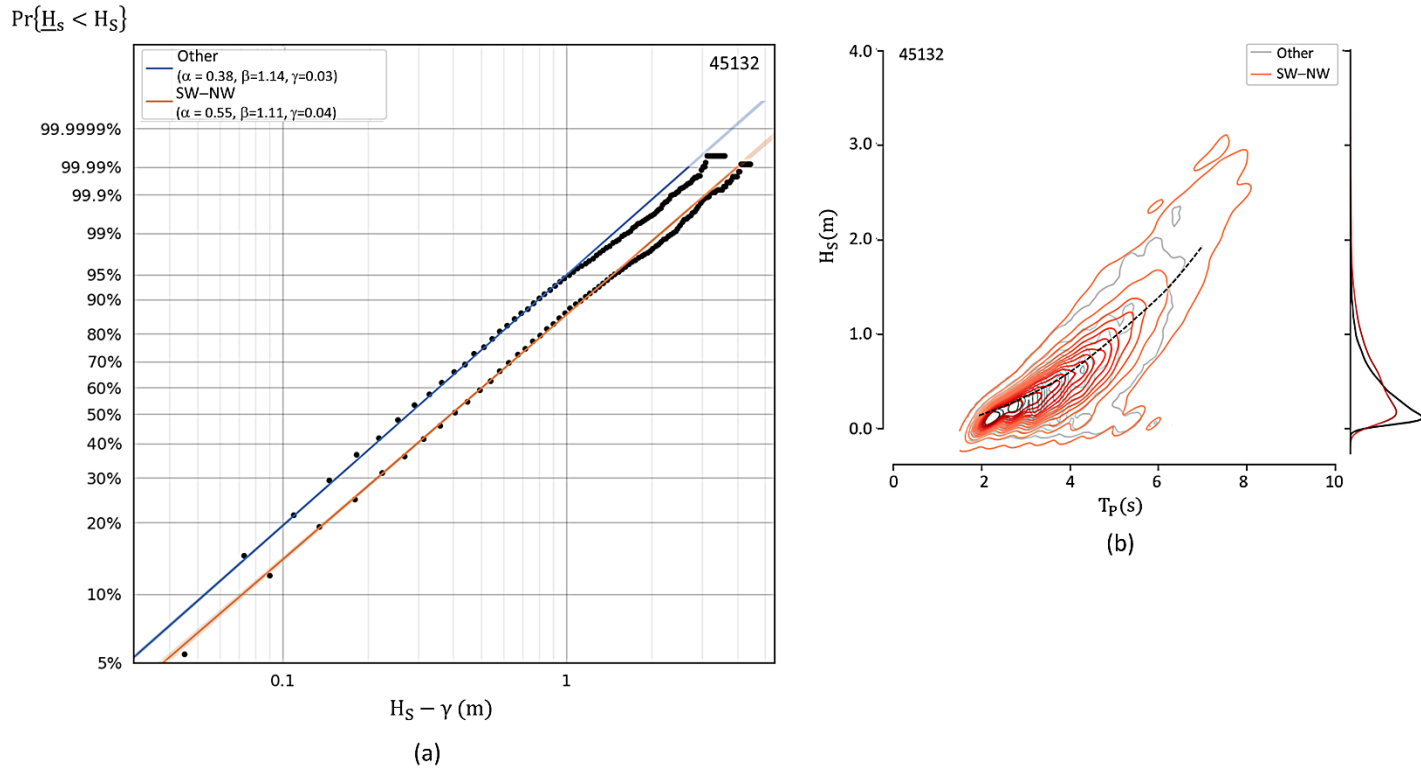
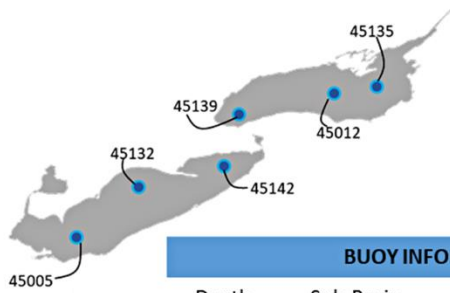


Figure 30: Data recorded at buoy 45132, in Lake Erie (Central Basin), for the period 2002–2010. (a) The long-term Weibull distribution of significant wave heights, for wave parameters recorded under westerly winds (red), or other wind directions (blue). Each black dot gives the binned observations for the 2002–2010 distributions, while the straight lines show the best-fit candidate distributions (maximum likelihood). (b) The joint distribution of significant wave height, H_s , and peak wave period, T_p . Observations were classified by local wind direction: westerly winds (SW–NW; red lines), or others (gray lines). The dashed black line gives the wave steepness, H_s/L , 1:40. The inset on the right shows the probability distribution of wave height.

Table 6: Wave statistics for Lakes Erie and Ontario, for the period 1980–2010. Data were classified according to local winds observed at the time of recording, i.e. north (NW–NE), east (NE–SE), south (SE–SW), or west (SW–NW) winds. The blue lines indicated wind direction associated with major wave events for each of the lake sub-basins. Columns indicate: water depth at buoy locations; lake sub-basins in which the wave buoy is moored; period or record; percentage of data available during the period of record; percentage of data recorded under calm conditions ($H_s < 0.05$ m); the wind direction; the percentage of occurrence of a specific wind direction in the dataset; the mean (and variance) of the significant wave height (based on the best-fit Weibull distribution); the 99th percentile of the wave

height distribution (and the absolute maximum value); and the median peak wave period (with the 2.5th and 97.5th percentiles).



	BUOY INFORMATION					WINDS		WAVES		
	Depth (m)	Sub-Basin	Years	Data (%)	Calm (%)	Direction	Occurrence (%)	H _s (m)	H _s 99 (max) (m)	Tp (s)
<i>Lake Erie</i>										
45005	9.8	Western	1981–2010	78	18	NW–NE	20	0.67 (0.16)	1.9 (3.7)	3.3 (3.9 ; 5.9)
						NE–SE	25	0.63 (0.15)	1.8 (3.4)	4.0 (3.3 ; 5.9)
						SE–SW	30	0.48 (0.07)	1.2 (2.6)	3.3 (2.9 ; 4.8)
						SW–NW	25	0.63 (0.14)	1.8 (2.9)	3.5 (3.0 ; 4.8)
45132	21	Central	2002–2010	48	2	NW–NE	22	0.38 (0.07)	1.2 (2.0)	3.2 (2.7 ; 4.8)
						NE–SE	22	0.42 (0.14)	1.7 (2.6)	3.2 (2.7 ; 5.3)
						SE–SW	27	0.38 (0.10)	1.5 (3.1)	3.2 (2.7 ; 4.8)
						SW–NW	29	0.55 (0.21)	2.1 (4.1)	3.7 (2.7 ; 5.9)
45142	27	Eastern	1995–2010	69	3	NW–NE	18	0.35 (0.08)	1.3 (2.8)	3.2 (2.7 ; 6.9)
						NE–SE	18	0.26 (0.04)	0.9 (1.8)	3.2 (2.7 ; 6.4)
						SE–SW	26	0.37 (0.09)	1.4 (3.3)	3.7 (2.7 ; 5.9)
						SW–NW	38	0.66 (0.31)	2.5 (4.9)	4.3 (3.2 ; 6.9)
<i>Lake Ontario</i>										
45139	35–126*	Niagara	1992–2010	59	10	NW–NE	26	0.28 (0.07)	1.3 (2.6)	3.2 (2.7 ; 21.3)
						NE–SE	21	0.37 (0.18)	2.0 (3.2)	3.7 (2.7 ; 10.2)
						SE–SW	22	0.19 (0.03)	0.8 (1.4)	2.7 (2.2 ; 18.3)
						SW–NW	31	0.25 (0.04)	0.9 (1.9)	2.7 (2.2 ; 5.3)
45012	143	Mississauga	2002–2010	78	18	NW–NE	15	0.67 (0.15)	1.8 (3.0)	3.9 (3.2 ; 5.6)
						NE–SE	22	0.57 (0.13)	1.6 (2.9)	3.6 (3.0 ; 5.0)
						SE–SW	25	0.53 (0.11)	1.5 (2.9)	3.5 (3.0 ; 5.0)
						SW–NW	38	0.74 (0.27)	2.4 (5.9)	3.9 (3.3 ; 6.3)
45135	47–68*	Rochester	1992–2010	48	9	NW–NE	20	0.40 (0.18)	2.0 (3.4)	3.7 (3.2 ; 7.9)
						NE–SE	15	0.31 (0.10)	1.5 (5.3)	3.2 (2.7 ; 5.3)
						SE–SW	27	0.38 (0.13)	1.7 (3.7)	3.7 (2.7 ; 5.3)
						SW–NW	38	0.60 (0.30)	2.6 (5.3)	4.3 (3.2 ; 6.9)

Table 6 presents long-term statistics of buoy-observed waves for six offshore locations in Lakes Ontario and Erie, with each moored buoy being representative of a sub-basin of the lake. Although the NDBC has maintained instrumented buoys in the Great Lakes since the early 1980s, the

buoys were not deployed at the same time, and the available data are generally sparse with no persistent temporal coverage. To avoid annual irregularity in the wave statistics that would preferentially weight some months over others, only years with 60% temporal coverage for the period April–November were retained, thus eliminating incomplete years from the analysis. The long-term average wave climate for the reference period (1980–2010) therefore included wave measurements recorded prior to 2010, with year-varying contribution.

In Lake Erie, the major wave events are generated by westerly winds (SW-NW), with an upper limit for the significant wave height (99th percentile) of 2–2.5 m and maximum absolute observed values of 4–5 m. These waves are mainly detected in the Central and Eastern Basins, and benefit from longer fetches and deeper bathymetry, which allow wave propagation. The mean wave climate remains relatively gentle, with a mean H_s of 0.26–0.67 m, the highest nominal condition experienced in the Western Basin. The western part of the lake appears to be influenced by complex wave dynamics with no preferential wind direction. Overall, the mean peak period, which corresponds to the 50th percentile, is within the range of 3.2 and 4.3 s, well below the swell period observed in Great Lakes (10 s; e.g. Tsanis and Brissette, 1992), with a higher value of 6–7 s that appears typical of the Eastern Basin (97,5th percentile). The joint distribution of significant wave height and period (Figure 30b) reveals that the largest events are associated with higher wave periods, consistent with wind-wave growth in the deep portion of the lake, where wave-breaking processes are not dominant and mean wave energy and frequency depend on wave age (Badulin *et al.*, 2005).

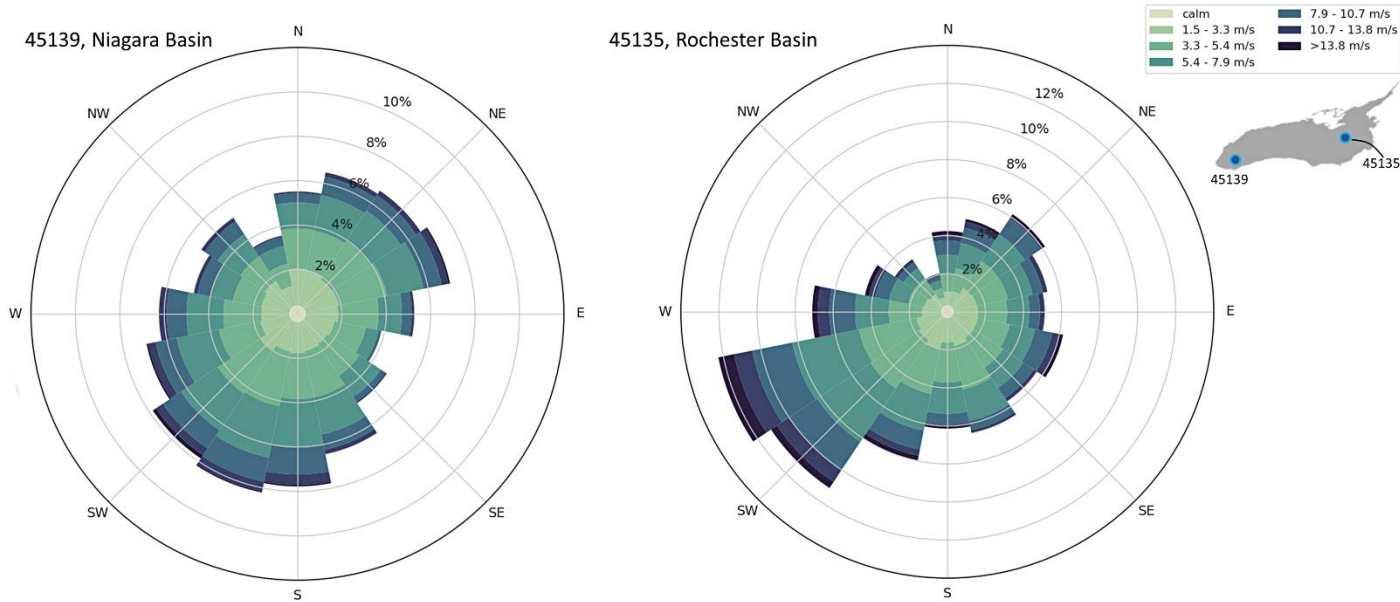


Figure 31: Wind roses for winds observed between April–November at buoys 45139 (Niagara Basin) and 45135 (Rochester Basin) in Lake Ontario, for the period 1980–2010. The winds were extracted from the homogenized dataset (cf. Section 2.3.1).

In Lake Ontario, wave characteristics are essentially similar to those observed in Lake Erie: wind-sea, with a nominal period of 2.7–4.3 s and gentle significant wave height, with a mean value 0.28–0.74 s. The main difference comes from the extreme values, especially in the Mississauga (mid-lake) and Rochester (eastern end) Basins, where the maximum significant wave height reaches 5.9 and 5.3 m, respectively, under a predominant west-to-east wind fetch. These values are close to the 99.9th percentile wave height events impacting Eastern Lake Ontario shorelines based on the 36-year climatology wave heights provided by the Wave Information Study (WIS; Grieco and DeGaetano, 2019), a model-derived dataset published by the US Army Corps of Engineers (<http://wis.usace.army.mil>). The Niagara Basin displays a more specific wave climate, primarily influenced by easterly winds associated with periodic storms (Figure 31) and distinguished by swell waves of period > 10 s (95th percentile; Table 6). These long waves do not necessarily follow the local wind direction, but rather the longer fetch direction (Tsanis and Brissette, 1992), and were likely generated in the eastern part of the lake.

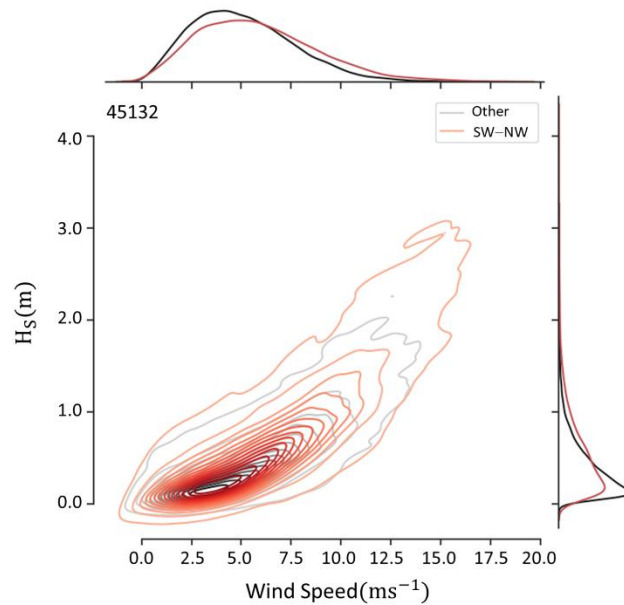


Figure 32: The joint distribution of significant wave height and wind speed for buoy 45132, in Lake Erie (Central Basin). The insets at the right and top show the respective probability distributions. Observations were classified by local wind direction: westerly winds (SW–NW; red lines), or others (gray lines).

In both lakes, there is evidence of reset phases: as soon as the wind starts to calm, short and long waves decay, leaving a quiescent basin ($H_s < 0.05$ m; % calm in Table 6). Lakes Erie and Ontario are therefore devoid of swell energy. Wave activity is directly linked to observed wind conditions, as illustrated in Figure 32, with extreme wave events typically occurring in early spring (March–April) and fall (September–November; e.g. Niu *et al.*, 2016; Grieco and DeGaetano, 2019; Angel *et al.*, 1995), consistent with seasonal variations in surface winds (e.g. Figure 14 in Section 2.3.1). Anderson *et al.* (2015) showed that changing wind direction is responsible for interannual variations in wave climate in Lake Superior, which was found to be equally important for Lake Erie (Niu *et al.*, 2016). A strong correlation between periods of high wave energy and high lake levels was also denoted by Meadows *et al.* (1997). This causal relationship appears to be related to significant changes in the cyclone climatology of Great Lake Basin. The eastern Great Lakes were identified as an area of maximum storm frequency and deepening, with storm tracks varying in response to the El Niño-Southern Oscillation (ENSO; Colucci, 1976), a large-scale atmospheric circulation feature.

Although the buoy data mainly report deep-water wave conditions, which limits the description of wave climate to the offshore area, the observed wave conditions can be used as an indicator of local nearshore dynamics. Incoming wave energy is crucial for shallow-water waves, as local wave height is a function of deep-water wave characteristics: they set the initial conditions that

will subsequently evolve as a function of wind, bathymetry, and coastline. Exposed shorelines, such as the northern shores of Lake Erie and the eastern shores of Lake Ontario, are more likely to be subject to extreme wave steepness, H_s/L ($\propto H_s/T^2$ in deep water) than protected areas.

3.3. Mean lake level modelling

Lake modelling must consider both long- and short-term fluctuations that modulate water levels, both being very important to wetland ecosystems although they do not operate on the same time scale. The former refers to seasonal and interannual variations that follow the change in net basin supply, while the latter responds primarily to physical processes that set the water surface in motion. To properly simulate change in levels over time, lake models must therefore rely on inflows/outflows, tributary discharges, as well as overlake precipitation and lake evaporation that collectively determine the overall variation in water storage for a specific basin. While the historical period can be modeled using observations and reanalysis gridded data sets, which provide good estimates of past climate conditions, the past and future levels projected by climate scenarios must be obtained from simulation results. Work is hence needed to determine, from the general output variables provided by the AOGCM-RCMs, all components of net basin supply (hereafter referred to as NBS), including runoff and connecting channel flows, which are typically used in hydrodynamic modelling. NBS is defined as:

$$NBS = P_{lake} - E_{lake} + R \quad 3.4$$

where P_{lake} and E_{lake} are the overlake precipitation and evaporation, respectively, and R , the runoff, i.e. the sum of the water flowing into the lake from all surrounding rivers, excluding inflow from upstream lake if any. The change in storage, ΔS (in m^3s^{-1}), which can be converted in change in lake-depth, ΔH (in m), using lake surface area and time, is related to the NBS through the budget equation of the lake,

$$\Delta S = NBS + I - O \pm D \quad 3.5$$

with I and O , the inflow from the upstream lake and outflow from downstream lake, respectively, and D , any diversions into and out the lake. The AOGCM-RCMs provide direct projections for precipitation and evaporation, but all other components of the above equations must be estimated based on model outputs, using a routing model to track tributary and connecting channel flows.

The change in mean lake level is obtained from the change in ΔH , which is typically calculated on a quarter-month basis in the Great Lakes system, which is roughly one week (cf. Section 3.7.2.1).

Depending on the hydrodynamic model, mean lake level, inflow/outflow, diversion, or river discharge were used to constrain the two-dimensional simulations. These force annual and seasonal fluctuations that are determined by observed or projected climatic conditions, depending on the period considered. In the second case, i.e. projections, these conditions were extracted from the work done by Seglenieks and Temgoua (2022), who analyzed hydroclimatic variables and future Great Lakes levels from 5 dynamically downscaled CMIP5 AOGCMs, which include the models selected for this study (i.e. CanESM2 and GFLD-ESM2M, downscaled with CRCM5). The following paragraphs provide a general description of the method used by these authors to generate lake levels and connecting channel flows for the past (1980-2009) and future (2070-2099) periods, as well as a brief presentation of the resulting time series.

3.3.1. Component Net Basin Supply and projections

For this project, Seglenieks and Temgoua (2022) estimated mean lake levels and connecting channel flows from the net basin supply.

First, each component of the NBS was extracted or calculated from model outputs. As explained earlier, overlake evaporation and precipitation are directly provided by the AOGCM-RCMs, while runoff must be estimated from a routing scheme designed to follow water from land to river network, ensuring proper timing and mean outflow. The WATFLOOD model (Kouwen *et al.*, 1993; Wijayarathne and Coulibaly, 2020), which is a semi-empirical physical based model, was employed to calculate runoff in each lake from temperature and precipitation datasets extracted from the AOGCM-RCMs. This hydrological model is commonly used in the Great Lakes, and a set of validated calibration parameters already exist for the entire basin (Pietroniro *et al.*, 2007).

Second, precipitation, evaporation and runoff were debiased on a monthly basis using a multivariate bias adjustment function (Cannon, 2016), and the NOAA Great Lakes Environmental Research Laboratory (GLERL) hydrometeorological database (1961–2000; Hunter *et al.*, 2015), which was selected as the reference dataset. The three components were adjusted individually, with correction factors estimated from the 1961–2000 period and subsequently applied to the entire time series (1961–2099) before being summed to obtain the projected NBS for each lake.

3.3.1.1. Mean lake levels and connecting channel flows

The resulting debiased NBS components for past and future periods were finally used to estimate projected mean lake levels and connecting channel flows for the Great Lakes Basin, including Lakes St. Clair and Michigan-Huron, the latter being considered as a single entity in terms of water storage. Since the regulation plans control outflows from Lakes Superior and Ontario, specific models must be employed to calculate levels according to rules adopted (e.g. Clites and Lee, 1998). These models use projected NBS as inputs and provide quarter-month mean lake levels and connecting channel flows that meet the fixed regulatory measures. For their analyses, Seglenieks and Temgoua (2022) generated data based on regulation plans currently used by the International Lake Superior Board of Control and the International Lake Ontario St. Lawrence Regulation Board, which are responsible for regulating outflows on the St. Marys River and at Moses-Saunders Dam in the St. Lawrence River. These plans, known as Plan 2012 (Lake Superior) and Plan 2014 (Lake Ontario), were implemented in 2014 and early 2017, respectively. Since there is no way to predict future changes to the regulation plans, lake levels were projected assuming that both plans will remain in place under future climate change. As explained by Seglenieks and Temgoua (2022), this hypothesis may be violated if extreme climatic conditions bring more (or less) water into the system than ever seen in the past.

3.3.2. Projected time series

Projected time series for the mean levels of the Lower Great Lakes, including Lake Michigan-Huron and St. Clair, are presented in Figure 33 and Figure 34. They include the set of AOGCM-RCMs analyzed by Seglenieks and Temgoua (2022), following the NBS debiasing technique previously explained, and the two commonly used representative concentration pathways, i.e. RCP4.5 (left panels) and 8.5 (right panels). Observed levels for each lake are also plotted in black for the reference period (1980–2010). Additional graphs for connecting channel flows are also available in the report published by Seglenieks and Temgoua (2022).

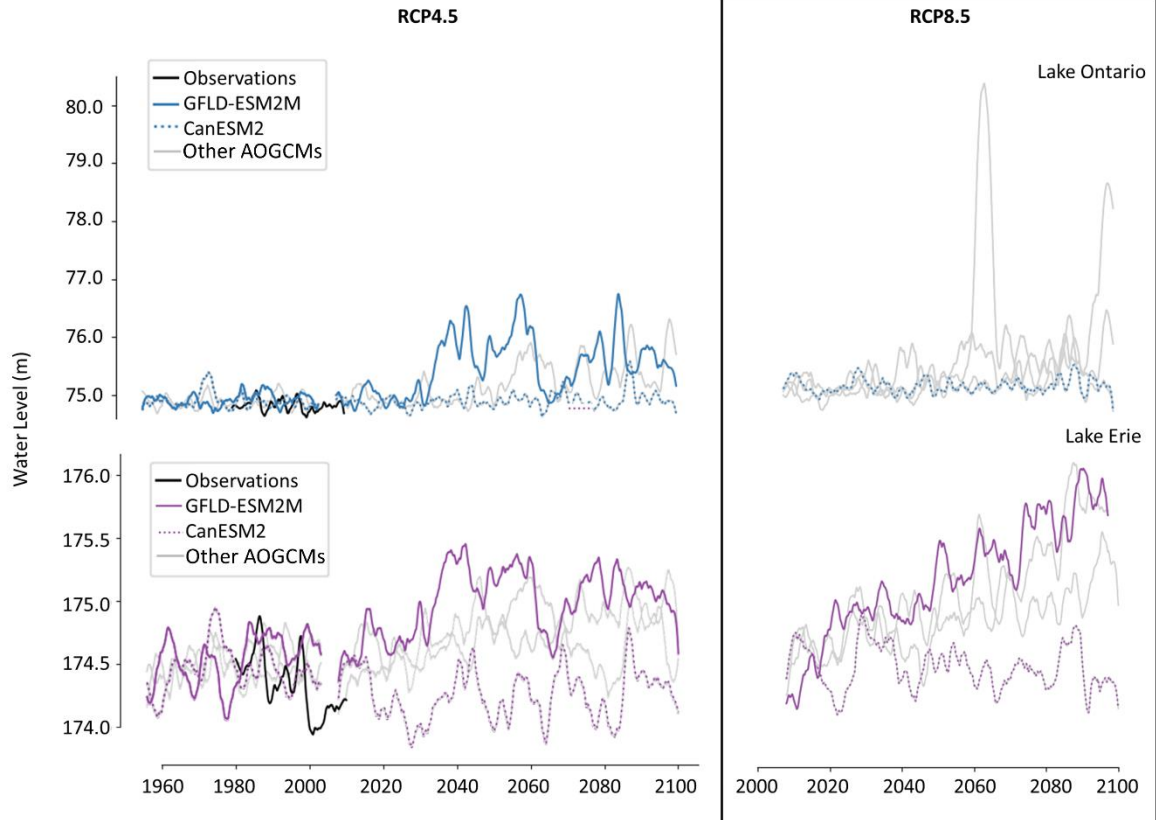


Figure 33: The projected past and future mean levels for Lakes Ontario (upper panels) and Erie (lower panels). The two selected AOGCM-RCMs are highlighted in each graph, with dashed lines for CanESM2 (or SIM01 and SIM02 for RCP4.5 and 8.5, respectively), and solid lines for GFLD-ESM2M (or SIM03 and SIM04 for RCP4.5 and 8.5, respectively). The grey lines provide the results obtained from other CMPI5 AOGCMs included in the NA-CORDEX project, while the black lines give the observed historical time series. One of the Lake Ontario time series illustrates doubtful results obtained under the regulation rules for the high emission scenario (RCP8.5). Note: the GFLD-ESM2M time series is missing for Lake Ontario, since this scenario was removed from the study due to unrealistic projections. Details are given in the text.

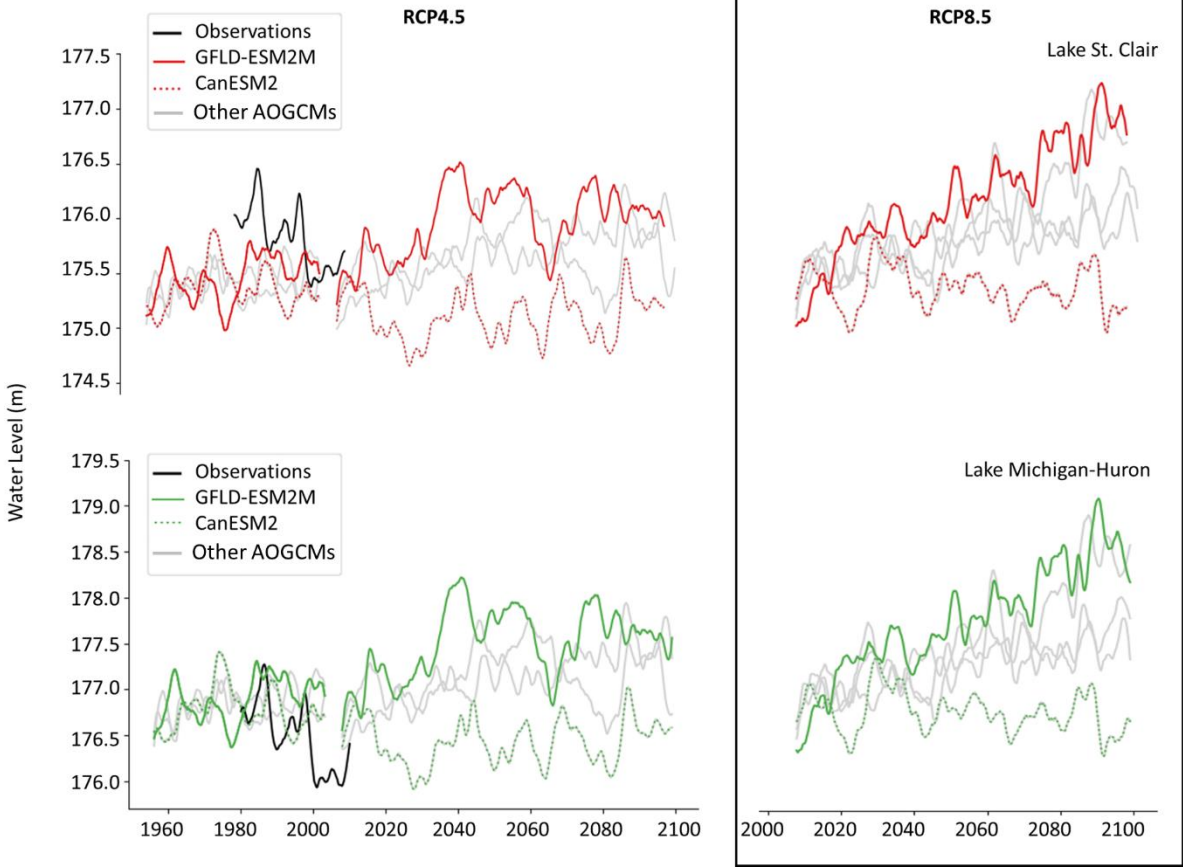


Figure 34: Idem as Figure 33, but for Lakes St. Clair (top panels) and Michigan-Huron (bottom panels).

The projections obtained for the two selected AOGCMs, namely CanESM2 (or SIM01 and SIM02, according to RCP4.5 and 8.5) and GFLD-ESM2M (or SIM03 and SIM04, according to RCP4.5 and 8.5; cf. Table 1) are highlighted in the graphs presented, with dashed lines representing the CanESM2 time series and the solid lines, its counterpart.

3.3.2.1. The case of Lake Ontario

Based on the results obtained by Seglenieks and Temgoua (2022), some climate models project a significant increase in Lake Ontario levels in the last decades of the century (Figure 33). One of them, the GFLD-ESM2M downscaled by the CRCM5 and forced by RCP8.5 scenario, even projects a monotonic increase in mean lake levels beyond 2070, which seems unrealistic given the interannual variation normally expected (not shown). This behavior appears to be directly related to the assumption of fixed regulation rules, which are not designed to handle the extreme high amounts of water entering the Great Lakes system as projected by some of the AOGCMs. In its current form, Regulation Plan 2014 limits the maximum Lake Ontario outflow to $\sim 10.7\text{--}11.5 \times 10^3 \text{ m}^3\text{s}^{-1}$ (IJC, 2014), which is likely not sufficient to manage extremely wet years, when

inflows from the upper lakes far exceed any historically observed values. However, given the rarity of such inflows, the physical characteristics of the St. Lawrence River, the duration of outflows in excess of $11 \times 10^3 \text{ m}^3\text{s}^{-1}$ that would be required to significantly reduce similar Lake Ontario levels, and the levels of forecasting expertise required to effectively manage such situations, it appears unlikely that a regulation plan could effectively mitigate such extreme conditions. In addition, the validity of routing is questionable under extreme flows since connecting channels, which have a limited capacity, may respond differently than normally expected by regulation. As a result, and due to the large uncertainty in future Lake Ontario levels under the higher emission scenario (RCP8.5), only simulations forced by the RCP4.5 scenario were retained to project future Great Lakes conditions and wetland evolution in the decades 2070s to 2090s. For the same reasons, some AOGCMs were removed from the analysis conducted by Seglenieks and Temgoua (2022).

3.4. Hydrodynamic modelling

This section provides a general overview of the different numerical approaches used to model the Great Lakes system.

3.4.1. Numerical solver

The hydrodynamic simulations performed in this project were carried out using the H2D2 software (version 19.04p2; Secretan, 2013), which is a two-dimensional finite element model that allows for robust, distributed, and shared-memory computation of large systems and non-stationary problems. This model solves the two-dimensional Navier-Stokes equations, which describe shallow water motion, using an implicit time scheme and a special treatment of the drying-wetting zones to compute the temporal evolution of the wetted surface area and discharges (Heniche *et al.*, 2000). The parameterization used by H2D2 relies on several assumptions, namely incompressibility, hydrostatic pressure, and stable bathymetry (e.g., Bois, 2000). For more information on the finite element discretization, the reader is referred to Heniche *et al.* (2000) and Dhatt *et al.* (2005). Further details on the implementation of the H2D2 model can be found online (<http://www.gre-ehn.ete.inrs.ca/H2D2>), including the conceptual description of the drying-wetting model.

3.4.2. Two-dimensional modelling and assumptions

3.4.2.1. 2D Saint-Venant equations

The description of the fluid motion in shallow-water environments is derived from the Navier-Stokes equations by assuming that the water column is well mixed, and the displacement roughly two-dimensional, i.e. that horizontal motion is much larger than vertical motion, so that the vertical derivatives can be ignored. Therefore, the vertical acceleration is assumed negligible (i.e. hydrostatic assumption) and the flow, strictly 2D, resulting in the depth-integrated formulation of the equations of motion, which in final form are known as the St-Venant equations. These equations govern the mass and momentum conservation through two variables, the discharge (or flow rate), $q(q_x, q_y)$, and water level, h , and are respectively defined as:

$$\frac{\partial pH}{\partial t} + \frac{\partial q_x}{\partial x} + \frac{\partial q_y}{\partial y} = 0 \quad 3.6$$

and

$$\frac{\partial q_x}{\partial t} + \frac{\partial}{\partial x} \left(\frac{q_x q_x}{H} \right) + \frac{\partial}{\partial y} \left(\frac{q_x q_y}{H} \right) = \sum F_x \quad 3.7$$

$$\frac{\partial q_y}{\partial t} + \frac{\partial}{\partial x} \left(\frac{q_x q_y}{H} \right) + \frac{\partial}{\partial y} \left(\frac{q_y q_y}{H} \right) = \sum F_y \quad 3.8$$

where x, y are the Cartesian coordinates, t , the time, $H (= h - z)$, the water depth, with h and z the water surface level and the bed level, respectively, and F_x, F_y are the external forces in the x and y directions.

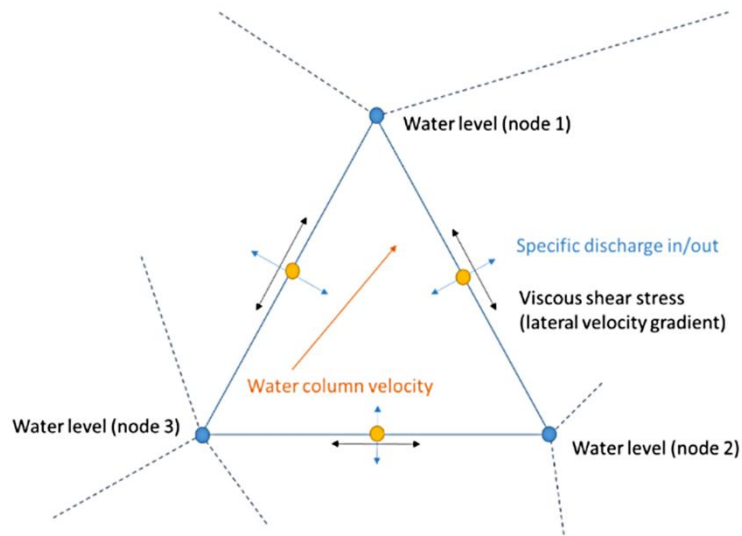


Figure 35: 2D Quadratic element and its interconnection with adjacent cells

In the H2D2 solver, various external forces can be considered to determine the equilibrium state at each cell of the mesh, ensuring conservation of mass and momentum. The main terms in the equations include: gravitational acceleration; bottom friction, which depends on the Manning roughness coefficient; surface friction, which is related to ice cover, if any, and surface wind stress; and viscous forces, which control turbulence and mixing. Additional source terms that account for over-lake precipitation and evaporation can also be included in the first mathematical description above to add or remove mass on specific mesh elements (Figure 35 and Figure 36).

These equations cannot be solved explicitly, except under very large hypothesis that are unrealistic in most situations, and numerical schemes are normally used to resolve the 2D surface dynamics, i.e. the spatial distribution of water levels and velocities.

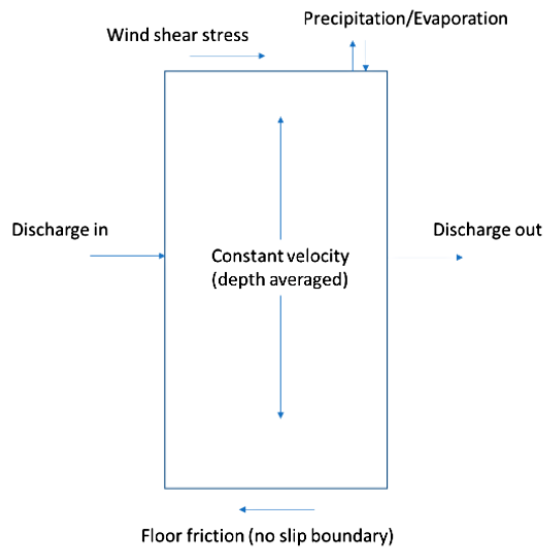


Figure 36: External forces on a 2D mesh cell

3.4.2.2. Single-layer assumption and surface Ekman layer

The 2D assumption is reasonable in rivers, where along-channel (and cross-channel) gradients are high, and in shallow lakes, where surface motion can be approximated using a homogeneous, single-layer model in which surface stress is felt from the surface to the bottom. However, when dealing with deeper lakes and periods of strong stratification, this approximation is no longer valid, and three-dimensional (i.e. baroclinic) effects become important. For hydrodynamic modelling, this can lead to inaccurate estimation of water-level fluctuations since the main physical processes (i.e. wind set-ups) can be misrepresented. While the depth-integrated St. Venant equations consider that the entire water column is set in motion by a wind acting on the surface, only the well-mixed layer is affected to a depth that depends on the wind intensity. The motion is then constrained to the so-called upper Ekman layer (cf. Section 3.2.2), which has a typical thickness in mid-latitudes of 50 m to 100 m for wind speeds of 10 ms^{-1} to 20 ms^{-1} when the stratification is weak or absent (Pond and Pickard, 1983; Figure 37). An important note here is that the Ekman-layer formulation assumes no vertical density stratification (e.g. Cushman-Roisin and Beckers, 2011). Stratification is a major factor as it can hinder vertical movements, thereby reducing mixing momentum by turbulence initiated by the wind-driven flow and, thus, the depth of penetration of wind energy into the upper layers (e.g. Price and Sundermeyer, 1999). Consequently, the vertical density gradient reduces the thickness of the Ekman Layer, and only severe, long-lasting storms can counteract this effect by generating a deepening of the well-mixed surface layer, thus reducing the stability of the water column. The occurrence of storms is

therefore particularly critical to the dynamics of the Great Lakes during the summer months, as the latter are highly stratified between May and October, especially in their deep, central basins.

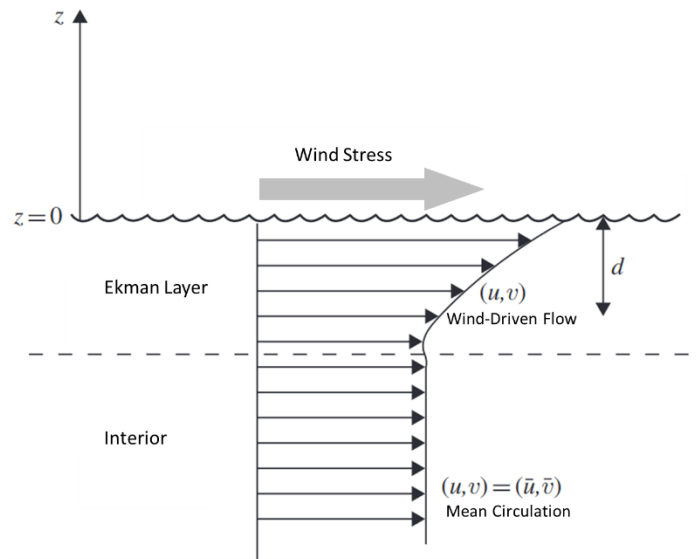


Figure 37: The surface Ekman layer generated by a wind stress (adapted from Cushman-Roisin and Beckers (2011)).

While shallow lakes are well approximated by the 2D assumption, this is not the case for Lakes Ontario and Huron, where the depth reaches more than 200 m and the single-layer hypothesis is no longer valid at the basin scale. Since the displacement is restricted to the surface Ekman layer, an alternative modelling approach that artificially constrains the calculation to the upper layers was developed to obtain reliable estimates of the surface dynamics.

3.4.2.3. Deep lakes and 2D modelling

To approximate the deep lake dynamics with a 2D numerical scheme, the depth of the surface layer was artificially modulated to mimic the action of winds on the water surface, allowing for greater penetration of wind energy into the water column under strong, sustained atmospheric conditions. This idea relies on the inherent dynamics of wind set-ups that are generated by the displacement of the surface layer, which is considered as moving freely over the thermocline when subjected to surface stress. In this description, the motion modelled is that which could be observed from the surface mixed layer alone, regardless of the dynamics of the underlying layers that may respond oppositely to the wind stress. The depth of this 'active' layer varies according to the wind intensity, which means that the bathymetry used by the model in its parametrization of the lake must be modified to suit the imposed atmospheric forcing (Figure 38). Several calibrations must then be performed to provide valid solutions for any wind, whether low, moderate, strong, or even extreme. The set of depth-wind solutions thus created is used to

determine, at any time step, the state of the system, which is assumed the equilibrium state reached by the lake under static conditions, i.e. under a wind of constant intensity blowing on the surface of the lake for a time long enough to be considered infinite. The static hypothesis is critical here as a change in water depth implies a change in volume, which may lead to a violation of mass conservation if this situation occurs between two successive time steps of a simulation.

Although a true steady state is extremely unlikely, since adjustment (or set-up) time scale is longer than the time that large wind events usually last (Simons, 1971), this hypothesis is postulated in first approximation as will be discussed below (cf. Section 3.4.3.2). In reality, the lake responds to any change in winds when fresh injection of energy forces free surface motion, and a slow adjustment of the basin-scale circulation ensues that seeks to counteract the new wind-force distribution. If change in wind speed and direction occurs before the full basin-wide adjustment, no steady state is reached and the lake remains in transient state. The wind set-ups therefore rarely attain their full equilibrium amplitude, except in the case of strong, slow-moving storms.

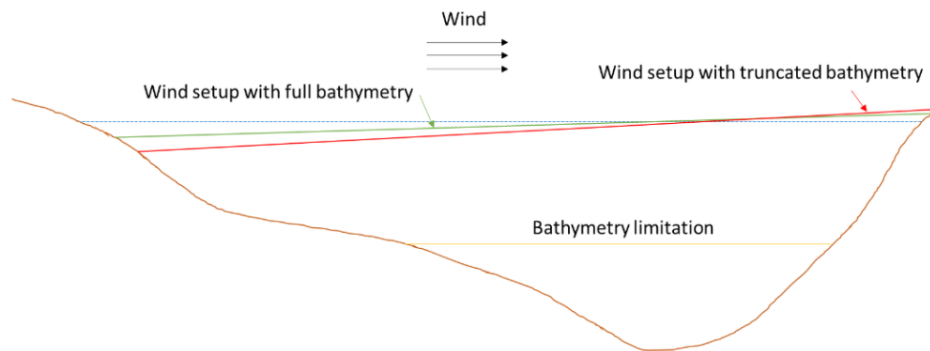


Figure 38: Illustration of the effect of limiting depth on the wind setup in a 2D model

3.4.3. Modelling approaches: Complex vs. scenario-based

Two modelling approaches were adopted to simulate long- and short-term fluctuations in water levels as a function of the lake being modelled, whether it can be considered as a single-layer model or not.

3.4.3.1. Shallow lakes modelling: Complex physics

Lakes Erie and St. Clair are the shallowest lakes in the Great Lakes system with average depths of 19 m and 3 m, respectively. Lake Erie is a special case, since its Central and Eastern Basins (maximum depth of 25 m and 64 m, respectively) can be stratified as early as May, and retain a vertical thermal structure that is almost absent in its western part. However, this lake is very

susceptible to strong wind impulses, especially during the early stage of the stratification when the water column stability is relatively low. Basin-scale oscillations, internal waves, upwelling, and inter-basin advection also promote enhanced mixing of the upper water column (Bouffard *et al.*, 2012; Liu *et al.*, 2014; Beletsky *et al.*, 2012; Boegman *et al.*, 2001; Lin *et al.*, 2021; Bocaniov *et al.*, 2014), and increase the sensibility of thermal structure to atmospheric forcing (Austin and Allen, 2011). Spring and summer storms can therefore cause momentary mixing of the deeper basins and weaken their stratification, which causes a deepening of the thermocline (Beletsky *et al.*, 2013) and leave a nearly uniform surface to bottom temperature profile in mid-September and mid-October (Schertzer *et al.*, 1987). Because the influence of a strong, shallow stratification in Lake Erie remains limited, this lake can be approximated by a one-layer model. Although this assumption may be violated under certain circumstances, particularly in the deep eastern basin, wind-induced surface motions modelled at the basin scale are not expected to be significantly affected.

The single-layer assumption is therefore valid in first approximation for lakes Erie and St. Clair, and the 2D numerical scheme can be used to simulate the free-surface motions, as well as the general dynamics of Lake Erie and the Huron-Erie Corridor, which includes the St. Clair River, Lake St. Clair and the Detroit River. Simulations were therefore performed under time-varying conditions to account for the transient nature of these systems (Figure 39), providing real-time solutions that offer a complete description of the wind-induced physical processes, i.e. wind set-ups and surface seiches (cf. Sections 3.2.1.1 and 3.2.1.2). This approach offers a realistic numerical representation since all forcing fields are dynamic, which is necessary to simulate an unsteady and highly stochastic phenomenon. However, this method is by far the most demanding in terms of computational and storage resources since each time step of a simulated period is calculated once at a time, providing one- to three-hour gridded time series. For one year of simulation, this means over 5000 lake level maps in Lake Erie (e.g.).

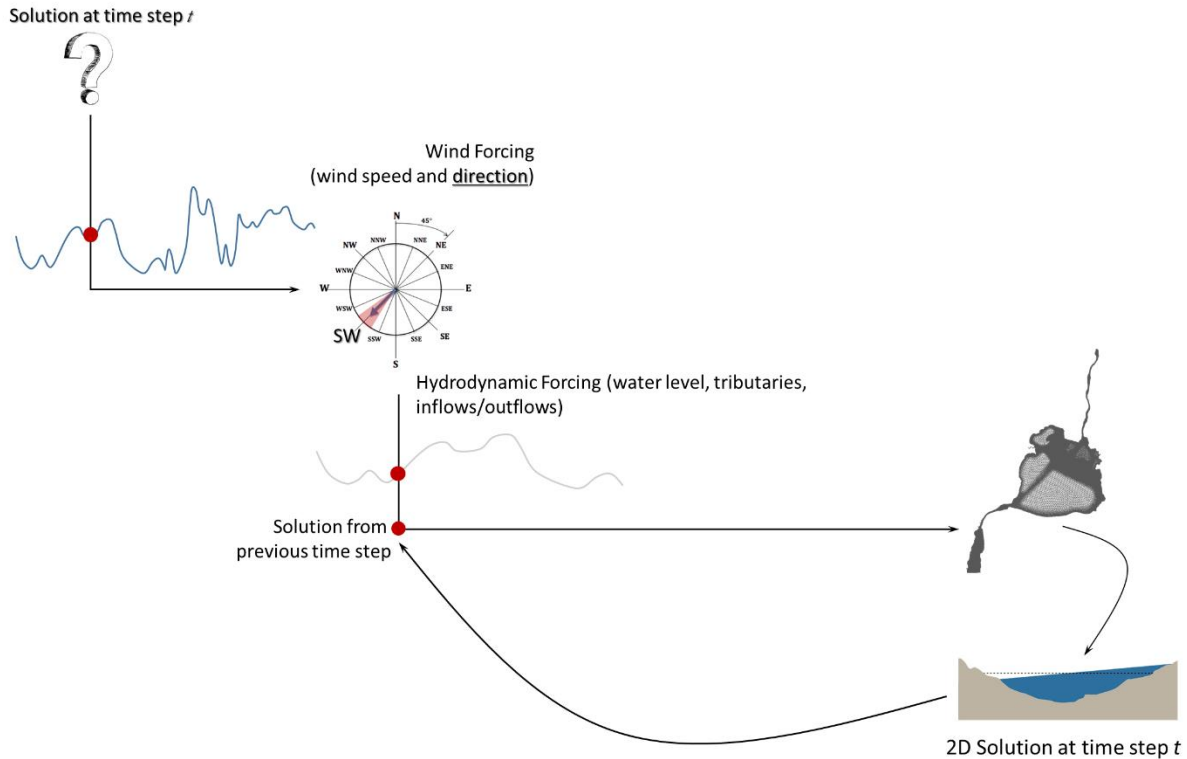


Figure 39: Complex physics approach, using unsteady simulations.

3.4.3.2. Deep lakes modelling: Scenario-based approach

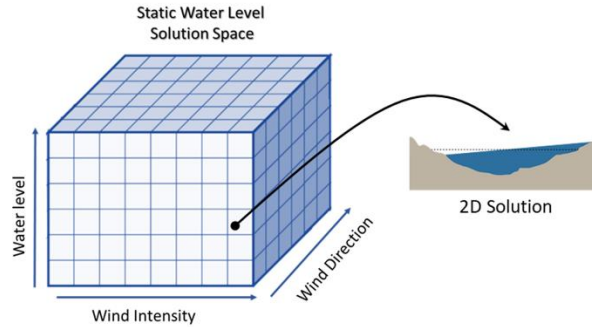
The second modelling approach seeks to reproduce the physics of free-surface motions as observed in the mixed layer of a stratified system by assuming that the upper layer moves freely, with no frictional effects at the thermocline. This assumption is often used in oceanography to describe surface motions in a two-layer system when strong stratification reduces turbulent frictional coupling between the upper and lower layers (e.g. Pond and Pickard, 1983). This approximation has been applied to the modelling of deep lakes, when the vertical structure cannot be assumed homogeneous and three-dimensional dynamics neglected. This is the case for Lakes Ontario and Huron, which have a maximum (mean) depth of ~244 (86) m and 230 (59) m, respectively.

As explained earlier, the motion initiated by the atmospheric forcing is restricted to the surface Ekman layer whose depth varies with the wind intensity. To mimic this depth-varying process, the adopted numerical scheme simulates only the surface layer dynamics by artificially modulating the lake bathymetry since the water column depth is used to estimate the wind effect in 2D parametrization. To provide a good representation of the wind set-ups amplitude, a calibration of the 'effective' depth under different wind conditions must be performed, considering both direction

and speed, as the wind origin modifies the fetch and, hence, the lake response. In this approach, only static solutions can be obtained to avoid a violation of conservation of mass as mentioned previously. In order to reproduce the transient water level fluctuations, the time series is reconstructed from precomputed solutions rather than simulated on an hourly basis, as is the case for the classical non-stationary method.

3.4.3.2.1. Steady-state solution space

The use of 2D steady-state solutions to approximate the transient state of the lake presupposes the existence of a set of precomputed solutions, which are sufficient to reproduce all hydrodynamic (i.e. mean lake level) and atmospheric (i.e. wind intensity and direction) conditions. Since it is not realistic to model all possible forcing combinations, a solution space was developed and used to estimate the state of the system, i.e. the tilt of the lake surface once in equilibrium with the wind (Figure 38). In this representation, only the initial deflection of the lake surface is modelled: the surface seiches initiated by the relaxation of the lake surface are not parametrized since it is an oscillatory process resulting from an instability. Part of the energy will be therefore missing from the final time series reconstructed with the steady-state solutions.



STATIC FORCING								
Mean Lake Level		Winds						
Lake Ontario	Lake Huron	Wind Intensity			Wind Direction			
(m)	(m)	Speed Classes		Forcing				
		km h ⁻¹		km h ⁻¹ (ms ⁻¹)				
1	73.75	175.40	1	No Wind	< 7	0 (0)	1	N
2	74.0	175.78	2	Gentle	7–12	10 (2.8)	2	NNE
3	74.5	176.18	3	Low	12–27	20 (5.6)	3	NE
4	75.0	176.59	4	Moderate	27–43	35 (9.7)
5	75.5	177.0	5	High	43–57	50 (13.9)	16	NNW
6	76.0	177.42	6	Strong	57–73	65 (18.1)		
7	76.5	177.83	7	Extreme	> 73	80 (22.2)		
8	77.0	178.24						
9	77.5	178.67						
10	78.0	179.09						

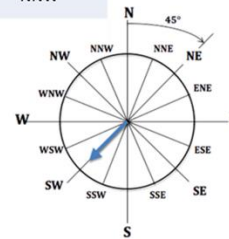


Figure 40: The solution space, with its several mean lake level and wind classes.

Because long-term fluctuations are an important component of the simulated physics, the mean lake level must follow realistic trends. The solution space is therefore composed of ten discrete levels that span the range of variability observed in the past and expected from climatic projections (e.g. from 73.75 m to 77.0 m in Lake Ontario, with an average increment of 0.5 m; Figure 40). For each lake level, several simulations were run under varying atmospheric conditions to provide a set of possible tilts and, from these, a representative spatial distribution of wind set-ups in each grid cell. The wind compass rose was divided into 16 equal subdivisions, offering a resolution in wind direction of 22.5°. The sub-directions included the eight principal winds (i.e. N, NE, E, SE, S, SW, W, NW, and N), as well as the eight half-winds (i.e. NNE, ENE, ESE, etc.). For wind speed, five to seven wind classes were selected based on the wind climatology behind the observed 1980–2010 set-up events in Lakes Ontario and Huron (e.g. Figure 41). The first class, which

includes wind speeds below 2.78 ms^{-1} (or 10 km h^{-1}), is defined as the no-wind category, meaning that any wind speed below 2.78 m s^{-1} is considered too weak to generate significant surface deflection. This is the so-called “still water” case.

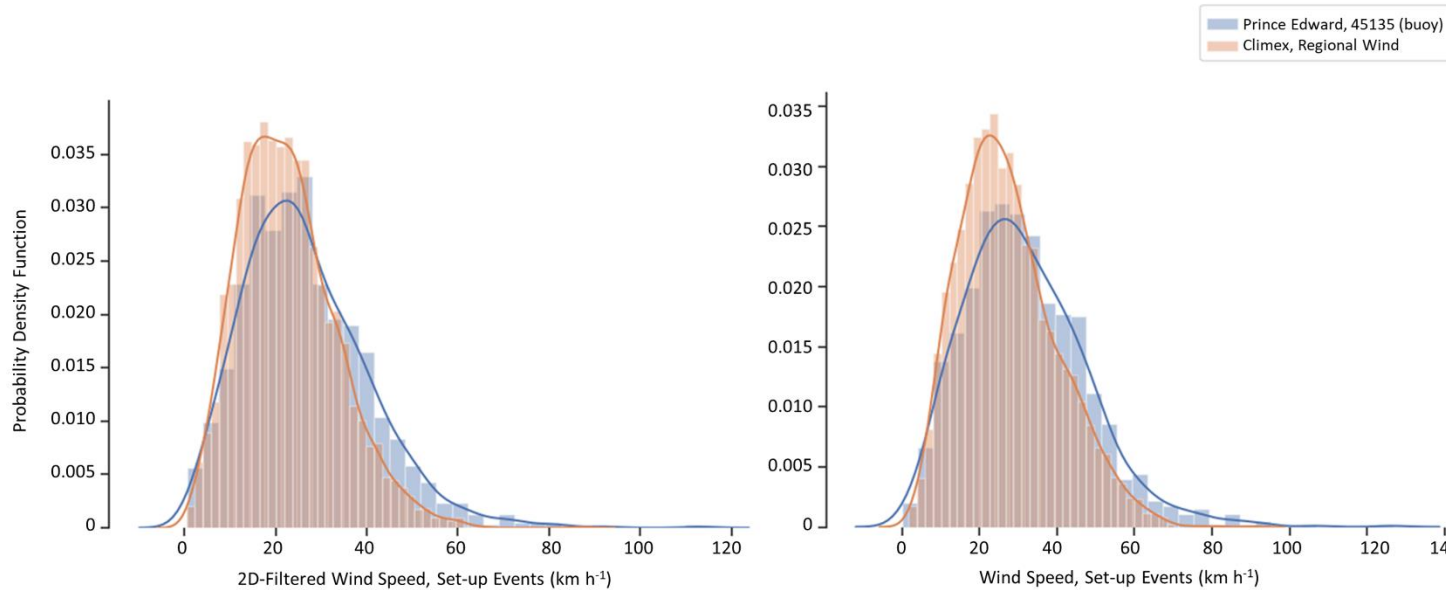


Figure 41: Empirical distribution of observed wind speed during identified wind set-ups in Kingston, Lake Ontario. Wind values refer to observations recorded offshore, at the Prince Edward buoy (in blue; cf. Section 2.3.1), or values extracted from the regionally averaged Climex series (in orange). Solid line gives the estimated PDF, while empirical is provided by the shaded boxes. The left panel shows results obtained from 2days-filetered time series, while the right panel, from unfiltered series. Details are given in the text.

Hence, for each combination of lake level, wind speed, and wind direction, only one 2D steady solution is simulated. Depending on the wind speed used, the bathymetry of the lake is adapted to provide a correct estimate of the displacement in the surface mixed layer, independent of the motion experienced in the lower part of the water column. The system is therefore reduced to a single-layer model, with an effective depth that changes with the atmospheric forcing used. The effective depth to be used was set during the model calibration, which is discussed below.

Although the mixed layer is also affected by meteorological forcing that forces surface heat fluxes, and causes a deepening or shallowing of the surface layer, this influence was neglected in the scenario-based modelling approach. First, because no concurrent simulations were performed to project changes in lake surface temperature, any estimates of changes in surface heat flux and its consequences would have been speculative. Second, based on previous studies conducted on the response of the thermal structure to changes in air temperature and wind speed (Huang *et al.*, 2012; Liu *et al.*, 2014), the thermocline depth is more sensitive to winds, which is mainly related to the enhanced influence of upwelling events when wind speeds increase. Changes in

air temperature primarily affect the time of onset and breakdown of the stratification (Robertson and Ragotzkie, 1990; Huang *et al.*, 2012), with increasing air temperature leading to earlier onset and later breakdown, which is not accounted for in the solution space calibration. However, wind speeds also have a strong effect on this aspect (Liu *et al.*, 2014; Huang *et al.*, 2010; Austin and Allen, 2011).

3.4.3.2.2 Filtered winds: Atmospheric forcing and wind set-ups

To generate steady-state scenarios, the lake models must be forced with a constant wind field, i.e. wind blowing in one direction, with a given wind speed. Since the main objective here is to simulate the short-term water level fluctuations associated with set-ups, i.e. the tilting of the lake surface under constant surface forcing, local variations in the wind field are assumed negligible for the lake dynamics and only basin-wide perturbations are considered. Furthermore, it has been shown (cf. Section 3.2.2) that the response of the lake is in phase with atmospheric systems with a return period greater than 2 days, which is the typical period of synoptic-scale systems (or storm track) in mid-latitudes (e.g. Blackmon *et al.*, 1977). Therefore, only large-scale, long-lasting atmospheric disturbances are assumed significant for basin-scale dynamics, and only similar disturbances were used to force steady-state solutions. These perturbations can be extracted from the low-frequency components of the wind time series, which includes all fluctuations with period > 2 days. In the scenario-based approach, the wind used to trigger a basin-scale motion is thus the wind field obtained by filtering out all high frequency fluctuations in the zonal, u , and meridional, v , components (here after referred to as 2days-filtered or 2D-filtred time series). Figure 41 shows the observed wind speed during set-up events for the filtered and unfiltered time series, while Figure 43 displays a snapshot of the time series (2days-filtered in blue).

This distinction between filtered and unfiltered winds is important because the events to be modelled have a period that matches the periodicity of large-scale synoptic systems. This is directly related to the high inertia of lakes, which adjust slowly under the action of a surface constraint. Since the scenario-based approach relies on steady-state solutions, any wind event is assumed sufficiently long to generate basin-scale motion, which is not the case when a rapid change in the wind field occurs. The unfiltered, hourly time series typically used to force the hydrodynamic models include temporal and spatial variations that do not generate any tangible lake level response other than local scale disturbances. Therefore, using these time series would result in unrealistic short-term fluctuations that do not replicate the expected lake behavior.

3.4.3.2.3. Regionally averaged winds

In the complex hydrodynamic approach, the lake models are forced with gridded wind data, which give the detailed wind field at a horizontal spatial resolution of ~ 12 km, a resolution small enough to allow representation of some mesoscale features and local variations that induce basin-wide gradients. With the scenario-based approach, the use of similar wind data is impossible as the 2D solutions are precomputed based on specific wind conditions (Figure 40). The lake models are forced with a constant wind field, which has no variation in space and time, restricting the atmospheric forcing to one speed and direction. Realistic short-term fluctuations are nevertheless expected, as if the models were run with a gridded dataset, extracting the significant influence of wind from the spatial distribution at each time step.

In order to provide a realistic forcing that properly reproduces the non-steady behavior of the lakes, a single point time series was used for each simulation period. This time series was created from the gridded datasets by reducing the spatial distribution to a regional description of the wind, which is intended to be representative of the predominant wind condition, experienced (on average) by the basin. Since wind is a vector field, the averaging procedure used must take into account the spatial distribution of the two wind components, zonal and meridional, and thus obtain a representative wind speed and direction for each gridded map in the dataset. Such averaging is not straightforward because there is a correlation between the two wind components, which must be maintained to avoid unwanted changes in the atmospheric pattern.

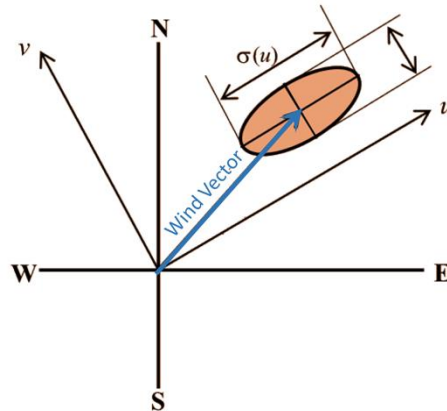


Figure 42: The conceptual ellipses used by Harris and Cook (2014) to define the joint PDF of wind speed and direction. Details given in the text.

To extract prevailing weather patterns over a given region, model-based clustering can be applied (e.g. Clifton and Lundquist, 2012; Kazor *et al.*, 2015). This technique assumes that the

observations are generated from a mixture of probability distributions, each of which represent a different cluster or, put another way, one of the components of spatial wind variability. The data can therefore be classified into several subsets according to their probability of belonging to one or the other, and a mixture model can be used to characterize the set of solutions thus obtained. For wind regimes, joint probability density functions (PDF) of wind speed and direction can be used. This distribution follows the description of Harris and Cook (2014), which describes the 2-dimensional wind distribution as ellipses in a rotated reference frame aligned with the principal axes of the wind (Figure 42). In this description, the two orthogonal wind components, u and v , are uncorrelated. The PDF can therefore be defined as (Cook, 2019):

$$p(u, v) = \frac{1}{2\pi\sigma_u\sigma_v} \exp \left[-\frac{1}{2} \left(\frac{(u - \bar{u})^2}{\sigma_u^2} + \frac{(v - \bar{v})^2}{\sigma_v^2} \right) \right] \quad 3.9$$

with overbar denoting means, and σ , standard deviations. The distribution is now a joint Gaussian distribution, where the standard deviations give the axis of the ellipse, and (\bar{u}, \bar{v}) , the position of the ellipse in geographical space. When the wind field is clustered into multiple ellipses according to the individual vectors in the gridded map, the joint PDF of the mixture is the sum of the N component PDFs, each weighted by its relative frequency, f :

$$p(u, v) = \sum_{i=1}^N f_i \times p_i(u, v) \quad 3.10$$

This model can therefore be used to extract, from a number of clusters, the frequency (or weight) of a specific subset of characteristic winds, along with their mean components, (\bar{u}, \bar{v}) , which provide wind speed and direction. These variables can then be used to define the regional wind regime of a 2D spatial distribution at any time step.

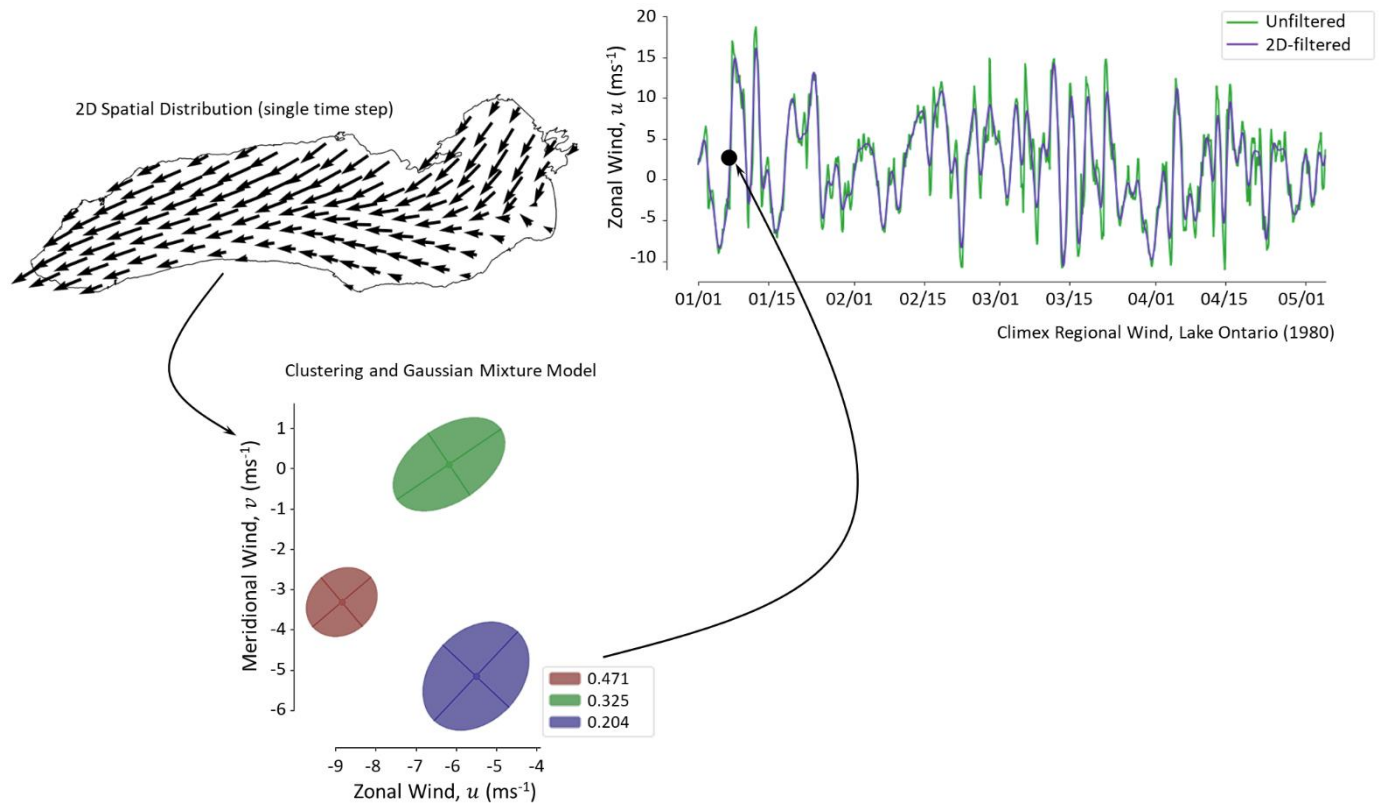


Figure 43: Example of a regionally averaged wind time series (upper right panel), along with the clustering results obtained for the presented 2D spatial wind distribution (upper left panel). The clusters, shown as ellipses in the u, v space, display shaded colors that refer to their frequency (or weight) in the mixture model. Filtered and un-filtered time series are also presented.

In the scenario-based approach, the time series of lake level fluctuations is reconstructed based on the single-point wind time series obtained by the Gaussian Mixture Model explained here, using a fixed number of three clusters to describe the lake-wide spatial variation. Figure 43 shows an example of a regionally averaged time series, along with a snapshot of the spatial distribution and clustering results. As previously mentioned, 2D-filtered data are used, a filtering process that was applied once the averaged time series was produced. For each simulated period, a new wind time series is therefore generated for Lakes Ontario and Huron separately. For this purpose, only grid points included within the geographical boundaries of the lake are retained to force each model with over-lake atmospheric conditions only (Figure 43, upper left panel).

3.4.3.2.4. Interpolation: Creating the time series

The creation of a continuous series of 2D maps of simulated levels relies on the use of the solution space, which provides the set of precomputed solutions, and the point series of winds and mean lake level, which give the hydrological and atmospheric forcing that determines the state of the

lake at each time step. The idea is to select from the precomputed solutions the one that best fits the conditions under which the lake evolves, and to recreate artificially the chronological sequence that provides the change in lake dynamics through time. Since the number of lake level and wind classes is limited, the best solution is determined from four candidate solutions, using a bilinear interpolation technique (Figure 44).

The candidate solutions share a common wind direction, which corresponds to the wind origin at time t according to the regional wind time series, but have different wind speeds and mean lake levels. These wind and level conditions are selected to restrict, using lower and upper bounds, the solution space to four possibilities, which offer simulated solutions with conditions (wind speed and mean level) slightly lower or higher than those imposed at time t . For example, if the wind speed at time t is 27 km h^{-1} , the 2D maps computed under a wind of 20 and 35 km h^{-1} (cf. Figure 40) in the solution space will be selected as candidate solutions.

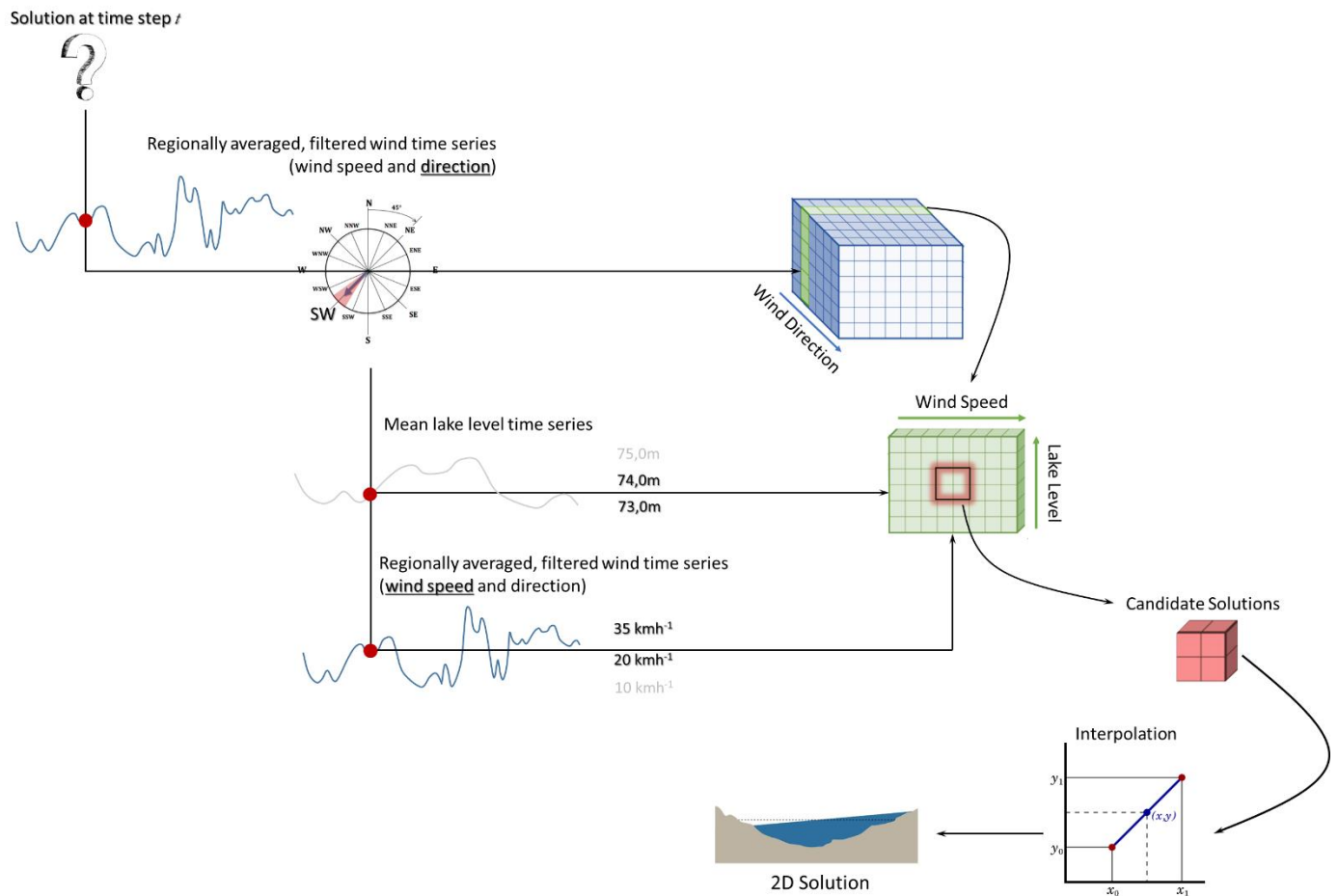


Figure 44: The bilinear interpolation process. Details given in the text.

The final solution is therefore the result of the bilinear interpolation performed using these four candidate solutions, which is computed at each time step of the simulated period. Since time series of mean lake level is a prerequisite for the interpolation process, these time series are either calculated from observations recorded during the historical period (1980–2018) or provided by the climate projections (cf. Section 2.3.1 and 2.3.2; 1980–2009 and 2070–2099). For the historical period, the stations used by the NOAA Great Lakes Environmental Research Laboratory were selected to calculate lake-wide average levels, i.e. stations Rochester, Oswego, Port Weller, Toronto, Cobourg, and Kingston in Lake Ontario, and Ludington, Mackinaw City, Harbor Beach, Milwaukee, Thessalon, and Tobermory in Lake Michigan-Huron.

3.4.3.2.5. Wind and depth calibration

Initialization and calibration of lake models in the scenario-based approach require more work than is typically required to parametrize a 2D hydrodynamic model, since multiple models must be calibrated and validated for a single lake. Each wind condition available in the solution space must be associated with a specific basin-wide effective depth to artificially increase (or decrease) the surface layer in which wind-driven flow is constrained. The calibration should then use the observed data to adjust the bathymetry for each wind speed and direction, as the origin of the wind can influence the fetch length and hence, the wind stress acting on the lake surface (e.g. Richards *et al.*, 1966).

This calibration was realized in several steps:

1. Creation of a database that includes the observed set-ups and wind amplitude. This database is created following the identification process explained in Section 3.2.2, which is designed to detect lake level anomalies that correspond to wind events in the filtered time series. All gauge stations were included in the database, and the set-up amplitudes were extracted for the 16 binned wind directions to capture any asymmetry in the lake dynamics along the fetch direction.
2. Creation of several lake models with varying bathymetry, or depth, for use with the different wind classes in the solutions space (cf. Figure 40).
3. Creation of the optimal depth-wind set, which identifies the effective depth to be used under a specific wind speed and direction to reproduce events included in the database created in 1). For this step of the calibration, the mean lake level was kept constant. The variation of the mean level is negligible for the dynamics of the surface layer, which depends on the depth of the water column considered.
4. With the optimal set of depth-wind combinations, the solution space was completed by varying the mean lake level (cf. Figure 40).

More details on the specific lake models are given in Sections 3.5.1 through 3.5.5.

3.4.3.3. The Upper St. Lawrence River: A specific case

The Upper St. Lawrence River (here after referred to as USLR) is the second connecting channels modelled in this project, apart from the St. Clair–Detroit system. It is located at the outlet of Lake Ontario, and is largely influenced by the dynamics of the lake that modulates the outflows and hence, the flow of the river. This portion of the Great Lakes Basin is therefore characterized by a significant change in water level that describes a slope between the lake, near Kingston (Ontario) and Cape Vincent (New York, USA), and the downstream portion of the USLR, near Cornwall (Ontario), where Lake Ontario outflows are regulated.

The Upper St. Lawrence could have been successfully modelled by either modelling approach, as no three-dimensional dynamics are involved and conventional 2D modelling is well designed to simulate river flow regimes. However, due to the influence of Lake Ontario levels at the mouth of the USLR, the scenario-based method was chosen to facilitate the simulation process, using the simulated water level at Kingston, as well as the observed or projected discharge values as inputs. For this specific section of the Great Lakes, the contribution of atmospheric forcing to water level fluctuations is therefore assumed negligible compared to the lake itself, which force the flow in the upstream part of the river. As stated by Paturi *et al.* (2012), the northeastern section of the Upper St. Lawrence is preliminary hydraulically driven, with both long- and short-term disturbances induced by lake dynamics. It is only during strong, easterly storms ($\sim 10 \text{ m s}^{-1}$ or 36 km h^{-1}) that the influence of wind cannot be excluded, as similar conditions generate flow reversal near Kingston (Paturi *et al.*, 2012). Such events are not captured by the interpolation process used to model the USLR, as no wind was considered, which represents a limitation of the modelling. More details regarding this specific model are given in Section 3.5.1.

3.4.4. Summary table: lake-specific approaches and water level uncertainties

Table 7 below shows the post-calibration uncertainties on water level and the approach used for each water body of the system. More details on the calibration process for each lake are given in Section 3.5.

Table 7: Summary table for the different lake models.

	Modelling Approach	Mesh Size ($\times 10^3$)	Seasonal Water Level Uncertainty	
			Sub-Basin	RMSE (cm)
Upper St. Lawrence River	Scenario-based	750		1.7–3.0
Lake Ontario	Scenario-based	590		2.6
Lake Erie	Complex	323		2.9
Huron-Erie Corridor	Complex	600	St. Clair River	4.0
			Lake St. Clair	4.2
			Detroit River	4.8
Lake Huron	Scenario-based	1,800	Lake Huron	4.1
			Georgian Bay	4.8

3.5. Lake models

This section presents the methodology used to create reliable water level scenarios for the historical and projected time periods, as well as the accuracy of the models developed for each lake and connecting channels considered in this project.

3.5.1. Upper St. Lawrence River

3.5.1.1. Bathymetry and modelling approach

Only the western part of the Upper St. Lawrence River was modelled for the project, which provides the physical conditions in the vicinity of Hill Island, near Alexandria Bay (New York, USA), the only selected site located in this connecting channel (cf. Figure 2). The model therefore covers the northeastern portion of Lake Ontario, between Kingston (Ontario) and Cape Vincent (New York, USA), and the upstream section of the Upper St. Lawrence River ending at the Iroquois Dam, 46 km west of the Moses-Saunders Dam, where Lake Ontario outflows are regulated. The section of the river between Kingston and Iroquois Dam, in the middle of the USLR, was directly derived from the St. Lawrence Seaway model, which was calibrated and validated for operational use in 2020.

The river is generally shallow (Figure 45) and has alternating sections with rapids, where flow velocities are high, and quiet sections. Consequently, the slope of the river is not constant, and velocities vary greatly with river discharge. As previously mentioned, the effect of wind on the local dynamics is considered negligible, and the USLR is defined as a system essentially forced by hydraulics, which include the effect of wind on Lake Ontario itself. The scenario-based modelling approach was adopted for this connecting channel, and static solutions were generated with an imposed lake level at the Lake Ontario outlet and a fixed discharge at Iroquois Dam (Figure 45). The outflows used as boundary conditions are either from observed values, which are consistent with the regulation history of Lake Ontario (1980–2018), or those projected by mean lake level simulations (cf. Section 3.3), which are in accordance with Plan 2014 guidelines.

3.5.1.1.1. Interpolation: Lake Ontario levels and outflows

Since no atmospheric forcing was included in the Upper St. Lawrence modelling scheme, the steady-state solutions that fill the solution space were generated with a bilinear interpolation that accounts for Lake Ontario levels and outflows, the unique dimensions of the solution space, which are reduced to two. The Lake Ontario levels used here are the observed and simulated levels obtained from the lake model (cf. Section 3.5.2), time series that include all long- and short-term

fluctuations that drive changes in discharge, with both seasonal fluctuations and wind set-ups. The St. Lawrence model thus depends on the Lake Ontario model for climate projections.

Inset in Table 8 shows the gauging stations in the USLR that historically recorded water levels, i.e. Brockville (Ontario), and Alexandria Bay (New York, USA).

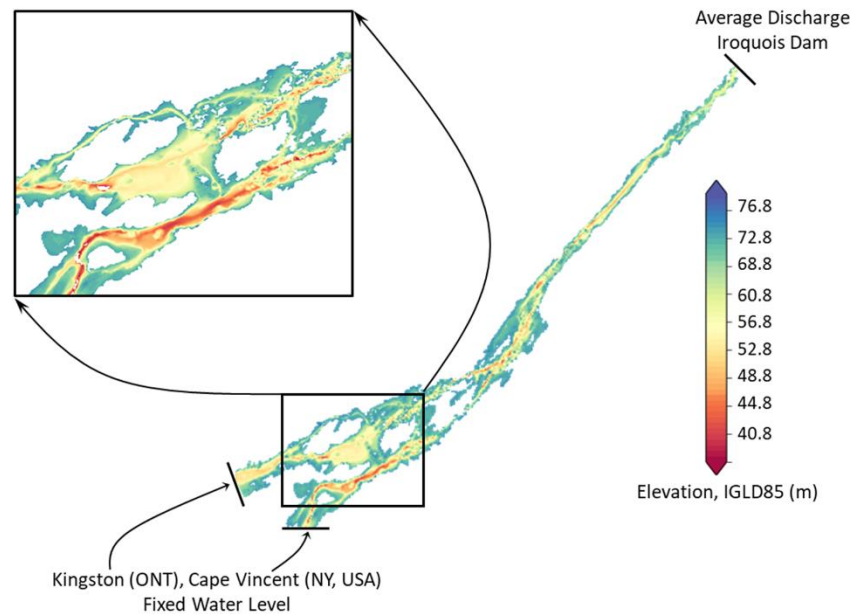


Figure 45: Bathymetry of the Upper St. Lawrence River and boundary conditions used for the modelling.

3.5.1.2. Computational grid

The computational grid used for the USLR contains 748k nodes and 370k quadratic elements, which allows for a good parametrization of the numerous islands that shape the topography of the upstream section of the river, namely the Thousand Islands. The resulting mesh is composed of more elements than the entirety of Lake Ontario, and it is characterized by a marked change in bathymetry in the along-channel direction.

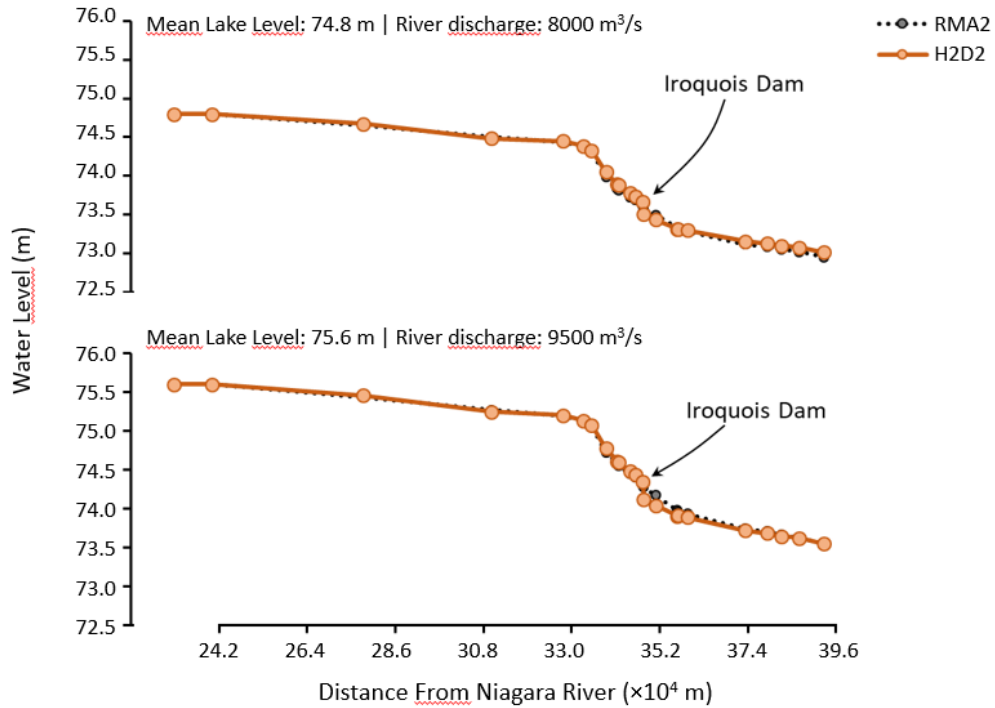
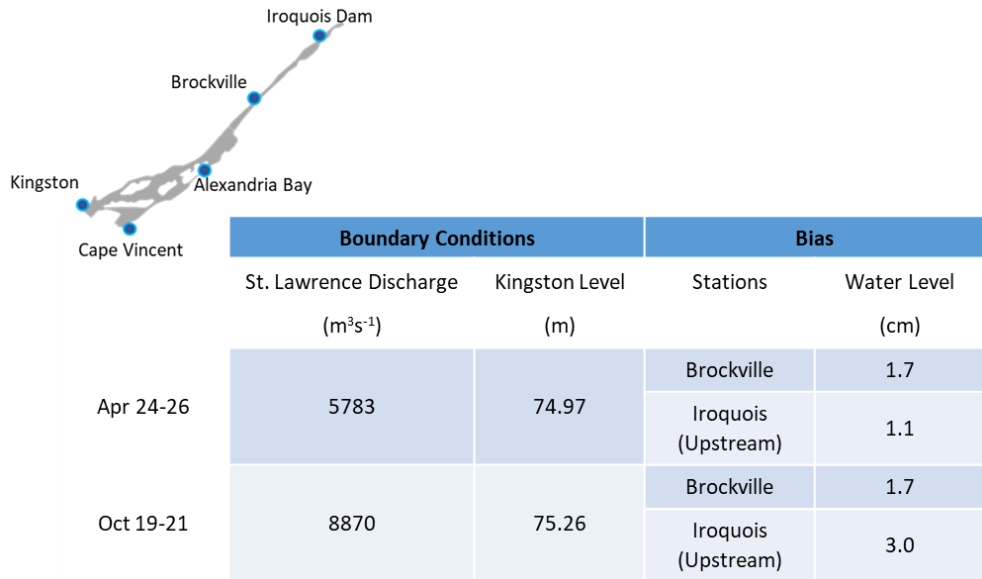


Figure 46: Modelled water levels obtained for the RMA2 model and the calibrated USLR model. The x-axis gives the distance from the mouth of the Niagara River, representing water levels along an axis that follows the course of the Upper St. Lawrence.

3.5.1.3. Calibration and validation

The calibration of the Upper St. Lawrence River was performed with two datasets: (1) results obtained from a pre-existing calibrated and validated model, using the RMA2 solver (Thompson and Moin, 2003; Thompson, 2006); and (2) observations collected from two distinct time periods, i.e. April and October 2019, for which accurate discharge measurements were available. The results of this calibration process are presented in Table 8 and Figure 46. Although Figure 46 shows results obtained for the entire Upper St. Lawrence River, from Lake Ontario to Moses-Saunders Dam, only the upstream section is considered for this project.

Table 8: Calibration results for the USLR model.



3.5.2. Lake Ontario

3.5.2.1. Bathymetry and modelling approach

The morphology of Lake Ontario is characterized by its elongated shape, which runs from west to east, and its deep eastern Basin (i.e. Rochester Basin), where the depth reaches over 240 m (Figure 47). The scenario-based approach is therefore the modelling technique adopted for this lake.

The Lake Ontario model ends at the entrance of the Upper St. Lawrence River, between Kingston (Ontario) and Cape Vincent (New York, USA). Toward the east, the dynamics are mainly described by a river-like flow as water levels are primarily determined by discharge, resulting in high current velocities. This section was modelled separately as described in Section 3.5.1. In its western part, the model was forced with mean discharge data at the downstream end of the Niagara River, which controls the outflow from Lake Erie (via the Niagara Falls) and, hence, one of the main water supplies to the basin (5000–7000 m³s⁻¹). In its eastern part, water levels were imposed between Kingston and Cape Vincent, and this boundary condition was used to generate the different static solution space scenarios. The mean lake level used in the interpolation process is therefore the average water level obtained under this set of static forcing (cf. Section 3.4.3.2).

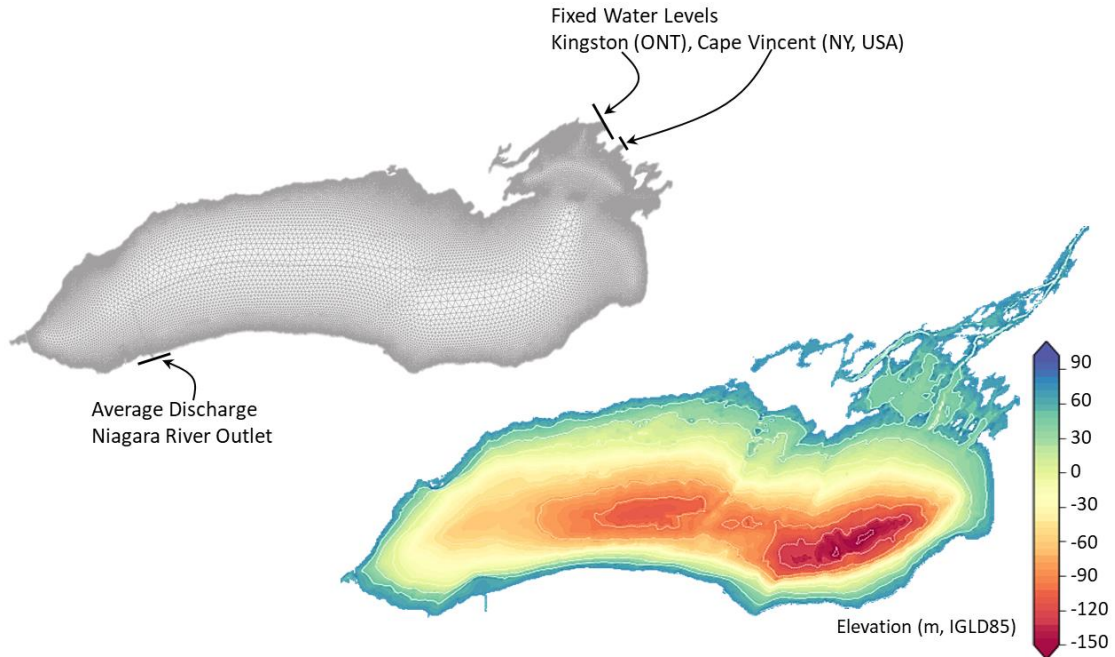


Figure 47: Mesh details (upper panel) and bathymetry (lower panel) used for the Lake Ontario model. Boundary conditions are also defined.

3.5.2.2. Computational grid

As with other lakes in the Great Lakes system, the Lake Ontario model displays relatively low mesh density in its center, but an increasing number of elements near the coasts and islands, bringing the total number of nodes and triangular cells to 590k and 286k, respectively (Figure 47).

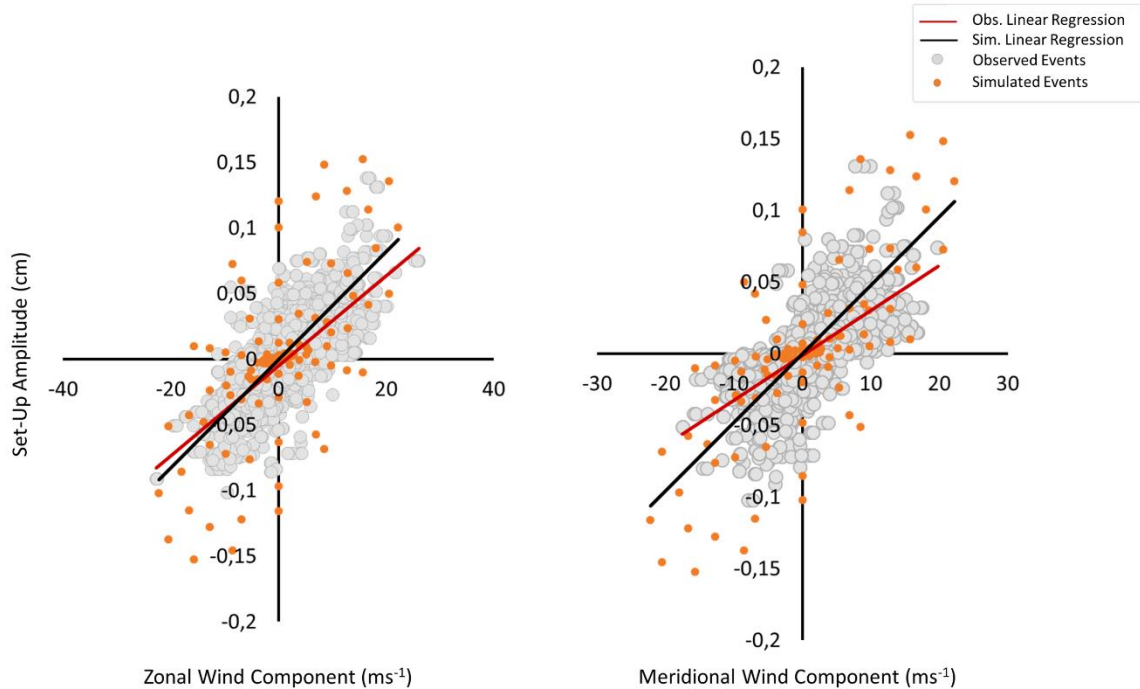


Figure 48: Observed (grey dots) and modelled (orange dots) wind-driven set-ups at Kingston, Lake Ontario. The black and red lines show the linear regression obtained from the detected events, i.e. the relationship between event amplitude and wind speed for the zonal (left panel) and meridional (right panel) wind components.

3.5.2.3. Calibration and validation

Several gauging stations are located on either side of Lake Ontario, as shown in Table 9. Historical water levels observed in these locations, along with offshore wind data recorded in the central portion of the basin, at Prince-Edward buoy (station 45135), were used to populate the database of set-up events needed to calibrate the scenario-based approach (cf. Section 2.3.1). The calibration period extends from 1990 to 2010, which encompasses the operational period of the moored buoy.

Figure 49 shows a comparison between the amplitude of observed and modelled set-up events for Kingston (Ontario) following the calibration process. These results were obtained with the optimal depth-wind combination, i.e., the combination that provides a good representation of the surface layer dynamics under different wind intensities and directions. Some adjustments were necessary to reduce the overall root-mean square error (or RMSE) of the water level estimates, which remains under 3 cm for the 1990 series reconstructed with the bilinear interpolation technique explained earlier (cf. Section 3.4.3.2; Table 9 and Figure 49).

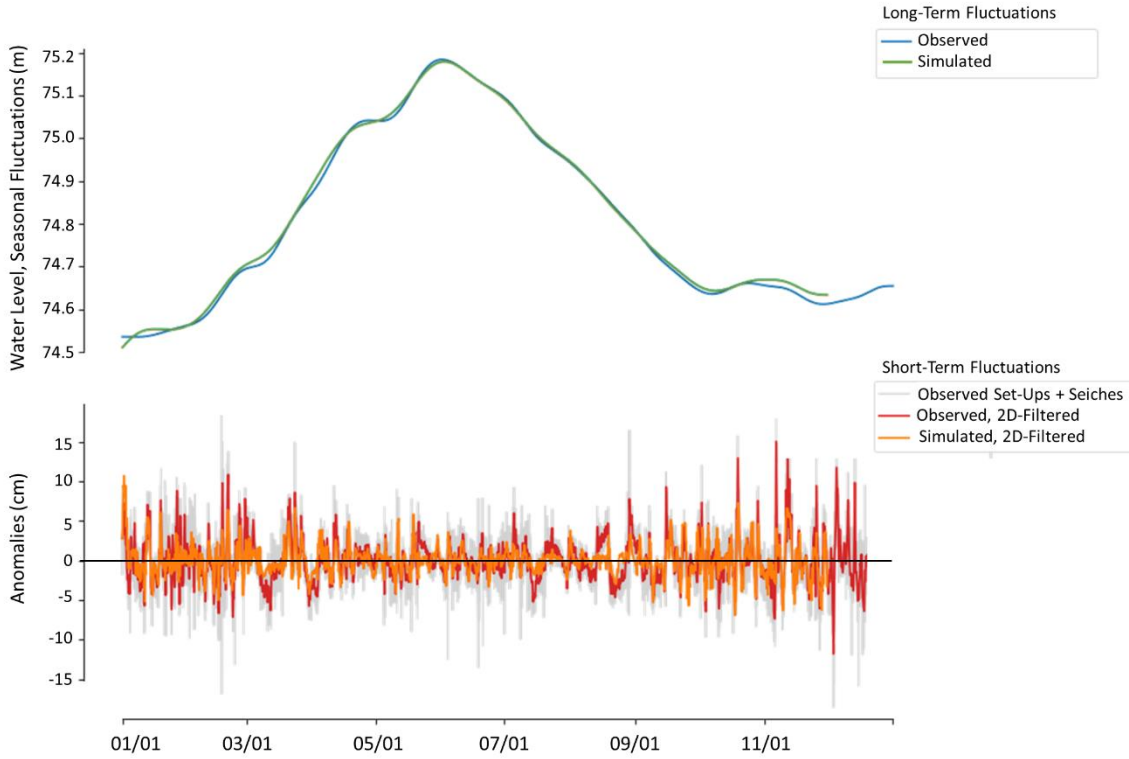
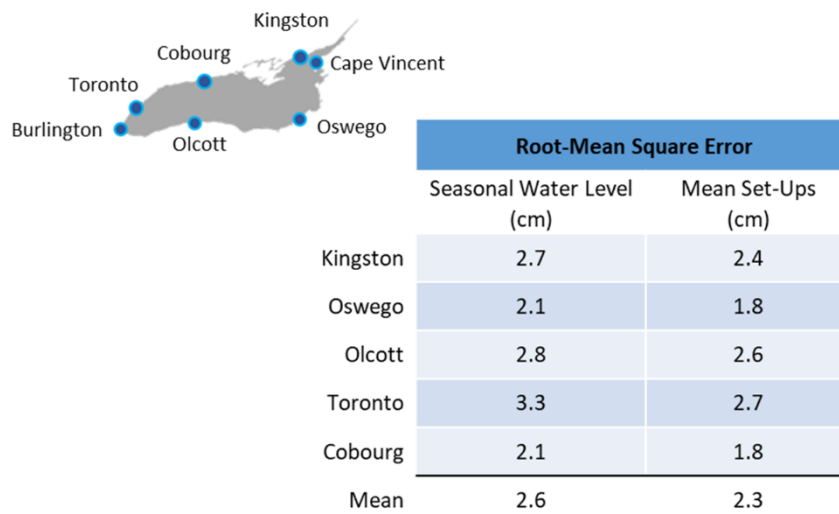


Figure 49: Upper panel: Observed (blue) and modelled (green) seasonal water level fluctuations for year 1990 at Kingston, in Lake Ontario. Lower panel: Idem, but for the short-term fluctuations, which include only the set-up events for the 2days-filtered time series (orange and red). The grey line gives the full detailed series of observed short-term disturbances, including surface seiches (which are not modelled) and set-ups.

Table 9: The errors (RMSE) obtained for the long- and short-term fluctuations in Lake Ontario, according to the calibrated model.



3.5.3. Lake Erie

Past modelling effort dedicated to Lake Erie have mainly focused on three-dimensional simulations, which are used to predict seasonal water levels, as well as large-scale circulation, thermal structure, and ice cover (e.g. Bai *et al.*, 2013; Dupont *et al.*, 2012). Reasonable agreements between simulated and observed hourly water levels were obtained with the Lake Erie Operational Forecast System (LEOFS-FVCOM, NOAA) over a two-year period, including seiche representation following strong wind events (Kelley *et al.*, 2018; Xu *et al.*, 2018). However, the amplitude and timing of extreme set-up events were interpreted as deficient, with RMSEs ranging from 4 to 18 cm, with the largest errors at the lake ends. Few attempts have been conducted with two-dimensional hydrodynamic models, although these can improve the depiction of nearshore dynamics, especially with respect to currents in shallow water areas. It is possible to mention the high-resolution model implemented by Dibling (2012) for Lake Erie, which is based on ADCIRC-SWAN (ADvanced CIRCulation Simulating WAVes Nearshore), a coupled hydrodynamic and wave model that provides a fine scale description of coastal dynamics, including flooding.

3.5.3.1. Two-Dimensional Lake Erie model

The Lake Erie model, which includes the downstream portion of the Detroit River and the upstream portion of the Niagara River, is based on an unstructured, finite element mesh grid that allows for good definition of shorelines, shallow water areas and harbours. The grid has a resolution of ~10 m to 3 km and includes over 323k nodes (150k triangular elements; Figure 50). Lateral boundaries were placed at Fort Wayne (Detroit River) and Fort Erie (Niagara River), in line with known gauging stations. The downstream course of major tributaries was also included in the mesh to provide adequate runoff forcing for historical modelling. River discharges can be significant to the overall net basin supply, especially during the spring freshet when total river flow rate can episodically reach $1000 \text{ m}^3\text{s}^{-1}$. Main tributaries include the Maumee River (Ohio, USA) and the Grand River (Ontario, Canada), which are by far the most significant inflows outside of the Detroit River.

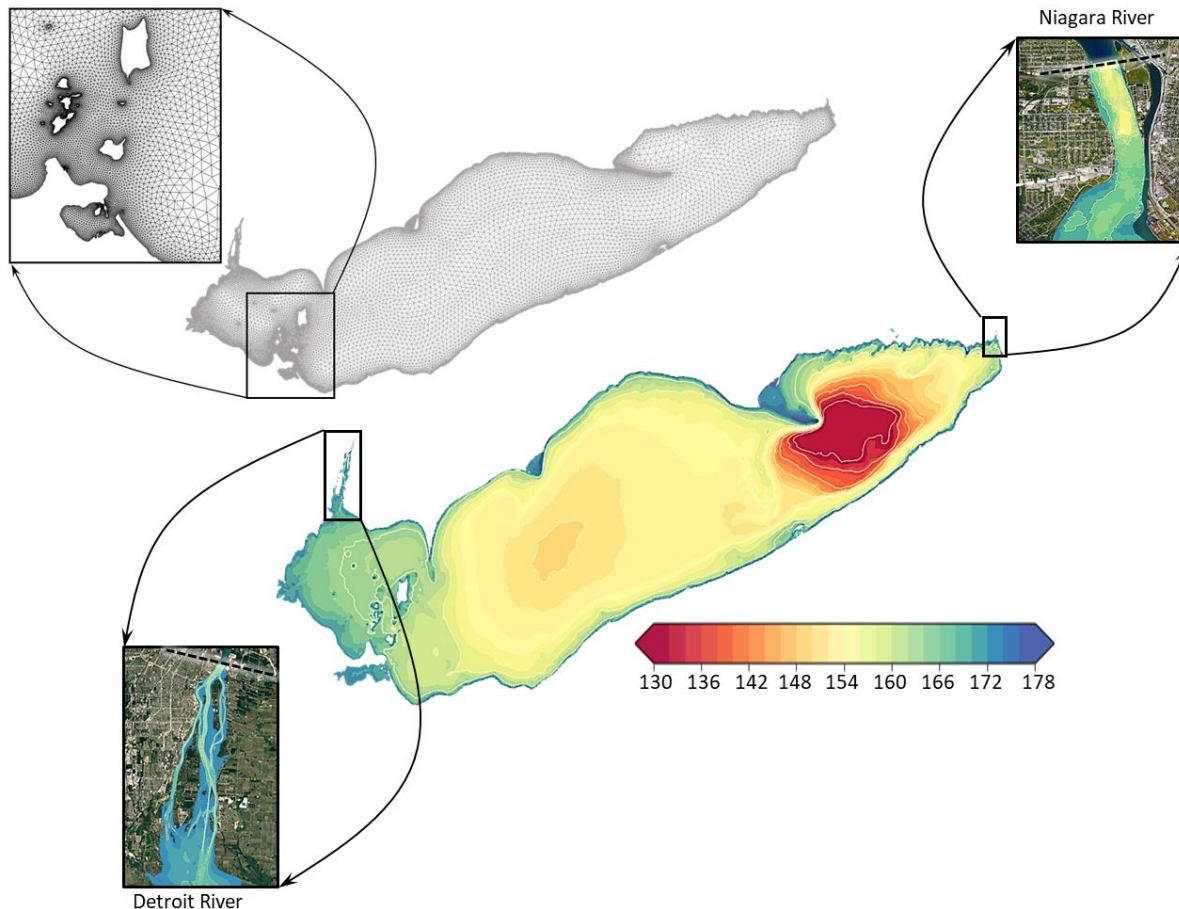


Figure 50: The mesh (top) and the bathymetry (bottom) of the Lake Erie hydrodynamic model. Insets show details of the lake's inlet (Detroit River) and outlet (Niagara River).

The bathymetry was constructed using a linear interpolation method, which uses a priority-based ranking process to avoid overlapping (and conflicting) datasets and ensure that the best available depth measurement is used at each grid node. The datasets employed comprise high-resolution bathymetry of the Detroit¹⁷ and Niagara Rivers, hydrographic surveys collected by the NOAA along the southern shores of the lake and in the Buffalo area (<https://maps.ngdc.noaa.gov/viewers/bathymetry/>), as well as the official Lake Erie bathymetric grid distributed by the NOAA (<https://www.ngdc.noaa.gov/mgg/greatlakes/>). Some bathymetric LiDAR and high-resolution sounding data were also added at specific locations on the lake, near and within the wetland sites included in the project. The uplands and beaches observed at Long Point, located on the northeast shore of the lake (Figure 2), were added to the mesh to allow for

¹⁷ The bathymetry used for the Detroit River was first created for the Detroit River and Lake St. Clair waterways hydrodynamic model, which included 2000 surveys collected by the NOAA.

(potential) flooding of the land under an extreme high water levels scenario. Figure 51 shows the final bathymetry grid obtained after the interpolation process.

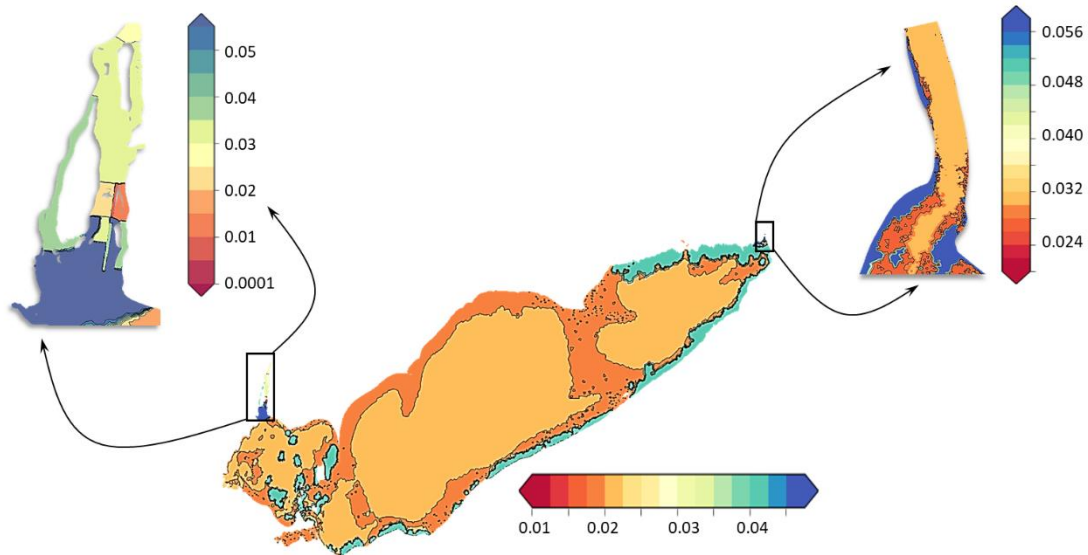


Figure 51: The Manning's coefficient in the lake, and in the Detroit and Niagara Rivers.

The Manning's coefficient, or bed roughness, was determined based on the substrate as defined by the Great Lakes Aquatic Habitat Framework dataset (<https://www.glahf.org/data/>), with a varying coefficient for sand, mud, gravel, rock, or clay (Figure 51). A more specific calibration was realized within the lake inlet/outlet, where bottom friction greatly influences the amount of water entering or leaving the basin, the mean annual discharge of the Detroit and Niagara Rivers being close to $6000 \text{ m}^3\text{s}^{-1}$. For the Detroit River, the roughness applied replicates that used in the pre-existing Huron-Erie corridor hydrodynamic model (Holtchang and Koschik, 2002), as it has already been calibrated to ensure proper flow rate through the waterways (CHC, 2009). The Manning's coefficient in the headwaters of the Niagara River was calibrated over a one-year period to preserve the seasonal trend in lake levels and prevent long-term deviation. A depth-related coefficient was selected, with three different values that follow bank topography (Figure 51). While the simulated water levels are consistent with observations, non-negligible errors are obtained in the outflows at Fort Erie, which are highly variable depending on the period simulated (Figure 52). Published discharge data, however, are subject to known errors. Uncertainty in headwaters flow measurements has been estimated to 4% (200 to $250 \text{ m}^3\text{s}^{-1}$) at a 95% confidence level (Bruxer, 2010). The Ontario Power Corporation River Controllers, who are in charge of the Robert Moses Niagara Power Plant, also apply correction factors to the observations, based on downstream gauges and actual power plant flows, to account for losses due to weeds and ice

(pers. comm.). Therefore, no further calibration was attempted to correct for the flow discrepancy at the Lake Erie outlet, and, as explained in the following sections, this error has no direct impact on the long-term simulated water levels due to the simulation strategy chosen for the project.

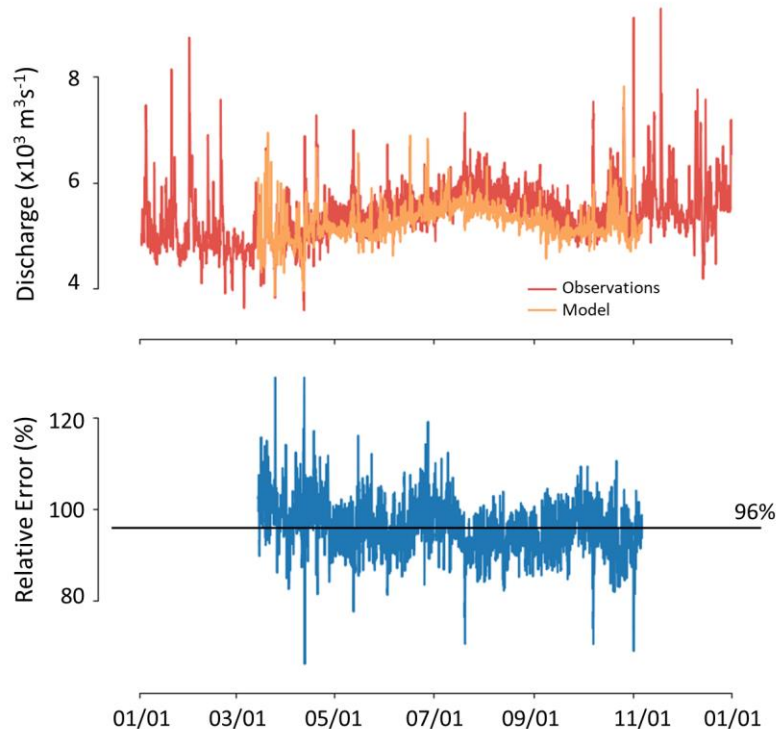


Figure 52: Top panel: Discharge simulated (orange) and observed (red) in 2013, at Fort Erie station (Niagara River). Bottom panel: relative error (%) between the simulated and observed discharge (blue), and relative mean error (black line) computed for the period April–November 2013. The relative error ranges from 86–107 % according to the 2.5 and 97.5 centiles, for this specific year.

The Lake Erie model was run with a 6-minute time step, which was found to be optimal for rapid convergence and reliable modelling of the lake’s response to winds. The simulations provide water level estimates from April through November only, to cover the growing season and avoid any ice cover that is not accounted for in the modelling.

3.5.3.2. Hydrodynamic forcing: Seasonal cycle and Interannual Variability

To create the historical time series, which covers the period 1980–2018, the hydrodynamic forcing included all components of the net basin supply that control the water level seasonal cycle: overlake precipitation, overlake evaporation, runoff, inflow/outflow, and diversion (through the Welland Canal, which connects Lake Erie to Lake Ontario). Several datasets were used to provide adequate forcing throughout the recent past period, based on the best available products (cf. Table 11).

3.5.3.2.1. Inflow/outflow, diversion and runoff

Lateral boundary conditions for the Lake Erie model were specified using real-time measurements recorded at the lake inlet and outlet: discharge at Fort Wayne, in the Detroit River (USGS station 04165710; Michigan, USA), and water level at Fort Erie, in the Upper Niagara River (CHS station 02HA013; Ontario, Canada). In the first case (Detroit River), high-resolution discharge data (6-minute time scale) were available for the last decade of the calibration period (2008–2018). Prior to these dates, only daily average flow (1990–2007) or daily flows estimated through the stage-fall-discharge equations developed by Fay and Kerslake (2009), with wintertime adjustment for ice retardation, were obtainable.

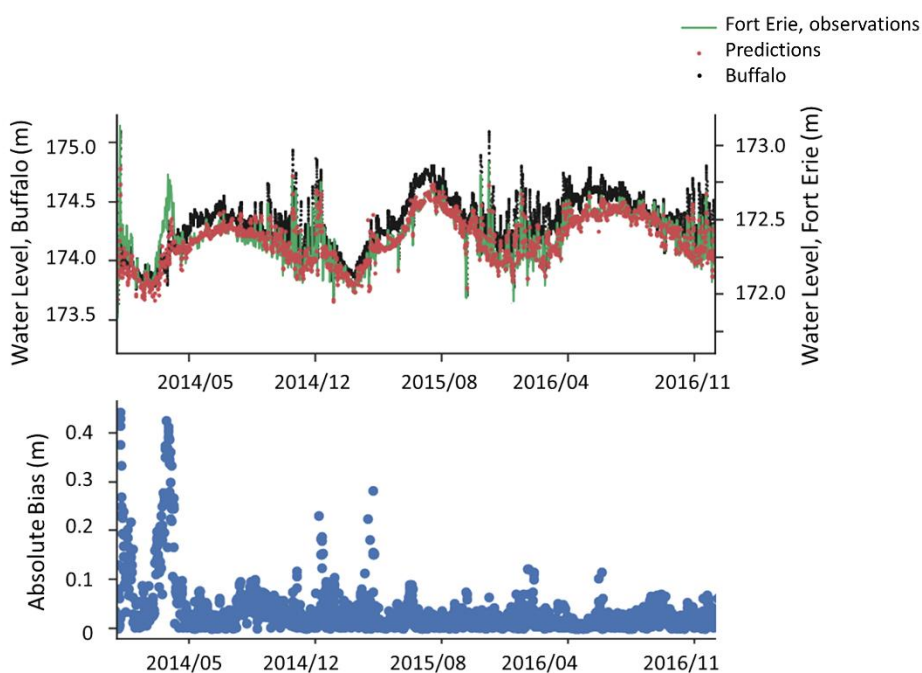


Figure 53: Top panel: Water level observed time series at Buffalo (black dots) and Fort Erie (green line), at the mouth of the Niagara River. The reconstructed Fort Erie time series, estimated using a Gradient Boosting regression algorithm, is shown by the red dots. Bottom panel: Absolute bias calculated from the estimated and observed water level time series at Fort Erie.

In the second case (Niagara River), continuous water level measurements at Fort Erie have only been recorded since 2009. Missing data (1980–2008) were reconstructed based on historical water levels observed at Buffalo (station 9063020; New York, USA), using a Gradient Boosting regression algorithm that employs a machine learning technique to obtain the best least-squares regression estimates. One regression estimate was obtained for every day-of-year, using a 31-

day moving window¹⁸, to provide values that reflect the seasonality observed in the (water levels) correlation, which is related to weed growth and change in bed roughness. The regression was performed over the low-frequency components of the time series, which include seasonal variability and wind set-up events. Comparison of predicted and observed water levels at Fort Erie on a sample dataset revealed a RMSE of ~5 cm, with a maximum absolute bias of 14 cm observed in winter (97.5 centile; Figure 53).

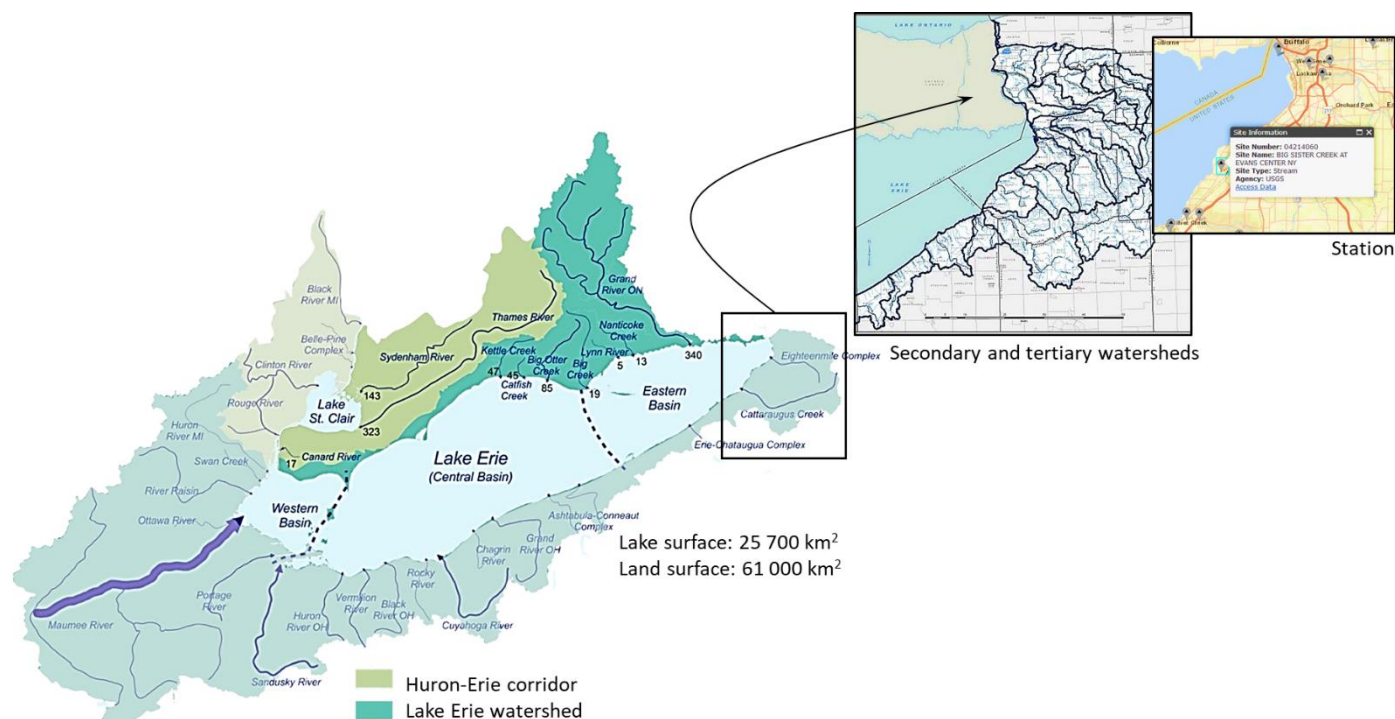


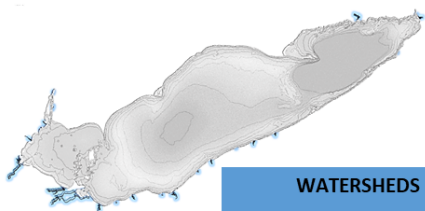
Figure 54: The Lake Erie watershed, with details of some of its secondary and tertiary watersheds, and the location of one hydrometric (gauging) station (adapted from <https://www2.erie.gov/environment/index.php?q=lake-erie-watershed-protection-alliance> and ECCC-OMECC, 2018).

The drainage basin of Lake Erie covers parts of Indiana, Michigan, Ohio, Pennsylvania, New York and Ontario, and it includes numerous small rivers that drain one of the secondary watersheds. Overall, 61 000 km² of the land surface contribute to the runoff, most of which is provided by the Detroit River that controls the water flows from Lake Huron through the St. Clair River, Lake St. Clair, and Detroit River system. As previously stated, the downstream course of 18 tributaries of the lake’s sub-basins were included in the grid, and inflow at tributary boundaries was used to ensure adequate drainage from surrounding land to the lake and capture peak flows. To do so, all secondary and tertiary watersheds were inventoried and associated with stream gauging

¹⁸ The use of a moving window avoid the creation of discontinuities from month to month.

stations where available (Figure 54), and then the gauged drainage areas were estimated. A correction factor was computed for each available stream gauge to obtain accurate estimates of total streamflow for a secondary watershed based on the associated gauging stations. The ungauged basins, which are primarily located on the northern shores of the lake (Table 10), were quantified with the drainage-area ratio method, i.e. the ungauged flow is estimated according to the nearby gauging station. Table 10 lists the gauged and ungauged secondary watersheds, their major tributary, which includes the tributaries used as boundary conditions in the hydrodynamic model (indicated by a star in Table 10), and the percentage of the gauged drainage area. The inventoried watersheds contained two drainage areas located in the downstream portion of the Detroit River (i.e. Cedar Creek and Detroit watersheds), as their flow is not captured by measurements recorded at Fort Wayne. For the historical period (1980–2018), the correction factors used to compensate for the ungauged drainage fraction change based on data availability, as some stations have only been operating for the last decade(s) (e.g. Black River, USGS station 04200500).

Table 10: Lake Erie secondary watersheds, their major tributary, including tributaries used as boundary conditions in the hydrodynamic model (indicated by a star, *), their associated gauging station, as well as the drainage (in km²) area and percentage of the gauged area.



WATERSHEDS	TRIBUTARIES	STATION ID	TOTAL AREA	% GAUGED AREA
<i>Western Basin</i>				
Maumee River (OH)	Maumee River*	04193500	17 018.2	96.1
Cedar-Portage (OH)	Lower Portage*	04195820	2 510.0	51.0
Detroit (MI)	Lower Rouge*	04167000	1 518.3	32.0
Huron (MI)	Huron River (via Raisin River)	04174500	2 378.3	79.0
Ottawa-Stony (MI)	Ottawa River*	04177000	1 806.3	30.0
Raisin (MI)	Raisin*	04176500	2 753.3	78.0
Cedar Creek (ONT)	Canard*	02GH003	814.8	20.0
<i>Central Basin</i>				
Sandusky (OH)	Sandusky*	04198000	4 732.0	68.5
Huron-Vermillon (OH)	Huron River* Vermillon River*	04199000 04199500	1 979.8	90.0 80.0
Black-Rocky (OH)	Black River* Rocky River*	04200500 04201500	2 324.7	70.0 80.7
Cuyahoga (OH)	Little Cuyahoga*	04208504	2 040.9	97.1
Ashtabula-Chagrin (OH)	Chagrin*	04209000	1 641.5	38.8
Grand River (OH)	Grand River*	04212100	1 827.5	64.2
Chautauqua-Conneaut (PA)	Conneaut*	04213000	2 246.9	20.0
Big Creek (ONT)	Big Creek (via Grand River)	02GC007	3 971.5	14.0
Rondeau (ONT)	(via Grand River)		966.9	0
<i>Eastern Basin</i>				
Grand (ONT)	Grand River*	02GB001	7 197.9	70.0
Cattaraugus (NY)	Cattaraugus*	04213500	1 449.5	77.9
Buffalo-Eighteenmile (NY)	Buffalo River*	04214500	1 856.1	20.0

The Welland Canal, which connects the lower lakes for navigation, diverts annually about 260 m³s⁻¹ of water from Lake Erie to Lake Ontario. This canal was included in the grid to account for diversion, and daily discharge was used (CHS station 02HA019) to provide a good estimate of the outflow through this canal.

The temporal resolution of boundary conditions, whether it is river outflows, inflows/outflows or diversion, varies with the available observations, ranging from 6-minute data to daily values.

3.5.3.2.2 Overlake precipitation and evaporation

Two different gridded datasets were used to provide the overlake precipitation, which is maximum in late summer and early fall according to the climatology. The Canadian Precipitation Analysis (CaPA) was selected first, as it provides the best possible estimate of 24-h accumulated precipitation over the North American domain. Several complementary CaPA products were available at the beginning of the project, including the Regional Deterministic Precipitation Analysis (RDPA-10 km; Lespinas *et al.*, 2015), which covers the period 2002–2021, and the Regional Deterministic Reforecast System (RDRS-10 km; Gasset *et al.*, 2021), which covers the period 2010-2014. The latter offers surface reanalysis, which assimilates additional 24-h total precipitation observations to improve precipitation analysis.

Prior to 2002, a complementary dataset was selected to fill in the missing years in the CaPA analysis, which does not cover the entire historical period. Since a gridded source was needed, the Multi-Source Weighted-Ensemble Precipitation (MSWEP) was identified as a potential product. MSWEP V1.1 (1979–2015; Beck *et al.*, 2017), which is a global-scale precipitation dataset at high spatial (~30 km) and temporal resolution (3-h), produces estimates based on daily gauge observations, satellite remote sensing data, as well as reanalysis datasets, in addition to including automatic bias-correction for gauge under-catch and orographic effects. This product showed good performance in estimating daily precipitation values over the period 2008–2017 compared to a set of 10 other gauge-corrected precipitation datasets (Beck *et al.*, 2019). A rapid comparison of the quality obtained from RDPA-CaPA and MSWEP over the Great Lakes region against a gauge-adjusted precipitation dataset, the CPC global unified daily analysis (<https://psl.noaa.gov/data/gridded/data.cpc.globalprecip.html>), showed similar performance for years 2002–2010. The observed biases were comparable over the March–November period, with the greatest dissimilarity noticed during the summer months (June, July and August), when RDPA-CaPA displays significant underestimation of daily precipitation accumulation over the southwestern portion of the Great Lakes Basin compared to MSWEP (not shown). However, RDPA-CaPa is known to be less efficient in summer due to its difficulty in correctly reproducing convective precipitation (Lespinas *et al.*, 2015). When used to force the Lake Erie hydrodynamic model, both products (RDPA-CaPA and MSWEP) show good performance when combined with other dynamic forcings, i.e. runoff and evaporation (Figure 55; blue and orange lines). The long-term, seasonal trend obtained under realistic transient forcing will be discussed in Section 3.5.3.5

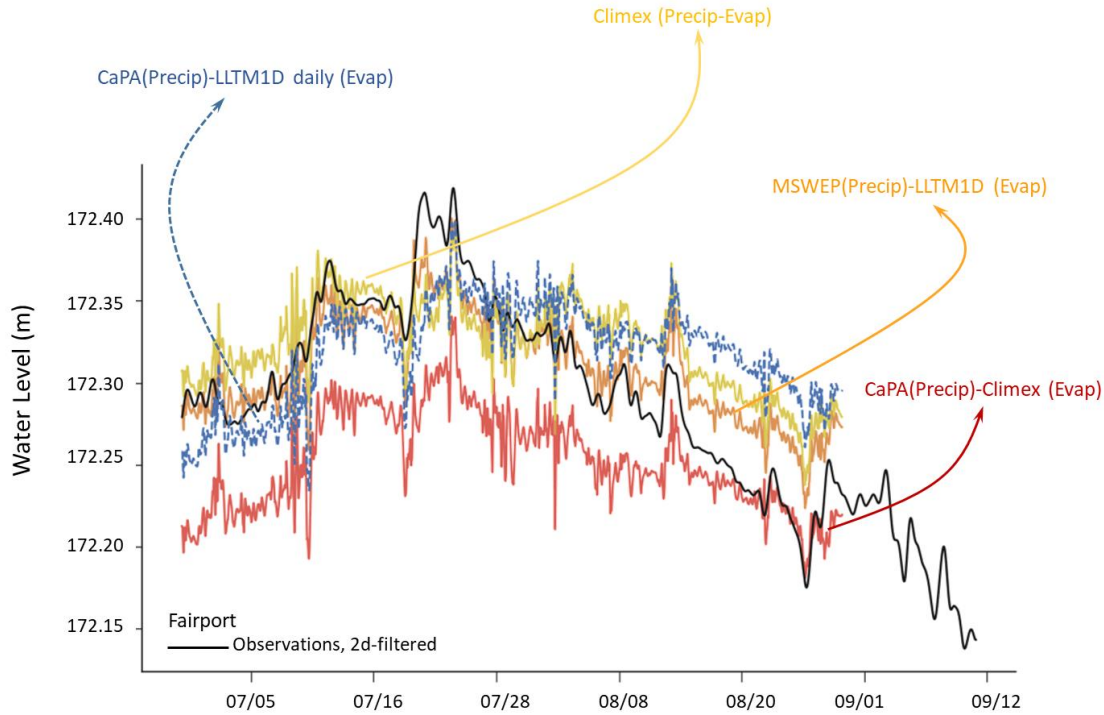


Figure 55: Simulated water levels obtained for Fairport, between May– September 2013, obtained using various evaporation and precipitation datasets: CaPA, the Canadian Precipitation Analysis, MSWEP, the Multi-Source Weighted-Ensemble Precipitation, and LLTM-1D, the Large Lakes Thermodynamics Model, and Climex.

The primary gap in dynamic forcing comes from overlake evaporation, which is a key component of the Great Lakes water balance: on an annual time scale, the latter is roughly equivalent to the sum of overlake precipitation and tributary runoff (Gronewold *et al.*, 2013; Spence *et al.*, 2013). Although evaporation is expected to vary temporally and spatially, as spatial patterns tend to follow synoptic-scale air masses travelling over the lakes (Spence *et al.*, 2011), spatially distributed estimates of evaporation are rare and almost non-existent for long, extended periods. Promising findings have been obtained using model-simulated latent heat flux, which can be translated into a total lake-wide evaporation estimate (Gronewold *et al.*, 2019), but this use is still recent and no data currently cover the entire historical period. Only seven monitoring stations adapted to evaporation rate measurements are installed at offshore locations as part of the Great Lakes Evaporation Network (GLEN), which further limits any spatial analysis of over-lake observations.

For the current project, the over-lake evaporation extracted from the NOAA model developed by Croley (1989) was used, the so-called Large Lakes Thermodynamics Model (LLTM). This one-dimensional fixed-parameter model includes schemes for wind mixing (Croley, 1992) and ice thermodynamics (Croley and Assel, 1994). It is used in the NOAA Great Lakes Advanced

Hydrologic Prediction System (AHPS), which provides reasonable forecasts of net basin supplies and water levels (Croley, 2005; Gronewold *et al.*, 2011). Daily lake-wide values obtained from the NOAA for the period 1980–2018 (in mm; person. comm.) were therefore employed to specify a homogeneous, evaporation rate over the lake (in m s^{-1}) in the hydrodynamic model.

3.5.3.2.3. Recent past and future periods: Mean lake level and inflow projections

Under climatic scenarios (recent past and future periods), the Lake Erie simulations were strictly forced with mean lake levels and Detroit River outflow projections. The mean lake level, which encompasses all the water balance components, obviates the need for separate surface forcing fields and river inflow boundary conditions. As with the historical time series, the Fort Erie level was estimated using a Gradient Boosting regression algorithm, utilizing the projected mean lake level as the explanatory variable rather than the observed level at Buffalo. Tested over the same historical period (2009–2018; cf. Figure 53), and using the levels obtained from Port Stanley, Port Colborne, Toledo and Cleveland gauging stations as the observed mean lake levels (<https://www.tides.gc.ca/C&A/historical-eng.html>), the goodness of fit of the predicted Fort Erie levels is slightly lower than otherwise obtained from the Buffalo time series: a RMSE of ~9 cm, and a maximum absolute bias of 26 cm (97.5 centile). The use of a mean smooths the observed water levels at stations, which have significant fluctuations related to wind set-ups. The increase in errors is mainly due to the absence of these events in the predicted values. Since water level and outflow times series provided by the net basin supply analysis are only on a quarter-month scale (cf. Section 3.3), and are not intended to reproduce daily or sub-daily fluctuations, the predictions obtained from the projected mean levels are deemed acceptable. Furthermore, the Lake Erie model was found to be insensitive to the forced water level at its outlet: the bathymetry of the Niagara River largely controls the amount of water leaving the lake (through the outlet), and proper inflow conditions assure a good representation of the absolute mean water level (i.e. seasonal cycle).

3.5.3.3. Atmospheric forcing: Set-ups and seiches

Depending on the period being simulated, the gridded datasets used to model the lake's response to winds are those detailed in Section 2.3: Climex, for the historical period, and debiased winds extracted from selected climatic scenarios, for the recent past and future periods. Both give 3-hourly estimates (or projections), and are interpolated to a common horizontal resolution of ~10 km, which reflects the original Climex grid.

Since the Climex dataset only covers the period 1980–2013, forecasts provided by the Global Environmental Multiscale Model (GEM, Canadian Meteorological Center) were used to fill the gap in the historical time series (2014–2018). The GEM model is an integrated atmospheric environmental forecasting and simulation system that incorporates both global and regional data assimilation. The latter is achieved by the Regional Deterministic Prediction System that produces hourly estimates at a horizontal grid spacing of approximately 10 km, which covers North America (e.g. Caron *et al.*, 2015). Surface winds were extracted from archived data produced between 2014 and 2018 (Table 11).

Table 11: Summary of hydrodynamic and atmospheric forcing datasets used for the historical period (1980–2018; observations), and recent past and future periods (1980–2010, 2070–2100; climatic projections).

	Historical Period	Recent Past and Future Periods
<u>Hydrodynamic Forcing</u>		
River Outflows	All major tributaries	
Inflows (Discharge) Detroit River at Fort Wayne	Fort Wayne	Fort Wayne (projections)
Outflows (Water Levels) Niagara River at Fort Erie	Fort Erie (2009-2018) Buffalo (1980-2008)	Mean Lake Levels (projections)
Diversion	Welland Canal	
Evaporation	CaPA (2010-2018) MSWEP (1980-2009)	
Precipitation	LLTM-1D	
<u>Atmospheric Forcing</u>		
Winds	Climex (1980-2013) GEM-10 km (2014-2018)	Debiased Scenarios (projections)

3.5.3.4. Modelling framework and data assimilation

The various tests performed during calibration showed that modelled water levels are in good agreement with observations in the first half of the annual simulated period, from early April to late July, but gradually deviate from expected values thereafter, during late summer and fall (Figure 55, blue and orange lines). This discrepancy occurs when overlake evaporation begins to be significant, relative to the other net basin supply components (<https://qlisa.umich.edu/sustained-assessment/erie-climatology/>), due to the increase in air-lake temperature difference and winds speed. Several experiments were conducted with diverse combinations of evaporation and precipitation to determine the impact of the gridded datasets on

the annual change in water levels (Figure 55)¹⁹. The Lake Erie model appears to be very sensitive to changes in water balance in late July, and evaporation observations are too sparse, both temporally and spatially, to properly estimate the bias adjustment that would correct the LLTM data (if any).

To overcome this problem, the simulations were performed with a data assimilation process, which provides an estimate of the system state based on “observations” to adjust the model trajectory (Fletcher, 2017). This process was designed to be applicable to both intended uses, namely (1) historical simulations, for which observed water levels are known at each gauging station, and (2) climate change simulations, which use projected mean lake levels.

3.5.3.4.1. First guess and wind set-ups

The state of the system at a specific time step is defined by a mean lake level, which gives the seasonal variability, as well as anomalies, which define the response of the lake to surface wind forcing. The surface seiches, which explain the high-frequency components of these anomalies, are an oscillatory phenomenon that cannot be predicted: they are initiated by the relaxation of the surface waters following a wind set-up event (cf. Section 3.2.1.2). The data assimilation process therefore focuses on the slope of the lake surface (i.e. the set-ups) to prescribe water level anomalies, a slope that is directly determined by the atmospheric conditions used to force the model.

Past climatic observations provide a comprehensive datasets of synoptic- scale atmospheric patterns that characterize the Great Lakes region. These data can be used as a database, i.e. a large collection of possible wind fields for which the state of the lake is known, based on the water levels recorded at gauging stations. Under a similar wind pattern, the lake is assumed to respond similarly, with a surface slope that generates a rise/fall in water level at the same geographical locations (e.g. rise at Toledo and fall at Buffalo). Since the winds and water levels show good coherence for periods of 2 days or more (cf. Section 3.2.2), the lowpass-filtered wind and water level time series can be used to populate the database that will serve as “observations” in the data assimilation process.

¹⁹ Overlake evaporation and precipitation extracted from the Climex dataset, described in Section 2.3.1.1, were used to provide a comparative view of the impacts of surface forcing fields on the observed discrepancy between recorded and predicted water levels at the end of the summer period.

3.5.3.4.2 Wind patterns and historical database

The zonal (“ u ”) and meridional (“ v ”) wind components were extracted from the homogeneized dataset used to validate the Climex outputs (cf. Section 2.3.1). Only stations located in the nearshore or offshore areas of the lake were retained, resulting in a set of eight meteorological stations. The database was restricted to the longest common period of record available, which spans from 2005 to 2015, and only observations obtained between March and November were preserved, to eliminate any potential influence of the ice cover on lake dynamics. Since only wind pattern is of interest for the data assimilation, i.e. the relative importance of the wind vectors, and following the work of Weber and Kaufmann (1994), the components u and v included in the database were normalized. This normalization was performed using the mean absolute value, which is defined, for a given wind field with j different locations (or observations), as:

$$s_t = \frac{1}{N} \sum_{j=1}^N (u_{j,t}^2 + v_{j,t}^2)^{1/2} \quad 3.11$$

, with N , the number of stations available at each t time step of the recording period²⁰. All individual wind observations, $\tilde{u}_{j,t} = u_{j,t}/s_t$ or $\tilde{v}_{j,t} = v_{j,t}/s_t$, were used to define the dimensionless wind fields. In total, over 29k observations were included in the historical database.

This database also contains the (lowpass-filtered) water level time series observed during the same period (2005–2015), at each Lake Erie gauging station.

²⁰ A minimum of five simultaneous observations at different locations was required to maintain a date in the wind database.

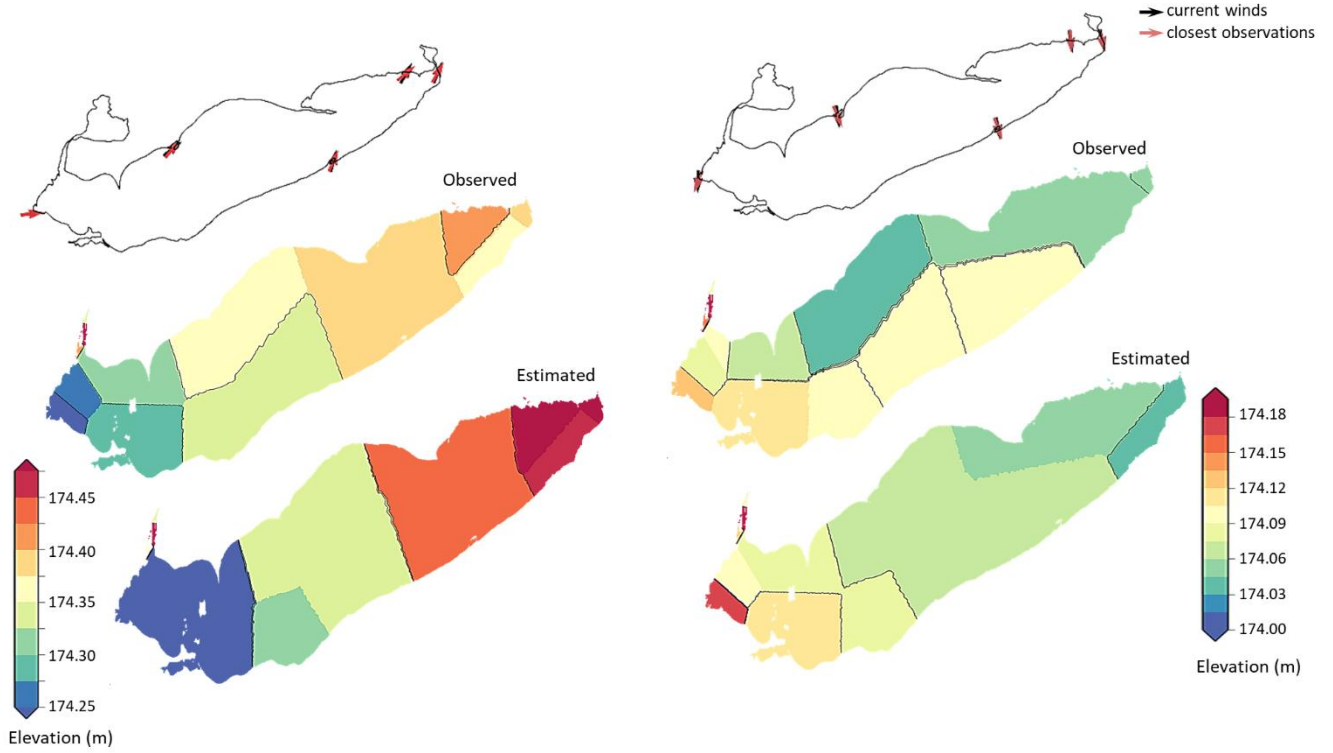


Figure 56: Examples of results obtained from step 3 of the data assimilation process for (left) westerly winds, and (right) northerly winds. Top panels: The wind pattern extracted from the forcing database at initialization time T (black arrows) opposed to closest wind pattern extracted from the historical database at time t' (red arrows). Bottom panels: The lake' slope "observed" at time T opposed to the lake' slope "estimated" based on water level records extracted from the historical database, at time t' . Details given in the text.

3.5.3.4.3. Data assimilation

Several steps are taken to determine the "first guess" that defines the state of the system at model initialization, which is the combined sum of the mean lake level and wind set-up amplitude:

1. Wind time series are extracted from the gridded dataset used to force the model, at the geographical position of each of the eight meteorological stations (j) included in the historical database. They are then filtered and normalized, using the same method explained above, and stored in a separate database called the forcing database, with components $\tilde{U}_{j,t}$ and $\tilde{V}_{j,t}$.
2. At simulation initialization (time T), the wind field used to force the model is extracted from the forcing database. The distance between this wind field and the 29k observations of the historical database is calculated according to (Weber and Kaufmann, 1994):

$$D_t = \left\{ \frac{1}{N} \sum_{j=1}^N [(\tilde{U}_{j,T} - \tilde{u}_{j,t})^2 + (\tilde{V}_{j,T} - \tilde{v}_{j,t})^2] \right\}^{1/2} \quad 3.12$$

The process is repeated for the wind field extracted from the forcing database at the time $T - 6h$ and for all observed winds extracted from the historical database at time $t - 6h$, giving D_{t-6h} . This procedure allows the identification of a persistent wind field, lasting at least 6 hours, which would be sufficient to counteract the lake's inertia and induce a displacement of the surface waters.

3. Among the 29k wind fields, the date $t = t'$ of the observation that yields the minimum distance $D_t + D_{t-6h}$ is selected as the best wind pattern estimate for the initialization. At this historical date, the lake was responding to a wind field that can be stated similar to the wind used to initialize the model.
4. The observed water levels at the date t' are extracted from the historical database and used to create the initialization state. Since these water levels give the correct lake slope (anomalies), but not the correct absolute mean level (seasonal variability), a simple bias adjustment is then performed. To do so, the estimated bias between the mean lake level at the date t' and the observed or projected mean lake level at initialization time T , depending on the period simulated (historical or recent past/future periods), is used to correct the water levels extracted from the historical database.
5. The initialization state (or initial water level) at each grid node is obtained from the observed (and corrected) water level at the nearest gauging station (nearest neighbour search), at date t' .

Figure 56 gives an example of result obtained after step 3 for two distinct wind patterns, westerly (left panels) and northerly winds (right panels). Data assimilation is performed every 48 hours in the adopted modelling framework, and the simulation then proceeds freely over a 60-hour time window. The first 12 hours of each simulation step are suppressed to eliminate the stabilization phase, which can present large numerical instabilities depending on the forcing applied at time T , especially with respect to runoff and inflow/outflow. Each 60-h time window of the simulation is therefore independent, and several can be performed simultaneously.

3.5.3.5. Model performance

The performance of the Lake Erie model was tested over the baseline period, 1980–2010, using the historical time series, which was intended to replicate the observed water level over the past several decades. Data assimilation was utilized to perform the simulations, with the observed mean lake level and winds as “observations”, as well as the Climex wind dataset that is known to be biased (Section 2.3). Here, it is the model performance under its scenario-based configuration approach that is tested, rather than its ability to be used as an operational product, with the best forcing datasets. In hydrodynamic models, much of the uncertainty comes from the uncertainty in climate forcing, which cannot be avoided.

3.5.3.5.1. Seasonal water level and Interannual Variability

To determine the ability of the two-dimensional model to reproduce year-to-year lake levels, which reflect the annual and interannual variations experienced by the lake due to the changing importance of the net basin supply components, lowpass-filtered time series were first compared. Simulated water levels at each of the lake' gauging stations were archived during the simulations and then lowpass-filtered to remove any influence of wind (i.e. wind set-ups and surface seiches). Only variations with periods greater than 30 days were retained to focus on monthly fluctuations. The error was quantified using the bias, defined as the difference between the predicted P_i and observed O_i values at time i , i.e. $P_i - O_i$, as well as the root mean square error (here after referred to as RMSE):

$$RMSE = \left[\frac{1}{n} \sum_{i=1}^n (P_i - O_i)^2 \right]^{1/2} \quad 3.13$$

with n , the number of observed or predicted values.

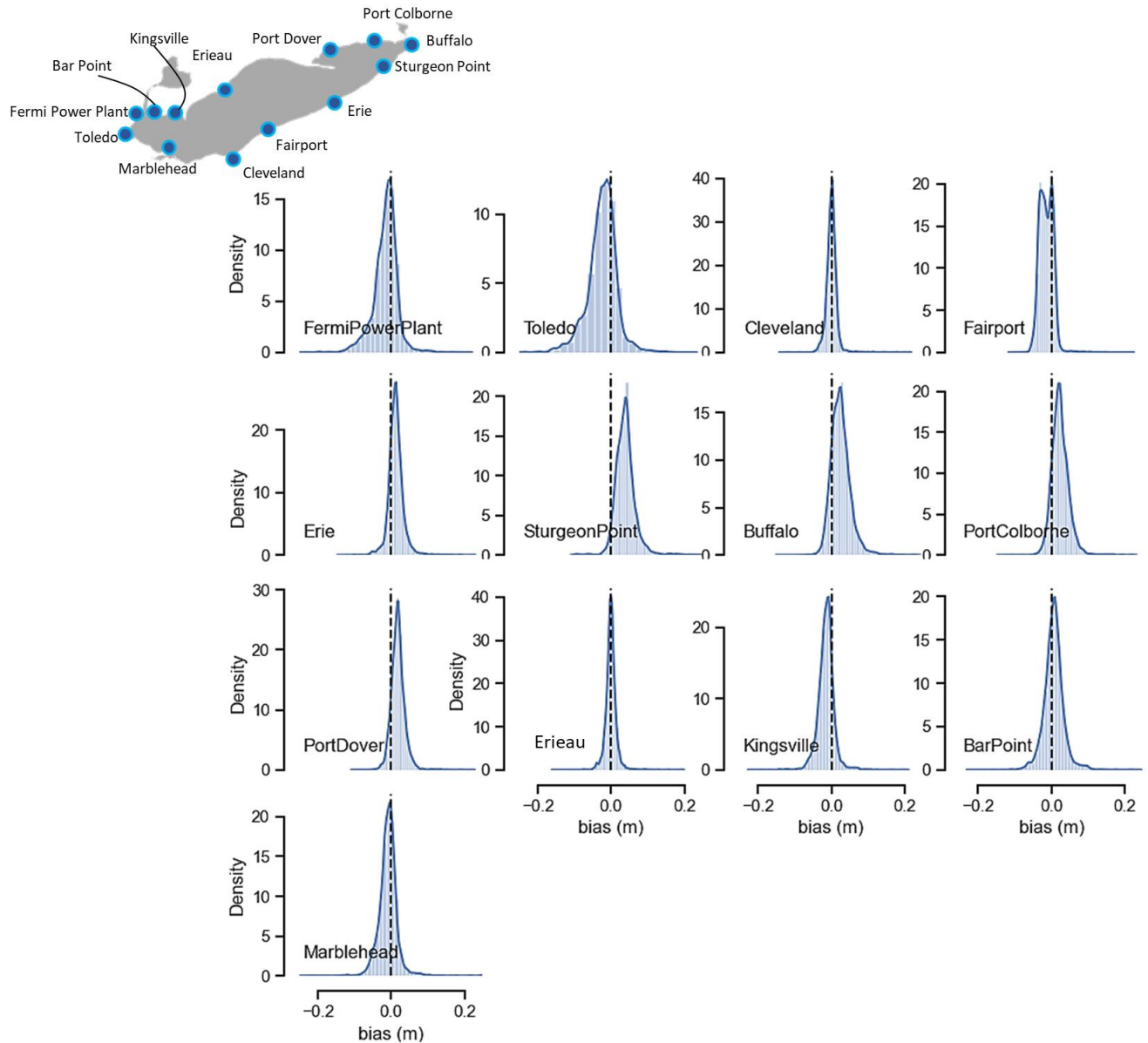


Figure 57: Bias distributions calculated from the observed and simulated (historical) monthly water level series (1980–2010) for each Lake Erie station, starting with the westernmost station, Toledo (upper left corner), and sorted by longitude.

The simulated time series show good agreement with the historical levels recorded at the stations. Figure 57 displays the bias distributions computed from the lowpass-filtered time series at each lake locations, sorted by longitude, starting with the westernmost station, Toledo. For most stations, the errors remain between 5 and 10 cm for the 30-year period compared, with a maximum absolute value of ~15 cm (e.g. Toledo), which is within the acceptable error magnitude used as a standard criterion by the National Ocean Service (NOAA; Hess *et al.*, 2003). While centred distributions are noticed at Fermi Power Plant, Bar Point, Marblehead, Erieau and

Cleveland, the model tends to underestimate water levels at the western end of the lake, and overestimate them on the opposite side. The largest discrepancies are observed at Toledo and Sturgeon Point, where the mean biases reach -2.1 (-4.1; -0.5) cm and 3.8 (2.4; 5.0) cm respectively (with first and third quartiles in brackets). The results from Fairport should be taken with caution, as the water level gauge is sitting over a salt mine, where the area is known to have subsided in the past. The observations were adjusted in September 2006 with an overall correction of ~-5 cm (NOAA, pers. comm.), which is consistent with the left-skewed distribution observed in Figure 57. Since 2006, the vertical motion of the gauging station has been continuously monitoring, and the recorded water levels are in agreement with those simulated, which explains the bimodal distribution obtained at this station.

Table 12: Mean bias (with first and third quartiles) and RMSE calculated from the observed and simulated water level series (1980–2010), and detailed for monthly variations (seasonal water level), wind set-ups event, and surface seiches.

	Seasonal Water Level		Mean Set-Ups	Surface Seiches
	Bias (cm)	RMSE (cm)	Bias (cm)	Bias (cm)
Toledo	-2.1 (-4.1 ; -0.5)	4.6	3.7 (-0.3 ; 6.1)	-3.2 (-4.2 ; -2.3)
Fermi Power Plant	-1.1 (-2.8 ; 0.1)	3.4	4.0 (0.1 ; 5.9)	-2.1 (-3.0 ; -1.2)
Bar Point	0.6 (-0.6 ; 1.8)	2.5	2.5 (-0.5 ; 4.2)	-3.2 (-4.0 ; -2.0)
Kingsville	-1.4 (-2.3 ; 0.5)	2.5	2.6 (0.0 ; 3.8)	-2.3 (-3.0 ; -1.7)
Erieau	0.0 (-0.7 ; 0.4)	1.5	2.1 (0.2 ; 3.2)	-2.7 (-1.7 ; -1.2)
Port Dover	1.8 (0.9 ; 2.7)	2.6	1.8 (-0.2 ; 3.7)	-1.9 (-2.7 ; -1.3)
Port Colborne	2.2 (1.1 ; 3.5)	3.2	2.4 (-0.3 ; 4.9)	-2.1 (-2.8 ; -1.4)
Buffalo	2.3 (1.0 ; 3.5)	3.5	2.0 (-1.4 ; 4.9)	-3.3 (-4.2 ; -2.4)
Sturgeon Point	3.8 (2.4 ; 5.0)	4.7	2.0 (-0.6 ; 4.0)	-2.2 (-3.1 ; -1.2)
Erie	1.2 (0.3 ; 2.2)	2.4	1.7 (-0.5 ; 3.8)	-1.6 (-2.2 ; -1.1)
Fairport	-1.5 (-2.8 ; -0.0)	2.4	0.2 (-0.6 ; 1.1)	-2.2 (-2.5 ; -1.9)
Cleveland	0.0 (-0.6 ; 0.6)	1.5	0.9 (-0.3 ; 2.0)	-2.2 (-2.6 ; -1.8)
Marblehead	-0.7 (-1.8 ; 0.2)	2.5	2.6 (-0.5 ; 4.1)	-1.9 (-2.5 ; -1.3)

Overall, the mean bias errors stay within 5 cm, as do the root mean square error (Table 12).

3.5.3.5.2 Wind set-ups and surface seiches

To highlight the ability of the hydrodynamic model to capture the lake' response to winds, and to properly reproduce the specific dynamics of the system, the water level anomalies were considered separately. While the wind datasets used to force the model has a direct influence on the generation of set-up events and their amplitude, the barotropic surface motions are only

partially related to atmospheric forcing. The initial amplitude of the seiches is dictated by the initial surface motion, but the subsequent propagation and damping of the oscillations are prescribed by the model parametrization, which controls internal lake processes as near-bottom friction.

The predicted and observed hourly time series at the stations were first highpass-filtered to remove the seasonal variability prescribed by the hydrodynamic forcing (periods > 30 days). The resulting anomalies were then divided into their low- and high-frequency components, defined as water level fluctuations with periods greater or less than 2 days, respectively (cf. Section 3.2.2). Since the initial wind set-up amplitude is critical for the lake dynamics, individual events were identified in each (low-frequency) anomalies time series, following the procedure explained in Section 3.2.2, and taking care to compare the common events in each series. Surface seiches were analyzed via the daily range fluctuations estimated from the high-frequency anomalies.

Several statistical measures were used to determine the model skill with respect to each of the frequency components, related to set-ups and surface seiches. In addition to the bias (Table 12), the measures included the RMSE, and its systematic, $RMSE_s$, and unsystematic parts, $RMSE_u$ which are defined as:

$$RMSE_s = \left[\frac{1}{n} \sum_{i=1}^n (\hat{P}_i - O_i)^2 \right]^{1/2} \quad 3.14$$

and

$$RMSE_u = \left[\frac{1}{n} \sum_{i=1}^n (P_i - \hat{P}_i)^2 \right]^{1/2} \quad 3.15$$

with \hat{P}_i , the regressed predictions obtained from the linear least-squares regression model $\hat{P}_i = a + bO_i$. The $RMSE_s$ estimates the linear (or systematic) error of the model, due to inputs or model deficiency, while the $RMSE_u$ quantifies the amount of difference between the predicted and observed values that results from random processes or influences outside the legitimate range of the model, due to lack of model refinement or grid resolution. For good model performance, the systematic difference should approach zero, while the unsystematic difference, approach $RMSE$ (Willmott, 1982). The standard deviation (or square variance) was also considered by the computation of:

$$s_o = \left[\frac{1}{n} \sum_{i=1}^n (O_i - \bar{O})^2 \right]^{1/2} \quad 3.16$$

and

$$s_p = \left[\frac{1}{n} \sum_{i=1}^n (P_i - \bar{P})^2 \right]^{1/2} \quad 3.17$$

with \bar{P} and \bar{O} , the mean of the observed and predicted values at the selected station. Finally, two standardized measures were included in the analysis, as such unitless quantities are widely applied to perform cross-model comparisons. The first is the index of agreement (IOA), which is defined as (Willmott, 1982):

$$IOA = 1 - \left[\frac{\sum_{i=1}^n (P_i - O_i)^2}{\sum_{i=1}^n (|P_i - \bar{O}| + |O_i - \bar{O}|)^2} \right] \quad 3.18$$


This index takes a value between 0 and 1, with 1 indicating perfect agreement between P and O . It can be interpreted as the measure of the relative average error between the model and observations. Although a modified and improved version of the IOA exists, the original definition presented by Willmott (1982) was used for consistency with other studies (e.g. Chu *et al.*, 2011). The last quantity evaluated is the amplitude skill, AS, which is a skill test developed by Dingman and Bedford (1986) to assess model credibility in simulating major water level events. This test assigns a score to each prediction based on the difference between the observed and computed values, with a minimum score of 0 when the difference is greater than 0.5 m, and a variable score for lower values (Table 13).

Table 13: Amplitude skill score rules for water level anomalies.

Point	Absolute Difference (cm)
10	$ P_i - O_i < 5$
9	$5 \leq P_i - O_i < 10$
8	$10 \leq P_i - O_i < 15$
7	$15 \leq P_i - O_i < 20$
6	$20 \leq P_i - O_i < 25$
5	$25 \leq P_i - O_i < 30$
4	$30 \leq P_i - O_i < 35$
3	$35 \leq P_i - O_i < 40$
2	$40 \leq P_i - O_i < 45$
1	$45 \leq P_i - O_i < 50$
0	$50 \leq P_i - O_i $

Comparison of the biases calculated from set-up events and daily range values first reveals an inherent feature of the hydrodynamic model: a systematic bias in the modelled amplitude of surface seiches. While the initial set-ups causing the seiches are mostly overestimated regardless of station, with errors of 0.2 to 3.7 cm, the mean estimated biases for barotropic motions range from -3.2 to -1.6 cm, with a maximum error of -4 cm at the ends of the lake (Table 12), where observed seiches amplitude is maximum (e.g. Toledo and Buffalo; cf. Section 3.2.2.1). This error is well captured by the systematic RMSE, which remains close to the total RMSE for most stations (Table 14). The lake's parametrization induces excessive damping of the long-standing waves in the basin, but no adjustment was found to be effective in reducing dissipation based on tests conducted during the calibration. For instance, the damping coefficient that acts as a linear friction parameter was set to 0 in present application, as were the free surface smoothing viscosities. According to the amplitude skill score (i.e. AS), the absolute difference between daily range values remains between 5 and 10 cm for the baseline period (1980–2010), which is equivalent to a maximum error of 5 cm in absolute amplitude (since the daily range is about twice the amplitude). The standard deviation of the predicted values, s_p , is also similar to that estimated from observations, s_o : the relative daily variations are consistent over the 30-year period, which is an important result for wetland modelling. The low values obtained for IOA also highlight a general lack of mean seiche amplitude rather than inconsistency in relative values.

Table 14: Statistics and amplitude skill scores for set-ups events (left) and surface seiches (right) in Lake Erie, for the reference period (1980–2010).



	Set-Ups, Skill Scores								Surface Seiches, Skill Scores						
	s_o (cm)	s_p (cm)	RMSE (cm)	RMSE _s (cm)	RMSE _u (cm)	IOA	AS	n	s_o (cm)	s_p (cm)	RMSE (cm)	RMSE _s (cm)	RMSE _u (cm)	IOA	AS
Toledo	9.6	14.8	8.9	4.9	7.4	0.86	9.35	157	3.2	3.3	7.0	6.5	2.7	0.47	9.20
Fermi Power Plant	6.3	11.2	7.8	5.1	5.9	0.80	9.46	164	2.9	2.9	5.3	4.2	2.4	0.55	9.77
Bar Point	5.2	8.8	5.9	3.2	4.9	0.82	9.68	157	3.7	2.7	7.3	6.8	2.6	0.43	9.62
Kingsville	4.0	7.0	5.2	3.1	4.2	0.78	9.69	137	2.2	2.0	5.0	4.7	1.7	0.43	9.27
Eriean	1.6	3.5	3.4	2.2	2.6	0.60	9.83	64	1.2	1.2	3.0	2.9	0.9	0.43	9.98
Port Dover	5.9	7.1	4.2	1.8	3.9	0.89	9.75	177	2.5	2.2	4.3	4.0	1.7	0.52	9.60
Port Colborne	9.0	10.8	5.8	2.5	5.2	0.91	9.60	214	2.9	2.6	4.6	4.2	1.9	0.58	9.70
Buffalo	11.3	13.2	6.5	2.1	6.1	0.93	9.52	222	3.9	2.9	7.0	6.7	2.1	0.50	9.87
Sturgeon Point	9.4	11.6	5.7	2.2	5.3	0.92	9.65	151	3.9	2.8	5.4	4.8	2.4	0.54	9.65
Erie	6.2	8.0	4.5	1.8	4.2	0.89	9.74	148	1.9	1.9	3.6	3.2	1.5	0.51	9.18
Fairport	1.5	1.6	1.3	0.5	1.2	0.80	10.0	57	1.3	0.9	4.4	4.3	0.8	0.33	9.63
Cleveland	2.6	2.3	2.3	0.9	2.1	0.85	9.96	116	1.6	1.2	4.5	4.3	0.9	0.38	9.69
Marblehead	5.4	5.8	5.8	2.9	5.0	0.82	9.63	138	1.9	2.0	4.1	3.7	1.6	0.48	9.77

The wind set-up events identified in the simulated series show better agreement with observations than seiches, with a RMSE of less than 5 cm, mainly due to unsystematic errors. The IOA remains above 0.6, with values exceeding 0.8 at most stations. The amplitude skill score is also high, with a minimum value of 9.35 estimated at Toledo, where water level variations due to prevailing westerly winds are known to be significant (cf. Section 3.2.2.1). The calculated biases over the 30-year period are largest on the west side of the lake, at Fermi Power Plant and Toledo. These discrepancies are due in part to the biases observed in the wind data, Climex particularly overestimating the wind speed in this part of Lake Erie. Figure 58 details the observed and simulated winds that promoted the water level rise (or fall) identified as set-up events in the analysis, for station Toledo. The bar plots provide the monthly distributions of wind set-ups and wind speeds as calculated for the baseline period, and specify the magnitude of each when (1) all individual events are considered (referred to as *mean* in Figure 58) or (2) when only the maximum monthly values are retained (referred to as *max* in Figure 58). The maximum distributions of simulated events show larger discrepancies, which follow the trend observed for wind speeds, with greater overestimation leading to larger error in the magnitude of modeled

events. The mean distributions show better agreement between simulations and observations, demonstrating the model's ability to reproduce lake motions in terms of water surface fluctuations following wind forcing.

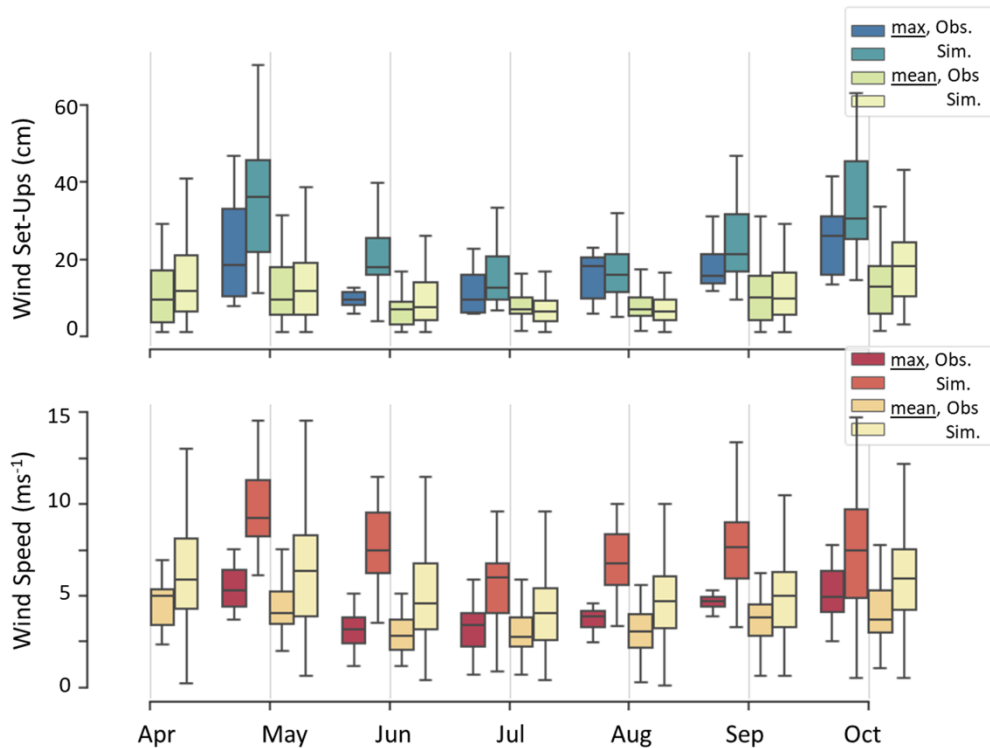


Figure 58: Monthly bias distributions for wind set-ups amplitude and wind speed at Toledo, for the period 1980-2010. The bar plots give the errors as estimated from (1) all identified individual events (referred to as mean, clear colors), and (2) the maximum monthly values only (referred to as max, dark colors). Wind speed refers to the magnitude of the wind that generated the events in the simulated and observed time series. The observed winds were extracted from the homogenized observational dataset, while the simulated winds were extracted from Climex, at Toledo location (cf. Section 2.3). Only distributions with a minimum of ten values have been retained.

Figure 59 and Figure 60 show examples of the observed total monthly biases for the period 1980–2010 at two stations, Kingsville and Toledo, with short snapshots of the simulated and observed hourly time series (lower panels). The error distributions provide explicit information about expected biases when all the frequency components are considered, including seasonal variations, set-ups and surface seiches (although figures also detail the expected error difference when seiches are neglected, which is referred to as *2d-filtered* in Figure 59 and Figure 60). Even at Toledo, where the errors were found to be maximal (Table 12 and Table 14), the monthly mean biases remained less than 5 cm for hourly values, and 10 cm based on the first and third quartiles, which is within the acceptable error range according to standard NOS criteria. When the influence of the seiches is removed from the time series (i.e. the *2d-filtered* series), the maximum estimated bias is reduced, as expected from the previous results. Most importantly, the model captures

major set-up events with accurate simulated water level (when forcing allows), as shown in Figure 60, where a water level rise of approximately 1 m was observed at Toledo.

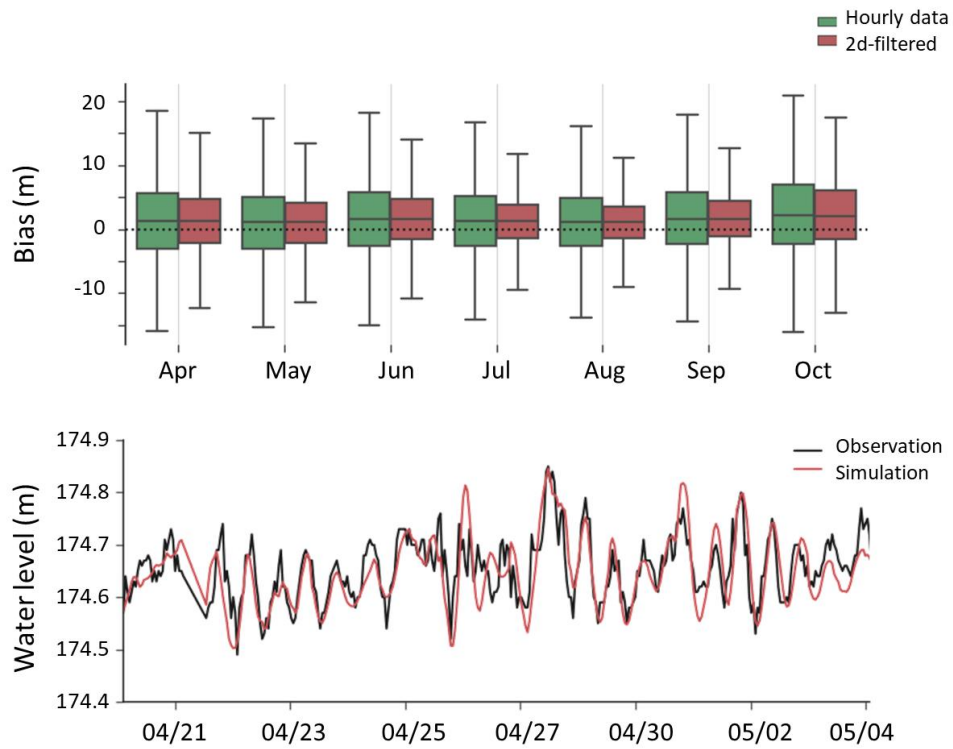


Figure 59: Upper panel: monthly bias distributions for hourly (green) and lowpass-filtered (red) time series at Kingsville, for the period 1980–2010. Lower panel: snapshot of the observed (black) and simulated (red) hourly time series at Kingsville for late April, early May 2016.

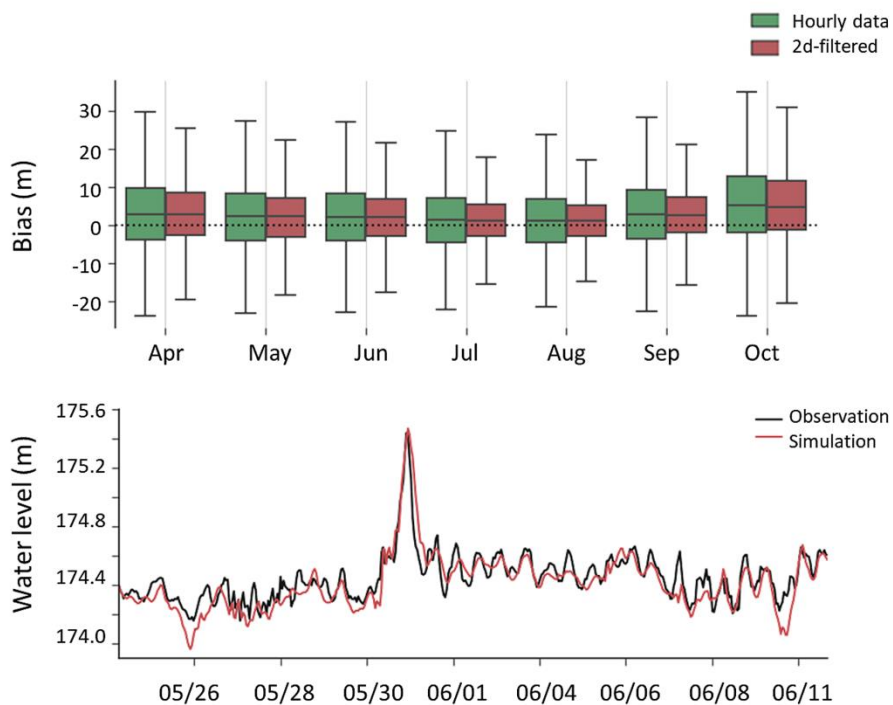


Figure 60: Upper panel: monthly bias distributions for hourly (green) and lowpass-filtered (red) time series at Toledo, for the period 1980–2010. Lower panel: snapshot of the observed (black) and simulated (red) hourly time series at Toledo for late May, early June 2015.

3.5.4. Lake St. Clair

3.5.4.1. Bathymetry and modelling approach

Lake St. Clair is the smallest and shallowest lake in the Great Lakes Basin, with its deepest zone reaching only about 8 m. This water body is particularly well suited for a classical 2D hydrodynamic simulation, which allows for realistic water level fluctuations, including surface seiches, and time-evolving flows along the St. Clair and Detroit Rivers. Although highly comprehensive, this modelling approach has a much higher computational cost due to the mesh density required to resolve river flows, and the large amount of time steps needed to cover the entire historical and projected periods.

Figure 61 details the bathymetry within the Huron-Erie Corridor that connects the upper Great Lakes to the lower Great Lakes, providing an average flow of $5200 \text{ m}^3\text{s}^{-1}$ to Lake Erie (Holtschlag and Koschik, 2002), or 80% of its total water supply (Bolsenga and Herdendorf, 1993). This channel includes the St. Clair River, Lake St. Clair, and Detroit River. The former is a relatively straight river of 64 km that flows from Lake Huron to Lake St. Clair, with an elevation drop of 1.6 m from end to end. In addition to Lake Huron outflows, this river receives inputs from the Pine, Black

and Belle Rivers located along the US side of the river. The Detroit River connects Lakes St. Clair and Erie, and runs along 52 km, with a drop in elevation of about 0.9 m. Its main flow is maintained by Lake St. Clair outflows, as well as the Rouge River (Michigan, USA). Lake St. Clair, which occupies the center of the system, is dynamically different from the other lakes of the Great Lakes Basin since 98% of its water supply comes from the St. Clair River and only 2% from its net basin supply. Consequently, even small seasonal changes in the inflow and outflow of its connecting channels can have a marked influence on its water levels. This is especially true during the ice seasons, when the lake is affected by ice retardation in the St. Clair and Detroit Rivers. Frequent ice jams are observed in the St. Clair River, which can restrict up to 50% of the flow (Quinn, 2002).

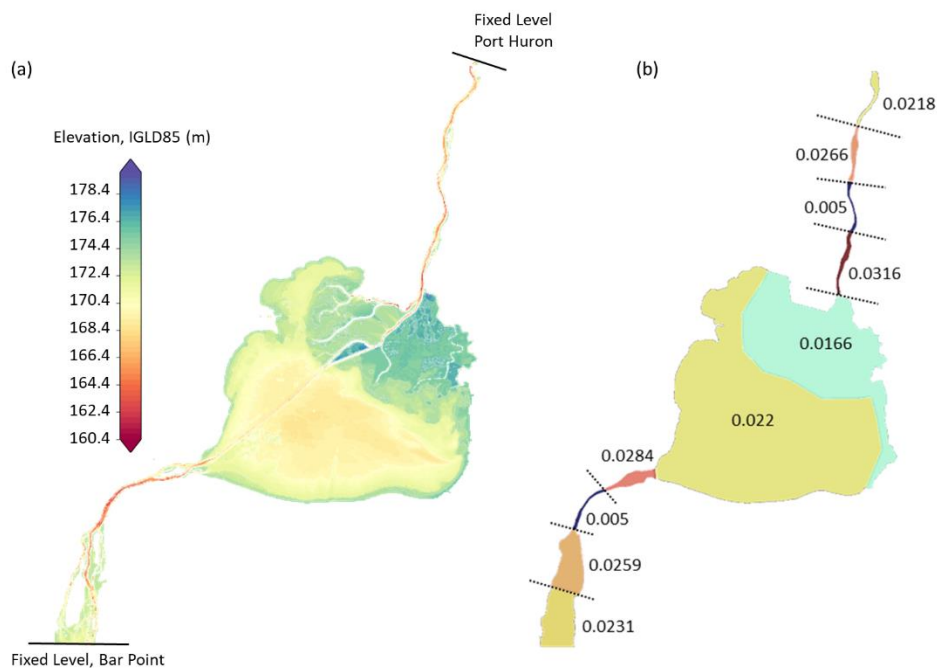


Figure 61: Details of the bathymetry (left panel) and Manning's coefficients (right panel) used in the Huron-Erie Corridor model.

The set of boundary conditions used for the Huron-Erie Corridor consists of: (1) Lake Huron water level imposed at Fort Gratiot (Michigan, USA), near the outlet of the lake; (2) Lake Erie water level at Bar Point (Ontario), near the mouth of the Detroit River, on the eastern side of the Lower Detroit River; and (3) main tributary inflows along the system, which can have a noticeable effect on the downstream water levels. Because hydraulic conditions in the Lower Detroit River highly depend on the dynamics of Lake Erie, which forces surface seiches and set-up events in the river, simulations performed under the projected climate (past and future) used outputs from Lake Erie model at Bar Point. The two models are thus linked in the classic 2D modelling approach to provide realistic short-term water level fluctuations.

3.5.4.2. Mesh details

The mesh density used for the Huron-Erie Corridor consists approximately of 600k nodes and 300k quadratic elements, with average element size ranging from 75 m in the St. Clair and Detroit Rivers to 750 m in the lake. The number of elements were kept high within the St. Clair–Detroit Seaway, as well as in vicinity of the St. Clair Delta, where the St. Clair River enters the northern portion of Lake St. Clair via several channels (Figure 62).

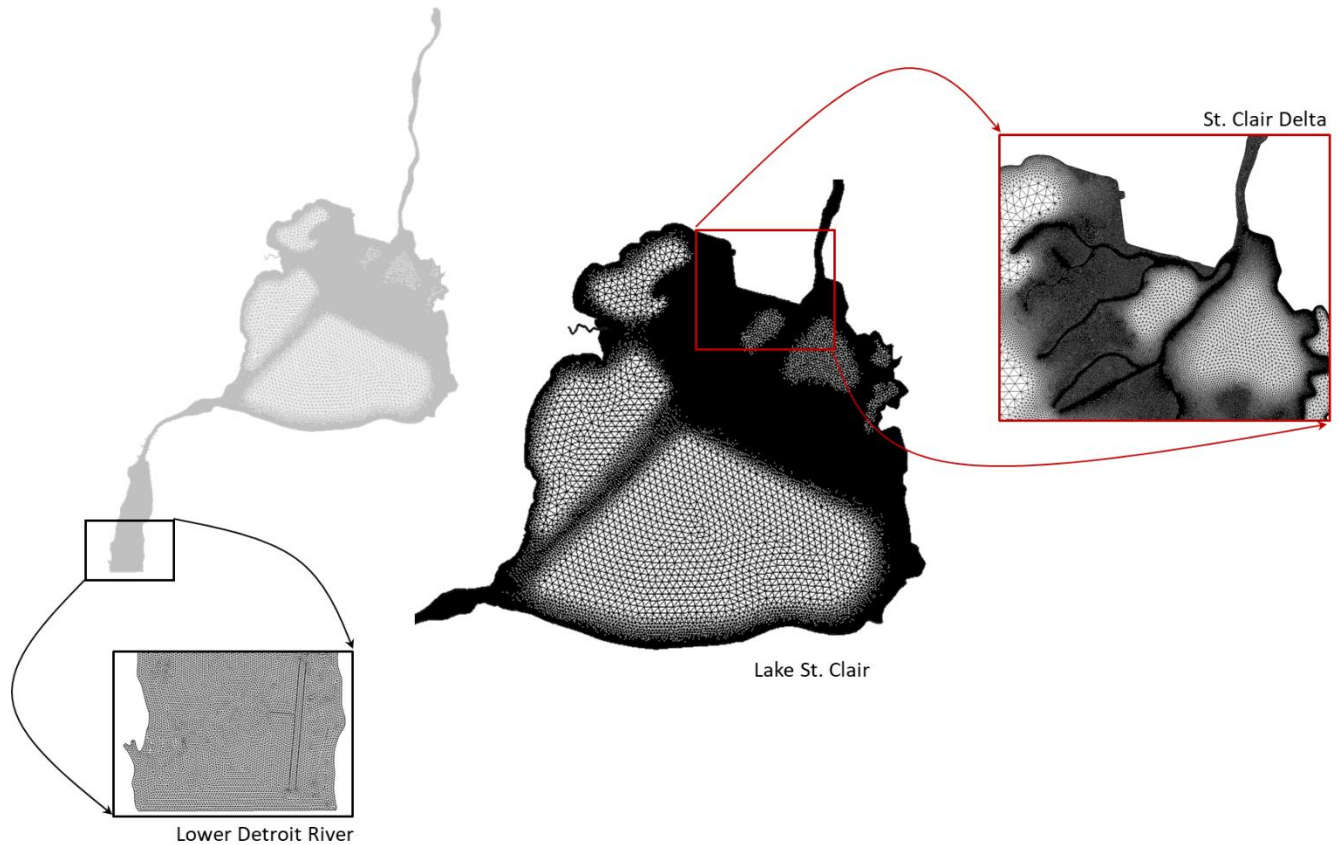


Figure 62: The computational grid used for the Huron-Erie Corridor model, with details in vicinity of the St. Clair Delta and the mouth of the Detroit River.

3.5.4.3. St. Clair and Detroit River calibration and model validation

The calibration of the St. Clair–Detroit River system was especially challenging in the upper and lower parts of the channel, where flow passes through riverine sections that are hydraulically driven by the dynamics of Lakes Huron and Erie (cf. Section 3.2.2). Because the water depth is quite shallow in these areas and flow velocities can be large, small changes in local Manning coefficients and hence, bottom friction, can induce marked changes in discharge. Since the use of suboptimal friction values can bias Lake St. Clair inflows/outflows, and thus simulated water levels, a rigorous calibration was necessary. This calibration was performed with the help of the

numerous gauging stations located in the course of the system, as well as with the discharge measurements obtained through past field campaigns. Only a lack of data was noted at Lake St. Clair, which limited the parametrization of wind set-ups and surface seiches amplitude that can reach 5.3 cm and 1.8 cm, respectively (cf. Section 3.2.2). Therefore, the standard surface wind stress formulation proposed by Kumar *et al.* (2009) was used without further adjustment. This formulation, which accounts for the influence of waves on the surface drag coefficient and was primarily designed for oceanic applications, was also employed for the Lake Erie modelling (cf. Section 3.5.3).

The Huron-Erie corridor model was calibrated for ice-free, plant-free conditions, and different areas were used to modulate the Manning coefficient between the mouths of the St. Clair and Detroit Rivers (Figure 61). The root-mean square errors obtained for the calibration period, i.e. the first week of May 2016, were about 4.5 cm in the St. Clair River, 1.8 cm in Lake St. Clair, and 2.6 cm in the Detroit River, considering all stations included in either of these sections.

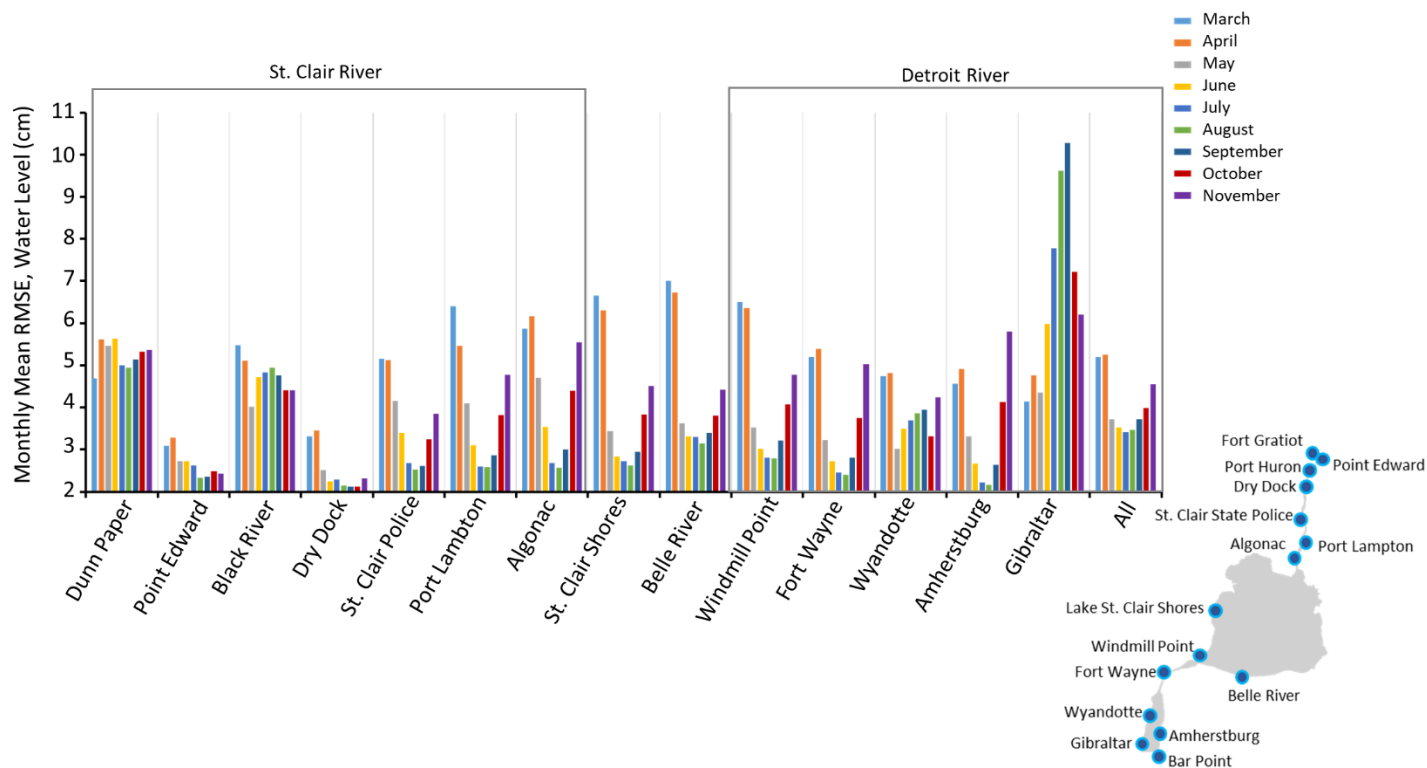


Figure 63: Monthly mean water level errors (RMSE) at several gauging stations, for the period 1980–2018. Errors are broken down by month.

Validation was performed on the entire historical period, i.e. 1980–2018, using water level and discharge measurements, the latter provided at Port Huron (Michigan, USA), at the mouth of the St. Clair River, and Fort Wayne (Michigan, USA), in the Upper Detroit River. Overall, the annual

mean water level errors (RMSE) remain below 5 cm (Table 15 and Figure 63). When the errors are broken down by month, an increase in the difference between observed and modelled levels is observed in early spring (March–April), especially during years 1982, 1984–1987, and 1996 when errors reach 10–25 cm at stations (not shown). These RMSEs are likely related to freezing conditions that altered the flow in the system, a secular situation that can lead to flow reversal (e.g. Derecki and Quinn, 1990). Errors also tend to be noticeably smaller in summer in all sections of the connecting channel except near Gibraltar (Michigan, USA), in an area known to be influenced by submerged vegetation (Figure 63).

Table 15: Water level errors obtained for different sections of the Huron-Erie Corridor for years 1980–2018, according to two different periods. The first (Mar 15th to Nov 15th) includes late spring, when ice conditions can be observed in the St. Clair and Detroit Rivers.

RMSE, Water Levels		
(cm)		
	Mar 15–Nov 15	May 1–Nov 15
St. Clair River	4.2	3.8
Lake St. Clair	4.8	3.6
Detroit River	4.9	4.6
All	4.6	4.0

A similar behavior is observed for discharge values (Figure 64), with maximum errors in March and April, particularly in the Upper Detroit River whose entrance is frequently obstructed by ice jams.

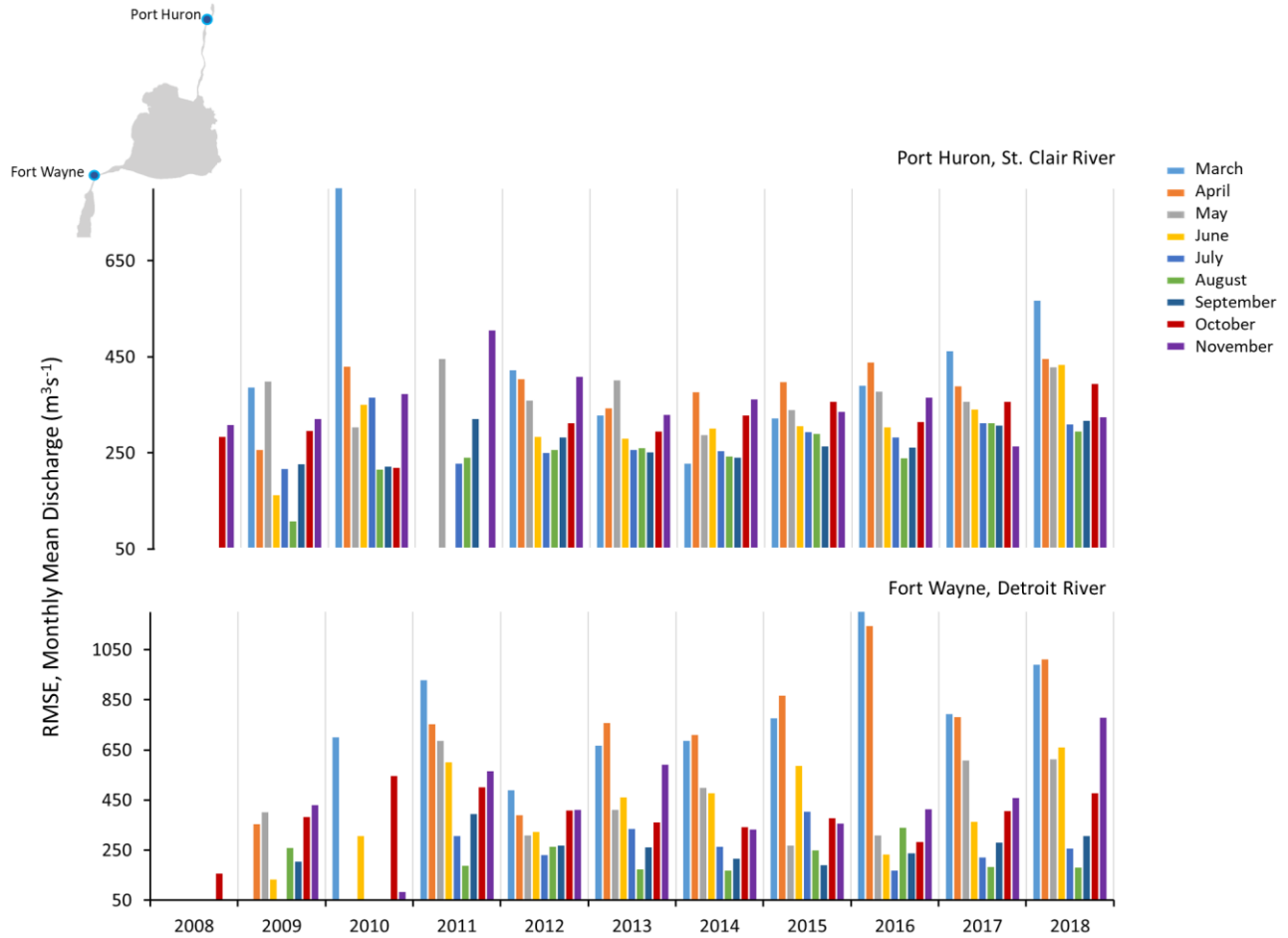


Figure 64: Idem as Figure 63, but for discharge values at Port Huron (St. Clair River) and Fort Wayne (Detroit River).

3.5.5. Lake Huron

3.5.5.1. Bathymetry and modelling approach

Lake Michigan-Huron is one of the largest lakes in the Great Lakes Basin with a total area of 117400 km². This lake is characterized by a large ratio of lake surface area to drainage basin, which damps the seasonal hydrologic fluctuations usually seen in the lower lakes. Because Lakes Michigan and Huron are connected through the Straits of Mackinaw, which is 6 km wide at the narrowest point, they exhibit similar behavior and are generally treated together when considering water levels and hydrodynamics. The mean annual net flow observed in the straits is on the order of 1400 m³s⁻¹, but shows high variability from year to year (Quinn, 1977). The presence of this channel section in the system as a large influence on the surface seiches dynamics, as it initiates bi-lake oscillations and complex interactions with atmospheric forcing (Anderson and Schwab, 2013).

For this project, the focus is primarily on the Lake Huron system, although both lakes were included in the hydrodynamic model to ensure adequate physical modelling. Lake Huron is a relatively complex basin composed of several entities. Its main water body, oriented North-South, is connected to Lake Superior via the St. Marys River that flows through several channels and provides a mean inflow of about $2100 \text{ m}^3\text{s}^{-1}$ to the system, which is controlled by the Lake Superior Regulation Plan. In its southern and northern portions, the lake is connected with the St. Clair–Detroit system by the St. Clair River, near Port Huron, and to Lake Michigan via the Straits of Mackinaw, respectively. Finally, narrow passages in its northeastern part drain Lake Huron water into two nearly distinct water bodies, the North Channel and the Georgian Bay. Georgian Bay is a deep basin ($>100 \text{ m}$) oriented along a northwest–southeast axis (Figure 65).

The scenario-based approach was used to model the dynamics of Lake Huron owing to its deep bathymetry. Three open boundaries were used that force: (1) inflows to Lake Huron from Lake Superior, via the St. Marys River, and Michigan, via Mackinaw Straits, and (2) the mean level at the outlet of Lake Huron, near Port Huron, which controls outflows. While the first two were held constant for all simulated solutions, using mean values, the latter was modulated to provide the discrete water levels required for the solutions space (cf. Section 3.4.3.2). Lake Michigan inflow was imposed near Ludington (Michigan, U.S.A), on the eastern side of the lake (Figure 65), to provide a realistic water supply to Lake Huron, which must compensate for precipitation, evaporation and run-off from the Michigan watershed. The bathymetry used for Lake Huron is shown in Figure 65, along with the geographical location of the boundary conditions.

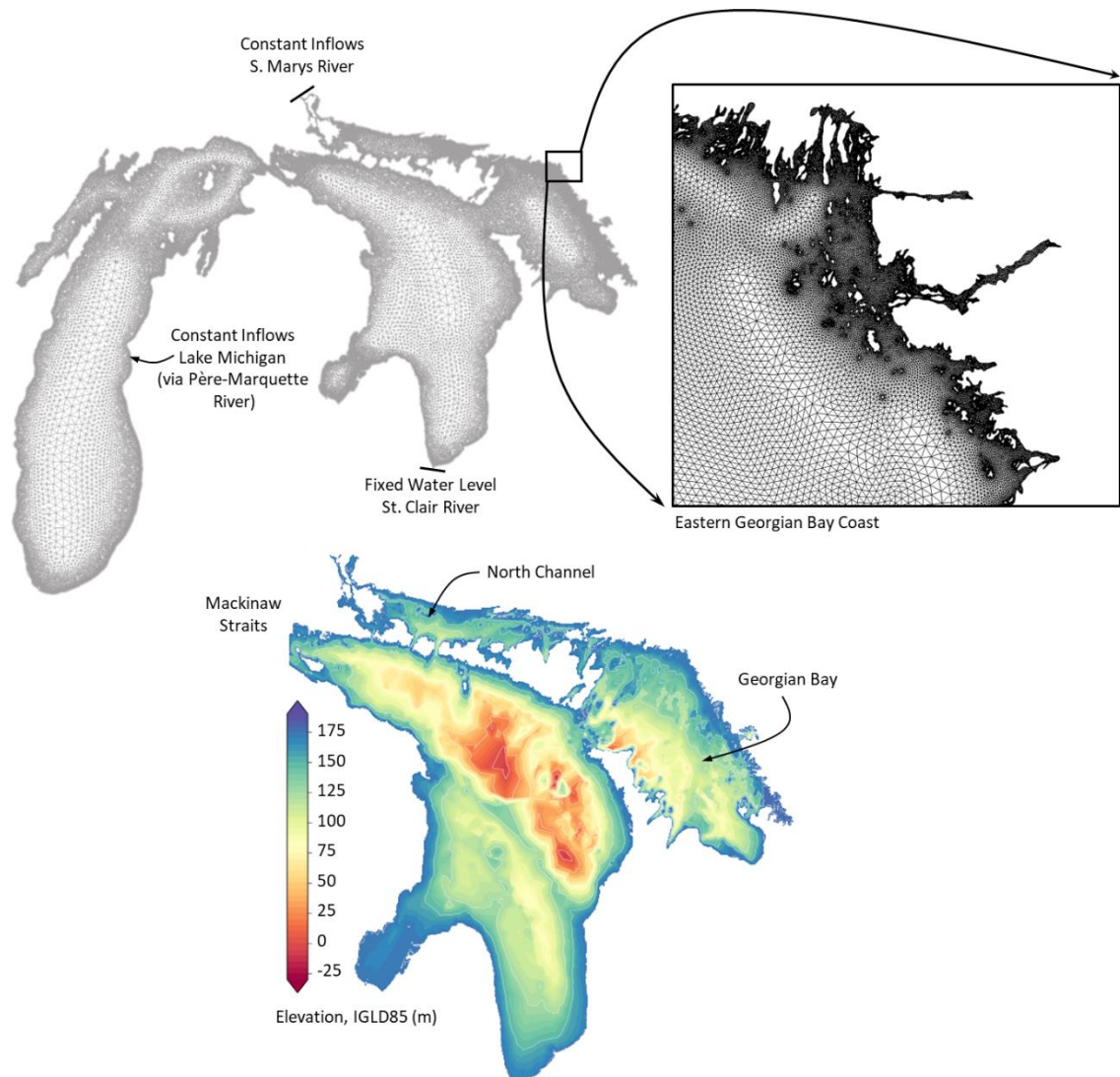


Figure 65: Mesh details (upper panels) and bathymetry (lower panel) used for the Lake Huron model. Boundary conditions are also defined.

3.5.5.2. Computational grid

As explained earlier, the Lake Huron model includes Lake Michigan, as it influences the amount of water entering the system, as well as the overall dynamics. While the choice of an open boundary in the Straits of Mackinaw would have precluded the need to include this large water body in the computational grid, initial tests have shown that winds can greatly alter the flow in the Straits, leading to numerical instability and convergence problems that hamper the simulations. Therefore, the inclusion of Lake Michigan, although costly in terms of number of elements and computational time, prevented numerical instability by moving the boundary condition far from the connecting channel, into eastern Lake Michigan (Figure 65), which improved convergence behavior. Since Lake Michigan is used only to provide appropriate hydrologic forcing, a coarse

set of bathymetry was used for this lake and no calibration was undertaken to optimize the modelled hydrodynamics west of the Straits of Mackinaw. The final mesh consists of about 1840k nodes and 888k elements (Figure 65).

3.5.5.3. Calibration and validation

Since Lake Huron and Georgian Bay differ in orientation, with the Georgian Bay facing slightly westward relative to Lake Huron, their main basin responds distinctly to atmospheric forcing. The effect of winds on lake surface motion will therefore be variable depending on wind direction, with a greater influence of NW-SE winds in Georgian Bay due to longer fetch along this axis, which is nevertheless limited given the size of this sub-basin. Therefore, the selection of the optimal wind-depth combination was realized separately for these two entities during the calibration process, leading to a variable effective depth in both basins for the same wind direction and intensity. Figure 66 shows an example of the results obtained from the set-up events calibration at Collingwood, in southern Georgian Bay.

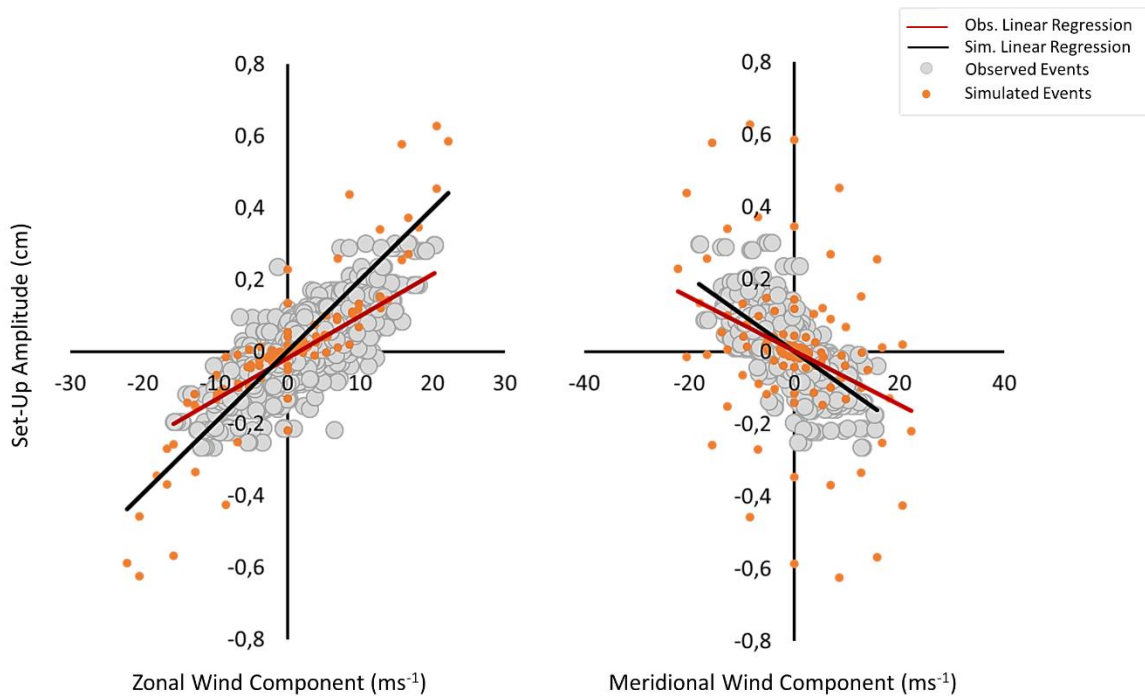
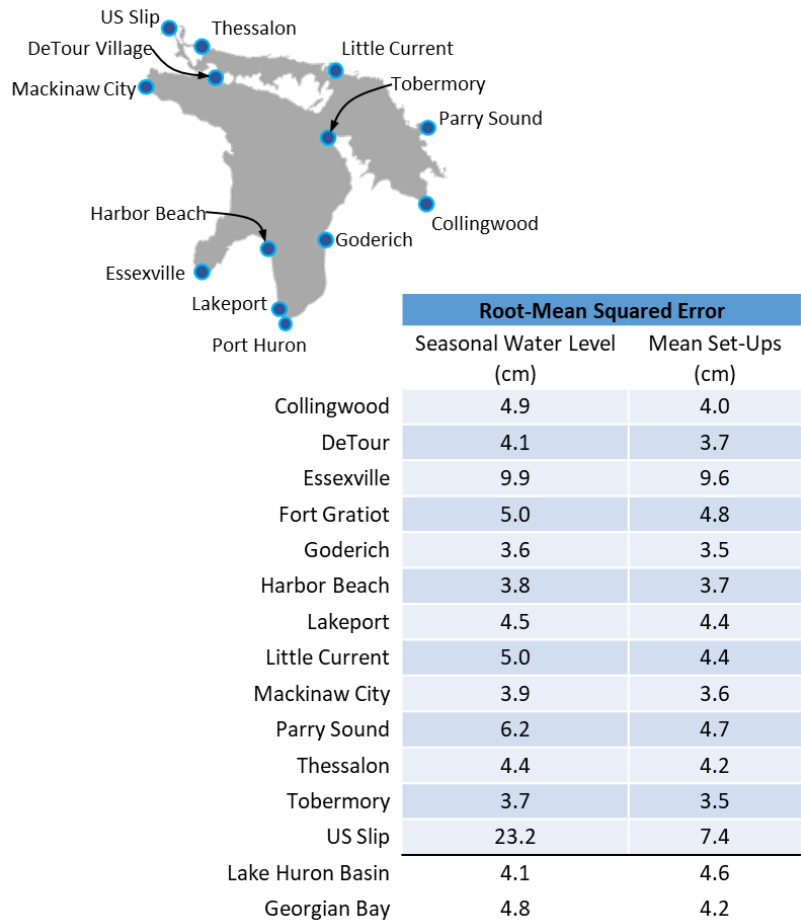


Figure 66: Observed (grey dots) and modelled (orange dots) wind-driven set-ups at Collingwood, Georgian Bay. The black and red lines show the linear regression obtained from the detected events, i.e. the relationship between event amplitude and wind speed for the zonal (left panel) and meridional (right panel) wind components.

The calibrated Lake Huron model gives an overall root-mean square error of 4.6 cm and 4.2 cm for the amplitude of wind-generated events in Lake Huron and Georgian Bay for the year 1990, respectively (Table 16). These errors must be added to errors observed in the seasonal water

level fluctuations, which is reproduced with a mean RMSE of 4.1 cm and 4.8 cm in both basins. Figure 67 provides an overview of the simulated time series at Collingwood for this specific year.

Table 16: The errors (RMSE) obtained for the long- and short-term fluctuations in Lake Huron, according to the calibrated model.



As revealed by the data in Table 16, two stations have significant errors: US Slip, in the Upper St. Marys River, and Essexville, in the Saginaw Bay, which is the large, elongated bay on the western side of Lake Huron. The former is located near the open boundary, downstream of the locks that enable ships passage between Lake Superior and Lake Huron, and is strongly influenced by the flow regime of the river and hence, the gates that control the Lake Superior outflows. Since this boundary condition is held constant in the modelling approach adopted, without any consideration of flow at the control structures, the change in water level induced by the rapids flow (e.g. Bachand *et al.*, 2017) is not captured by the model, thus the observed error. This approximation is valid here given the limited effect of flow variation on lake level, which is the primary concern in this project. The latter, Essexville, is located within an elongated bay that is large enough (~87 km x

46 km) to be influenced by local wind-driven fluctuations, which can enhance the surface water deflection otherwise observed in the main basin. This bay would have benefited from a separate calibration to improve the water level estimated locally. However, since there is no wetland site in this part of Lake Huron, as in the Upper St. Marys River, no additional work was undertaken to reduce the divergence observed at US Slip and Essexville.

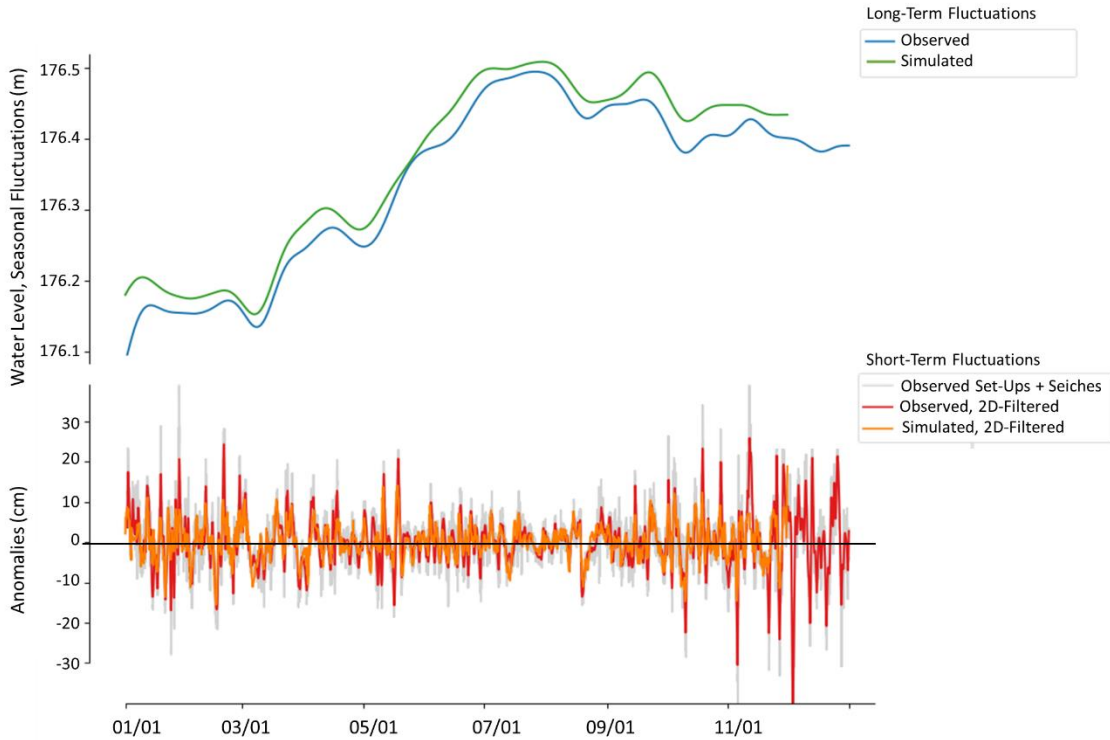


Figure 67: Upper panel: Observed (blue) and modelled (green) seasonal water level fluctuations for year 1990 at Collingwood, in Georgian Bay Lower panel: Idem, but for the short-term fluctuations, which include only the set-up events for the 2days-filtered time series (orange and red). The grey line gives the full detailed series of observed short-term disturbances, including surface seiches (which are not modelled) and set-ups.

3.6. Wave modelling

The wave climate that shapes the physical environment of wetlands at selected sites in the Great Lakes Basin was estimated using wave modelling, which is a numerical description of the sea state and the evolution of wind-generated waves (Cavaleri *et al.*, 2007). Since the Great Lakes are large, closed basins with both deep and shallow water areas, the modelling approach used had to be adapted to the changes that a wave undergoes as it moves toward the coast. The behaviour and structure of this type of wave are progressively modified and subject to physical processes that differ considerably from those governing deep-water waves (e.g., shoaling, refraction, diffraction, wave breaking). While some wave models are specifically designed to capture open ocean conditions, others are more dedicated to the transition zone, where waves undergo substantial changes, or even closer to shore, where morphodynamic processes come into play (i.e. surf and swash zones).

The models selected to construct the recent past wave climate and projections must therefore reflect the complexity of wave dynamics in coastal environments. This section provides a general description of the selected models, the nesting process used to provide a good representation of waves in shallower areas of the wetlands (Section 3.6.1), and the two modelling approaches adopted for Lakes Erie and Ontario (Section 3.6.2). While the former provides a comprehensive description of transient wave dynamics under unsteady and time-evolving conditions, the latter takes advantage of a scenario-based strategy that mimics the method used to generate the Lake Ontario/Huron water level time series (Section 3.4.2.3). No wave modelling was performed for Lake Huron due to time constraints and limited computer resources. The results of the validation are presented in Section 3.6.3.

3.6.1. Spectral wave models: WWIII and SWAN

There are two main families of wave models: phase-resolved models, which simulate wave processes based on conservation laws (mass and momentum), and phase-averaged models. Phase-resolved models aim to describe rapidly changing waves in environments where diffraction and wave-wave interactions are predominant (e.g. harbours, near coastal structures). These models simulate individual waves, which requires a high spatial resolution to resolve all wavelengths (typically a few metres). Their use is computationally demanding (Monbaliu *et al.*, 2000), and is therefore mainly dedicated to engineering studies and small coastal areas. Phase-averaged models are based on the action balance equation (described below), and describe the temporal and spatial evolution of the wave energy spectrum (Monbaliu, 2003). Waves are

simulated stochastically, by computing sea surface and wave statistics rather than the full range of waves. Wave conditions are assumed to evolve slowly, as opposed to phase-resolved models. The wave energy spectrum is computed on each grid cell of the computational domain, resulting in a representation of the wave field.

3.6.1.1. Third-generation wave models

The most up-to-date models, called third generation wave models, were first developed in the mid-1980s by Hasselmann *et al.* (1985), and Hasselmann and Hasselmann (1985). They explicitly include a source term for the wave-wave interactions that control the wind-sea evolution, in addition to the wind input (wave generation) and dissipation: the discrete interaction approximation (or DIA) that is still widely used in modern models. This range of models solves the wave transport equation determining the wave energy density in the time-space and frequency domain without any a priori assumptions.

The wave parametrization used to simulate coastal waters in phase-averaged models is similar to that of ocean models. The main difference lies in the term sources that are more complicated and complex in shallow waters, where several processes may control the propagation of the wave energy (shoaling, refraction, diffraction, quadruplet wave-wave interactions, bottom friction and depth-induced breaking). Two classes of spectral models are therefore employed, depending on the domain modelled (Figure 68): offshore and nearshore models, which use respectively a formulation adapted to open ocean or coastal conditions. The most commonly used models included WAM (WAMDI Group, 1988) or WaveWatch III (referred to as WW3; Tolman *et al.*, 2002), for the first class, and SWAN (Simulating Wave Nearshore; Booij *et al.*, 1999) or STWAVE (Steady State Spectral Wave model; Smith *et al.*, 1999), for the second²¹.

²¹ Commonly used nearshore wave models also included XBeach (Roelvink *et al.*, 2010) and SWASH (Simulating Waves till Shore; Zijlema *et al.*, 2011), which are defined as phase-resolving nonlinear shallow-water models preferentially dedicated to coastal engineer studies.

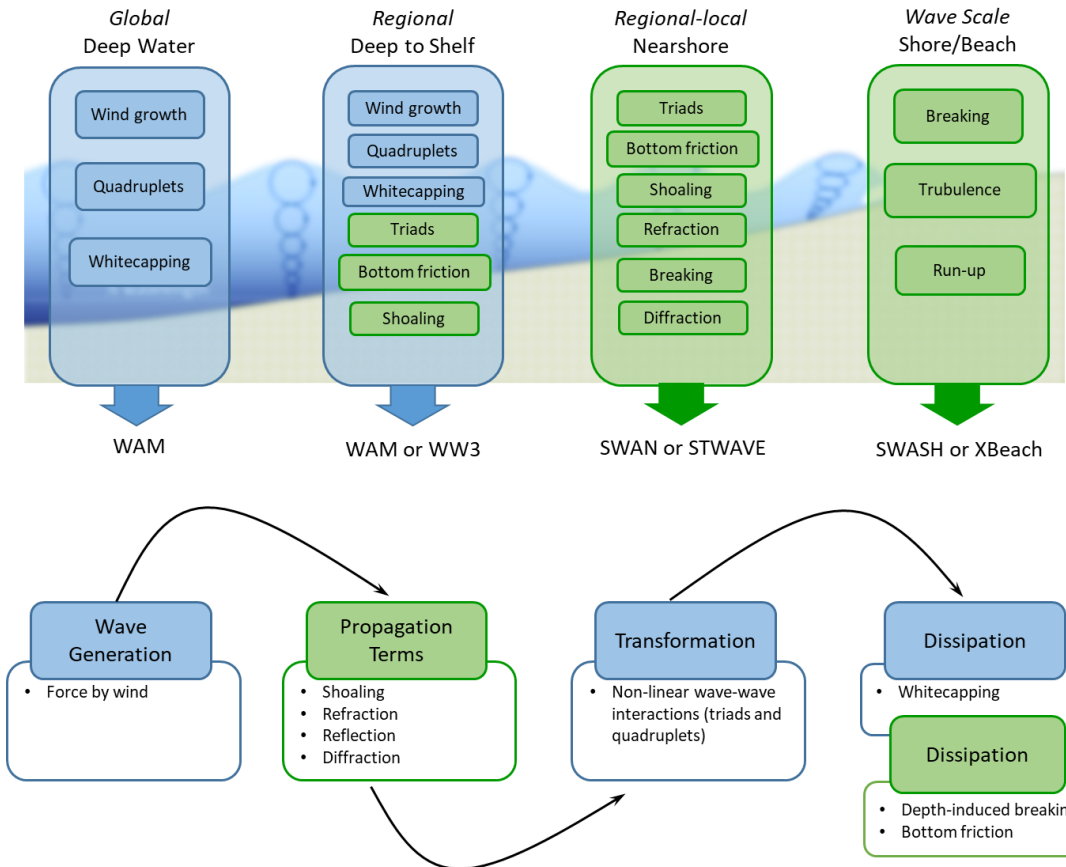


Figure 68: Top panel: Comparison of the most popular numerical wave models, the processes involved and their application (adapted from Roelvink, 2011). Bottom panel: Summary of physical processes in commonly used wave models. Green boxes indicate processes exclusively related to shoreline dynamics.

The evolution of wave energy in the phase-averaged models is determined by the wave action, $N = E/\sigma$, which depends on the wave density spectrum, E , that distributes wave energy over discrete frequencies, σ , and directions, θ . The action balance equation is expressed as:

$$\frac{dN}{dt} = \frac{S_{tot}}{\sigma} = \frac{S_{in} + S_{wc} + S_{nl4} + \dots}{\sigma} \quad 3.19$$

with S_{tot} , the sum of the source terms that consists of various contributions depending on the model. In deep water, the dominant source terms include wave generation, through the transfer of energy from wind to the waves, S_{in} , dissipation of wave energy due to whitcapping, S_{wc} , and non-linear transfer of wave energy due to quadruplets (four-wave interactions), S_{nl4} . Closer to the coast, in intermediate depths and shallow waters, more complex processes most by considered, as bottom friction, S_{bot} , dissipation due to depth-induced breaking, S_{brk} , non-linear three-wave interactions (triads), S_{nl3} . In the nearshore zone, localized effects such as coastal reflection, refraction, diffraction, and wave damping by vegetation may also be involved. Figure 68 gives a

summary of the physical processes included in SWAN, when the model is used to simulated nearshore dynamics.

3.6.1.2. Running the wave simulations: Workflow

In order to provide realistic simulations of sea conditions at the boundary of a wetland site, several steps must be followed to set up a wave model. The workflow includes the creation of the computational grids and nesting approach, definition of the wave models, generation of boundary conditions, and selection of outputs. Figure 69 summarizes these steps, which are defined in the following subsections.

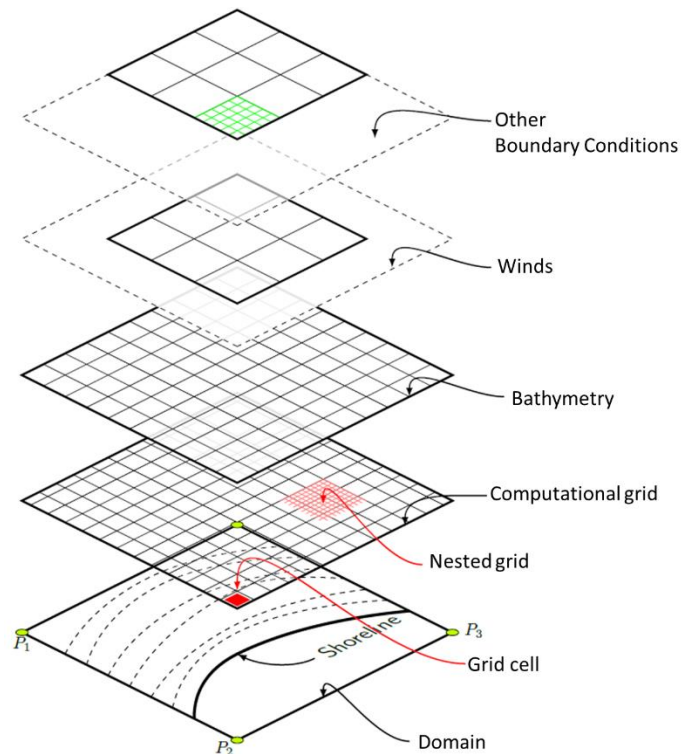


Figure 69: Schematic of the steps required to build and set-up a wave model (adapted from <https://texample.net/tikz/examples/swan-wave-model/>).

3.6.1.2.1. Computational grids, nesting and bathymetry

The first step in the model set-up is to define the domain and resolution of the computational grid, i.e. the X,Y geographic space in which the simulation will be run and the size of the cells (pixel size or point distance). All the computational grids used are regular, i.e. uniform in X,Y and rectangular, and in spherical coordinates.

A first spatial grid is defined that encompasses the entire lake, with a cell resolution of 500 m. This regular grid is dedicated to the WaveWatchIII model (version 5.16) which provides the offshore conditions, and includes only wet cells (i.e. without landward extension). Two intermediate SWAN grids (version 41.31) are then used to progressively transport the waves into the nearshore zone, where propagation terms such as shoaling and refraction come into play. Their use is necessary to provide a consistent physical representation of wave energy transport from one grid to another, as a change in resolution implies a change in bathymetry, which has a crucial influence on wave dynamics. In this nesting approach, each cell of the parent grid located at the boundaries of the intermediate (finer or child) grid is used to force the incoming wave energy (Figure 70). These boundary conditions are therefore extracted from simulations previously computed with the coarser (parent) grid.

At each boundary node, the wave energy spectrum is prescribed at a given time step, but the waves then evolve according to local conditions. The deep-water boundary of the first SWAN intermediate grid is located in the WW3 grid at points where the effects of shallow water are negligible, thus avoiding large discontinuities between the two models. In the Great Lakes, where the wave climate is devoid of swell energy (low frequency waves), the deep-water approximation is valid to a water depth of 10–15 m. Wave energy is therefore brought from a basin-wide resolution of 500 m (WW3) to intermediate resolutions of 150 m and 50 m (SWAN), before reaching the final grid that covers the terrestrial and lacustrine area of the wetlands, with a resolution of 20 m (SWAN; Figure 71). Each successive grid is dependent on the previous (coarser) one, ensuring that offshore wave information is transferred to smaller scales. Overall, one WW3 was constructed for the lake, and three SWAN grids for each of the wetland sites, for a total of 13 models for Lake Ontario and 16 for Lake Erie (Table 17).

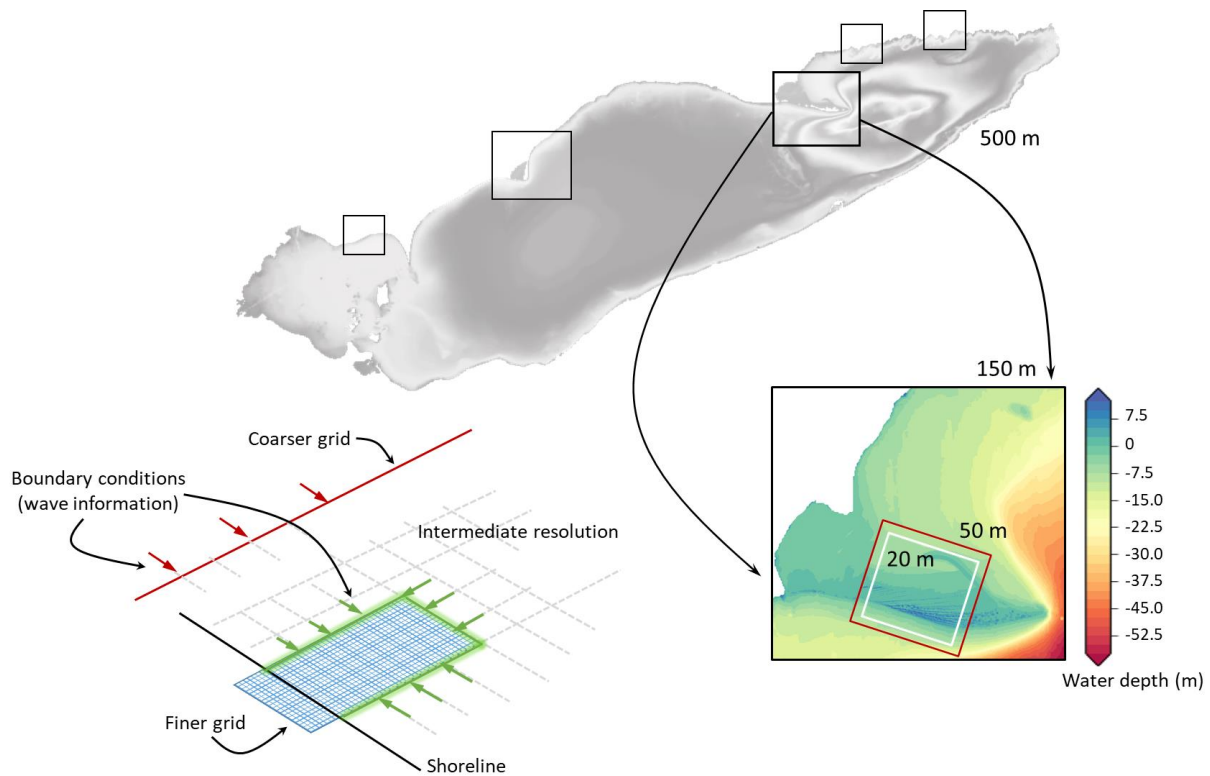


Figure 70: Nesting approach for wave modelling. Details are given in the text.

The same bathymetry and topography datasets used for the Lake Erie and Lake Ontario hydrodynamic models were used to create the grids, using a linear interpolation technique with a priority-based ranking that favours specific datasets to avoid any overlap. For the final grid, which covers the wetland area of interest, the digital elevation model was included in the interpolation process to provide a good digital representation of the topography, especially in the terrestrial portion of the site. In SWAN, dry cells are removed from the calculation at each computational time step, allowing the number of active (or wet) cells to change with water levels.

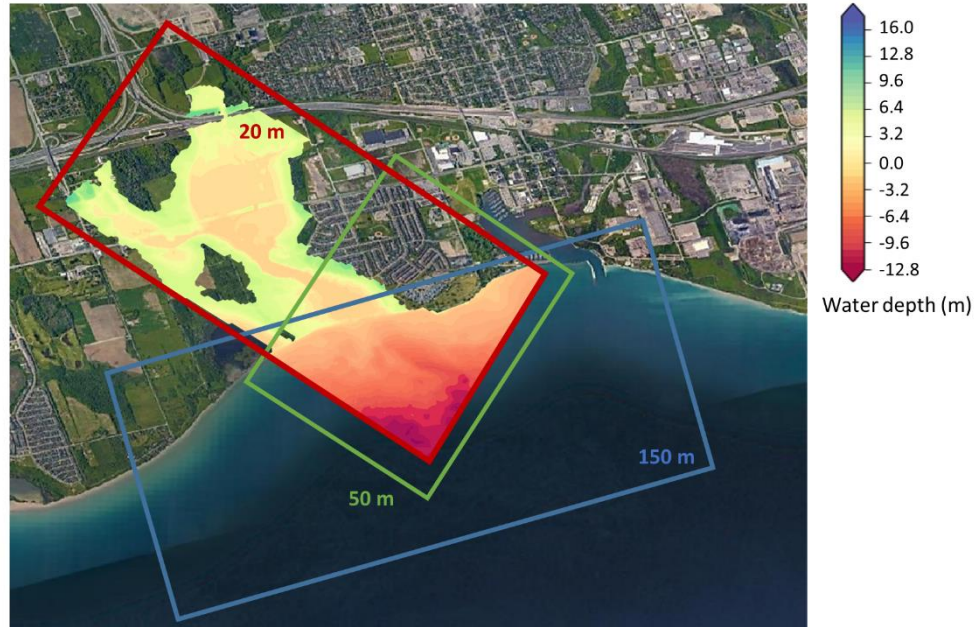


Figure 71: The nested SWAN grids for the Lynde Creek marshes (5LCM, Lake Ontario). The shaded colors show the bathymetry, relative to IGLD85, generated for the finer computational grid, which has a resolution of 20 m and extends over the terrestrial area of the site. Dry cells are removed from the calculation and updated at each forcing time step (i.e., 1 hour), based on water level fluctuations. Uncolored areas are masked cells.

3.6.1.2.2 Models set-up: Numerical and physical schemes

The spectral wave models estimate the wave spectrum at each point of the computational grid based on discrete frequencies and directions. For WW3 and SWAN grids, the same spectral resolution was chosen, based on what is used for the operational Great Lakes wave forecasting system developed by NOAA' National Centers for Environmental Prediction (NCEP; Alves *et al.*, 2014). This model operates with a discrete spectrum of 29 frequencies ranging from 0.05 to 0.72 Hz, emphasizing the importance of short waves typical of wind-sea. From 24 (WW3) to 36 (SWAN) angular directions were selected for wave propagation, allowing a directional resolution of 10–15° and a good computational efficiency.

While WW3 is sensitive to the CFL (Current-Friedrichs-Lewy) stability criterion, the numerical propagation scheme in SWAN is unconditionally stable, especially on a regular mesh, and very robust in shallow coastal applications due to the mutual independence of spatial and temporal resolutions. The CFL number, which determines the time that the fastest waves spend in a cell of the mesh, limits the time step needed to simulate adequately the geographical propagation of wave energy. The smaller the spatial resolution, the smaller the time step required to resolve nearshore processes (e.g., Monbaliu *et al.*, 2000). All non-stationary runs of WW3 were therefore performed with a global time step of 6 minutes, while the SWAN runs used a time scale of 3 minutes, which is small enough to handle any changes in physical conditions (offshore waves,

water levels, or winds). These time scales apply strictly to the Lake Erie wave models, as we will be discussed later (cf. Section 3.6.2).

Both WW3 and SWAN were run with the so-called observation-consistent wind input and whitecapping dissipation scheme, known as the ST6 physics, which is based on field observations at moderate-to-strong wind-wave conditions (Rogers *et al.*, 2012). This scheme is based on a nonlinear wind input that relaxes in strong winds and steep waves to parametrize airflow separation (Donelan *et al.*, 2006). A wave-breaking threshold is also used for the whitecapping dissipation (Babanin *et al.*, 2001), as well as cumulative behavior at small-scales for dissipation under breaking waves (e.g. Young and Babanin, 2006). Bottom friction (JONSWAP formulation), swell dissipation (Ardhuin *et al.*, 2010), and depth-induced breaking (Battjes and Janssen, 1978) were activated, as well as the Lumped Triad Approximation (LTA; Hasselmann *et al.*, 1985) and the Discrete Interaction Approximation (DIA; Eldeberky, 1995), for triad and quadruplets wave-wave interactions. The models used Message Passing Interface (MPI) with a distributed memory. Table 17 summarizes the characteristics of each computational grid and numerical scheme used.

Table 17: Characteristics of the computational grids and numerical schemes used for WW3 and SWAN models. Acronyms refer to wetland sites.

	Lake	Wetlands			
	WW3	SWAN 150m	SWAN 50m	SWAN 20m	
<u>Lake Erie</u>					
Elements/cells	795 x 396	7GRM 8SPP 9LPW 10RBY 11FCK	90 x 42 74 x 70 248 x 188 142 x 173 173 x 92	155 x 52 139 x 67 181 x 174 270 x 317 138 x 50	361 x 367 320 x 209 378 x 342 605 x 713 300 x 242
Sea points	115668	9LPW 7GRM 8SPP 9LPW 10RBY 11FCK	35197 3114 4459 35197 11892 12072	22323 4400 5840 22323 31890 4622	82574 23486 26266 82574 139809 17719
Land points	199152 (inactive)	7GRM 8SPP 9LPW 10RBY 11FCK	53 40 3479 135 179	208 262 9143 9653 118	37143 12477 46564 99205 26177
Average water depth	18 m	7GRM 8SPP 9LPW 10RBY 11FCK	11 m 11 m 13 m 13 m 9 m	7 m 5 m 5 m 6 m 5 m	6 m 4 m 4 m 4 m 4 m
<u>Lake Ontario</u>					
Elements/cells	626 x 240	2ACM 3SBM 5LCM 6JSM	165 x 69 76 x 87 31 x 20 36 x 25	85 x 229 64 x 120 44 x 48 48 x 22	207 x 490 141 x 262 90 x 257 94 x 231
Sea points	74595	2ACM 3SBM 5LCM 6JSM	2763 3375 509 751	3313 2277 1211 845	17440 10514 4885 5549
Land points	75645 (inactive)	2ACM 3SBM 5LCM 6JSM	155 117 6 4	357 1120 19 32	18364 6929 7722 2682
Average water depth	90 m	2ACM 3SBM 5LCM 6JSM	3 m 13 m 10 m 10 m	4 m 5 m 7 m 5 m	4 m 3 m 6 m 2 m
<u>Numerical Scheme</u>					
Integration and source time step (sec)	30/360	180			
Max iterations/time step	1	5			
Wind/Water level input time step (hour)	1–3/1	1–3/1			
Nesting time step (hour)		1			
Model output time step (hour)	1	1			

3.6.1.2.3. Boundaries conditions: Atmospheric and oceanic forcing

The wind data used to force the wave models were extracted from the datasets generated for the hydrodynamic modelling (cf. Table 11, Section 3.5.3). For non-stationary simulations (Lake Erie), the gridded wind fields were updated every 1 or 3 hours depending on the period being simulated (historical or recent past and future periods). Since water level fluctuations influence the depth-induced breaking process in the nearshore zone and hence the wave intensity along the coast (e.g., Meadows *et al.*, 1997), waves were calculated with fluctuating water levels. Depending on the simulation approach chosen (temporal or scenario-based method), gridded water level time series or static water level scenarios were used, as explained hereafter (cf. Section 3.6.2).

Although wave-current interactions (WCI) can have a significant impact on wave dynamics, particularly under fetch-limited conditions (Brissette *et al.*, 1993) by causing, for example, change in wave age, energy dissipation, change in wave frequency, and refraction, no current forcing was used for the simulations. The two-dimensional hydrodynamic models developed for the Great Lakes are unable to resolve the basin-wide circulation, which is largely three-dimensional, and the nearshore dynamics, which are dominated by several specific features such as upwelling or downwelling and coastal jets (Valipour *et al.*, 2019). Therefore, no reliable current was available to predict this WCI, which is mainly confined to extremely shallow regions that exhibit large variations in current intensity and water depth (Dodet *et al.*, 2013). This lack of information is a limitation of the wave simulations performed in this project. However, and since the shaping of wetlands (in time and space) related to wave activity is primarily predicted as a function of relative wave intensity (or near-bottom orbital velocity) in the area of interest, rather than in terms of absolute values, no significant drawbacks are expected from this limitation.

3.6.1.2.4. Outputs

From intermediate grids (WW3 and SWAN), only the hourly mean wave statistics were saved as outputs, i.e. the significant wave height (H_S), mean wave period (T_p and/or T_{m02} according to model), and mean wave direction (DIR). In the final stage of the modelling (SWAN 20 m), the near-bottom orbital velocity (u_{bot}) was also saved on the original 20 m grids and then interpolated to the CWRM grid, providing results at a final 10 m resolution for wetland modelling.

3.6.2. Modelling approaches: Time-varying and scenario-based methods

Two numerical approaches were taken to run the wave models, mimicking the methods used for hydrodynamic modelling of Lakes Erie and Ontario. In the first case (Lake Erie), the simulations

were run in a non-stationary mode, from mid-March to early November with a (global) time step of 3-6 minutes. The first two weeks of simulation are used as an initialization period (or spin-up), i.e. the time required by the model to reach a statistical steady state under non-stationary forcing. Water levels and winds are updated at each one-hour time step, as well as the wave forcing at the boundaries, to give a realistic simulation framework. In this configuration, continuous and gridded time series of wave statistics are obtained, with a time resolution of one hour.

3.6.2.1. **Scenario-based wave modelling: Lake Ontario**

In the second case (Lake Ontario), the wave models were run in stationary mode ($\partial N/\partial t=0$): the solution obtained is the quasi-equilibrium state of the waves under static forcing. Since atmospheric (wind intensity and direction) and hydrodynamic (water level) conditions change during the growing season, the wave climate must be inferred from a time series that integrates spatial and temporal variations. To do this, an interpolation technique similar to that described in Section 3.4.3.2 was used to construct the wave time series based on the prevailing physics, by grouping in chronological order several static solutions, each of which being a representation of waves at a given time step.

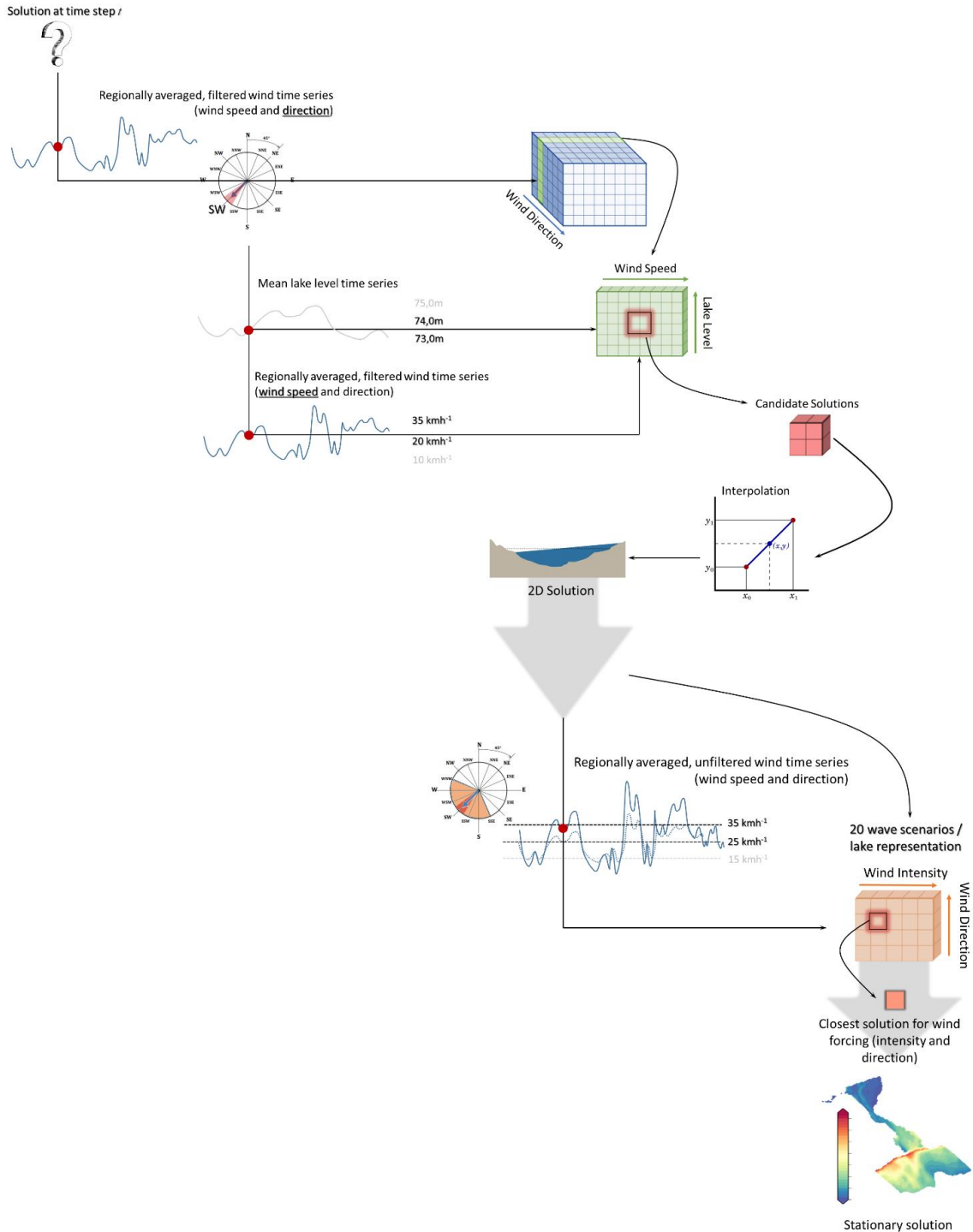


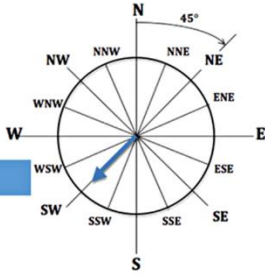
Figure 72: Schematic illustration of the scenario-based approach to wave modelling (Lake Ontario). The selection of the standing wave scenario at a specific time step is performed in two steps. First, the selection of the closest hydrodynamic forcing, which depends on the wind speed and direction observed at time t in the filtered and regionally averaged wind time series (first half of the diagram). Second, the selection of the closest wave scenario, which is based on the wind speed and direction observed at time t in the regionally averaged unfiltered wind time series (second half of the diagram).

The first phase in this modelling approach is to define the state of the lake, in terms of water levels, from the mean lake level and regional (filtered) winds, which determines the dominant atmospheric system responsible for the set-ups (Section 3.4.3.2). This state is chosen from a subset of four solutions, grouping the solutions simulated with the two closest water level scenarios and the two closest wind intensities scenarios, as described in Section 3.4.3.2 (Figure 72). These solutions are therefore taken from the database previously created for hydrodynamic modelling purposes, which include 970 lake representations (but only the first 776 are used for wave modelling, which includes the first eight levels in Figure 40, cf. Section 3.4.3.2). Unlike hydrodynamic modelling, which interpolates the lake state from the four solutions in the created subset, wave modelling uses only the closest solution in that set as a forcing.

Where the static wave modelling approach differs from the method explained in Section 3.4.3.2 is in the choice of atmospheric forcing used to generate the wave solutions. The response of surface gravity waves to changes in wind is a rapidly evolving process that responds quickly to any deviation in wind direction and intensity, especially in fetch-limited seas (e.g., Günther *et al.*, 1981). Scenario-based wave modelling must therefore include this degree of complexity, which involves selecting a static wave solution that matches the wind conditions at each one-hour time step of the simulated time series. While the two-day filtered regional winds are used to select the hydrodynamic forcing, i.e., the lake condition in terms of water levels and set-ups, the unfiltered regional winds were chosen to force the wave models. At a specific time step, the wind intensity and direction used to generate the waves are directly related to the unfiltered, regional average values, based on predetermined wind classes that included 5 intensities and 16 directions (Table 18). In doing so, two wind time series are used to determine the correct wave scenarios at time t , i.e., the two-day filtered and regionally averaged wind time series, which defines the hydrodynamic state of the lake, and its corresponding unfiltered series, for the surface forcing (Figure 72).

Table 18: Wind classes used for the scenario-based modelling approach.

Wind Intensity			Wind Direction		
	Intensity (Unfiltered series)	Forcing	Direction (Filtered series)	Available Forcing (Unfiltered series)	
	km h ⁻¹	km h ⁻¹ (ms ⁻¹)			
1	No Wind	< 10	0 (0)	1 N	NW, NNW, N, NNE, NE
2	Low	10–20	15 (4.17)	2 NNE	NNW, N, NNE, NE, ENE
3	Moderate	20–30	25 (6.94)	3 NE	N, NNE, NE, ENE, E
4	Strong	30–40	35 (9.72)
5	Extreme	> 40	45 (12.5)	16 NNW	WNW, NW, NNW, N, NNE



For any wind less than 10 km h⁻¹ (or 2.8 ms⁻¹), calm conditions are assumed and no significant wave energy is expected in nearshore areas. While each wind intensity class (unfiltered) was used to create a distinct wave climate in combination with the lake level representations, the variability in wind direction was limited to five directions. These directions are centred on the (filtered) wind direction used to simulate the hydrodynamic scenario used as forcing (Table 18). This choice allows for a non-negligible reduction in computational time and data storage requirements since all 13 Lake Ontario models must be run for each of the solutions included in the wave database to provide accurate nesting between grids. Based on the analysis conducted on the historical wind time series (1980–2010), i.e. the regionally averaged filtered and unfiltered Climex series (cf. Section 3.4.3.2), the use of five directions ($\pm 45^\circ$) around each filtered wind direction encompasses up to 88-96% of the variability between the two series (not shown). Overall, for each of the 776 lake representations, 20 wave scenarios were computed, for over 15k scenarios per model.

3.6.2.2. Expected bias of the scenario-based waves modelling

Although the scenario-based approach is very efficient, providing a quick way to create a wave climate based on time series of water levels and winds, the use of stationary solutions forced under constant physical conditions can lead to a bias in the estimation of wave statistics. Wave simulations performed under spatially constant wind by Nekouee *et al.* (2016) were found to be deficient, as the predicted significant wave height was up to 38% higher than that of a spatially

variable wind field. Small-scale wind effects can have a significant impact on surface waves: omitting them can increase uncertainties in modelling outputs, which is the case when spatially constant fields are used.

3.6.3. Validation: Historical period, 1980–2010

Since wetland models use the relative wave intensity across the study sites to shape the plant communities and their spatial extent, contrasting the observed wave conditions across the grid, no calibration was performed to improve the numerical wave models. Calibration is used to correct for bias in the wind field, providing a possible adjustment to the wind drag coefficients and the strength of the swell decay due to wind effects (via the input term, S_{in} ; e.g. Fernández *et al.*, 2021), and to improve the modelling for local conditions (e.g., calibrating the wave breaking coefficients). While wave observation data are available from buoys deployed in the central portion of the lakes via the National Data Buoy Center, no observations are accessible for the nearshore areas of the selected wetland sites. This lack of information limits the feasibility of a reliable calibration and does not ensure an optimal representation of wave characteristics along the shoreline in the shallower areas of the lakes. Therefore, the quality of the uncalibrated wave simulations was evaluated to determine the accuracy of the predicted values in deep water only.

3.6.3.1. Errors and biases

For both lakes (Lakes Erie and Ontario), deep-water wave statistics were extracted from simulations at the geographic position of surface buoys for which measurements are available since early 1980 (cf. Section 3.6.3). Because the WW3 models have a horizontal spatial resolution of 500 m, the four grid points located closest to each buoy location were used to generate time series of simulated values for the reference period, 1980–2010. The model-predicted values were then compared to the measurements using bias, root mean square error (RMSE), percent mean absolute error (MAPE), and dispersion index, SI:

$$BIAS = P_i - O_i \quad 3.20$$

$$MAPE = \left\langle \left| \frac{P_i - O_i}{O_i} \right| \right\rangle \times 100 \quad 3.21$$

$$RMSE = \sqrt{\frac{1}{N} \langle (P_i - O_i)^2 \rangle} \quad 3.22$$

$$SI = \sqrt{\frac{\langle [(P_i - \bar{P}) - (O_i - \bar{O})]^2 \rangle}{\langle O_i^2 \rangle}} \quad 3.23$$

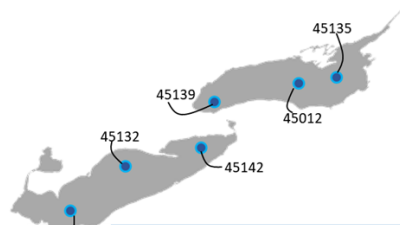
with P_i and O_i , the simulated and observed values at time i for a specific station, respectively, and over bar or angle brackets denoting mean. The bias was calculated from the wave climatology, using the long-term time series of significant wave height and the best-fitted Weibull distribution (mean; cf. Section 3.6.3), as well as for individual realizations along the selected period (with mean and 2.5th/97.5th quantiles). The SI is a measure of variability, i.e., it gives the expected percentage error for the parameter. Bias, RMSE, and SI are standard statistical values used in wave modelling studies to quantify the accuracy of simulations (e.g. Hu *et al.*, 2021). A final statistical indicator was used to evaluate model performance, the index of agreement, IOA, defined by Willmott (1982) and presented in Section 3.5.3.5. The IOA indicates a perfect agreement between the predicted and observed values when it is equal to 1.

3.6.3.2. Lake Erie

The significant wave height, H_s , and peak period, T_p , simulated by the model were compared to available buoy observations in Lake Erie for the baseline period, which provide deep-water wave characteristics. The statistics for each wave parameter used for the model accuracy evaluation are presented in Table 19, along with the observed errors in the wind inputs at the station positions (i.e. Climex data). These time series were compared to the post-processed in situ winds as described in Section 2.3.1.

Table 19: Summarized validation statistics of WW3 wave models data relative to in-situ measurements in Lakes Erie and Ontario. Statistics for winds (wind speed at 10 m), significant wave height, and wave period are presented at buoy locations, along with detailed statistics broken in wind directions for Lake Ontario. Statistics include bias, root-mean-square error (RMSE), Mean Absolute Percentage Error (MAPE), scatter index (SI), and index of agreement

(IOA). H_S Weibull refers to the mean of the best-fitted Weibull distribution, while $H_{S,95}$, to waves in the upper range of the distribution (> 95th quantile).



		WINDS			SIGNIFICANT WAVE HEIGHT							WAVE PERIOD		
Direction		Bias (ms ⁻¹)	RMSE (ms ⁻¹)	H _S Weibull		H _S 95		Bias (m)	RMSE (m)	SI	IOA	Bias (s)	RMSE (s)	SI
				Bias (m)	MAPE (%)	Bias (m)	MAPE (%)							
<i>Lake Erie</i>														
45005	All	0.5 (-5.0 ; 6.4)	2.8	< 0.01	< 1	-0.25	15	0.01 (-0.63 ; 0.62)	0.31	0.43	0.82	-0.3 (-2.1 ; 1.2)	0.9	0.21
45132	All	1.0 (-4.4 ; 8.5)	3.1	0.14	30	0.05	3	0.14 (-0.43 ; 0.87)	0.35	0.53	0.77	-0.1 (-1.7 ; 1.6)	0.9	0.23
45142	All	1.0 (-4.5 ; 7.3)	2.8	0.09	18	-0.03	2	0.09 (-0.52 ; 0.79)	0.33	0.45	0.81	-0.3 (-3.0 ; 1.7)	1.2	0.29
<i>Lake Ontario</i>														
45139	NW-NE	0.8 (-4.3 ; 6.1)	2.7	-0.16	29	-1.51	60	0.08 (-0.55 ; 0.82)	0.35	0.82	0.75			
	NE-SE	0.0 (-5.1 ; 5.4)	2.6	-0.10	20	-0.79	36	-0.08 (-0.80 ; 0.67)	0.37	0.56	0.77			
	SE-SW	0.5 (-4.6 ; 5.7)	2.8	0.09	40	0.01	3	0.10 (-0.33 ; 0.77)	0.30	0.99	0.74			
	SW-NW	1.0 (-4.2 ; 6.3)	2.7	0.16	58	0.14	15	0.16 (-0.33 ; 0.91)	0.35	0.93	0.70			
45012	NW-NE	-0.2 (-5.8 ; 5.1)	2.6	-0.16	23	-0.65	36	-0.17 (-0.90 ; 0.59)	0.40	0.45	0.74	-1.3 (-2.5 ; 0.0)	1.4	0.20
	NE-SE	-0.2 (-5.0 ; 4.6)	2.4	-0.11	17	-0.33	21	-0.10 (-0.78 ; 0.64)	0.37	0.50	0.77	-1.2 (-2.4 ; 0.1)	1.3	0.21
	SE-SW	0.5 (-4.2 ; 5.0)	2.3	0.02	4	-0.02	< 1	0.03 (-0.57 ; 0.87)	0.36	0.55	0.76	-1.0 (-2.2 ; 0.3)	1.2	0.22
	SW-NW	-1.0 (-6.8 ; 4.1)	2.9	-0.24	30	-0.83	31	-0.23 (-1.13 ; 0.65)	0.50	0.44	0.70	-1.4 (-2.7 ; 0.1)	1.5	0.20
45135	NW-NE	1.0 (-3.9 ; 6.6)	2.9	0.04	7	-0.50	23	-0.03 (-0.68 ; 0.68)	0.35	0.54	0.78			
	NE-SE	0.7 (-4.2 ; 6.0)	2.6	0.04	10	-0.60	23	0.05 (-0.61 ; 0.77)	0.39	0.71	0.70			
	SE-SW	0.4 (-4.5 ; 5.7)	2.6	0.05	11	-0.15	8	0.05 (-0.64 ; 0.87)	0.36	0.62	0.76			
	SW-NW	0.7 (-4.9 ; 7.2)	3.1	-0.11	16	-0.82	30	-0.11 (-1.05 ; 0.80)	0.46	0.50	0.71			

The simulated deep-water wave climatology for the historical period (1980-2010) is in good agreement with the observations, with a bias of 0.04–0.15 m for the significant wave height based on the mean of the best-fit Weibull distribution. This bias reflects a slight overestimation of H_S at all stations, in agreement with the observed errors in the wind field (0.5–1.0 ms⁻¹). Similar model behaviour can also be observed in the extracted time series for the year 2008, where the simulated data remain higher than the observations in the lower range of values, especially for station 45132 (Figure 73). This station (Port Stanley) has the largest deviations, with a bias of 0.14 m, or 30% of the observed mean value. Inspection of the data reveals that the simulated waves are particularly overestimated in the peak of the distribution, where the waves reach their nominal value of ~30–70 cm (cf. Table 19, Section 3.6.3). The RMSE remains between 0.31 and 0.35 m, which is comparable to the results obtained by Niu and Xia (2016) with their Finite-Volume

Coastal Ocean Model (FVCOM)-based Lake Erie surface wave model (i.e., up to 0.26–0.28 m), and by Alves *et al.* (2014) with NOAA's Great Lakes wave forecasting system (i.e., 0.14–0.37 m, all lakes combined).

The scatter index varies between 0.43 and 0.53, providing information on the validity of the model estimates relative to the observations (acceptable < 1). For the highest waves ($H_s > H_{s,95}$, the 95 percentile), the absolute bias varies between 0.05–0.25 m (2–15%), with underestimates at stations 45005 and 45142, and a small overestimate in the central basin (45132), where the model accuracy is slightly lower (AOI < 0.80). Wave models generally underestimate storm peaks, which is one of the most challenging aspects of physics-based wave models (Cavaleri, 2009). During extreme events, nonlinear effects can potentially come into play and alter the wave dynamics, which is poorly captured by current wave models.

The Q-Q plots in Figure 73 confirm the above results: overestimation of significant wave heights, with a maximum deviation observed at the top of the distribution, around the nominal wave climate amplitude (~ 0.3 – 0.7 m). The upper quantiles of the predicted distribution show small overestimates, revealing that wind input, more than model parameterization, may be responsible for the negative bias observed at the highest significant wave heights ($H_{s,95}$). The model simulated consistent storms and intense wave conditions, but there is a lack of temporal synchronization between the major events associated with $H_s > 1.2$ – 1.4 m in Lake Erie. In the Great Lakes, the majority of the sea state can be characterized by moderate to low wave energy (Alvers *et al.*, 2011), with larger waves observed in early spring and late fall as expected from the wind climatology (cf. Figure 14), two periods that are at the limits of the modelling time window. The validation period may therefore hide the actual capacity of the model to reproduce more severe sea state.

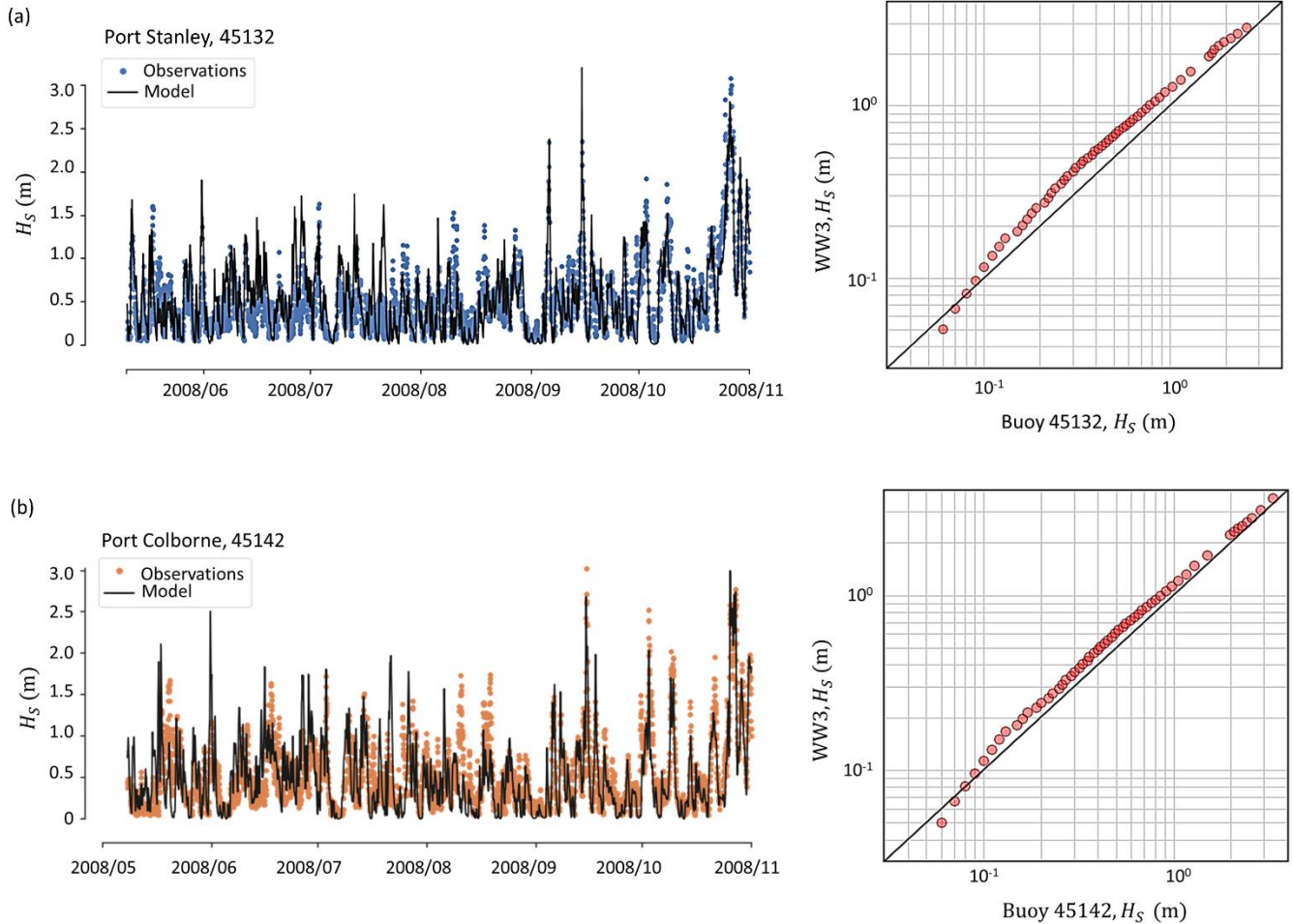


Figure 73: Time series (left panels) and Q-Q plots (rights panel) of observed and simulated significant wave heights at buoys 45132 (a) and 45142 (b), in Lake Erie.

Predictions of peak periods, T_p , systematically underestimate observed values, as shown by biases that remain between -0.1 and -0.3 s, with a maximum absolute error of 3.0 s. The bias is mostly observed in the lower and upper quantiles, i.e., below 3 s or above 6 s (not shown), outside the range of nominal values observed in the in situ data (cf. Table 19, Section 3.6.3). The RMSEs range from 0.9 to 1.2 and the dispersion of the predicted values is quite small, with an SI score of 0.21–0.29, which is similar to the results obtained by Alves *et al.* (2014).

Overall, the agreement between the model and in situ measurements is satisfactory, although the performance of the WW3 model for Lake Erie could be improved by specific tuning of the wind input term: the accuracy of wave models depends strongly on the accuracy of the wind fields (Alves *et al.*, 2014; Cavaleri, 1994). Since the wave modelling was performed with Climex data,

which have a temporal resolution of 3 h, an improvement could also be expected using hourly winds, as would be possible with the reanalysis outputs from the Global Environmental Multiscale Atmospheric Model (GEMR; Gasset *et al.*, 2021) that were not available at the beginning of the project.

3.6.3.3. **Lake Ontario**

Because surface waves dynamics in Lake Ontario were modelled using a scenario-based approach with limited flexibility in terms of wind definition, with only five intensity levels (including calm conditions; Table 18), the objective of the simulations was primarily to replicate observed nominal conditions rather than individual realizations. Validation therefore focused on wave climate and upper quantile statistics to reflect the intended use of the wetland models, which are firstly concerned with the average wave conditions encountered during the growing season and storms, as explained in Section 3.2.4.3.

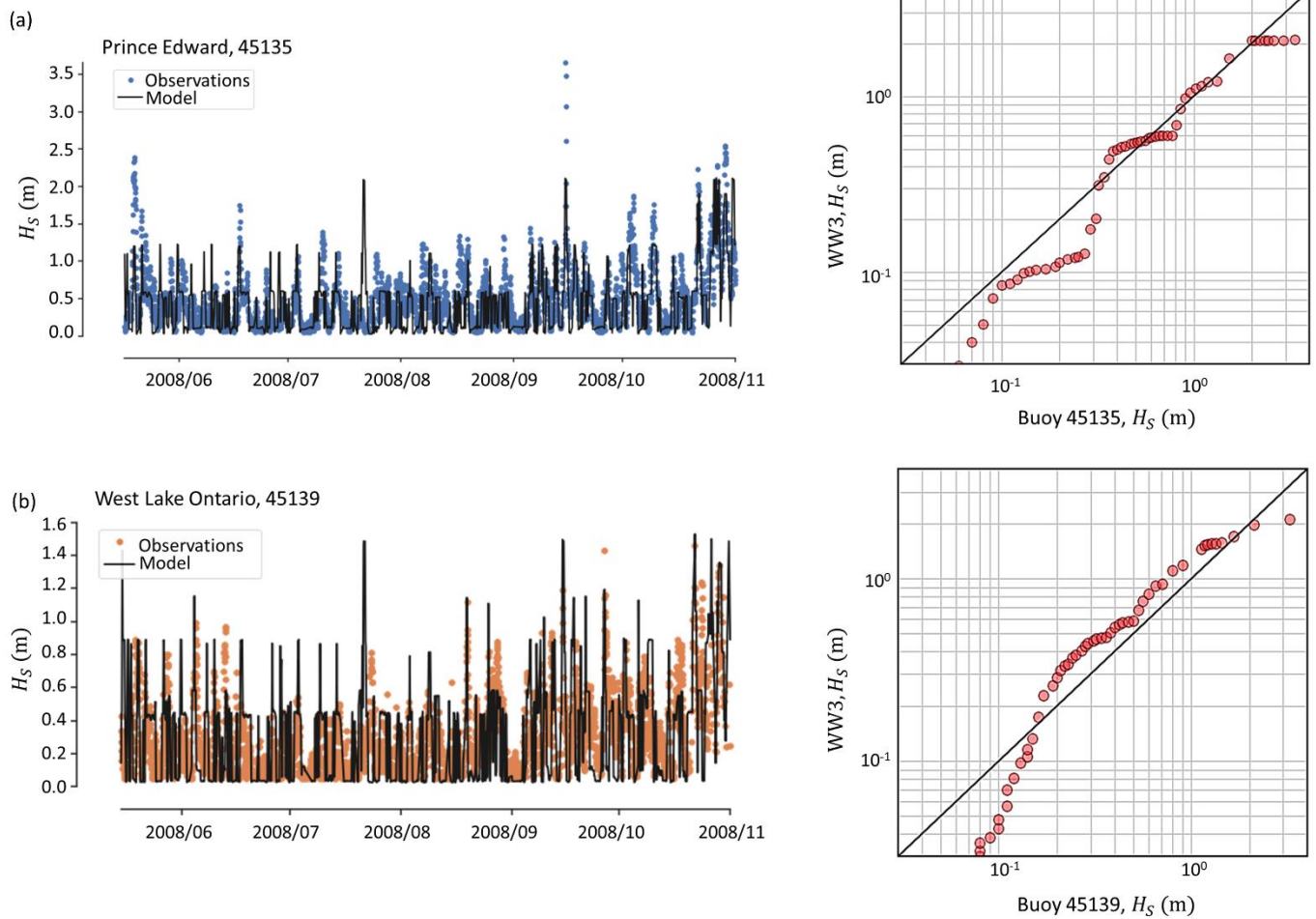


Figure 74: Time series (left panels) and Q-Q plots (rights panel) of observed and simulated significant wave heights at buoys 45135 (a) and 45139 (b), in Lake Ontario.

The long-term statistics for the wave parameters show a variable bias depending on the observed local wind direction, revealing an asymmetric behaviour of the model depending on the atmospheric forcing. Therefore, the results in Table 19 were broken down into the four main geographical directions, namely north (NW–NE), east (NE–SE), south (SE–SW) and west (SW–NW).

The absolute bias estimated from the mean of the best-fit Weibull distribution ranges from 0.02 to 0.24 m, with an absolute relative error that remains mostly below 25%. This error increases beyond 40% at station 45139 for south and west winds, the directions associated with the shortest fetches relative to station position in Lake Ontario, as well as the smallest recorded waves (<0.25 m; cf. Table 19, Section 3.6.3). Thus, the model overestimates the significant wave height under short fetch conditions, as predicted by previous studies (e.g. Toumi *et al.*, 2012). The bias

extracted from individual observations is generally consistent with the biases observed in the winds. It remains within the error range of the NOAA Great Lakes wave forecasting system for most cases (i.e. below an absolute error of 0.10 m), but with a slightly higher RMSE than those obtained for Lake Erie (0.30–0.50).

The scattering of the simulated values is also greater, with values ranging from 0.44 to 0.99. In the upper quantiles ($H_s > H_{s95}$), waves are globally underestimated as in the Lake Erie model, except for short fetch conditions (station 45139, SE–SW and SW–NW directions). However, the observed discrepancies are larger, with a MAE of 0–60%. The largest inaccuracies detected in the Lake Ontario model are reflected in the IOA, which remains below 0.8 for all stations. With respect to the predicted wave period, only the mean wave period, T_{m02} , was extracted from the Lake Ontario scenarios, which reduces the comparison to the observed values at station 45012 (buoys operated by ECCC strictly record the maximum wave period). As described above, WW3 systematically underestimates this wave parameter, with a bias ranging from -1.4 to -1.0 s, which is significantly higher than the error observed in Lake Erie. However, T_{m02} is sensitive to the entire density spectrum, which is largely biased in the low frequencies (highest waves), which may explain the observed difference between the two models.

Overall, the Lake Ontario steady-state solutions provide reasonable long-term wave climate, but with significant errors in the station point estimates, especially in the upper quantiles of the significant wave height distribution ($H_s > H_{s95}$; Figure 74, left panels). The use of five intensity levels, with a maximum wind speed of 45 kmh^{-1} (12.5 ms^{-1}), and a constant, uniform wind field clearly limits the ability of WW3 to reproduce wave generation under the atmospheric conditions that characterize the Great Lakes, with rapidly changing wind fields and intense wind gradients (Alves *et al.* 2011). The Q-Q plots in Figure 74 (right panels) show how the static wind scenarios can fit the mean climate on average (black line in Figure 74), but with significant biases due to the use of discrete wind classes. As demonstrated by Cavaleri (1994), a 10% error in the surface wind speed estimate can lead to a 10–20% error in H_s , which is not negligible. For an observed wind speed of 5.7 ms^{-1} , the Lake Ontario wave model is forced with a wind speed of 6.94 ms^{-1} , which represents a 17% error in the intensity of the atmospheric forcing, which can have important consequences on the predicted wave height. Although it would have been possible to increase the number of wind classes, this would have significantly increased the total number of wave scenarios, with each of the additional wind speed classes adding 3200 scenarios per wave model.

Given the final use of the wave statistics, which focuses on the relative difference in wave activity in the wetlands during the growing season, the Lake Ontario WW3 model and the scenario-based approach were considered acceptable. Any future improvement of the method should focus on the calibration of the wave models for use in a quasi-steady state and optimization of the number of wind classes used.

3.7. Physical variables for wetland modelling

Ecohydraulic modelling focuses on the changing hydrological conditions that largely control the location, extent, productivity and diversity of wetlands (Mortsh, 1998). These conditions define the pattern of water-level fluctuations that shape wetlands and are indirectly influenced by important climatic factors, such as solar radiation, precipitation, evaporation and wind. In order to inform wetland modelling with a reliable description of short- and long-term water level fluctuations, the simulated data were post-processed to extract meaningful metrics that emphasize the timing, duration, and extent of observed fluctuations in the system. Although simple at first glance, this information must include the details of the complex water level dynamics that characterize the Great Lakes, including seasonal variations, set-ups, seiches, and waves. The set of physical variables selected must therefore be representative of these features and their specific importance in both terrestrial and lacustrine areas of the ecosystems, in order to reflect the environment-specific spatial and temporal variability.

In this section, the post-processing technique used to aggregate the data is presented (Section 3.7.1), along with the physical variables extracted from the physical modelling (Section 3.7.2). The wave modelling variables are discussed separately in Section 3.7.3.

3.7.1. Wavelet analysis

To provide a complete description of the fluctuations that modulate Great Lakes water levels, in terms of frequency, duration and time, a wavelet analysis was used. Such an analysis is specifically dedicated to time series showing multiple, periodic or episodic influences, each with its own time-frequency specificity. It is widely used in geophysical studies, including climate science (e.g. Tan *et al.*, 1996) and oceanographic research (e.g. Elsayed, 2010). This section provides a brief review of this processing technique. A detailed description can be found in Torrence and Compo (1998).

3.7.1.1. Wavelet transform and power spectrum

To determine the dominant modes of variability within a time series, it is convenient to decompose the signal into time-frequency space. This decomposition is more complex than the classical Fourier transform, which converts the signal from the time base to the frequency base, assuming temporal stationarity, which translates into a constant frequency content over time (i.e. harmonic components). While this frequency analysis is performed by projecting the signal onto a number

of sinusoids of infinite extent in time, the wavelet analysis is performed by projecting the signal onto a set of localized functions in time and frequency space, called wavelets. These wavelets, $\psi_{a,\tau}$, are created from a parent wavelet, $\psi(t)$, which is a wave oscillation that can take many mathematical forms. For example, the Morlet wavelet, which consists of a plane wave modulated by a Gaussian:

$$\psi(t) = \pi^{-1/4} e^{i\omega_0 t} e^{-t^2/2} \quad 3.24$$

with t , the time, and ω_0 , the nondimensional frequency, usually taken to be 6. A wavelet family thus groups a set of similar wavelets obtained by varying the scale, s (dilatation), and translating the oscillation along the localized time index, τ (translation; Figure 75):

$$\psi_{a,\tau} = \frac{1}{s^{1/2}} \psi\left(\frac{t-\tau}{s}\right) \quad 3.25$$

The continuous wavelet transform is thus defined as a convolution of a discrete sequence of data (with equal time spacing) with a scaled and translated version of the parent wavelet, usually denoted by $W_\tau(s)$. The convolution is run N times for each scale, where N is the number of points in the (discrete) time series. It provides the wavelet power that is equal to the square modulus $|W_\tau(s)|^2$, analogously to the power spectral density. The scalogram (or wavelet power spectrum) finally obtained gives the absolute value of the continuous wavelet transform of the signal, in the time-scale domain (Figure 75).

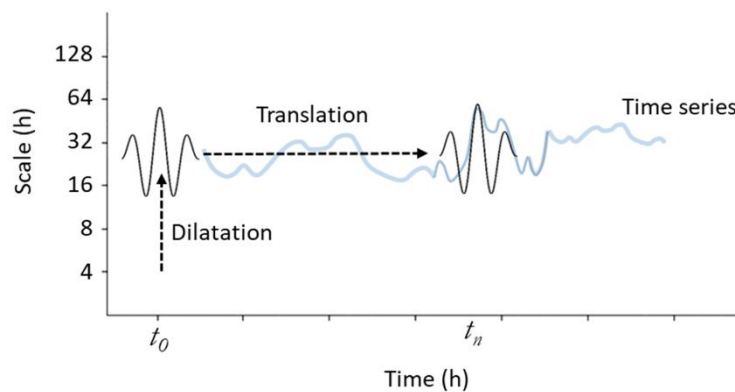


Figure 75: Schematic of wavelet analysis, with the concepts of translation, dilatation and convolution. The wavelet is represented by the black sinusoid.

3.7.1.2. Wavelet scale and scale-averaged wavelet power

The set of scales s used in the wavelet transform is preselected, and usually defined as a fractional power of two:

$$s_j = s_0 2^{j\delta_j}, j = 0, 1, \dots, J \quad 3.26$$

where $s_0 = 2\delta t$, the smallest resolvable scale, and J , the largest scale. For the Morlet wavelet, adequate scale sampling is achieved with a scale resolution, δ_j , less than 0.5. This specific mathematical function is also characterized by a wavelet scale that is nearly equal to the Fourier period, i.e., $T = 1.03s$. For a time series with $N = 5160$ points, $\delta_t = 1$ h, $\delta_j = 0.05$, and $J = 140$, the spectral space of the wavelet function is composed of 227 scales ranging from 2 h to 256 h, which is sufficient to resolve the physical processes that change Great Lakes water level in a quarter-month (~7–8 days), the typical time scale used by wetland models (briefly explained in Section 3.7.2.1).

When the wavelet plot is averaged over a specific range of scales, using the weighted sum of the power calculated along a vertical slice of the scalogram, between scales s_1 and s_2 , the result gives the fluctuation of the power with time. The scale-averaged wavelet power (hereafter referred to as SAWP) is defined as follows:

$$\bar{W}_n^2 = \frac{\delta_j \delta t}{C_\delta} \sum_{j=j_1}^{j_2} \frac{|W_n(s_j)|^2}{s_j} \quad 3.27$$

with $C_\delta = 0.776$, the reconstruction factor, kept constant for each wavelet function. The SAWP provides the time series of the average variance in a band of scales, similar to the variance density spectrum used in wave analysis (cf. Section 3.6.3). It can therefore be viewed as a measure of the average energy carried by the fluctuations, which is why it is sometimes referred to as the scale-averaged wavelet energy (e.g., Ma *et al.*, 2009).

3.7.2. Water-level fluctuations

The idea behind using a pre-selected set of physical variables is to aggregate the information provided by physical modelling to inform ecosystem models on a time scale relevant to them. Plant community structure varies seasonally and annually in response to mean lake levels, while short-term disturbances affect organisms and processes with daily or small turnover times

(Keough *et al.*, 1999). While a single event is unlikely to generate a response, successive episodes of rise and fall can induce significant changes in population trends, as seen in Lake Erie, which is subject to major fluctuations in a single day (e.g., Herdendorf 1992). Physical variables extracted from simulated water level time series must therefore capture all aspects of dynamics, including short- and long-term changes, duration, frequency, and amplitude, in a time step close to a year, the relevant time step for wetland models. To maintain better temporal resolution and allow for flexibility in modelling (e.g., estimating the influence of spring and fall conditions on wetland extent and composition), details of physical processes were extracted on a quarter-month basis.

3.7.2.1. Quarter-months

The quarter-month is conventionally used in Great Lakes studies (e.g., Razavi *et al.*, 2014; Steinschneider, 2021) to highlight changes induced by regulation plans that control Lake Ontario outflows at Moses Saunders Dam, particularly under extreme water supply conditions. The regulation time step is four times per month, with a new flow calculated after every quarter month: this is the native temporal resolution of the Lake Ontario management model. The year is therefore divided into 48 time windows, each of which is seven to eight days long depending on the month. This time step was chosen to create the physical variables, providing a time scale over which the different values were averaged or estimated.

3.7.2.2. Vegetation growing seasons

Since wetland models only consider observed and modelled physical conditions during the growing season, when plants can develop with rainfall, daylight and air temperature (e.g.), the calculations were restricted to this time of year. Therefore, only the quarter-months within this predefined period are kept, which changes by lake as the geographical area considered by the models encompasses a wide range of latitudes. The start and end of the growing seasons (in quarter-month) were chosen based on the historical conditions encountered in the Great Lakes Basin in terms of monthly mean air temperature only (MacKey *et al.*, 1996), between 1980–2018 (Table 20). Growing season length may change in the future, but they are held constant for all modelling periods, including the last decades of the century (i.e. projected future period) for the GLPI project. Simulations from the SeedGrow model from Natural Resource Canada were consulted to determine future growing season length (Mackey *et al.*, 1996). After study, it was noted that not the same climate models were run by SeedGrow and that the air temperature time series produced were not debiased.

Table 20: Growing seasons in quarter-months. * For Lake Erie, hydrodynamic modelling was initiated prior to the definition of the growing season and limited to the beginning of April to the end of October. This period was retained.

	Growing Season	
	(quarter-month)	
	Start	End
Upper St. Lawrence River	14	44
Lake Ontario	14	44
Lake Erie*	15	43
Huron-Erie Corridor	13	44
Lake Huron	15	43

3.7.2.3. Wet/dry cycles-and long-term fluctuations

Since a temporal and spatial description of the hydrodynamics of the sites is required, the set of grid points for a given CWRM was analyzed separately. The simulated years were also considered one at a time as the simulations only cover a portion of the year, the growing season which generally extends from late spring to early fall (Table 20).

All gridded hydrodynamic data were first projected onto the final CWRM grids, defined during DEM creation, using a linear interpolation technique. The water level time series extracted at each grid point were subsequently converted to water depth by subtracting the site elevation, z (cf. Section 5), from the simulated level, h : $d = h - z$. To describe the rise and fall of the water level at a point, the resulting series were analyzed to identify the localized time index(es) where the water depth crosses through zero (Figure 76), meaning that a grid cell has changed from a dry state ($h < 0$) to a wet state ($h > 0$). This step is used to identify the existence of dry/wet cycles, as well as to detect cells that have remained flooded or dried out for a period of several days, or even the entire quarter-month (Figure 76).

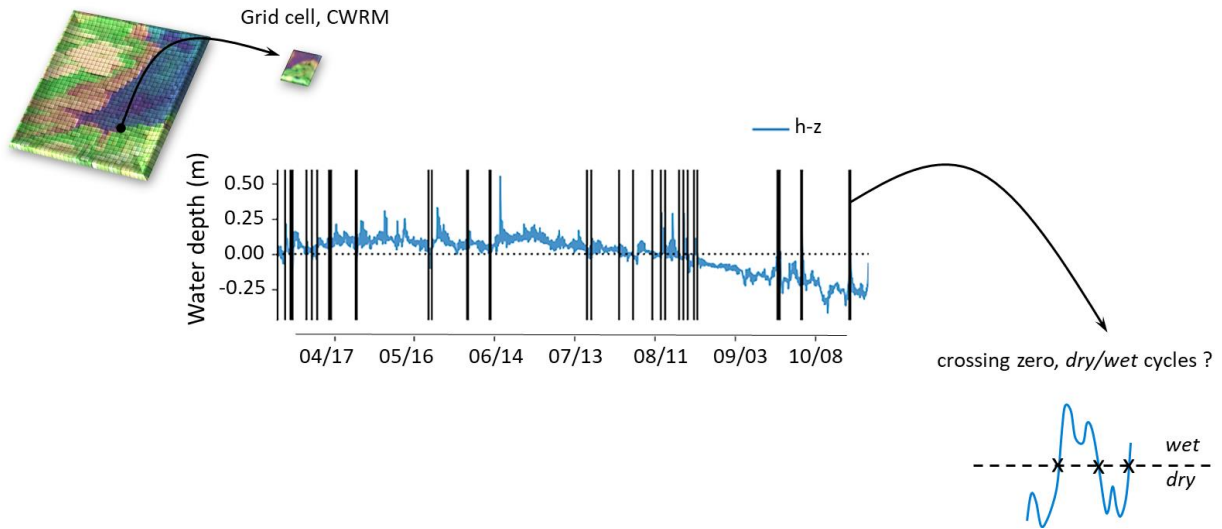


Figure 76: Example of a water-depth time series extracted from the simulated data, for a given grid cell, with the wet/dry cycle detection scheme. The vertical black lines in the middle graph indicate the time index where the water depth changes from $h > 0$ to $h < 0$, indicating a change in cell state (from wet to dry or inversely).

As the wavelet analysis was performed on scales ranging from 2 h to 256 h, with a maximum scale slightly larger than the total number of hours in a quarter-month (i.e. 192 h), the time series were filtered to remove long-term trends that could not be detected by the analysis. A Butterworth high-pass filter was applied, which retains only frequency components with periods less than 30 days. The quarter-monthly water level variations, which follow seasonal changes in lake levels, were instead extracted from the 7-day low-pass filtered series. To inform the wetland model about the range of average lake variation, the mean, d_{7m} , maximum, d_{7x} , and minimum, d_{7i} , water level observed during a quarter-month were estimated. These variables constitute the first set of values included in the list of physical variables extracted from the hydrodynamic simulations (Table 21). When the model also includes realistic flow velocities, as is the case with the Huron-Erie Corridor, the maximum flow velocity in the x and y directions were also extracted for each quarter-month, which are named u_{7x}, v_{7x} respectively.

Table 21: The physical variables selected to aggregate the hydrodynamic data.

Variables	Name	Units	Description
d_{7m}	Mean water depth	m	Mean water depth extracted from the 7-day, high-pass filtered time series, for the quarter-month.
d_{7x}	Maximum water depth	m	Maximum water depth observed in the 7-day, high-pass filtered time series, for the quarter-month.
d_{7i}	Minimum water depth	m	Minimum water depth observed in the 7-day, high-pass filtered time series, for the quarter-month.
u_{7x}, v_{7x}	Maximum flow velocity	ms ⁻¹	Maximum flow velocity in the x and y directions, respectively, for the quarter-month.
T_c	Mean cycle period	h	Average period obtained from the significant period estimated at each time step of the rise/fall events detected during the quarter-month.
T_x	Maximum cycle period	h	Maximum significant period of the detected events.
T_q	Maximum detectable cycle period	h	Maximum significant period allowed for the quarter-month, based on the maximum observed wavelet power.
W_c	Duration of dry/wet cycles	h	Duration of detected cycles during the quarter-month.
saP	Scale-averaged wavelet power	m ²	Mean of the scale-averaged wavelet power calculated at time points t of the detected events.
$saPx$	Maximum scale-averaged wavelet power	m ²	Maximum scale-averaged wavelet power reached during the quarter-month.
P_{cF}	Percent time flooded	%	Percentage of time during the quarter-month that the grid cell is strictly flooded with no cycles detected.
P_{cD}	Percent time dried out	%	Percentage of time during the quarter-month that the grid cell is in strictly dry condition with no cycles detected.

3.7.2.4. Short-Term Fluctuations

The high-pass filtered series were post-processed with the wavelet analysis technique described in Section 3.7.1. Because the primary objective of this analysis is to detect and characterize the timing, duration, and frequency of wet/dry cycles that characterize the physical environment of wetland plant communities, only grid cells with detectable cycles were processed.

3.7.2.4.1. Wavelet power spectrum and significant cycle period

The wavelet power spectrum was generated for the extracted time series at each grid point, keeping only the signal within the 95% confidence level (Figure 77b). This level is defined based on a background spectrum, which determines the minimum acceptable power to assume a feature observed in the scalogram to be true with a given percentage confidence. Fourier red noise, or

Brownian noise, was chosen as the reference signal, which allows differentiation between real frequency content and randomly generated artifacts.

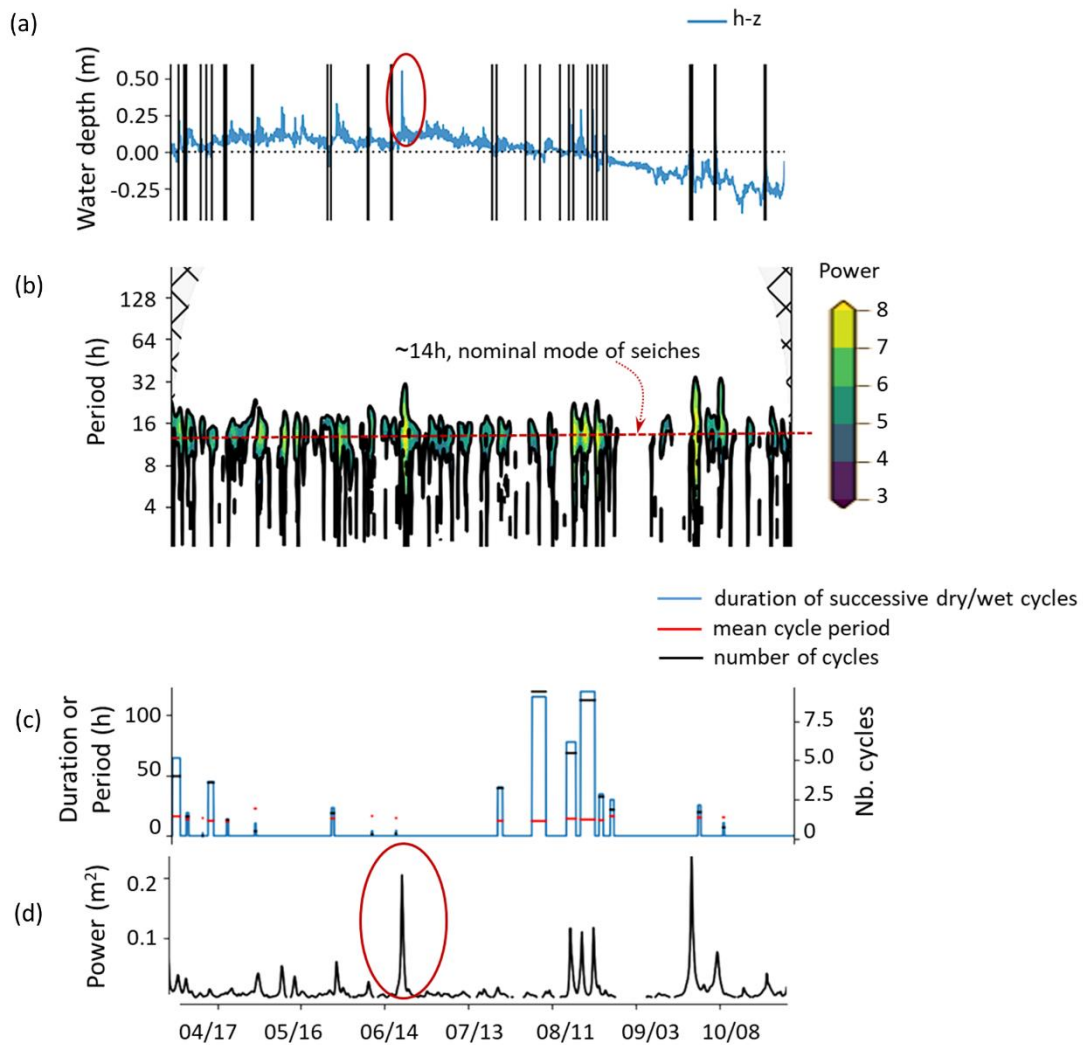


Figure 77: Post-processing technique used to analyze hydrodynamic data: (a) time series of water depth at a point, with detection of dry/wet cycles (black vertical lines); (b) scalogram; (c) physical variables extracted from the event analysis, i.e. total cycle duration (blue), average cycle period (red), and number of cycles included in an event (separate bars in the graph); (d) scale-averaged wavelet power.

For each quarter-month, a detailed inspection of the spectral content in relation to the cycles was performed (Figure 77). First, based on the wavelet plot, the period range of the detectable features was determined using the signal enclosed within the 95% confidence level. All cycles included in the quarter-month that had a period less than the minimum detected period were merged to form a temporal sequence of consecutive dry/wet cycles, the so-called event. Conversely, any cycles associated with a period greater than the maximum period detected in the scalogram were discarded: they reflect a change in the state of the cell, which goes from flooded to dry (or vice

versa) without showing any cyclicity. An event can be understood as the fluctuations experienced by a grid cell located at the altitude of the mean lake level. This cell is subject to seiche-induced changes and, under constant level conditions, will see several water level rises and falls in a single day. Such a grid point should therefore be identified as periodically inundated, associated with a cycle period similar to the typical seiche period, as well as a number of cycles per quarter-month that is representative of this periodicity.

For identified events, the so-called significant period is determined at each time step t that covers the duration of the event. The significant period is the period for which the maximum wavelet power is observed at each localized time index in the series (within the 95% confidence level; Figure 77b).

3.7.2.4.2 Selected physical variables

Since quarter-month is the temporal resolution chosen for the wetland models, all information extracted from the wavelet analysis was averaged based on this definition. Thus, for a quarter-month, the physical variables selected to characterize short-term water level variations are (Table 21):

1. Mean Cycle Period, T_c : Average period obtained from the significant period estimated at each time step of the rise/fall events detected during the quarter-month.
2. Maximum Cycle Period, T_x : Maximum significant period of the detected events.
3. Maximum Detectable Cycle Period, T_q : Maximum significant period allowed for the quarter-month, based on the maximum observed wavelet power.
4. Duration of dry/wet cycles, W_c : Duration of detected cycles during the quarter-month, which gives the estimated number of cycles when divided by T_c .
5. Scale-Averaged Wavelet Power, saP : Mean of the scale-averaged wavelet power calculated at time points t of the detected events.
6. Maximum Scale-Averaged Wavelet Power, $saPx$: Maximum of the scale-averaged wavelet power calculated at time points t of the detected events.
7. Percent Time Flooded, P_{CF} : Percentage of time during the quarter-month that the grid cell is strictly flooded with no cycles detected, which includes cycles with a significant period greater than the maximum period allowed based on spectral content.
8. Percent Time Dried Out, P_{CD} : Same as P_{CF} , but for the time spent in a strictly dry condition.

Figure 77c presents the results obtained from the analysis of the series shown in Figure 77a for W_c (blue line) and T_c (red line), as well as the estimated number of cycles (black line), defined as the ratio of these two variables. For ease of interpretation, the entire time series is presented without considering the quarter-month. Figure 77d displays the scale-averaged wavelet power

time series obtained for this particular example, which reveals high values during the set-up events. This variable is therefore representative of the major water-level changes observed at a specific location in the wetland, capturing any extreme water level fluctuations that may result in a change in physical conditions.

The spatial distribution obtained for the average period of characteristic fluctuations observed at Long Point, Lake Erie, is provided in Figure 78 for a given quarter month. This site is exposed to the lake dynamics and can be defined as an open coastal wetland. As can be seen, grid cells located on the fringe of the peninsula experience seiches, which have a nominal period of ~14 h in Lake Erie. Landward, the typical period of fluctuations increases, revealing that these land areas are mostly flooded during extreme water level rise and fall events, with a period of 2–3 days in the lowest elevations (green and yellow colours in Figure 78), and more than 4 days in the upland areas. Conversely, the majority of the lake points remain strictly flooded, while some land areas stay dry throughout the quarter-month. This is most easily seen in the lower panel of Figure 78, which shows the percentage of time a grid cell is subject to water depth fluctuations over the quarter-month, a value obtained from $100 - P_{CF} - P_{CD}$. All blue-shaded areas include strictly flooded or dried out points (i.e., no discernible cycle).

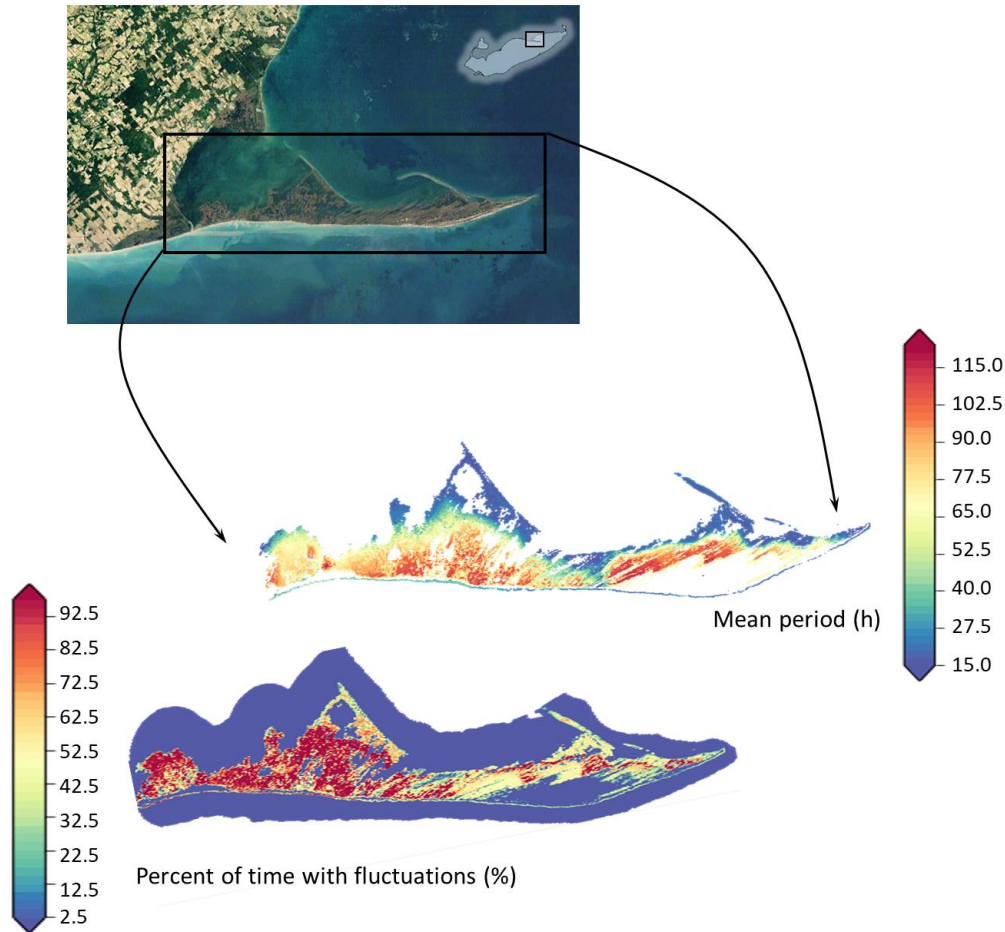


Figure 78: Example of results for Long Point Wetland, Lake Erie: the average period (top panel) and the percentage of time a grid cell is subject to water level fluctuations (dry/wet cycles; bottom panel). Results are presented for a given quarter-month.

These seven variables are primarily used to quantify short-term fluctuations and capture any wind-induced changes in Great Lakes water level dynamics, which are closely related to seiche and set-up intensity.

3.7.2.5. Scenario-based physics

The mathematical description of the physical variables and their selection were made from data extracted from the Lake Erie and Huron-Erie Corridor models, which were developed in a non-stationary modelling framework. These models provide a comprehensive representation of the physics of the lakes, with their characteristic seiche-induced modulations that generate sub-daily changes in water levels. In the scenario approach adopted for Lakes Ontario and Huron, as well as the Upper St. Lawrence River (cf. Section 3.4.2.3), none of these fluctuations are modelled: the simulated hydrodynamics provide an estimate of the direct response of the lake surface to

surface wind forcing, but not of the ensuing physics, which cannot be parameterized in static mode.

To determine if the variables listed in Table 21 are still relevant to scenario-based modelling, a quick test was performed for Lake Erie, the only lake for which static scenarios and non stationary time series were produced. These scenarios were initially developed to compare the performance of the two modelling approaches. Two gridded water level datasets were generated for the year 2014 (April–November) with the same wind input, i.e., GEM. As explained in Section 3.4.2.3, the winds were regionally averaged for use with the stationary scenarios, so that a single time series is employed to force the static model rather than a meshed dataset, as is the case in non-stationary modelling. The simulated water-depth time series at a specific location in the lake was extracted from both scenarios, specifically at a grid cell located in Rondeau Bay Wetland (Lake Erie). The results of the post-processing technique explained in Section 3.7.1 are shown in Figure 79, with the non-stationary and stationary examples displayed in the left and right panels respectively.

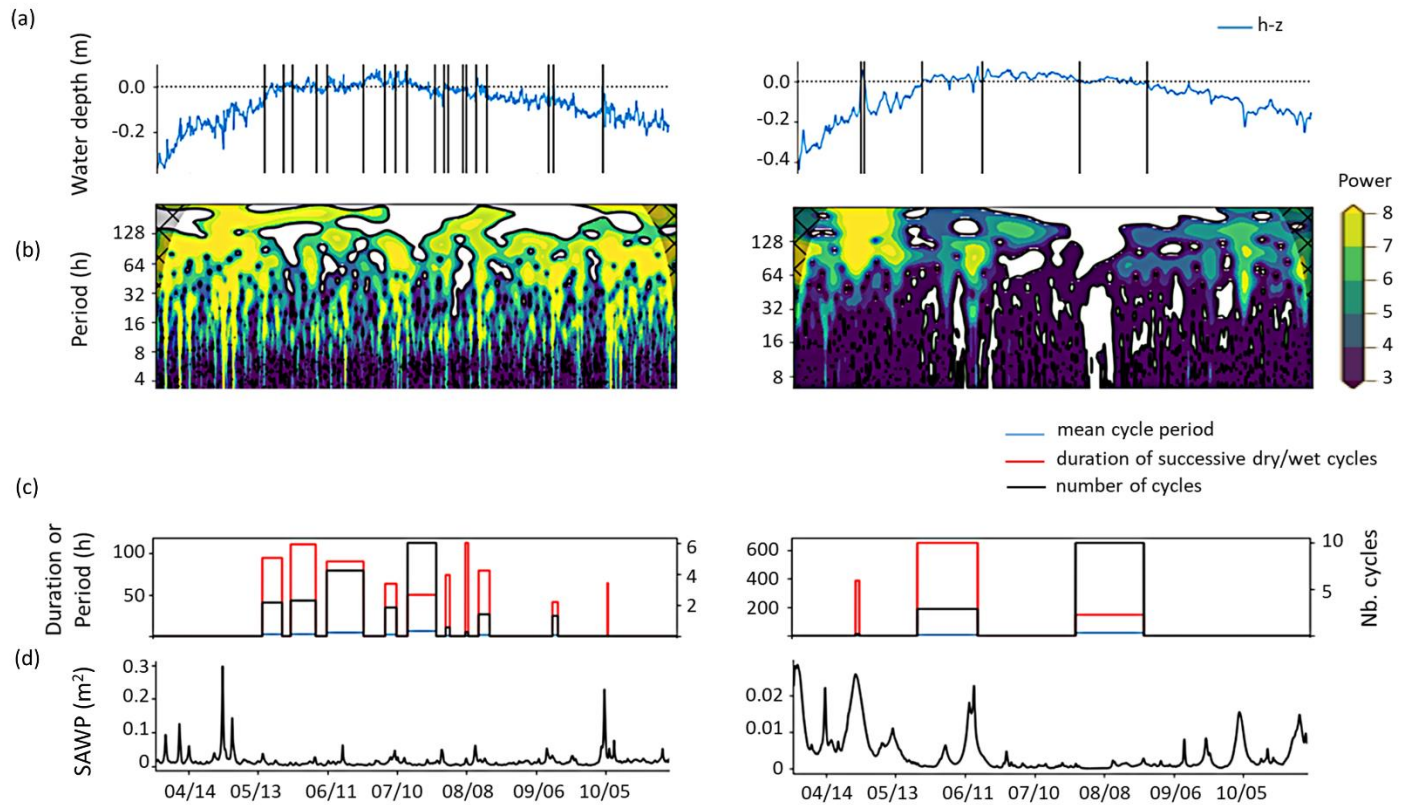


Figure 79: Same as Figure 77, but for a grid cell located in the Rondeau Bay wetland in Lake Erie. Left panels: results obtained from non-stationary scenarios. Right panels: results obtained from stationary scenarios (i.e., the scenario-based approach).

Regardless of the difference in absolute water depth, Figure 79 shows that the wavelet analysis is still effective in describing the spectral content of the time series and detecting periods characterized by multiple dry/wet cycles. The scalogram obtained from the stationary scenarios clearly shows the absence of seiche activity in the simulated data, as no significant features are observed below a 16 h period. The number of detected events is also less, with only three windows delineated instead of ten (Figure 79c), but representative of what can be observed in the top panel: the selected grid cell remains strictly flooded or dried out for several days. The detected dry/wet events extend over a longer time, with a total duration of 200–600 h, a result consistent with the modelled dynamics, which does not allow for as much variability due to the absence of long surface motions. These movements account for 4–16 cm of the observed daily variability (cf. Table 5, Section 3.2.2), which is sufficient to generate successive dry/wet cycles over grid cells located near the mean lake level elevation, as is the case here. As a direct consequence, the absence of the sub-daily motions significantly alters the energy (or variance) contained in the signal, with a maximum value of 0.02 m² instead of 0.3 m² for the non-stationary

case (Figure 79d). Although several peaks can be distinguished at the same time index, the relative importance of changes in water depth observed in early May and October, e.g., is lost in the scenario-based approach. The seiches that followed the setups have a non-negligible influence on the final estimate of the scale-averaged wavelet power, which averages the wavelet power by a factor of $1/s$. The smaller the scale s (or period), the higher the contribution of wavelet power to the final estimate.

Overall, the dissimilarity observed in the results is due to the spectral content, which is not as complete in the scenario-based approach, which does not simulate seiches. Nevertheless, the wavelet analysis provides meaningful information, as the defined physical variables are representative of the modelled dynamics and consistent with the need for wetland modelling. Therefore, the same variables were used for both modelling approaches (Table 21).

3.7.3. Waves

As explained in Section 3.2.4.3, wave activity and its relative importance in the spatial extent of the wetlands are estimated using the near-bottom orbital wave velocity, u_{bot} . This variable represents the maximum root mean square value attained by the modelled velocity in a time step. In previous modelling efforts, mean values calculated over the growing season or sub-seasonal periods (i.e., spring/fall) have been used to quantify the impact of waves in ecosystem models. However, careful inspection of the data generated for the Great Lakes revealed that the distribution of this variable is predominantly bimodal, and has a Weibull shape that is the common candidate distribution employed in long-term wave statistics (cf. Section 3.2.4.4; Figure 30). The use of an arithmetic mean can therefore hide useful information, particularly with respect to extreme events and cyclic storms, which cause deterioration and erosion of coastal wetlands, resulting in habitat loss.

3.7.3.1. Weibull mixture model

To highlight this asymmetry in wave dynamics, which is related to the site specificity and episodic nature of the storms observed in the Great Lakes, the physical variables used to characterize the wave climate were revised. Instead of time-averaged values, wave action in the wetlands was estimated from a two-component Weibull mixture model, with the density function defined as follows (Razali *et al.*, 2013):

$$g(x) = \sum_{j=1}^k w_j f_j(x) \quad 3.28$$

$$f_j(x) = \frac{\beta_j(x)^{\beta_j-1}}{\alpha_j^{\beta_j}} \exp \left[- \left(\frac{x}{\alpha_j} \right)^{\beta_j} \right] \quad 3.29$$

with k , the number of components in the system, w_j , the proportion of the j th component in the mixture, and $f_j(x)$, the density function of the sub-population j of the Weibull distribution. Here $w_j \geq 0$, $j = 1, 2, \dots, k$, and $\sum_{j=1}^k w_j = 1$. The adopted model uses $k = 2$, allowing the characterization of the nominal wave activity and extreme events, the latter being associated with intense wave climate and high values of u_{bot} .

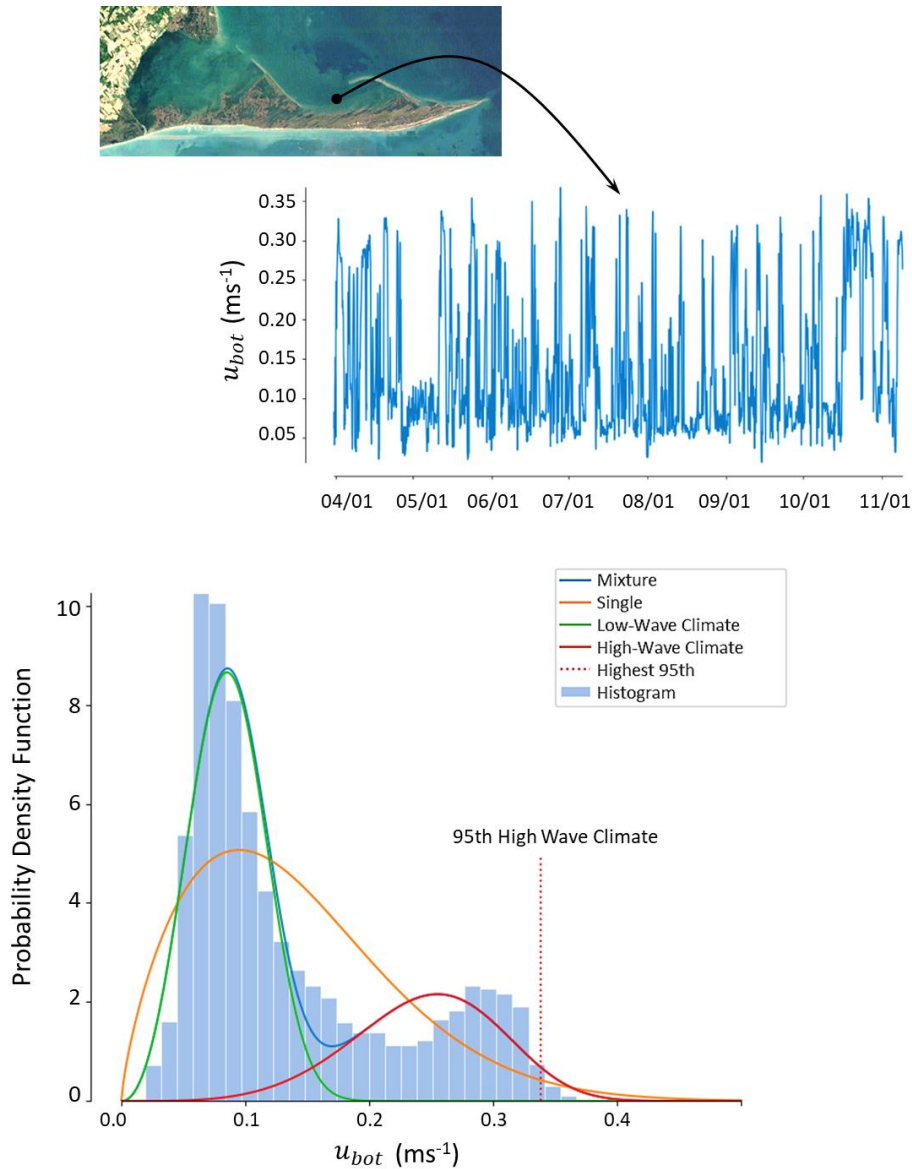


Figure 80: Upper panel: extracted near-bottom wave orbital velocity for a randomly selected grid cell in the Long Point Wetland, Lake Erie, for the year 2013. Lower panel: near-bottom wave orbital velocity histogram and associated distributions, i.e., Weibull mixture model (blue), simple Weibull distribution (orange), simple Weibull distribution fitted for low-wave climate (green), and simple Weibull distribution fitted for high-wave climate (red).

An example of the anticipated mixture Weibull model is shown in Figure 80 for a randomly selected grid cell in Long Point Wetland, for the time series extracted from the simulation carried between April and November 2013. As shown in the figure, the data distribution is formed by two wave climates, defined here as representative of the low and high conditions observed during the growing season (green and red lines in Figure 80, respectively). The two climates can be defined by a distinct Weibull distribution, with their own shape, α , and scale, β (cf. Section 3.2.4.4), and thus a different expected value (i.e., the mean of the Weibull distribution).

3.7.3.2. Selected physical variables: Wave exposure

Because plants can be affected by nominal wave activity as well as storms, two main features were extracted from the annual statistics: the mean and the 95th percentile. While the former is used to determine the ongoing wave-associated stress that shapes plant communities (Croft and Chow-Fraser, 2007) and the range of elevations occupied by wetland species (Keddy *et al.*, 1983), the latter is used to identify highly exposed areas devoid of vegetation. These shorelines typically have consolidated substrate (e.g., rocky, bedrock), sandy soil, or low organic matter content, as sustained wave action promotes erosion and offshore sediment transport (e.g., Hawley and Niester, 1993; Thomas *et al.*, 2006). Exposure, estimated by the tail of the high wave climate, can therefore be used to identify unfavourable habitats for submerged aquatic species and floating plants, which are generally intolerant of wind and waves. It can be considered a surrogate indicator for soil type, which generally gives indications of the likelihood of presence or absence of specific species. Plant models do not otherwise use any substrate-related data.

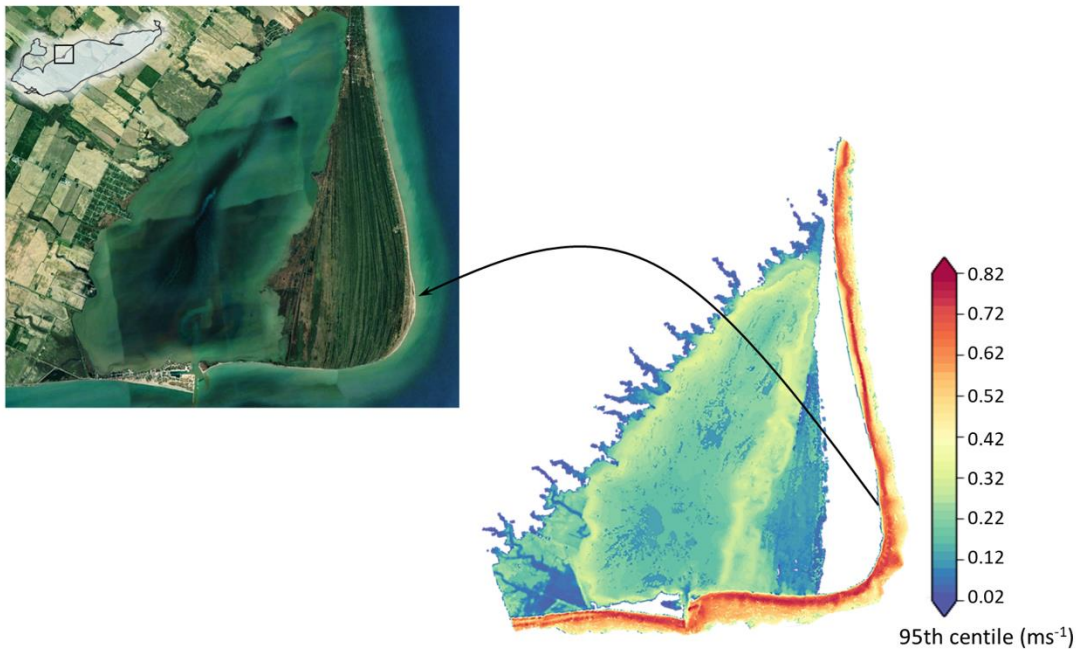


Figure 81: Example of results from the highest 95th percentile in the Rondeau Bay wetland (Lake Erie). The area exposed to wave activity at the tip of the peninsula is characterized by high 95th percentile values (i.e., strong waves climate). This area is occupied by long sandy beaches, which is expected when physical conditions are highly unfavorable for submerged aquatic vegetation.

Figure 81 shows the predicted results from the 95th percentile. The data presented were extracted from 1-year simulated wave time series for the Rondeau Bay wetland, located on the north shore of Lake Erie. As shown by the spatial distribution of this variable, the fringe of the site exposed to

incoming wave energy is characterized by high wave orbital velocity, in contrast to the interior of the bay, where quiescent conditions are detected. The sandy beaches observed on the lakefront along the eastern and southern margins of the bay are therefore correlated with high u_{bot} values as anticipated.

Table 22: The physical variables selected to aggregate the wave data.

Variables	Name	Unit	Description
μ_{low}	Mean low-wave orbital velocity	ms^{-1}	Mean of the near-bottom wave orbital velocity-adjusted Weibull distribution for the low-wave climate observed during the growing season.
μ_{high}	Mean high-wave orbital velocity	ms^{-1}	Mean of the near-bottom wave orbital velocity-adjusted Weibull distribution for the high-wave climate observed during the growing season.
p_{95}	Highest 95th	ms^{-1}	95th percentile of the adjusted Weibull distribution for the high-wave climate.
p	Proportion	1	Proportion of data included in the leftmost distribution.

Table 22 summarizes the variables selected to inform the wetland models of wave activity: near-bottom orbital wave velocity extracted from the low- and high-wave climate, μ_{low} and μ_{high} , the highest 95th percentile, p_{95} , and the proportion of data included in the leftmost distribution, p . For wave statistics, all variables were estimated over the entire growing season, rather than on a quarter month basis. Each grid cell was handled independently, as described in the previous section (cf. Section 3.7.2).

3.8. Projected changes

3.8.1. Lake dynamics: Long and short-term fluctuations, waves climate

The projected changes in lake dynamics are presented in Table 23, with detailed description of changes for long- and short-term water level fluctuations, as well as for wave climate. The significance of projected changes was determined following the method described in Section 3.3, with statistical tests for mean and variance. Changes are also expressed in absolute and relative values, the latter being defined as the absolute change divided by the present climate from the model simulation.

3.8.1.1. Long-term water level fluctuations: Mean lake levels

A complete analysis of the projected changes in mean lake levels can be found in Seglenieks and Temgoua (2022). The following paragraph provides only general conclusions drawn for the various parts of the Great Lakes systems, with the exception of Lake Superior. The analysis is limited to the selected AOGCMs, which provides the lower and upper bound limits of expected values for a restricted set of climatic conditions (cf. Section 2.2.3, Figure 7). The results are presented in Table 23, with changes defined as the difference between the distributions of future (2070–2099) and the recent past (1980–2009) annual values, considering all quarter-months included in the 30-year periods. Differences are given for the growing season only, as described in Table 20 (cf. Section 3.7.2.2). Interannual variability was assessed via the standard deviation of the distributions (hereafter referred to as STD).

3.8.1.1.1. Change in mean

By the horizon 2085, no clear projection in mean lake level is obtained for the Great Lakes Basin, with the exception of Lake Ontario and the upstream section of the Upper St. Lawrence River (i.e. Alexandria Bay), where levels are likely to increase by up to ~0.7 m (Table 23). While the lower bound scenario tends to predict a smaller relative change, with a decline between -0.12 and -0.23 m for Lakes Erie, Huron, and the Huron-Erie Corridor, the AOGCMs do not agree on the sign of changes, revealing large model uncertainty. The overall variation in long-term fluctuations, however, is large compared to the observed natural variability for the period 1980–2009, which remains between 0.26 and 0.39 m (STD in Table 23). According to the climate change envelope, the absolute change in mean level is 0.5 to more than 2.5 times the year-to-year variation, which can have a significant impact on the composition and positioning of wetland vegetation (e.g. Wilcox and Nichols, 2008). The response of plants to such a long-term change in water levels can

force an up- or down-slope migration that goes beyond the historical cycle. Anthropogenic stressors, such as urbanization (i.e. land use), could then trigger an abrupt shift in wetland quality, especially under the upper bound scenario. A decrease in total habitat area can be expected by the end of the century in sites where any landward re-establishment is restricted (e.g. Gottgens *et al.*, 1998).

3.8.1.1.2 Change in Interannual Variability

Interannual variability, expressed here as standard deviation, is expected to increase by more than 25% in the upcoming decades for the Lower Great Lakes, including the Lower Detroit River near Amherstburg (Table 23, dark orange color). Variability in Lake Ontario and the Upper St. Lawrence (i.e. Alexandra Bay) is particularly marked, with an absolute change in standard deviation of up to 0.23–0.24 m, which represents a relative increase of 88–94%. No significant change in IV was projected for Lakes St. Clair and Huron.

Large fluctuations in water levels can dramatically alter plant communities from year to year when periods of extremely high or extremely low lake levels occur. Anthropogenic disturbances, such as land use alterations, can also have a greater impact on wetland conditions during similar extreme events (Uzarski *et al.*, 2017). In terms of wetland composition, there is empirical evidence that invasive species, like *Typha X glauca* and *Phragmites*, are favored by interannual water-level fluctuations, taking advantage of water levels declines to establish in newly exposed substrate (Frieswyk and Zedler, 2007; Lishawa *et al.*, 2010; Tulbure and Johnston, 2010; Wilcox, 2012). The projected increase in IV may therefore threaten the ecological integrity of Great Lakes wetlands (DeRoy and Maclsaac, 2020).

Table 23: Projected changes in lakes dynamics for the period 2070-2099. Results are presented for change in means and interannual variability, described here by the standard deviation. Changes are provided with missing values (or dash, -) when statistical tests did not meet the 10% significance level (i.e. U-test for the mean and Levene' test for the variance). Shaded colors indicate relative changes that reach at least 5 or 25% and reveal a clear signal of change, i.e. when the two scenarios agree on the sign of the projected changes (positive, in orange, or negative, in green). Grey boxes indicate no data.

	LONG-TERM FLUCTUATIONS			SHORT-TERM FLUCTUATIONS						WAVES							
	Mean Lake Levels (m)			Stations	Maximum Set-up (cm)			Surface Seiches (cm)			Buoys	Significant Wave Height (m)			Wave Period (s)		
	Reference	Projected Changes			Reference	Projected Changes		Reference	Projected Changes			Reference	Projected Changes		Reference	Projected Changes	
	Mean (STD)	Mean	STD	Mean (STD)	Mean	STD	Mean (STD)	Mean	STD	Mean (STD)	Mean	STD	Mean (STD)	Mean	STD		
<u>Upper St. Lawrence</u> (Alexandria Bay)	74.74 (0.26)	0.04 ; 0.73	(0.09 ; 0.23)		6.4 (4.2)	-0.4 ; -		2.5 (0.6)									
<u>Lake Ontario</u>	74.88 (0.26)	- ; 0.71	(- ; 0.24)	Toronto	4.3 (2.1)	-0.4 ; -		3.1 (0.9)		45139	0.27 (0.06)	-0.02 ; -	(- ; 0.03)	4.3 (4.0)	-0.01 ; -	(-0.01 ; -)	
				Cobourg	3.0 (1.3)	-0.2 ; 0.5	(- ; 0.4)	2.9 (0.4)		45012	0.65 (0.19)	-0.03 ; 0.01	(-0.01 ; 0.02)	3.9 (1.0)	-0.01 ; 0.01	(-0.01 ; 0.01)	
				Kingston	4.9 (2.7)	-0.3 ; -		3.1 (0.6)		45135	0.47 (0.27)	-0.03 ; 0.01	(-0.01 ; 0.02)	4.1 (1.9)	-0.01 ; -	(- ; 0.01)	
				Rochester	3.0 (1.1)	-0.1 ; -	(- ; 0.4)	2.7 (0.4)									
<u>Lake Erie</u>	174.41 (0.27)	-0.14 ; 0.45	(- ; 0.07)	Toledo	26.6 (15.7)	-3.9 ; -	(- ; 10.5)	12.9 (2.2)	-1.8 ; -	45005	0.60 (0.13)	-0.03 ; 0.01	(-0.02 ; 0.02)	3.8 (0.9)	-0.06 ; 0.02	(-0.02 ; 0.02)	
				Erieau	5.1 (3.2)	-0.1 ; -	(- ; 2.3)	4.2 (0.7)	-0.3 ; -0.2	45132	0.44 (0.13)	-0.04 ; 0.01	(-0.02 ; 0.02)	3.5 (1.0)	-0.06 ; 0.02	(-0.03 ; 0.03)	
				Buffalo	27.0 (19.8)	-2.0 ; -	(- ; 8.7)	11.1 (2.6)	-1.1 ; -0.5	45142	0.45 (0.17)	-0.03 ; 0.01	(-0.02 ; 0.02)	3.9 (1.5)	-0.04 ; 0.02	(-0.03 ; 0.01)	
				Cleveland	8.0 (4.7)	-0.6 ; -		5.2 (1.0)	-0.3 ; -0.2								
<u>Detroit River</u> (Amherstburg)	176.55 (0.26)	-0.12 ; 0.44	(0.01 ; 0.05)		12.1 (6.8)	-0.9 ; -	(- ; 2.1)	5.6 (0.9)	-0.2 ; 0.7	(- ; 0.3)							
<u>Lake St. Clair</u>	175.89 (0.30)	-0.17 ; 0.52		St. Clair Shores	5.3 (3.4)	- ; 1.2	(1.3 ; 2.9)	1.8 (0.5)									
<u>Lake Huron</u>	176.55 (0.39)	-0.23 ; 0.63		Essexville	18.7 (11.0)	-0.2 ; -0.1		6.7 (0.8)									
				Mackinaw City	5.7 (2.6)			4.6 (0.5)									
				Tobermory	8.3 (4.1)			2.0 (0.3)									
				Fort Gratiot	13.0 (6.4)			6.3 (0.9)									
				Thessalson	6.9 (3.1)			3.9 (0.6)									
				Parry Sound	13.4 (7.6)	-0.6 ; -		3.9 (0.8)									
				Collingwood	12.9 (7.1)			4.5 (0.7)									

<u>Negative Changes</u>		<u>Positive Changes</u>	
> 5%	> 25%	> 5%	> 25%

Table 24: Idem as Table 23, but for some of the physical variables developed for wetland modelling: strictly flooded area, defined as the % of the site kept flooded during the growing season; cycle period, which is the mean period of dry/wet cycles detected in the transition zone (ignoring zero values); maximum scale-averaged wavelet power, defined as the mean annual maximum values observed in the quarter-months; the cycle duration, defined as the total time (in days) that a grid cells is subject to fluctuating water levels during the growing season; near bottom wave orbital velocity; and partially flooded area, defined as the % of sites included in the transition zone, where dry/wet cycle are observed. Details are given in the text.

Strictly Flooded Area (%)				Mean Cycle Period (h)			Scale-Averaged Wavelet Power (x10 ² m ²)			Total Cycle Duration (d)			Near-Bottom Wave Orbital Velocity (ms ⁻¹)			Partially Flooded Area (%)			
Reference	Projected Changes		Reference	Projected Changes		Reference	Projected Changes		Reference	Projected Changes		Reference	Projected Changes		Reference	Projected Changes			
Mean (STD)	Mean	STD	Mean (STD)	Mean	STD	Mean (STD)	Mean	STD	Mean (STD)	Mean	STD	Mean (STD)	Mean	STD	Mean (STD)	Mean	STD		
<i>Lake Ontario and Upper St. Lawrence</i>																			
1HIE	55 (2)	0.4; 9.9	(-; 1.9)	96.9 (3.7)		(-; 1.5)	3.2 (0.5)					7.4 (3.2)	-3.2; -2.6	(-2.1; -)				11.1 (2.1)	-5.1; -
2ACM	39 (1)	-; 3.8	(-; 2.7)	94.0 (5.6)			2.2 (0.4)	-; 0.1	(-; 0.3)			15.2 (5.2)	-3.6		0.39 (0.13)		(-0.04; -)	6.0 (2.5)	1.4; 6.1
3SBM	55 (1)	-; 3.6	(-; 2.3)	100.9 (3.0)		(-; 2.0)	2.8 (0.3)	-0.5; -				12.0 (3.2)	-3.6; -2.3		0.25 (0.08)	-0.10; 0.01	(-0.03; -)	5.5 (2.4)	1.5; 4.6
5LCM	21 (2)	-0.7; 8.4	(-; 3.2)	99.5 (6.0)	-; 0.9		2.9 (0.7)	-0.5; -				11.3 (3.3)	-2.5; -		0.93 (0.23)	-0.10; 0.06	(-0.11; -)	13.2 (4.5)	2.4; 2.6
6JSM	66 (3)	-; 4.0	(0.4; 3.1)	101.2 (5.3)	-3.7; -		2.0 (0.4)	-0.1; -				14.5 (6.6)			0.39 (0.14)	-0.14; 0.03	(-0.05; -)	10.3 (6.3)	3.3; 5.5 (-1.1; -0.3)
<i>Lake Erie</i>																			
7GRM	24 (2)	-0.7; 4.8	(-; 4.2)	27.3 (3.6)		(-; 1.3)	9.8 (2.8)					13.5 (7.3)	-4.9; -4.8		0.30 (0.13)	-; 0.15		33.1 (6.9)	-; 4.0 (-; 4.4)
8SPP	54 (3)	-1.3; 2.1	(-; 0.6)	32.6 (3.9)	-1.6; -	(-; 1.5)	11.1 (2.9)					16.4 (5.0)	-2.8; -		0.53 (0.30)			6.6 (2.6)	-0.6; 1.1 (-; 0.5)
9LPW	65 (9)	-4.4; 8.1	(-4.3; -)	39.9 (5.5)			13.0 (4.1)					20.0 (6.8)			0.51 (0.38)	0.47; 0.57		19.8 (7.5)	-5.9; 4.0 (-3.6; -)
10RBY	51 (5)	-3.0; 8.3	(-1.2; -)	61.4 (9.9)	-3.0; -		6.6 (1.7)					17.4 (3.7)	-2.1; -	(-1.7; -)	0.50 (0.18)	0.31; 0.53		12.7 (2.6)	-2.3; 1.5
11FCK	25 (2)	-; 0.7		27.2 (2.9)	-0.7; -		8.4 (1.9)	-; 0.8				10.9 (4.4)		(-1.4; -)	0.32 (0.16)			3.7 (1.4)	0.5; 1.8 (-; 0.8)
<i>Huron-Erie Corridor</i>																			
12DRM	56 (6)	-2.3; 11.3		57.1 (6.8)	-3.8; -		6.5 (1.4)	0.5; 0.8				23.8 (7.0)	-3.2; -	(-1.7; -)				16.4 (3.2)	-5.6; - (-; 1.5)
13LSC	93 (6)	-1.6; 1.4	(-0.8; -)	69.6 (6.5)	-2.3; -		9.2 (4.5)	-; 1.3	(-; 0.7)			17.5 (6.0)	-2.1; -					5.6 (5.7)	-0.8; 1.3 (-0.7; -)
14SAM	86 (10)	-2.5; 2.5	(-2.0; -)	72.1 (6.2)			10.6 (8.2)	-; 0.7	(-; 0.8)			16.5 (7.2)	-2.9; 3.2	(-1.7; -)				10.3 (9.1)	-1.7; 1.3 (-1.9; -)
<i>Lake Huron</i>																			
15BDD	54 (5)	-3.5; 6.1		86.6 (5.3)			5.4 (2.0)		(-1.0; -)			15.7 (4.5)	-; 1.6					4.7 (1.7)	0.6; 0.7
16HBW	35 (4)	-2.8; 3.5	(-1.5; -)	96.2 (4.2)			4.1 (1.2)					18.5 (6.2)	-; 1.7					4.2 (1.5)	-0.8; 0.5 (-0.8; -)
18HGW	40 (2)	-1.1; 2.3		96.8 (5.9)			2.6 (0.5)					22.1 (5.4)	-; 2.5					2.6 (0.9)	0.3; 0.4
19TBY	51 (4)	-2.2; 4.8		96.9 (5.8)			2.6 (0.5)					22.5 (5.3)	-; 1.8					5.0 (1.4)	-; 0.6
22WHW	60 (14)	-7.1; 13.6	(-2.2; 3.4)	100.7 (4.0)			2.4 (0.5)					23.8 (6.2)						15.5 (6.1)	-4.9; 2.1 (-; 1.7)
23ACK	14 (3)	-2.0; 3.9	(-1.1; -)	99.3 (4.6)			2.7 (0.6)	-; < 0.1				20.3 (7.6)						3.8 (2.4)	-0.6
27FPT	55 (5)	-2.8; 8.0		97.4 (5.3)			2.6 (0.5)					23.1 (5.4)						7.0 (1.7)	-1.4; 0.5

Negative Changes Positive Changes

>5% >25% >5% >25%

3.8.1.2. Short-term water level fluctuations and waves

Because lake dynamics respond to surface stresses that force water surface motion, generating set-ups, surface seiches, and surface gravity waves, the expected changes from climate disturbances follow what was observed for winds (cf. Section 2.4). Table 23 displays results consistent with the projected wind climate, i.e. a decrease in the maximum monthly wind set-ups amplitude in most lakes by the end of the century due to decreasing wind speeds by the end of the century. The lower bound of changes in mean annual maximum winds (cf. Table 3) therefore has a significant impact on the modelled lakes dynamics, particularly in the Lower Great Lakes, including the Lower Detroit River (i.e. Amherstburg). However, the relative changes remain less than 10% for most of stations, or less than 4 cm in Lake Erie and 1 cm in Lake Ontario. These changes may not be relevant to wetland plant communities, which typically occupy large elevation ranges, e.g., from 74.4–75.0 m and 75.8–76.0 m for emergent marsh and meadow marsh in Lake Ontario (Grabas *et al.*, 2019).

Lakes St. Clair and Huron show different behavior, with up to 22% increase in the mean annual monthly maximum set-ups amplitude for the former, or 1.2 cm, and almost no significant change for the latter. Given that marsh areas in Lake St. Clair are characterized by very low topographic relief, dikes that limit wetland migration, and the dominance of submerged or emergent aquatic vegetation (Mortsch, 1998), changes in mean lake level in 2070–2099 are likely to have a more pronounced effect on the vegetation pattern than changes in sub-daily fluctuations.

3.8.1.2.1. Surface seiches

Since only Lakes Erie and St. Clair (including the Huron-Erie Corridor) were modelled under unsteady, time-evolving conditions that allow a complete physical description of barotropic surface motions, changes in daily-range values of high frequency fluctuations are obtained only for these specific lakes. As noted for the set-up events, the amplitude of surface seiches is projected to decrease, especially in Lake Erie, as expected for a gentle wind climate.

3.8.1.2.2. Interannual Variability of short-term fluctuations

Finally, the year-to-year variability in monthly maximum set-ups events is projected to increase in the Lower Great Lakes, including Lake St. Clair, similarly to what was drawn from the wind speeds analysis (cf. Table 3). This variation is quite large relative to observed values for the period 1980–2009, and reach 8–93% depending on stations, with the greatest changes expected in Lakes Erie (41–54%) and St. Clair (35–93%). More than the means, the IV of short-term fluctuations can

have marked influence on species richness (e.g. Grabas *et al.*, 2019), notably wet meadow communities whose diversity relies on temporary cycles of flooding and drying (Gathman *et al.*, 2005). Again, no significant climate signals were detected in Lake Huron.

3.8.1.2.3. Wave climate: Lakes Ontario and Erie

Past and future wave characteristic were defined based on long-term wave climate statistics calculated over the 30-year time series (i.e. according to the best-fitted Weibull distribution, cf. Section 3.2.4.4).

The projected future wave climate for Lakes Ontario and Erie is similar to that observed during the baseline period. The relative changes in significant wave height and wave period were estimated to be less than 5% (Table 23), with no agreement on bound values. The same conclusions can be formulated for the inter-year variability. The mean wave climate on the lakes reflects the shape of the basins and the fetch length, which determines the surface wave dynamics, as well as the annual frequency and magnitude of the winds. As wave generation during large storm events is mostly fetch-limited in the Great Lakes, which restricts the wave height, the potential impact of modest changes in wind climate as projected here (Table 3) remains limited (Wuebbles *et al.*, 2019).

These results provide guidance for the two AOGMs used, for deep-water waves, and for months within the growing season, which excludes late fall (November) and winter (December–January–February). The greatest changes in wave activity are expected during the cold weather season, as projected decrease in ice cover extent by the end of the 21st century (Filazzola *et al.*, 2020) will likely increase wave energies throughout the Great Lake Basin. Lake ice almost completely inhibits waves under heavy-ice conditions (Bai *et al.*, 2020), which are expected to become rare in the future, while the number of ice-free years will increase (Filazzola *et al.*, 2020). Since storm activity in the Great Lakes is generally higher in winter (e.g. Byun *et al.*, 2019), the loss of lake ice will certainly affect the mean annual wave climate.

3.8.2. Site-scale dynamics

While wetland areas and plant communities are expected to respond to changes in mean lake level, they may be affected differently depending on their topography, even for sites belonging to the same basin (e.g. Wu and Zheng, 2020). A change in mean lake level variably alters wetland area based on the complexity of the bank landform. To determine whether a specific site has

experienced changes in its physical environment, some key variables extracted from the hydrodynamic and wave simulations were analyzed (cf. Section 3.7). Table 24 summarizes the results of this analysis, with detailed description of changes in mean and interannual variability between recent past and future periods. The data give spatial averages of mean annual values calculated over the site area of interest. The wetland sites selected for this project are introduced and described in details in Section 4.

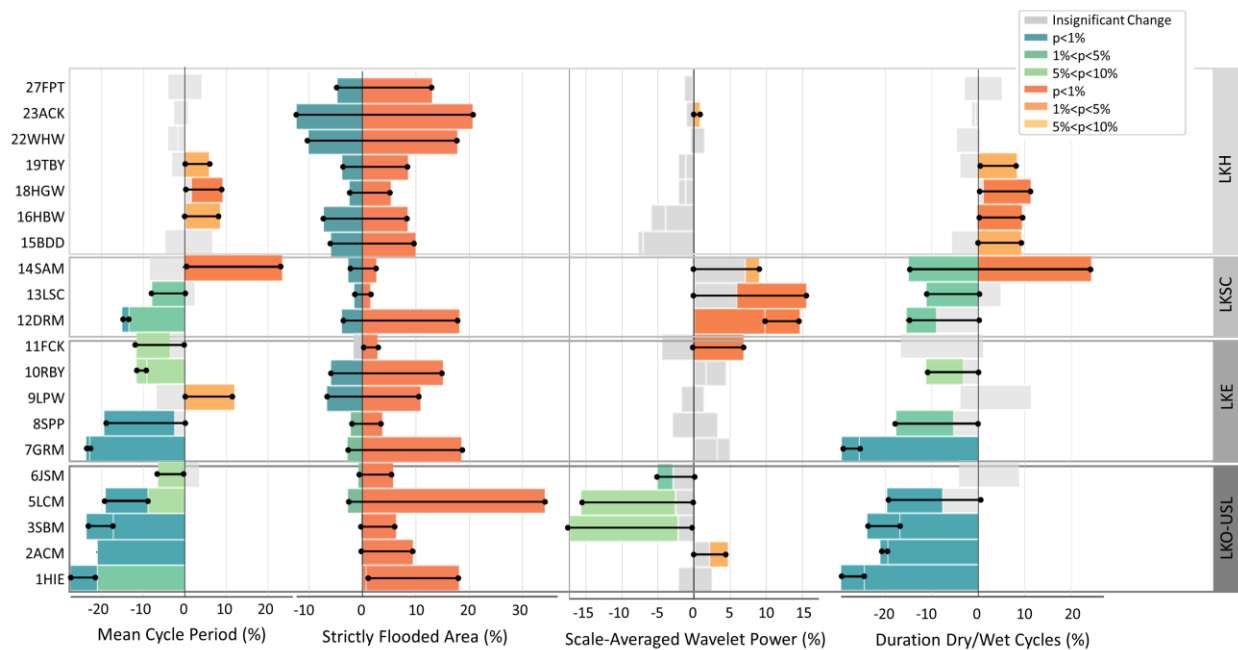


Figure 82: Range of relative changes from baseline projected by the lower and upper bound scenarios for some of the key physical variables. Shaded colors indicate the sign of changes (positive in orange, and negative in green), as well as the level of significance of each projections. The black lines make the projected range explicit, based on the significant values. This figure should be read as a clustered bar chart with overlapping bars, where the lengths represent actual values rather than proportional ones.

3.8.2.1. Changes in flooded area

Under a change in mean lake level, the percentage of habitat areas inundated throughout the growing season will likely increase or decrease if the nominal conditions are significantly altered. This may affect the dominance of submerged aquatic vegetation (Hudon *et al.*, 2005), change the overall low marsh habitat (i.e. aquatic habitat; Weller and Chow-Fraser, 2019a), and potentially the total area defined as open water if the depth of inundation in the lacustrine boundary of coastal wetlands is substantially increased. Projected changes in the extent of the strictly flooded area of each wetland are given in Table 24, as well as in Figure 82, which illustrates the range of possible futures under the lower and upper bound scenarios (relative to baseline).

All Lake Ontario sites (including 1HIE) display a clear increase in the mean annual number of grid points defined as strictly flooded during the growing season. An additional 6–34% of the deepest portion of the wetlands will likely be inundated by 2070–2099 and will not experience any wet/dry cycles on a sub-daily or seasonal basis. Only Lynde Creek Marshes (5LCM) reveal a possible decline in flooded extent, but with a relative value that remains small, i.e. less than 3%, and a lower bound projection that is less significant than its counterpart value ($p < 5\%$ rather than $p < 1\%$). According to the reference period, the percentage of permanently flooded zone at this site is also less compared to other Lake Ontario marshes, with only 21% of points remaining below the water line against 39–66% (Table 24). This is similar to the proportion found in other riverine systems, such as Grand River Mouth Wetland (7GRM; Lake Erie) and Anderson Creek Marshes (23ACK; Lake Huron), where the upper limit projection is also large relative to basin-scale predictions. The projected rise in mean lake level by the end of the 21st century may therefore have a greater impact in steeply topographic drowned river mouths primarily characterized by high marsh habitat (i.e. wet meadow or shrubby swamp) during the period 1980–2009.

With the exception of most of the riverine systems (7GRM, 8SPP, and 11FCK), for which the decrease in permanently flooded area is small (<3%) and less ($p < 5\%$) or not significant ($p > 10\%$), the projections for the remaining wetlands are not robust and fluctuate as expected by the projected lake levels (Table 23). Although the projected increase in mean lake conditions by horizon 2085 is significantly larger than any possible decrease, some sites respond equally to the two bound scenarios, with a similar relative decrease or increase: Lake St. Clair marshes (13LSC and 14SAM), as well as Hay Bay and Hog Bay Wetlands in Lake Huron (16HBW and 18HGW).

3.8.2.1.1. Interannual Variability

The extent of the annual strictly flooded area is expected to be more stable in 2070–2099 for several sites in Lakes Erie, St. Clair and Huron. A relative decrease of 32–89% is projected for the interannual variability, with a more pronounced effect observed in Lake St. Clair, where the relative year-to-year variation for Lake St. Clair Marshes and Johnston Bay ranges from 78–89%. These sites are characterized by diked areas that limit the shoreward migration of low marsh when lake levels are high and, at the same time, the extent of wetland habitat. This is well illustrated by the low variability observed during the reference period, which is only 6–12% of the average values for 13LSC and 14SAM. Since the relative changes in the annual inundated areas are projected to be quite small for these sites, i.e. between -3% and 3%, the decrease in variability suggests more stable conditions over time, with no major changes over the 30-year period. The transition zone of these sites, where sub-seasonal wet/dry cycles are observed, also shows a

similar drop in IV, with a relative decrease of 80–91%. Therefore, there is a heightened risk of perennial habitat loss in Lake St. Clair under the upper bound projection.

More generally, decreased IV can support a stable extent of low marsh habitat from year to year when the flood depth allows the establishment or persistence of submerged vegetation and floating plants. Otherwise, open-water area will increase at the expense of aquatic species. Since annual and perennial aquatic species are recognized to be resilient to change in water levels from year to year (Gathman *et al.*, 2005), due to their rapid response to water depth variation, change in interannual variability should not be a threat to low marsh habitat, except in the case of an extreme increase in mean annual lake level.

Again, Lake Ontario and riverine systems (7GRM and 8SPP) show different behavior, with a likely increase in interannual variability of the permanently inundated area by the end of the century, which follows the projected variability in lake levels (cf. Table 23). The relative increase in variability is especially important compared to reference values, representing one to 5 times the estimated IV for 1980–2009. However, since Plan 2014 was used to project past and future water level scenarios (Seglenieks and Temgoua, 2022), even though it was not implemented until early 2017, comparison to absolute reference values should be taken with caution.

3.8.2.2. Changes in transition zone

The area of wetlands subject to daily or sub-seasonal fluctuations (here after referred to as the transition zone) is an important component of the ecosystem biodiversity, the latter being critical to the establishment and persistence of wet meadows (Gathman *et al.*, 2005), the most species-rich habitat type in Great Lakes coastal wetlands (Keddy and Reznicek, 1986; Wilcox *et al.*, 2005).

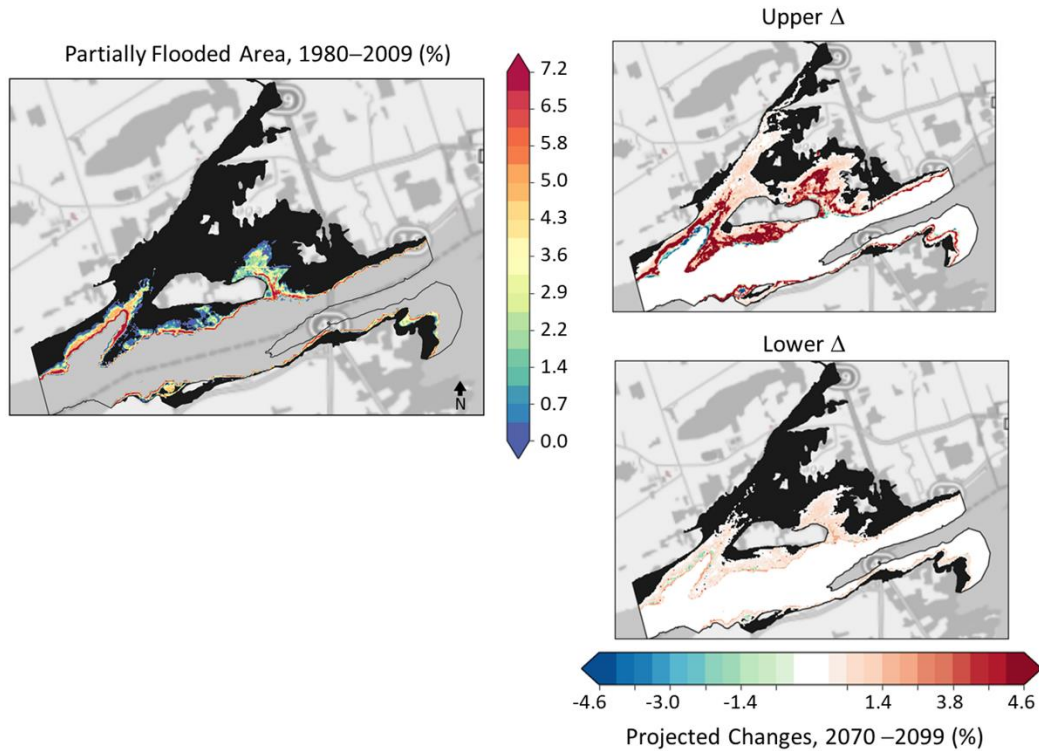


Figure 83: Left panels: Climate reference map for mean annual partially flooded area, which gives the % of time a grid cell is subjected to fluctuating water level during the growing season, for the period 1980–2009 in Airport Creek Marshes, Lake Ontario. Right panels: The upper and lower bound of the projected change for this variable by 2070–2099 relative to baseline.

The data presented in Table 24 reveal a clear positive change in the extent of the transition zone by the end of the century for the Lake Ontario sites. The mean annual percentage of grid points subject to wet/dry cycles changes by up to +6% for the 2070–2099 period, which represents an increase of 24–103% relative to baseline. Airport Creek Marshes (2ACM) show the largest shift, with a projected increase in mean annual spatial values of 3.3 to 5.5 % (in absolute value), which is comparable to the historical variability of 6.3%. Figure 83 details the spatial distribution of this variable in 2ACM, with the reference state on the left and projected changes on the right. The black areas in maps highlight zones that remain dry throughout the 30-year period and, conversely, white (or uncolored) areas indicate the strictly flooded sectors. As expected from results in Table 24, major changes are projected for the 2070–2099 period, with increasing fluctuations under the upper bound scenario in areas that are already favorable to wet meadow and emergent plants (left panel in Figure 83). While 13% of grid points show physical conditions that could potentially support high marsh habitat during the recent past, this value will likely increase by 8 to 24% by the end of the century. The net effect will be a decrease in upland area

in 2070–2099 (i.e. black areas in Figure 83), with a possible impact on the upper wetland (i.e. swamp).

Similar dynamics can be expected at the other Lake Ontario sites, as well as in Lake Erie riverine system (7GRM and 11FCK), and at some Lake Huron sites (15BDD, 18HGW, and 19TBY). Conversely, a significant decrease in partially flooded areas is projected for the connecting channel sites, i.e. Hill Island East (1HIE; down to -48%) in the Upper St. Lawrence, and Detroit River Marshes (12DRM, down to -33%) in the Huron-Erie Corridor.

3.8.2.3. Characteristics of short-term fluctuations

Changes in sub-annual water level fluctuations can also be analyzed in terms of changes in the mean characteristics of the dry/wet cycles, i.e. cycle period (in hours), total duration of level fluctuations during the growing season (days), and the energy carried by short-term disturbances, as explained by the scale-averaged wavelet power (cf. Section 3.7.1.2). Table 24 lists results for these three variables, and Figure 82 details projected changes for each site along with the significance level. As explained in Section 3.7.2.4, the cycle characteristics were extracted from high-pass filtered water levels simulated over a quarter-month, i.e. regardless of the weekly variation in mean lake level. Therefore, they include only the high-frequency components of the signal with periods < 7 days. Furthermore, to determine whether a change is projected in the nearshore dynamics indifferently of the projected change in the extent of the transition zone, only grid points with non-zero values were considered when dealing with short-term fluctuations. Annual means are thus calculated on quarter-month spatial means, rather than on the individual annual mean of each grid points, to eliminate any influence of landward or lakeward wetland migration.

3.8.2.3.1. Wet/dry cycle periods

The mean dry/wet cycle periods obtained from the reference dataset are representative of the physical processes that modulate nearshore dynamics at each site. While Lake Erie and the Huron-Erie Corridor were modelled under unsteady conditions, which allow a good representation of surface seiches and set-ups, the simulated water level scenarios for Lakes Ontario and Huron only admit wind-driven fluctuations with periods of > 2 days (cf. Section 3.4.2.3). This explains the difference in values presented in Table 24, where typical fluctuation periods range from 87–101 hours (~ 4 days) in Lakes Ontario and Huron, and 27–72 hours (1–3 days) in Lakes Erie (including the Lower Detroit River) and St. Clair. Most of Lake Erie sites show quite a low mean annual

average (< 2 days) that demonstrates the dominant influence of seiches, which typically have period of ~14 hours, over wind-induced displacements.

As expected, no significant changes in shoreline dynamics are observed between 1980–2009 and 2070–2099. Typical drying and wetting periods are essentially similar, with almost no significant change in Lakes Ontario and Huron, and a relative difference of less than 6% in Lake Erie and the Huron-Erie Corridor (Figure 82). Projected changes in mean lake level do not alter the physics of surface seiches, which is highly dependent on basin morphology, and no significant shift in wind event frequency is notable in the compiled data. The rise and fall of water levels in the transition zones are likely to be driven by synoptic-scale systems of periods of 2–4 days in the last decades of the 21st century, as typically observed in mid-latitudes (Trigo *et al.* 1999). Although research conducted with CMPI5 GCMs point to a decrease in the frequency of cyclone storm tracks over North America (Chang *et al.*, 2013; Lehmann *et al.*, 2014) and the Great Lakes system (Turner *et al.*, 2013) by 2100, no similar drop was clearly identified in the analysis of strong wind events in this study (events with wind speed > 13.9 ms⁻¹ or 46.8 kmh⁻¹; not shown in Section 2.4).

3.8.2.3.2 Mean annual duration and scale-averaged power

An overall decrease in the mean annual duration of periodic events is projected for a majority of sites in Lakes Ontario, Erie, and St. Clair, including the Lower Detroit River (Table 24). While grid cells experienced between ~7–24 days of short-term disturbances during the past growing seasons, this number is reduced by ~2–3 days by 2070–2099 (Figure 82), with the greatest relative change projected for Grand River Mouth (7GRM) and Hill Island East (1HIE; up to 30%) wetlands. These changes are large relative to the natural variability, especially in Lake Ontario where the STD estimated for the reference period is less than 5 days for the majority of sites²². The projections obtained for Lake Huron are somewhat opposite, with a likely increase in mean annual duration of 8–11% (or 1.8–2.5 days) in half of the wetlands studied.

Although projected changes in event intensity (i.e. seiche and set-up amplitude; Table 23) can partially explain these results, the complex dynamics linking short-term disturbances, mean lake level and site topography are likely at play here. The same conclusions can be drawn for the mean annual maximum scale-averaged wavelet power, for which projections vary by site with no general trend, except for a somewhat stronger decrease or increase in this variable in Lake Ontario and Huron-Erie Corridor, respectively. A positive increase in maximum scale-averaged

²² Again, a caveat must be added to this observation as Lake Ontario projections were conducted under regulation Plan 2014.

wavelet power is expected when the event amplitude is significantly amplified or the transition zone substantially increases without sufficient change in water depth to inhibit or lessen dry/wet cycles²³. Both explanations can be applied to Lake St. Clair, the only lake where a significant increase in set-ups amplitude is projected by the end of the century relative to baseline.

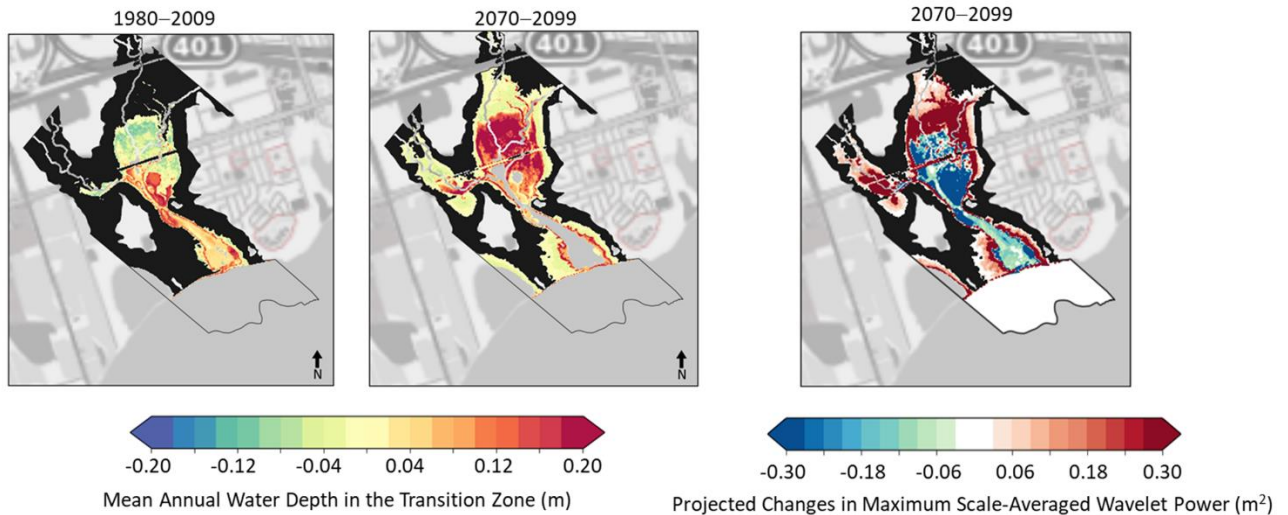


Figure 84: Example of changes in mean water depth across the transition zone for Lynde Creek Marshes, in Lake Ontario, for past and future periods (left panels), as well as projected changes in the maximum scale-averaged wavelet power (right panel). Black shaded areas in all maps indicated zones that remain strictly dry during the 30-year periods.

The consistent decrease obtained for both cycle duration and scale-averaged wavelet power is generally related to increasing water depth throughout the partially flooded areas, which reduces and inhibits the fluctuations and, therefore, the energy carried by them. An example of similar dynamics is presented in Figure 84 for Lynde Creek Marshes in Lake Ontario. A negative mean water depth in the left panels indicates trend toward dryness over the 30-year period considered, while uncolored areas reveal strictly flooded zones. As can be seen in the left panels, a large portion of the site in the center of the wetland is inundated in 2070–2099 relative to baseline, and an increase in water depth is projected at the margin of it. The projected negative changes in maximum scale-averaged wavelet power by the end of the century (right panel) are related to this increase in water depth in the transition zone, which limits the influence of dry/wet cycles.

In general, a reduction in the richness of emergent marsh and meadow communities can be expected when the magnitude of successive cycles of drying and flooding that characterize the transition zone is reduced (e.g. Grabas *et al.*, 2019).

²³ Again, it is important to note that this variable is set to zero when no cycles are detected.

Figure 85 gives a second example that clearly illustrates the complexity of site-wide dynamics. It shows the spatial distribution of projected changes for the cycle duration in Rondeau Bay Wetlands (10RBY), with reference values. As can be seen from the reference period (left panel), areas in the interior of the peninsula, on the bay side, are frequently exposed to water level fluctuations, as are lands bordering tributaries flowing along the coast. With projected changes in mean lake levels, the transition zone moves landward (lakeward) on the northern (southern) shores of the bay under the upper bound scenario, and conversely under the lower bound scenario (right panels). While the number of grid points subjected to wet/dry cycles is projected to decrease by 5% in the lower case, as illustrates black shaded area in Figure 85, no significant change is observed in the mean annual duration across the site ($p > 10\%$; Table 24). In contrast, the number of grid points exposed to sub-seasonal fluctuations is projected to increase by 7% in the upper case although much of the peninsula and land along the tributaries are expected to flood more frequently. These changes result in a significant decrease of about 2 days in the mean annual cycle duration (Table 24). Therefore, to obtain a complete picture of the projected changes in site dynamics, each wetland must be considered individually to derive results that go beyond the general conclusions extracted for the lakes as a whole.

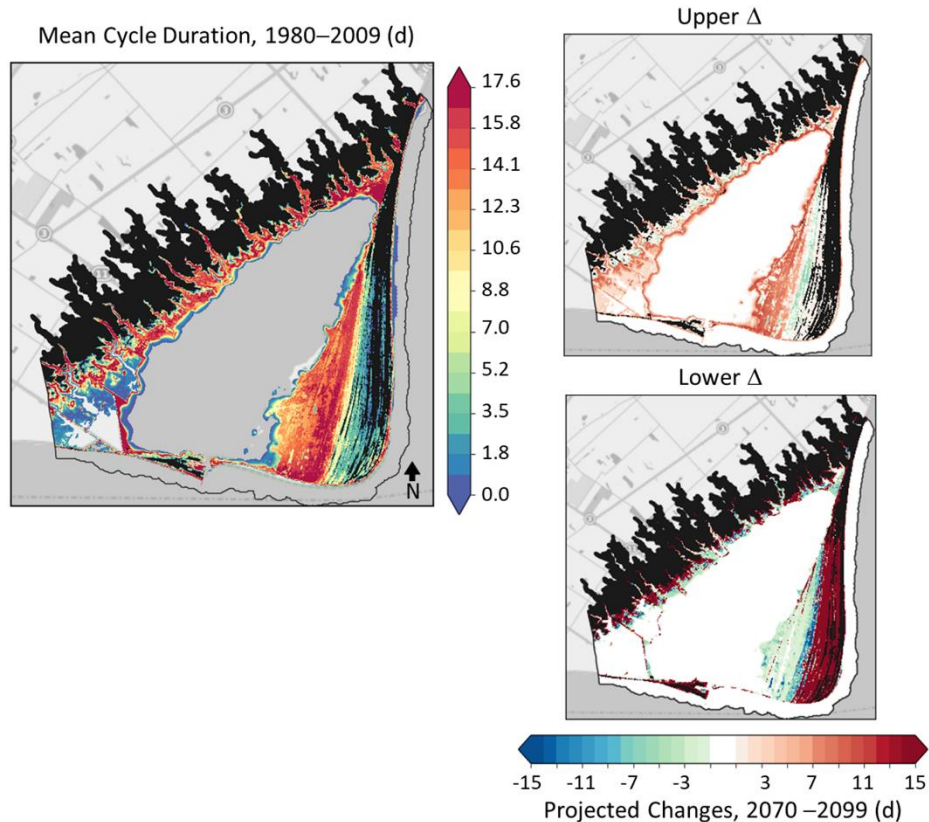


Figure 85: Left panel: Climate reference map for mean annual cycle duration for the period 1980–2009 in Rondeau Bay Wetlands, Lake Erie. Right panels: The upper and lower bounds of projected change for this variable by 2070–2099 relative to baseline. Duration gives the total number of days during the growing season that a grid cell is subject to sub-seasonal water level fluctuations.

3.8.2.4. Waves: Near-bottom orbital velocities

Only grid points experiencing wave activity were considered here to explore changes in near-bottom orbital velocities, i.e. grid points with a non-zero mean annual value.

No clear signal of change in near-bottom wave orbital velocities is observed in Lake Ontario, although a more pronounced decrease is to be expected according to the lower bound scenario (-12,-39% compared to +5,+10%; Table 24). Opposite projections are obtained for Lake Erie, where wave intensity is likely to increase by the end of the century along wetland shorelines under both scenarios, with major relative changes expected in lacustrine sites like Long Point (6LPW, 52–81%) and Rondeau Bay Wetlands (7RBY, 28–52%). Because no such differences in offshore wave climate were observed between past and future periods (Table 23), changes in site-scale statistics are likely due to changes in mean lake level, which alters water depth (or bathymetry) and thus, nearshore dynamics. An increase in exposure to wave action is likely to influence plant composition of the offshore fringe of open shore wetlands (Albert *et al.*, 2005; Angradi *et al.*, 2013;

cf. Section 3.2.4.3). High activity can limit the establishment and survival of much of the emergent plants and submerged aquatic vegetation.

3.8.3. Summary

From the results described in the previous sections, some general conclusions can be drawn about projected changes in site-scale dynamics, which are related to mean lake level, site topography, and nearshore dynamics:

1. Most Lake Ontario sites (including 1HIE, in the Upper St. Lawrence) display a 6-34% increase in mean annual strictly flooded area in 2070–2099 relative to baseline. Drowned river mouths, such as Grand River Mouth Wetland (7GRM; Lake Erie) and Anderson Creek Marshes (23ACK; Lake Huron), also show high upper bound projections compared to basin-scale values. In general, the riverine systems are more likely to be flooded by the end of the century.
2. The transition zone is projected to expand by 2070–2099 in Lake Ontario wetlands, and Lake Erie riverine systems (7GRM and 11FCK), as well as in specific sites in Lake Huron (15BDD, 18HGW, and 19TBY).
3. A significant decrease in the areal extent of the transition zone is projected for connecting channel sites, i.e. Hill Island East, in the Upper St. Lawrence, and Detroit River Marshes, in the Huron-Erie Corridor.
4. An 80–90% decrease in interannual variability of flooded and partially flooded area of Lake St. Clair marshes is projected by the end of the century. More stable physical conditions can be expected from year to year in this lake, which heightens the risk of perennial habitat loss if mean lake level increases significantly.
5. A general decrease in the mean annual duration of periodic events is projected for a majority of sites in Lakes Ontario, Erie, and St. Clair, including the Lower Detroit River. Projections for Lake Huron are somewhat opposite, with a likely increase in the mean annual duration in half the wetlands.
6. Wave exposure is likely to increase in the offshore fringe of Lake Erie's open shore wetlands (i.e. Long-Point and Rondeau Bay Wetlands), with a 52–81% relative increase in wave activity by the end of the century, which is likely to limit aquatic species establishment.

4. SELECTED SITES

The Great Lake Protection Initiative focuses on 20 sentinel wetlands that represent the diversity of coastal wetlands found along the Canadian shoreline of the Great Lakes. In this study, the CWRM is used to show how these sentinel wetlands might evolve under the different climatic scenarios.

In 2004, the Great Lakes Coastal Wetland Consortium (GLCWC) identified 4511 coastal wetlands (>2ha) along the Canadian shoreline of the Great Lakes, covering roughly 700 km² (Ingram, *et al.*, 2004). Moreover, it is recognized that the GLCWC inventory underrepresents the number of coastal wetlands in Lake Huron, particularly in eastern Georgian Bay (Ingram, *et al.*, 2004; Midwood *et al.*, 2012). Therefore, twenty coastal marshes, representative of the dominant hydrogeomorphological systems found within lakes Huron, St. Clair, Erie and Ontario, were selected to be studied, as well as locations in the St. Marys River, the Detroit River and the Upper St. Lawrence River (Figure 2). It was mandatory to represent the dominant hydrogeomorphological systems found within each basin for making sure that the variation in the exposure of coastal marshes to lake-level changes was properly captured. Daily, seasonal and annual water-level change controls the distribution of vegetation communities in Great Lakes coastal wetlands (Keddy & Reznicek, 1986; Wilcox & Meeker, 1991; Wilcox, *et al.*, 2002), and the influence of water levels is moderated by the hydrologic connection between wetland and lake (Keough *et al.*, 1999; Wilcox, *et al.*, 2005; Wilcox, 2012; Grabas & Rokitnicki-Wojcik, 2015).

Coastal wetlands throughout the Great Lakes can be classified as lacustrine, riverine or barrier-protected based on their primary hydrologic source and hydrologic connection with the lake. Within these systems, coastal wetlands can be further separated based on their geomorphic features and coastal processes (Albert *et al.*, 2005). A hierarchical diagram illustrating the variation in coastal wetland hydrogeomorphology is shown in Figure 86. Lacustrine systems are directly controlled by Great Lakes levels, and are heavily influenced by lake-level fluctuations as well as erosive and depositional processes. In this study, riverine sites occur at the confluence of a tributary and a lake and are partially controlled by the river watershed. However, lake waters flood the lower portions of these systems, influencing water levels and fluvial processes. Lastly, barrier-protected systems may have a lacustrine or riverine origin, but they become separated from the lake by a barrier beach or beach ridges often forming a coastal lagoon (Albert *et al.*, 2005; Wilcox, 2012). Table 25 details the hydrogeomorphology of the 20 coastal wetlands

selected, and Figure 87 illustrates the relative surface area of each hydrogeomorphological system in each basins.

Barrier beach lagoons are a notable omission from sites selected on lakes Huron and Ontario. The sand barrier that forms in these systems can sever the hydrologic connection between wetland and lake for an extended period of time (Albert *et al.*, 2005). These barriers are dynamic and are the result of sediment transport. They can breach as water levels rise or through erosion on the lakeward side of the barrier causing rapidly changing water levels (see Figure 5 within Grabas & Rokitnicki-Wojcik, 2015). The CWRM does not model the changes in sedimentation since it uses a static digital elevation model (DEM). The inability to predict when and for how long the barrier beaches form and when breaches occur challenges the ability to model the distribution of wetland vegetation since the water depths are most likely inaccurate in such sites using the proposed approach.

In addition to lake-level fluctuations, several other environmental variables can influence the distribution of vegetation communities of Great Lakes coastal wetlands (Wilcox, *et al.*, 2005). These are both natural and anthropogenic and include, but are not limited to:

- Temperature;
- Latitude;
- Sediment supply and transfer (e.g. longshore drift) and associated disruptions (e.g. shoreline hardening, dredging);
- Ice and storm events;
- Biological stressors, including invasive species (e.g. *Typha x glauca*, *Phragmites australis* spp. *australis*, common carp);
- Wetland impoundment, including dike construction;
- Water chemistry including pollutants (e.g. herbicides), nutrients (e.g. nitrogen and phosphorus), turbidity and temperature; and
- Other human-related disturbances such as land conversion (Wilcox, 2012).

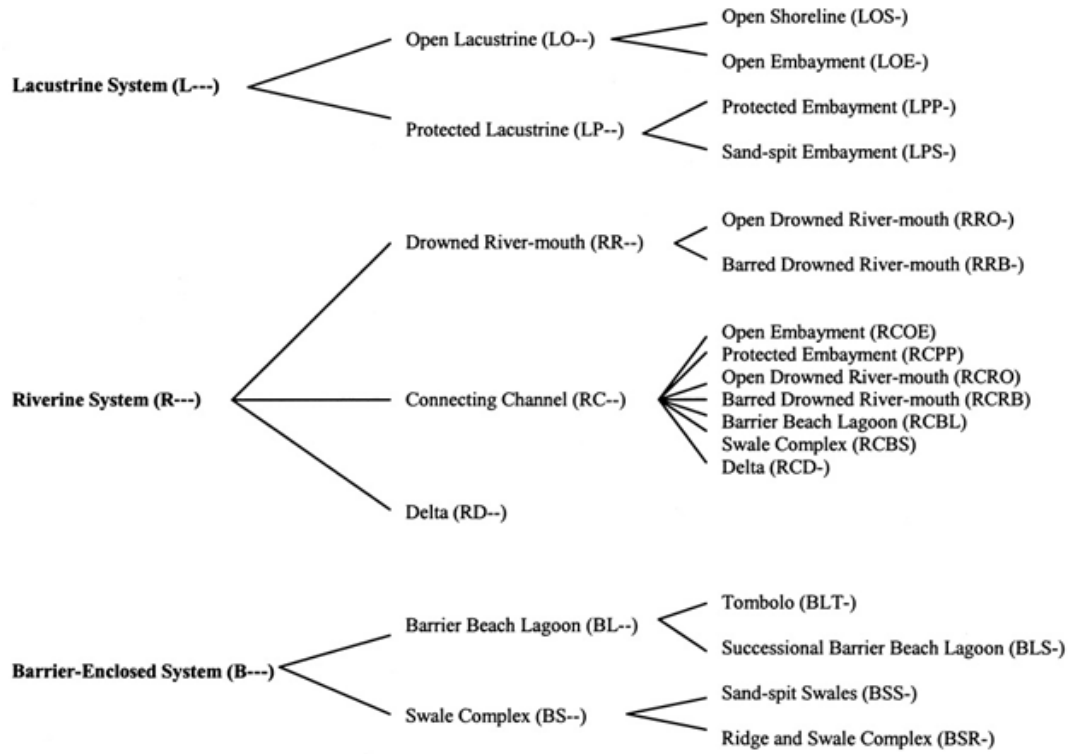


Figure 86: Hydrogeomorphic classification of Great Lakes coastal wetlands (Albert et al., 2005).

Table 25: Hydrogeomorphology (HGM) and land tenure for twenty Great Lakes coastal wetlands assessed. ¹ - Refers to a wetland managed by a provincial conservation authority.

Basin	Site	HGM	Private	First Nation	Provincial	Federal	Crown Land
St. Lawrence River	Hill Island East (1HIE)	RCPP				X	
Lake Ontario	Airport Creek Marsh (2ACM)	RRO		X			
	South Bay Marsh (3SBM)	LOE	X				
	Lynde Creek Marsh (5LCM)	RRB			X ¹		
	Jordan Station (6JSM)	RRB	X		X ¹		
Lake Erie	Grand River Mouth Wetlands (7GRM)	RRB	X		X ¹		
	Selkirk Provincial Park (8SPP)	RRB	X		X		
	Bouck's Bond, Long Point National Wildlife Area (9LPW)	LPS				X	
	Rondeau Bay (10RBY)	LPS	X		X		
	Fox Creek/ Dolson's Creek Marsh (11FCK)	RRB	X		X ¹		
Huron – Erie Corridor	Detroit River Marshes (12DRM)	RCOS	X		X ¹		
	Lake St. Clair Marshes (13LSC)	LOS	X			X	
	Johnston Bay / Saint-Ann Marshes (14SAM)	RCD		X		X	
Lake Huron	Baie Du Doré (15BDD)	LOE	X				
	Hay Bay Wetland (16HBW)	LPP				X	
	Hog Bay (18HGW)	LPP	X				
	Treasure Bay (19TBY)	LPP				X	
	Frances Point Marsh (27FPT)	LPP					X
	Whiskey Harbour Wetland (22WHW)	LPP		X			
St. Marys River	Anderson Creek (23ACK)	RCRO	X				

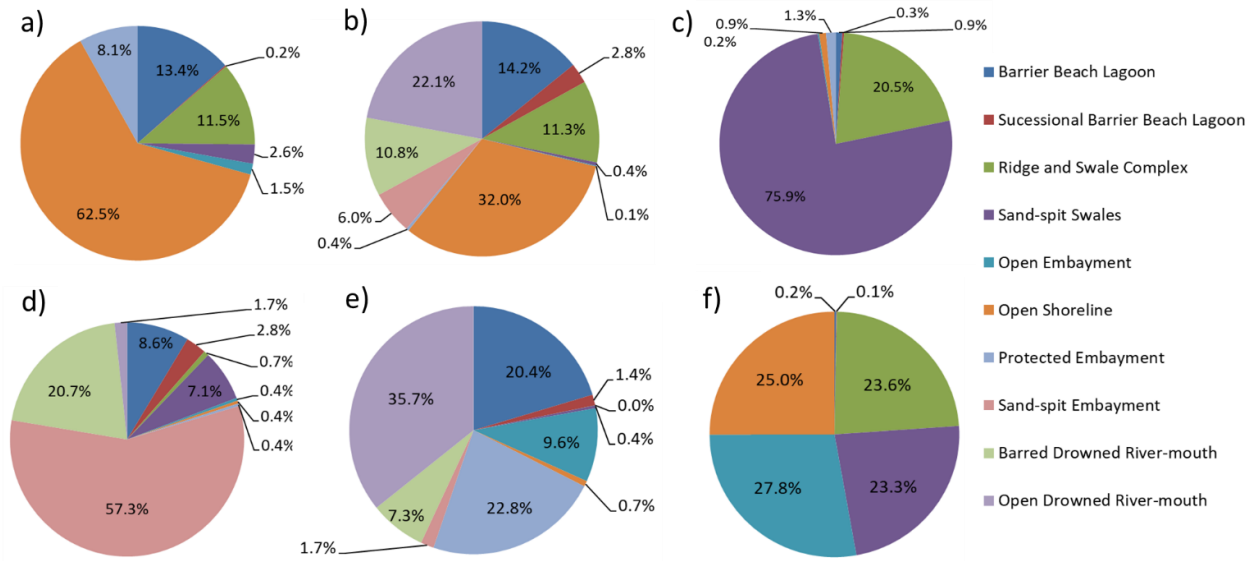


Figure 87: Relative surface area of each hydrogeomorphic system in: (a) the St. Marys River; (b) Lake Huron; (c) the Huron-Erie Corridor; (d) Lake Erie; (e) Lake Ontario and (f) The St. Lawrence River as quantified through the GLCWI (Ingram et al. 2004).

4.1. Site description

4.1.1. St. Lawrence River

1HIE - Hill Island East

Hill Island East is a protected embayment on the eastern edge of Hill Island, Thousand Islands National Park. It is the only study site located in the Upper St. Lawrence River. Protected embayment coastal marshes are the most common hydrogeomorphological type observed along the Upper St. Lawrence River, representing 45% of all coastal wetlands as quantified through the Great Lakes Coastal Wetland Inventory (GLCWI) (Ingram *et al.*, 2004; Figure 87).

Thousands Island National Park is located where the St. Lawrence River and Frontenac Arch meet, serving as a transitional zone between eastern deciduous and boreal forests. The geology and unique climatic characteristics of the Park provide a diversity of habitats that support several species at the northern or southern limit of their range (Parks Canada Agency, 2019). Hill Island is designated as an Area of Natural and Scientific Interest by the Province of Ontario, and Hill Island East is an evaluated Provincially Significant Wetland.



Figure 88: Hill Island East, Thousand Islands National Park, Ontario. Photo Credit: Canadian Wildlife Service – Ontario Region, Environment and Climate Change Canada, August 2002

4.1.2. Lake Ontario

2ACM - Airport Creek Marsh

Airport Creek Marsh is an open drowned river-mouth wetland located on Tyendinaga Mohawk Territory in the Bay of Quinte, Lake Ontario. Open drowned river-mouth coastal marshes are the most common hydrogeomorphological type observed in Lake Ontario, representing 30% of all coastal wetlands as quantified through the GLCWI (Ingram *et al.*, 2004; See Figure 87).

Airport Creek Marsh is also designated as a Provincially Significant Wetland. Amongst coastal wetlands within the Bay of Quinte Area of Concern, the water quality and biotic condition of Airport Creek Marsh are considered 'Good' to 'Excellent' (Environment Canada - Canadian Wildlife Service, 2007). Airport Creek Marsh is monitored by Quinte Conservation and ECCC with support from the Mohawks of the Bay of Quinte.



Figure 89: Airport Creek Marsh, Deseronto, Ontario. Photo Credit: Canadian Wildlife Service – Ontario Region, Environment and Climate Change Canada, August 2019.

3SBM - South Bay Marsh

South Bay Marsh is an open embayment located along the eastern edge of Prince Edward County, Ontario. Open embayment coastal marshes are an uncommon hydrogeomorphological type within Lake Ontario, representing only 7% of all coastal wetlands as quantified through the GLCWI (Ingram *et al.*, 2004; See Figure 87).

South Bay Marsh is designated as a Provincially Significant Wetland and a part of the Prince Edward County South Shore Important Bird and Biodiversity Area (Birds Canada, 2018). Like Airport Creek Marsh, water quality and biotic data have been collected at South Bay Marsh by the Canadian Wildlife Service – Ontario Region for nearly two decades. This information has supported the development of a submerged aquatic vegetation (SAV) community index of biotic integrity (IBI) for use in Lake Ontario coastal wetlands (Grabas *et al.*, 2012), and has furthered research relating the influence of daily, seasonal and annual water level fluctuations to the composition of Lake Ontario coastal wetland vegetation communities (Wilcox, *et al.*, 2005; Grabas & Rokitnicki-Wojcik *et al.*, 2015; Grabas *et al.*, 2019).



Figure 90: South Bay, Milford, Ontario. Photo Credit: Canadian Wildlife Service – Ontario Region, Environment and Climate Change Canada, September 2016.

5LCM - Lynde Creek Marsh

Lynde Creek Marsh is a barred drowned river-mouth, Provincially Significant Wetland located in Lynde Shores Conservation Area, Whitby, Ontario. Unlike open drowned river-mouths, barred drowned river-mouths have a barrier that constricts streamflow as it enters the lake, often forming a lagoon. Barred drowned river-mouth coastal marshes are a fairly common hydrogeomorphological type observed in Lake Ontario, representing 25% of all coastal wetlands as quantified through the GLCWI (Ingram *et al.*, 2004; See Figure 87).

The biological and geophysical condition of Lynde Creek Marsh have been monitored by the Central Lake Conservation Authority (CLOCA) and ECCC for nearly two decades as part of the Durham Region Coastal Wetland Monitoring Project (Environment Canada and Central Lake Ontario Conservation Authority, 2007) and the Coastal Wetland Monitoring Program (CWMP; Uzarski, *et al.*, 2017). Relative to other coastal wetlands throughout the Great Lakes, the condition of Lynde Creek Marsh is considered “Moderately Impacted” to “Moderately Degraded” as measured through the composition of the bird, anuran, fish and vegetation communities.



Figure 91: Lynde Shores Conservation Area, Whitby, Ontario.

6JSM – Jordan Marsh

The most appropriate hydrogeomorphological classification for Jordan Station Marsh would be a barred drowned river-mouth; however, the Queen Elizabeth Way (QEW) is located across the barrier beach that once sheltered this coastal wetland. Barred drowned river-mouth coastal marshes are a common hydrogeomorphological type observed in Lake Ontario, representing 25% of all coastal wetlands as quantified through the GLCWI (Ingram *et al.*, 2004; See Figure 87).

Jordan Station Marsh is evaluated as a Provincially Significant Wetland that overlaps two Provincial Areas of Natural and Scientific Interest - Jordan Valley and Twenty Mile Creek Drowned River Mouth. Jordan Harbor is surrounded by private residences and agricultural land, with exception of two Provincial Conservations Areas – Ball’s Falls and Jordan Harbour, both of which are managed by the Niagara Peninsula Conservation Authority (NPCA). Like South Bay Marsh, the condition of Jordan Station Marsh has been monitored by the Canadian Wildlife Service – Ontario Region for nearly two decades (Wilcox *et al.*, 2005; Grabas *et al.*, 2012; Grabas & Rokitnicki-Wojcik *et al.*, 2015; Uzarski *et al.* 2016; Grabas *et al.*, 2019). Relative to other coastal wetlands throughout the Great Lakes, the condition of Jordan Station Marsh is considered to be ‘Moderately Impacted’ to ‘Degraded’ as measured through water quality and surrounding land use, and the composition of the bird, anuran and fish communities.



Figure 92: Jordan Harbour, Jordan Station, Ontario. Photo Credit: Canadian Wildlife Service – Ontario Region, Environment and Climate Change Canada, September 2016.

4.1.3. Lake Erie

7GRM - Grand River Mouth Wetlands

The wetlands at the outlet of the Grand River can be considered a large, barred, drowned river-mouth complex. However, like Jordan Station Marsh, the mouth of the Grand River has been stabilized through jetties in Port Maitland, Ontario. Barred drowned river-mouth coastal marshes are a common hydrogeomorphological type observed in Lake Erie, representing 28% of all coastal wetlands as quantified through the GLCWI (Ingram *et al.*, 2004; See Figure 87).

The Grand River Mouth Wetlands are designated as a Provincially Significant Wetland Complex. It is located at the outlet of southern Ontario's largest watershed (6800 km²), and it is heavily influenced by agriculture (70% agricultural land; Grand River Conservation Authority, 2018). A significant portion of the marsh is owned by the Grand River Conservation Authority and leased to the Broad Creek Recreation Club. The Canadian Wildlife Service – Ontario Region has monitored the condition of the Grand River Mouth Wetlands for the past decade, on a three-year basis (unpublished data). Relative to other Lake Erie coastal wetlands, the water quality of the Grand River Mouth Wetlands is considered to be 'Very Degraded'. Despite this, the biotic condition appears to be 'Very Good' as measured through the composition of aquatic macroinvertebrate and bird communities.



Figure 93: Byng Island, Dunnville, Ontario. Photo Credit: Grand River Conservation Authority, 2010.

8SPP - Selkirk Provincial Park

Selkirk Provincial Park contains a barred drowned river-mouth wetland at the confluence of Sandusk and Spring Creeks in Haldimand County, Ontario. Barred drowned river-mouth coastal marshes are a common hydrogeomorphological type observed in Lake Erie, representing 28% of all coastal wetlands as quantified through the GLCWI (Ingram *et al.*, 2004; See Figure 87).

Selkirk Provincial Park is an evaluated Provincially Significant Wetland, surrounded largely by agriculture. The Canadian Wildlife Service – Ontario Region has monitored the condition of Selkirk Provincial Park for the past decade, on a three-year basis (unpublished data). Relative to other Lake Erie coastal wetlands, the water quality of the Selkirk Provincial Park is considered to be 'Moderately Degraded'. Despite this, biotic condition, as measured through the composition of aquatic macroinvertebrate and bird communities is considered to be 'Very Good'.



Figure 94: Selkirk Provincial Park, Selkirk, Ontario. Photo Credit: Canadian Wildlife Service – Ontario Region, Environment and Climate Change Canada, July 2019.

9LPW - Bouck's Pond, Long Point National Wildlife Area

Bouck's Pond is one of several sand-spit embayments on Long Point National Wildlife Area. Sand-spit embayment coastal marshes are the most common hydrogeomorphological type observed in Lake Erie, representing 43% of all coastal wetlands as quantified through the GLCWI (Ingram *et al.*, 2004; See Figure 87).

The coastal marshes of Long Point, including Bouck's Pond serve as one of the most important staging grounds on the continent for waterfowl (Government of Canada, 2020). Because of this, Long Point is recognized provincially and internationally as a wetland complex of extraordinary ecological and social importance. Long Point is a Wetland of International Significance under the Ramsar Convention, a UNESCO World Biosphere, a Provincially Significant Wetland, and an Important Bird and Biodiversity Area. Relative to other Lake Erie coastal wetlands, the water quality of Bouck's Pond is considered to be 'Good' and the biotic condition as measured through the composition of submerged aquatic vegetation, aquatic macroinvertebrate and bird communities is considered to be 'Very Good' to 'Excellent'.



Figure 95: Bouck's Pond, Long Point National Wildlife Area, Ontario. Photo Credit: Canadian Wildlife Service – Ontario Region, Environment and Climate Change Canada, November 2018.

10RBY - Rondeau Bay

Rondeau Bay is a large sand-spit embayment in southwestern Ontario in the Municipality Chatham-Kent. Rondeau Provincial Park is located on the east side of Rondeau Bay and contains several sand-spit embayment coastal marshes, much like Long Point National Wildlife Area. Sand-spit embayment coastal marshes are the most common hydrogeomorphological type observed in Lake Erie, representing 43% of all coastal wetlands as quantified through the GLCWI (Ingram *et al.*, 2004; See Figure 87). The west or landward side of Rondeau Bay contains several drowned river-mouth wetlands in a landscape dominated by agriculture.

Rondeau Provincial Park protects a unique diversity of habitats including oak savannah, Carolinian forest, dune and coastal wetland (Friends of Rondeau, 2016). The marshes of the Greater Rondeau Area are also considered to be a major waterfowl staging area (Birds Canada, 2018). In recognition of its ecological and social importance, Rondeau Provincial Park is designated as an Area of Natural and Scientific Interest, a Provincially Significant Wetland, and as an Important Bird and Biodiversity Area.



Figure 96: Rondeau Provincial Park, Ontario. Photo Credit: Ontario Parks, August 2010.

11FCK – Fox Creek/Dolson’s Creek Marsh

A barred drowned river-mouth coastal marsh exists at the confluence of Fox and Dolson’s Creeks in Harrow, ON. Barred drowned river-mouth coastal marshes are a common hydrogeomorphological type observed in Lake Erie, representing 28% of all coastal wetlands as quantified through the GLCWI (Ingram *et al.*, 2004; See Figure 87).

Fox Creek/ Dolson’s Creek Marsh is evaluated as a Provincially Significant Wetland in a landscape dominated by agriculture. The Canadian Wildlife Service – Ontario Region has

monitored condition of Fox Creek/ Dolson's Creek Marsh for the past decade, on a three-year basis (unpublished data). Relative to other Lake Erie coastal wetlands, the water quality of the Fox Creek/ Dolson's Creek Marsh is considered to be 'Moderately Degraded'. Despite this, the biotic condition, as measured through the composition of the submerged aquatic vegetation, aquatic macroinvertebrate and bird communities is considered to be 'Good' to 'Very Good'.



Figure 97: Fox Creek Marsh, Harrow, Ontario. Photo Credit: Canadian Wildlife Service – Ontario Region, Environment and Climate Change Canada, July 2019.

4.1.4. Huron – Erie Corridor

12DRM - Detroit River Marshes

The Detroit River Marshes are a riverine, open shoreline coastal wetland complex in LaSalle, Ontario. Open shoreline marshes are a common hydrogeomorphological type observed in the Huron – Erie Corridor (Detroit River, Lake St. Clair, St. Clair River), representing 28% of all coastal wetlands as quantified through the GLCWI (Ingram *et al.*, 2004; See Figure 87).

Located in the Detroit River Area of Concern (AOC), the water quality and condition of the submerged aquatic vegetation community within the Detroit River Marshes are considered 'Good' and comparable to coastal wetlands outside of the AOC. Despite this, the biotic condition as measured through the composition of local the bird community is considered to be 'Poor' relative to non-AOC sites (ECCC, 2017). The Detroit River Marshes are designated as Provincially Significant Wetland and an Important Bird and Biodiversity Area. Petite Côte Conservation Area is also situated in the Detroit River Marshes east of Fighting Island, an international wildlife refuge (Essex Region Conservation Authority, 2020).



Figure 98: Detroit River Marshes, LaSalle, Ontario. Photo Credit: Canadian Wildlife Service – Ontario Region, Environment and Climate Change Canada, July 2012.

13LSC – Lake St. Clair Marshes

The marshes along the eastern shoreline of Lake St. Clair can be considered as a large, open shoreline coastal wetland complex. Open shoreline marshes are a common hydrogeomorphological type observed in the Huron – Erie Corridor (Detroit River, Lake St. Clair, St. Clair River), representing 28% of all coastal wetlands as quantified through the GLCWI (Ingram *et al.*, 2004; See Figure 87).

The eastern shoreline of Lake St. Clair is designated as an Area of Natural and Scientific Interest, a Provincially Significant Wetland Complex and an Important Bird and Biodiversity Area. South of James Bay, Lake St. Clair and adjacent marshes are the most important staging area for waterfowl in Ontario (Government of Canada, 2020). St. Clair National Wildlife Area (NWA), located adjacent to the southeastern shore, is a Wetland of International Significance under the Ramsar Convention and sees up to 360 000 individual waterbirds in the spring and up to 150 000 in the fall (Canadian Wildlife Service - Ontario Region, 2001). The Canadian Wildlife Service of ECCC continues to monitor the biotic and geophysical condition of the Lake St. Clair Marshes to inform NWA management and the remediation of the St. Clair River Area of Concern (Environment Canada - Canadian Wildlife Service, 2016).



Figure 99: St. Clair National Wildlife Area – St. Clair Unit, Pain Court, Ontario. Photo Credit: Canadian Wildlife Service – Ontario Region, Environment and Climate Change Canada, September 2017.

14SAM – Johnston Bay/St. Anne Marsh

The marshes of Johnston Bay and the southern portion of St. Anne Island, Ontario are part of the St. Clair River delta, the largest delta in the Laurentian Great Lakes (Thomas *et al.*, 2006). The eastern portion of the St. Clair River Delta is Bkejwanong Territory (Walpole Island First Nation). Not surprisingly, delta marsh habitat is the most common hydrogeomorphological type observed in Huron – Erie Corridor (Detroit River, Lake St. Clair, St. Clair River), representing 54% of all coastal wetlands as quantified through the GLCWI (Ingram *et al.*, 2004; See Figure 87).

Walpole Island supports a mosaic of biologically diverse natural landscapes, including tall grass prairies, oak savannahs and coastal wetlands. Not only do these habitats support over 70 species at risk, but they are also of cultural and social importance to the Bkejwanong people (Beckford *et al.*, 2010). Walpole Island, including the marshes of Johnston Bay and the southern portion of St. Anne Island are designated as an Area of Natural and Scientific Interest by the Province of Ontario and are also part of the Eastern Lake St. Clair Important Bird and Biodiversity Area.



Figure 100: Johnston Bay/ St. Anne Marsh, Walpole Island First Nation, Ontario. Photo Credit: Canadian Wildlife Service – Ontario Region, Environment and Canada, June 2019.

4.1.5. Lake Huron

15BDD - Baie du Doré

Baie du Doré is an open embayment, coastal marsh adjacent to the Bruce Power Nuclear Station in Tiverton, Ontario. Open embayment coastal marshes are an uncommon hydrogeomorphological type within Lake Huron, representing only 5% of all coastal wetlands (not including eastern Georgian Bay), as quantified through the GLCWI (Ingram *et al.*, 2004; See Figure 87).

Baie du Doré is also evaluated as a Provincially Significant Wetland. Since 2014, Bruce Power and Municipality of Kincardine have supported the monitoring and management of the invasive common reed, *Phragmites australis* sp. *australis* (Phragmites) within the coastal wetlands between Baie du Doré and MacGregor Point Provincial Park. The monitoring and management of Phragmites along this stretch of the Lake Huron shoreline have been coordinated and implemented the Lake Huron Centre for Coastal Conservation, the Invasive Phragmites Control Centre and the Saugeen Ojibway Nation (Bruce Power, 2019).



Figure 101: Bruce Power Nuclear Plant, Tiverton, Ontario. Photo Credit: Bruce Power, 2019.

16HBW – Hay Bay Wetland

Hay Bay is protected embayment located in Fathom Five National Marine Park, a National Marine Conservation Area in Lake Huron. Protected embayment coastal marshes are the most common hydrogeomorphological type within Lake Huron, representing 51% of all coastal wetlands (not including eastern Georgian Bay), as quantified through the GLCWI (Ingram *et al.*, 2004; See Figure 87).

Fathom Five National Marine Park is part of the Niagara Escarpment Plan and World Biosphere Reserve, and harbours several species at risk endemic to wetlands (Parks Canada Agency, 2016a). The southern portion of Hay Bay is also evaluated as a Provincially Significant Wetland (Barney Lake).



Figure 102: Hay Bay, Fathom Five National Marine Park. Photo Credit: Southwestern Ontario Orthoimagery Project (SWOOP), Ontario Ministry of Natural Resources and Forestry, 2015.

18HBW – Hog Bay

Hog Bay is a protected embayment located in Severn Sound, Lake Huron near Midland, Ontario. Protected embayment coastal marshes are the most common hydrogeomorphological type within Lake Huron, representing 51% of all coastal wetlands (not including eastern Georgian Bay) as quantified through the GLCWI (Ingram *et al.*, 2004; See Figure 87).

Hog Bay is evaluated as a Provincially Significant Wetland that serves as an important staging area for waterbirds (Weseloh *et al.*, 2002). In 2003, Severn Sound was delisted as an Area of Concern having sufficient restored all beneficial use impairments identified in Annex 2 of the Great Lakes Water Quality Agreement (1987). The Severn Sound Environmental Association continues to monitor the condition of Severn Sound, including the evaluation of wetlands to determine their significance for land use planning.



Figure 103: Hog Bay, Midland, Ontario. Photo Credit: South Central Ontario Orthoimagery Project (SWOOP), Ontario Ministry of Natural Resources and Forestry, 2013.

19TBY – Treasure Bay

Treasure Bay is a protected embayment located on Beausoleil Island within Georgian Bay Islands National Park near Port Severn, Ontario. Georgian Bay is the world's largest freshwater archipelago, containing roughly 30 000 islands and over 3700 coastal wetlands (Fracz & Chow-Fraser, 2013). These wetlands provide important habitat for migratory fish, birds, mammals and herptiles, including several species at risk (Fracz & Chow-Fraser, 2013; Parks Canada Agency, 2016b). In recognition of its ecological importance, Georgian Bay was designated as a UNESCO World Biosphere in 2004 (Georgian Bay Biosphere Reserve, 2020).

For nearly two decades, the laboratory of Dr. Chow-Fraser (McMaster University) has mapped and studied the ecology of coastal wetlands within Georgian Bay (Wei & Chow-Fraser, 2007;

DeCatanzaro *et al.*, 2009; Midwood & Chow-Fraser, 2010; Cvetkovic & Chow-Fraser, 2011; Rokitnicki-Wojcik *et al.*, 2011; Midwood *et al.*, 2012). The research undertaken by McMaster University has futhered our understanding of how the quality and quantity of spawning and nursery habitat for migratory fish are influenced by Great Lakes water levels (Cvetkovic *et al.*, 2010; Midwood & Chow-Fraser, 2012; Fracz & Chow-Fraser, 2013; Weller & Chow-Fraser, 2019a, b).



Figure 104: Treasure Bay, Beausoleil Island, Georgian Bay. Photo Credit: BC2 Groupe, July 2018.

27FPT – Frances Point Marsh

Frances Point Marsh is a protected embayment located on the northeastern tip of Franklin Island near Brooks Landing, Ontario. Like Beausoleil Island, Franklin Island is one of the 30 000 islands in eastern Georgian Bay, Lake Huron – a UNESCO World Biosphere Reserve (Georgian Bay Biosphere Reserve, 2020).

Georgian Bay contains over 3700 coastal wetlands (Fracz & Chow-Fraser, 2013). These wetlands provide an important habitat for migratory fish, birds, mammals and herptiles, including several species at risk (Fracz & Chow-Fraser, 2013). Like Treasure Bay, Frances Point Marsh has and continues to be studied by the laboratory of Dr. Chow-Fraser at McMaster University, Ontario.



Figure 105: Frances Point, Franklin Island, Ontario. Photo Credit: Canadian Wildlife Service – Ontario Region, Environment and Climate Change Canada, May 2019.

22WHW – Whiskey Harbour Wetland

Whiskey Harbour is a protected embayment located on Wiikwemkoong Unceded Territory, towards the northeastern tip of Manitoulin Island. Protected embayment coastal marshes are the most common hydrogeomorphological type within Lake Huron, representing 51% of all coastal wetlands (not including eastern Georgian Bay) as quantified through the GLCWI (Ingram *et al.*, 2004; See Figure 87).

Manitoulin Island supports a diversity of globally rare vegetation communities, including Great Lakes coastal wetlands and alvars that provide habitat for a number of species at risk (e.g. Pitcher's thistle, *Cirsium pitcheri*; lakeside daisy; *Teranearis herbacea*; and dwarf lake iris, *Iris lacustris*; (Kraus *et al.*, 2006). Whiskey Harbour was recently surveyed as part of the Coastal Wetland Monitoring Program and is considered undisturbed or of reference quality with respect to water quality and surrounding land use (Central Michigan University, 2018).

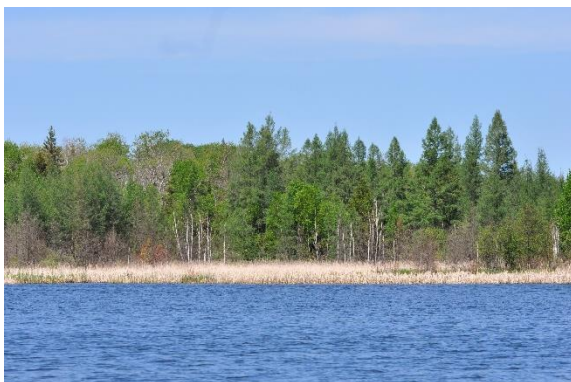


Figure 106: Whiskey Harbour, Wiikwemkoong Unceded Territory. Photo Credit: Canadian Wildlife Service – Ontario Region, Environment and Climate Change Canada, May 2018.

23ACK – Anderson Creek

Anderson Creek is an open drowned river mouth wetland on the St. Marys River near Desbarats, Ontario. Open drowned river-mouth coastal marshes are a common hydrogeomorphological type observed on the St. Marys River, representing 14% of all coastal wetlands as quantified through the GLCWI (Ingram *et al.*, 2004; See Figure 87).

To assess the impairment of fish and wildlife habitat within the St. Marys River Area of Concern (AOC), the biotic conditions of Anderson Creek and other non-AOC locations were studied between 2013 and 2015. Relative to AOC and other non-AOC locations along the St. Marys River, the water quality of Anderson Creek is considered 'Good' and the biotic condition, as measured through the submerged aquatic vegetation is considered 'Very Good' (Environment and Climate Change Canada, 2016).

Anderson Creek is also part of a Provincially Significant Wetland Complex (Kensington Point).



Figure 107: Anderson Creek, Desbarats, Ontario. Photo Credit: Canadian Wildlife Service – Ontario Region, Environment and Climate Change Canada, July 2015.

4.2. Area of Interest (AOI)

To take into account the capacity of wetlands to migrate over time, it is necessary that the CWRM represents areas larger than the present-day footprint of the selected wetlands. Nevertheless, since CWRM relies on a large amount of data that implies considerable computing capacities, modelling unnecessarily large areas could quickly create a major burden. Thus, an Area of Interest (AOI) for each sentinel site was carefully delimited to precisely identify the zones where CWRM results are computed. AOI delineation is based on the following criteria:

1. Inland boundary based on the contour line at an elevation 5 m higher than each lake historical high-water level (based on monthly averaged values; see Table 26). For instance, the historical high water level value in Lake Erie is 175.04 m, thus the contour line at 180 m was selected as the area of interest inland limit for all sites in this lake;
2. Offshore boundary based on the isobaths 5 m lower than each lake historical low water level (based on monthly averaged values; see Table 26); and
3. Lateral boundaries based on a maximum 2 km buffer around each sentinel wetland.

From those general areas, some site-specific adjustments were made to:

1. Include adjacent wetlands²⁴;
2. Exclude areas where some datasets are not available (for instance no LIDAR coverage);
3. Exclude areas where hydrodynamics are strongly altered by artificial structures (for instance, upstream of dams);
4. Exclude areas that are not included on wave modelling; and
5. Limit the size of areas of interest in flat areas.

Table 26: Historical high and low water levels per lake (based on monthly averaged values):

Lake	Historical High Water Level (m)	Historical Low Water Level (m)	Maximum fluctuation (m)
Lake Ontario	75.81	73.74	2.07
Lake Erie	175.04	173.18	1.86
Lake St. Clair	175.96	173.24	2.72
Lake Huron	177.5	175.57	1.93

²⁴ Based on the Great Lakes Coastal Wetland Consortium dataset produced in 2004, available at https://services.arcgis.com/cJ9YHowT8TU7DUyn/arcgis/rest/services/site_view_regions_totals/FeatureServer

Based on those criteria, the Lake St. Clair (13LSC) and Ste. Anne Marsh (14WID) sites share the same AOI since their offshore and inland boundaries overlap. Therefore, there are 19 AOIs that cover the 20 coastal wetlands of this study. In total, the AOIs represent 1243 km², where the biggest AOI is 13LSC with 823 km² and the smallest is Whiskey Harbour Wetland AOI (22 WHM) with 0.62 km² (Table 27). The difference in AOI size is due to the different wetland sizes, the topographic variation in the surrounding area and LIDAR dataset availability.

Table 27: CWRM Areas of Interest.

Wetland name	AOI Unique ID	Area (km ²)	Centroid
Hill Island East	1HIE	1.81	(-75.94447, 44.36419)
Airport Creek Marsh	2ACM	11.53	(-77.1053, 44.17545)
South Bay Marsh	3SBM	5.94	(-77.03756, 43.92051)
Lynde Creek Marsh	5LCM	4.77	(-78.96122, 43.85026)
Jordan Marsh	6JSM	2.65	(-79.37247, 43.17268)
Grand River Mouth Wetlands	7GRM	42.13	(-79.56829, 42.88277)
Selkirk Provincial Park	8SPP	9.95	(-79.96888, 42.80461)
Long Point Wetland	9LPW	168.84	(-80.26006, 42.5744)
Rondeau Bay	10RBY	94.42	(-81.89018, 42.29585)
Fox Creek / Dolson's Creek Marsh	11FCK	14.06	(-82.84263, 42.00215)
Detroit River Marshes	12DRM	38.45	(-83.09983, 42.21204)
Lake St. Clair Marshes	13LSC	822.67	(-82.461, 42.47129)
Walpole Island			
Baie du Doré	15BDD	8.73	(-81.55927, 44.3434)
Hay Bay Wetland	16HBW	4.38	(-81.69429, 45.2371)
Hog Bay Wetland	18HBW	5.62	(-79.79481, 44.73929)
Treasure Bay	19TBY	3.44	(-79.85815, 44.86591)
Whiskey Harbour Wetland	22WHW	0.62	(-81.65468, 45.85941)
Anderson Creek	23ACK	1.56	(-83.96795, 46.33117)
Frances Point Marsh	27FPT	1.25	(-80.33368, 45.41806)

4.3. Masked areas

4.3.1. Masks related to physical variable

Within each site's AOI, there are areas where it is assumed that CWRM results will not be accurate due to 1) the large influence of groundwater seepage, 2) the occurrence of pools (pounds, lake), 3) areas protected from flooding (dykes) or 4) the absence of accurate elevation information. Within each AOI, such areas were identified and used to form a mask where CWRM will not computed results.

The absence of accurate elevation data occurs mostly in tributary channels or where bathymetric data are not available (Figure 108). In addition, inland water bodies (i.e. pools) that are not connected to the lake were assumed to have inaccurate elevation information since they were covered by LIDAR surveys (which reflects on water surface as described in Section 5). These zone were identified by comparing the flooded area of an AOI and the corresponding topometric coverage.

Most pools were identified with the Ontario Hydro Network (OHN) Waterbody dataset (Ontario Ministry of Natural Resources and Forestry, 2018) and cross-validated with satellite imagery. Finally, when inland water streams were identified on OHN Watercourse dataset (Ontario Ministry of Natural Resources and Forestry, 2010) and were visible on satellite imagery, a 20 m buffer was created on each side of the stream and this zone was added to the mask (Figure 109).

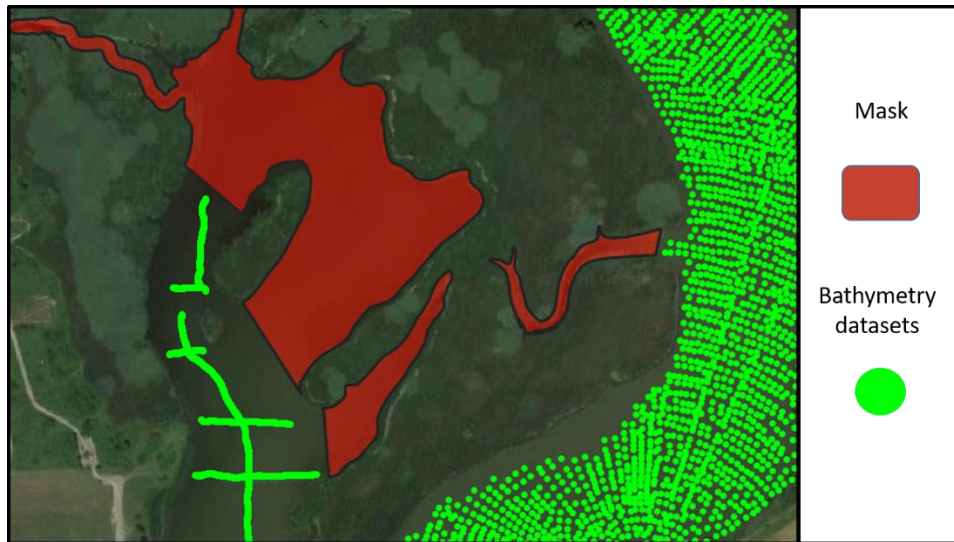


Figure 108: Part of the mask (in red) applied on water portions of Rondeau Bay's (10RBY) area of interest where bathymetry datasets (bright green) are not available.

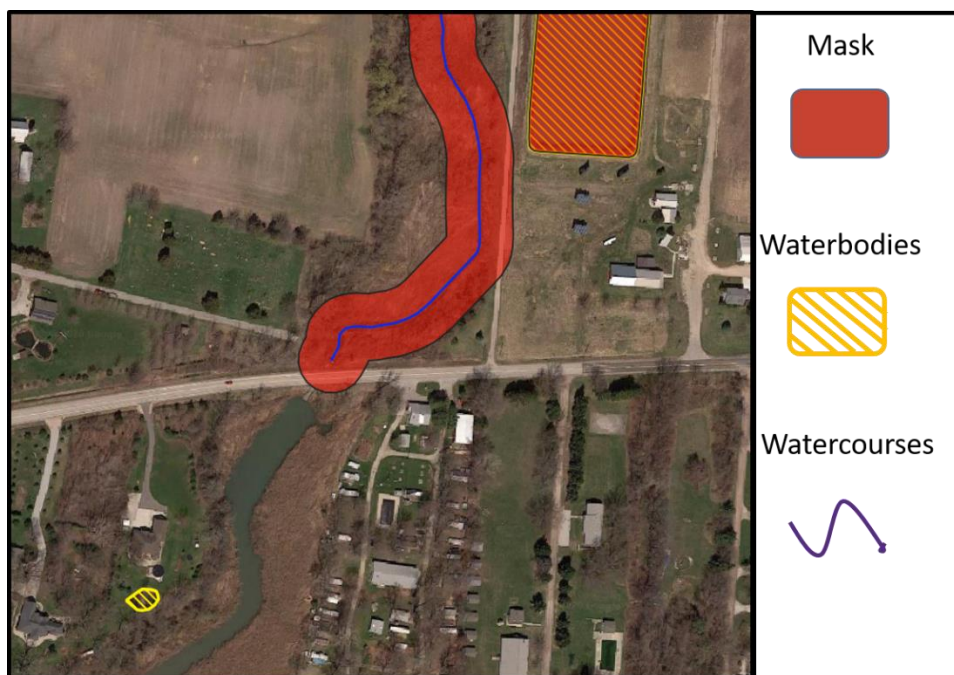


Figure 109: Part of the mask (in red) applied on Fox Creek (11FCK) area of interest, based on a 20 m buffer applied on each side of watercourses and on waterbodies disconnected to the lake (yellow hashed) that also appear on satellite's imagery.

No dataset that precisely identifies dyke locations could be found (Figure 110 and Figure 111). Therefore, dyke systems have been manually delineated based on LIDAR data, satellite imagery, field photographs and *GoogleStreetView*. Also, it is assumed that upland areas, mainly on the landward side from main roads are mostly anthropized (housing, commercial, industrial, etc.).

These roads act as dykes and water levels are not controlled solely by lakes (Figure 112). Thus, those areas were also masked.



Figure 110: In Rondeau Bay (10RBY), dyke and pump system regulates water level near agricultural lands.



Figure 111: In Lake St-Clair (13LSC), water level on agricultural lands (left side) is maintained artificially low compared to the lake's level (right side).



Figure 112: In Detroit River Marsh (12DRM), upland area from the road is mostly anthropogenic. Therefore, it was assumed that the road would act as a dyke and areas upland have been masked (yellow).

As described in Table 30, the extent of masked area varies from one site to the other, ranging from 0% to 57.9% of total AOI, with an average value of 9.6%. Most extended masks occur in anthropic settings such as Lake St. Clair (13LSC) shores or Grand River Mouth (7GRM) wetlands, while sites in more natural environment such as Hill Island or Whiskey Harbor will have reliable CWRM results throughout the whole AOI.

4.3.2. Masks related to land use

Land use has to be considered in AOI masking. For instance, wet meadow species will not grow on asphalted roads nor intensively cultivated areas even if favorable hydrologic conditions occur.

Therefore, it is necessary to mask areas that cannot support wetlands migration, based on the land use information available. The Ecological Land Classification (ELC) was used for this purpose. It is a collection of ecological classes delineated based on satellite imagery that covers the majority of the study sites. Even though it was primarily intended to delineate ecological classes, anthropized land areas are also identified with precision.

Based on ELC classes descriptions (Ontario Ministry of Natural Resources and Forestry, 2019b), the ELC codes listed in Table 28 were considered unsuitable for wetland migration and were masked.

Table 28: ELC classes present in the AOIs and considered not suitable for wetland (please refer to Ontario Ministry of Natural Resources and Forestry, 2019b for description of each class).

ELC Codes	Land use class
CS	Constructed
CSC	Civic
CSE	Extraction
CSI	Industry & Utility
CSR	Residential
CST	Transportation
CSU	Urban Core
CT	Cultivated
CTO	Open Cultivated
CTS	Shrub Cultivated
CTT	Treed Cultivated
CTR	ARI – Monoculture
CTM	ARI - Mixed
CTP	ARI - Unimproved
RB	Rock Barren
CL	Cliffs and Talus
CLO	Open Cliff and Talus
BL	Bluff
BLO	Open Bluff

The ELC dataset only partially covered the AOI of 7GRM, 10RBY, 14WID, and 15BDD. In these areas, the Southern Ontario Land Resource Information System (SOLRIS) version 3.0 (Ontario Ministry of Natural Resources and Forestry, 2019a) was used instead of ELC to delineate unsuitable areas for wetland migration (Figure 113). SOLRIS is a land cover/land use inventory covering Southern Ontario from 2000 to 2015. It is the third update (after 2.0 and 2.1) since the initial SOLRIS version 1.0 was created in the late 1990's. It is mainly based on Landsat-5 TM, Landsat-7 ETM+ and Radarsat-1 image classification (using *eCogintion image object technology*) with a minimum mappable unit of 0.5 ha (Ontario Ministry of Natural Resources and Forestry, 2019a). Therefore, features less than 0.5 ha or less than 90 m wide cannot be reliably detected. This explains why areas delimited with this dataset can have a “pixelized” aspect and are only

used where the ELC dataset is not available. The land use classes of SOLRIS included in the mask are listed in the following table (Table 29).

Table 29: SOLRIS land use classes present in the AOIs and considered not suitable for wetland (please refer to Ontario Ministry of Natural Resources and Forestry (2019a) for description of each class).

SOLRIS CODE	Land use class
41	Open Cliff and Talus
64	Open Bedrock
193	Tilled
201	Transportation
202	Built-Up Area – Pervious
203	Built-Up Area – Impervious
204	Extraction –Aggregate
250	Undifferentiated



Figure 113: Mask related to land use in Rondeau Bay (10RBY) site, determined from a combination of ELC and SOLRIS 3.0 datasets.

The combination of ELC and SOLRIS datasets did not provide satisfying results for 16HBW and 18HBW, as clear discrepancies between land use classification and satellite imagery occur. In these cases, we performed a manual delineation of land uses within the AOI based on satellite imagery, field photographs and *Google StreetView* (Figure 114).

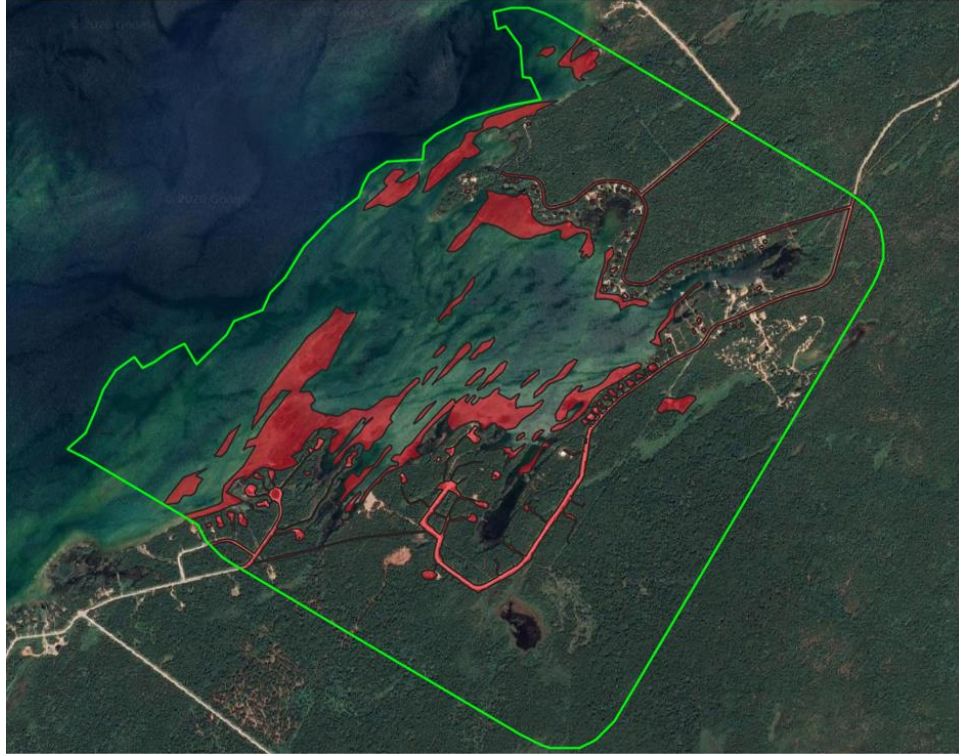


Figure 114: Mask related to land use for Hay Bay (16HBW) site, delineated manually.

Finally, 19TBY and 27FPT have many underwater hard rock outcrops where wetland migration cannot occur. A substrate hardness value was derived from side scanning and sonar surveys collected at those sites by an external consultant (Georgian Bay Forever, 2020). Post collection data processing was created using the embedded reflectance data, allowing bathymetric isobaths and bottom hardness determinations to be charted. Bottom hardness values were then examined along with existing charts, historic imagery, and local observations to determine rock shoal extent. On a second visit, visual confirmation of the rock shoals was possible in most instances and, where necessary, real-time imaging was examined to confirm the siting. Surface and subsurface georeferenced photographs were taken for several reference points at each site. Underwater rock shoal extent maps were derived from those observations and were included in the land use mask of the surveyed sites.

As described in Table 30, land use masked area varies greatly from one site to the other, ranging from 0% to 63% of total AOI with a mean value of 11%. Most extended masks occur in intensive agricultural settings such as FoxCreek, while sites in more natural environment such as Hill Island or Whiskey Harbor have land uses that can support wetlands throughout the whole AOI.

Table 30: Area of interest (AOI) for the twenty Great Lakes Coastal Wetland sites and their respective masked areas (physical modelling and land use masks. Non-masked AOI area is the resulting AOI after applying physical modelling and land use masks.

Site	AOI area (ha)	Physical modelling mask area (ha)	% masked (physical modelling)	Land use mask area (ha)	% masked (land use)	% masked (total)	Non-masked AOI area (ha)
1HIE	181	0	0.0%	0	0.0%	0.0%	181
2ACM	1153	0	0.0%	179	15.5%	15.5%	974
3SBM	594	0	0.0%	129	21.7%	21.7%	465
5LCM	377	17	4.6%	104	27.5%	32.0%	256
6JSM	265	1	0.4%	18	6.8%	7.2%	246
7GRM	4213	2390	56.7%	381	9.1%	65.8%	1442
8SPP	995	3	0.3%	232	23.3%	23.6%	761
9LPW	3434	0	0.0%	0	0.0%	0.0%	3434
10RBY	9442	1848	19.6%	1113	11.8%	31.4%	6482
11FCK	1406	52	3.7%	886	63.0%	66.7%	468
12DRM	3845	2228	57.9%	359	9.3%	67.3%	1258
13LSC	22238	6849	30.8%	574	2.6%	33.4%	14816
14SAM	14167	0	0.0%	156	1.1%	1.1%	14012
15BDD	873	87	10.0%	13	1.5%	11.5%	773
16HBW	438	3	0.6%	58	13.3%	13.9%	377
18HGW	562	30	5.3%	59	10.5%	15.8%	473
19TBY	344	0	0.0%	4	1.2%	1.2%	340
22WHW	62	0	0.0%	0	0.0%	0.0%	62
23ACK	156	4	2.4%	2	1.5%	3.9%	150
27FPT	125	0	0.0%	2	1.3%	1.3%	124

5. HIGH-RESOLUTION DIGITAL ELEVATION MODELS OF COASTAL WETLANDS

Authors: Antoine Maranda, M.ATDR., Mathieu Roy, Ph.D., Marianne Bachand, Ph.D., Jean Morin, Ph.D.

5.1. Introduction

Wetland classes are mainly structured along a topographical gradient, and the elevation range (relative to water level) in which certain species can persist is often narrow (<1 m). Thus, wetland structure and plant spatial distribution are especially sensitive to changes in elevation relative to water level. An accurate characterization of elevation is therefore critical in wetland plant succession models like the one included in the Coastal Wetland Response Model (CWRM). This characterization is done through high-definition Digital Elevation Models (DEMs). Primary terrain attributes such as the slope, aspect (slope orientation) and terrain curvature can influence wetland structure and plants. This information is retrieved from elevation values of the DEM and can then be generalized at different resolutions to describe terrain attributes from small to local scales.

5.1.1. Definitions and key concepts:

5.1.1.1. Digital Elevation Models

A DEM is a digital representation of the terrain elevation (Figure 115). DEM is a generic term that includes Digital Surface Model (DSM), which represents the elevation of the terrain including all objects on it, like trees or buildings, and Digital Terrain Model (DTM), which represents the bare ground surface (without objects). For the scope of this study, DTMs were produced since physical and ecological processes modelled by the CWRM rely on bare ground elevation values. However, the more generic term DEM is used in this report.

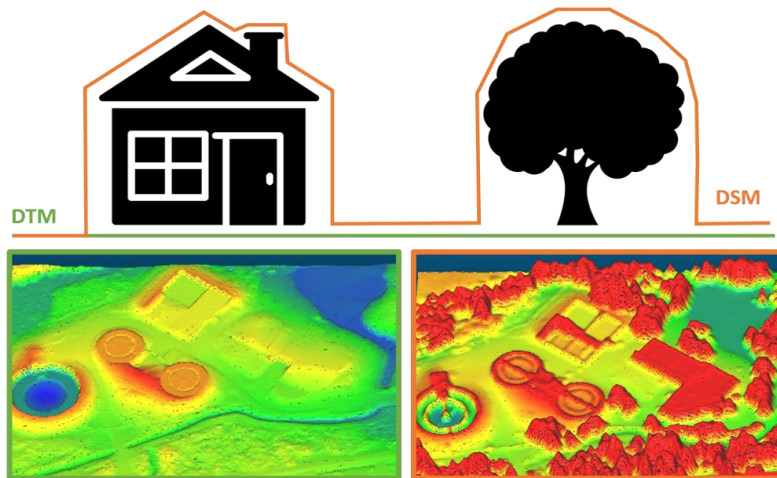


Figure 115: Difference between Digital Surface Model and Digital Terrain Model.

A DEM represents the topography of an area at a scale defined by its cell (or pixel) size in a regular grid setup. Finer cell size will provide more information on the topographic variability while increasing file size and computing time. A DEM cannot provide information more precise than the original topographic and bathymetric data used to create it. Considering the precision of datasets available for all the study sites and computing capacity, a 2 m resolution DEM was created for each wetland AOI. These DEMs provide elevation information at every 2 m that is then transposed on the CWRM 10 x 10 m computational grid.

Since AOIs cover the land-water interface across the entire Great Lakes region, several bathymetric and topographic elevation datasets were used to create each DEM. Merging these multiple datasets to produce consistent and flawless DEMs contributed to processing complexity.

A large amount of ground-truth data collection and data manipulations, based on statistical modelling and multispectral image analysis, were used to produce the most accurate DEM for each sites. The following sections describe the sources of all the topographic and bathymetric data that were used and the transformations that were needed to create the most precise, accurate and seamless DEMs as possible.

5.1.1.2. Primary terrain attributes

Several terrain attributes can be generated as derivatives of elevation values. In this study, the bottom slope, aspect and the profile curvature were extracted, which are commonly used variables in ecological studies (Morin *et al.* 2003), at five different resolutions (i.e. 10, 30, 130, 250, and 310 m).

The slope expresses the rate of change in elevation values between a DEM cell and its neighbours (expressed in degrees or percent). Basically, the lower the slope, the flatter the terrain is within that cell. The aspect gives each DEM cell's slope orientation in degrees clockwise from North. The profile curvature is the second derivative of the topographic surface defined by a DEM, and expresses the degree of downslope acceleration or deceleration within the landscape in a specific direction (Gallant and Wilson, 2000), i.e. in the slope orientation. Values are negative when the slope is increasing downhill (convex profile) and positive when it is decreasing (concave profile). Calculation details will be described in the methods section.

5.2. Methods

5.2.1. Coordinates reference systems

5.2.1.1. Horizontal coordinate reference systems

Study sites cover two different Universal Transverse Mercator (UTM) zones. Therefore, two different horizontal coordinate reference systems were used, which were assigned to the different sites as presented in Table 31. Each dataset used to create the DEM of a specific site was projected in the appropriate coordinate system before being integrated into the DEM.

Table 31: Study sites and the associated horizontal coordinate reference systems.

	Sites	Reference System	EPSG
Upper St. Lawrence Lake Ontario	1HIE 2ACM, 3SBM	NAD83 (CRS)/UTM18N	2959
Lake Ontario Lake Erie Huron-Erie Corridor Lake Huron	5LCM, 6JSM 7GRM, 8SPP, 9LPW, 10RBY, 11FCK 12DRM, 13LSC, 14SAM 15BDD, 16HBW, 18HGW, 19TBY, 22WHW, 23ACK, 27FPT	NAD83(CRS)/UTM17N	2958

5.2.1.2. Vertical coordinate reference system

The International Great Lakes Datum 1985 (IGLD85) is the vertical coordinate reference system used for the CWRM, which provides dynamic heights. However, all topographic datasets used to create the DEMs were provided in the Canadian Geodetic Vertical Datum 1928 (CGVD28) or in the Canadian Geodetic Vertical Datum 2013 (CGVD2013) that give normal-orthometric and orthometric heights. The conversions of heights related to these different vertical reference frames usually necessitate knowledge of heights in the two systems at a common benchmark (Véronneau, pers. comm.). Therefore, a series of benchmarks provided by the Canadian Geodetic

Survey was used, which gives height conversion between CGVD28, CGVD2013 and IGLD85 at various points along the coast of the study zone. For each site, the closest benchmark was identified, and the appropriate height conversion was applied to the datasets. In the case that many benchmarks were close to one wetland, benchmark values were averaged. When bathymetry datasets provided depth measurements instead of elevation values, the official Low water datum elevation of the corresponding lake was added to depth values to obtain IGLD85 elevation values (Table 32).

Table 32: Conversion values between different vertical datum and Lake low water datum for each study site.

	IGLD85 - CGVD2013	IGLD85-CGVD28	Low Water Datum
	(m)	(m)	(m)
Lake Ontario	1HIE	0.373	74.2
	2ACM	0.397	
	3SBM	0.395	
	5LCM	0.462	
	6JSM	0.513	
Lake Erie	7GRM	0.463	173.5
	8SPP	0.463	
	9LPW	0.462	
	10RBY	0.459	
	11FCK	0.467	
Huron-Erie Corridor	12DRM	0.479	174.4
	13LSC	0.455	
	14SAM	0.455	
Lake Huron	15BDD	0.452	176.0
	16HBW	0.447	
	18HGW	0.462	
	19TBY	0.428	
	21KRW	0.465	
	22WHW	0.472	
	23ACK	0.474	
	27FPT	0.436	

5.2.2. Topographic datasets

For 19 of the 20 sites, airborne LIDAR point clouds were used as primary topographic datasets. The point clouds originated from the following three sources:

1. LIDAR Eastern Acquisition Project (LEAP) acquired in 2009, covering 3 sites with an average density of 1.3 points/m², .las files version 1.2 (for more information see Government of Ontario, 2018);

2. Land Information Ontario (LIO) dataset acquired from 2016 to 2018 covering 7 sites, with an average density of 8 points/m², .las files version 1.4 (for more information see Government of Ontario, 2019);
3. LIDAR point clouds collected for Natural Resources Canada during summer 2018, covering 9 sites with an average density of 15 points/m², .las files version 1.4 (for more information see KBM Resources Group, 2018);

Please refer to Appendix A to see which LIDAR dataset was used for each site.

No LIDAR point cloud was available for Frances Point (27FPT). For this specific site, 2 m resolution DEMs from the South Central Ontario Orthophotography Project (SCOOP) and the Central Ontario Orthography project (COOP) were used as primary topographic datasets (Government of Ontario, 2016 and 2017). The DEM for this site will be referred to as an imagery-derived DEM in the following sections.

5.2.2.1. LIDAR-derived DEM correction method

Airborne LIDAR is amongst the most advanced and accessible technologies to collect precise topographic data over large areas, which makes it a popular option for measuring the bare ground elevation height and creating DEMs. However, the laser pulse is often unable to penetrate the dense vegetation canopy, and so it fails to provide accurate bare earth elevations in such areas. This greatly limits the accuracy of LIDAR-derived DEMs in areas such as coastal wetlands, as plants create a positive bias in elevation that results in significant vertical errors (Buffington *et al.*, 2016; Hladik and Alber, 2012; Montané and Torres, 2006; Rosso *et al.*, 2005; Sadro *et al.*, 2007; Schmid *et al.*, 2011).

Since DEM accuracy is critical to wetland succession models, an error correction method was applied to LIDAR datasets. A technique named the *LIDAR Elevation Adjustment with NDVI (LEAN)* was used (Buffington *et al.*, 2016). This technique uses multispectral imagery information coupled with ground truth points to develop a statistical correction model that is then applied to the original LIDAR-derived DEM.

5.2.2.1.1. LEAN Modified Technique inputs

The LEAN technique was slightly adapted to study needs and datasets availability and will be referred to as the *LEAN Modified Technique (LMT)* in the subsequent sections. While the LEAN technique was applied to a 1 m resolution DEM in Buffington's work, there was an interest to see if LEAN method could be more performant in error reduction at a different resolution. Therefore, the technique was tested at 11 different resolutions ranging from 1 to 20 m. This multi-resolution

approach is relevant since DEMs created with other ground filtering techniques such as Minimum-bin gridding can have accuracy values that strongly vary according to the DEM's resolution . It was therefore desirable to see if the same accuracy variation was observed under the LEAN method for different resolutions and, if so, to determine the resolution that maximized the corrected DEM's accuracy.

Ground truth points collection

Elevation data were collected at 300 – 600 survey points per study site, distributed uniformly across 20 transects predetermined by ECCC. These values, along with elevation data collected by vegetation surveys described in Section 4.1, were used to ground-truth and assess the accuracy of LIDAR-derived DEMs, develop a correction model, and quantify precision gain. These values will be referred to as ground-truth points hereafter.

Ground-truth points were collected using Trimble R8 and R10 Global Navigation Satellite System (GNSS) receivers operating in Real-time Kinematic (RTK) mode, providing centimeter accuracy (Z error \pm 5 cm) and post-processing capability. Surveys were conducted on foot in 2018 and 2019 when plant growth (early spring, late fall) or risk of disturbance to marsh-nesting birds were low (early spring, mid- to late summer). In remote areas without network access (e.g. eastern Georgian Bay, Lake Huron), ground control points (GCPs) were logged over a four-hour period and corrected using the Canadian Spatial Reference System Precise Point Positioning (CSRS-PPP) tool (Natural Resources Canada, 2020). Raw positional data were then post-processed from corrected GCPs using Trimble Business Center 4.10 (Trimble Inc., Sunnyvale, CA) and ArcGIS 10.5.1 (ESRI Inc., Redlands, CA).

Topographic transects spanned terrestrial and aquatic systems, extending from the forest edge to the flooded areas, to a maximum water depth of 1.2 m. In addition to basin morphology, the orientation and length of transects were predetermined to capture elevation points in each vegetation community present, as determined through contemporary aerial imagery and Ecological Land Classification (Lee *et al.* 1998). The dense canopy cover occasionally precluded the collection of ground-truth points at a higher elevation. In these instances, staff drew upon their understanding of wetland systems to find a suitable location no more than 10 m off the predetermined transect. If surveying was still not possible, the transect was relocated to an alternate location following the elevation gradient in the study site to achieve the desired number of survey points.

Uncorrected LIDAR-derived DEM elevation values

Uncorrected LIDAR-derived DEM elevation values are one of the LEAN method's inputs. Since no LIDAR-derived DEM existed for all sites, it implied creating uncorrected DEMs from the raw LIDAR point clouds. To do so, the minimum-bin gridding technique was used, which assigns to each grid cell the elevation value of the lowest LIDAR point that lies within the cell's extent. Since the LEAN method was to be tested at different resolutions, the lowest LIDAR point falling within 11 different grid cell sizes was identified, ranging from 1 m to 20 m, creating 11 different uncorrected LIDAR-derived DEMs for each site. Elevation values from each DEM at each ground-truth point location were then extracted as a LEAN method input.

The error of each uncorrected DEM was then calculated at each specific ground-truth point location as:

$$Error_{lidarij} = Z_{lidarij} - Z_{RTKi} \quad 5.1$$

, where, $Z_{lidarij}$ is the elevation of the uncorrected DEM of resolution j at the location of ground-truth point i , and Z_{RTKi} , the elevation of ground-truth point i .

For each uncorrected DEM, the Root Mean Square Error (RMSE) was calculated as:

$$RMSE_j = \sqrt{\sum (Error_{lidarij})^2 / n} \quad 5.2$$

, where $RMSE_j$ is the Root Mean Square Error of a DEM of resolution j , and n , the number of ground truth points.

RMSE is used for accuracy assessment. This error helps to determine for each site which resolution provides the most accurate uncorrected LIDAR-derived DEM when created with the minimum-bin gridding technique (Figure 116). For comparison purposes, the RMSE of a DEM created with the average LIDAR elevation values in a 2 m resolution grid cell was also estimated.

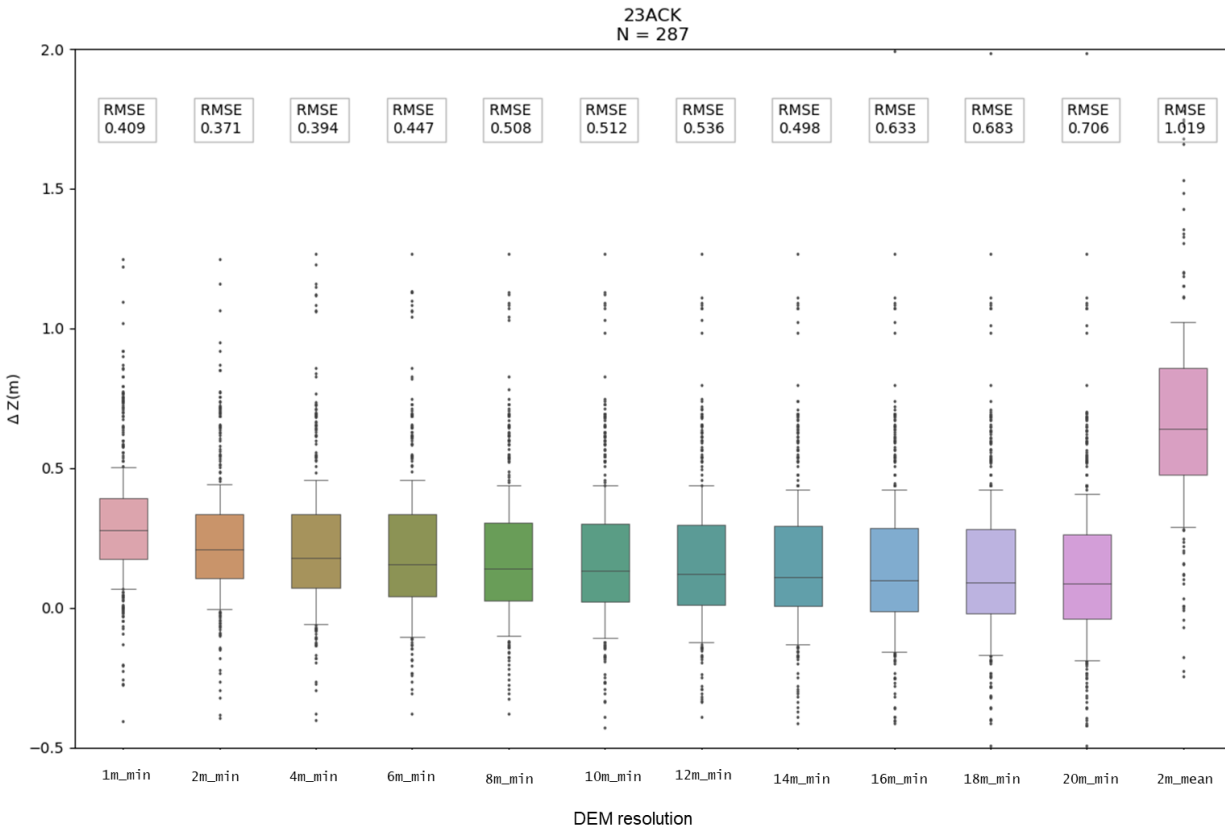


Figure 116: Errors obtained by comparing minimum-bin gridding LIDAR derived DEM values and ground-truth values at 11 different resolutions for the Anderson Creek (23ACK) site. On the right-end, errors obtained with the average bin gridding at 2 m resolution.

Multispectral image statistics

The LEAN method uses vegetation information derived from multispectral imagery to correct LIDAR DEMs. Therefore, a collection of multispectral images that covers each wetland during the leaf-on period was gathered. Images were precousiously selected with a preference for highest resolution, lowest cloud coverage and acquisition date as close as possible to LIDAR surveys. These images came from *Geoeye*, *WorldView-2*, *WorldView-3*, *Pleiades* and *Ikonos* sensors, and ranged from 80 cm to 2 m resolution. Please refer to Appendix B to see which multispectral image was used for each site. Images were cropped to each wetland area of interest and then georeferenced with a 1 m resolution intensity image generated from the LIDAR cloud. In the few cases where more than one image were needed to cover a specific area of interest, a mosaic was created by using the *Large blending feathering method* from the *Mosaic tool* in *OTB/Monteverdi* open source software (ORFEO Toolbox, 2017). This ensured that the multispectral values were as consistent as possible throughout the mosaic. Most of the image manipulations were done using the *GDAL* library (GDAL, 2019) in *Python*.

With the multispectral image of each site, the Normalized Difference Vegetation Index (NDVI) was first calculated as:

$$NDVI = \frac{NIR - R}{NIR + R} \quad 5.3$$

where NIR is the near-infrared band value (band number 4 on 4 band images, and band number 7 on 8 band images), and R, the red band value (band number 1 on 4 band images, and band number 5 on 8 band images). NDVI is a relative index that ranges from -1 to 1, with values close to 1 generally associated with dense vegetation. The pigment in plant leaves, chlorophyll, strongly absorbs visible light (including red band) for use in photosynthesis, and the cell structure of the leaves strongly reflects near infrared light. Thus, the more leaves a plant has, the higher the value of the NIR band and the lower the value of the red band when represented on a multispectral image.

Second, the NDVI average value of the pixels falling into 11 different window sizes (corresponding to uncorrected DEMs resolution) around each ground-truth points was calculated. Those NDVI average values were then used as LEAN method's input. Calculations were performed using *Rasterio* (Gillies *et al.*, 2019) *Python* library.

All calculated data were gathered in such a way that each ground truth point was associated with an uncorrected LIDAR-derived DEM elevation value, as well as a NDVI average value at 11 different resolutions.

5.2.2.1.2 Correction model development

As suggested in Buffington's work, a site-specific multivariate approach was used to model the relationship between the LIDAR error, NDVI values, and uncorrected LIDAR elevation. This model was defined as:

$$E = c + l + l^2 + v + v^2 + l * v + l * v^2 + l^2v + l^2v^2 \quad 5.4$$

where, E is the predicted error (LIDAR elevation minus ground-truth point elevation), l , the uncorrected LIDAR DEM elevation, v , the NDVI, and c , a model specific constant value. The model aims to predict an error for each pixel of a LIDAR derived DEM, based on its NDVI and elevation values.

In implementing LEAN, the Least Absolute Shrinkage and Selection Operator (LASSO) regression was employed to fit models, which include (3) independent variables. For each of them, the LASSO's shrinkage hyper-parameter was chosen using 100-fold cross-validation. A supplementary 100-fold cross validation analysis was run to validate each LEAN model and keep potential outliers in check, by randomly withholding 30% of the dataset for testing at each iteration. The average model correction from individual cross-validation runs was calculated, as well as RMSE mean and standard deviation. Statistical analysis was performed using *glmnet R* package (Freidman *et al.*, 2019).

For each site, the LEAN method was applied at 11 different resolutions ranging from 1 to 20 m (Figure 117), to identify the resolution that offers the best performing model (lowest RMSE). Outputs also specify the elevation range for which the model is valid. Please refer to Appendix C for each set of site model parameters. Examples of model outputs are provided in Figure 117.

Lynde Creek Marsh

Information

Unique ID	5LCM
Lake ID	LKO
SCR	UTM17N
EPSG	2958
Validity range (m)	73.77, 78.72

Best model's parameters

	Coefficients
Constante	0.168
l	0.000
l^2	0.000
v	-1.247
v^2	0.000
$l \cdot v$	0.000
$l \cdot v^2$	12.985
$l^2 \cdot v$	5.172
$l^2 \cdot v^2$	0.000

Residual errors at different DEM's resolution

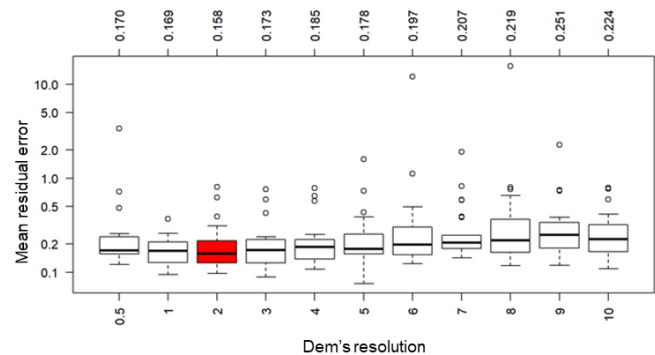


Figure 117: Example of the correction model outputs for Lynde Creek Marsh (5LCM). The red shaded box gives the resolution with the lowest RMSE, while values of the nine terms involved are listed in the lower table.

5.2.2.1.3. Applying the correction model

To apply the correction method to each site, a corrected DEM was produced by applying the statistical model to a raw LIDAR-derived DEM, using the resolution that provides the lowest RMSE.

To do so, a two-band raster dataset covering the whole site's AOI was first created, with one band containing NDVI values and the other raw LIDAR-derived elevations (the lowest LIDAR point identified in each raster cell). For each raster cell, these two values were then entered into the model equation, which returned an estimated error. This error was finally subtracted from the raw LIDAR elevation, resulting in a new corrected elevation value for each raster cell within the elevation range deemed valid for the model (Figure 118).

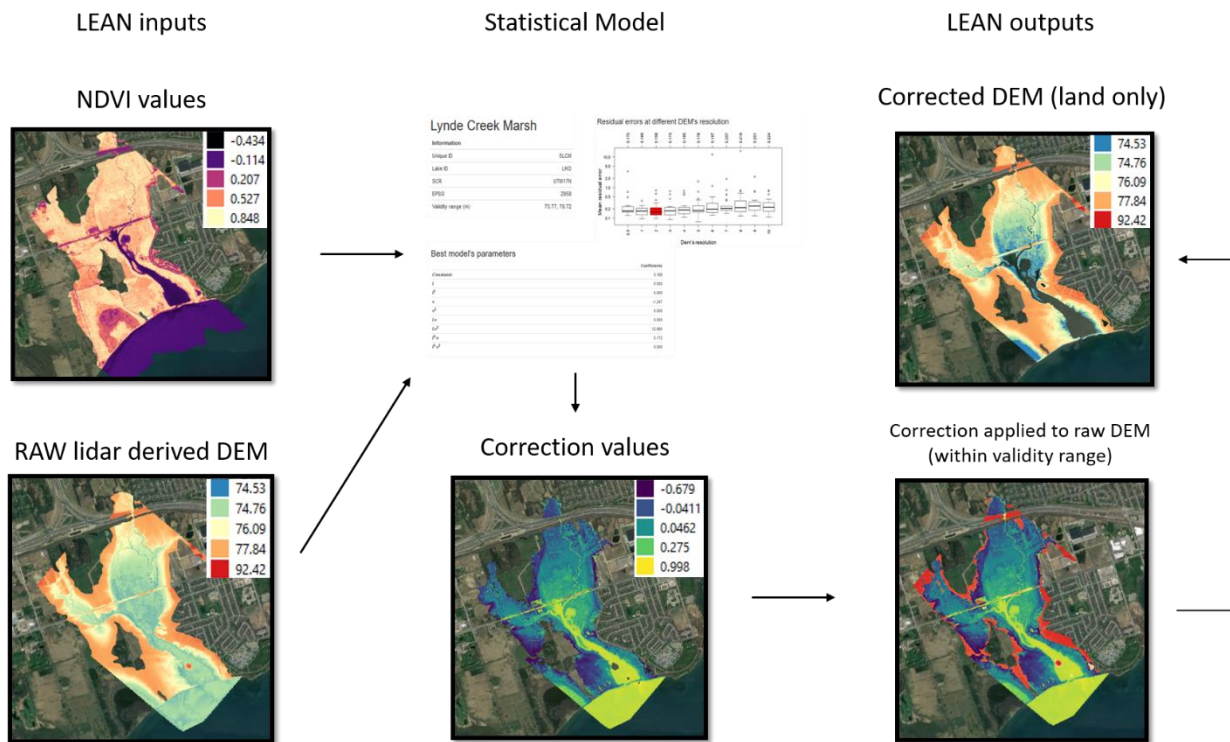


Figure 118: Workflow for applying the correction model on the raw LIDAR-derived DEM.

5.2.2.1.4. Identify the land-water interface

The near-infrared laser (1064 nm) that is typically used for airborne topographic LIDAR survey only penetrates the first few centimeters of the water surface before being completely absorbed. Therefore, it cannot be used as a reliable data source for bathymetric measures, and LIDAR-derived DEMs should only cover the land part of wetland area of interest. Thus, the coastline, as

it appeared when the LIDAR data was collected, was accurately located and georeferenced for each site.

For most sites, the point cloud classification was used, where “class 9” identifies laser pulses that land on the water. Keeping only point class 1-2-3-4-5-6-10-11 (refer to Appendix D for ASPRS Standard LIDAR Point Classes), a 2 m resolution raster dataset was first generated, using the point count as pixel value. Only pixels with a value of 10 or higher were kept and identified as being part of the land surface. Second, this raster was converted to a polygon shapefile, eliminating any parts that were less than 400 m². Finally, a smoothing algorithm (*Polynomial Approximation with Exponential Kernel* with a 10 m tolerance from *Smooth Polygon ArcGIS Pro’s toolbox*) was applied to create a smooth coastline.

For the three sites covered by the LEAP LIDAR dataset (cf. Appendix A), point cloud classification did not correctly identify the pulses that landed on the water (Figure 119). Therefore, coastline delineation was realized by extracting the extent of the water bodies from *Satellite* images using the *Quick OSM* extension in *QGIS*. This method has the advantage to quickly extract a smooth coastline, but it cannot guarantee an identical water level at the acquisition date of the satellite image and LIDAR, which explains why it was only applied when the first technique did not give consistent results. The corrected LIDAR-derived DEMs were then clipped with the coastline to keep only the inland portion of each site area of interest.



Figure 119: For sites covered by LEAP dataset, point classification is not reliable to identify laser pulses that hit water surface. Here, points in pink are classified as water (class 9) and green, as ground (class 2). On the right, satellite image of the same sector.

5.2.2.1.5. Performance assessment

To assess the performance of the applied correction technique, corrected DEMs accuracy was compared with four other DEMs obtained from widely used LIDAR ground filtering techniques (Figure 120): *Minimum-bin gridding* (MBG), *Ground classified points* (GCP), *Kraus and Pfeifer's ground filter* (KGF) (Kraus and Pfeifer, 1998) and *Zhang et al.'s progressive morphological ground filter* (PGF) (Zhang et al., 2003). For MBG, the DEM was created with the *LAS Dataset To Raster tool* in *ArcGISPro* with the minimum binning technique and linear void-filling method at a 2 m resolution. GCP was obtained by filtering the LIDAR cloud, keeping only "class 2" points, and using the same tool as MBG, with the average binning technique and linear void fill method at a 2 m resolution. KGF and PGF were applied to the raw LIDAR cloud via *PyFor* (Frank B., 2019), a *Python* package that holds ground filtering modules based on these two techniques. A 2 m window cell, as well as default parameters were used in this case.

The government of Ontario recently created 0.5 m and 1 m resolution DEMs with the LEAP and LIO LIDAR point clouds (Government of Ontario, 2019). These DEMs (named ONT in the following tables and figures) include coverage for nine of the selected sites, which in these cases allows additional accuracy comparison with the corrected DEMs developed for this study.

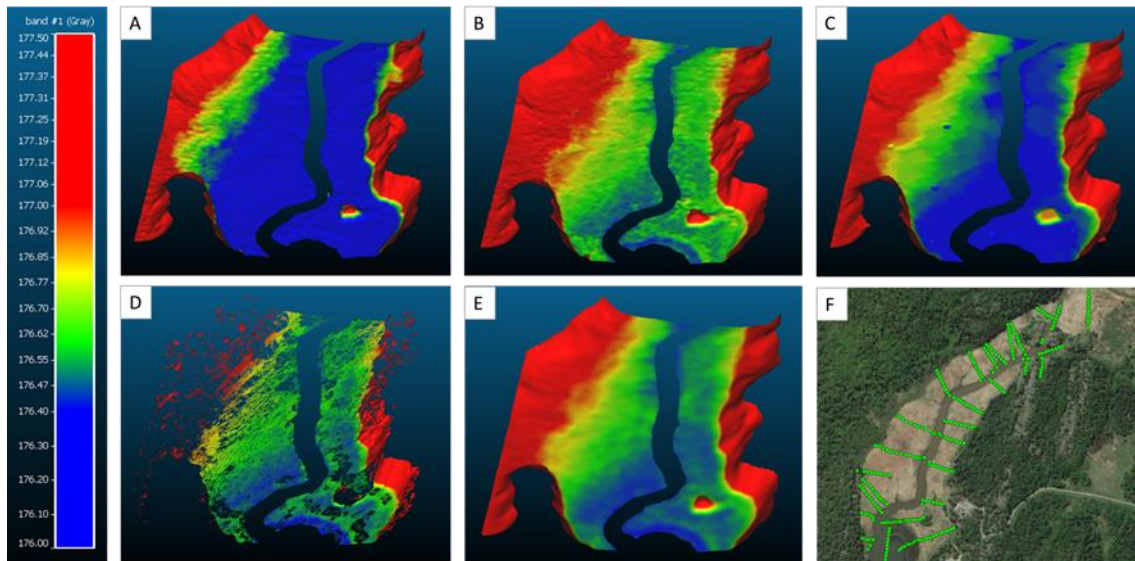


Figure 120: DEM generated with five different techniques on a portion of Anderson Creek (23ACK). A) LMT B) GCP C) PGF D) KGF E) MBG. F) Satellite image of the sector with ground truth points in green. (Z=10x)

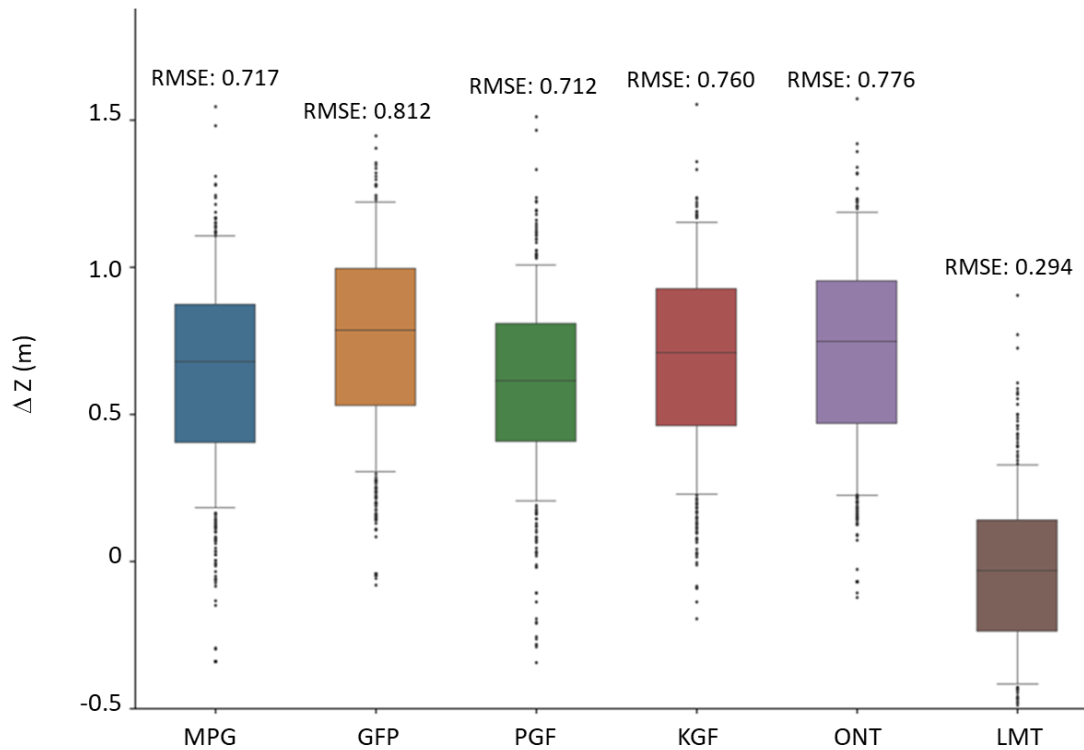


Figure 121: Error values obtained when comparing elevation values from 6 LIDAR-derived DEMs and ground-truth points for Long Point Wetlands (9LPW). Corrected DEM is on the right end and is identified as LMT (LEAN modified technique).

The RMSE relative to ground-truth point elevations was calculated for each DEM to support an accuracy comparison (Figure 121). Outliers, detected as values outside an interval spanning over the mean plus/minus three standard deviations, were removed to avoid extreme elevation values. For each site, DEM accuracy was then compared based on their respective RMSE. In spite of drawbacks observed in the analysis of the spatial variability of errors, RMSE-based comparison of DEM elevations with ground-truth values offers an appropriate way to provide error estimate and has been used in several previous studies (Gonga-Saholiariliva *et al.*, 2011).

As illustrated by the results obtained (Table 33 and Table 34), the modified LEAN technique (LMT) provided the most accurate DEM for 16 of 18 sites²⁵ (most accurate was PGF for 2 sites), with an average RMSE of 25 cm (with minimum and maximum values of 15.6 cm and 42.5 cm, respectively). On average (Table 34), this technique reduces the error by 45% (20.8 cm)

²⁵ Please note that since Lake St. Clair (13LSC) and Johnston Bay (14SAM) area of interest are overlapping, only one DEM has been generated covering both sites AOs. It is referred to as 13LSC in the tables and figures of that section.

compared to MBG, 55% (30.9 cm) compared to GCP, 38% (15.4 cm) compared to PGF, 53% (28.5 cm) compared with KGF, and 51% (25.9 cm) compared to ONT. For a vast majority of tested sites, the LMT created a more accurate DEM than the five other methods and, on average, reduced elevation errors by 48% (24.3 cm). This technique performed best in South Bay Marsh (3SBM), with an average reduction of 66% (39.8 cm) in RMSE; however, it was less effective in Jordan Station (6JSM), with 1% (0.15 cm) increase in average error over other DEMs.

Table 33: Root mean square errors (in meter) between ground-truth points and DEMs generated with 6 different techniques.

	Post-Processing Technique					
	MBG	GCP	PGF	KGF	ONT	LMT
1HIE	0.374	0.398	0.277	0.586	0.391	0.257
2ACM	0.353	0.544	0.261	0.543		0.294
3SBM	0.501	0.638	0.454	0.628	0.587	0.189
5LCM	0.27	0.351	0.205	0.343		0.174
6JSM	0.43	0.454	0.359	0.451		0.425
7GRM	1.017	1.222	0.719	1.171	0.409	0.34
8SPP	0.394	0.56	0.357	0.477	0.427	0.204
9LPW	0.717	0.812	0.712	0.76	0.776	0.294
10RBY	0.496	0.637	0.465	0.553	0.558	0.306
11FCK	0.258	0.351	0.259	0.303	0.314	0.189
12DRM	0.384	0.488	0.35	0.441	0.449	0.247
13LSC	0.603	0.737	0.558	0.67	0.672	0.295
15BDD	0.415	0.47	0.396	0.465		0.212
16HBW	0.399	0.474	0.382	0.433		0.252
18HGW	0.446	0.529	0.443	0.505		0.19
19TBY	0.294	0.356	0.268	0.345		0.156
22WHW	0.532	0.601	0.5	0.552		0.248
23ACK	0.369	0.438	0.305	0.403		0.235
Average	0.458	0.559	0.404	0.535	0.509	0.250
Min	0.258	0.351	0.205	0.303	0.314	0.156
Max	1.017	1.222	0.719	1.171	0.776	0.425

It is worth noting that the LMT correction technique showed the poorest performance and was outperformed by PGF (2ACM and 6JSM) at sites where the statistical model returned only one significant term, the constant c . Thus, a constant pixel-independent value was subtracted from each of the raw elevation values, rather than a specific value derived from each pixel elevation and NDVI values, as it was the case at the other sites.

Table 34: Comparison of RMSE values from DEMs created with LEAN modified technique (LMT) and five other ground filtering techniques.

	RMSE Difference		Nb of Sites
	(cm)	(%)	
MBG-LMT	20.8	45	18
GCP-LMT	30.9	55	18
PGF-LMT	15.4	38	18
KGF-LMT	28.5	53.2	18
ONT-LMT	25.9	50.8	9
Average	24.3	48.4	

An average residual error of 25 cm might seem relatively high for flat areas such as coastal wetlands. However, given the swampy and muddy nature of wetlands (Figure 122), as well as the accuracy of GNSS receivers (~5 cm) which can result in errors of several centimeters when measuring ground truth elevations, this error range is acceptable and the precision of the resulting elevation values is considered suitable for the CWRM.



Figure 122: Pictures taken in South Bay Marsh (3SBM) showing the swampy and muddy nature of the terrain, which can leads to errors of several centimeters when measuring ground truth elevations.

5.2.2.2. Imagery-derived DEMs correction

Since LIDAR point cloud data were not available for Frances Point (27FPT), the imagery derived DEM was used as primary topographic datasets for this site.

This DEM is derived from digital imagery acquisition at 20 cm Ground Sample Distance. The image is first classified by an automated filtering routine to identify the ground surface and remove above-ground features, and remaining points are then triangulated and interpolated on a regular

2m grid (Government of Ontario, 2016 and 2017). When the ground is not visible in the original imagery, as is often the case in areas such as wetlands or dense forests, the automated routine cannot identify ground points, and low points in the canopy can be misinterpreted as ground values. This is an important limitation of imagery-derived DEMs, and these digital models cannot be considered accurate representations of the bare-earth elevation surface.

Thus, a correction process similar to the one applied to LIDAR-derived DEMs was used to correct this imagery derived DEM to minimize elevation errors and improve accuracy. Mainly, the LEAN correction method (Buffington *et al.* 2016) was applied to the 2 m resolution DEM. RMSE value of 27.3 cm was obtained for 27FPT, which is similar to LIDAR-derived DEM values but represents a reduction in error values of only 6.5% compared to the uncorrected DEM (29.2 cm). Therefore, the LEAN correction method was less performant for this imagery-derived DEMs than it was for LIDAR-derived DEMs, for which the average error reduction was 45% (cf. Table 34).

Since the topographic datasets used for Frances Point differ from those used for the other sites, this wetland was not included in the accuracy assessment (cf. Section 5.3.1).

5.2.3. Bathymetry datasets

DEMs had to be completed using bathymetric datasets as each AOI spanned both aquatic and terrestrial environments, and LIDAR datasets are not reliable on water (cf. Section Identify the land-water interface). As no recent bathymetric survey campaign was available for the entire Great Lakes region, multiple datasets were used to cover the selected sites. These datasets were collected by various organizations, using several technologies, at different periods and times. Even after consolidating all available bathymetric information, ECCC had to conduct bathymetric surveys at some study sites to fill outstanding data gaps.

5.2.3.1. Targeted bathymetric surveys

Within predetermined, spatially explicit polygons, ECCC and BC2, an independent contractor, collected depth data relative to water-level surface elevation at the time of the survey. By following the Ministry of Natural Resources and Wildlife's Bathymetric Inventory Standardization Guide (Arvisais & Demers, 2011), bathymetry transects were positioned based on the area and morphology of each wetland. These transects were located perpendicular to the shore, with multiple crossings and shore-side branches (Figure 123) to validate the accuracy of the collected RTK topographic data (cf. Section Ground truth points collection).

The bathymetric surveys were performed by motor boat (Zodiac or Jon boat), using a single beam echosounder to ensure sufficient sampling in shallow (≤ 1.2 m in depth) and open water habitats (>1.2 m). BC2 collected sonar data using an Echotrac CV100 (Teledyne Technologies Inc., Thousand Oaks, CA), and recordings were georeferenced using an Arrow 200 RTK GPS Receiver (Eos Positioning Systems Inc., Terrebonne, QC). ECCC logged water depth using a HydroBox v. 2.45 (SyQwest Inc., Cranston, RI), and recordings were georeferenced horizontally using a Trimble GeoXH GPS unit (Trimble Inc., Sunnyvale, CA). Collected water depths were exported and corrected using daily water levels (measured *in situ*; cf. Section Ground truth points collection), as well as the transducer draft. HYPACK (Xylem Inc., Rye Brook, NY) was the hydrographic software employed by both teams for navigation and data acquisition, recording one point every tenth of a second. Collected bathymetric data were exported via HYPACK, and post-processed with ArcGIS 10.5.1.

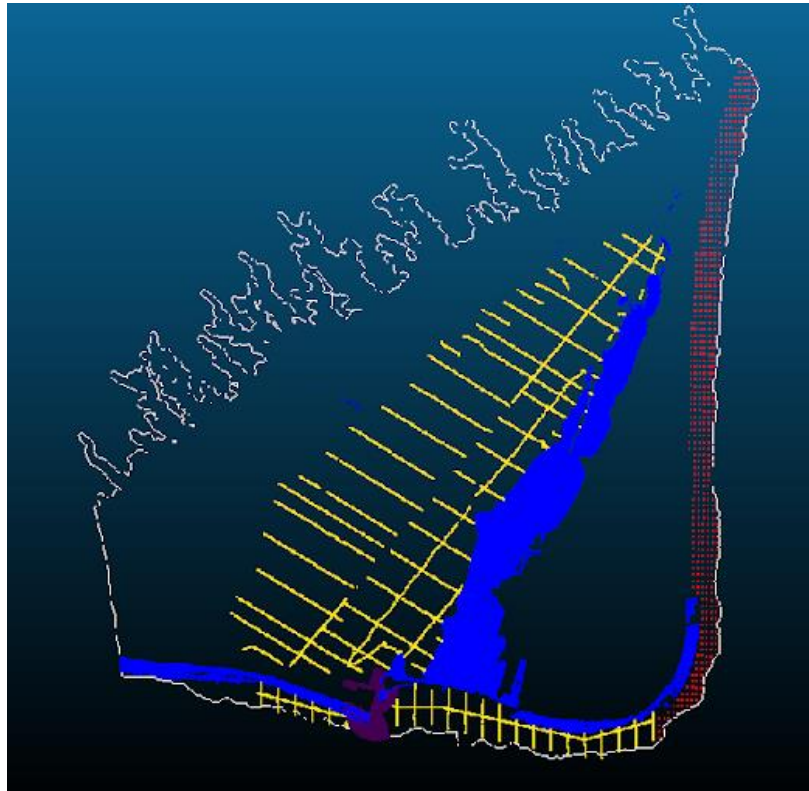


Figure 123: Different bathymetry datasets used for 10RBY DEM. Blue: bathymetric LIDAR dataset; Yellow: echosounder dataset from BC2; Purple: echosounder dataset from Fisheries and Oceans Canada; Red: Bathymetry grid from NOAA; White: Area of interest boundaries.

5.2.3.2. Dataset prioritization and elevation shift

Since more than one bathymetric dataset were used to cover the lacustrine area in most sites, the datasets had to be ordered in priority, with the best bathymetric measurements defined as the preferred measurements. Precision and accuracy are the two main characteristics that were used to quickly assess datasets quality and facilitate prioritization. Accurate data have values that are close to reality (low RMSE when compared to ground truth points), while precise data are linked to high spatial resolution, which takes good account of the elevation variability.

For many sites, bathymetric LIDAR datasets (IIC Technologies, 2018) were available. Those datasets are covering a large portion of the nearshores area with high point density (1.6 to 8 points per m²) and detect bathymetric variability with high precision. However, when compared to bathymetric data collected by BC2 and CWS (hereafter referred to as echosounder datasets), these more precise bathymetric LIDAR datasets appeared less accurate since they had larger elevation difference with ground truth points (e.g. Figure 124).

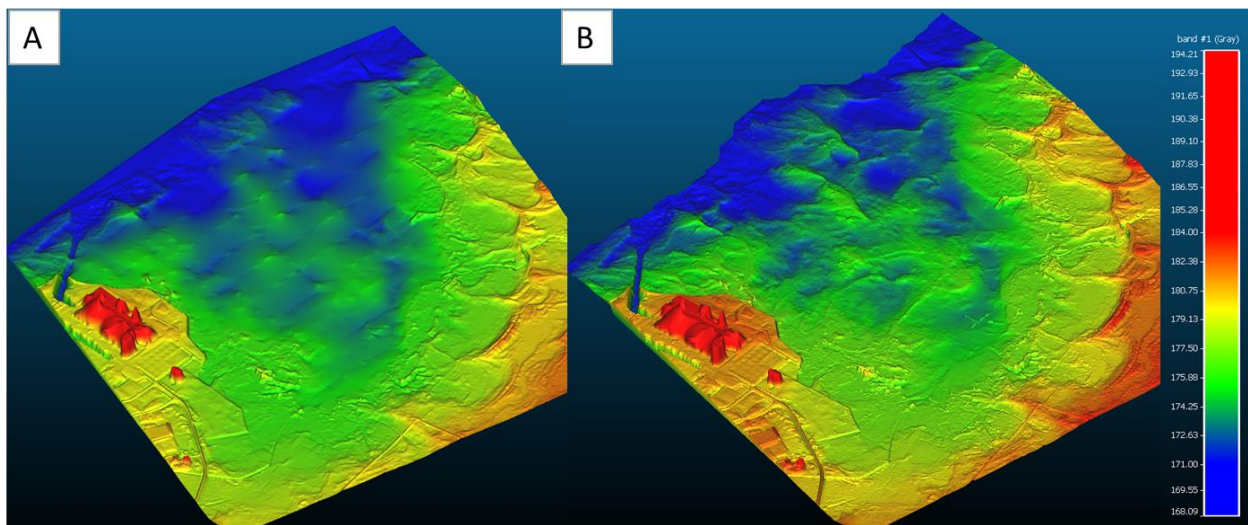


Figure 124: A) DEM of Baie du Doré (15BDD) generated with echo-sounder dataset for the water portion of the lake; RMSE=0.57m; B) DEM of Baie du Doré (15BDD) generated with bathymetric LIDAR dataset for the water portion of the lake; RMSE=0.87m; (Z=10x).

In order to take advantage of the precision of one dataset while maintaining the accuracy of the second, bathymetric LIDAR elevation values were modified to recover the accuracy otherwise obtained from the echo sounder data. This correction was made by plotting the observed difference in elevation between the echo-sounder and bathymetric LIDAR points, within 0.5, 1.0, and 1.5 m from each other. The error calculated from these different radii was found to be relatively constant, with a small distribution of values around the mean and median (Figure 125),

indicating the existence of a systematic error between the two datasets. It was therefore possible to correct the bathymetric LIDAR dataset based on the difference in median elevation between the two datasets. The resulting bathymetric LIDAR dataset is precise and accurate, with high resolution elevation values closer to ground truth points. This method increases bathymetric LIDAR accuracy and provides better consistency between the two bathymetric datasets, creating seamless DEMs (Figure 126).

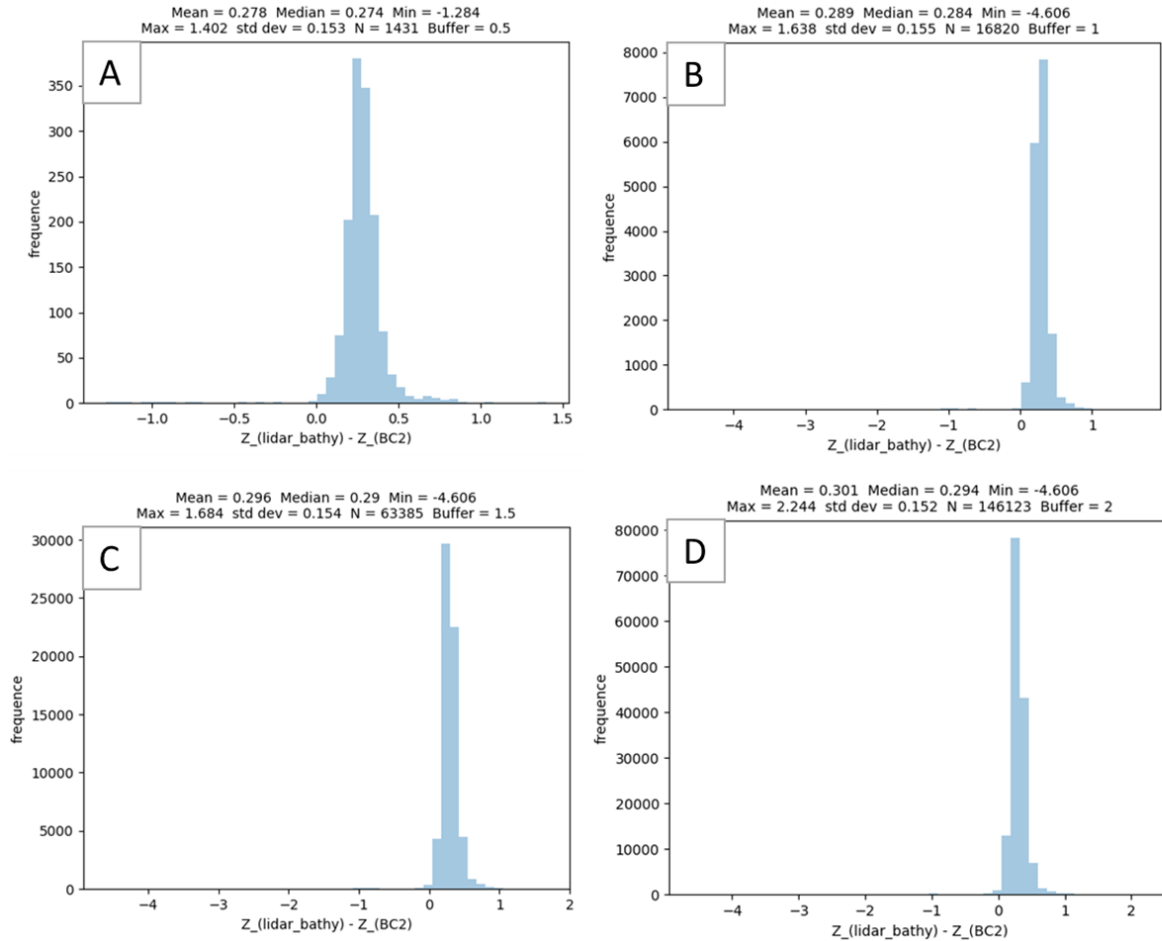


Figure 125: Elevation difference between echosounder points and bathymetric LIDAR points that are within a 0.5 (A), 1m (B), 1.5m (C) and 2m (D) radius from each other. In this case, 0.28m was subtracted from bathymetric LIDAR elevation values.

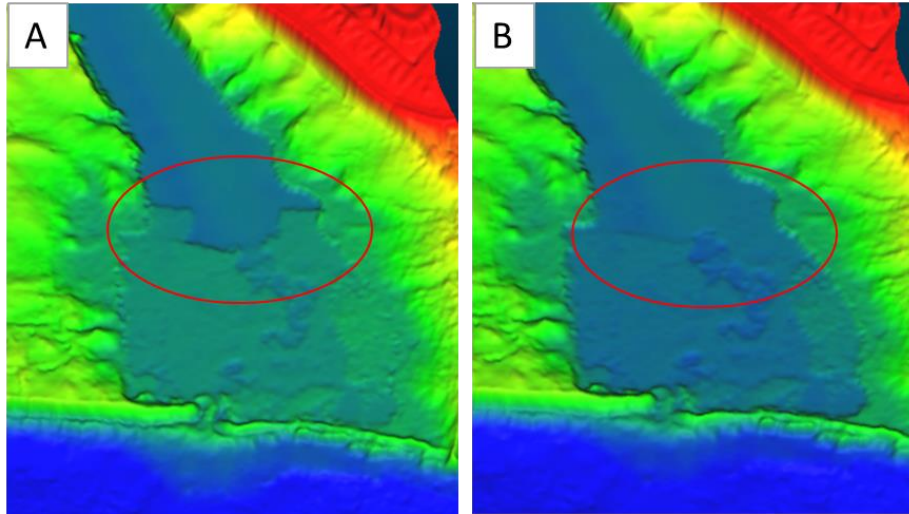


Figure 126: Bathymetric LIDAR elevation shifts ensure seamless DEMs in transitions zones between two different bathymetric datasets (circled in red). A) DEM generated without elevation shift and B) DEM generated with elevation shift at 5LCM ($Z=10x$).

With a few exceptions, when bathymetric LIDAR datasets were available for one site, the data were modified according to the technique described above and used as a primary source of bathymetric data to generate the DEM. Then, soundings datasets were used to complete areas that were not covered by the bathymetric LIDAR. Finally, other bathymetric datasets collected from *Fisheries and Ocean Canada* or NOAA were used to fill gaps when necessary.

5.2.4. DEM creation and interpolation methods

As mentioned previously, DEMs are grids where each cell value represents the elevation of the terrain. To generate a regular grid with point clouds and datasets of different density, these datasets need to be interpolated to the DEM grid. The DEM spatial resolution is 2 m, which is lower than most of the datasets used. Therefore, several elevation values can be assigned to the same grid cell, which corresponds to the different points within that cell. Since the DEM seeks to represent the bare earth, each cell was assigned the lowest elevation value available, which is known as the minimum-bin gridding interpolation technique.

While this technique works in areas covered by datasets of high point density, it fails in areas covered by sparse datasets, where elevation value cannot be assigned to many grid cells. In these instances, elevation was estimated from surrounding measurements using an alternative interpolation technique. This interpolation method has to be chosen with caution since it can introduce errors. In most cases, a Natural Neighbour interpolation method (with *LAS Dataset To Raster* tool in *ArcGIS PRO*) was selected. It is an area-based interpolation technique that better

accounts for data density variation than distance-based techniques (Amidor, 2002) such as Inverse Distance Weight or Nearest Neighbour (Figure 127). This approach is quite useful here since data density varies greatly from one dataset to the other and an empty grid cell's elevation can be interpolated from different datasets.

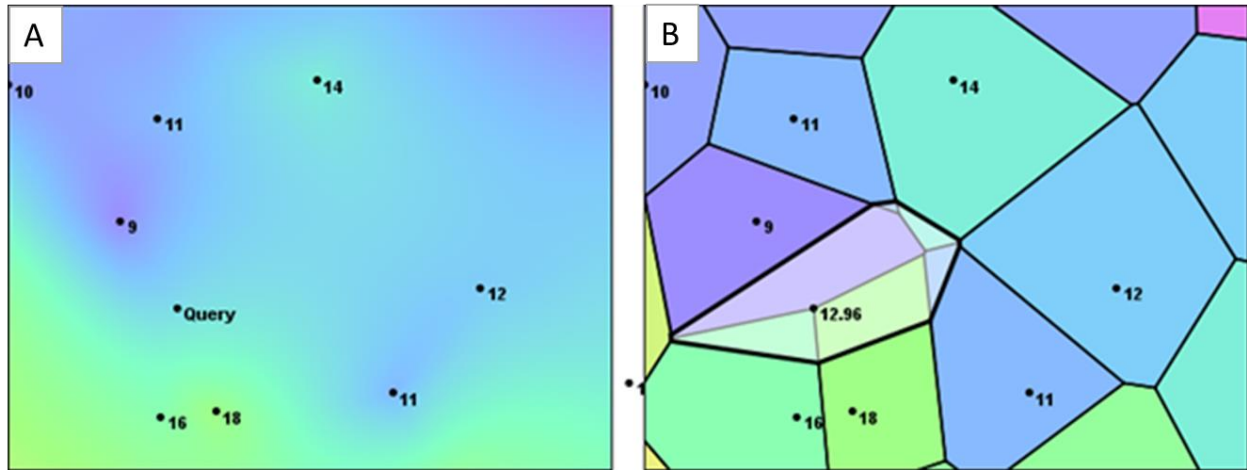


Figure 127: With distance-based weight interpolation (A) query point's value would be the average of the 3 surrounding known values (14.33) over-representing the dense values (16 and 18), while area-based interpolation (B) would give a lower value (12.96). Source: (Lucas G., 2011)

However, the Natural Neighbour technique is unsuccessful in creating discontinuity-free DEMs when used to interpolate echosounder datasets collected along transects. These datasets have high point density along localized lines that can be as much as 100 m apart. When interpolated with Natural Neighbour technique, these datasets created important artifacts that do not accurately represent real terrain bathymetry. Therefore, Ordinary Kriging interpolation was used for echosounder data, using a Spherical Variogram on a 5 to 10 m grid (depending on site size and computation capacities; e.g. Figure 128). Ordinary kriging was performed with *PyKriging* Python toolkit (Copyright (c) 2015-2018, PyKriging Developers), with 12 lags and more weight given to first lags.

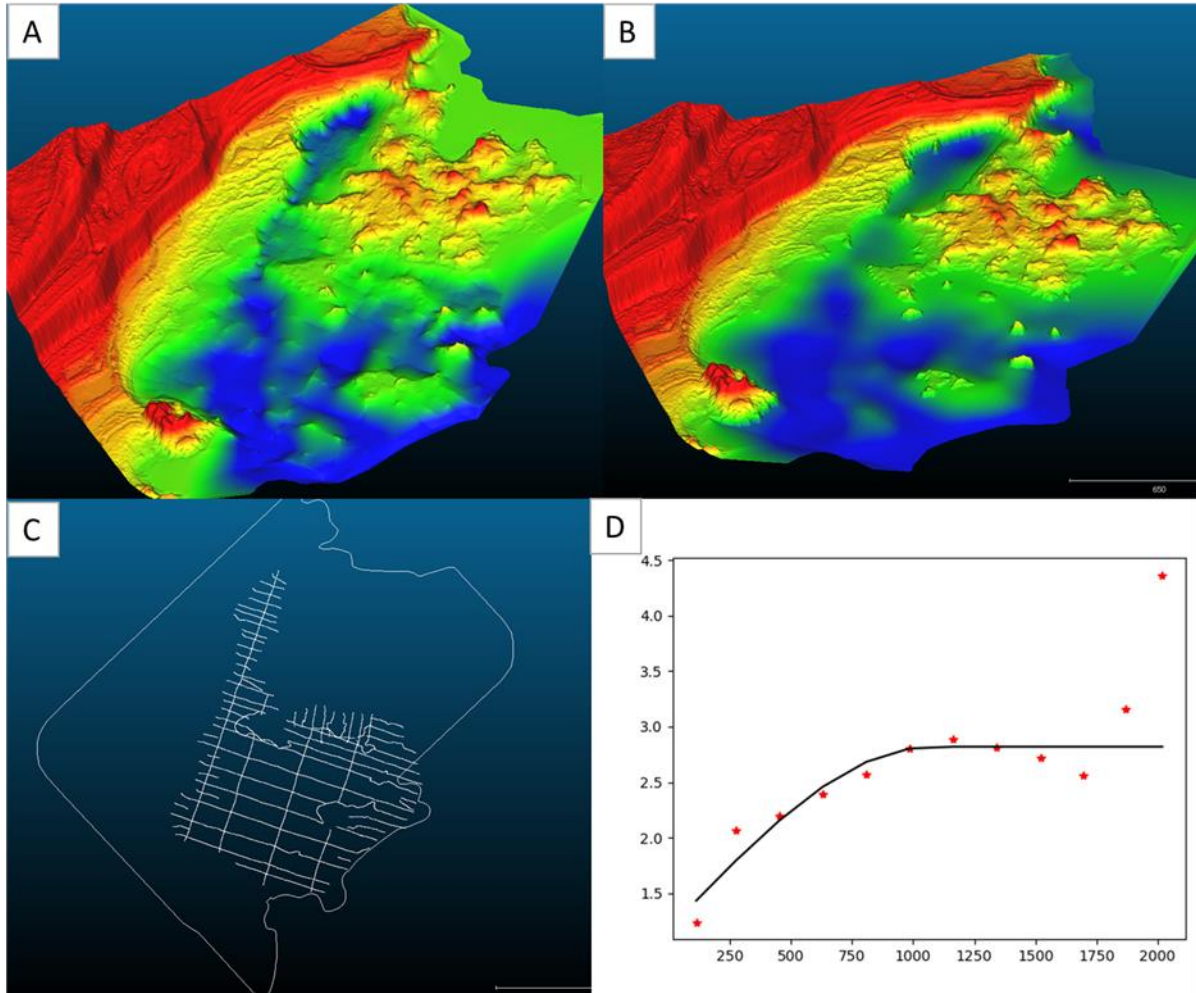


Figure 128: A) 19TBY DEM created with echosounder dataset interpolated with Natural Neighbour technique. B) Treasure Bay's DEM created with echosounder dataset interpolated by Ordinary Kriging. C) Treasure Bay echosounder dataset. D) Spherical variogram.

5.2.5. DEMs filtering

Outliers may persist as a result of the post-processing treatments described above, creating unwanted noise and peak and dips in the final DEM (e.g. Figure 129). To create flawless DEMs, image-filtering techniques were applied to the corrected models to eliminate questionable values. There are many filters that can be combined and applied with different intensities to achieve cumulative effects. It is therefore important to carefully select which filters to apply and how to apply them in order to properly remove outliers without altering the original DEM accuracy.

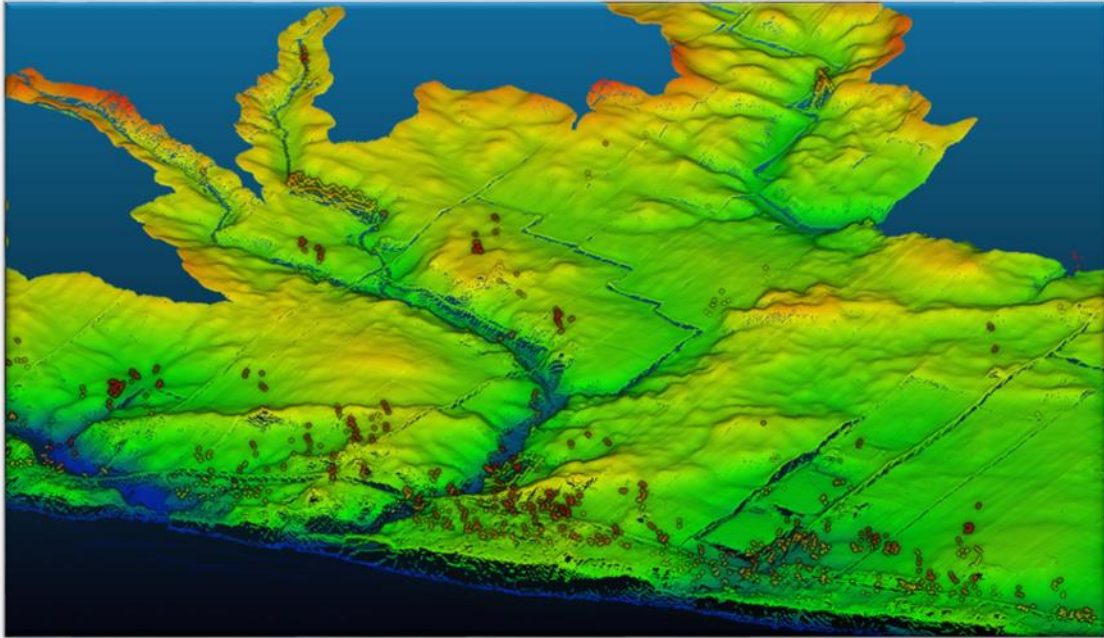


Figure 129: Fox Creek's DEM (11FCK) before filters were applied (outlier values appear in red).

After some literature review and a trial and error process, the *RemoveOffTerrainObjects (ROTO)* filter developed by John Lindsay from University of Guelph (Lindsay J., 2018) was used, followed by a *Gaussian* filter. *ROTO* is described as a tool that “is typically applied to LIDAR DEMs which frequently contain numerous off-terrain objects (OTOs) such as buildings, trees and other vegetation, cars, fences and other anthropogenic objects” (Lindsay, 2018). The filter was applied with the *WhiteboxTools Python* package (Copyright (c) 2017-2019 John Lindsay), with the filter parameter set at 15 and slope, at 10. Gaussian filter was also applied via *WhiteboxTools* with sigma value set to 1, which corresponds to a 9-pixel kernel size. This combination achieved removal of outliers without altering DEM quality and was used for all selected study sites (e.g. Figure 130).

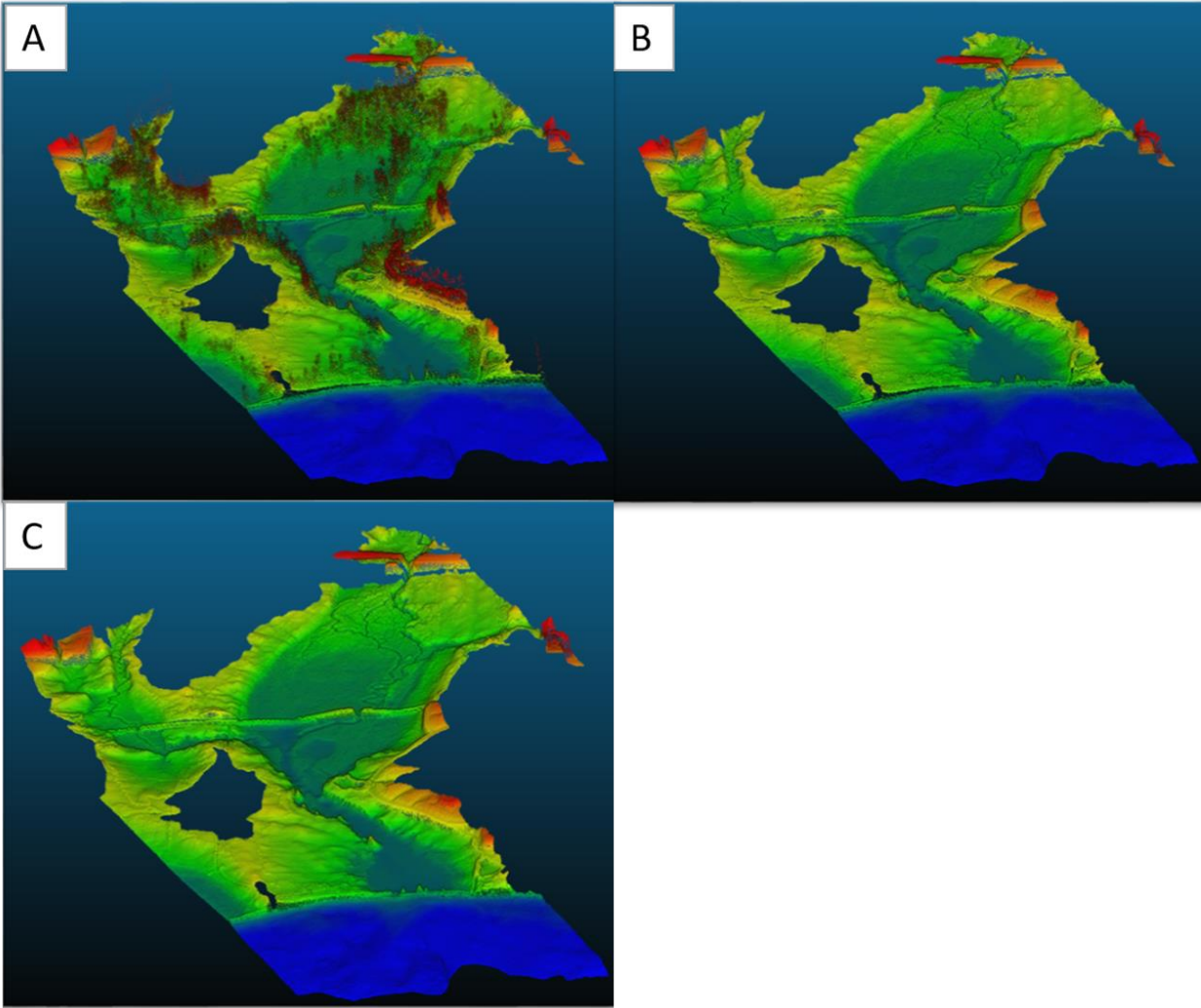


Figure 130: Lynde Creek Marsh's DEM: A) With no filter applied; B) With ROTO filter applied; C) with ROTO and Gaussian filters applied.

5.2.6. Extraction of elevation values on CWRM grid

To meet the needs of the CWRM, elevation values from 2 m resolution DEMs were interpolated on to CWRM 10 x 10m grids. A k-dimensional tree was created from the 2x2 m elevation data using the *ckDTree* class from *Scipy Python* library (Jones *et al.*, 2001), with a leaf size of 16. This tree was then used to identify the closest elevation value of the 10 x 10m grid points, assign it to the point grid and thus provide the final elevation value for the CWRM (Nearest Neighbour Interpolation; Figure 131).

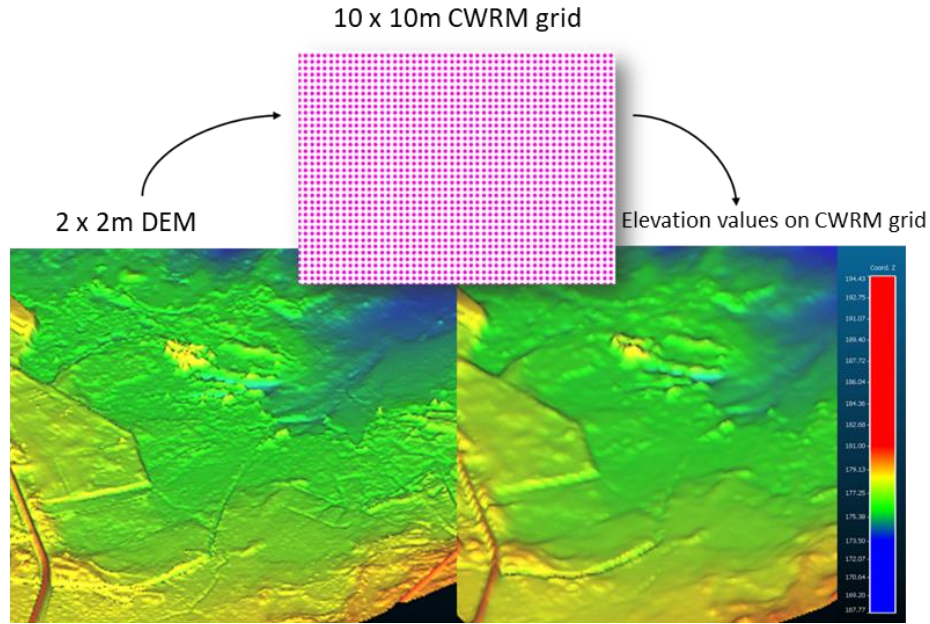


Figure 131: Baie du Doré's (15BDD) 2 m resolution DEM elevation values are transferred on the 10 x 10m CWRM grid.

5.2.7. Primary terrain attributes

From the 10 m resolution DEMs three, primary terrain attributes were calculated and generalized at 5 different resolutions (10, 30, 130, 250 and 310 meters).

5.2.7.1. Slope

Slope calculation was realized using the "Slope" tools from *WhiteboxTools Python* package (Copyright (c) 2017-2019 John Lindsay). The tool uses Horn's 3rd-order finite difference method to estimate slope (Horn, 1981). Following the clock-type grid cell numbering scheme presented in Figure 132, the slope of cell 9 in degree is calculated as:

$$Slope = \arctan(f_x^2 + f_y^2)^{0.5} \quad 5.5$$

$$f_x = (z3 - z5 + 2(z2 - z6) + z1 - z7) / 8 * \Delta \quad 5.6$$

$$f_y = (z7 - z5 + 2(z8 - z4) + z1 - z3) / 8 * \Delta \quad 5.7$$

, where Δx and Δy are the grid resolution in the x and y directions, respectively, which is 10 meters here. Mainly, this slope calculation technique uses a moving 3x3 window, which predicts the slope of the central cell, based on its eighth neighbours. The Horn equation (also known as

Neighbouring technique) tends to smooth the slope surface, and so it may lead to a loss of local variability in the spatial distribution of slopes over the domain (Dunn *et al.*, 1998).

7	8	1
6	9	2
5	4	3

Figure 132: Clock-type grid cell numbering scheme.

5.2.7.2. Aspect

Aspect (or slope orientation) was calculated using the « aspect » mode of « gdaldem » tool of the GDAL library (GDAL, 2019). This tool also uses Horn's 3rd-order finite difference method to estimate the slope (Horn, 1981) from which it extracts the angle between the x and y components of the slope (equation 5.6 and 5.7):

$$\theta = \tan^{-1}\left(\frac{f_y}{f_x}\right) \quad 5.8$$

, where θ is the angle between the 2 slope components, which is then adjusted to give a slope of 0° for a slope facing North, and 90° , for a slope facing east. Aspect values are finally grouped in 8 categories corresponding to the cardinal (N, E, S, W) and ordinal (NE, SE, SW, NW) directions.

5.2.7.3. Profile curvature

Profile curvature was calculated from DEMs values using the “ProfileCurvature” tool from *WhiteboxTools Python* package (Copyright (c) 2017-2019 John Lindsay). This algorithm uses the plan curvature formula defined by Gallant and Wilson (2000). It expresses the degree of downslope acceleration or deceleration within the landscape in a specific direction, which is chosen here as the slope orientation. Curvature values are grouped in convex (negative values) and concave (positive values) categories.

5.2.7.4. Multi-scale moving window average

In order to describe primary terrain attributes global patterns and micro-topographic variations, slope, aspect, and profile curvatures were calculated at 5 different resolutions (10, 30, 130, 250,

and 310 meters). Coarser resolutions were obtained by averaging the 10 m slope, aspect and curvature gridded data within moving windows of 3x3, 13x13, 25x25 and 31x31 pixels. This task was performed using the “MeanFilter” tool from the *WhiteboxTools Python* package (Copyright (c) 2017-2019 John Lindsay).

5.3. Results

5.3.1. DEMs accuracy assessment

5.3.1.1. Root Mean Square Error

The accuracy of the DEMs was assessed by calculating the RMSE between DEM elevation values and all available ground truth points (located in the land and lacustrine portion of the wetlands). The accuracy of DEMs was also analyzed through the error frequency distribution, which details the dispersion of values and proportion of sampled points with errors below a particular threshold. Here, the proportions of the distribution with absolute error less than 50 cm, 25 cm and 15 cm were calculated. Table 35 shows the accuracy assessment results obtained for all LIDAR-derived DEMs.

Table 35: Accuracy assessment of the final DEMs.

	Nb.	Errors			Proportion < Threshold			
		Control points	RMSE*	Mean**	Median**	< 15 cm	< 25 cm	< 50 cm
			(m)	(m)	(m)	(%)	(%)	(%)
1HIE	356	0.20	0.15	0.10	65	79	97	
2ACM	260	0.29	0.23	0.20	35	60	92	
3SBM	449	0.26	0.18	0.14	52	76	93	
5LCM	422	0.16	0.12	0.10	70	90	99	
6JSM	356	0.33	0.28	0.27	29	47	90	
7GRM	384	0.38	0.28	0.21	37	59	83	
8SPP	390	0.22	0.16	0.12	57	80	95	
9LPW	467	0.36	0.28	0.21	39	57	84	
10RBY	317	0.37	0.27	0.20	37	62	85	
11FCK	363	0.20	0.14	0.10	62	83	98	
12DRM	528	0.29	0.26	0.20	40	56	85	
13LSC	727	0.31	0.22	0.16	48	69	90	
15BDD	378	0.25	0.18	0.13	56	72	94	
16HBW	380	0.32	0.26	0.22	34	58	90	
18HGW	361	0.22	0.17	0.14	52	75	98	
19TBY	438	0.24	0.17	0.11	64	79	94	
22WHW	251	0.23	0.18	0.15	50	71	96	
23ACK	388	0.24	0.19	0.17	42	70	96	
Average	401	0.27	0.21	0.16	48	69	92	
Min	251	0.16	0.12	0.10	29	47	83	
Max	727	0.38	0.28	0.27	70	90	99	

*Outliers were removed based on standard deviation and average values (plus and minus 3 x standard deviation).

** Median and mean calculated on absolute values.

Based on 7215 sample points throughout 18 wetlands²⁶, average RMSE was estimated at 27 cm (ranging from 16 to 38 cm), with an average median error of 16 cm (ranging from 10 to 27 cm).

Nearly half of the points sampled (48%) had an error less than 15 cm, 69% less than 25 cm and 92% less than 50 cm. The environmental conditions underlying the data collection (i.e. unconsolidated earth) must be considered when interpreting these results, as well as the accuracy of the GNSS receiver (~5 cm) that can produce errors of several centimeters when recording elevation. In this context, results shown in Table 35 are acceptable for the needs of the CWRM, which must integrate robust and representative elevation data in wetlands.

²⁶ Please note that since Lake St. Clair (13LSC) and Johnston Bay (14SAM) area of interest are overlapping, only one DEM has been generated covering both sites AOIs. It is referred to as 13LSC in the tables and figures of that section.

As a comparison, the accuracy of the recently created DEMs by the Government of Ontario (Government of Ontario, 2019) was estimated based on the same set of ground-truth points. Only inland ground-truth points of the area of interest were kept for this analysis since no bathymetric datasets were used to create these DEMs. The inclusion of all ground-truth points would have exaggerated the error and underestimated the accuracy of the Government of Ontario DEMs.

Table 36: Accuracy assessment of Government of Ontario DEMs.

	Nb.	Errors			Proportion < Threshold		
		RMSE*	Mean**	Median**	< 15 cm	< 25 cm	< 50 cm
		(m)	(m)	(m)	(%)	(%)	(%)
1HID	214	0.39	0.32	0.26	27	46	80
3SBM	342	0.59	0.57	0.57	1	2	34
7GRM	329	0.41	0.36	0.35	16	32	81
8SPP	342	0.43	0.36	0.36	21	38	75
9LPW	407	0.77	0.69	0.74	9	20	27
10RBY	263	0.56	0.47	0.48	18	24	55
11FCK	251	0.31	0.27	0.28	27	43	93
12DRM	426	0.45	0.37	0.35	26	40	66
13LSC	541	0.56	0.50	0.50	8	18	51
Average	346	0.50	0.43	0.43	17	29	62
Min	214	0.31	0.27	0.26	1	2	27
Max	541	0.77	0.69	0.74	27	46	93

*Outliers were removed based on standard deviation and average values (plus and minus 3 x standard-deviation).

** Median and mean calculated on absolute values.

Based on 3115 sampled points through nine wetlands (Table 36), the average RMSE for the Government of Ontario's DEMs is 50 cm (compared to 29 cm for their corresponding corrected DEMs), with an average median error of 43 cm (compared to 16 cm). About 17% of sampled points have an error of less than 15 cm, 29% less than 25 cm, and 62% less than 50 cm (compared to 49%, 70%, and 91%). Thus, the corrected DEMs developed for this study were found to be more accurate for all sites, with a 42% decrease in RMSE compared to Ontario's products and a 63% decrease in mean median error.

Table 37 shows RMSE values for imagery-derived DEMs, which tends to be slightly higher than those observed from LIDAR-derived DEMs.

Table 37: Accuracy assessment of imagery derived DEM.

	Nb.	Errors			Proportion < Threshold		
		RMSE*	Mean**	Median**	< 15 cm	< 25 cm	< 50 cm
		(m)	(m)	(m)	(%)	(%)	(%)
27FPT	430	0.34	0.26	0.20	40	56	85

5.3.1.2. DEM error distribution

As shown in Figure 133, most of the corrected DEM error distributions are centered near zero. The LIDAR-derived DEM’s correction technique, as well as the interpolation used to produce the bathymetric data, did not introduce a systematic elevation bias. As mentioned previously, a positive elevation bias is generally associated with uncorrected, LIDAR-derived DEMs, which leads to a shift in the error distribution curves. Such a shift can be observed in the error distribution of the Government of Ontario’s products (Figure 134), and for sites where the correction method did not work properly (i.e. 2ACM, 6JSM; Figure 133). It is therefore possible to conclude that, for most sites, the *LEAN Modified Technique* removed most of the positive elevation bias typically associated with LIDAR-derived DEMs. The same result was observed in the imagery-derived DEM that was created for 27FPT, where the LEAN correction method also performed well.



Figure 133: Distribution of DEM's elevation error for the 19 study sites²⁷. Most sites have a distribution centered on 0 (red line). Only sites where the LIDAR correction method was less effective (2ACM, 6JSM) still have a positive elevation bias (curve shift to the right).

²⁷ Please note that since Lake St. Clair (13LSC) and Johnston Bay (14SAM) area of interest are overlapping, only one DEM has been generated covering both sites AOIs. It is referred to as 13LSC in the tables and figures of that section.

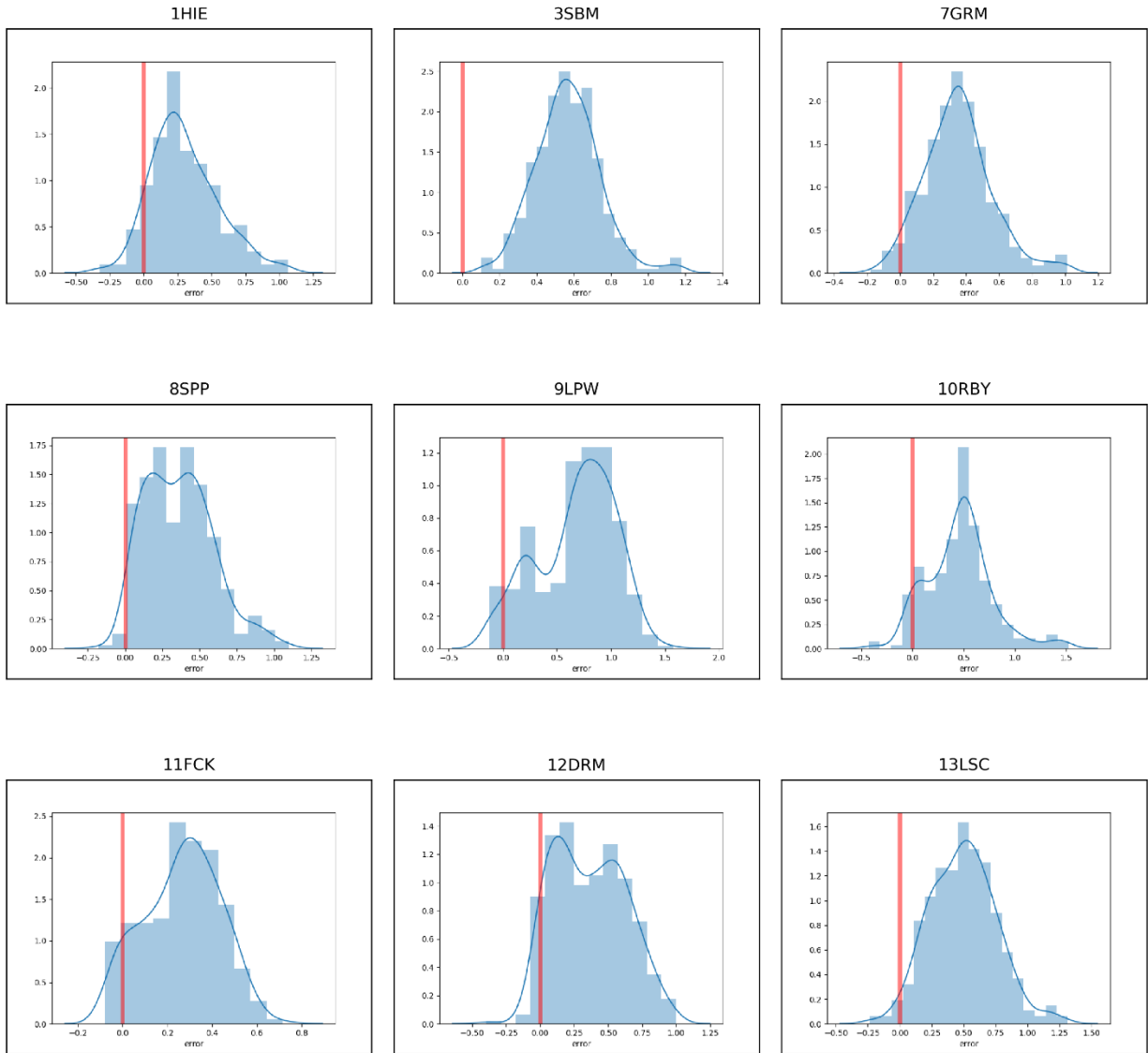


Figure 134: Error distribution between Government of Ontario DEMs and ground truth points for the 9 study sites. All sites show positive elevation bias (curve shifts to the right) which is typical of uncorrected LIDAR-derived DEMs.

5.3.1.3. Spatial distribution of errors

No trend was observed in the spatial distribution of errors extracted from the corrected DEMs (Figure 135). Nevertheless, the finer-scale spatial variability of DEM error has received much attention in recent years from the scientific community (Gonga-Saholiariliva *et al.*, 2011; Wilson, 2012), and many investigators have suggested that a better description of how these elevation errors may affect any further use (i.e. modelling) is needed. Methods such as the Local indicator of Spatial Association (LISA) (Anselin, 1995) have proven to be effective (Gonga-Saholiariliva *et al.*, 2011) and could be implemented through GeoDa open source software (Anselin *et al.*, 2006)

in further studies. Information on the spatial distribution of elevation errors coupled with satellite image classification techniques could likely help develop more efficient LIDAR-derived DEM correction methods.

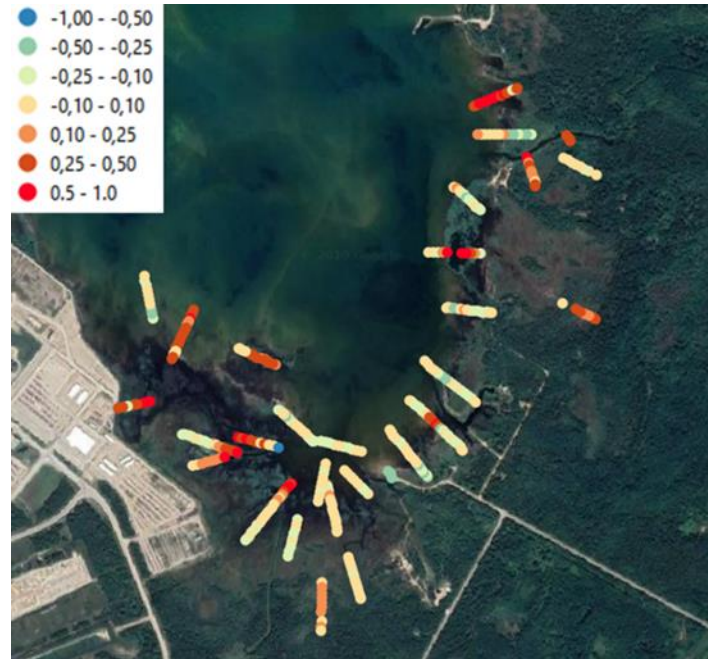


Figure 135: Residual elevation error in Baie du Doré DEM (15BDD) don't show any spatial distribution pattern. (Errors in m, final DEM elevation minus ground-truth point values).

5.3.2. Primary terrain attributes

Slope, aspect, and curvature gridded data were calculated at resolutions of 10, 30, 130, 250 and 310 m to describe global primary terrain attribute patterns, as well as small-scale topographic variations. Since no ground-truth measurements were collected for these parameters, it was not possible to conduct accuracy evaluation. Despite this, and given the accuracy results obtained for the corrected DEMs, key terrain attributes are based on robust, precise and accurate elevation values.

5.4. Summary

The post-processing technique described in this section led to the creation of 2 m resolution seamless DEMs, representing the integrated topography and bathymetry for 19 coastal

wetlands²⁸ in the Great Lakes region. Classified LIDAR point clouds were used as primary topographic datasets for 18 sites, and then corrected using the LEAN method (Buffington *et al.*, 2016) to overcome the deficiencies of raw LIDAR in providing accurate bare earth elevations in densely vegetated areas like coastal wetlands. Based on multivariate correlations between the collected ground-truth elevation, uncorrected DEM elevation, and Normalized Difference Vegetation Index (NDVI), this method estimates the error in each pixel of a LIDAR-derived DEM. This error is then subtracted from the original DEM to create a corrected DEM, which provides elevation values that are closer to ground-truth observations.

With this correction technique, the terrestrial portion of the 18 DEMs have an average RMSE value of 25 cm. Compared to DEMs created with other ground-filtering techniques, the corrected DEMs had the most accurate elevation values in 16 out of 18 cases, with a RMSE 38 to 55% (15 to 31 cm) lower than other DEMs. Thus, the chosen correction technique created more accurate DEMs, and thus helped to significantly reduce elevation errors on the land portion in the 18 wetlands where it was applied. For the site where LIDAR point clouds were not available, a similar correction technique was applied on imagery-derived DEM created by the Government of Ontario, although this achieve less error reduction (6.5%).

Multiple bathymetry datasets were used to complete the water-covered area of each wetland. Prioritization of the dataset and multiple manipulations (e.g. elevation corrections and vertical datum conversions) were required to create consistent and seamless datasets that could be interpolated on the DEM grids. Minimum-bin gridding interpolation was used where bathymetry datasets were denser, while Kriging and Natural Neighbour interpolation were preferred in areas covered by sparser datasets. Final DEMs were then filtered with *RemoveOffTerrainObjects* (ROTO) (Lindsay, 2018) and Gaussian filters.

Based on 7215 sample points throughout 18 wetlands²⁸, average LIDAR-derived DEMs' RMSE was 27 cm (ranging from 16 to 38 cm), with a mean median error of 16 cm (ranging from 10 to 27 cm). In comparison, the land portion of the DEMs created by the Government of Ontario had an average RMSE of 50 cm. Thus, the technique described in this section reduced the error by 46% (23 cm) on average.

²⁸ Please note that since Lake St. Clair (13LSC) and Johnston Bay (14SAM) area of interest are overlapping, only one DEM has been generated covering both sites AOs. It is referred to as 13LSC in the tables and figures of that section.

Considering the environmental conditions underlying the data collection (i.e. unconsolidated earth), and the sampling accuracy of the ground truth elevations on which the DEMs are based, the results obtained were judged acceptable for the needs of the CWRM, which must integrate robust and representative elevation data in wetlands. The elevation error distribution for each DEM was found to be centered on zero, which confirms that the applied DEM correction technique removed the systematic (positive) bias that is typically associated with LIDAR-derived DEMs.

Slope, aspect, and curvature were calculated from the elevation values of the corrected DEMs at a 2 m resolution. In order to describe the global pattern of these primary terrain attributes and their small-scale topographic variations, they were resampled at five different resolutions (10, 30, 130, 250 and 310 m). Finally, elevation and primary terrain attributes were interpolated on to each CWRM grid point (10 m x 10 m), based on nearest neighbour interpolation techniques.

In further studies, analysis on DEM error spatial distribution coupled with image classification and/or plant species clustering techniques could help to develop more advanced error correction methods and create DEMs that are even more accurate.

6. GREAT LAKES COASTAL WETLAND MODELLING

Authors: Dominic Thériault, M. Sc., Marianne Bachand, Ph.D., Sandrine Hogue-Hugron, M. Sc., Mathieu Roy, Ph.D., Jean Morin, Ph.D.

6.1. Vegetation modelling

Coastal wetlands are dynamic ecosystems influenced by abiotic factors such as nutrients, temperature and water level fluctuations. Water levels in the Laurentian Great Lakes fluctuate over various time scales. Long term fluctuations are driven by annual water budgets, whereas short term fluctuations are driven by wind tides and seiches (Fortin & Gronewold, 2012; Trebitz, 2006). Wetland plant species dominance and extent are directly linked to fluctuating water levels (Smith *et al.*, 2021).

Wetland plant species mainly grow in accordance with their water-depth tolerance, resulting in stratified vegetation communities (hereafter called wetland classes) along the elevation gradient called the hydrosere (Figure 136). By definition, wetlands are terrestrial areas saturated with water for periods sufficiently long to influence their abiotic and biotic components, favoring the occurrence of hydromorphic soils, hydrophilic vegetation and biological processes associated with humid environments (Couillard & Grondin, 1986; Zoltai, 1988). Hydrological variables such as water level fluctuations, water velocity and wave energy are recognized as highly influential on hydrophilic species habitat and niche. At a larger scale, those processes influence the structure of the hydrosere in the wetland ecosystems (Ellison & Bedford, 1995; Mitsch & Gosselink, 2000; Odland & Del Moral, 2002; Smith *et al.*, 2021; Tabacchi *et al.*, 1998; Tessier *et al.*, 1981; Townsend, 2001; van der Valk *et al.*, 1994). As a result, wetlands are dynamic ecosystems that are highly responsive to changes in hydrology, either natural or anthropogenic. For example, wetlands can migrate with changes in water level, causing the overall area of wetland in a given water body to fluctuate through time. In addition to fluctuations in wetland area, the structure of one given wetland ecosystem will respond to changes in the hydrological regime. Periodic events, like prolonged flooding, can cause the mortality of shrubs and be responsible for a shift in wetland classes from swamp to marshes within a few seasons. Between open water (OW) and upland (UPL), the typical wetland classes of the hydrosere are the submerged aquatic vegetation (SAV) below the surface of the water, emergent marshes (EM) in shallow water or inundated substrate, wet meadows (WM) above the shoreline, followed by shrubby (SS) and treed swamps (TS) at the inland limit of the wetland.

In order to model the vegetation response to change in water levels, three types of models were developed:

1. Wetland succession model;
2. Invasive species suitable habitat; and
3. Invasive species population growth models.

The different types of models are based on the same assumption: the distribution of hydrophilic species and wetland classes is strongly influenced by hydrological processes (Nilsson & Keddy, 2011; Toner & Keddy, 1997). The following sections present each of these models.

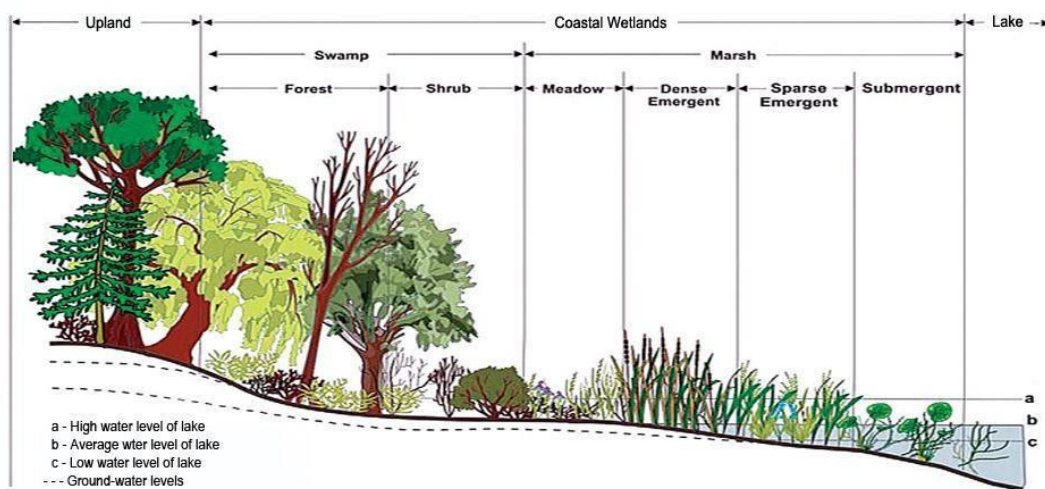


Figure 136: Typical sequence of coastal wetland classes observed on a gradient of elevation (IJC.org, url: <http://www.ijc.org/loslr/en/background/wetlands.php>)

6.1.1. Wetland succession modelling

The objective of the CWRM is to predict the spatial distribution of submerged aquatic vegetation (SAV), emergent marshes (EM), wet meadows (WM), shrubby swamps (SW) and treed swamps (TS). Although open water (OW) and upland (UPL) are not wetland class *per se*, we also included them in this effort to limit the spatial distribution of SAV lakeward and swamps landward. The selected method for modelling combines three components: 1) a clustering analysis to classify the vegetation data from the field surveys into large wetland classes (Section 6.1.2); 2) a supervised machine learning (here Random Forest) to link wetland class distribution to physical variables (Section 6.1.4) and 3) a succession algorithm to differentiate the variable progression of the different wetland classes (Section 6.1.6, Figure 137).

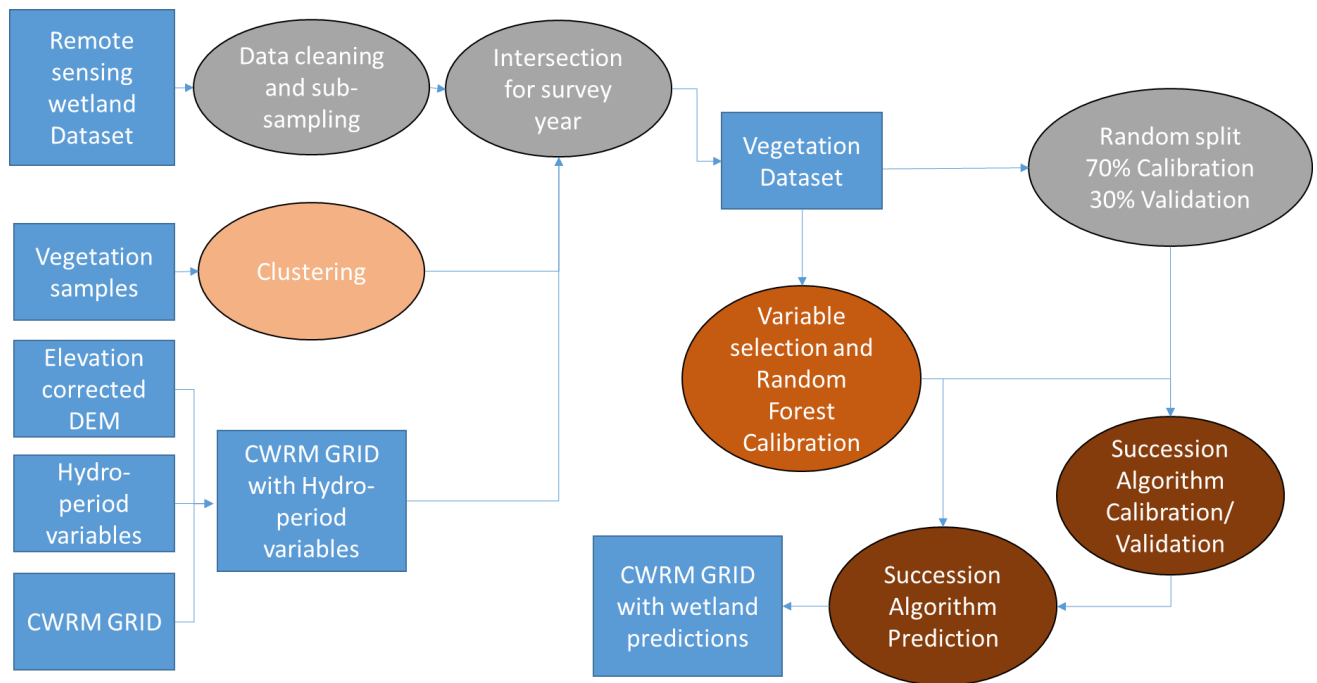


Figure 137: Coastal Wetland Response Model (CWRM) Framework. Blue squares are for data, grey ellipses are data operation (i.e. sampling, geospatial operation) and other colored ellipses are modelling operations.

6.1.2. Wetland class datasets

To generate a dataset containing a relatively balanced number of nodes of the different wetland classes, five datasets were used: GLPI vegetation surveys, Ecological Land Classification (ELC; Ontario Ministry of Natural Resources and Forestry Ontario, 2019b), other CWS surveys, the Great Lakes Shoreline Ecosystem (GLSE) inventory (Ontario Ministry of Natural Resources and Forestry, 2019c) and the Wetlands Trends through Time (WTT) (Snell and Cecile Environmental Research, 2001). The information on the vegetation surveys used is detailed in Table 39, and the various surveys are further discussed in the following sub-sections.

6.1.2.1. GLPI Vegetation surveys

The current GLPI project financed an important vegetation survey. For each wetland site, a vegetation survey measured 150 to 200 quadrats along 15 to 20 transects during 2018 and 2019. The numbers of transects and quadrats per site was determined by the size of the wetland. The transect locations were determined before sampling to capture a variety of habitats along the hydrosere and the elevation gradient. If transects needed to be shortened to fit within a site, additional transects were added to cover the wetland site for a maximum of 20 transects per site. Sampling quadrats were uniformly distributed along each transect with a general rule of 10

quadrats per transects. The Canadian Wildlife Service (CWS), Natural Resource Solutions Inc. and Dillon Consulting performed vegetation surveys in both years for the benefit of the modelling effort. Quadrats of 1.0 m x 0.5 m were distributed along transects. The total percentage of vegetation cover was estimated, as well as the percentage of cover for each species present for each quadrat. Plants that were difficult to identify to the species level (e.g., Characeae) were identified at the genus. Species cover ratio was estimated by vertical projection from 0 to 5%, then by increments of 5% until 95% and from 96 to 100%. Two surveyors evaluated vegetation cover to minimize sampling error and species misidentification. If quadrats were in deep water, and the vegetation cover could not be accurately estimated, surveyors used a rake device to identify the taxa in the quadrat and cover was estimated from the raked vegetation. Positioning and elevation data (X, Y and Z) were recorded for each quadrat using a GPS-RTK providing a high precision topographic survey (see Section 5 for more details).

Another vegetation dataset was used to improve the representation of SAV. It was obtained from surveys conducted by the CWS under the Coastal Habitat Assessment and Monitoring Program (CHAMP) for other studies. The sampling methodology is described in Grabas *et al.* (2012) and it focused on the SAV species, but the dataset also contains species of other wetland classes. The SAV community was sampled using 20 randomly located quadrats of 1 m x 1 m within the open water portion of each wetland from 2003 to 2019. Relative species abundance for the 20 most abundant species of each lake are presented in Appendix E, and the list of all the species identified in the study are presented in Appendix F.

6.1.2.2. Ecological Land Classification (ELC)

ELC is a dataset describing the ecological land use classes delineation (including wetland classes) at different scales and covering the majority of the study sites (Ontario Ministry of Natural Resources and Forestry, 2019b). It is based on satellite imagery and aerial photography. The scale at which vegetation types and wetland classes are identified in the ELC dataset ranges from 1:2000 to 1:10 000 depending on the imagery used. The years of wetland observations range from 2008 to 2015 depending on the site (Table 39).

6.1.2.3. Great Lakes Shoreline Ecosystem (GLSE) inventory

GLSE is a geospatial digital inventory containing ecosite polygon mapping, field survey calibration points and associated ground level ecological data (Ontario Ministry of Natural Resources and Forestry, 2021). Mapping and ground sampling adheres to the Great Lakes Shoreline Ecosystem

classification system (Lee *et al.*, in prep.), which is a detailed ecological classification and surveying method. It covers the entire Lake Erie shoreline, from the land to water or wetland to water interface to two kilometers inland. It also covers Lake Ontario, Detroit River, Lake St. Clair, Lake Huron and southern Georgian Bay shorelines.

6.1.2.4. Wetlands Trends through Time (WTT)

The WTT dataset is a spatial database of wetland vegetation delineation for 6 wetland sites along the shores of Lake St. Clair, Lake Erie and Lake Ontario that was developed as part of the Wetland Vulnerability to Climate Change project (Mortsch *et al.*, 2006) initiated by CWS and the Adaptation and Impacts Research Group (AIRG) of ECCC. For each wetland site, aerial photographs for different years representing periods of low, medium or high lake levels, from the 1920s to 2001, were acquired. Wetlands and other land use classes were manually delineated by photointerpretation on mylar map sheets at a scale of 1:10 000. Those delineations were then digitized and converted into a Geographical Information System (GIS) compatible format.

6.1.2.5. Merging the different sources of data into a single wetland class dataset

Data processing was performed on the vegetation datasets prior to the wetland model calibration and validation. The species distribution data obtained through vegetation surveys were used to derive wetland class distribution using clustering analysis (see Section 6.1.3). The wetland classes in the classification datasets were matched with the CWRM classes. Nodes of each class (OW, SAV, EM, WM, SW, UPL) were extracted by intersecting the mapping polygons and the CWRM nodes, and the number of nodes between classes was balanced by random sub-sampling. Examining the GLSE and ELC datasets, which were both generated through areal image delineation, revealed mismatched classifications at some locations for the same year. To alleviate this issue, only the CWRM grid nodes for which the two sources indicated the same wetland class were retained in the dataset. When possible, data intersection was done on delineations of the same year. Otherwise, a maximum five-year gap between the two delineations was considered, and only for persistent plant communities (EM, WM, SS and TS). In those instances, the selected CWRM nodes were considered to have the same wetland classification over the five (or less) years interval. For the WTT dataset, no processing was performed since there was no temporal overlap with the other data sources, as this classification dates mostly before the 2000s. Also, in order to improve confidence in wetland delineation data, areas showing differences in land use changes between the year of the delineation and the current year were removed from the dataset. For instance, polygons that belonged to a wetland class in the 1980s

but that are now agricultural crops or urban areas were removed. The final datasets for each wetland class in each lake are described in Table 38

Table 38: Description of the datasets used to calibrate and validate the wetland models.

Site/Lake	Wetland Class	Origin of vegetation nodes			Total number of nodes
		Vegetation surveys *	Photointerpretation		
			GLSE/ELC	WTT	
1HIE	OW	3	-	500	503
	SAV	54	-	500	554
	EM	19	-	500	519
	WM	14	-	50	64
	SW	0	-	500	500
	UPL	2	-	500	502
LKO (2ACM, 3SBM, 5LCM, 6JSM)	OW	401	3999	0	4400
	SAV	927	1588	1647	4162
	EM	602	358	3390	4350
	WM	564	1352	2454	4370
	SW	306	1228	3546	5080
	UPL	77	3479	795	4351
7GRM	OW	74	126	154	354
	SAV	118	1	164	284
	EM	164	36	42	242
	WM	21	179	156	356
	SS	-	-	123	123
	TS	-	200	164	364
	UPL	12	188	164	364
LKE (8SPP, 9LPW, 10RBY, 11FCK)	OW	72	7927	5914	13913
	SAV	356	7645	5994	13995
	EM	196	7805	212	8213
	WM	33	7967	5772	13772
	SS	10	7990	6000	14000
	TS	1	8000	5672	13673
	UPL	28	7974	5927	13929
12DRM	OW	62	363	-	425
	SAV	425	-	-	425
	EM	93	332	-	425
	WM	21	126	-	146
	SW	12	413	-	425
	UPL	4	421	-	425
LSC (13LSC, 14SAM)	OW	71	1429	-	1500
	SAV	385	1115	-	1500
	EM	147	1353	-	1500
	WM	-	1500	-	1500
	SW	-	713	-	713
	UPL	-	1500	-	1500
LKH (15BDD, 16HBW, 18HBW, 19TBY, 22WHW, 23ACK, 27FPT)	OW	0	2000	500	2500
	SAV	367	1875	431	2673
	EM	315	1723	434	2472
	WM	389	809	453	1651
	SW	155	1645	462	2262
	UPL	0	2000	500	2500

* Vegetation surveys includes the samples from the GLPI project surveys of 2018-2019 and other vegetation surveys done by CWS.

Table 39: Wetland classification dataset used in the study and the respective survey years for each sites.

Lake	Site	GLPI survey	Other CWS surveys	ELC	GLSE	WTT
Upper St. Lawrence	1HIE	2019	2003	-	-	1987, 1999
Lake Ontario	2ACM	2018, 2019	2006-2019	2008	2015	-
	3SBM	2018, 2019	2003, 2009, 2011, 2015, 2018	2008	2015	1986, 1999
	5LCM	2018, 2019	2003, 2009, 2011, 2012, 2015, 2018	2010	2015	1986, 2001
	6JSM	2018, 2019	2003, 2009, 2012, 2015, 2018	2008	2015	1986, 1988, 2001
Lake Erie	7GRM	2018, 2019	2010, 2013, 2016, 2019	2010	2015	1983, 1988, 1995, 2000
	8SPP	2018, 2019	2010, 2013, 2016, 2019	2010	2015	-
	9LPW	2018, 2019	2010, 2013, 2016, 2019	2006, 2010, 2015	2015	1985, 1995, 1999
	10RBY	2018, 2019	2014	2010	2015	1985, 1988, 1995
	11FCK	2018, 2019	2010, 2013, 2016, 2019	2010	2015	-
Lake St. Clair	12DRM	2018, 2019	2008, 2011-2018	2015	2015	-
	13LSC	2018, 2019	2007, 2008, 2011-2018	2010	2015	1985, 1988
	14SAM	2018, 2019	2007, 2008, 2011-2018	2010	2015	-
Lake Huron	15BDD	2018, 2019	-	-	-	1985, 1988, 1995
	16HBW	2018, 2019	-	2015	-	-
	18HGW	2018, 2019	-	-	-	-
	19TBY	2018, 2019	-	2015	-	-
	22WHW	2018, 2019	-	-	-	-
	23ACK	2018, 2019	-	2009	-	-
	27FPT	2019	-	2015	-	-

6.1.3. Clustering analysis

In order to assign a wetland class to each vegetation survey point presented in the previous section (Section 6.1.2.1), clustering analysis were performed for each lake independently. The clustering analysis allows associating a wetland class to vegetation species occurrences.

In order to minimize the bias induced by rare species, only species with a frequency higher than 3% in each lake were included in the analyses. Forb and graminoid species with a frequency lower than 3% were grouped based on the combination of their growth form and wetness index (Table 40). Wetness index, also named wetland indicator status, indicates the probability that individual species of vascular plants are present in freshwater (see Reed (1997, 1998) for more details on wetness index). Some groups were also created prior to the clustering analyses, regardless of the frequency of the species for four situations (Table 40):

1. SAV: because the goal of this project was not to model the different submerged vegetation communities, this group represents all submerged species present in one quadrat except *Hydrocharis morsus-ranae* and *Myriophyllum spicatum*, two exotic and invasive species, were added to form the AQUATIC group;
2. CAREX: a group named CAREX_WET covering all *Carex* species associated to wetland habitats (wetness indexes OBL and FACW) was created;
3. TREES: trees and shrubs were all grouped according to their wetness index;
4. DRY: Upland species.

Table 40: Regrouping of species with rare frequencies or with interest prior to clustering analysis. WET group includes FACW and OBL. DRY group includes FACU and UPL, see Reed (1997, 1988) for more definitions on the wetness index.

Groups	Growth form	Wetness index	Rare species	All species grouped
FORB_WET	Forb	WET	X	
FORB_FAC	Forb	FAC	X	
FORB_DRY	Forb	DRY	X	
GRAM_WET	Graminoid	WET	X	
GRAM_FAC	Graminoid	FAC	X	
GRAM_DRY	Graminoid	DRY	X	
SHRUB_WET	Shrub	WET		X
SHRUB_FAC	Shrub	FAC		X
SHRUB_DRY	Shrub	DRY		X
TREE_WET	Tree	WET		X
TREE_FAC	Tree	FAC		X
TREE_DRY	Tree	DRY		X
SAV	SAV			X
CAREX_WET	Carex	WET		X
DRY		UPL		X

In cases where the frequency of a group remained under 3% after grouping, the group was either discarded for the analysis or grouped with another growth form with the same wetness index (for example: SHRUB with TREE_DRY). Finally, the vegetation cover matrix was transformed with the Hellinger distance coefficient, which reduced the importance given to differences in the abundance of rare species (double-zeros; Legendre & Legendre, 1998).

The *clValid* R package (Brock *et al.*, 2008) was used to determine the best clustering method (between Ward's Hierarchical and Kmeans) and the optimal number of clusters according to the Connectivity, and Silhouette and Dunn Indexes. Clustering analyses were performed step by step, removing from the dataset the quadrats that were classified into an ecologically meaningful wetland class in the first step, while keeping the unclassified quadrats for the subsequent clustering steps. This approach was used to avoid the subdivision of ecologically meaningful wetland classes into smaller clusters with similar plant composition (but with different covers). In the rare cases where the clustering method and/or number of clusters suggested by the *clValid* package did not result in the creation of a meaningful ecological wetland class, the number of clusters or the clustering method was modified. In general, between 4 and 8 clustering steps were necessary for each study site to create between 5 and 15 wetland clusters.

Clusters were associated to one of the seven classes listed in Table 41. *A posteriori* modification of classifications was performed for quadrats that did not follow the classification rules. For example, a few quadrats containing both *Typha x glauca* and shrubs (OBL or FACW) could be classified in a cluster dominated by *T. x glauca* emergent marsh. In such cases, the quadrats exhibiting a shrub cover greater than 25% were transferred *a posteriori* to the SS wetland class.

Table 41: Description of the wetland classes modelled in the CWRM.

Acronym	Wetland Class	Criteria ¹	Example of communities
UPL	Upland	Dominated by FACU and UPL species	Goldenrod prairies Agricultural wastelands dominated by ruderal species Oak forest
TS	Treed swamp	> 25% of hydrophyte tree species	Eastern white cedar forest Red ash forest Tamarack forest
SS	Shrubby swamp	> 25% of hydrophyte shrub species	Alder swamp Willow swamp Dogwood thickets
MM	Meadow marsh	25% of emergent macrophytes	Bluejoint meadow marsh Sedge meadow marsh Reed canary grass meadow marsh
EM/NPE	Emergent marsh and nonpersistent emergent marsh	25% of <i>Typha</i> or <i>Phragmites</i> spp. Submerged aquatic plants are often present or 25% of NPE indicator species	<i>Phragmites australis</i> marsh <i>Typha</i> marsh Bur-reed marsh Wild rice marsh Arrowhead marsh
SAV	Submerged aquatic vegetation	> 25% of aquatic plants	Eelgrass beds Pondweed beds Algae beds
OW	Open water	< 25% of aquatic plants Dominated by open water	

¹ Adapted from Warner and Rubec 1997; Bazoge *et al.* 2015. Classification criterias follow a top-down hierarchy where the classification depends on the abundance of a strata at the highest vertical layer (canopy, shrub layer, persistent emergent vegetation, non-persistent emergent vegetation and submerged aquatic vegetation).

6.1.4. Supervised machine learning model: Random Forest

Seven distinct wetland models were calibrated using a Random Forest classifier (RF) using the wetland class distribution as dependent variables and the physical variables as predictors. The latter, such as the minimum, maximum and mean water depth, the percentage of time a given node is flooded, the mean length of the cycle period, and the amplitude of the cycles period in the previous growth seasons (aggregated on 1, 2 and 3 previous growth season) are calculated for every node of the CWRM grid and for each year of the observed period (Section 3.7.2.3).

RF is an ensemble learning method used for regression and classification. This model iteratively uses many permutations of the dataset to calibrate and validate an ensemble of decision trees where each tree votes for a given class. The class with the majority of the votes is then predicted. At each iteration, calibration and validation datasets are randomly selected, and the thresholds and the variables used at each branch of the trees are adjusted iteratively to reduce the error on the validation dataset (out-of-bag error). The RF iteratively builds a set of rules using various explanatory variables to identify features describing each wetland class. RF classifiers are widely used in remote sensing for wetland classification (Banks *et al.*, 2019; Battaglia *et al.*, 2021; Bourgeau-Chavez *et al.*, 2017; Mahdianpari *et al.*, 2020). Some studies have proven the performance of RF over traditional machine learning methods, such as multiple logistic regression models in ecohydrological modelling (Peters *et al.*, 2007), and to study the response of wetlands to global warming (Liu *et al.*, 2011; Peng *et al.*, 2020). The RF algorithm has many advantages such as (Breiman, 2001):

- Handles high dimensional data;
- Has a quick calibration/prediction time;
- Is robust to outliers and non-linear data;
- Handles unbalanced data;
- Has a low bias and moderate variance;
- Gives useful internal estimates of error, strength, correlation and variable importance.

The Python implementation of the RandomForestClassifier function by *Scikit-learn* (Pedregosa *et al.*, 2011) was used to calibrate and validate the RF models and to predict the wetland classes.

6.1.5. Selection of the explanatory variables

The different physical variables used as predictors of wetland communities comprise two groups: terrain variables and hydroperiod variables. The terrain variables are the curvature and the slope at different scales, whereas hydroperiod variables describe the water level fluctuations during a given time window. Hydroperiod variables include minimum, maximum and mean water depth, percentage of inundation, and the period and amplitude of the dry-wet cycles (Section 3.7). To calibrate the wetland model, the variables were aggregated into time windows prior to sample acquisition. It has been demonstrated that the distribution of wetland classes such as EM is influenced by water levels of the two or three previous years (Morin *et al.*, 2005; Turgeon *et al.*, 2004). The aggregation of the variables on such time windows allowed us to predict the presence of wetlands in areas where conditions were suitable over a sufficient period and to reduce the influence of extreme water level years.

In order to select the significant explanatory variables, we first made a RF model exclusively using the terrain variables, slope and curvature, and selected the scale between 10, 30, 130, 250 and 310 m that had the highest importance explaining the wetland class distribution. For the hydroperiod variables, we used the same approach grouping the variables for different time windows (two and three growth seasons preceding the sampling growth season). The hydroperiod variables tested were the water depth, dry-wet cycle period, scale-averaged wavelet power, percent time flooded or stranded, flow velocity, and wave orbital velocity. Mean, maximum and minimum of each variable were calculated and tested for each time window. First, we selected the time window resulting in the highest accuracy. Then, we selected the hydroperiod variables that had the highest importance and that were minimally correlated with each other.

The importance of variables is obtained using the Mean Decrease Accuracy and the Mean Decrease in Gini metrics. Mean Decrease Accuracy uses the out-of-bag (OOB) validation samples to compute the importance of the variable by assessing the prediction error when removing each variable from the model. Mean Decrease in Gini assesses the impurity of the variables by iteratively removing each variable from the model. The higher the value of Mean Decrease Accuracy or Mean Decrease in Gini score, the higher the importance of the variable in the model (Hong Han *et al.*, 2016). The best variables among each group were then grouped and included into another RF. We looked at the importance of the variables and aimed to improve the accuracy for the classes that had the poorest performance. We recursively added and removed

variables from the model and saved the performance metrics for each model. Finally, we selected the model that had the highest performance on the OOB validation.

6.1.6. Wetland succession algorithm

Wetland succession occurs when the change in environmental conditions is maintained for a given time period. The succession algorithm modulates the transition time between wetland classes and ensures that it follows the observed wetland succession. In other words, based on the prediction of the RF and certain physical thresholds, it ensures that the succession of wetland classes for each CWRM grid node follows the ecology of the different wetland classes. For example, the succession algorithm ensures that one node does not transition from SAV to TS within a single year, as trees take years to grow. It also takes into consideration the level of tolerance of different wetland classes to an increasing or decreasing water level before changing state. For example, a single season with high water levels is not enough to induce a dieback of EM species like *Phragmites* or *Typha* (Seabloom *et al.*, 2001; van der Valk *et al.*, 1994; van der Valk & Davis, 1978), but will be enough to eliminate a plant community dominated by annual plants, like SAV (Morin *et al.*, 2005). Another interesting example is the transition from swamp to an upland forest when experiencing receding water levels. As the conditions get drier, the growth or survival of most species of wetland trees will not be impeded and, to the contrary, will likely be improved by better growing conditions. As the substrate gets drier, it also becomes more suitable for the establishment of mesic tree species, that are, in general, more competitive than wetland tree species. As the density of trees increases over the years, evapotranspiration increases, further contributing to the reduction of the humidity content of the soil (a phenomenon often called biological drainage; Jutras *et al.*, 2006). Over the years, competition for resources will disadvantage wetland trees at the expense of mesic tree species, up to a point where mesic trees will become dominant and the node will be classified as an upland forest.

The succession algorithm predicts the distribution of each wetland class according to the temporal variations of the physical variables, mainly hydroperiod variables, under each climate change scenario. It predicts the wetland class at each grid node using the wetland class predicted by the RF for the current year, the physical variables occurring during the previous growing season, the wetland class predicted in the previous years, and the time required before environmental conditions result in a change of wetland class.

The succession algorithm is represented as a tile system where all the possible wetland “states” and transition between them are defined. The tiles system represents the entire hydrosere where tile #1 is the lower boundary class “open water” (OW) and tile number 105 is the upper boundary class “upland” (UPL) (Morin *et al.*, 2005; 2016). Each wetland class was assigned an “optimum tile” representing the state where the environmental conditions are ideal for a wetland class. Some classes encompass more than one tile to represent a “transitioning community” towards a drier or wetter class. For every CWRM grid node and every year of the time series, the RF predicts a wetland class based on physical variables experienced at that location the preceding growing season. Since this prediction is based on an array of physical variables, the predictions are used in the succession algorithm as an estimation of the environmental conditions prevailing at that node. If the RF predicts a wetter community than the one that was present the previous year, it indicates that environmental conditions for that year were wetter and will generally lower the tile number for that grid node compared to the previous year. If the RF predicts the same community that was prevailing the year before, the tile number will generally go back to the optimal tile number for that community. Finally, if the RF predicts a drier community, the tile number will generally increase (Figure 138).

More specifically, the following section will describe each wetland class and the rationale behind the numbering of the tiles that are represented in Figure 138. In the figure, the full red square represents a transition state that occurs when the wetland grid area is flooded or dried for too long a period. This transitional state is the succession from one class to another according to the prediction of the RF model and the environmental conditions. The succession of the wetland classes is presented by arrows indicating transition to drier (green arrow) or wetter (blue arrow) wetland classes. The succession conditions are written on each arrow. The notation {wetland class} + stands for {wetland class} and the other drier classes (ex. SS+ = SS, TS, UPL). Inversely, {wetland class} – stands for {wetland class} and other wetter classes (ex. SS- = SS, MM, EM, SAV, OW). For example, for SAV: p=EM or p=SS+ & FI>50% means that for SAV to become EM, the RF prediction has to be EM or SS+ (Shrubby swamp and drier) and the grid node should be flooded for more than 50% of the growing season.

Open water (OW) was assigned **tile #1** (Figure 138, blue square). This community contains only one tile because drier conditions can lead to the establishment of vegetation within one year. More specifically, OW will transition to SAV if water levels are receding gradually. In cases where the water level decrease is large and swift, substrate gets exposed (i.e. mudflats), which offers a suitable germination bed for forbs or graminoids species. Depending on the prediction of the RF,

it is thus possible for OW to evolve towards an EM or WM community within one year (depending on the RF prediction). It is however impossible for ligneous species to become dominant only one year after water recedes, so if the prediction of the RF is SS+ (SS, TS or UPL), the node will evolve towards an EM or a WM community, depending on the proportion of time that the node was flooded over the growing season. Periods of extremely low water expose unvegetated lagoon bottoms as mud flats, providing a substrate for new plant colonization. Annuals and other opportunistic species such as *Schoenoplectus tabernamontani* rapidly increase in abundance, and are typically replaced by cattail as the plant community matures (Bosley, 1978; Harris *et al.*, 1978).

Submerged and aquatic vegetation (SAV) was assigned **tile #6** (Figure 138, violet square). This community contains only one tile because most of the species occupying this wetland class are annuals (Turgeon & Morin, 2005). More specifically, the community can evolve into OW in cases of water level increases or into EM or WM if water levels are decreasing. Similar to OW, SAV cannot evolve within one year into a swamp and will be directed towards EM or WM with the same flooding threshold if the prediction of the RF is SS+.

Emergent marsh (EM) was assigned **tiles #13 to 17**, with an **optimum at tile #15** (Figure 138, red square). This community is largely dominated by cattail species and *Phragmites*. Although it encompasses the highly invasive species *Phragmites australis* and *Typha x glauca*, this class is not intended to reproduce the dynamics of a biological invasion. The invasion aspect will rather be taken into account by the species models described in Section 6.2. Here, EM was considered to be able to tolerate 2 consecutive years of wetter conditions. In fact, several studies observed that it takes two to three years of unsustainably high water level to eliminate species of EM (Seabloom *et al.*, 2001; van der Valk *et al.*, 1994; van der Valk & Davis, 1978). More specifically, if the prediction of the RF is SAV-, the tile number will be lowered to 14 or 13 that represents EM transitioning towards a wetter community, but that still remain dominated by emergent plant species. If the prediction the next year is EM+, then the node will transition toward tile #15 (the optimum). EM can thus evolve toward SAV or OW only if the prediction of the RF is SAV- for three consecutive years. Conversely, if the conditions are getting drier (prediction of the RF is WM+), we considered that two consecutive years of drier conditions were necessary before experiencing a change in plant community. Tile #16 can thus be seen as an EM that starts to be invaded by WM species or shrubs. More specifically, EM can evolve towards a WM or a SS after two consecutive years of RF prediction of WM+.

The succession time for EM is the same for Upper St. Lawrence, Lake Ontario, Lake Erie and Lake St. Clair sites. For Lake Huron, we used a slightly different succession time for EM, since there is a higher richness of wetland species in this Lake and because the EM are highly dominated by non-persistent-emergent (NPE) species. In this Lake the EM may go to a wetter class such as OW or SAV if the wetter conditions persist for two consecutive years (one year less than other lakes) and require three consecutive years of dry conditions to become a WM.

Wet meadow (WM) was assigned **tiles #23 to 30**, with an **optimum at tile #25** (Figure 138, yellow square). WM can also be affected by the percentage of time they are flooded during the growing season (Millar, 1973; Squires & Valk, 1992). Gathman *et al.* (2005) documented the quick response of wetland plant species to a three-year (1996-1998) water level change in coastal Lake Huron wetlands. In their study, stem density, per plot species richness, and Shannon diversity in the WM and transition zones decreased as water depth increased from 1996 to 1997. An increase in these same measures was noted in 1998 with the decrease in water level (Gathman *et al.*, 2005). We estimated that it takes 5 years of continuously dry conditions before the WM becomes dominated by shrubs.

In Lake Erie, the model predicts two distinct classes for swamps, the **shrubby swamps (SS)** and the **Treed swamp (TS)**. In the other lakes there was not enough available data to model the two classes of swamps. **Shrubby swamp (SS)** was assigned **tiles # 34 to 40**, with an **optimum at tile #35** (Figure 138, pink square). **Forested swamp (FS)** was assigned **tiles #63 to 80**, with an **optimum at tile #65** (Figure 138, turquoise square). It has been suggested that the growth of forested wetlands, such as shrubby swamps (SS) and forested swamps (FS), was reduced and the regeneration of these ecosystem was interrupted when they were flooded for more than 40 to 50% of the time over two growing seasons (Ernst & Brooks, 2003; Hall & Smith, 1955; Kozlowski, 1997; Toner & Keddy, 1997). Inversely, SS flooded for less than 50% of the growing season or for which we predicted a drier wetland class for 15 consecutive years were assumed to change into FS. Finally, we assumed that FS had to be flooded for less than 50% of the growing season and found at water depths < 0.5 m for 20 consecutive years to change into terrestrial forests, called here “upland” here (Gauvin *et al.*, 1998). In the other lakes, both classes were merged into a single **Swamp (SW)** class including the shrub and the trees. **Swamp (SW)** was assigned to **tiles #34 to 50**, with an **optimum at tile #35** (not represented in Figure 138). The succession time for this class has been modified to 20 consecutive years for the swamp class to transition into terrestrial forest, called “upland” here.

Upland (UPL) was assigned **tiles #103 to 105** (Figure 138, green square), with an **optimum at tile #105**. The upland species can persist through two consecutive years of wet condition before transitioning to a wetland.

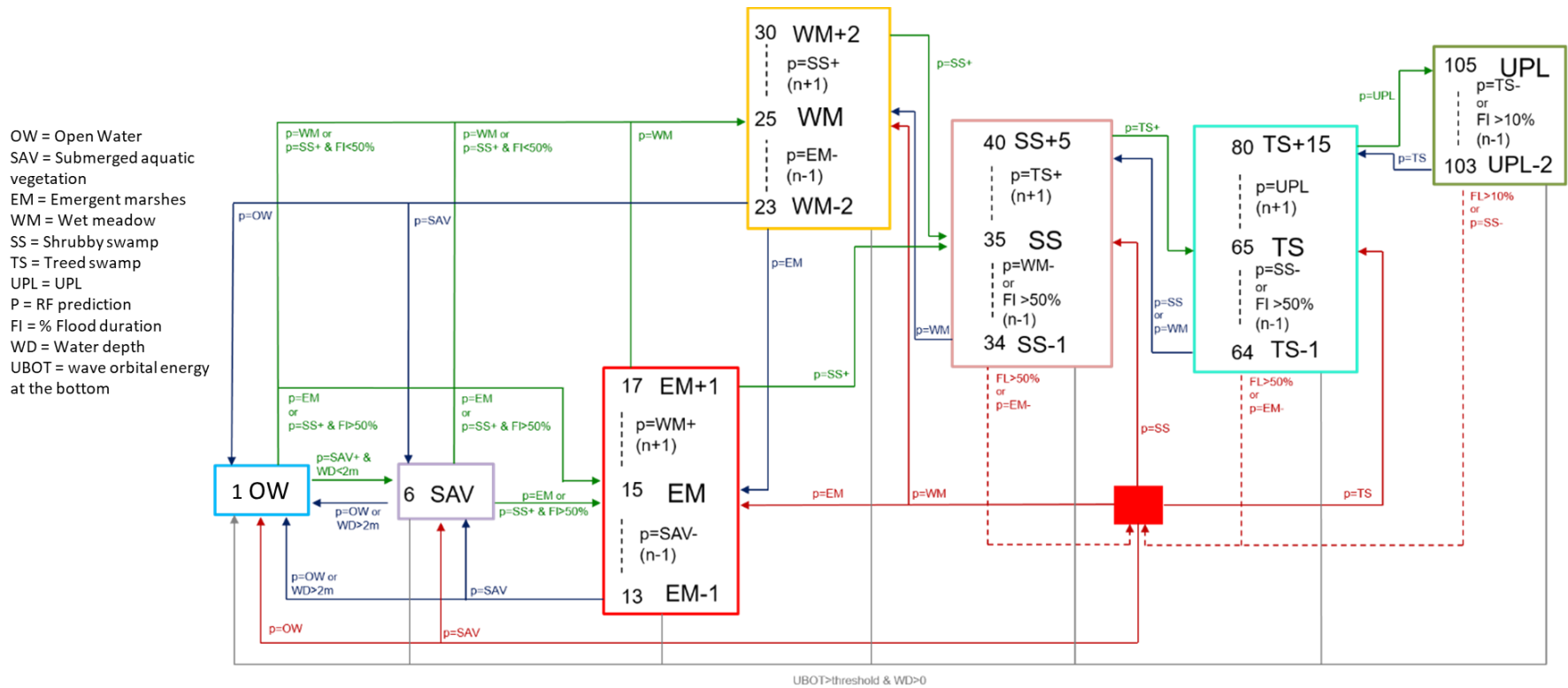


Figure 138: Wetland succession algorithm scheme. Green arrow signifies a transition towards a drier class, whereas red arrow signifies a transition towards a wetter class. The red square corresponds to the re-initialization of the wetland following a disturbance. Each wetland class has their respective tile numbers and the proposed conditions for transition are presented along the transition arrows.

6.1.7. Variable importance for each wetland class

The wetland modelling aims to find descriptive features linking wetland class distribution to hydrology and topography. The OW and UPL classes are the lower and upper limits of the wetlands and are generally identified accurately. In all lakes, for OW, the water depth is higher than all other classes, flooded all the time with low period of water level fluctuations (Figure 142, 144 and 152). Upland are terrestrial ecosystem that are rarely flooded. The water depth is lower than all other classes (Figure 140, 142, 144, 146, 148 and 150).

Water level fluctuations and wave energy are recognized as the main factors regulating the growth and distribution of SAV (Madsen *et al.*, 2001). Water depth and hydroperiod are also important factors controlling their distribution and abundance in lake ecosystems (Turgeon & Morin, 2005). According to the wetland models of the different water bodies, the variables that describe SAV distribution and increase its distinction in comparison with other wetland classes are:

- Higher water depth than other wetland classes (Figure 140, 142, 144, 146, 148 and 150);
- Mean dry-wet cycle period higher than OW but lower than EM with a high variability in most models (Figure 142, 144, 148 and 150);
- Mean flooded period lower than OW but higher than EM (Figure 142, 146 and 148);
- Mean velocity is lower than OW but higher than other classes in Detroit River (Figure 148);
- Wave exposure (mean orbital velocity of the Weibull distribution) higher for SAV than EM but lower than OW in Lake Erie (Figure 144).

In general, the most important hydroperiod variables for SAV is the maximum water depth, but other variables are also important in specific water body, such as the flood duration in Lake Ontario (Figure 141) and the mean period of dry-wet cycles in the Lake Erie (Figure 143).

EM are generally located at the land-water interface exposed to water level fluctuations and are subject to frequent or seasonal flooding. The observed distribution of water depth variables for this class are generally similar to WM. According to wetland observations, the variables that describes EM and increase its distinction with other classes are:

- Mean flooded duration is generally higher for EM than WM, SW and UPL but lower than SAV (Figure 140, 142 and 146);
- Mean dry-wet cycle period and maximum scale average power is generally higher for EM than for other classes, which means that this wetland class is more exposed to water level fluctuations (Figure 142 and 148);
- Wave exposure, which is used in the Lake Erie and Grand River Mouth models, is higher for EM than for WM and SW but is lower than SAV (Figure 144 and 146).

In exception of the topographic variables, the most important variables for EM are the water depth variables and hydroperiod variables such as the mean period of dry-wet cycles and maximum scale-average power. In Lake Erie, the most important hydroperiod variables for this class are the mean period of dry-wet cycles and the minimum water depth (Figure 143). In Detroit River Marsh, the maximum scale-average power, mean period and maximum water depth are the most important hydroperiod variables (Figure 147). In Lake Huron, the minimum, maximum water depths and the maximum scale-average power are the most important variables (Figure 151). In Lake Ontario and Lake St. Clair, the importance of the explanatory variables are similar (Figure 141 and 149).

WM are composed of flood-tolerant species but can also be favored by low water levels as they support conditions at the boundary of the terrestrial and aquatic habitats better than wetlands associated with wetter conditions (Wilcox *et al.*, 2008), such as SAV and EM. According to wetland observations, the variables that describe WM and increase its distinction in the models are:

- Mean and maximum period lower than EM but higher than SW (Figure 140, 142, 144 and 148);
- Maximum scale-average power lower than EM but higher than SW (Figure 142, 144, and 148);
- Mean flooded duration higher than SW but lower than EM (Figure 140 and 148);
- Wave exposure lower than SAV and EM but slightly higher than SS and TS in Lake Erie (Figure 144).

Across all models, the maximum scale-average power is among the most important hydroperiod variables for WM, along with water depth variables. Minimum water depth is important in Lake Ontario, Lake Erie and Lake Huron (Figure 141, 143 and 149). In Lake St. Clair, the maximum water depth is the most important hydroperiod variable in this lake (Figure 149). Other explanatory variables such as the mean and maximum period are also important in some models, such as the Lake Erie and Grand River Mouth models (Figure 143 and 145).

SW are at the intermediary between the wetlands and the terrestrial ecosystems. The species included in that class are flood resistant shrubs and trees (shrubby swamps and treed swamps). SW is favored by occasional flooding but shrub and trees growth may be reduced and regeneration interrupted if the flooding duration exceeds 40 to 50% over two growing seasons (Ernst & Brooks, 2003; Hall & Smith, 1955; Kozłowski, 1997; Toner & Keddy, 1997). According to wetland observations, the variables that describe SW and increase its distinction in the models, including SS and TS in Lake Erie sites, are:

- Flood duration lower than WM but higher than UPL (Figure 140 and 144);
- Mean period of cycles lower than WM but higher than UPL (Figure 140, 142, 144, 148 and 152);
- Water depth slightly lower than WM but higher than UPL (Figure 140, 142, 150 and 152);
- Wave exposure in Lake Erie is slightly lower than WM but higher than UPL (Figure 144).

For SW, slope and curvature have an high importance for most models but the most important hydroperiod variables varies from one model to another. In Hill Island, the SW distribution is mainly explained using water depth (minimum and maximum) and with mean period of dry-wet cycles (Figure 139). In Lake Ontario, the mean water depth and the mean period are the most important hydroperiod variables (Figure 141). In Lake Erie, the minimum water depth and the mean period are important for SS distribution, while the maximum depth and the maximum scale-average power are more important for TS (Figure 143). In Grand River Mouth, the mean and maximum period and the maximum scale-average power are the most important hydroperiod variables (Figure 145). In Detroit River Marsh, the maximum water depth and the mean velocity allow to discriminate this class (Figure 147). In Lake St. Clair, the maximum water depth is the main hydroperiod variable used for this class (Figure 149). In Lake Huron, the minimum, maximum and mean water depth are the most important predictors (Figure 151).

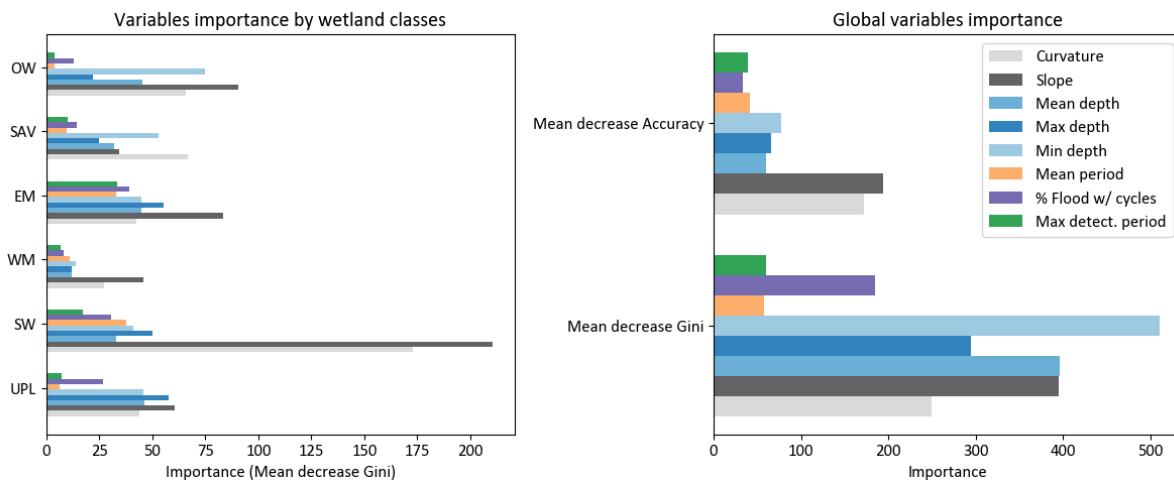


Figure 139: Variables importance by wetland classes (left) and global variable importance (right) for the Hill Island East random forest model.

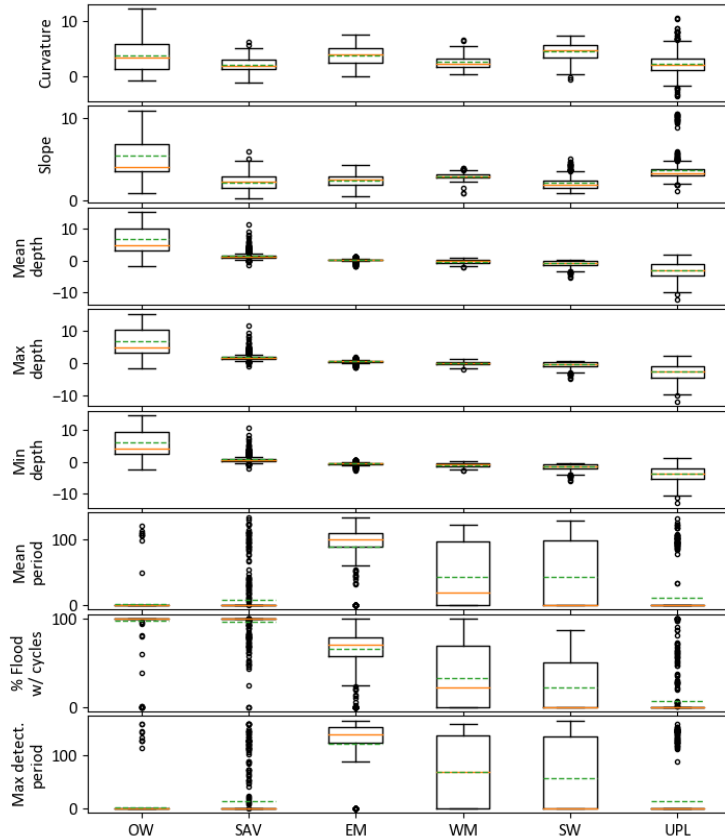


Figure 140: Physical variables distribution by wetland class for the Hill Island East vegetation dataset. Orange line corresponds to the median while green dashed line corresponds to the mean.

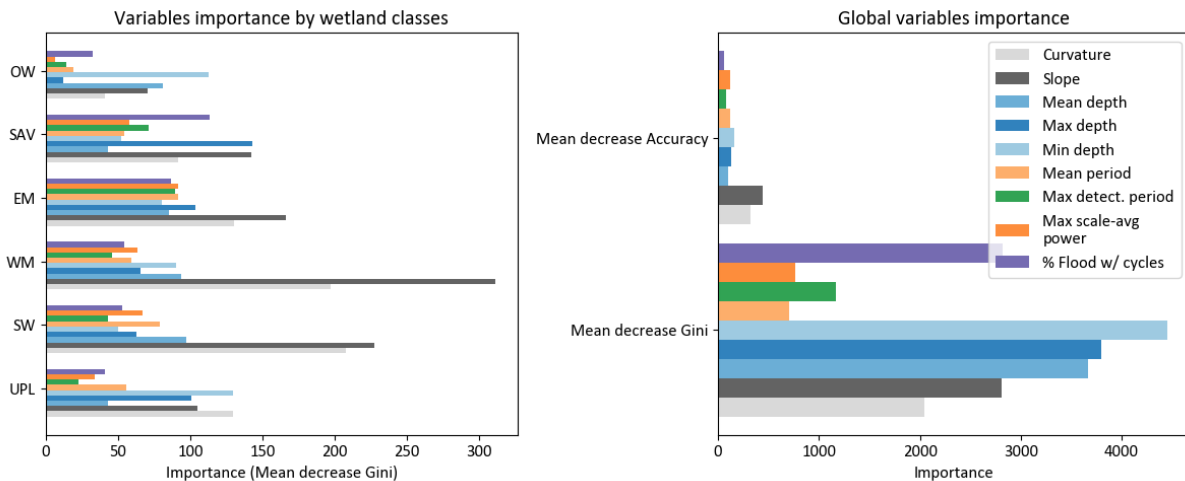


Figure 141: Variables importance by wetland classes (left) and global variable importance (right) for the Lake Ontario random forest model.

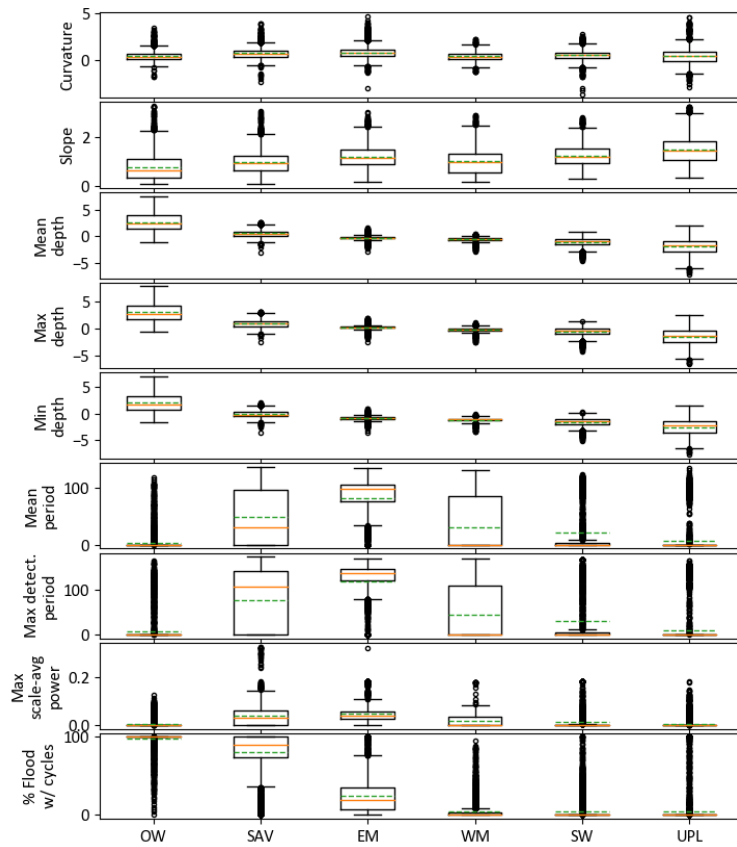


Figure 142: Physical variables distribution by wetland class for the Lake Ontario vegetation dataset. Orange line corresponds to the median while green dashed line corresponds to the mean.

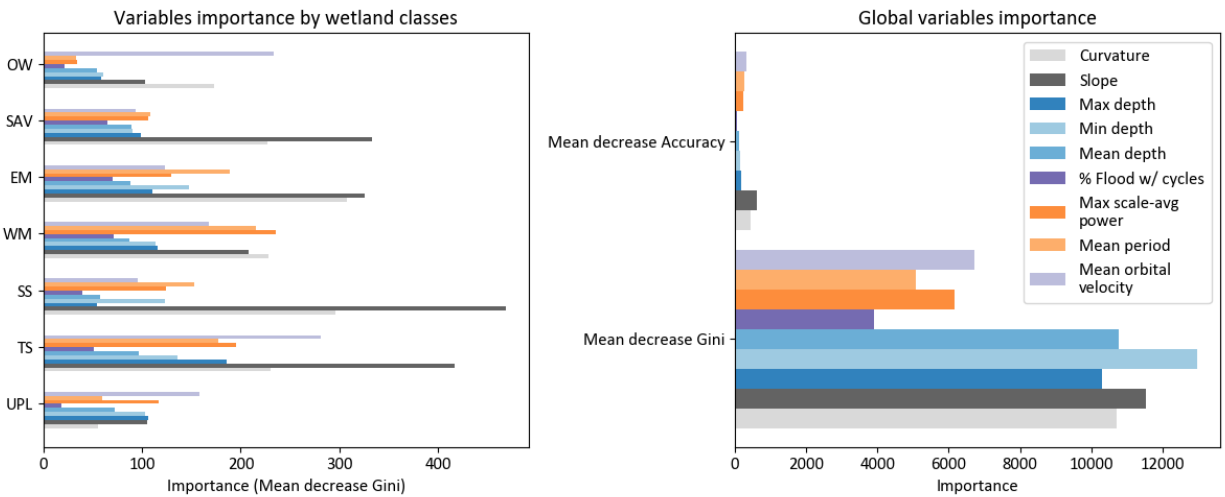


Figure 143: Variables importance by wetland classes (left) and global variable importance (right) for the Lake Erie random forest model.

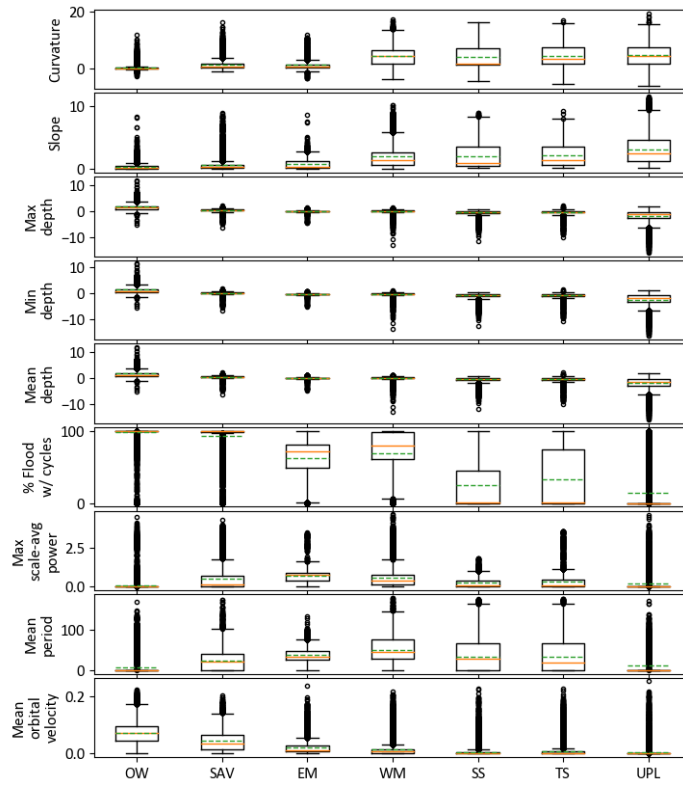


Figure 144: Physical variables distribution by wetland class for the Lake Erie vegetation dataset. Orange line corresponds to the median while green dashed line corresponds to the mean.

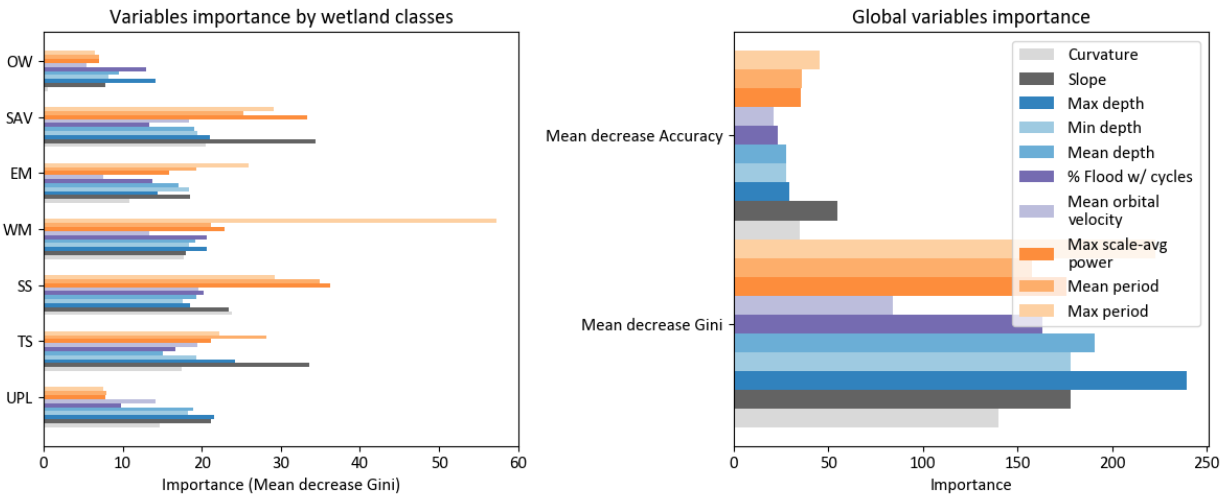


Figure 145: Variables importance by wetland classes (left) and global variable importance (right) for the Grand River Mouth random forest model.

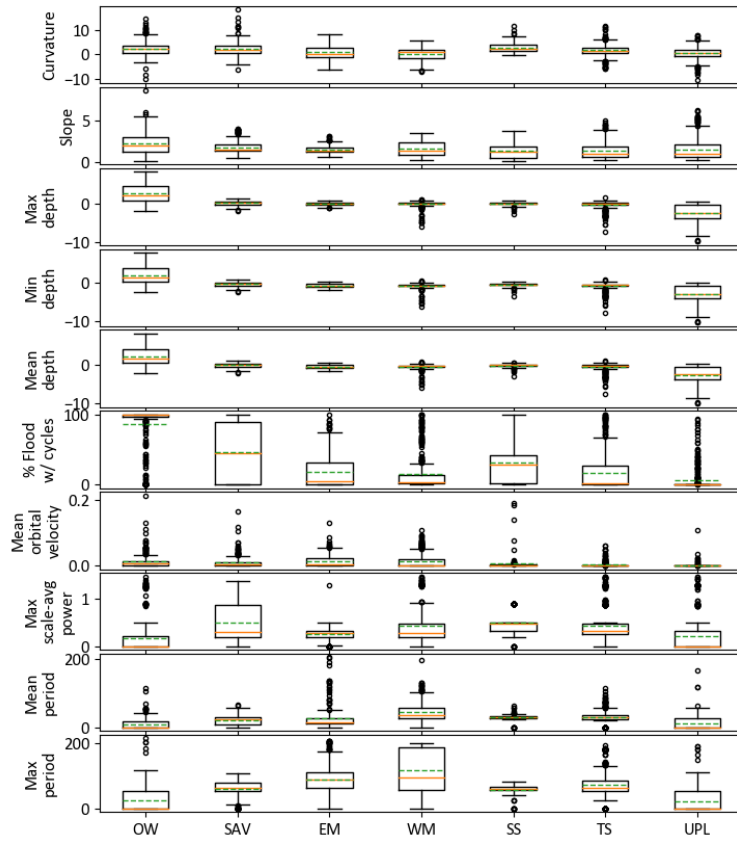


Figure 146: Physical variables distribution by wetland class for the Grand River Mouth vegetation dataset. Orange line corresponds to the median while green dashed line corresponds to the mean.

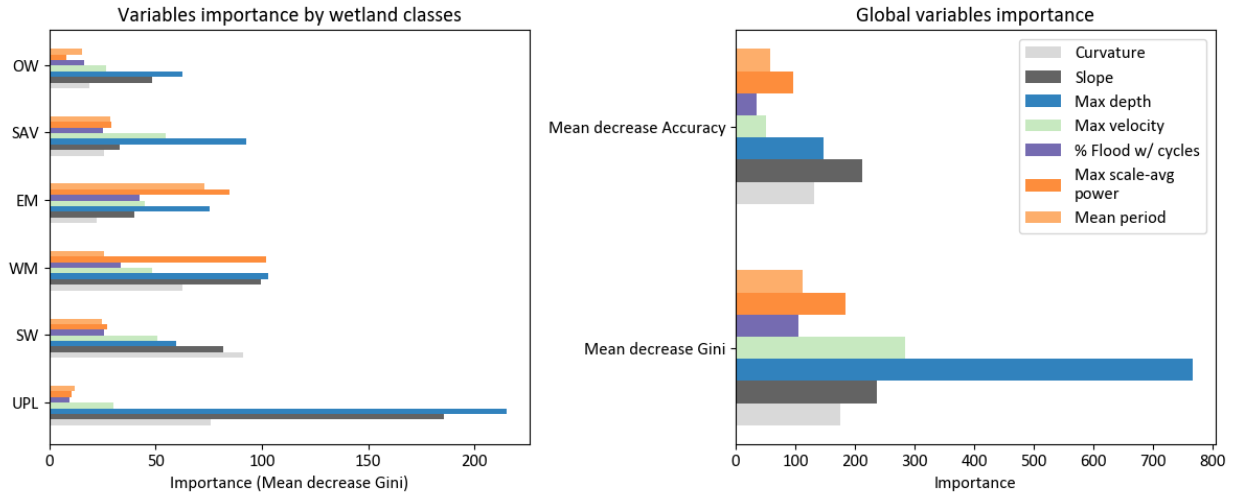


Figure 147: Variables importance by wetland classes (left) and global variable importance (right) for the Detroit River Mouth random forest model.

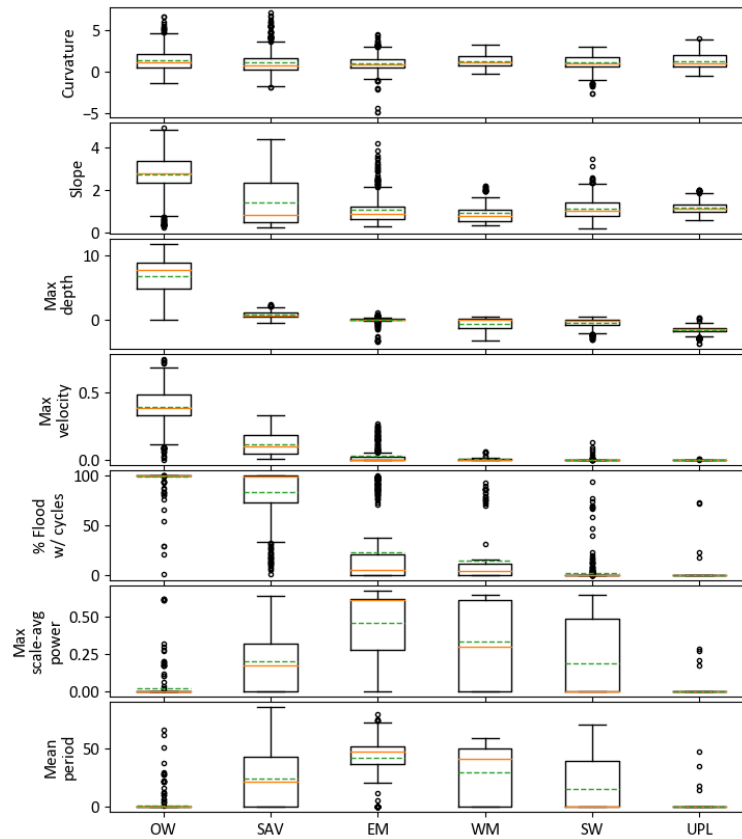


Figure 148: Physical variables distribution by wetland class for the Detroit River Marsh vegetation dataset. Orange line corresponds to the median while green dashed line corresponds to the mean.

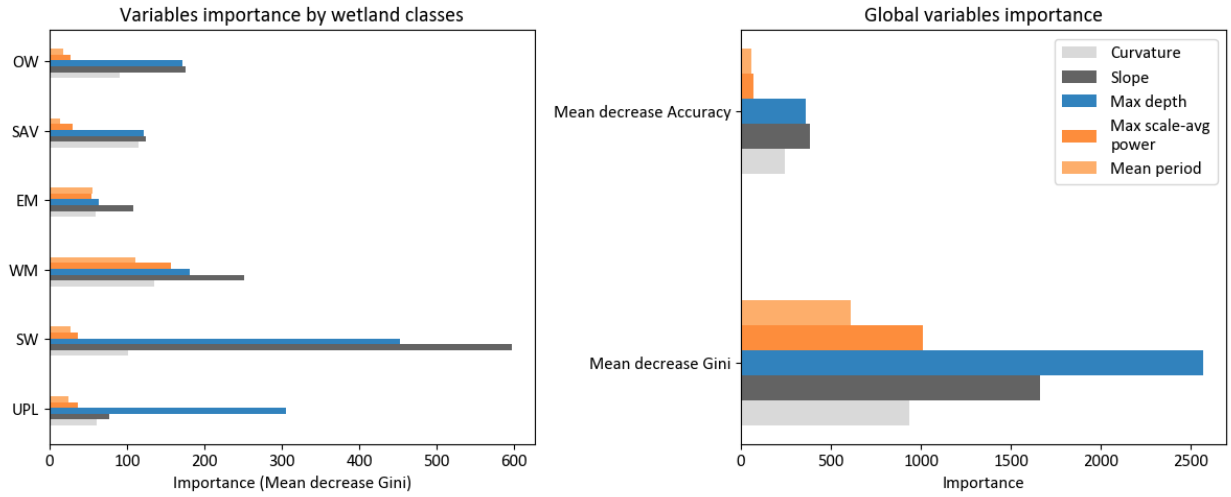


Figure 149: Variables importance by wetland classes (left) and global variable importance (right) for the Lake St. Clair random forest model.

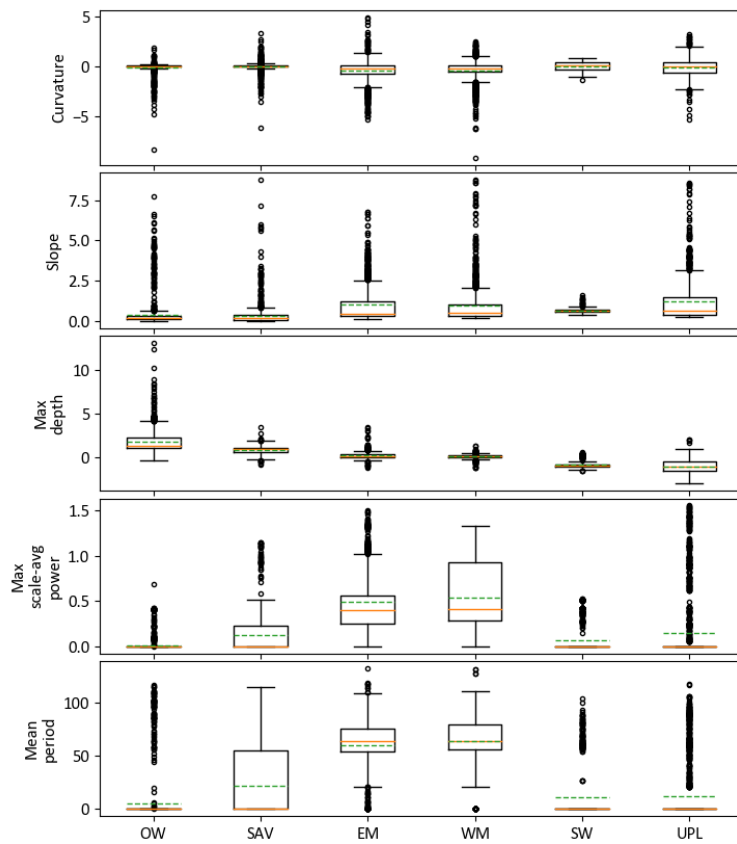


Figure 150: Physical variables distribution by wetland class for the Lake St. Clair vegetation dataset. Orange line corresponds to the median while green dashed line corresponds to the mean.

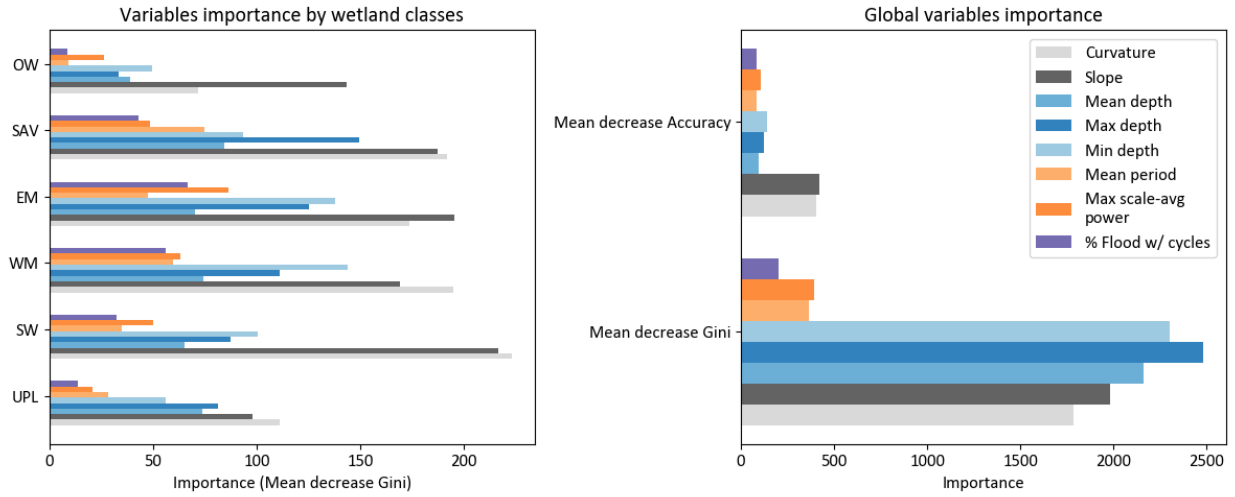


Figure 151: Variables importance by wetland classes (left) and global variable importance (right) for the Lake Huron random forest model.

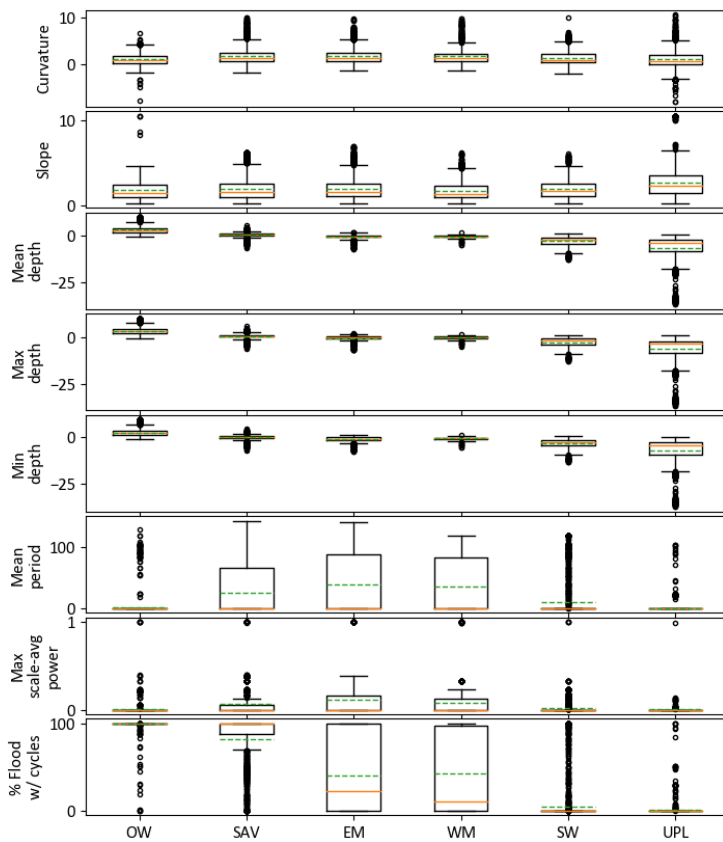


Figure 152: Physical variables distribution by wetland class for the Lake Huron vegetation dataset. Orange line corresponds to the median while green dashed line corresponds to the mean.

6.1.8. Wetland model calibration and validation

The RF models are calibrated using hydroperiod variables aggregated on a two to three year time window with all the vegetation samples available. The RF model is trained using bootstrap aggregation, where each new tree is fit from a bootstrap sample of the training observations $z_i = (x_i, y_i)$. The *out-of-bag* (OOB) error is the average error for each z_i calculated using predictions from the trees that do not contain z_i in their respective bootstrap sample. This allows the RF model to be fit and validated whilst being trained (Hastie *et al.*, 2009). The *out-of-bag* samples are used to calculate the confusion matrix and other validation metrics such as the Global Accuracy, Precision, Recall, F1-Score, and Cohen's kappa score (Cohen, 1960; Powers, 2008) in comparison with the ground truth samples. The global accuracy is the number of correct predictions in relation to the total number of samples. Precision measures the number of correct predictions in relation to the total number of predictions, thus measuring the overestimation. Recall measures the number of correct predictions in relation to the total number of occurrence, thus measuring the underestimation. A low precision score signifies the class is overestimated, whereas a low recall score signifies the class is underestimated. The F1-Score is the harmonic mean between the recall and precision. Kappa score measures the proportion of specific agreement of the model ranging from -1 to 1. This metric assesses whether model prediction could result from chance alone, as a kappa value of zero indicates no differences with random predictions (Cohen, 1960). Kappa scores less than 0.4 are considered low and indicate a poor performance of the model, whereas scores between 0.4 and 0.6 are considered moderate, and scores greater than 0.6 are considered high and indicate excellent performance of the model.

Two different succession algorithms have been calibrated, one for the southern sites (Upper St. Lawrence, Lake Ontario, Lake Erie and Lake St. Clair) and one for Lake Huron. The succession algorithms were calibrated on a subset of the Lake Erie vegetation dataset and the Lake Huron vegetation dataset. The Lake Erie dataset was chosen because it is the dataset with the most high-quality data including two classes of swamps. Since most Lake Huron sites contain an exceptional biodiversity and high abundance of non-persistent emergent marshes, a different succession algorithm was calibrated for this lake using a subset of the vegetation samples. Succession periods and conditions were fine-tuned based on the literature and using the calibration dataset composed of 70% of the samples. Once a satisfying model was obtained, it was validated on the remaining subset of the vegetation samples.

Overall, the validation suggests that most models have good performance with Kappa scores ranging from 0.52 to 0.78 on the succession algorithm validation (Tables 42 to 48). The model with the highest performance is the 1HIE model (0.78 Kappa score) followed by the 12DRM model (0.75 Kappa score). Lake Ontario and Lake Erie models have good overall performance and estimate all classes with a F1-Score greater than 0.58. The Lake St. Clair model also demonstrates good overall performance (0.63 Kappa score), but it has a poor performance for WM that is confused with EM. Lake Huron model suggest some confusion between EM and WM but presents an overall high performance (0.6 Kappa score). The lowest performing model is the 7GRM model (0.52 Kappa score), where there is some confusion for WM, SS and TS classes. CWRM predictions were compared to wetland classifications, and mapping results are presented in Figures 153 to 156 for some sites in Lake Erie and Lake Ontario. The results presented suggest performance from good to excellent for all the models. Most wetland classes present also good scores, maybe with an exception of WM that can have low precision or recall scores in some lakes. In some case, this can be due to the sparse presence of WM in the calibration dataset. Also, the wetland succession model does not take into account invasive species, such as cattail, which have a wide range of tolerance to hydrophilic conditions and that are invading WM in some locations. This may lead to an overestimation or underestimation of WM in some sites. But overall, performance for most wetland class stands between good and excellent.

Table 42: Validation metrics for Hill Island (1HIE) wetland community model.

Random Forest							
	Model	OW	SAV	EM	WM	SW	UPL
OOB error	0.16						
Accuracy	0.84						
Kappa	0.80						
Recall		0.78	0.88	0.78	0.28	0.80	0.87
Precision		0.93	0.89	0.73	0.51	0.85	0.84
F1-score		0.94	0.88	0.76	0.36	0.82	0.86

Succession Algorithm							
Accuracy score	0.83						
Kappa	0.79						
Recall		0.98	0.76	0.768	0.75	0.76	0.89
Precision		0.85	0.92	0.746	0.39	0.75	0.899
F1-score		0.91	0.83	0.757	0.51	0.80	0.895

Table 43: Validation metrics for Lake Ontario wetland community model.

Random Forest							
	Model	OW	SAV	EM	WM	SW	UPL
OOB error	0.20						
Accuracy	0.80						
Kappa	0.76						
Recall		0.92	0.86	0.79	0.72	0.72	0.80
Precision		0.95	0.85	0.75	0.71	0.73	0.83
F1-score		0.94	0.86	0.77	0.72	0.73	0.81

Succession Algorithm							
Accuracy score	0.74						
Kappa	0.68						
Recall		0.88	0.80	0.72	0.69	0.59	0.71
Precision		0.92	0.85	0.61	0.59	0.56	0.97
F1-score		0.90	0.82	0.66	0.63	0.58	0.82

Table 44: Validation metrics for Grand River Mouth (7GRM) wetland community model.

Random Forest								
	Model	OW	SAV	EM	WM	SS	TS	UPL
OOB error	0.26							
Accuracy	0.74							
Kappa	0.69							
Recall		0.80	0.73	0.78	0.70	0.73	0.71	0.71
Precision		0.89	0.70	0.77	0.70	0.76	0.67	0.72
F1-score		0.84	0.71	0.78	0.70	0.74	0.69	0.72

Succession Algorithm								
Accuracy score	0.59							
Kappa	0.52							
Recall		0.81	0.46	0.76	0.50	0.30	0.51	0.62
Precision		0.95	0.86	0.44	0.40	0.20	0.58	0.88
F1-score		0.87	0.60	0.56	0.44	0.24	0.54	0.73

Table 45: Validation metrics for Lake Erie wetland community model.

Random Forest								
	Model	OW	SAV	EM	WM	SS	TS	UPL
OOB error	0.19							
Accuracy	0.81							
Kappa	0.78							
Recall		0.92	0.82	0.87	0.75	0.81	0.76	0.78
Precision		0.96	0.83	0.87	0.77	0.80	0.77	0.73
F1-score		0.94	0.83	0.87	0.76	0.80	0.77	0.76

Succession Algorithm								
Accuracy score	0.70							
Kappa	0.65							
Recall		0.89	0.66	0.82	0.70	0.73	0.50	0.68
Precision		0.78	0.84	0.60	0.54	0.70	0.70	0.85
F1-score		0.83	0.74	0.69	0.61	0.71	0.58	0.76

Table 46: Calibration and validation metrics for the Detroit river marsh (12DRM) wetland community model.

Random Forest								
	Model	OW	SAV	EM	WM	SW	UPL	
OOB error	0.14							
Accuracy	0.86							
Kappa	0.83							
Recall		0.92	0.95	0.81	0.72	0.77	0.88	
Precision		0.98	0.90	0.80	0.89	0.77	0.92	
F1-score		0.95	0.92	0.80	0.80	0.77	0.90	

Succession Algorithm								
Accuracy score	0.80							
Kappa	0.75							
Recall		0.96	0.70	0.60	0.47	0.94	0.91	
Precision		0.96	0.95	0.64	0.81	0.61	0.98	
F1-score		0.95	0.81	0.62	0.60	0.74	0.94	

Table 47: Calibration and validation metrics for the Lake Saint Clair (13LSC and 14SAM) wetland community model.

Random Forest							
	Model	OW	SAV	EM	WM	SW	UPL
OOB error	0.18						
Accuracy	0.82						
Kappa	0.78						
Recall		0.86	0.73	0.69	0.85	0.92	0.92
Precision		0.86	0.77	0.71	0.77	0.91	0.90
F1-score		0.86	0.75	0.70	0.81	0.92	0.91

Succession Algorithm							
Accuracy score	0.69						
Kappa	0.63						
Recall		0.94	0.72	0.85	0.21	0.81	0.66
Precision		0.99	0.97	0.45	0.62	0.43	0.98
F1-score		0.96	0.83	0.59	0.32	0.56	0.79

Table 48: Calibration and validation metrics for the Lake Huron wetland community model.

Random Forest							
	Model	OW	SAV	EM	WM	SW	UPL
OOB error	0.24						
Accuracy	0.76						
Kappa	0.72						
Recall		0.85	0.73	0.69	0.78	0.70	0.85
Precision		0.87	0.71	0.69	0.71	0.74	0.85
F1-score		0.86	0.72	0.69	0.74	0.72	0.85

Succession Algorithm							
Accuracy score	0.67						
Kappa	0.60						
Recall		0.88	0.40	0.46	0.78	0.71	0.83
Precision		0.87	0.79	0.53	0.39	0.66	0.88
F1-score		0.87	0.53	0.49	0.52	0.69	0.85

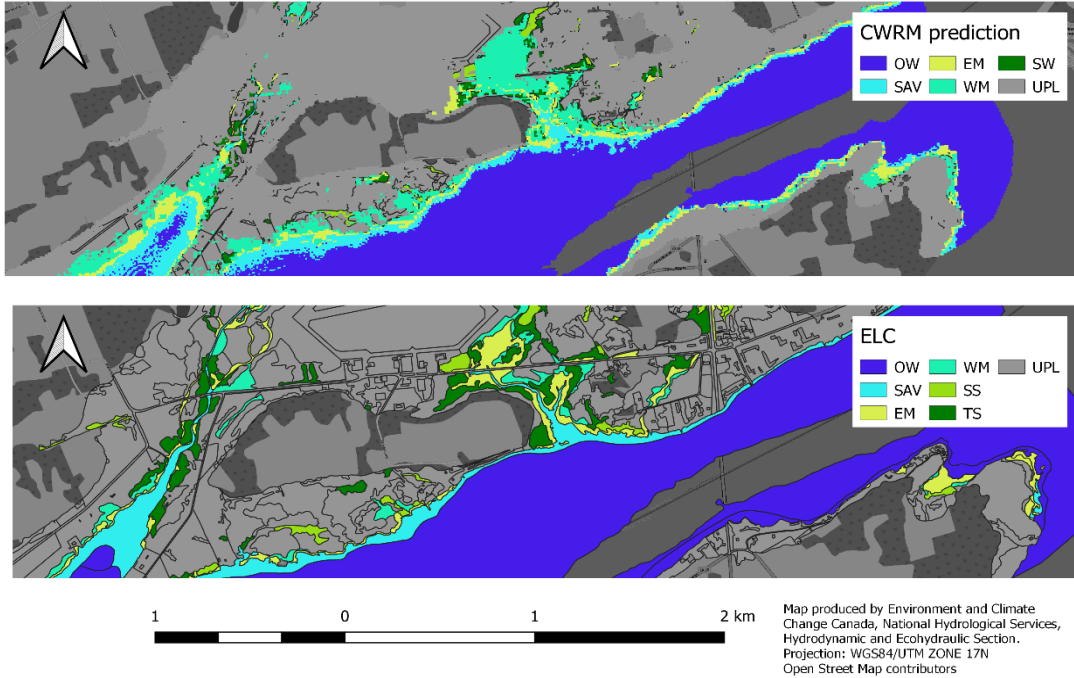


Figure 153: Wetland model prediction using the observed water levels time series (1980-2018) at Airport Creek Marsh (2ACM) in 2008 (upper) and observed wetland classes by ELC (lower) for the same year. ELC wetland classes were converted to match with CWRM wetland classes.

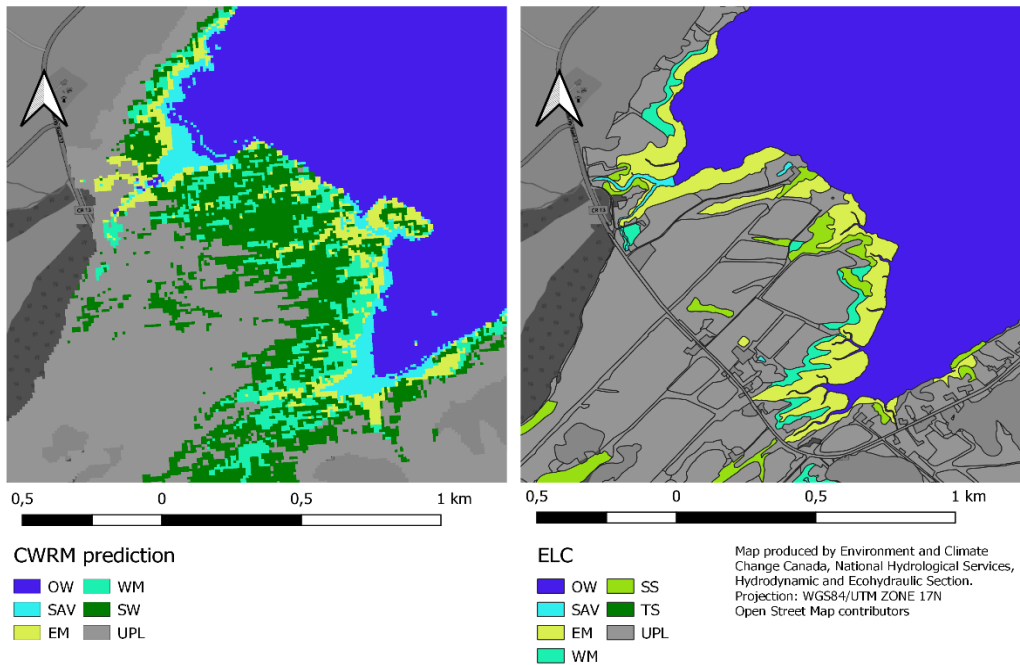


Figure 154: Wetland model prediction using the observed water levels time series (1980-2018) at South Bay Marsh (3SBM) in 2008 (left) and observed wetland classes by ELC (right) for the same year. ELC wetland classes were converted to match with CWRM wetland classes.

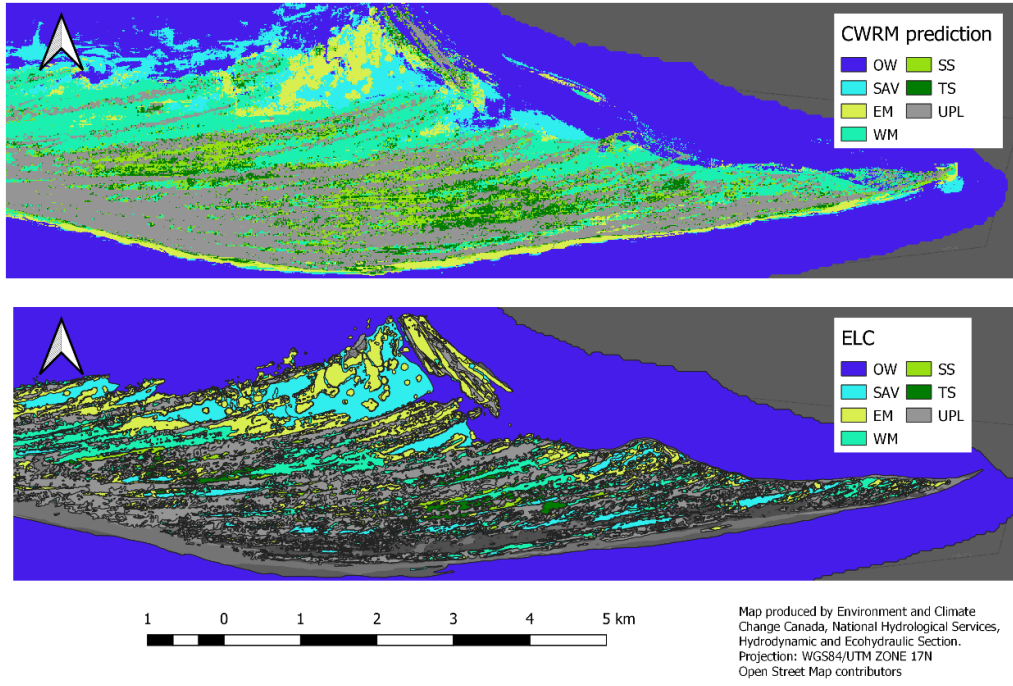


Figure 155: Wetland model prediction using the observed water levels time series (1980-2018) at Long Point (9LPW) in 2010 (upper) and observed wetland classes by ELC (lower) for the same year. ELC wetland classes were converted to match with CWRM wetland classes.

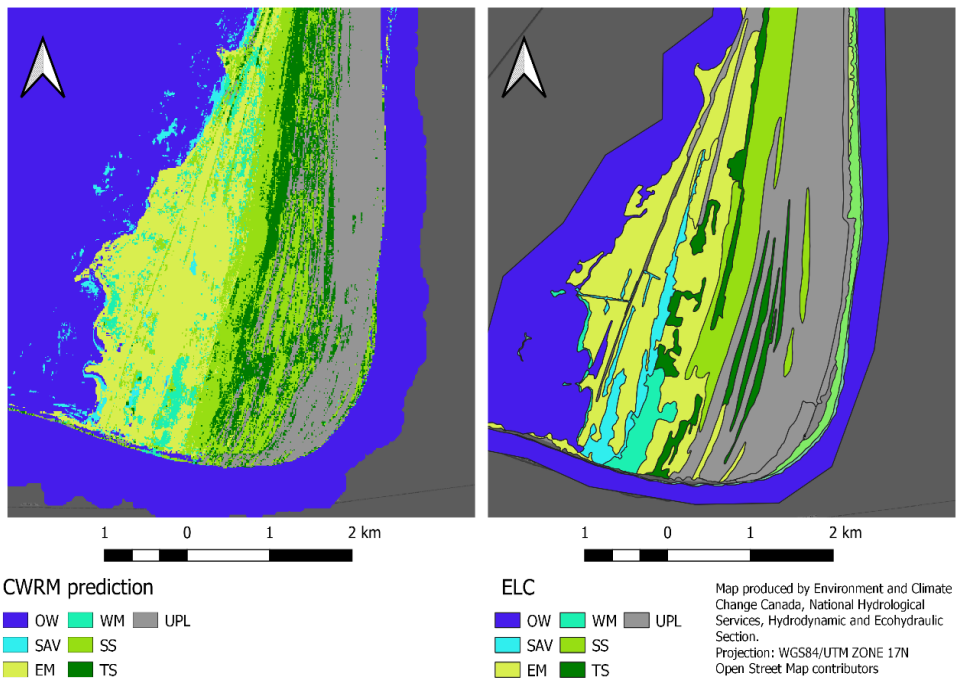


Figure 156: Wetland model prediction using the observed water levels time series (1980-2018) at Rondeau Bay (10RBY) in 2010 (upper) and observed wetland classes by ELC (lower) for the same year. ELC wetland classes were converted to match with CWRM wetland classes.

6.2. Invasive species modelling

Two invasive species were modelled in this study. These two plants are the two most abundant invasive plant species in the Great Lakes that threaten the biodiversity: the hybrid cattail (*Typha glauca*) and the invasive common-reed (*Phragmites australis*). These plants can be present in several wetland classes: SAV, EM, WM and SS. When the invasion of these classes is advanced, the wetland is trapped in an ecological “dead-end”, and the system cannot reverse to natural hydrosphere migration (Tougas-Tellier *et al.*, 2015; Lavoie *et al.*, 2012). Since both species do not currently fully occupy their ecological niche, it is difficult to dissociate the natural growth/invasion of the species with the expansion under climate change at the wetland class scale. That is why two distinct models were developed for these species:

1. Suitable habitat model (SHM) estimates the suitable habitat area based on the hydrological conditions of a given year. The comparison of suitable area between the recent past and future periods indicates the impact of climate change on the invasive species.
2. Population growth models (PGM) simulate the growth of invasive species and the impact on the other wetland classes.

SHM consists of modelling the potential ecological niche of the species. As suggested by Mazur *et al.* (2014), ecological niche models assume that an invasive species colonizing a new area conserves its prior niche (Fitzpatrick & Weltzin, 2005). The best modelling approach would be to use a correlative model based on a fully realized niche to inform the vulnerability of given site to invasion (Beaumont *et al.*, 2009). Since invasive species, such as *Phragmites*, do not fully occupy their respective ecological niche and are still expanding, there is no available data on the fully occupied niche of that species. Therefore, the current distribution of both species in its unrealized niche has been used to predict suitable habitat under different climate change scenarios and to assess the impact of climate change on the suitable habitat of both species (Peterson *et al.*, 2003).

A model predicting the presence or absence of each species has been developed by using vegetation samples from various sources. Similar to the wetland class modelling approach, this approach uses a Random Forest model and hydroperiod and topographic variables to predict if the habitat is suitable or not for the species. One model has been developed for each species using calibration datasets from different sites across Lake Ontario, Lake St. Clair and Lake Erie. The same model for each invasive species is applied for all 20 sites. The model calibration requires a balanced dataset where the number of presence equals the number of absence. Using the data available, all the presence and absence samples used are randomly selected nodes identified as

open water, swamps or upland. The other wetland classes were omitted from the absence record since those classes might correspond to the same ecological niche as both invasive species.

PGM simulates the growth of the two species exclusively based on the hydraulic conditions and topography. These models are based on the literature, and the parameters were fine-tuned so the predictions fit with observation data. Other factors such as the road density, urbanization and temperature were not considered.

PGM integrates three different models in sequence. The first part is the wetland model that predicts a wetland class for each node and for each year for the different climate change scenarios. The second part is the *Typha* PGM which uses the wetland model predictions as an input for the different functions such as the germination and the vegetative propagation (e.g. *Typha* will not germinate if the swamp class is predicted). The *Phragmites* model comes last and uses the *Typha* and wetland model outputs as input. Because *Typha x glauca* was present in the system prior to *Phragmites*, it was important to integrate the interaction between both species. We also assumed, based on observations and the scientific literature, that if both invasive species models predict a presence, the *Phragmites* will dominate because of its competitive advantage.

6.2.1. Cattail (*Typha*)

Cattail is an emblematic wetland species that is part of the biological cycle of several other wildlife species (e.g. muskrats, least bittern). Although only one cattail species is native to the Great Lakes system, three cattail species are now common throughout the system (*T. lagustifolia* (native), *T. angustifolia* (introduced) and *T. x glauca* (hybrid)). Their abundance can be linked to water-level management and can alter the biodiversity of the wetland plant community (Wilcox & Xie 2007; Morin *et al.*, 2016). The cattail models developed herein are used to simulate the growth of this plant under different climate-change scenarios and to evaluate the impact of this invasive plant on largewetland classes.

6.2.1.1. *Typha* ecology

Cattails belong to the *Typha* genus, a cosmopolitan taxa with about thirty species of monocotyledonous flowering plants within the *Typhaceae* family. *Typha* leaves are alternate and mostly basal on a single vertical stem reaching up to 3 m of height and a maximum single vertical stem up to approximately 2.5 m bearing the flowering spikes. This plant is monoecious, with numerous unisexual flowers developing in dense racemes (Apfelbaum, 1985). Male flowers form

a narrow spike at the top of the vertical stem, while female flowers form a dense, sausage-shaped spike just below the male spike (Ricketson, 2001). Cattails are prolific and can quickly dominate a wetland plant community (Zedler & Kercher, 2004). Monotypic stands of cattails reduce overall habitat value but are favorable for muskrats and breeding songbirds (Sojda & Solberg, 1993).

Cattails are found in shallow and deep marshes facing limited wave action (Morin *et al.*, 2005;; Turgeon & Morin, 2005; Morin *et al.*, 2016). Marshes with cattails are also characterized by gentle slopes, few flooding cycles and slow-to-moderate water velocity (Table 49). Although they are flood-tolerant, cattails are favored by moderate flooding (Bedish, 1967; Boers & Zedler, 2008; Ellison & Bedford, 1995; S. W. harris & Marshall, 1963; Zedler & Kercher, 2004), and water depths between 0.50 and 0.90 m appear to be optimal for the genus (Grace & Wetzel, 1981, 1982; Waters & Shay, 1990). *T. x glauca*, however, tolerates a wider range of depths than its parent species, as its vegetative shoots increase in height and dry mass along a water depth gradient up to 1 m (Waters & Shay, 1990). *T. x glauca* has been associated with high soil nutrients, low light, and large amounts of litter, contrary to the native *T. latifolia*, which produces shallow litter areas (Farrer & Goldberg, 2009; Waters & Shay, 1990). As such, invasions of *T. x glauca* can result in a 50% decline of plant diversity 10 to 25 years after the invasion and an increase in the organic layer of the soil after 35 years (Mitchell *et al.*, 2011).

Cattail can either be rooted in hydric mineral or organic soils or established on buoyant mats (Krusi and Wein, 1988). These mats contain belowground biomass, dead organic material, and minerals (Azza *et al.*, 2006). Most of the time, mat sections closest to shore are attached to the lakebed, while sections toward the lake are free-floating. The initiation of floating mats occurs when emergent vegetation detaches from the lakebed while bringing an upper layer of soil carrying rooted materials. As floating mats move with water levels and are not really affected by their variations (Krusi & Wein, 1988; Swarzenski *et al.*, 1991), the relation between their distribution and environmental variables is different than for rooted cattails. In Lake Ontario, floating mats of cattails occurred in some sites close to the shore just above the water and did not seem to respond to water-level variations (Wilcox & Xie, 2007).

Table 49: Cattail hydrological and topographical habitat requirements according to the life stages of the species.

Life stage	Criteria	Ideal	Suitable	Problematic
Germination	Water depth	2 to 16 cm ¹	0 to 2 cm ¹ 20 to 60 cm ⁷	>40 cm ² <0 cm
	Inter-annual fluctuations	Drawdown ¹⁴		
Seedling	Water depth	-20 to 0 cm ¹² 20 cm ⁷	-25 cm ¹²	>63 cm ⁶
Adults	Water depth	0.15 - 1.00 m ¹³	-0.15 to 1.00 ¹³ -20 cm to 20 cm ¹⁰	0.90-1.20 m over the top of existing shoots in spring ¹³
	Wave energy	Low ¹³	Moderate ¹³	High
	Wet-dry cycles	Stable ^{2, 13}	Moderate ¹³	Absent or frequent ¹³
	Slope	No slope ¹³	Low slope ¹³	Heavy slope ¹³
Vegetative propagation	Lateral spread	4m/yr ⁸	1m/yr ⁷	
	Water depth	2 to 5 cm ⁹	-20 cm or +20 cm ¹⁰	> 63 cm ⁵
	Wet-dry cycles	Stable ⁸	Moderate ⁸	High ⁸

¹ Meng *et al.*, 2016

² Bansal *et al.*, 2019; D. A. Wilcox *et al.*, 2008

³ Bourgeois *et al.*, 2012

⁴ Asamoah & Bork, 2010

⁵ Gucker, 2008

⁶ Snyder, 1985

⁷ Sharp, 2002

⁸ Boers & Zedler, 2008

⁹ Bedish, 1967

¹⁰ Bunbury-Blanchette *et al.*, 2015

¹¹ Frieswyk & Zedler, 2007

¹² Zedler & Kercher, 2004

¹³ Morin *et al.*, 2016

¹⁴ van der Valk & Davis, 1978

6.2.1.2. *Typha* in the Great Lakes

Even if it is possible to find cattail populations containing only one of the three taxa in the Great Lakes, most populations where both parental species (*T. latifolia* and *T. angustifolia*) are sympatric also contain the hybrid *T. x glauca* (Galatowitsch *et al.*, 1999). *T. latifolia* is a cosmopolitan species found in a variety of North American wetlands (Grace & Harrison, 1986). Although the status of exotic *T. angustifolia* is still debated (Shih & Finkelstein, 2008), it seems that this species was introduced on the Atlantic coast when the first European settlers arrived in the early 19th century (Stuckey & Salamon, 1987). By the end of the 19th century, the species was observed on the mainland east of the Great Lakes (Galatowitsch *et al.*, 1999). Shih & Finkelstein (2008) noticed that the distribution of *T. latifolia* and *T. angustifolia* has been expanding since the mid-20th century. The presence of *T. angustifolia* as a dominant species dates back to the 1970s (Travis *et al.*, 2010), and it is now abundant throughout southern Canada and northern United States, from the Atlantic coast to the Rockies (Grace & Harrison, 1986). The

expansion of *T. latifolia* and *T. angustifolia* distribution has resulted in a greater coexistence of these species and promoted the establishment of *T. x glauca*. *T. x glauca* has been present in the Great Lakes region for more than 50 years (Frieswyk & Zedler, 2007; Galatowitsch *et al.*, 1999; S. C. Lishawa *et al.*, 2013) and began to expand in some landscapes in the late 1980s (Frieswyk & Zedler, 2007). In different water bodies, *T. x glauca* expanded its distribution in response to higher and more stable water levels in regulated water bodies, like Lake Ontario (Seabloom *et al.*, 2001; Wilcox *et al.*, 2008).

6.2.1.3. **Typha dataset**

To calibrate the *Typha* SHM, various datasets were used for every site (Table 50). Presence data were taken from the vegetation surveys (CWS), ELC (Ontario Ministry of Natural Resources and Forestry, 2019b) and WTT (Snell and Cecile Environmental Research, 2001) datasets (see Section 6.1.3. for more details on the datasets) for the Grand River Mouth (7GRM), Long Point (9LPW), Rondeau Bay (10RBY), St. Clair (13LSC) and Johnston Bay (14SAM) sites (Section 6.1.3 for more details). Absence data were randomly selected to balance with the number of presence observations using samples that belong to the classes OW, SAV, SS, TS and UPL as identified by the wetland classification dataset.

Table 50: Description of the vegetation dataset used to calibrate the cattail suitable habitat models composed of presence and absence of various sources (Wetland Trends through Time, Ecological Land Classification and GLPI vegetation surveys).

Site	Survey year	Dataset	N presence Typha	N absence Typha
7GRM	1983	WTT	1000	789
	1988	WTT	1000	877
	1995	WTT	1000	1002
	2000	WTT	1000	1002
	2018	CWS	82	47
	2019	CWS	72	59
9LPW	1985	WTT	1000	1002
	1995	WTT	1000	1002
	1999	WTT	1000	1002
	2018	CWS	35	49
	2019	CWS	54	40
10RBY	1985	WTT	1000	678
	1988	WTT	32	550
	1995	WTT	1000	756
	2018	CWS	41	67
	2019	CWS	41	63
13LSC/ 14SAM	1985	WTT	1000	695
	1988	WTT	0	677
	2018	CWS	9	11
	2019	CWS	10	8
TOTAL			10376	10376

6.2.1.4. Typha SHM

The Hydrology and Ecohydraulic Section of ECCC has developed SHM for *Typha angustifolia* and *Typha latifolia* in the St. Lawrence River (Champoux *et al.*, 2002; Turgeon *et al.*, 2004) with an approach inspired by Toner and Keddy (1997). The section also developed an SHM for *Typha* ssp in the Rainy Lake – Namakan reservoir that predict where the habitat is suitable for the establishment of the gender using logistic regression (Morin *et al.*, 2016). The *Typha* SHM for the Great Lakes is a supervised model calibrated using absence/presence dataset (Table 50) as dependent variables and environmental variables (topographic and hydroperiod variables) as independent variables. The latter includes slope and curvature at 310 m scale, maximum, minimum and average water depth, average cycle period, as well as maximum scale-averaged wavelet power. The importance of the variables to the model is calculated with the Gini importance metric (hastie *et al.*, 2009). Slope was found to be the most important variable among the

predictors (Figure 157). The relative importance of the water depth variables (minimum, maximum and average water depths) is necessarily lower since these variables are highly correlated, which diffuses their feature importance (Perrier, 2015). Since the water depth variables each have a relatively high importance, water depth is a major component to the model and allows the comparison of water level scenarios. *Typha* habitat is characterized by low slope and near 0 m water depth (Figure 158). Variables related to short-term water level fluctuations, i.e. the mean cycle period and maximum scale-averaged power, do not significantly differ between absence and presence samples.

The model is applied to the recent past and future periods for each climate scenario in order to compare the change between both periods and to assess the impact of climate change on *Typha* suitable habitat.

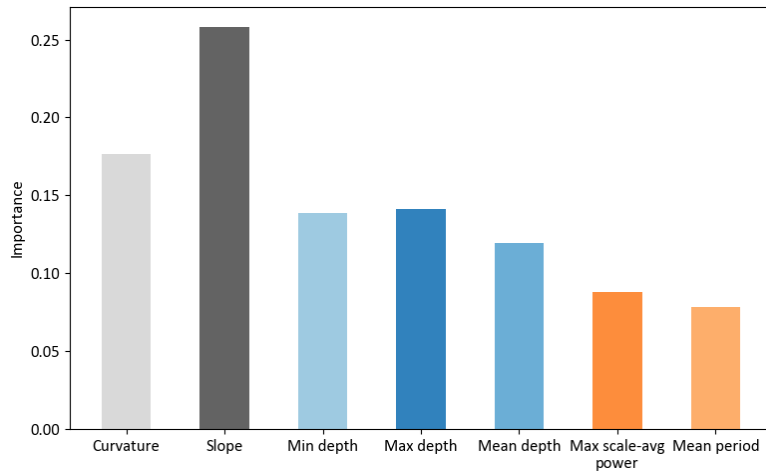


Figure 157: Independent variables relative importance of the cattail suitable habitat model.

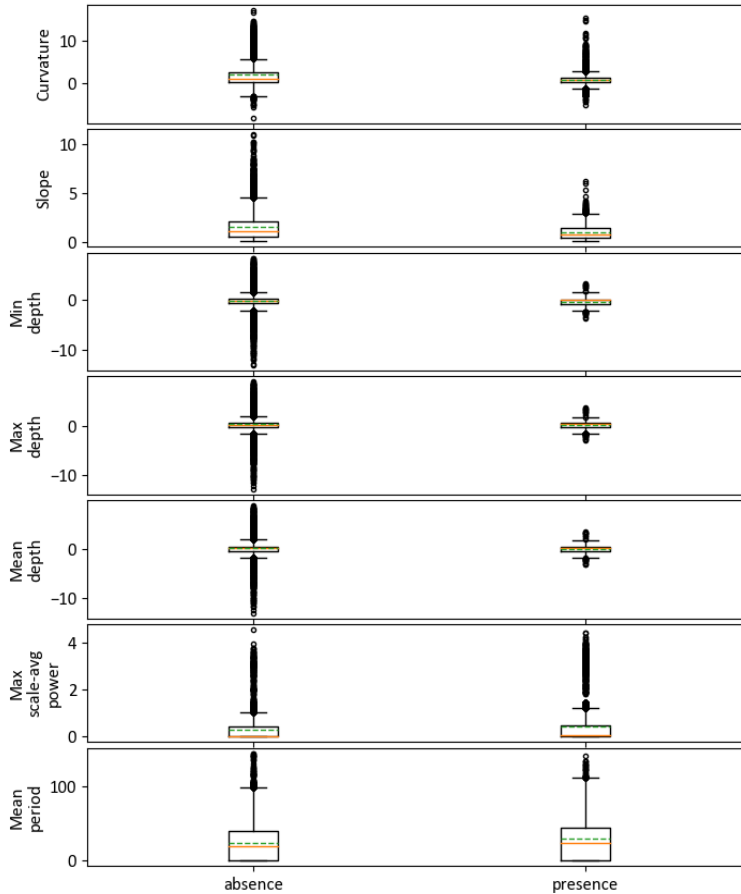


Figure 158: Boxplot distribution of the environmental variables of the cattail suitable habitat model dataset. Orange line corresponds to median, whereas green dashed line corresponds to mean.

6.2.1.5. *Typha* PGM

6.2.1.5.1. Model concept

The *Typha* PGM stochastically simulates the growth (expansion) of the species by reproducing in a simplified way some of the plant phenological stages and invasion mechanisms such as seed germination, survival of seedlings and adult plants, litter accumulation and vegetative propagation. PGM uses some of the concepts of the Gleasonian approach in which succession of freshwater wetlands is based on the life history traits of the species present (van der Valk, 1981). In *Typha* PGM, *Typha* seeds present germinate from the seedbank and grow as a result of a water level drawdown occurring during the previous growing season. In this approach, plant establishment is randomly influenced by seed dispersal. *Typha* PGM also included a litter accumulation algorithm slightly modified from the version proposed by Morin *et al.* (2016) in which wetland plant diversity decreases as litter accumulate (Lishawa *et al.*, 2010; Mitchell *et al.*, 2011) and the monotypic *Typha* stand can reach a floating mat stage that is no longer influenced by

interannual water level fluctuation (Mitchell *et al.*, 2011; White *et al.*, 2008). *Typha* PGM also simulates the vegetative propagation of the species to neighboring nodes, simulating the rhizome spread according to environmental conditions.

Typha PGM is then composed of five stages where different mechanisms are associated with each stage (Figure 159). The stages are: absence (no *Typha*), seedling, adult, monotypic stand and floating mat. The switch between stages may take one to several years, depending on the stages transition (e.g. No *Typha* to adult will take 1 year, whereas monotypic stand to floating mat requires at least 31 years).

Because *Typha* is monoecious, it reproduces primarily by seed dispersal. Seed germination is therefore a critical mechanism that controls the establishment of the species. Seed germination mostly occurs on exposed, saturated soils but can also occur under water where light can penetrate up to 40 cm of water depth (Bansal *et al.*, 2019). Germination in PGM occurs for nodes that were “No *Typha*” during the previous year and may present adequate conditions for seedling establishment.

Seedling survival is another critical mechanism, since flooding over 40 cm more than one month after germination can cause seedling mortality (Bansal *et al.*, 2019). A seedling survival function has been developed and applied during the year of germination. This function allows the node with a stage “seedling” facing adequate conditions to move to the stage “adult” or returns to the stage “no *Typha*” if the seedling does not survive.

The adult stage has two mechanisms to move to another stage: the adult survival and the litter accumulation. The adult survival function determines if the adult survives under specific environmental conditions. If the adult does not survive, it moves to the “No *Typha*” stage. If the adult survives, the litter accumulation function determines if the conditions are favorable for the node to move to the monotypic stage or not. Monotypic stands typically occur around 10 years after *Typha* establishment (Mitchell *et al.*, 2011). The litter accumulation function is an incrementer that counts the favorable (+1) and unfavorable years (-1). When the litter accumulation incrementer reaches +7, the adult transitions to monotypic stand.

The monotypic stand has three mechanisms involved in its change of stage: Adult survival, litter accumulation and vegetative reproduction. If the monotypic stand does not survive, it transitions to adult stage. If the litter accumulation incrementer is < 7 years, it will also transition to adult the following year. Inversely, if the litter accumulation incrementer is > 31 years, the monotypic stand

becomes a floating mat. In the literature, floating mat occurs after around 35 years cumulative years of favorable conditions (low interannual water level fluctuation; Mitchell *et al.*, 2011) and water level control strategy are no longer an option to control them. Monotypic stands also have the ability to propagate vegetatively to neighboring nodes. Once a neighboring node is colonized, it becomes a monotypic stand. The floating mat also propagates vegetatively colonizing neighboring nodes into monotypic stands.

In the following sections, more details are given concerning the stages and mechanisms involved in the *Typha* PGM.

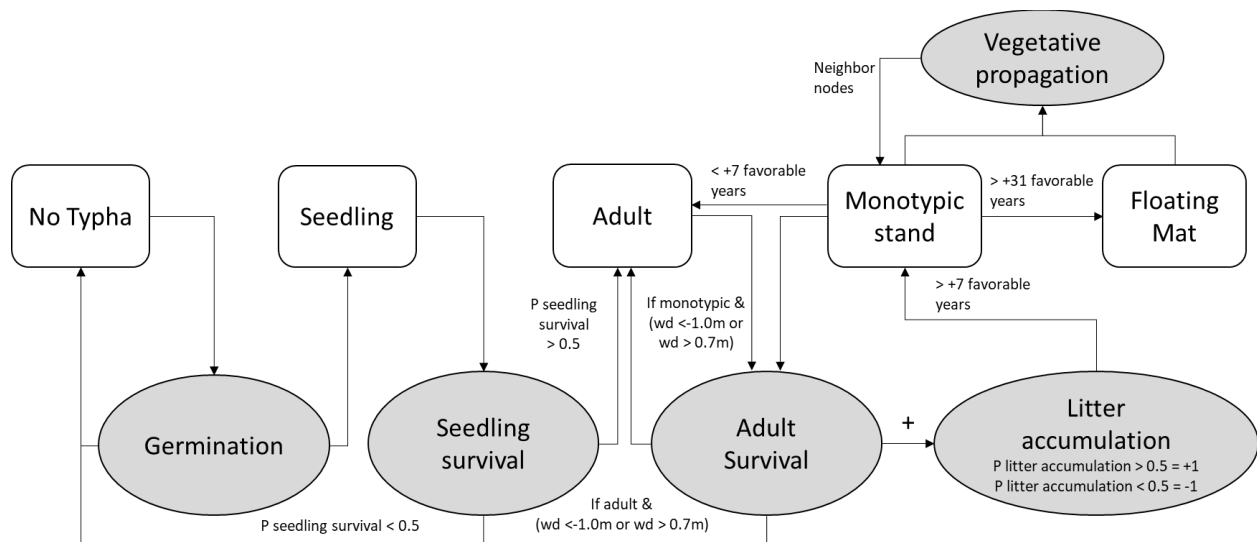


Figure 159: *Typha* Population Growth model conceptual scheme representing the different stages (white boxes) and the mechanisms (grey ellipses) that cause the change of stage from one year to another.

6.2.1.5.2 Germination

Germination occurs in exposed and saturated soils following a period of receding water level, which are characterized by mudflats with suitable water depth (Bansal *et al.*, 2019; Beule, 1979; Lorenzen *et al.*, 2000; Weller, 1975). During the germination phase, a node change from a state defined as unsuitable to suitable for the species (from NT to TSH; step 0 to 1; Figure 159). For a given CWRM node, the germination probability, P_g , is calculated as a function of the probability of water level drawdown (P_{wl}), the probability of water depth reaching a suitable level during the germination period (P_{wd}), and the establishment rate (E_r) (equation 6.1)

$$P_g = P_{wl} * P_{wd} * E_r \quad 6.1$$

The P_{wl} depends on the change in water level observed between the current and previous germination periods (start of the growing season to 1st week of July, QM25). When this change is less than 0, P_{wl} value is set to 0.0. When it is higher than 0.25 m, the probability is then 1.0. Between this depth range (0.0-0.25 m), the probability of drawdown is calculated linearly as presented by the preference curve in Figure 160.

The P_{wd} is the probability for a seed to germinate according to the water depth reached during the current germination period (Figure 161). *Typha* germination occurs generally where water depth is under 40 cm and under saturated substrate (Bansal *et al.*, 2019). The threshold used to predict the P_{wd} were determined based on the biology but also using a calibration via a trial and error approach. It was estimated that the substrate was saturated and can be suitable for germination if the mean water depth during the germination period is between -35 and 35 cm. P_{wd} value is 0.0 when the water depth drops below -0.35 m or rises above 0.35 m. When the water depth remains between -0.25 and 0.25 m, the probability value is equal to 1.0. Outside these ranges, P_{wd} is calculated linearly as presented by the preference curve in Figure 161.

Finally, the establishment rate (E_r) is set at a constant value of 0.001 to simulate the natural and random aspects of seed dispersal in the system. This factor restricts the maximum probability of germination and, hence, the number of nodes that are allowed to germinate into a seedling in a given year. The node germinates randomly, weighted by the probability of germination, P_g .

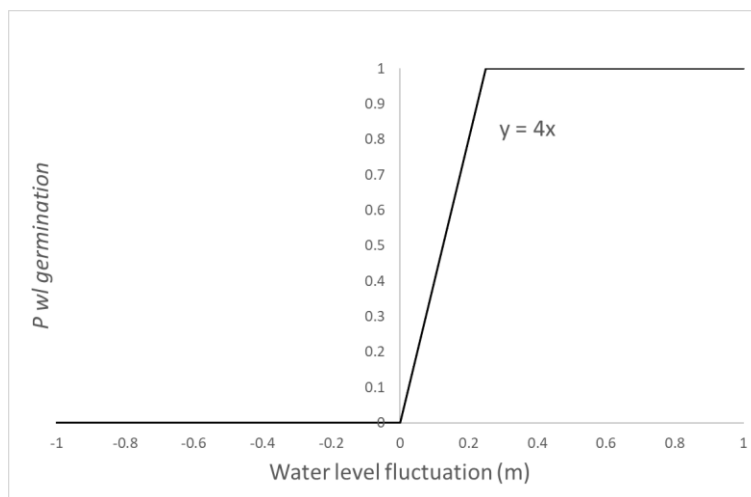


Figure 160: *Typha* germination probability as a function of the water level variation between the preceding year and the current germination period.

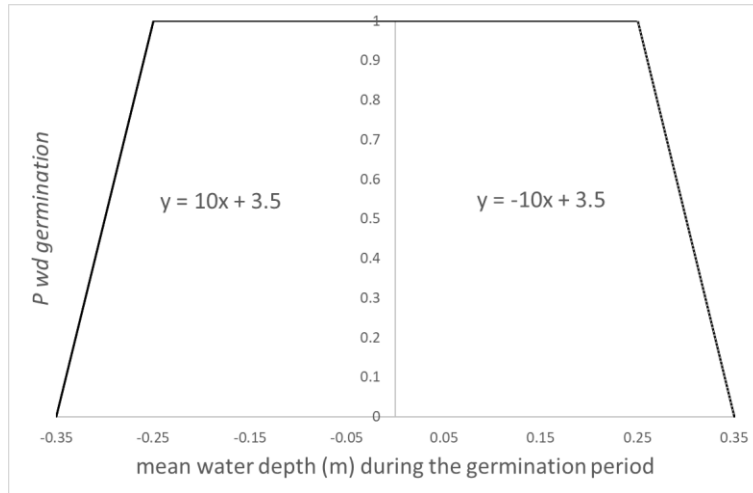


Figure 161: *Typha* germination probability as a function of the water depth during the germination period of the current year.

6.2.1.5.3. Seedling survival

After germination, seedlings need to survive water level fluctuations to become an adult. To survive seedling must be in saturated substrate and that seedling can tolerate a water depth under 40 cm one month after germination (Beule, 1979). Dry conditions also negatively affect the seedling survival, it was estimated that a substrate 35 cm higher than the mean water level during the growing season was unsuitable for *Typha* seedlings. Seedling survival in the PGM is a survival probability function (Figure 162) allowing the seedlings to become adults if the environmental during the whole growing season are favorable for its growth. Seedling survival probability value is 0.0 when water depth drops below or rises above an absolute value of 0.35 m during the entire growing season. When the water depth remains between -0.25 and 0.25 m, the probability is equal to 1.0. Outside these ranges, $P wd$ is calculated linearly as presented by the preference curve in Figure 162.

The probability must be > 0.5 to allow seedling survival, and initiate the transition of the node to move to adult stage the following year (Figure 159).

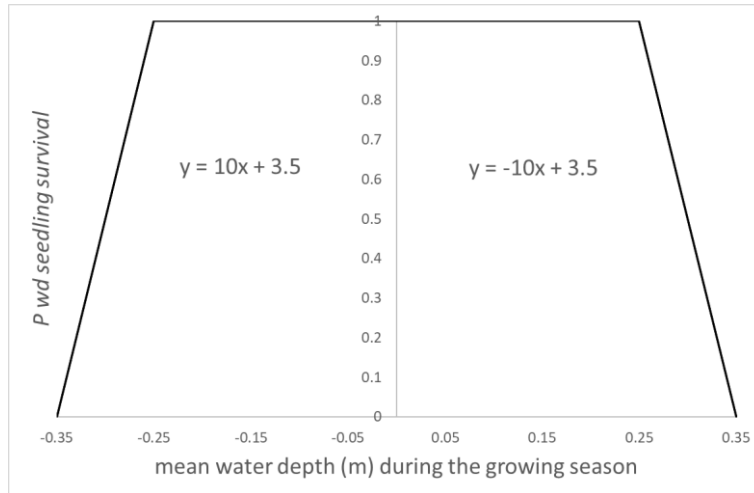


Figure 162: *Typha* seedling survival probability in function of the water depth during the current growing season.

6.2.1.5.4. Adult survival

The adult and monotypic stand stages include an adult survival mechanism (Figure 163) that determines whether the species survive or not. This mechanism acts as a hard reset when the *Typha* subsistence conditions are not met. *Typha* can generally tolerate up to 1.0 m of water over its top (Morin *et al.*, 2016). However, from wetland observations, it was possible to identify a significant loss of *Typha* in Crown Marsh area (Long Point, Lake Erie) during the 1986 high water levels associated to at least 70 cm of mean water depth during the growing season. It was thus determined, that water depth has to remain between -1.0 m and 0.7 m during the growing season so that *Typha* survives. If the node was an adult and the survival criteria is not met, the node moves to “no *Typha*”, whereas if the node was a monotypic stand and the survival criteria is not met, the node moves to adult stage and the litter accumulation increment is reset to 1.

6.2.1.5.5. Litter accumulation

Once the adult and monotypic stand stages survive, the litter accumulation algorithm is applied. This algorithm is an incremter that counts the favorable years. Once > 7 favorable years are accumulated, the node becomes a monotypic stand. When > 31 favorable years are accumulated, the node becomes a floating mat. Over time, the monotypic *Typha* stands lose biodiversity and the species become increasingly dominant. Organic matter accumulates in the monotypic stands, which eventually separate from the substrate, creating floating mats that are no longer influenced by environmental conditions.

Favorable years (+1 to the incremter) are defined as years where the litter accumulation probability exceeds 0.5 and unfavorable years (-1 to the incremter) occur when the litter accumulation probability is below 0.5.

The litter accumulation probability is 0.0 when water depth drops below -1.0 m or rises above 0.7 m during the current growing season. When the water depth remains between -0.35 and 0.35 m, the probability value is equal to 1.0. Outside these ranges, the litter accumulation probability is calculated linearly as presented by the preference curve in Figure 163.

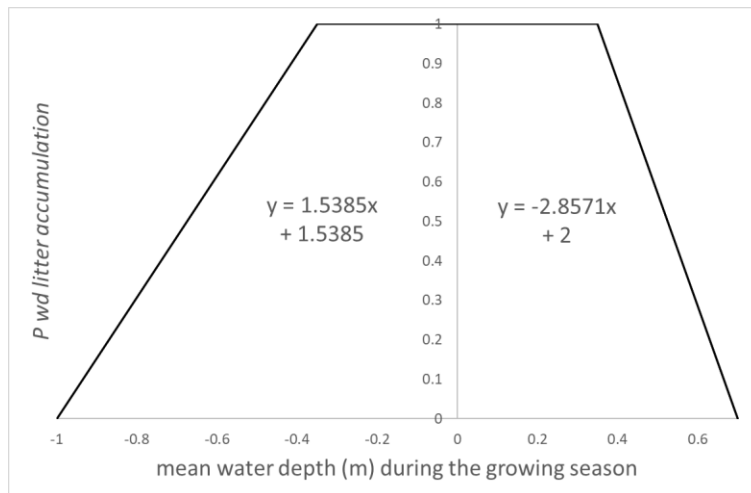


Figure 163: *Typha* litter accumulation probability as a function of the water depth during the current growing season.

6.2.1.5.6. Vegetative propagation

The vegetative propagation mechanism predicts the lateral propagation distance based on water depth, neighboring wetland class, and water level fluctuations. For any nodes reaching the monotypic stand or floating mat stages (Figure 159), vegetation propagation occurs to neighboring nodes. Neighbor nodes are colonized when this lateral distance becomes greater than the distance between the node and its neighbors, and colonized nodes are then assigned the monotypic stand stage.

The lateral vegetative propagation (V_g) is calculated using five components: the previous growth, the vegetative propagation probabilities associated with current water depth, P_{wd} (Figure 164), and year-to-year water level variation, P_{wl} (Figure 165), the propagation probability associated with the predicted wetland class in adjacent nodes, P_{we} (Table 51), and the maximum growth, which was estimated at 4 m for this study (Boers & Zedler, 2008).

For the first year, previous growth is equal to zero. The following years, if the $Vg < \text{distance to neighbors } (d)$, the previous growth is equal to the Vg . When Vg is greater than d , the previous growth is equal to $Vg - d$ (equation 6.3). This variable ensures that the growth in the previous years is accumulated when the distance to neighbors is not reached.

$$Vg(m) = (Max\ growth * P\ wd * P\ wl * P\ we) + previous\ growth \quad 6.2$$

$$previous\ growth = \begin{cases} Vg - d & \text{if } Vg > d \\ Vg & \text{if } Vg \leq d \end{cases} \quad 6.3$$

The vegetative propagation probability associated with water depth, $P\ wd$, is 0.0 when this depth remains below -1.0 m or above 0.7 m during the growing season. It is 1.0 when the water depth remains between these values, and is otherwise calculated linearly as presented by the preference curve in Figure 164.

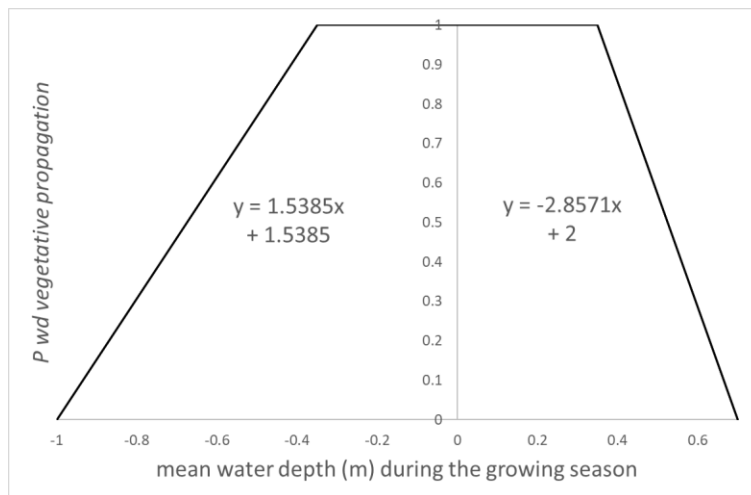


Figure 164: *Typha* vegetative propagation probability in function of the water depth during the current growing season.

The vegetative propagation probability in function of the water level variation ($P\ wl$) between the previous and current year is 1.0 when the variation goes between -0.125 to 0.125 m and 0.0 when is under -0.20 and 0.20 m. Between those values, $P\ wl$ is calculated linearly as presented by the preference curve in Figure 165.

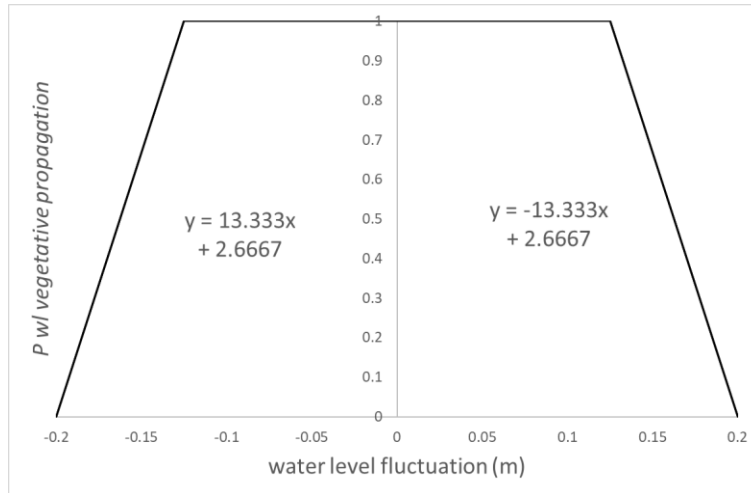


Figure 165: *Typha* vegetative propagation probability in function of the water level fluctuations between the preceding and current growing seasons.

Finally, *Typha* can only expand in wetland classes suitable for this species, i.e. OW, SAV, EM and WM (Table 51).

Table 51: Probability of vegetative propagation in the different wetland classes.

Wetland class	Probability
Open Water	1
Submerged aquatic-vegetation	1
Emergent marshes	1
Wet meadows	1
Shrubby swamps	0
Treed swamps	0
Upland	0

6.2.1.5.7. *Typha* PGM initialization

The year of *Typha* PGM initialization was selected based on literature review and the available data. The exact start date of *T. angustifolia* and hybridisation of *T. X. glauca* invasion in each lake is unknown, but pollen records of *Typha* in the Great Lakes date back to 1945 (Lishawa *et al.*, 2013) and can be used to roughly estimate the starting point. Therefore, the *Typha* model was started in 1956 in the Upper St. Lawrence, as well as in Lakes Ontario, Erie and St. Clair, at the beginning of the water level time series. For Lake Huron, pollen records show that *T. angustifolia* abundance was higher in the southern lakes than in Lake Huron wetlands before 1960 (Shih & Finkelstein, 2008), and that invasion significantly increased between 1960 and 2000. The low abundance of *T. angustifolia* and *T. x. Glauca* in the vegetation samples collected in Lake Huron

compared to those collected in southern lakes confirmed this trend. As a result, the *Typha* model was started in the 1980s at Lake Huron sites.

For the different climate change scenarios, the physical variables are simulated using hydrodynamic conditions for the recent past (1980-2009) and the future (2070-2099) periods. Although, during transition periods (i.e. <1980 and 2010-2069), hydrodynamic conditions are not simulated and the wetland class model is not used. Therefore, to initiate the model and ensure simulations continuity, the establishment and expansion of both invasive species during those transition periods are simply driven by quarter month mean water depth values.

6.2.2. Common reed (*Phragmites australis*)

Common reed, *Phragmites australis*, is a tall (3-5 m) perennial grass that colonizes a wide ecological niche among wetland ecosystems. It can be found in locations ranging from aquatic to terrestrial habitats and on different types of soils with a wide range of organic matter content, pH and nutrient concentrations (Mal & Narine, 2004; Packer *et al.*, 2017). Although native to North America, common reed is now considered as an aggressive exotic invader, thanks to the introduction of a non-native Eurasian genotype (halotype M) that started expanding in North Atlantic coastal marshes between 1960 and 1980 (Chambers *et al.*, 1999; Galatowitsch *et al.*, 1999; Marks *et al.*, 1994; Rice *et al.*, 2000).

The species possesses many characteristics that can explain its success at invading North American wetlands:

1. Reproduces both sexually and vegetatively from fragments, rhizomes or stolons that can advance up to 10 m/yr (Hudon *et al.*, 2005);
2. Produces a large number of seeds that are highly viable and that are dispersed over long distances by wind or water (Kettenring *et al.*, 2011);
3. Produces allelopathic gallic acid that inhibits the growth of co-occurring plants (Rudrappa *et al.*, 2007);
4. Grows taller than any other native marsh species and produces large amount of litter (Hudon *et al.*, 2004);
5. Not consumed by herbivores during the growing season (Dvorák *et al.*, 1998).

Other anthropogenic factors contributed to the success of the invasion in North American wetlands:

1. The eutrophication and disturbances of wetlands (e.g. encroaching on wetlands to perform work with heavy machinery or when creating or refreshing road or agricultural drainage ditches) favored *Phragmites* establishment and growth by eliminating competing vegetation, exposing mudflats that are suitable for reed germination and creating modified hydrological conditions that *Phragmites* can better tolerate than native species (Meyer *et al.*, 2001; Rice *et al.*, 2000; Warren *et al.*, 2001; K. L. Wilcox *et al.*, 2003);
2. The increased nitrogen and phosphorus runoff from agriculture favored the exotic common reed at the expense of the native subspecies of *Phragmites* because it tolerates and more efficiently assimilates high concentrations of nutrients (Chambers *et al.*, 1999; Galatowitsch *et al.*, 1999);
3. The development of the road network contributed to the spread of the species throughout the continent by creating a perfect habitat for common reed, i.e. road ditches (Lavoie, 2008);
4. Lower water levels and higher temperatures possibly induced by a more variable climate favor the spread of the species by exposing wetland substrate (Tougas-Tellier *et al.*, 2015).

Once the non-native Eurasian genotype establishes in a wetland, it expands rapidly at the expense of native wetlands communities, especially *Typha* marsh, wet meadows, sedge/grass meadows, and shallow aquatic vegetation (Jung *et al.*, 2017; Wilcox *et al.*, 2003). Dense *Phragmites* stands, which produce large quantities of litter, will eventually alter its surrounding environment by modifying soil properties, hydrology, nutrient cycling, temperature and incident light (Hudon *et al.*, 2004; Meyerson *et al.*, 2000; Warren *et al.*, 2001; Windham & Lathrop, 1999). Adverse effects of common reed invasion include a decrease in plant diversity; habitat loss of marsh-dependent birds, amphibians, and fishes; and negative effects on infrastructures (stems having the capacity to break up asphalt; Lavoie, 2019; Lavoie *et al.*, 2003; Meyer *et al.*, 2010; Meyerson *et al.*, 2000). Once established, *Phragmites* is hard to control or remove (Hazelton *et al.*, 2014), and management is very costly (Martin & Blossey, 2013). Recently, some researchers advocated that *Phragmites* control programs should prioritize the protection of non-invaded wetlands rather than trying to eliminate *Phragmites* in heavily invaded watersheds (Hazelton *et al.*, 2014). Other authors pointed out that reed beds also provide valuable ecosystem services that can be particularly useful in the context of global warming such as providing resilient vegetation, accretion rates that can keep pace with increasing sea level and nutrient removal (Ludwig *et al.*, 2003; Mozdzer *et al.*, 2010; Rooth *et al.*, 2003).

6.2.2.1. *Phragmites* ecology

Several studies report that *P. australis* seedlings emerge from soil seed banks. The seeds are dispersed in the environment by wind and water and can float on the water surface for a period

of up to 124 days in moving water (Wijte & Gallagher, 1996; van den Broek *et al.*, 2005). Seeds of *P. australis* germinate on bare non-inundated soils like mudflats because they require moist conditions along with light and large diurnal temperature variations to break dormancy (Armstrong *et al.*, 1999; Coops *et al.*, 2004; Haslam, 1971; Mauchamp *et al.*, 2001). Flooding, even by a few centimeters or water, reduces the germination rates (Table 52; Baldwin *et al.*, 2010; Coops & van der Velde, 1995; Haslam, 1971; Meng *et al.*, 2016; Yu *et al.*, 2012). Germination is also influenced by temperature, salinity, organic content of the substrate and fungal infection (Haslam, 1972; Packer *et al.*, 2017). Seed germination usually occurs within 2 to 14 days (Galatowitsch *et al.*, 1999; Packer *et al.*, 2017).

Phragmites seedlings can remain small (2-4 leaves / 2-5 cm tall) or even not develop to a further stage if favorable growing conditions are not present (Haslam, 1972). They grow faster without competition of other plants and in moist or saturated conditions (Mauchamp *et al.*, 2001). Periodic phases of submergence are well tolerated by seedlings, especially as they become older (Wijte & Gallagher, 1996; Baldwin *et al.*, 2010; Galatowitsch *et al.*, 1999; Mauchamp *et al.*, 2001). Seedlings survive if they are totally submerged by up to 80 cm of water during four to six consecutive weeks, but do not grow (Armstrong *et al.*, 1999; Coops & van der Velde, 1995; Mauchamp *et al.*, 2001). The major cause of seedling mortality is drought, although the species can tolerate drier conditions than most of the other wetland plants (Pagter *et al.*, 2005). In optimal conditions, seedlings can become mature plants over one growing season, but the process will take more time if conditions are sub-optimal.

The non-native *Phragmites* forms dense monotypic stands that produce three times more biomass than the native sub-species. *Phragmites* colonies grow best in shallow water (less than 50 cm) or in areas that are not permanently flooded (Byun *et al.*, 2014; Hudon *et al.*, 2005; Squires & Valk, 1992; M. G. Tulbure *et al.*, 2007). In flooded conditions (> 150 cm), the edge of a colony will retreat by a few meters, but stems located inside the colony are virtually immune from any adverse environmental conditions (Hudon *et al.*, 2005). Once a common reed colony is well established, it is very time- and cost-consuming to eradicate. Drowning *Phragmites* stands by at least 1.5 m of water (for a minimal duration of 6 weeks) is one of the options that can be used to control Common reed, but, in order to be effective, it needs to be coupled with other control measures like cutting, rolling or burning (Ontario Ministry of Natural Resources and Forestry, 2019).

Colonies expand rapidly by rhizomes or stolons that can grow up to 10 m within a single growing season. New erect stems grow at regular intervals (at each 10-20 cm) along the stolon, each of which is taking root. According to Hudon *et al.* (2005), the water depth of the previous growing season is the best predictor of the lateral expansion of colonies. In this study, lateral expansion of colonies was the highest at locations with the water table 40 to 60 cm below the ground and when there was no more than 20 days of flooding over the growing season. Another study in a Swedish lake with water depth ranging from 0.3 to 1.4 m found that rhizome length was negatively correlated with water depth (Weisner & Strand, 1996). Lateral expansion is generally accelerated in the year following a water level drawdown (Hudon *et al.*, 2005; M. G. Tulbure *et al.*, 2007). Flooding usually substantially slows lateral expansion, especially as flooding deepens or as duration of flooding is longer (Alvarez *et al.*, 2005; Hellings & Gallagher, 1992; Hudon *et al.*, 2005). For example, flooding for more than 100 days results in slow propagation (1-2 m/yr), while deeper flooding (more than 1.0 m) results in no vegetative growth at all (Hudon *et al.*, 2005).

Table 52: Effects of environmental conditions on the different *Phragmites australis* life stages.

Life stage	Criteria	Optimal	Tolerable	Problematic
Germination	Water depth	-4 to 4 cm ¹	4 to 10 cm ²	>15 cm ²
	Water level fluctuation	drawdown ³		
Seedlings	Water depth	-12 to 0 cm ⁴ 8 to 25 cm ⁵		
	Flooding duration	< 4 weeks ^{6,7}	4 to 8 weeks ^{6,7}	> 8 weeks ^{6,7}
Adults	Water depth	<-15 cm ⁸ shallow water ^{9,10}	1 to 1.5 m ³	<-1.5 m ¹³ >1.5 m for at least 6 weeks ¹⁴
	Flooding duration	not permanently inundated ^{9,10}		
	Water level fluctuations	stable		
Vegetative propagation	Water depth	-40 to -60 cm ¹¹	10 to 90 cm ^{9,11}	<-1 m ¹¹ >1.4 m ¹²
	Flooding duration	Flooding less than 3 weeks ¹¹	>100 days in previous growth season ¹¹	
	Water level fluctuations	drawdown ^{10,11}		

Clevering & Lissner, 1999¹

Coops *et al.*, 2004²

D. Wilcox, 2012; K. L. Wilcox *et al.*, 2003³

Haslam, 1971⁴

Meng *et al.*, 2016⁵

Yu *et al.*, 2012⁶

Byun *et al.*, 2014⁷

Weisner *et al.*, 1993⁸

Armstrong *et al.*, 1999⁹

Alvarez *et al.*, 2005¹⁰

Pagter *et al.*, 2005¹¹

Weisner & Strand, 1996¹²

Hudon *et al.*, 2005¹³

Ontario Ministry of Natural Resources and Forestry *et al.*, 2019¹⁴

6.2.2.2. **Phragmites in the Great Lakes**

Exotic reeds (subspecies native to Eurasia) have been present in the Canadian Great Lakes since the 1940s, but have only been expanding since the mid 1990s. A study by Wilcox (2012) at the Dickinson Island wetland site on the St. Clair River delta showed that even if non-native *Phragmites* invasion only started becoming apparent after the 1997 water level drawdown, the species was already established at the site since the mid-1980s. He showed that *Phragmites* initially established on exposed sediments after the 1986 water level drawdown, along with other native plants that were present in the seedbanks. The cover of *Phragmites* remained low during the next decade. The water-level drawdowns between 1997 and 1999 promoted the rapid expansion of the common reed in the wetland in the following decades.

This rapid expansion of *Phragmites* after the mid-1990s was observed in Lake Erie and Lake Michigan-Huron and was the result of water level drawdowns that occurred between 1997 and 2004, increases in ambient air temperatures and the establishment of the non-native Eurasian lineage (Jung *et al.*, 2017; Tulbure *et al.*, 2007; Tulbure & Johnston, 2010; Wilcox, 2012; Wilcox *et al.*, 2003). In Lake Ontario, water level regulation appears to have facilitated the establishment of *Typha spp.*, which might have prevented the establishment and proliferation of *Phragmites* because they share a similar ecological niche (Amsberry *et al.*, 2000; Keddy & Reznicek, 1986; Shay *et al.*, 1999; Wilcox *et al.*, 2008).

A study by Mazur *et al.* (2014) covering the entire Laurentian Great Lakes shoreline pointed out that wetland habitats that were the most vulnerable to invasion by *Phragmites* were those in proximity to developed lands and to a dense road network, coupled with minimal topographic relief. At Long Point National Wildlife Area, *Phragmites* invaded and replaced mostly *Typha* and wet meadows and, to a lesser extent, sedge/grass hummocks and mixed emergent marshes (Wilcox *et al.*, 2003).

6.2.2.3. **Phragmites dataset**

P. australis invasion in the Great Lakes most likely started after the 1987 mean annual water level drawdown which exposed bare soil and promote seed germination, but became apparent after the second drawdown in 1997 (Wilcox, 2012; Wilcox *et al.*, 2003). In order to ensure that the selected data were uniquely identifying the invasive *P. australis*, presence data from only 1995 and later were selected in the WTT dataset (Section 6.1.2). The presence data are more abundant in the 2010-2015 years since the invasion is more advanced (Table 53).

Table 53: Description of the vegetation datasets used to calibrate the *Phragmites* suitable habitat model composed of presence and absence of various sources (Wetland Trends through Time, Ecological Land Classification and GLPI quadrats surveys).

Site	Survey year	Dataset	N presence Phragmites	N absence Phragmites
7GRM	1983	WTT	0	359
	1988	WTT	0	378
	1995	WTT	50	434
	2000	WTT	0	439
	2010	ELC	1143	424
	2018	CWS	7	7
	2019	CWS	17	17
9LPW	1985	WTT	0	474
	1995	WTT	1000	434
	1999	WTT	1000	415
	2015	ELC	1171	406
	2018	CWS	12	12
	2019	CWS	14	14
10RBY	1985	WTT	0	291
	1988	WTT	0	253
	1995	WTT	267	324
	2018	CWS	7	7
	2019	CWS	2	2
13LSC/ 14SAM	1985	WTT	0	458
	1988	WTT	0	382
	2010	ELC	1342	502
	2018	CWS	73	73
	2019	CWS	51	51
TOTAL			6156	6156

6.2.2.4. *Phragmites* SHM

Phragmites SHM, like the *Typha* SHM (Section 6.2.1.4), is a supervised model calibrated using absence/presence data (Table 53) as dependent variables and physical variables (topographic and hydroperiod variables; Figure 166). The topographic variables used are the slope and curvature at 310 m scale. The hydroperiod variables are calculated for the previous growing season, and include maximum, minimum and average water depth, average cycle period and maximum scale-average wavelet power. The relative importance of the variables to the model is calculated with the Gini importance metric (Hastie *et al.*, 2009). Modelling results suggest that the

most important variables are the slope and curvature followed by the maximum scale average wavelet power. The minimum water depth is the most important water depth variable. The relative importance of the water depth variables are necessarily lower, since those variables are highly correlated and the feature importance is therefore diffused (Perrier, 2015). Since the water depth variables each have a relatively high importance, the water depth is a major component to the model and allows the comparison of water level scenarios. Suitable habitat for *Phragmites* is located at the interface of the land and water since most presence data have a water depth close to 0 m with low slope (Figure 167). *Phragmites* suitable habitat is associated with low water depths and with a 40-hour period of dry-wet cycles, which corresponds to the period of wind set-ups in Lake Erie.

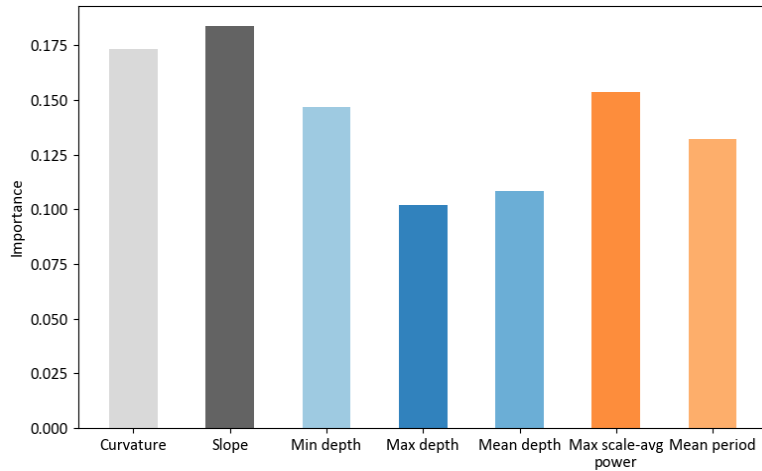


Figure 166: Independent variables relative importance of the *Phragmites* suitable habitat model.

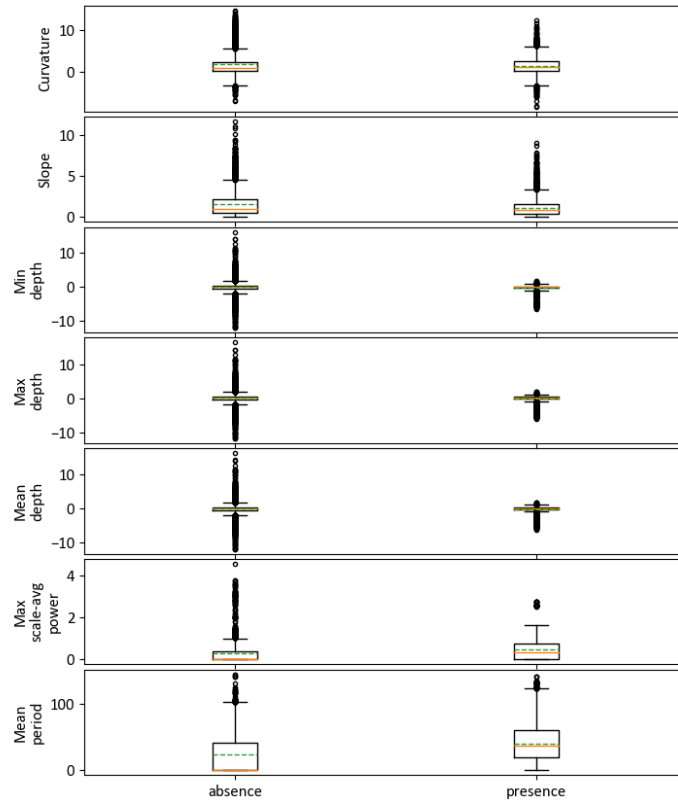


Figure 167: Boxplot distribution of the environmental variables of the *Phragmites* suitable habitat model dataset. Orange line correspond to median, whereas green dashed line corresponds to mean.

6.2.2.5. *Phragmites* PGM

The *Phragmites* PGM aims to reproduce the establishment of a common reed colony from the germination of seeds present in the seedbank to the expansion of the colony *via* vegetative propagation. Like other *Phragmites* models (i.e. Duncan *et al.*, 2017; Tougas-Tellier *et al.*, 2015), this one is theoretical. It is calculated according to the water depth during the germination and growing season period and inter-annual water level fluctuations. The different functions incorporated into the model (Figure 168) reproduce the different stages and mechanisms of the establishment of a *Phragmites* colony based on a thorough review of the literature of the species biology. A novelty of this 2D model is that, in addition to identifying the potential sites for common reed establishment, as done by Tougas-Tellier *et al.* (2015), it also includes a simplified seed propagation algorithm and predicts the advancement of the colonies by lateral vegetative propagation.

The *Phragmites* PGM has four stages: no *Phragmites*, seedling, adult, and colony. Between those stages, there are four mechanisms allowing the stages to change from one to another: germination, seedling survival, seed and vegetative propagation. The *Phragmites* PGM was

presented and approved by Claude Lavoie, a *Phragmites* specialist from Université Laval who also developed a *Phragmites* habitat model (Lavoie, 2007).

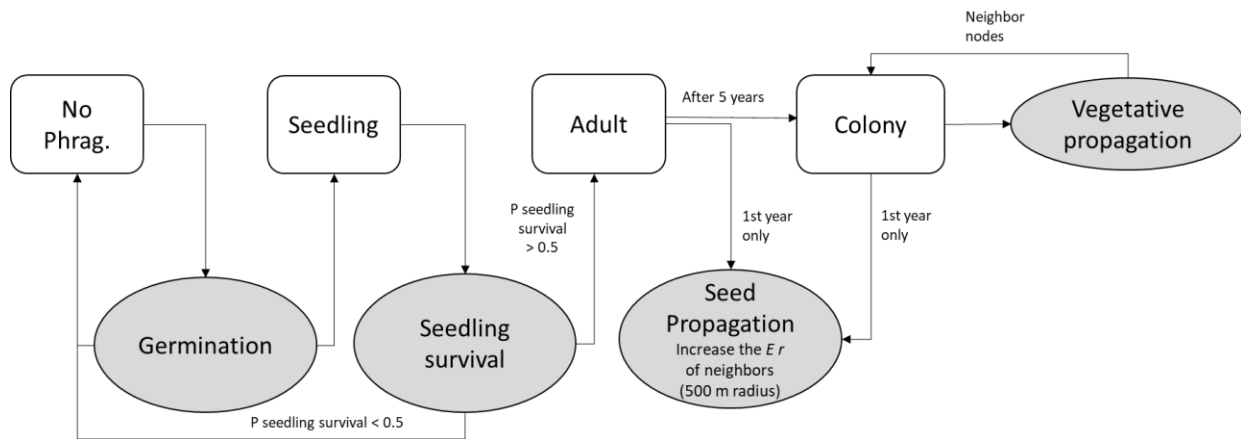


Figure 168: *Phragmites* population growth model scheme.

6.2.2.5.1. Germination

The first step for *Phragmites* establishment (going from No *Phragmites* to Seedling in Figure 168) consists of having appropriate conditions for seed germination. The model allows the germination for a random subset of the CWRM grid nodes weighted by the germination probability (P_g) on exposed mud flats in the spring following a receding water level. For each CWRM point, a germination probability (P_g) is calculated similarly to the *Typha* model (Section 3586.2.1.5.2) as a function of the probability of water level drawdown (P_w), the probability of water depth reaching a suitable level during the germination period (P_{wd}), probability to germinate associated with the various wetland classes (P_{we}), and the establishment rate (E_r).

$$P_g = P_w * P_{wd} * P_{we} * E_r \quad 6.4$$

P_w depends on the change in water level observed between the current and previous germination periods (start of the growing season to first week of July, QM25). When this variation is less than 0.125 m, P_w value is set to 0.0. When it is higher than 0.25 m, P_w is then 1.0. Between 0.125 and 0.25 m, the probability of drawdown is calculated linearly as presented by the preference curve in Figure 169.

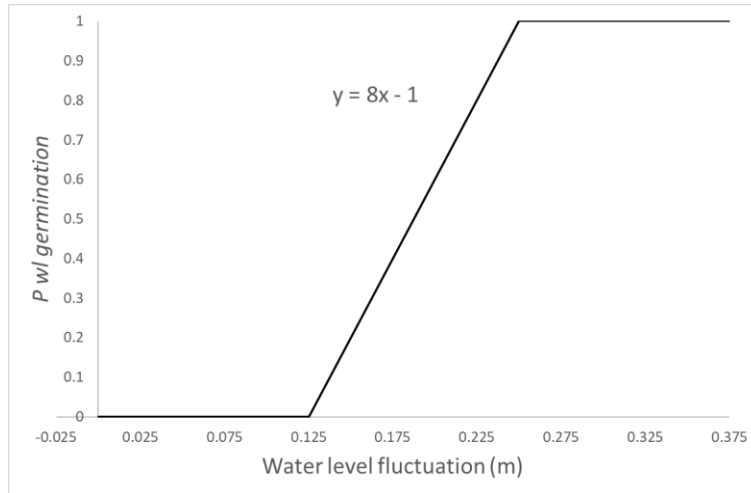


Figure 169: Germination probability according to the water level variation between the preceding year and the current germination period.

The P_{wd} is the probability for a seed to germinate according to the water depth reached during the current germination period (Figure 170). P_{wd} value is 0.0 when the water depth drops below -0.20 m or rises above 0.20 m. When the water depth remains between -0.1 and 0 m, the probability value is equal to 1.0 . Outside these ranges, P_{wd} follows a logarithmic function as presented by the preference curve in Figure 170.

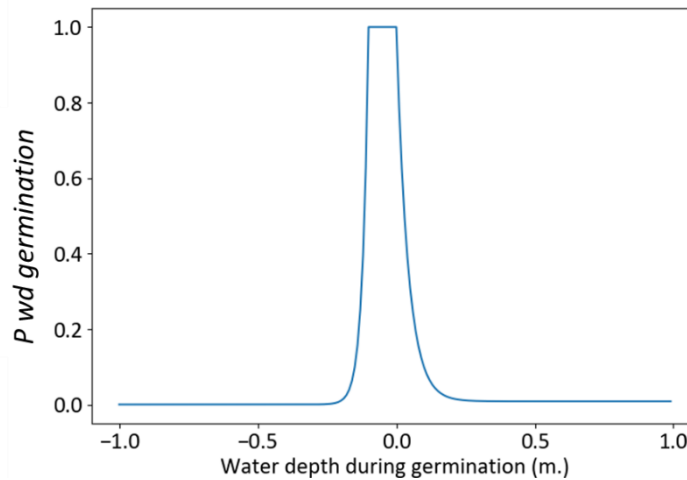


Figure 170: Germination probability according to the water depth during the germination period.

In the present model, there is also a probability to germinate associated with the various wetland classes (P_{we}) determine from literature review, expert consultation and iterative tries during the calibration process. *Phragmites* do not germinate in wetland classes with woody species or in upland sites (Table 54). A probability of 0.01 was given for *Phragmites* to allow the possibility of

Phragmites to germinate into cattail stands. However, *Phragmites* cannot germinate if the cattail stands is at the floating mat stage.

Table 54: Germination probability in function of the wetland class predicted by the wetland model and the cattail models.

Wetland class	Probability
Open Water	1
Submerged aquatic-vegetation	1
Emergent marshes	1
Wet meadows	1
Cattail stand	0.01
Shrubby swamps	0
Treed swamps	0
Upland	0

Finally, the establishment rate is a constant to integrate the natural and random aspect of seed dispersal in the system. This factor restricts the maximum probability of germination, restricting the number of nodes that can germinate at a given year. For example, with an establishment rate of 0.05, and optimal environmental conditions approximately 5% of the nodes will germinate.

6.2.2.5.2 Seedling survival

When a node is suitable for *Phragmites* germination, its stage transitions from no *Phragmites* to seedling. The second mechanism of the PGM is then to evaluate the seedling survival, which is required for the seedling to become an adult. The seedling has to survive one complete growing season in order to become a *Phragmites* adult or mature plant. The seedling survives and becomes an adult if the probability of seedling survival (P_{ss}) > 0.5.

$$P_{ss} = P_{wd} * P_{fw} \quad 6.5$$

P_{wd} is the survival probability of a seedling according to the mean water depth during the growing season of *Phragmites*. P_{wd} value is 0.0 when the water depth drops below -1.0m or

rises above 2.0 m. When the water depth remains between -1.0 and 2.0 m, the probability value is equal to 1.0 (Figure 171).

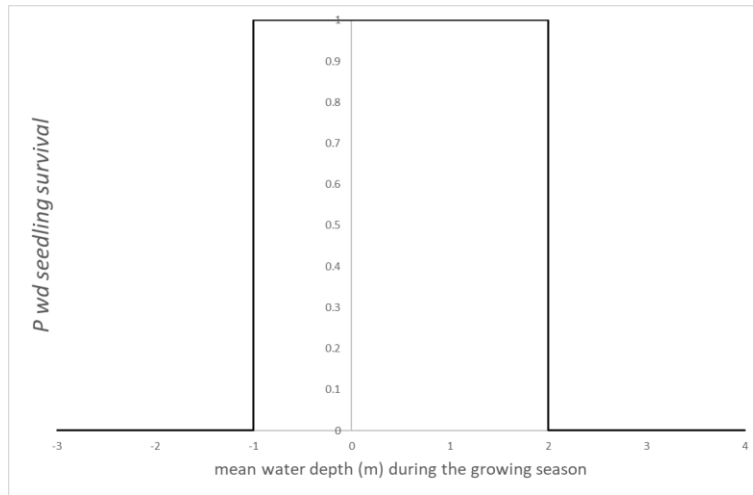


Figure 171: Seedling survival probability according to the mean water depth during the current growing season.

P_{fw} is the survival probability of seedlings as a function of the time a node is flooded consecutively during the growing season (Figure 172). *Phragmites* seedlings can completely survive ($P_{fw} = 1.0$) when six consecutive QM and less are flooded during the growing season. The P_{fw} value is 0.0 when the node is flooded for more than 14 consecutive QM. When the number of consecutive flooded QM is between 6 and 14, the P_{fw} value is calculated linearly as presented by the preference curve in Figure 172.

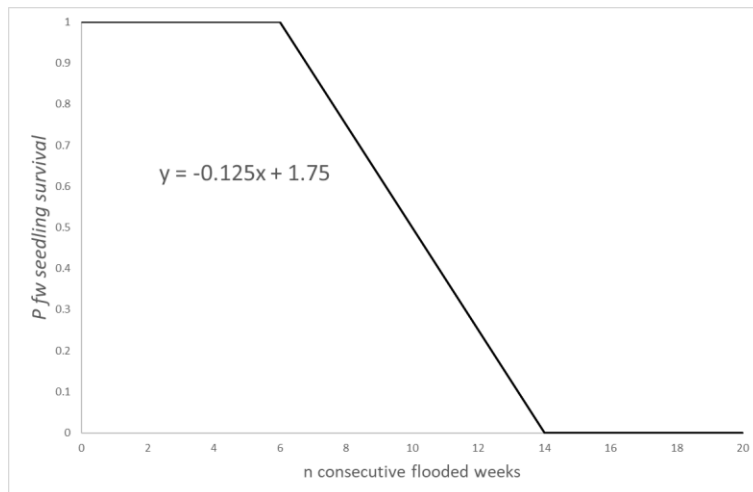


Figure 172: Seedling survival probability according to the number of consecutive flooded quarter-months.

6.2.2.5.3. Seed propagation

Once the seedling survives, the next year it becomes a *Phragmites* stand with adult plants. The model simulates the seed propagation of the *Phragmites* by increasing the Establishment rate (Er) of the neighboring points in a 500 m radius. The seed propagation increase is maximum for the points within a 100 m radius and decreases as the distance approaches 500 m. Between 100 and 500 m, the Er increase of the neighbor points is calculated linearly as presented by the preference curve in Figure 173.

We assumed that there is a lag time of 5 years for the *Phragmites* to fully occupy a 100 m² area (grid resolution) and thus establish a colony. The first time a node becomes an adult from germination or becomes a colony from lateral propagation (next section), it seeds/germinates in neighboring nodes and increases their respective establishment rate depending on the distance of the neighboring nodes to the adult (Figure 173). There are no condition in the model that can remove the *Phragmites* adult stage.

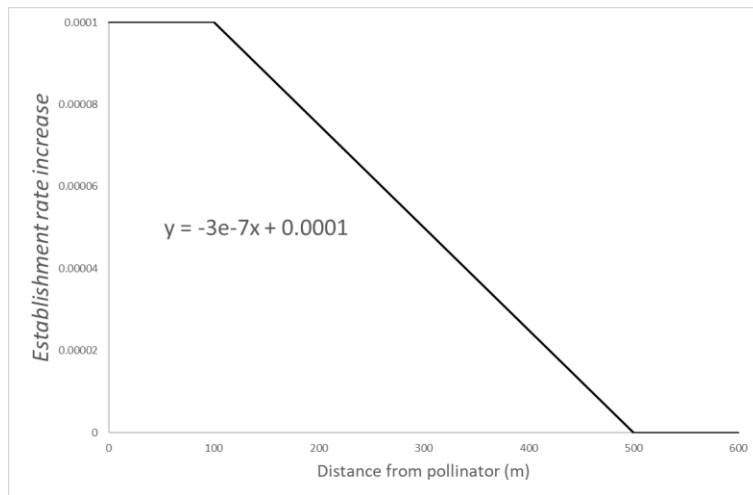


Figure 173: Establishment rate increase according to the distance between the neighbors and the pollinator.

6.2.2.5.4. Vegetative propagation: invasion

When the colony is well established, it can “invade” adjacent nodes of the CWRM grid by vegetative propagation. The vegetative propagation modelled in the *Phragmites* model is similar to the Cattail model (see Section 6.2.1.5.6). The lateral vegetative growth (Vg) is a function that calculates a distance of lateral propagation depending on the hydrological conditions and the wetland class predicted in the wetland model. The difference between the *Phragmites* adult and the colony is that during the five years lag time, there is no vegetative propagation possible to

neighboring nodes. Once it becomes a colony, the colonies expand to neighboring nodes by vegetative propagation.

The vegetative propagation (Vg) (equation 6.6) is calculated using six components:

- previous growth;
- vegetative propagation probabilities associated with current water depth, P_{wd} (Figure 174);
- slope, P_{sl} (Figure 175);
- year-to-year water level variation, P_{wt} ;
- propagation probability associated with the predicted wetland class in adjacent nodes, P_{we} (Table 51);
- maximum growth, which was estimated at 10 m/year for this species in this study.

For the first year, previous growth is equal to 0. The following years, if the $Vg < \text{distance to neighbors } (d)$, the previous growth is equal to the Vg . When Vg is greater than d , the previous growth is equal to $Vg - d$ (equation 6.7). This variable ensures that the growth in the previous years is accumulated when the distance to neighbors is not reached.

$$Vg (m) = (Max\ growth * P_{wd} * P_{sl} * P_{fw} * P_{we}) + previous\ growth \quad 6.6$$

$$previous\ growth = \begin{cases} Vg - d & \text{if } Vg > d \\ Vg & \text{if } Vg \leq d \end{cases} \quad 6.7$$

The vegetative propagation probability associated with water depth, P_{wd} , is 0.0 when this depth remains below -1.5 m or above 1.0 m during the growing season. It is 1.0 when the water depth stays between -0.6 and 0.0 m, and it is otherwise calculated linearly as presented by the preference curve in Figure 174.

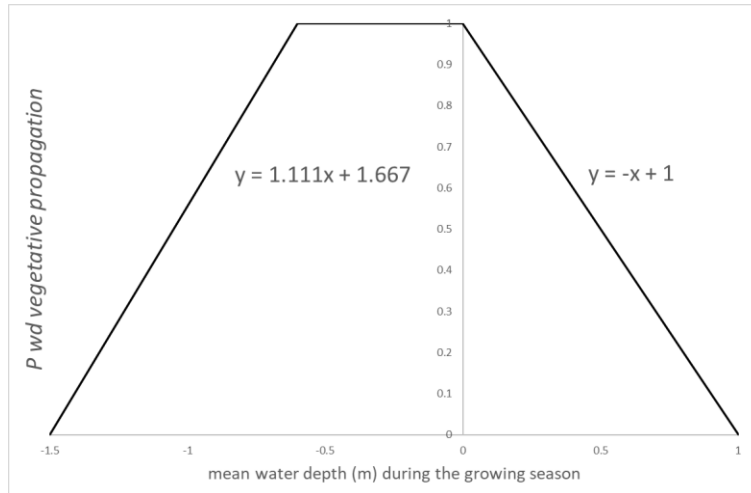


Figure 174: Vegetative propagation probability according to the mean water depth during the growing season.

P_{sl} is calculated by the preference curve presented in Figure 175. The value is 0.0 when the slope is under and over 50%. It is 0.5 when the slope is between -50 and -5% or between 5 and 50%. Finally, P_{sl} is at its maximum value, 1.0, when the slope is between -5 and 5%.

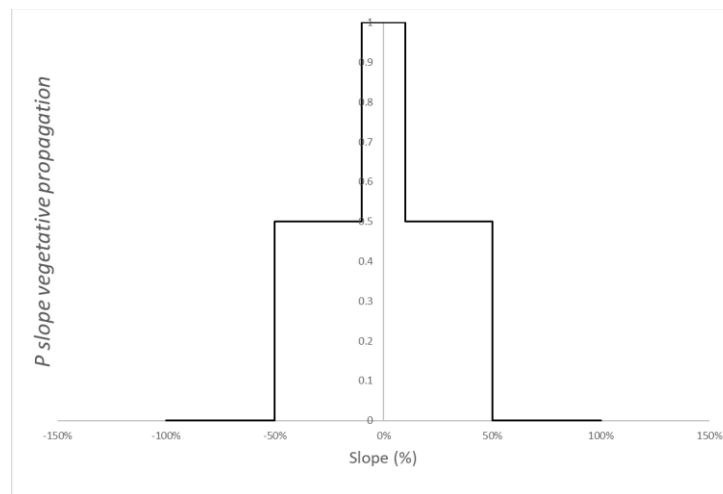


Figure 175: Vegetative propagation probability according to the slope with the neighboring points.

The vegetative propagation probability in function of the water level variation (P_{wl}) between the previous and current year is 1.0 when the water level declines (variation < 0.0 m) and is 0.0 when the water level rises (variation > 0.0 m). *Phragmites* can invade several wetland classes, but not all of them. The model considers the probability of *Phragmites* propagation maximum in OW, SAV, EM and WM. It is also possible for *Phragmites* to invade cattail stands but at a much lower probability than other EM. *Typha* growth is reduced when *Phragmites* are present and therefore, *Phragmites* are better competitor than *Typha* (Chun & Choi, 2009). The rate of expansion of

Phragmites under *Typha* cover is dependant of many factors, thus a heuristic is used to simplify this interaction. The vegetative propagation probability of *Phragmites* expansion under *Typha* cover has been selected iteratively during the calibration process. Finally, it is not possible for *Phragmites* to have vegetative propagation in SS, TS and Upland sites (Table 55).

Table 55: Vegetative propagation probability according to the wetland class of the neighbor point

Wetland class	Probability
Open Water	1
Submerged aquatic-vegetation	1
Emergent marshes	1
Wet meadows	1
Cattail stand	0.1
Shrubby swamps	0
Treed swamps	0
Upland	0

6.2.2.5.5. *Phragmites* PGM initialization

Studies showed that *Phragmites* invasion in Lake St. Clair and Lake Érié started in the 1980s but became significant after the 1997 water level drawdown (Wilcox, 2012; Wilcox *et al.*, 2003). Therefore, the *Phragmites* model was started in 1980 for the southern lakes. In contrast, for most Lake Huron sites except Baie du Doré, the invasion did not occur following the water level drawdowns of 1997 because the species was less present in the system. The exact date of the start of the invasion is also unknown for these sites, but since we know that it is currently happening in some sites, we decided to start all sites at 2010 (end of the recent past simulation).

For the different climate change scenarios, the physical variables are simulated using hydrodynamic and wave modelling for the recent past (1980-2009) and the future periods (2070-2099). To fill the gap between those periods, the models were applied by using only the water level time series (i.e., because the physical and wetland model simulations were not produce outside of those periods).

6.2.3. Models calibration and validation

6.2.3.1. Suitable habitat models

The SHM for *Typha* has a good overall performance (Kappa=62%, OOB error=19%, Table 56). The model seems to overestimate the presence of *Typha* slightly more than it is underestimating it. This species can sustain a wide range of environmental conditions, and this overestimation is

considered normal since many other factors are not considered by the model (ex: soil type, competition, etc). The temporal distribution of the calibration dataset is relatively uniform and should allow for identifying the potential habitat of *Typha* in different conditions and for different sites.

Table 56: Validation metrics for the *Typha* suitable habitat model OOB validation.

<i>Typha</i> suitable habitat model (Random Forest)			
	Model	Absence	Presence
OOB error	0.19		
Accuracy	0.81		
Kappa	0.62		
Recall		0.77	0.84
Precision		0.83	0.79
F1-score		0.80	0.81

The SHM for *Phragmites* has a strong performance overall (Kappa=78%, OOB error=11%, Table 57). The model slightly overestimates the presence of *Phragmites* by ≈12%. However, such overestimation is minimal and is considered normal giving the wide range of environmental conditions suitable for this species. Since this model is calibrated across different years and different sites, and the calibration years are representative of the invasion period of *Phragmites*, this model should be able to accurately predict the suitable *Phragmites* habitat at other sites and under various climate change scenarios

Table 57: Validation metrics for the *Phragmites* suitable habitat model OOB validation.

<i>Phragmites</i> suitable habitat model (Random Forest)			
	Model	Absence	Presence
OOB error	0.11		
Accuracy	0.89		
Kappa	0.78		
Recall		0.87	0.91
Precision		0.91	0.88
F1-score		0.89	0.89

6.2.3.2. Population growth models

6.2.3.2.1. Calibration and validation sites/data

PGMs were calibrated using water levels (1956-1980) and hydrodynamic simulations (1980-2018) from the measured time series of three sites in two lakes. Two calibration sites are located in Lake Ontario (South Bay Marsh, 3SBM and Airport Creek Marsh, 2ACM), where the invasion is mainly due to the expansion of *T. x glauca*. The invasion is promoted by past water level management favoring low interannual water level variability. Calibration at these sites is intended to replicate the invasion of *Typha* as well as the absence of *Phragmites* in Lake Ontario. The other calibration site is Thoroughfare (Long Point, 9LPW) located in Lake Erie, which faces an invasion of both species due to multiple factors. Since both species are present in this site from the late 1990s with various historical observations of both species available (see Table 58 for more details), this site was used to calibrate the interaction between both species along with their presence.

Heuristic parameters, simplifying growth mechanisms, such as the establishment rate and the expansion rate of *Phragmites* under *Typha* cover, were iteratively modified to best fit with the calibration data. Nevertheless, those modifications were done in the possible range of the biological requirements of both species. For example, *Phragmites* predicted patch size and shape in Lake Erie sites were compared with the observations, and the parameters were optimized to reproduce as best as possible the species distribution. The growth mechanisms and the parameters are the same for each site, even if some sites may be more vulnerable to invasion than others (e.g. due to higher seed density in the seed bank). This consistency between model parameters for different sites was chosen so that the models would represent plant growth and interaction instead of a site-specific calibration that reproduced the observations but did not necessarily reproduce the behavior. Since calibration data are not available for all sites, one model per species for all sites was required. In addition, to allow replicable results, the Random Number Generator algorithm was initialized with a fixed random seed value to assure that predictions are not caused by randomness but by different parameters.

To evaluate the calibration at each iteration, concordance between the species distribution predictions done by the model and the observations was done in order to ensure that predicted zones lie within the suitable habitat of the species. Also, the calibration aimed to reduce the error between the predicted and the observed total area occupied by each species by calculating the normalised root mean squared error (NRMSE) which is the root mean squared error divided by

the range of the observations. The NRMSE can be interpreted as a fraction of the overall range that is typically resolved by the model. Unfortunately, the NRMSE was calculated only based on the calibration data since there was not enough validation data available.

Lynde Creek (5LCM), in Lake Ontario, and Rondeau Bay (10RBY), in Lake Erie, were used as independent validation sites (Table 58). *Typha* presence and *Phragmites* absence were validated in Lynde Creek, whereas Rondeau Bay (10RBY) was used to validate the presence and interaction of both species.

Table 58: Sites and data used to calibrate and validate Population Growth Models for *Typha* and *Phragmites*

Lakes	Sites	Species	Calibration	Validation	Data origin and year
Lake Erie	9LPW	<i>Phragmites</i> & <i>Typha</i>	X		1985: WTT 1995: WTT 2015: ELC
	10RBY	<i>Phragmites</i> & <i>Typha</i>		X	2015: ELC
	2ACM	<i>Typha</i> & <i>Phragmites</i>	X		2008: ELC
Lake Ontario	3SBM	<i>Typha</i>	X		1986: WTT 1999: WTT 2008: ELC
	5LCM	<i>Typha</i>		X	1986: WTT 2001: WTT 2008: ELC

6.2.3.2.2 Overall calibration

Overall, the modelling approach is reproducing the *Typha* and *Phragmites* temporal and spatial distribution with more accurate predictions in some sites than others. The NRMSE of the *Phragmites* is 7% of the observed *Phragmites* area range, whereas the NRMSE for *Typha* is 15% of the observed *Typha* area range, using seven observations from the calibration dataset.

For the calibration site in Lake Erie, Thoroughfare, the *Typha* and *Phragmites* PGM accurately predicts the spatial and temporal distribution of **both** species. The *Typha* PGM reproduces the *Typha* die-off following the high water levels of 1986. The *Phragmites* PGM reproduces the *Phragmites* invasion starting at the beginning of the 1990s.

In Lake Ontario, the *Typha* PGM predictions closely reproduce the observations. However, the *Phragmites* PGM predictions are sparse and isolated. The modelling predicts more *Phragmites*

than what is actually observed, but the dominance of *Typha* over *Phragmites* in the calibration sites for this lake is well represented. Since the model allowed *Phragmites* to germinate where *Typha* is established with a 10% probability, it is expected that the model predicts some *Phragmites* stands in Lake Ontario. In addition, the *Phragmites* overestimation in Lake Ontario may be due to the underestimation of *Typha*. Since the modelling starts in the 1950s and *Typha* has always been present in the system at that time, *Typha* cover is most likely underrepresented.

6.2.3.2.3. Site-by-site calibration

The interaction between both species was calibrated in the Thoroughfare area of Long Point in Lake Erie (Figure 176). Calibration data come from WTT dataset (1985 and 1995) and the ELC dataset (2015) (Table 58). Note that for *Typha*, the shallow marsh class from ELC was used as presence observations.

High water level of 1985 and 1986 caused a loss of *Typha* in Thoroughfare (Figure 177). In 1985-1986, the model reproduces the major *Typha* die-off caused by the water level rise. *Typha* predicted area is 76 ha in 1985 and 37 ha in 1986, whereas observed area in 1985 is 45 ha (Figure 176). In 1995, the *Typha* PGM underestimated the presence of *Typha*, suggesting that the predicted *Typha* takes longer to recover from a major die-off. In 2015, the predicted area for *Typha* is exactly matching the observation (predicted 165 ha and observed 165 ha). In 1995, the observed *Phragmites* area is 2 ha, whereas the predicted area is 0.9 ha. The model predicts that *Phragmites* invasion begins around the mid-1990s, consistent with what is reported by Wilcox *et al.* (2003). In 2015, the predicted *Phragmites* area (20 ha) is close to the observed area (16 ha) (Figure 176). Overall, the model replicates well the temporal and spatial distribution of the *Phragmites*. Moreover, the *Phragmites* patch size and the general spatial distribution are similar to observations in the ELC dataset (Figure 178).

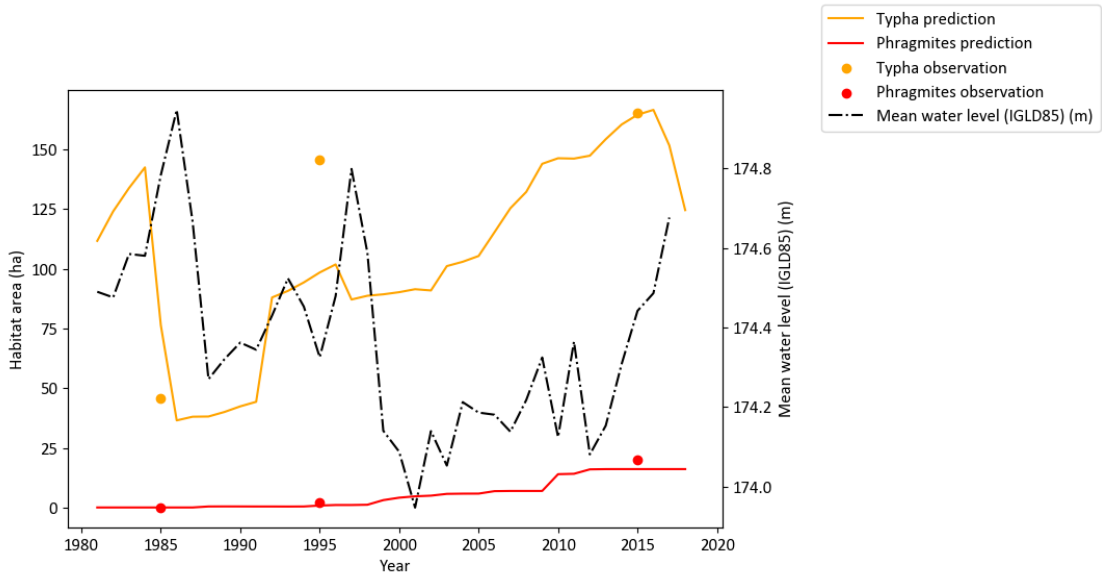


Figure 176: Predicted area (line) for *Phragmites* and *Typha* and observed area (point) for both species (*Phragmites*: red, *Typha*: orange) in Thoroughfare, Long Point (9LPW). Results produced using observed water level time series (black dash-dotted line).

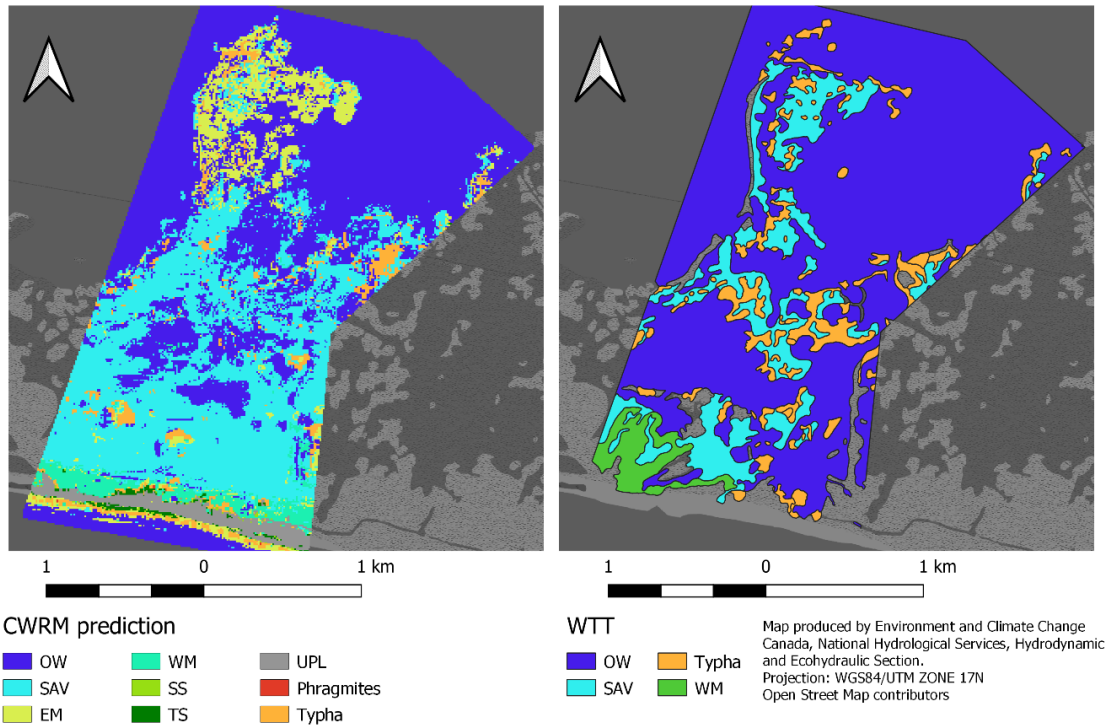


Figure 177: Invasive species model prediction using the observed water levels time series (1980-2018) at Thoroughfare, Long Point (9LPW) in 1985 (left) and observed wetland classes by WTT (right) for the same year. WTT wetland classes were converted to match with CWRM wetland classes.

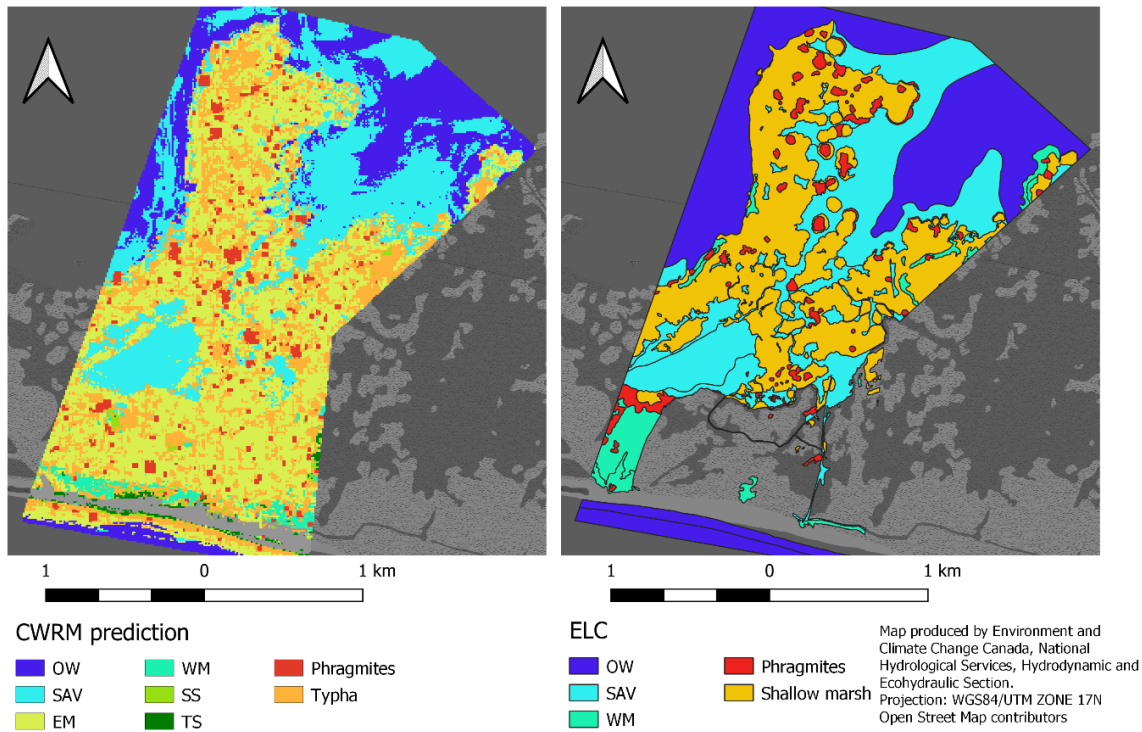


Figure 178: Invasive species model prediction using the observed water levels time series (1980-2018) at Thoroughfare, Long Point (9LPW) in 2015 (left) and observed wetland classes by ELC (right) for the same year. ELC wetland classes were converted to match with CWRM wetland classes. ELC Typha class corresponds to “shallow marsh” class.

In Airport Creek Marsh (2ACM), the *Typha* PGM overestimate the presence of *Typha* in comparison to the observations in 2008. The predicted presences are mostly located along the shores of the site, and the species is gradually expanding towards the higher elevation areas. For *Phragmites*, the predicted area is relatively close to the 2008 observed area (Figure 179). However, the model predicts *Phragmites* stands distributed across the study site, while observations are localized in the southeast (Figure 180). The difference between the predicted and observed *Phragmites* spatial distribution may be due to the random component of the germination function. Given the small germination probability of *Phragmites* into monotypic *Typha* stands, there is a small chance for *Phragmites* to germinate into *Typha* dominated area and create a dominant community in a specific location, as what seems to be the case in this site.

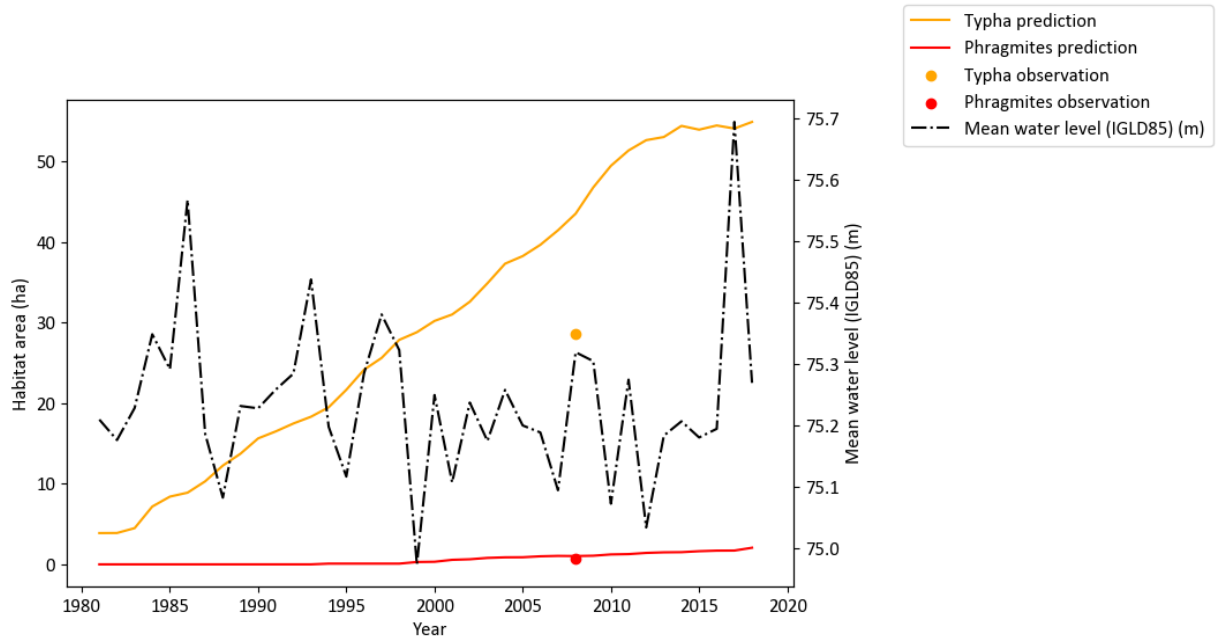


Figure 179: Predicted area (line) for Phragmites and Typha and observed area (point) for both species (Phragmites: red, Typha: orange) in Airport Creek Marsh (2ACM). Results produced using observed water level time series (black dash-dotted line).

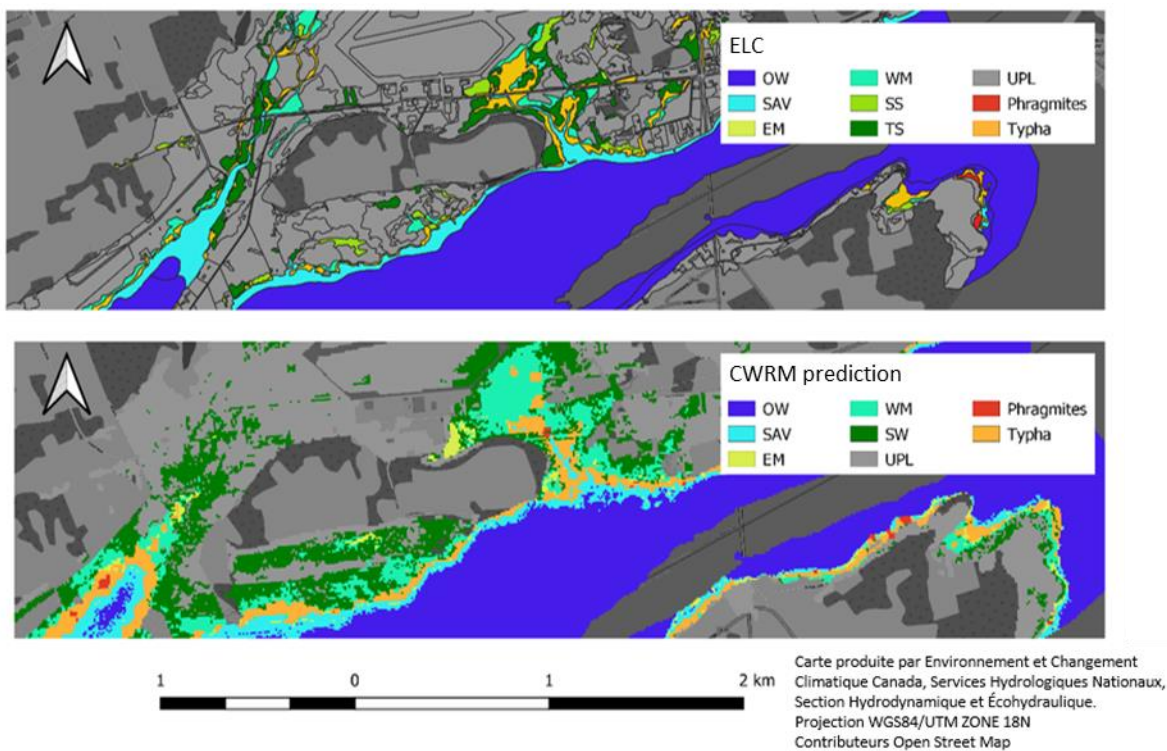


Figure 180: Invasive species model prediction using the observed water levels time series (1980-2018) at Airport Creek Marsh (2ACM) in 2008 (lower) and observed wetland classes by ELC (upper) for the same year. ELC wetland

classes were converted to match with CWRM wetland classes. ELC *Typha* class corresponds to “shallow marsh” class.

In South Bay Marsh (3SBM), *Typha* and *Phragmites* predicted area are relatively close to observations (Figure 181). For 1986, the model underestimates the *Typha* area (Figure 182). However, in 1999 and 2008, the predicted *Typha* area is relatively close to observations, and the predictions are located in the same area as observations (Figures 183 and 184). The model does not predict much *Phragmites* in this site (0.16 ha in 2008), consistent with the available data.

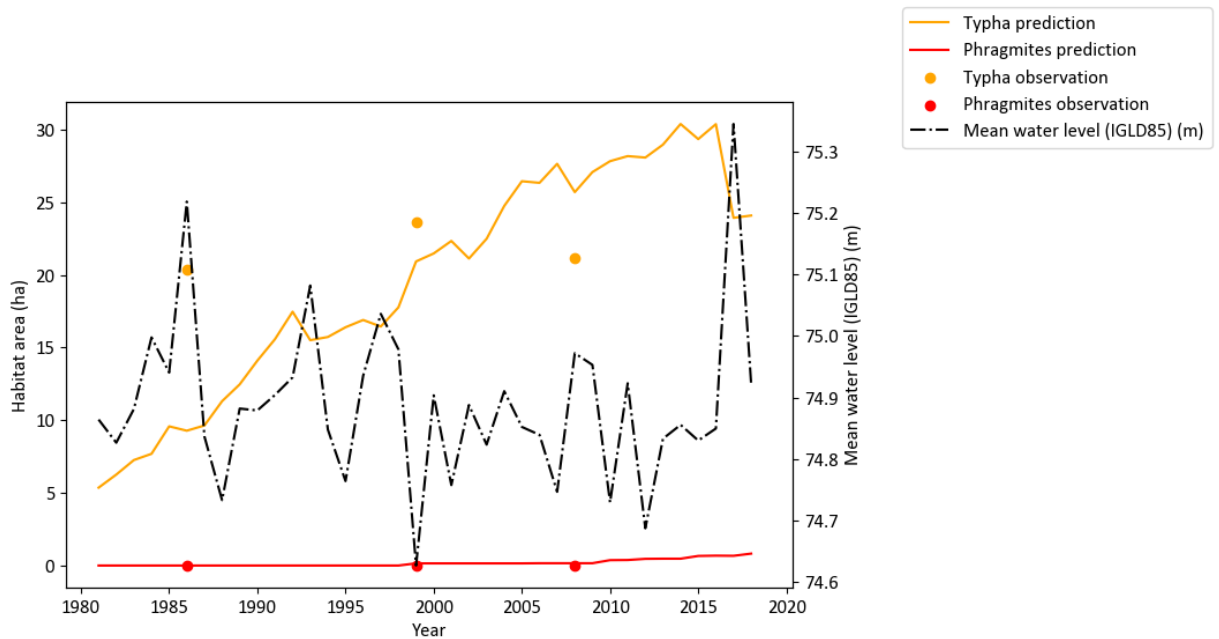


Figure 181: Predicted area (line) for *Phragmites* and *Typha* and observed area (point) for both species (*Phragmites*: red, *Typha*: orange) in South Bay Marsh (3SBM). Results produced using observed water level time series (black dash-dotted line).

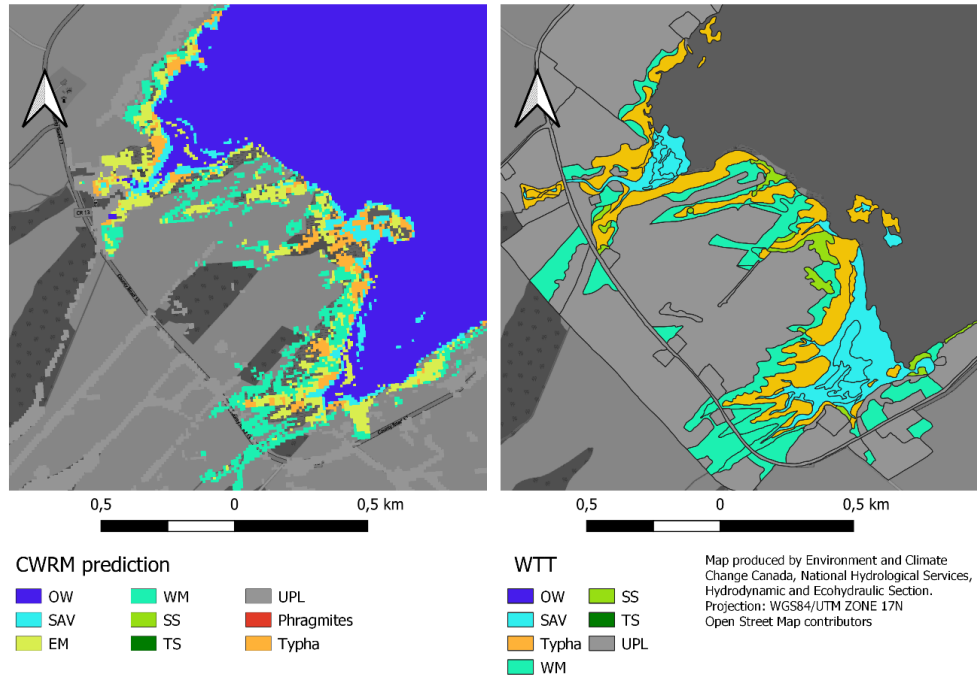


Figure 182: Invasive species model prediction using the observed water levels time series (1980-2018) at South Bay Marsh (3SBM) in 1986 (left) and observed wetland classes by WTT (right) for the same year. WTT wetland classes were converted to match with CWRM wetland classes.

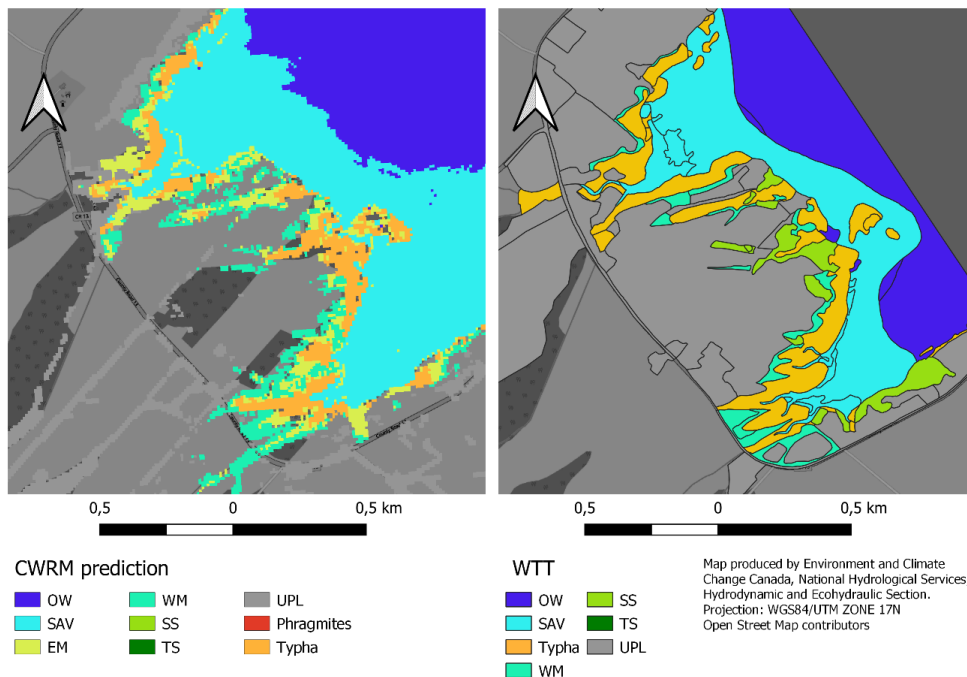


Figure 183: Invasive species model prediction using the observed water levels time series (1980-2018) at South Bay Marsh (3SBM) in 1999 (left) and observed wetland classes by WTT (right) for the same year. WTT wetland classes were converted to match with CWRM wetland classes.

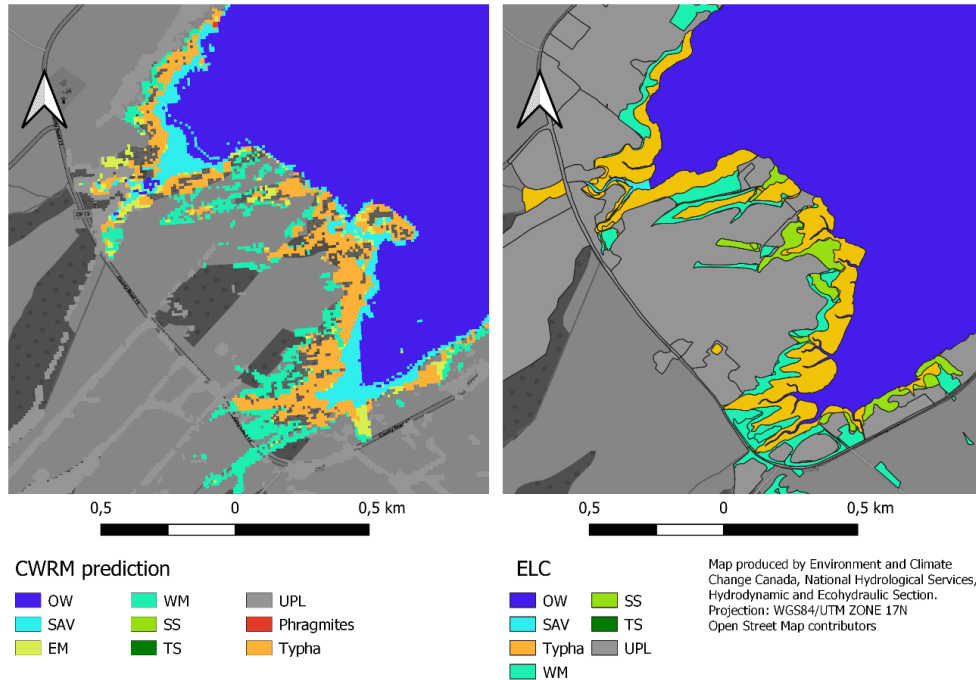


Figure 184: Invasive species model prediction using the observed water levels time series (1980-2018) at South Bay Marsh (3SBM) in 2008 (left) and observed wetland classes by ELC (right) for the same year. ELC wetland classes were converted to match with CWRM wetland classes. ELC *Typha* class corresponds to “shallow marsh” class.

6.2.3.2.4. Site-by-site validation

In Rondeau Bay, the predicted *Typha* area (501 ha) almost perfectly matches the observed areas (500 ha) in 2010 (Figure 185), but *Phragmites* area is underestimated by around 41 ha (predicted: 19 ha, observed: 60 ha). This site seems to be more vulnerable to *Phragmites* establishment because of the large flat area in the embayment where water level fluctuations are frequent. However, the general location of the predicted *Phragmites* and *Typha* corresponds to the observed distribution of both species (Figure 186). The *Phragmites* PGM model gives a conservative estimate of the *Phragmites* invasion for this site.

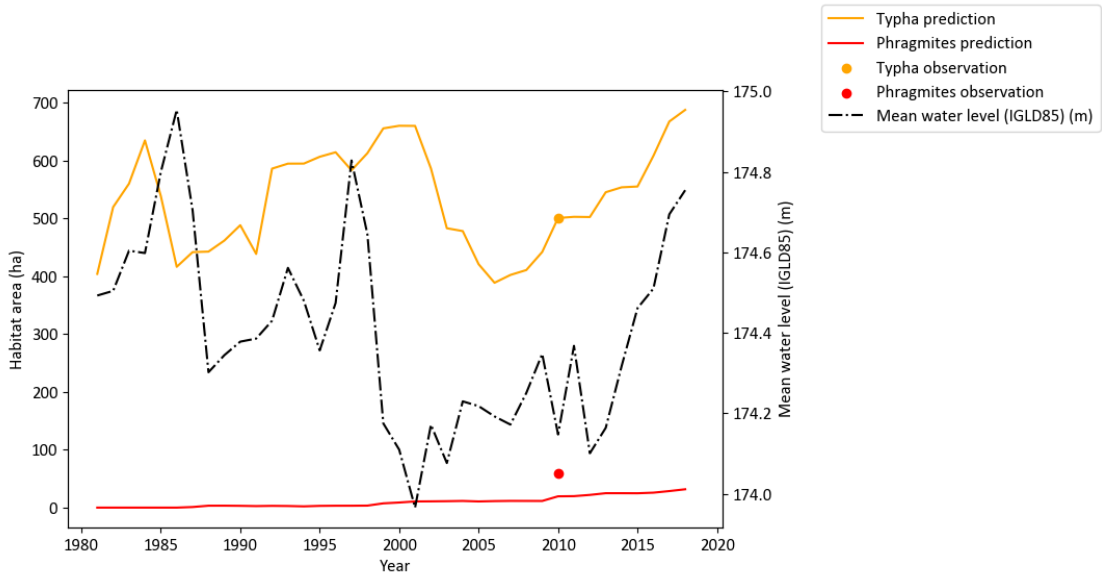


Figure 185: Predicted area (line) for Phragmites and Typha and observed area (point) for both species (Phragmites: red, Typha: orange) in Rondeau Bay (10RBY). Results produced using observed water level time series (black dash-dotted line).

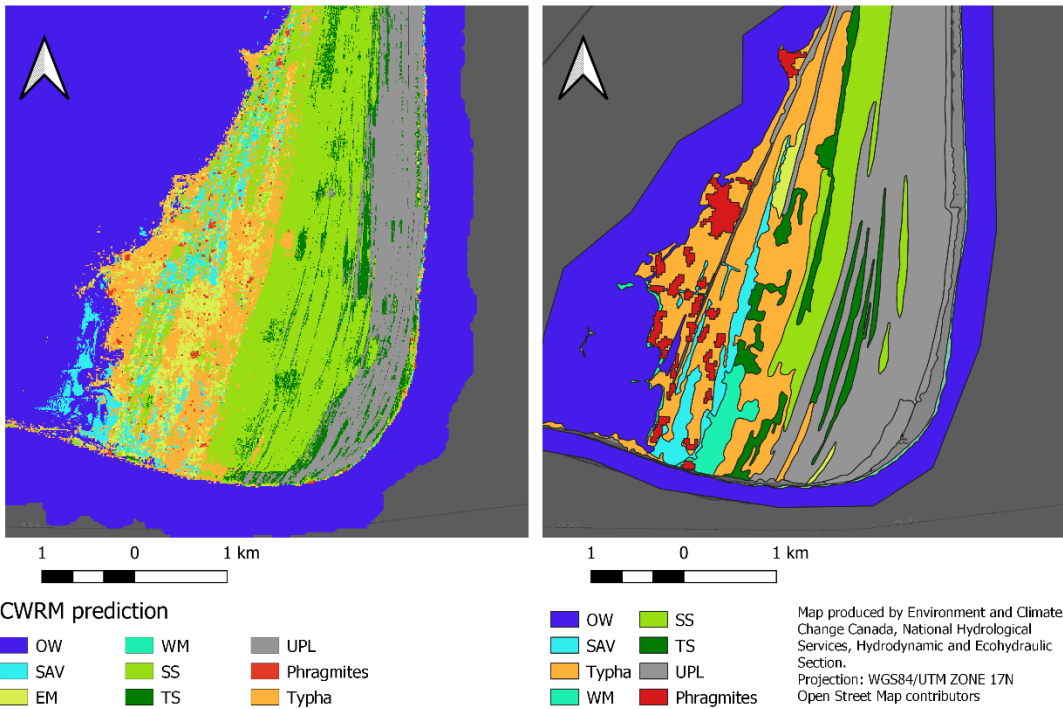


Figure 186: Invasive species model prediction using the observed water levels time series (1980-2018) at Rondeau Bay (10RBY) in 2010 (left) and observed wetland classes by ELC (right) for the same year. ELC wetland classes were converted to match with CWRM classes. ELC Typha class corresponds to "shallow marsh" class. Phragmites prediction data was provided by Ontario Ministry of Natural Resources and Forestry (OMNRF, 2010).

In Lynde Creek (5LCM), the predicted *Typha* area is underestimated in 1986 and overestimated in 2001 and 2008 (Figure 187). The location of the *Typha* predicted presences matches the observations relatively well (Figure 188 through Figure 190). The model allowed some nodes to germinate into a *Phragmites* stand, which is slowly expanding in 2001 and 2008 (Figures 189 and 190). These results might yield an overestimation of *Phragmites* in the future period since the species is not yet established in this site in reality.

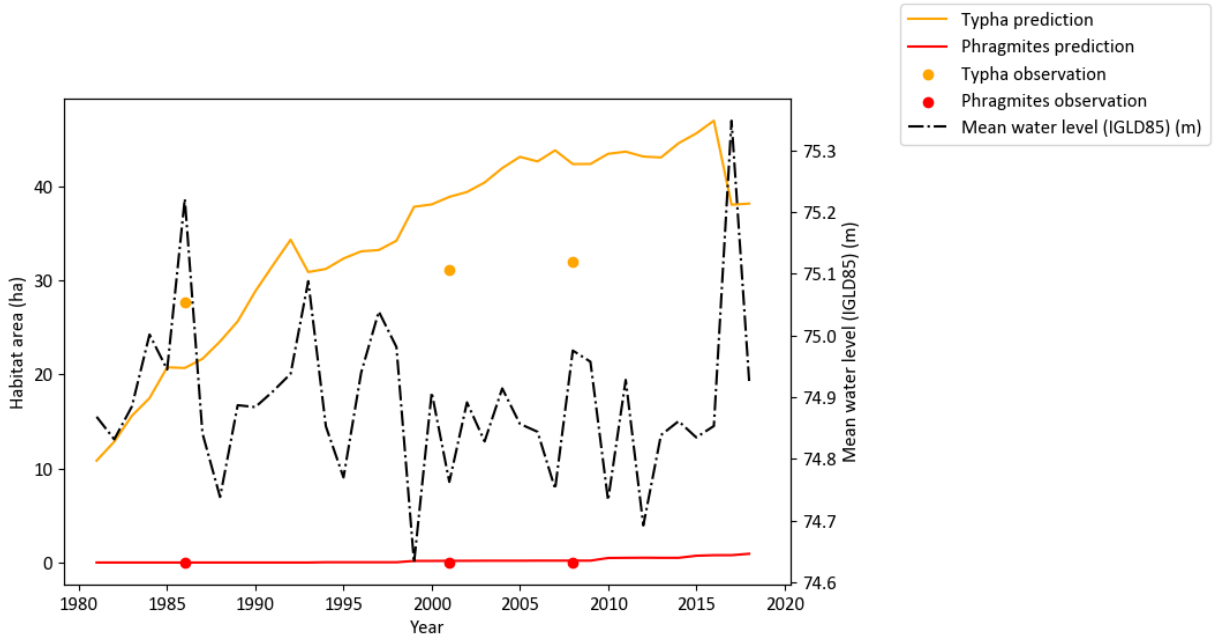


Figure 187: Predicted area (line) for *Phragmites* and *Typha* and observed area (point) for both species (*Phragmites*: red, *Typha*: orange) in Lynde Creek (5LCM). Results produced using observed water level time series (black dash-dotted line).

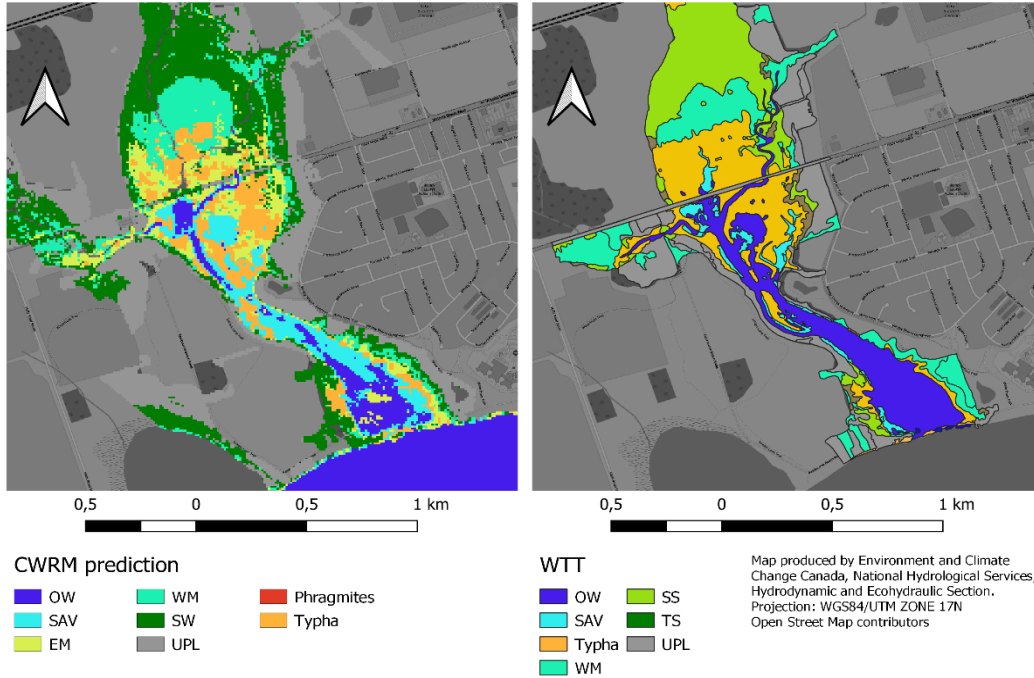


Figure 188: Invasive species model prediction using the observed water levels time series (1980-2018) at Lynde Creek (5LCM) in 1986 (left) and observed wetland classes by WTT (right) for the same year. WTT wetland classes were converted to match with CWRM wetland classes.

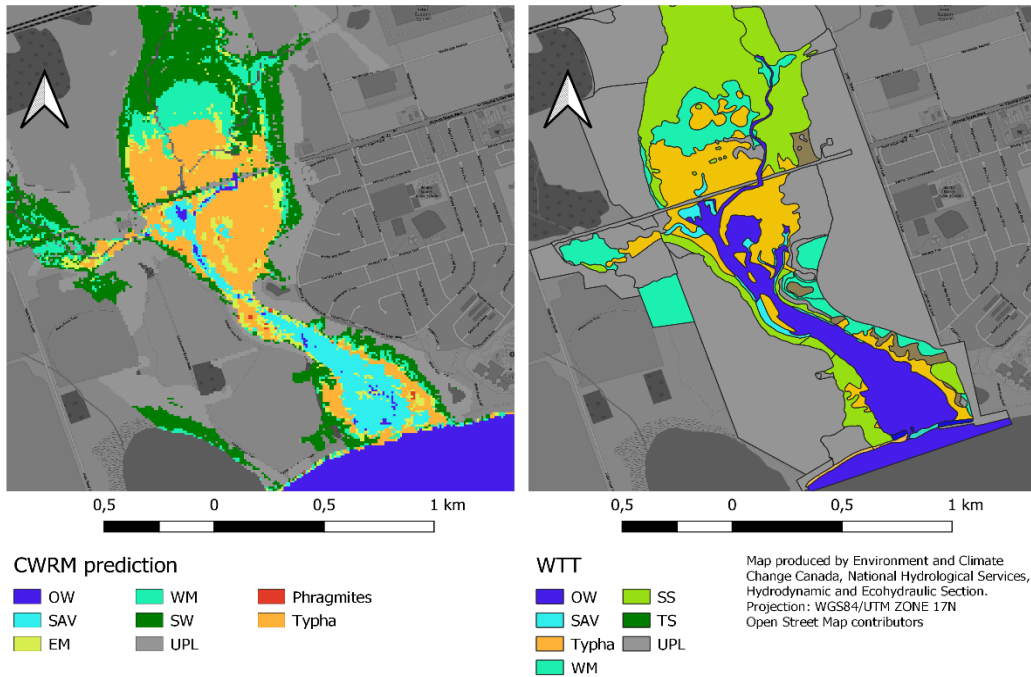


Figure 189: Invasive species model prediction using the observed water levels time series (1980-2018) at Lynde Creek (5LCM) in 2001 (left) and observed wetland classes by WTT (right) for the same year. WTT wetland classes were converted to match with CWRM wetland classes.

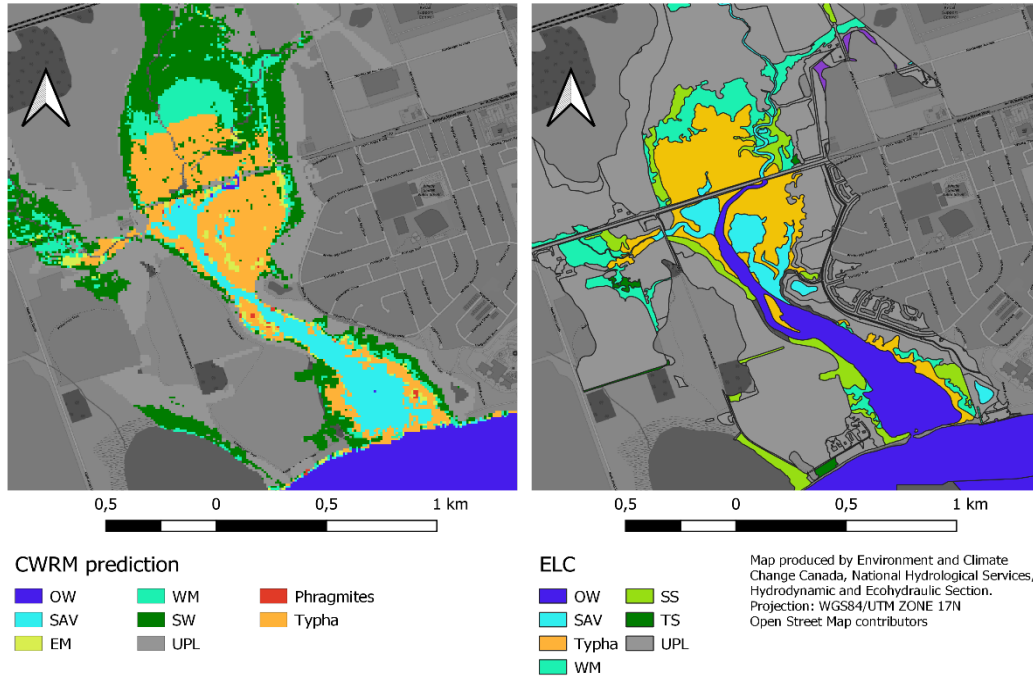


Figure 190: Invasive species model prediction using the observed water levels time series (1980-2018) at Lynde Creek (5LCM) in **2008** (left) and observed wetland classes by ELC (right) for the same year. ELC wetland classes were converted to match with CWRM wetland classes. ELC Typha class corresponds to “shallow marsh” class. Results and discussio

6.3. Results

6.3.1. Wetland succession modelling

6.3.1.1. Projected changes on total wetland area

To compare changes in wetland distribution and composition, the relative change of each wetland class between the recent past and future periods was calculated for each climate change scenario. The Mann-Whitney U statistical test ($\alpha=0.05$) (Mann & Whitney, 1947) was applied to evaluate the difference of mean area of each wetland class, including total wetland area, between the recent past and future periods for each wetland site. The variance in wetland class distribution has also been compared between the two periods for each climate change scenario using a Brown-Forsythe statistical test (Brown & Forsythe, 1974) ($\alpha=0.05$). The difference of variation coefficient between the recent past and future periods was used to measure the change in variance.

The range of relative projected changes in wetland area spans a decrease of 55% to an increase of 30% (Figure 191). Globally, for the upper-bound scenario, which has an associated average water level rise of 54.5 cm for all lakes (Table 59), there is an average loss of wetland area of 16% (Table 60). In contrast, the lower bound scenario, with an average water level decrease of 10.3 cm for all lakes (Table 59), shows an average wetland area gain of 7% (Table 60). However, the relative projected changes vary greatly among sites and among climate scenarios. The upper bound scenario shows mostly decreases in wetland area, with changes ranging from -55% to 12%, while the lower bound scenario shows mostly increases in wetland area, with changes ranging from -1% to 29% across all sites (Figure 191).

Under the upper bound scenario, in all Lakes apart Lake Ontario, a loss of total wetland area is predicted. The sites subject to experience the greatest changes are located in Lake Erie (9LPW: -55% and 10RBY: -33%) and Lake St. Clair (13LSC: -39% and 14SAM: -40%). On average, for Lake Erie, there is a simulated 31% loss of wetland area; similarly, wetlands are reduced by 35% for Lake St. Clair. Conversely, for Lake Ontario, the rise in water level suggested by the upper bound scenario results in an average increase in wetland area of 8%. In the Upper St. Lawrence River, site 1HIE experiences an average wetland loss of 19%. For Lake Huron, there is an average 11% predicted loss of wetlands under the upper bound scenario. However, it is important to note that the predicted 30% wetland loss in Whiskey Harbor (22WHW) is most likely overestimated the study area was restricted by a lack of LIDAR data. The sites experiencing the

greatest increase in wetland area under this scenario are located in Lake Ontario (6JSM: 27%) and Lake Erie (8SPP: 29%). Lake Ontario also has the highest average predicted increase for all wetlands with 11%. Lake Erie has an average increase of 10%, Lake St. Clair, 6% and Lake Huron, 4%. The simulated increase in wetland area is generally below 10% for most sites (17 of 20 sites). Of the three sites where the wetland area increases more than 10%, two are located in Lake Ontario (3SBM and 6JSM). The complete results of total wetland area changes are presented in Table 60 and the range of projected change are presented in Figure 191.

Table 59: Difference in median water level between recent past (1980-2009) and future (2070-2099) periods for the lower and upper bound climate simulations.

Water bodies	Range of variation in median water level (m) [lower, upper]
USL	[0.02, 0.62 m]
LKO	[0.01, 0.63 m]
LKE	[- 0.13, 0.46 m]
LSC	[- 0.15, 0.45 m]
LKH	[- 0.14, 0.64 m]

Table 60: Range of relative projected change in wetland area (%) in the future period (2070-2100) relative to the recent past period (1980-2009) for the lower-bound and upper-bound simulations. USL: Upper St. Laurence, LKO: Lake Ontario, LSC: Lake St. Clair – Detroit River, LKH: Lake Huron. Red indicates significant decrease, green

indicates significant increase and black indicates insignificant change in wetland area between the recent past and future periods. Statistical analysis were done using a Mann-Whitney U statistical test ($\alpha=0.05$).

Site	Water Body	Average wetland area (historic) (ha)	Projected % change in wetland area for two lake level scenarios [upper, lower]
Hill Island East(1HIE)	USL	69	[-18.9, -0.2]
Airport Creek (2ACM)	LKO	219	[25.4, 1]
South Bay (3SBM)	LKO	94	[0.3, 11.7]
Lyndee Creek (5LCM)	LKO	121	[-4.2, 3]
Jordan Station (6JSM)	LKO	88	[11.6, 26.7]
Grand River Mouth (7GRM)	LKE	649	[-22, 3.1]
Selkirk Provincial Park(8SPP)	LKE	59	[-22, 28.6]
Long Point (9LPW)	LKE	952	[-54.6, 6.8]
Rondeau Bay (10RBY)	LKE	1434	[-32.9, 7.6]
Fox Creek/Dolson's Creek(11FCK)	LKE	28	[-22.3, 5.2]
Detroit River(12DRM)	LSC	713	[-27.3, 2.9]
Lake St. Clair (13LSC)	LSC	1840	[-39.1, 7.7]
Johnston Bay (14SAM)	LSC	5367	[-39.7, 8.8]
Baie Du Doré (15BDD)	LKH	266	[-13.2, 0.7]
Hay Bay (16HBW)	LKH	104	[0.2, 1.9]
Hog Bay (18HGW)	LKH	95.3	[-17.1, 9.6]
Treasure Bay (19TBY)	LKH	102.2	[-12.9, 6.4]
Whiskey Harbor (22WHW)	LKH	38.9	[-30.0, 9.2]
Anderson Creek (23ACK)	LKH	42	[5.8, -0.8]
Frances Point (27FPT)	LKH	49	[-7.9, 0.8]

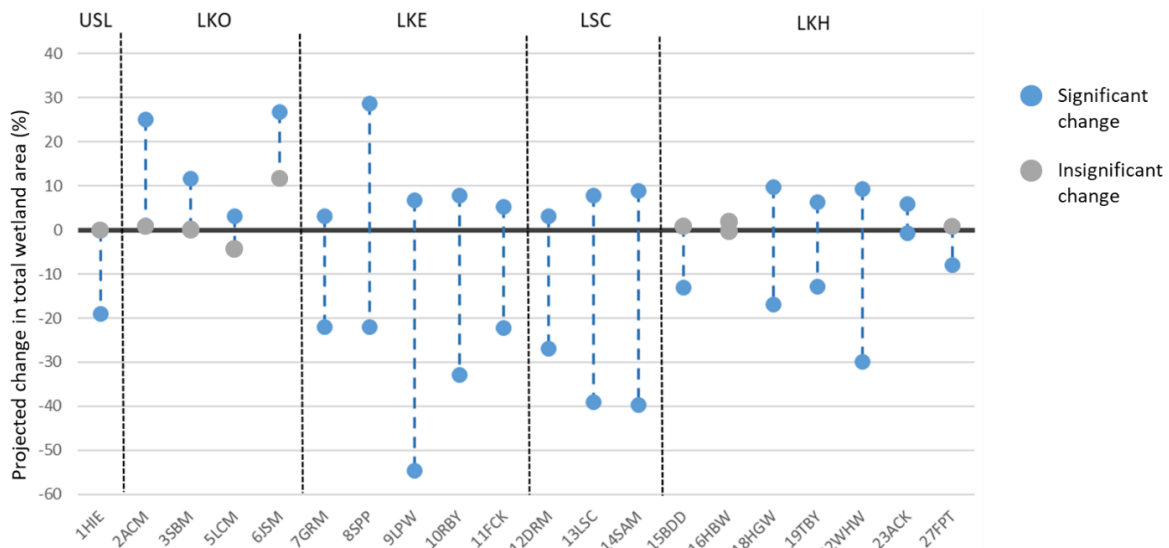


Figure 191: Range of relative projected change in wetland area (%) between recent past and future periods for all study sites, with changes defined as the difference in annual distributions between the future (2070–2099) and the recent past (1980–2009). Acronyms are defined in Table 60.

6.3.1.2. Projected changes in wetland class distribution

For most sites, even those with minor changes in total wetland area, a projected increase in water level will result in significant changes in wetland class distribution, as wetland classes may migrate or be replaced by other ones.

In the following subsections, the following elements are presented for each water body:

- Total area and relative abundance of each wetland class under the reference state (wetland class distribution according to the historical water-level time-series from 1980 to 2009) for each wetland site;
- The relative change in area for each wetland class between the simulated recent past and the simulated future time-series under the lower and upper bound. This gives an overview of the ranges of possible changes in terms of wetland class distribution under climate change;
- The relative change in the coefficient of variation of each wetland class between the recent past and future time-series for both simulations. This is an indication that the interannual variability of the wetland classes may be impacted by climate change. It indicates whether the wetland class distribution will be stable from year to year or may change abruptly;
- A map for a specific site of the lake showing the significant changes for two wetland classes between simulated recent past and future under the upper bound.

6.3.1.2.1. Upper St. Lawrence River

The Upper St. Lawrence River includes one site, Hill Island (1HIE). It is a protected embayment and a coastal marsh area of the natural landscape of Thousand Island National Park. Under the reference state, this site is mainly dominated by SAV and EM represents about a quarter of the total wetland, whereas WM and SW are much less present (Figure 192). The different wetland classes have a low standard deviation throughout the 30 year-period, indicating a low interannual variability.

Under the lower-bound scenario, the area of two wetland classes changes significantly. EM increases by 17%, while WM decreases by 35% in the future. It is important to note that WM does not occupy a very large proportion of the site in the baseline condition, which explains the large decrease in percentage. The total wetland area remains the same for this site. In addition, the variance of all the wetland classes does not change in the future under this scenario (Table 61).

Under the upper-bound scenario, EM decreases significantly (by 47%), and WM loses 29% of its area. The rise in water level causes those decreases because the topography of this site is not

suitable for inland wetland migration. The total wetland area is also significantly reduced by 19%. The mean area of SAV may be not significantly affected by the upper bound scenario, but its area is five times more variable from year to year in the future reacting to more variable water levels. The variance of EM area is also increased in the future under the upper bound scenario, as well as the total area of wetlands (Table 61).

6.3.1.2.2 Lake Ontario

In Lake Ontario, under the reference state most sites are dominated by SW and EM with the exception of the drowned river mouth wetlands of Jordan Station, where SAV and EM are predominant (Figure 192-A). SAV presents a high interannual variability in Airport Creek (2ACM), South Bay (3SBM) and Lynde Creek (5LCM) during the historical period.

Under the lower-bound scenario, most Lake Ontario sites are reacting the same way: an increase in SAV and EM. Those increases are associated with corresponding decreases of WM and SW areas. For Jordan Station (6JSM), WM is the only class presenting a loss of habitat (-48%), but it is also less variable. This WM decrease is associated with an increase of EM (20%) and SW (14%). All sites show an increase in inter-annual variability for SAV, with an increase in the variation coefficient between 16-24% (2ACM and 5LCM) to 71-75% (3SBM and 6JSM) (Table 61). The interannual variability also increases for SW in most sites. It also increases for WM in 2ACM and for EM in 6JSM.

Under the upper-bound scenario, impacts are more important but vary among sites (Figure 192-C), mainly because of the local topographical setup. For all sites in Lake Ontario, the area of SAV almost doubled. At Airport Creek Marsh (2ACM), an open drowned river mouth wetland, the rise in water levels leads to an increase in open water and to a migration of the wetland classes to the upland areas since the flat topography is suitable for inland wetland migration. At the three other sites, an increase in SAV leads to a decrease of all other wetland classes, with SW suffering the greatest losses in area. SW tend to have a lower capacity to migrate because of unfavorable topography (i.e. steep slopes) and land use, whereas EM tend to suffer lower losses, as they can migrate upland, in places where WM and SW have recently been dominant. This wetland migration is notably observed at Lynde Creek Marsh (5LCM), where EM migrated in areas that were occupied by SW in the recent-past (Figure 193). In addition, for all sites of Lake Ontario and for most of the wetland classes, variance significantly increases in the future with the exception of WM in 3SBM and 6JSM (Table 61). Facing climate change, Lake Ontario wetland class distribution will likely be more variable from year to year, especially for the SAV class.

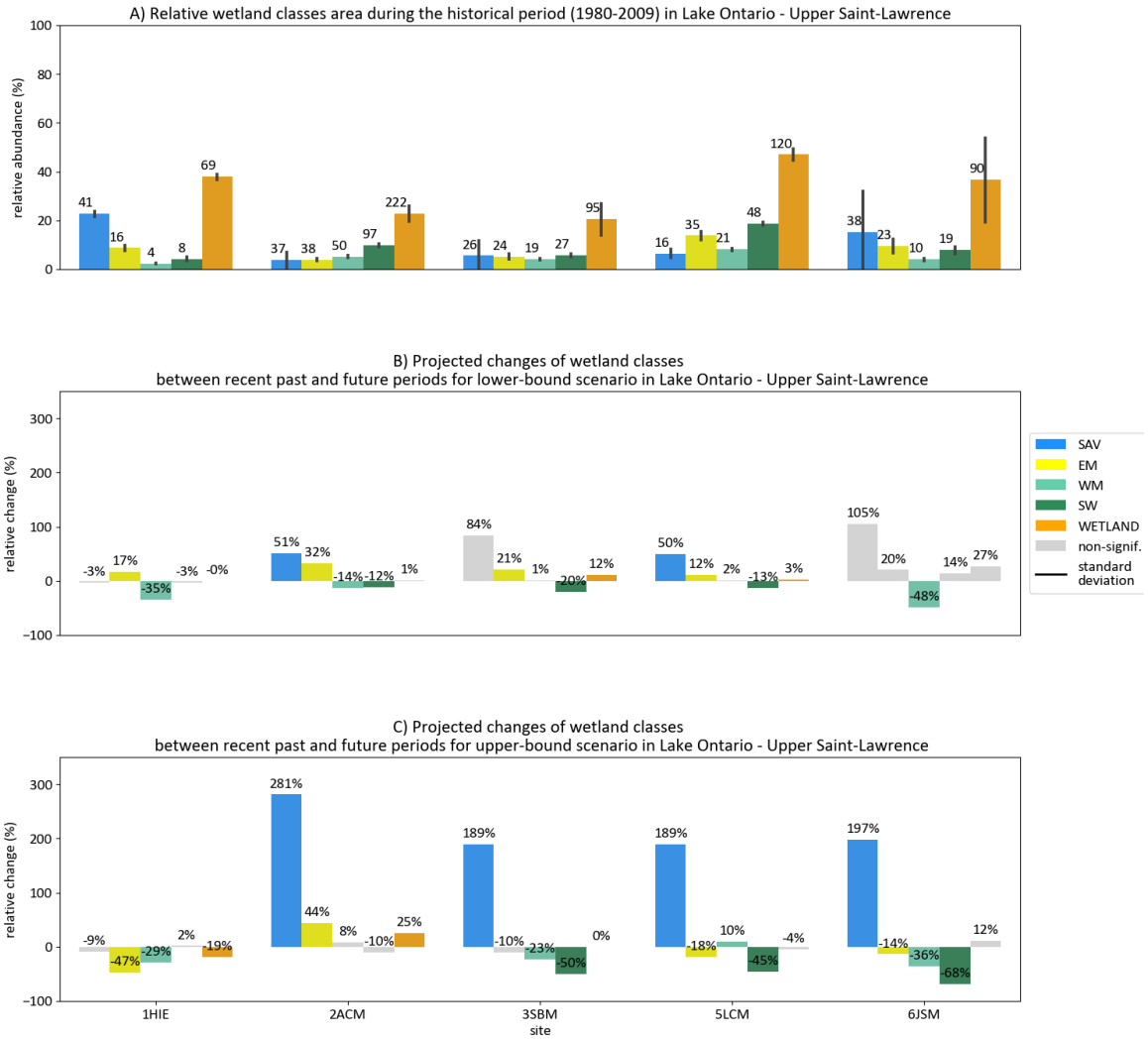


Figure 192: A) State of reference of wetland class area, as a proportion of total site area (%) in the recent past period (historic). Annotations on top of the bars represents the absolute area of the wetland class in hectares. Total wetland area (WETLAND) sums all classes, except OW and UPL. B) Variation (%) between the recent past and future periods for each wetland class for the lower-bound simulation and C) upper-bound simulation in Lake Ontario.

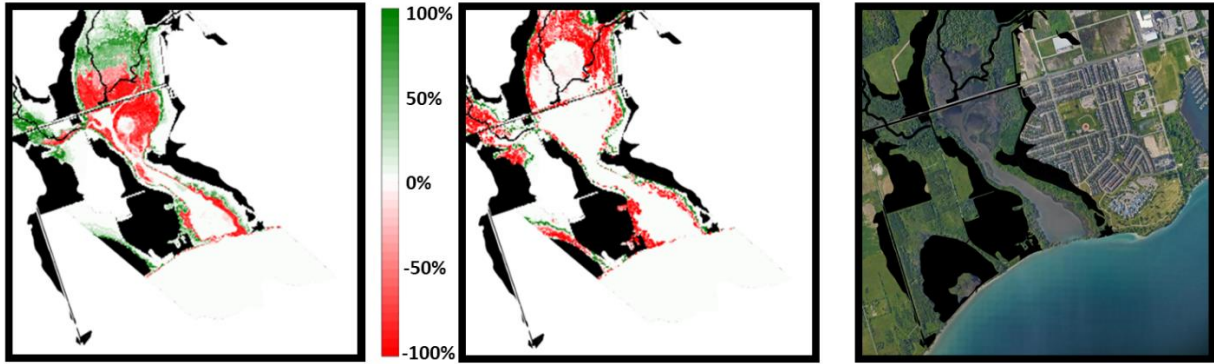


Figure 193: Changes in wetland class distribution between recent past and simulated future with the upper-bound scenario (red: loss, green: Gain, Black: Urban areas unsuitable to wetland establishment) at Lynde Creek (5LCM), Lake Ontario. Left: Upland migration of EM. Middle: Loss of SW. Right: Google Satellite imagery.

Table 61: Coefficient of variation difference between the recent past and future periods of the lower- and upper-bound scenario for the different wetland classes in Upper St. Lawrence and Lake Ontario sites. Difference in variance between the recent past and future periods that are statistically significant according to a Brown-Forsythe test ($\alpha=0.05$) are in bold.

Lake	SITE	CV difference SAV		CV difference EM		CV difference WM		CV difference SW		CV difference total Wetlands	
		Lower	Upper	Lower	Upper	Lower	Upper	Lower	Upper	Lower	Upper
Upper St. Lawrence	1HIE	5%	30%	-2%	48%	6%	14%	-1%	14%	5%	22%
	2ACM	24%	14%	-1%	29%	8%	19%	6%	20%	4%	7%
Lake Ontario	3SBM	71%	29%	2%	23%	-2%	12%	8%	6%	18%	15%
	5LCM	16%	3%	1%	12%	2%	4%	7%	19%	1%	10%
	6JSM	75%	26%	10%	32%	6%	20%	16%	10%	34%	25%

6.3.1.2.3. Lake Erie

In Lake Erie, under the reference state, the wetland class distribution varies among sites (Figure 194-A). In Grand River Mouth (7GRM) and Long Point (9LPW), SW and WM are the most abundant classes. In Rondeau Bay (10RBY), SW and EM are the most abundant wetland classes. While WM and EM are prominent in Selkirk Provincial Park (8SPP), EM is dominant in Fox Creek (11FCK).

For the lower-bound scenario, relative projected total wetland area changes are minor for most sites, except in 8SPP where wetland area increased by 29%, mainly due to an increase of SW (+59%) and EM (+60%) (Figure 194-B). Similar increases in EM and SW are observed, but to a lesser degree, at 9LPW and 10RBY (27 and 25% respectively). An increase in SW interannual variability is also observed in both of these sites. In 7GRM, there is an increase of SW (+11%)

and a decrease of EM (-13%). The variability increases for most wetland classes in this site, with the exception of SAV. In 11FCK, there is an increase of SW (+26%) and WM (+113%) and a decrease of SAV (-21%). The internannual variability of all wetland classes is increasing in this site (Table 62). Generally, the moderate decrease in median water level leads to a lakeward wetland migration and an increase in SW areas. In large sites such as 9LPW and 10RBY, water level changes cause major changes in wetland class distribution where the SW area is increased by ~59 ha in 9LPW and ~154 ha in 10RBY.

For the upper-bound simulation, all sites undergo an overall decrease in wetland area (Figure 194-C). For most sites, the rise in water level leads to a decrease of most wetland classes. In 7GRM, a barred drowned river mouth wetland, SAV increases by 98% while the SW is reduced by 64%. The variability of SW is also reduced in this site, while the variability of SAV and WM is increased (Table 62). High water levels in this scenario indicates a threat for this particular wetland, especially for the SW class. A similar threat is present for 8SPP where the high water levels reduce most wetland classes, reducing WM (-31%), SW (-19%) and EM (-13%) area. In 9LPW, most wetland class area are also reduced, with losses in SAV (-55%), EM (-35%), WM (-60%) and SW (-40%). The topography of this specific site is not suitable for wetland migration with rising water levels. The interannual variability of EM is also decreased, while SAV and WM variability is increased for 9LPW. In 10RBY, SW and SAV area is decreased by 50% and 53% respectively, while the WM area is increased by 24%. The variability for EM and WM also decreased in this sand-spit embayment. This site allows some wetland classes to migrate upland, but the overall suitable area for most wetland classes is reduced at higher elevations. In 11FCK, SAV and EM are negatively affected by 63% and 20% respectively. The interannual variability is increased for SAV and WM in this barred drowned river mouth wetland that is surrounded by human altered land use where wetland migration is impossible.

It is worth noting that in some cases, wetland classes can retain a similar coverage in terms of hectares, while migrating inside their AOI. This is the case in 10RBY where EM migrated in areas predominantly dominated by SW (Figure 195-left) while covering an area only 6% lower than what the recent past simulation indicates. However, due to a low availability of land suitable for wetland migration at higher elevation, the projected SW area is reduced by 53%. The same phenomenon is observed in 9LPW, where the topography limits the wetland migration. In 11FCK and 8SPP, the anthropogenic land use also limits wetland migration to higher elevations, explaining the loss of almost all wetland classes at those sites.

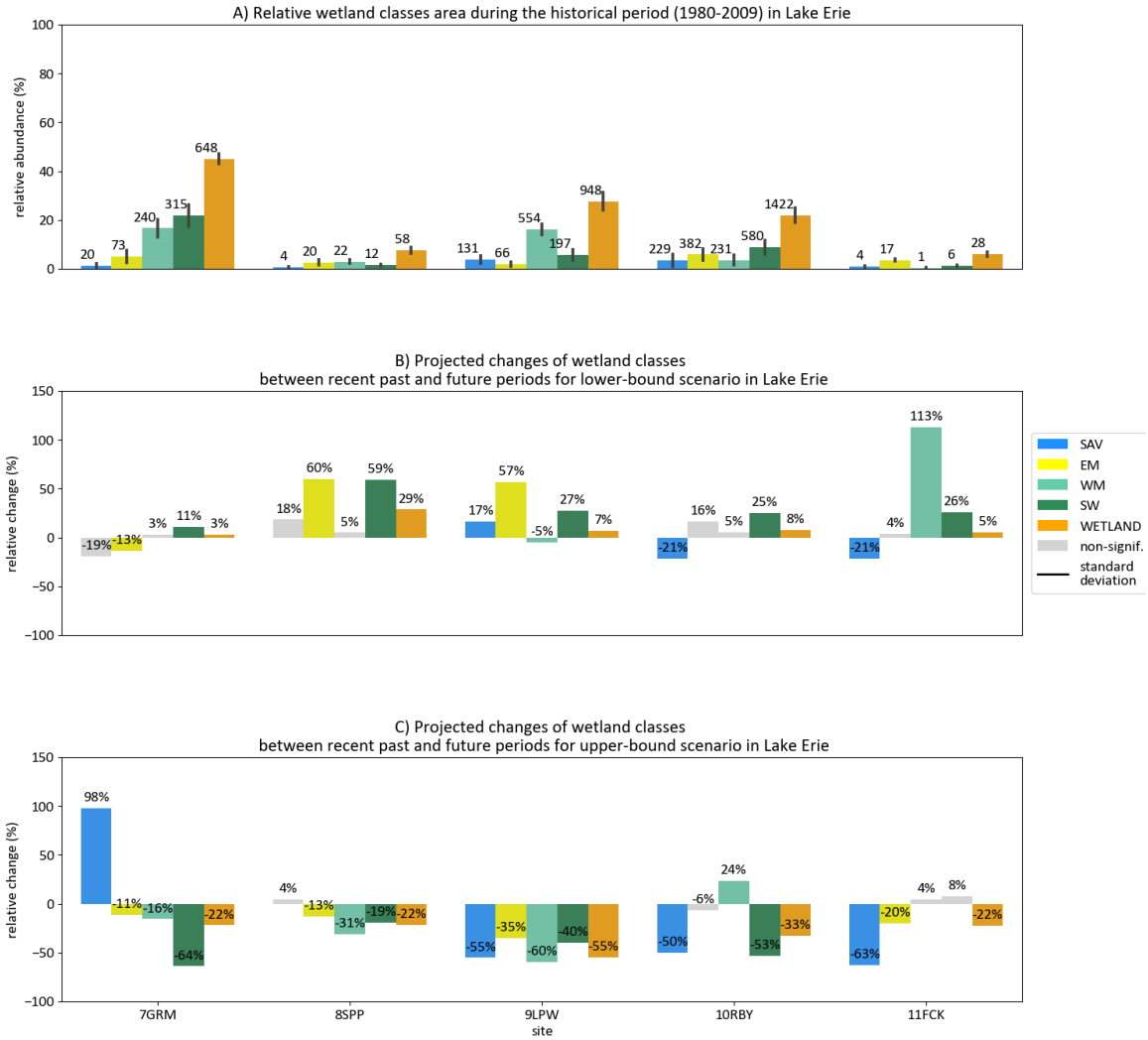


Figure 194: A) State of reference of wetland class area, as a proportion of total site area (%) in the recent past period (historic). Annotations on top of the bars represents the absolute area of the wetland class in hectares. SS and TS classes were summed into a single SW class. Total wetland area (WETLAND) sums all classes, except OW and UPL. B) Variation (%) between the recent past and future periods for each wetland class for the lower-bound simulation and C) upper-bound simulation in Lake Erie.

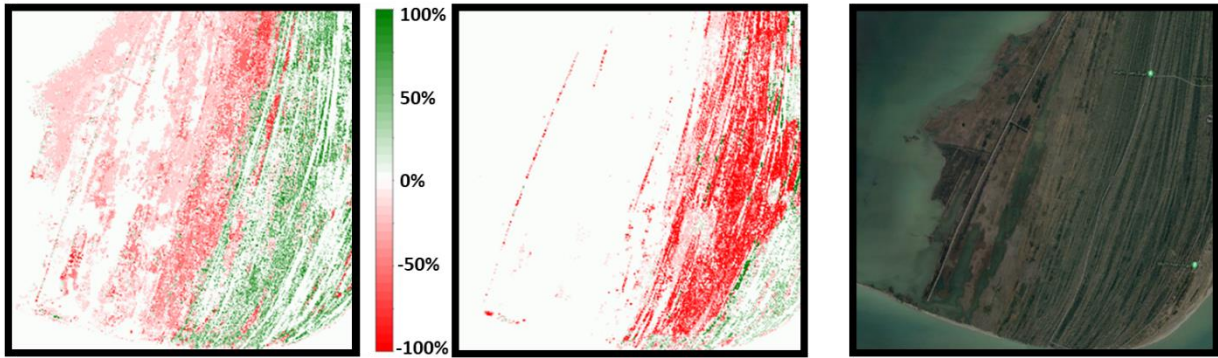


Figure 195: Changes in wetland class distribution between recent past and future with the upper-bound scenario (red: loss, green: Gain) at Rondeau Bay (10RBY), Lake Erie. Left: Upland migration of EM. Middle: Loss of SS. Right: Google Satellite imagery.

Table 62: Coefficient of variation difference between the recent past and future periods of the lower- and upper-bound scenario for the different wetland classes in Lake Erie sites. Difference in variance between the recent past and future periods that are statistically significant according to a Brown-Forsythe test ($\alpha=0.05$) are in bold.

Lake	Site	CV difference SAV		CV difference EM		CV difference WM		CV difference SW		CV difference total Wetlands	
		Lower	Upper	Lower	Upper	Lower	Upper	Lower	Upper	Lower	Upper
Lake Erie	7GRM	-10%	-2%	29%	3%	7%	10%	7%	-12%	1%	9%
	8SPP	-1%	-9%	2%	7%	10%	2%	17%	16%	10%	3%
	9LPW	-5%	12%	-6%	-33%	-2%	8%	12%	-2%	2%	9%
	10RBY	5%	21%	-10%	-31%	11%	-11%	18%	19%	3%	8%
	11FCK	21%	4%	4%	3%	36%	9%	18%	5%	1%	-2%

6.3.1.2.4. Huron-Erie Corridor

Under the reference state, SAV and EM are the most abundant wetland classes in the three Huron-Erie Corridor sites. In Detroit River Marsh (12DRM), some SW are present, but the WM presence is sparse. In the open shoreline of Lake St. Clair (13LSC), SW and WM are equally abundant. In Johnston Bay (14SAM), the wetland class distribution in this delta is similar to 13LSC (Figure 196-A).

For the three sites in Lake St. Clair and Detroit River, relative projected total wetland area (WETLAND) changes under the lower-bound simulation are minor ($< +10\%$) (Figure 196-B). The moderate decrease in water level under this scenario leads to a lakeward wetland migration and to a minor increase in wetland area. The area covered by SW increases in 13LSC and 14SAM sites by 105% and 64% respectively. However, SW are not abundant in those sites compared to other wetland classes (Figure 196-A). Moreover, EM is favored by lower water levels in 14SAM, where this class increases by 24%. In the open shoreline of Detroit River Marsh (12DRM), the

WM and SW area increase by 23% and 40% respectively. WM is not very abundant in this site during the historical period of the reference state, and thus lower water levels should be beneficial for this class. With this scenario, the interannual variability of the wetland class areas is similar for most classes except for SW where the coefficient of variation increases notably (Table 63). There is also an increase in variability for EM in 14SAM.

In contrast, in the upper-bound scenario, the rise in water level under this simulation leads to a decrease in all wetland classes of all sites. Being surrounded by dikes, agricultural lands or urban areas, the wetland sites located in the Huron-Erie corridor have a low capacity to migrate landward. Thus, the projected rise of water levels induces a reduction of wetland area in general, but mostly affects EM, SW and WM. 13LSC and 14SAM sites are located in the St. Clair River delta area and are characterized by a large shallow basin. A rise in water level in those sites causes major change in SAV area (-29% for both sites), increasing the open water area. In 12DRM, SAV migrates where EM was previously distributed (Figure 197), and because of the low availability of lands to migrate upland, significant losses of EM area are suggested by the upper-bound scenario. In 14SAM, similar to 12DRM, the SAV migrate where EM was present previously, and EM is unable to migrate inland because of the large diked area (Figure 198). In 13LSC, the SAV interannual variability increases with this scenario (Table 63). In 12DRM, the EM variability is reduced since the site is mostly flooded in the future, stopping the succession of EM to other wetland classes (to SAV for instance). SW variability is also reduced in this site since this class is mostly absent in the future. In 13LSC and 14SAM, the variability of EM distribution is increased. The EM establish in areas that were not suitable for this class in the past, such as previous SW areas. There is also a strong decrease in variability of SW in 13LSC because this class occurrence is sparse in the future time-series.

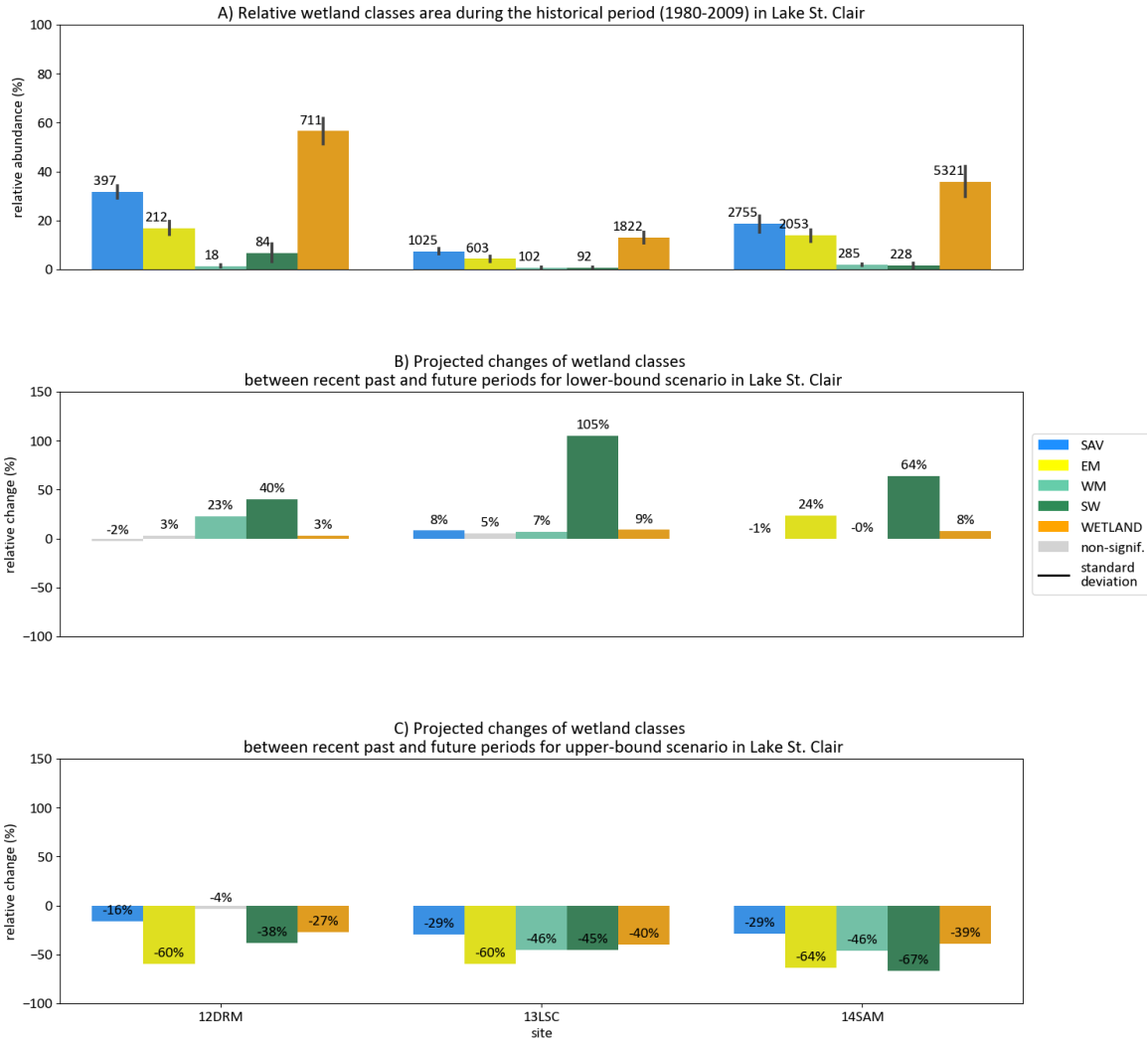


Figure 196: A) State of reference of wetland class area, as a proportion of total site area (%) in the recent past period (historic). Annotations on top of the bars represents the absolute area of the wetland class in hectares. Total wetland area (WETLAND) sums all classes, except OW and UPL.B) Variation (%) between the recent past and future periods for each wetland class for the lower-bound simulation and C) upper-bound simulation in Lake St. Clair – Detroit River.

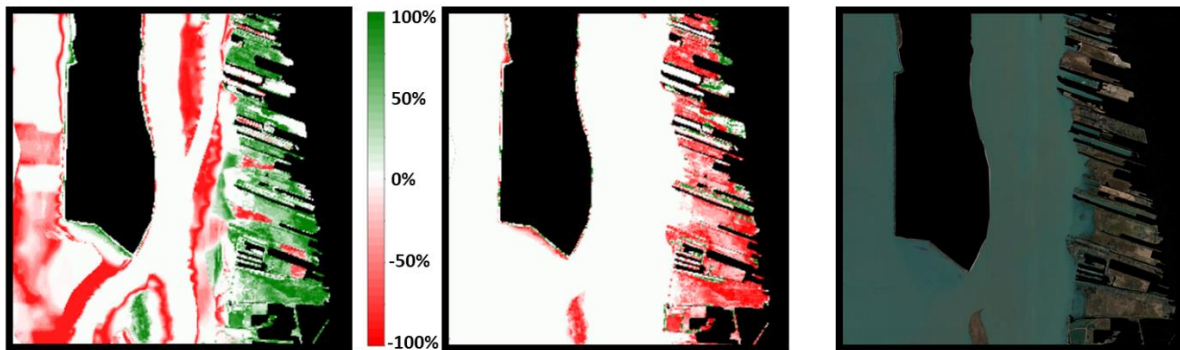


Figure 197: Changes in wetland class distribution between recent past and future with the upper-bound scenario (red: loss, green: Gain, Black: Urban areas unsuitable to wetland establishment or where the physical variables could not

be calculated) at Detroit River Marsh 12DRM. Left: Landward migration of SAV. Middle: EM habitat loss. Right: Google Satellite imagery.

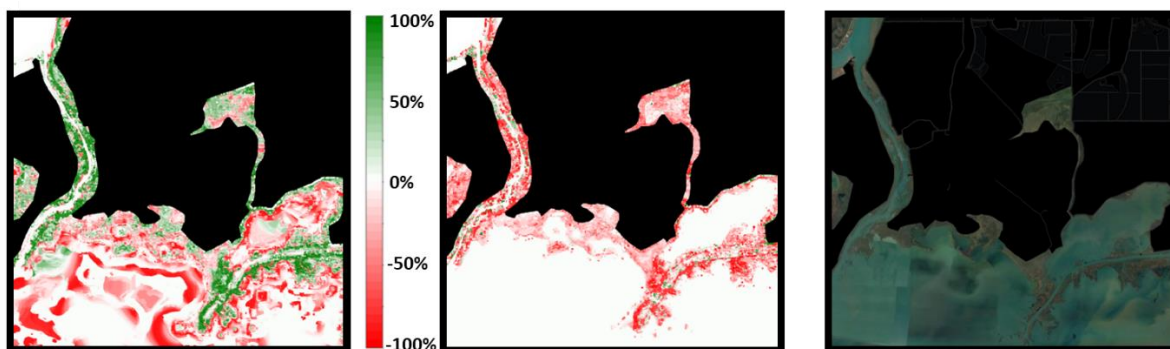


Figure 198: Changes in wetland class distribution between recent past and future with the upper-bound scenario (red: loss, green: Gain, Black: Urban areas unsuitable to wetland establishment or where the physical variables could not be calculated) at Johnston Bay (14SAM). Left: Landward migration of SAV. Middle: EM habitat loss. Right: Google Satellite imagery.

Table 63: Coefficient of variation difference between the recent past and future periods of the lower- and upper-bound scenario for the different wetland classes in Huron-Erie Corridor sites. Difference in variance between the recent past and future periods that are statistically significant according to a Brown-Forsythe test ($\alpha=0.05$) are in bold.

Lake	Site	CV difference SAV		CV difference EM		CV difference WM		CV difference SW		CV difference total Wetlands	
		Lower	Upper	Lower	Upper	Lower	Upper	Lower	Upper	Lower	Upper
Huron-Erie corridor	12DRM	2%	-1%	-3%	-8%	1%	-6%	32%	-1%	2%	-1%
	13LSC	0%	11%	-6%	2%	-22%	8%	54%	-20%	0%	10%
	14SAM	1%	7%	6%	11%	4%	7%	29%	3%	2%	7%

6.3.1.2.5. Lake Huron

Wetland sites of Lake Huron have the highest biodiversity among all Great Lakes sites and are characterized by a large amount of annual emergent plants. During the reference period, wetland class distribution is relatively similar among all sites where all classes are distributed uniformly (Figure 199-A). Lake Huron sites are located in a natural environment that has not been impacted as much as other lakes by human settlement. The migration capacity of the wetlands at these sites is mostly limited by topography and geology. The soil at Georgian Bay sites is generally composed of bedrock and may limit the establishment of wetlands at higher elevations. Areas where bedrock was visible on satellite imagery were considered unsuitable to wetland establishment, although such areas under forest cover might not have been identified as such.

Under the lower-bound scenario, total wetland area (WETLAND) remains stable or increases by less than 10% (Figure 199-B). Lower water levels projected with the lower-bound scenario cause an increase in SW area in four sites and a decrease in SAV for Baie du Doré (15BDD) and Francis

Point (27FPT). At the open embayment of 15BDD, the significant loss of SAV (-15%) and EM (-13%) is compensated by an increase in WM (25%). In Hog Bay (18HGW), a slight lakeward migration of wetlands occurs where EM increases by 17% and SW by 19%. For other sites, SW is the most affected class, increasing by up to 36% in Whiskey Harbor (22WHW). In terms of variance, WM area increases for nearly all wetland sites. The variation coefficient increases by up to 16% in 22WHW. In the protected embayment of Hay Bay (16HBW), the variance of every wetland class increases under the lower-bound scenario except for SAV, where the variance significantly decreases (Table 64).

Under the upper-bound scenario, the wetland area (WETLAND) of the future decreases significantly in comparison with the recent past period, associated with a decrease in EM by up to 38% in 18HGW and WM by up to 47% in 22WHW (Figure 199-C). In fact, in five sites (15BDD, 18HGW, 19BTY, 22WHM and 27FPT) all wetland classes are decreasing in the future in this scenario. However, the decrease is offset by an increase in SAV and/or SW caused by migration of wetlands in upland areas in 16HBW and Anderson Creek (23ACK). Wetland class landward migration is associated with the rising of median water level by 64 cm (Table 59), where EM, WM and SW migrate to higher elevations. This wetland migration can be observed in Treasure Bay (19TBY) where EM and WM establish in forested areas (Figure 200). In 22WHW, the limited LIDAR elevation data available might have restricted potential upland migration evaluation in the model outputs, since surrounding upland areas were not part of this site AOI. Therefore, modelling results for the simulation projecting a rise in water level (upper-bound) might overestimate wetland losses especially for wetland classes associated with higher elevation such as WM and SW for this specific site. Regarding the variance of the wetland class area, no evident pattern can be seen for Lake Huron sites, where significant changes in the variance are site and class specific. In general, the changes indicate a decrease in the interannual variability (Table 64).

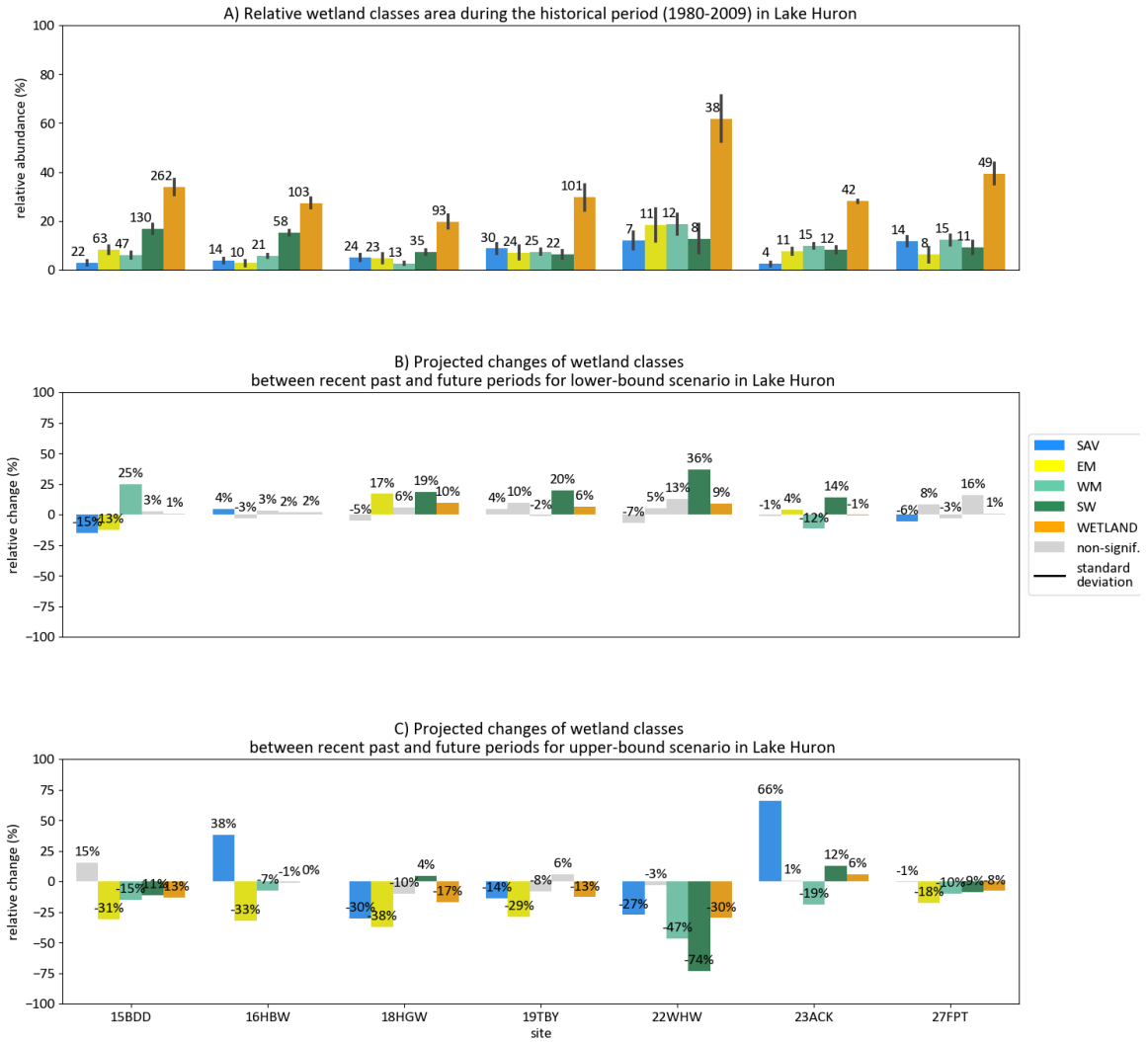


Figure 199: A) State of reference of wetland class area, as a proportion of total site area (%) in the recent past period (historic). Annotations on top of the bars represents the absolute area of the wetland class in hectares. Total wetland area (WETLAND) sums all classes, except OW and UPL. B) Variation (%) between the recent past and future periods for each wetland class for the lower-bound simulation and C) upper-bound simulation in Lake Huron.

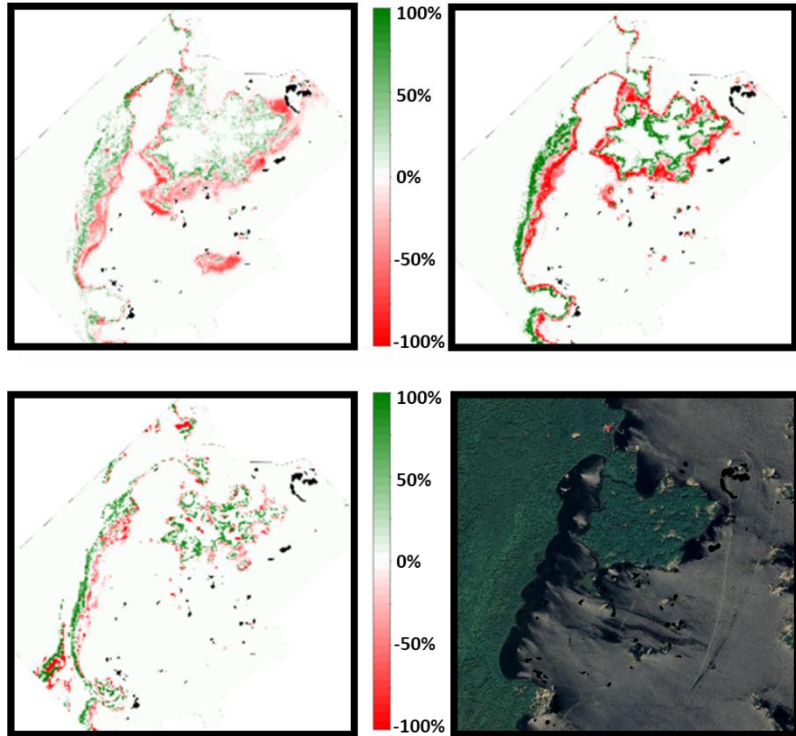


Figure 200: Changes in wetland class distribution between recent past and future with the upper-bound scenario (blue: loss, red: Gain, Black: Urban areas unsuitable to wetland establishment or where physical variables were unavailable) at Treasure Bay (19TBY). Up Left: EM landward migration, up right: WM landward migration, down left: SW landward migration, down right: Google Satellite imagery.

Table 64: Coefficient of variation difference between the recent past and future periods of the lower- and upper-bound scenario for the different wetland classes in Lake Huron sites. Difference in variance between the recent past and future periods that are statistically significant according to a Brown-Forsythe test ($\alpha=0.05$) are in bold.

Lake	Site	CV difference SAV		CV difference EM		CV difference WM		CV difference SW		CV difference total Wetlands	
		Lower	Upper	Lower	Upper	Lower	Upper	Lower	Upper	Lower	Upper
Lake Huron	15BDD	1%	12%	1%	3%	11%	1%	2%	-3%	1%	3%
	16HBW	1%	-1%	-2%	-8%	2%	-4%	2%	1%	1%	-1%
	18HGW	-6%	1%	4%	-4%	7%	8%	5%	0%	4%	-5%
	19TBY	-5%	0%	7%	-1%	3%	11%	0%	-7%	3%	-4%
	22WHW	2%	34%	3%	6%	16%	6%	9%	14%	-1%	9%
	23ACK	5%	-25%	0%	-3%	-1%	-6%	1%	-2%	0%	2%
	27FPT	3%	-1%	5%	-2%	3%	8%	3%	0%	3%	1%

6.3.2. Invasive species modelling

6.3.2.1. Projected change in area of suitable habitat for *Phragmites* and *Typha*

The relative change of invasive species suitable habitat area corresponds to the variation (%) of invasive species suitable habitat area between the recent past and the future periods which is calculated for the lower-bound and upper-bound scenario (Figure 201). In Figure 201, dark colored bars indicate a significant variation (using a Mann-Whitney U statistical test with $\alpha=0.05$) between the two periods according to the scenarios (teal for the lower-bound and orange for the upper-bound scenario). The black dotted line shows the significant range of possible outcomes.

6.3.2.1.1. Upper St. Lawrence River and Lake Ontario

In Lake Ontario and Upper St. Lawrence River, simulations from both scenarios indicate an important increase of *Phragmites* suitable habitat linked to climate change in all sites except 6JSM, with changes reaching up to 150%. The upper-bound scenario is more favorable to *Phragmites* suitable habitat than the lower-bound. However, the lower-bound scenario still increases the *Phragmites* suitable habitat in the future by 24% and 28% in 2ACM and 3SBM, respectively. The upper-bound scenario increases the *Phragmites* suitable habitat by up to 150% in 1HIE, which corresponds to an increase of 6 ha. 2ACM and 5LCM are also severely affected, where the upper-bound scenario increases the *Phragmites* suitable habitat area by 95% (23 ha) and by 66% (12 ha) respectively.

Suitable habitat area for *Typha* is also likely to increase in 2ACM and 5LCM, as both future scenarios indicate an increase. At those sites, the increase in *Typha* suitable habitat area is more important under the upper-bound scenario than the lower-bound (reaching more than 50% in 5LCM). In 6JSM, an important decrease in *Typha* suitable habitat area is projected, with a decrease of up to 60% (10 ha) with the upper-bound scenario. Hill Island East presents a similar trend with a decrease of 35% of *Typha* suitable habitat under the upper-bound scenario.

The upper-bound scenario appears to increase the suitable habitat area for both species in sites with a steady topographic gradient and natural landscape, such as 2ACM and 5LCM. Inversely, 6JSM site is less suitable for both species at higher water levels because the wetland is more constrained by agricultural and residential development and cannot migrate upland (Figure 201).

6.3.2.1.2 Lake Erie

In Lake Erie, it is difficult to draw clear basin-wide conclusions for both species. The lower-bound scenario increases the *Phragmites* suitable habitat by 50% (5 ha) in 8SPP, by 30% (81 ha) in 9LPW, and by 107% (2 ha) in 11FCK. The upper-bound scenario also increases the *Phragmites* suitable habitat but to a lesser degree, with increases of 28% (27 ha) in 7GRM and 16% (38 ha) in 9LPW. In 10RBY, the lower and upper-bound scenarios decrease *Phragmites* suitable habitat by 5 and 55% (35 to 311 ha), respectively.

The lower-bound scenario increases the *Typha* suitable habitat area by 17% (29 ha) in 9LPW and by 34% (5 ha) in 11FCK. The upper-bound scenario reduces *Typha* habitat area in most of the Lake Erie sites with reductions of 57% (15 ha) in 8SPP, 37% (46 ha) in Long Point, 37% (287 ha) in 10RBY and 21% (2 ha) in 11FCK.

Unlike Lake Ontario, the lower-bound scenario seems to be more favorable for both invasive species in most sites. However, in 10RBY, the suitable habitat of both species decreases under each scenario. This site is characterized by a large, shallow and flat terrain sensitive to water level fluctuations. While this shallow area is suitable for invasive species under historically observed lake level conditions, it becomes largely flooded and unsuitable under projected late-century levels, especially under a significant increase (Table 23) in mean lake level for the upper-bound scenario.

6.3.2.1.3 Huron-Erie corridor

For the Huron-Erie corridor sites, it is also difficult to distinguish a clear trend of the impact of climate change on both invasive species. The upper-bound scenario is generally unfavorable for both species in all sites, whereas the lower-bound scenario is favorable for *Phragmites* in 13LSC and for both species in 12DRM.

Under the lower-bound scenario, the *Phragmites* suitable habitat area increases by 21% (18 ha) in 12DRM and by 24% (80 ha) in 13LSC. With the upper-bound scenario, *Phragmites* habitat area decreases in all Huron-Erie corridor sites. Specifically, the habitat area is reduced by 34% (36 ha) in Detroit River Marsh, by 65% (104 ha) in Lake St. Clair and by 72% (532 ha) in Johnston Bay (14SAM).

Typha suitable habitat increases in 12DRM by 10% (8 ha) with the lower-bound and decreases by 9% (7 ha) with the upper-bound scenario. In other sites, the projected scenarios decrease the habitat area. In 13LSC, the habitat area is reduced by 51% (242 ha), while the *Typha* suitable

habitat is increased by 51% (772 ha) in 14SAM with the upper-bound scenario. The lower-bound scenario also decreases the *Typha* suitable habitat in Johnston Bay by 9% (139 ha).

In Detroit River Marshes (12DRM), the highest elevations of the site are occupied by agriculture and housing, limiting the inland progression of *Phragmites* or *Typha* under significant projected water level increases (Table 23), as expected from the upper-bound scenario. Dikes play the same role in 14SAM and 13LSC, which limits upland wetland migration and reduces suitable habitat area for invasive species (Figure 201).

6.3.2.1.4. Lake Huron

In sites of Lake Huron, there is no increase in *Phragmites* suitable habitat area in the future under both simulations except for 27FPT where the habitat area increases by 15 to 45%. In contrary, with the lower-bound scenario, a decrease in *Phragmites* suitable habitat area is projected in 16HBW and 23ACK, with habitat area reduction of 15% (1 ha) and 44% (2 ha), respectively. With the upper-bound scenario, a decrease in *Phragmites* suitable habitat area is projected for four sites in the future, i.e. 15BDD by 9% (2 ha), 16HBW by 31% (2 ha), 22WHW by 24% (1 ha), and 23ACK by 37% (2 ha). No significant changes for *Phragmites* suitable habitat area are projected for sites located in the southeast end of Georgian Bay (i.e. 18HGW, and 19TBY). It is worth noting that even if changes are statistically significant, simulated *Phragmites* habitat variations affects relatively small areas, with a maximum expected variation of 2 ha.

In all sites of Lake Huron sites, *Typha* suitable habitat area is predicted to reduce or to face no significant changes. The lower-bound scenario reduces the habitat area by 13% (10 ha) in 15BDD and by 15% (1 ha) in 16HBW. The upper-bound scenario reduces the habitat area by 37% (2 ha) in 18HGW, by 18% (2 ha) in 19TBY, by 44% (1 ha) in 22WHW, by 31% (0.2 ha) in 23ACK and by 10% (0.4 ha) in 27FPT. Overall, *Typha* is unlikely to be favored by climate change in Lake Huron, with all sites displaying a decrease of the suitable habitat area that reaches 10–50%.

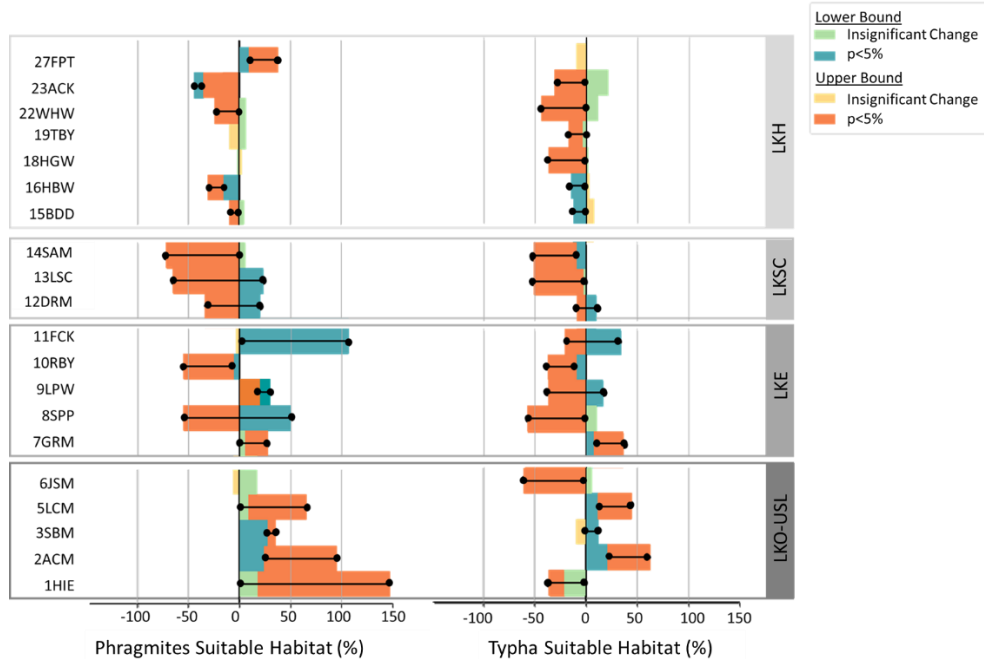


Figure 201: Range of relative changes of two invasive species habitat (%), between the recent past and the future periods, based on the lower-bound and upper-bound scenarios. Shaded colors indicate the scenarios (lower bound in teal, and upper bound in orange), as well as the level of significance of each scenarios (significant for $p < 5\%$). The black lines make the projected range explicit, based on the significant values. Statistically significant differences between recent past and future periods are calculated using Mann-Whitney U statistical test ($\alpha = 0.05$).

6.3.2.2. Projected changes in *Phragmites* and *Typha* expansion

To compare changes in *Typha* and *Phragmites* expansion between the recent past and future periods, the relative change in carrying capacity was estimated under each climate change scenario. Carrying capacity is defined as the maximum abundance of a species that a given habitat can support based on environmental conditions. The carrying capacity is obtained by fitting a logistic growth equation (Verhulst, 1838) to PGM simulations, which determines population size at time (t) as a function of maximum growth rate (r_{max}) and carrying capacity (K). Carrying capacity is expected to increase when environmental conditions (i.e. water depths distribution and water level variations) are more favorable to a species or to decrease when the species face competition. Species competition was integrated into the modelling approach by modelling the invasion of *Phragmites* into *Typha* stands. K was used to compare the maximum invasion extent of both species between climate change scenarios. To compare between sites, K was standardized by dividing it by the total wetland area simulated with the wetland succession model. Figure 202 presents standardized K values for each site for both invasive species and climate change scenarios and for the range of possible future invasion extents.

A different trend between the invasions of the two exotic species is observed between Lake Ontario and the other water bodies. In Lake Ontario, the upper-bound scenario supports *Phragmites* invasion, whereas the *Phragmites* invasion is limited by the dense *Typha* cover with the lower-bound scenario. It is only with the significant water level rises associated with the upper-bound scenario reducing the *Typha* coverage that *Phragmites* is able to invade and expand during the following years. On the other hand, in Lake Erie and Lake St. Clair, the interannual water level fluctuations are more frequent, and the *Phragmites* started to establish in the 1990s. With the lower-bound scenario, the water depth is more suitable for *Phragmites*, and the more frequent water level fluctuations promote the *Phragmites* invasion and limit the *Typha* invasion. With the upper-bound scenario, the wetlands migrate towards the higher elevations and the *Phragmites* establish in those disturbed areas, whereas the establishment and expansion are limited in the lower elevation areas.

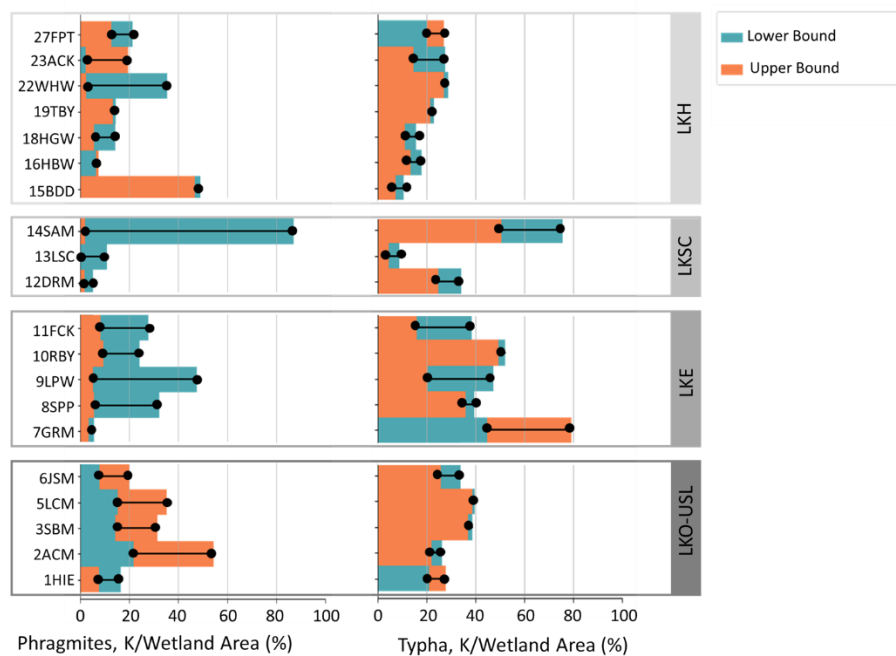


Figure 202: Range of Carrying capacity/Wetland area ratio projected by the lower and upper bound scenarios for *Phragmites* (left) and *Typha* (right) population growth models. Shaded colors indicate the scenarios (lower bound in teal, and upper bound in orange). The black lines indicate the range of projected change (difference between both scenarios).

6.3.2.2.1. Upper St. Lawrence River and Lake Ontario

In Hill Island East (1HIE), the lower-bound scenario indicates a *Phragmites* carrying capacity two times higher than what the upper-bound scenario suggests (Figure 204 left). An opposite trend is seen for *Typha* (Figure 204, right). According to modelling results, under the lower-bound

scenario, the conditions are not ideal for *Typha* to establish early in the 1980s in this site, allowing an easier *Phragmites* establishment at the beginning of the recent past time-series. However, *Typha* increases rapidly after that, covering more than 12.5 ha at the beginning of the 2000s and maintaining this area through the simulated future time-series. In 2000, *Phragmites* covers around 2.5 ha and continues increasing until 2100 when it covers around 10.0 ha (Figure 204). Under the upper-bound scenario, *Typha* establish and expand even more quickly than under the lower-bound scenario and more than *Phragmites*. Facing climate change, the wetlands of 1HIE should be dominated by *Typha* and may lose biodiversity in several wetland classes.

For all Lake Ontario sites, the upper-bound scenario predicts almost twice as much *Phragmites* as the lower-bound scenario. The major increase in water level in 2035 under the upper-bound scenario (Figure 203) causes a *Typha* die-off and allows *Phragmites* germination and expansion in the following years (Figure 205 through Figure 208). The *Phragmites* rate of expansion prior to the 2040s is slower under the upper-bound scenario because of less frequent water-level variations (Figure 203) and because the *Typha* is well established. It is only when the *Typha* die-off happens near 2040 that the *Phragmites* starts to germinate and expand. Under the lower-bound scenario, there are more frequent water-level drawdowns in the simulated future period (2070-2099), allowing the *Phragmites* to germinate; however, the pre-existent *Typha* cover limits *Phragmites* expansion.

The current Lake Ontario water-level regulation system facilitates the establishment of *Typha* which might have prevented the establishment and expansion of *Phragmites* in the simulations since both taxa share the same ecological niche (Amsberry *et al.*, 2000; Keddy & Reznicek, 1986; Shay *et al.*, 1999; D. A. Wilcox *et al.*, 2008). It is worth noting that for the reference period, the modelling results are slightly different from what is observed. The model tends to underestimate the *Typha* cover in Lake Ontario and leaves more room the *Phragmites* establishment and expansion, which makes it likely that the CWRM will overestimate *Phragmites* in the future period. Still, facing climate change, wetlands of Lake Ontario are at high risk to be dominated by *Typha* and with a prolonged water level increase and greater interannual water level variability, the models suggest that *Phragmites* could invade the Lake Ontario wetlands.

The main conclusions for the Upper St. Lawrence and Lake Ontario sites are:

- Under a climate change scenario that brings no significant change in mean lake levels (Table 23), such as the lower-bound scenario, and considering the current regulation plan for future outflow management (i.e. Plan 2014), *Typha* is likely to remain dominant in the

eastern Great Lakes, and the expansion of *Phragmites* should be less important than what is predicted by the models.

- Conversely, if lake levels are projected to rise above historical values, as projected by the upper-bound scenario (~24 cm increase by the end of the century), most wetland sites are likely to be flooded. The rules underlying Plan 2014 are not designed to handle more water than observed in the past, which results in a significant rise in model-predicted Lake Ontario levels. Under such conditions, emergent plants, including *Typha*, will likely die, facilitating the establishment and expansion of *Phragmites* in the upland portion of the wetlands.

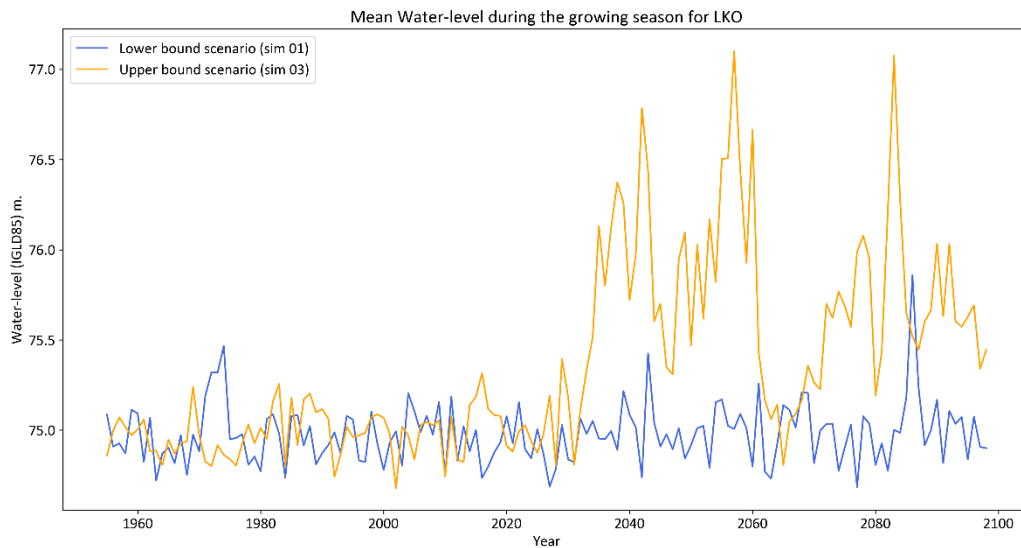


Figure 203: Projected water levels during the growing season for the lower and upper bound climate change scenarios in Lake Ontario (LKO).

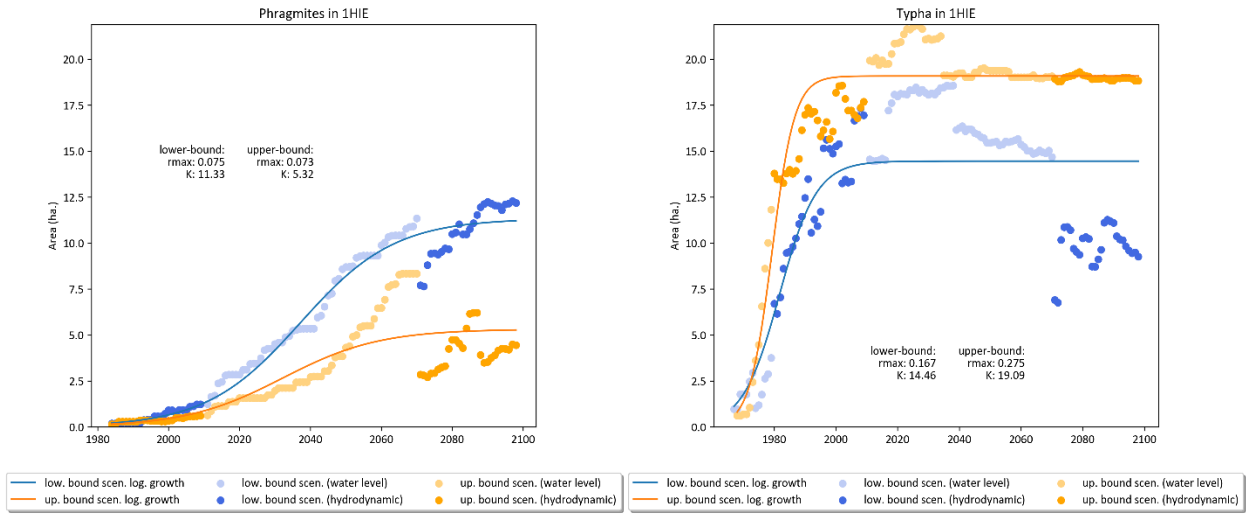


Figure 204: Phragmites (left) and Typha (right) evolution and logistic growth model in Hill Island East (1HIE) for lower (blue) and upper (orange) bound simulations.

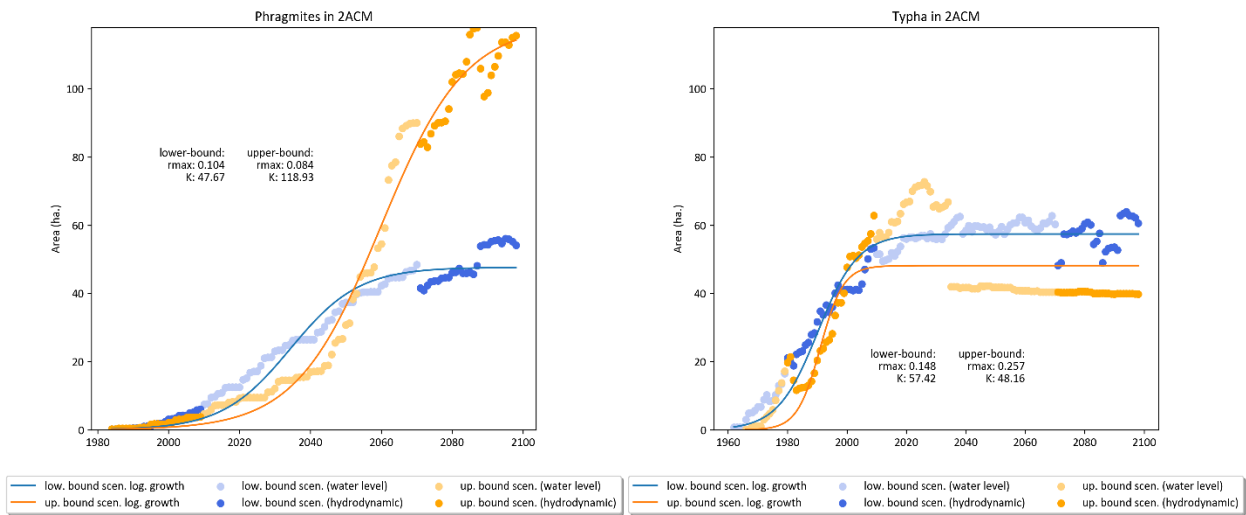


Figure 205: Phragmites (left) and Typha (right) evolution and logistic growth model in Airport Creek Marsh (2ACM) for lower (blue) and upper (orange) bound simulations.

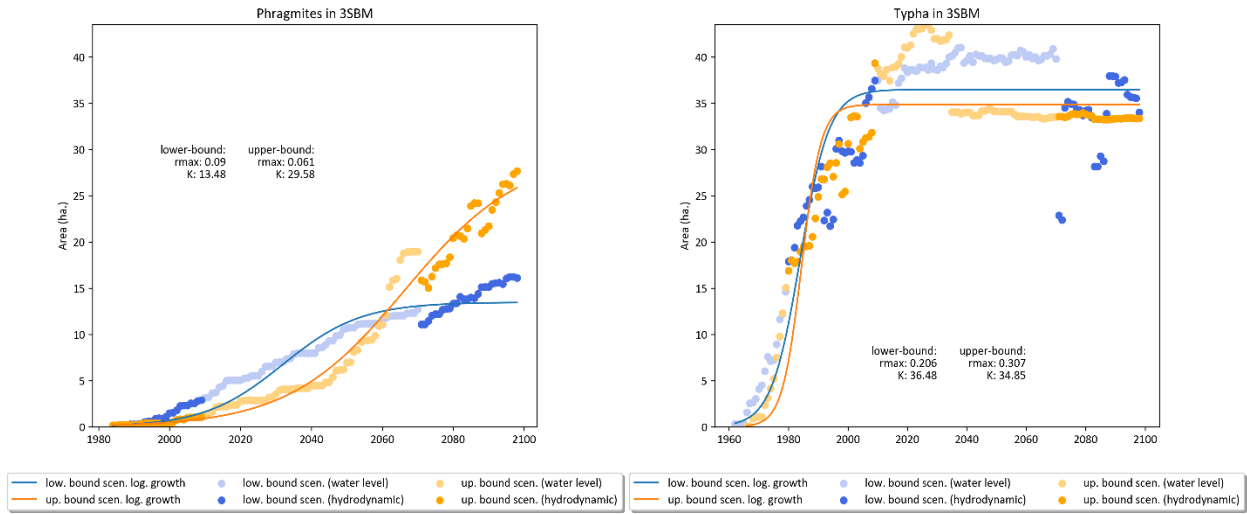


Figure 206: *Phragmites* (left) and *Typha* (right) evolution and logistic growth model in South Bay Marsh (3SBM) for lower (blue) and upper (orange) bound simulations.

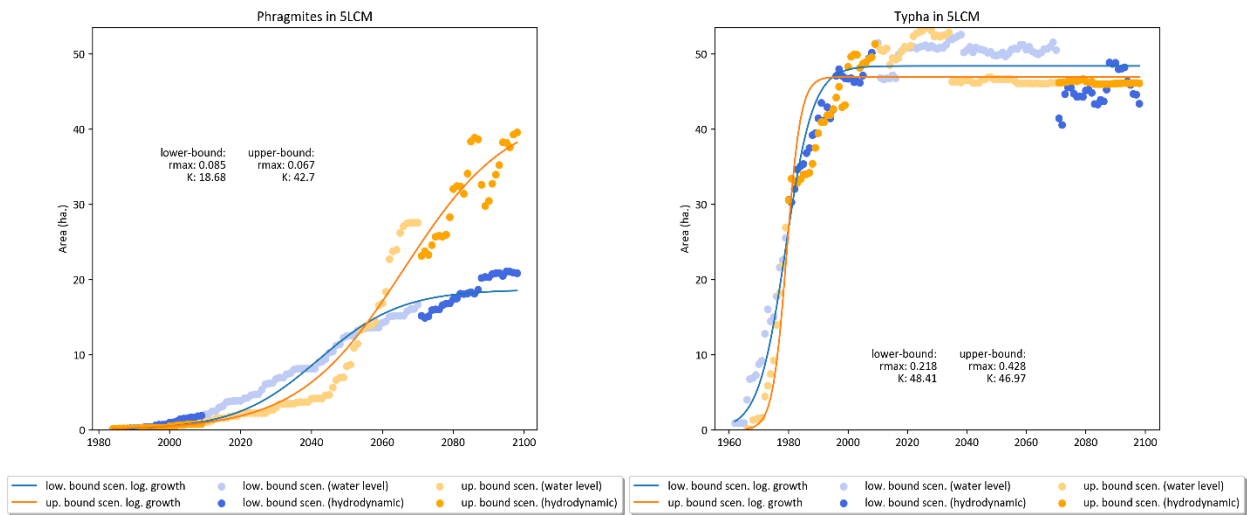


Figure 207: *Phragmites* (left) and *Typha* (right) evolution and logistic growth model in Lyndee Creek Marsh (5LCM) for lower (blue) and upper (orange) bound simulations.

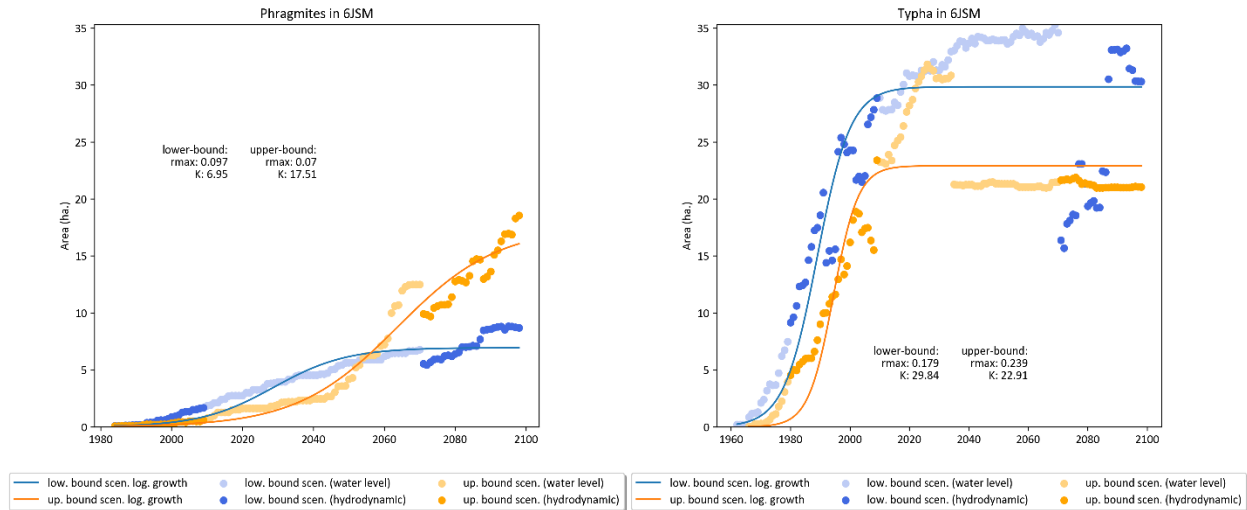


Figure 208: *Phragmites* (left) and *Typha* (right) evolution and logistic growth model in Jordan Station (6JSM) for lower (blue) and upper (orange) bound simulations.

6.3.2.2.2 Lake Erie

Under the lower-bound scenario, the median water level is decreasing (-13 cm) and the interannual variability is increasing between 2010 and 2099, causing many years of water level drawdowns that promote the *Phragmites* expansion (Figure 209). With the lower-bound scenario, we expect the *Phragmites* invasion to be much more important than with the upper-bound scenario across all Lake Erie sites, except for 7GRM (Figure 210). The water depth with the lower-bound scenario is generally suitable for *Phragmites*, but also for *Typha*. Between 2018 and 2038, there is a major expansion of *Typha* in 8SPP, 9LPW and 11FCK due to relatively stable interannual water levels. However, a major *Typha* die-off is caused by an increase in water levels in 2039 (Figure 209) and coincides with an important expansion of *Phragmites* from 2040 across most Lake Erie sites (Figure 210 to Figure 214).

With the upper-bound scenario, rising water levels moderate the *Phragmites* invasion. The water depth becomes unsuitable for *Phragmites* germination and for vegetative propagation. Some sites such as 8SPP and 11FCK become completely flooded and wetlands and *Phragmites* are unable to migrate upland because of land use limitations. In 9LPW, the topography limits the migration of wetland and of invasive species. In 10RBY, the wetlands and invasive species migrates upland. *Typha* remains the dominant species, but major *Phragmites* stands are present (Figure 215). Since *Phragmites* can tolerate high water levels, this scenario predicts *Phragmites* stands establishing in deeper water when the conditions were suitable. For this scenario, water levels variations are important, and high water levels do not favor *Typha* in most sites except Grand

River Mouth (7GRM). In this site, the topography favors the establishment of *Typha*, which can establish in higher elevations and survive through the water level fluctuations.

The main conclusions for Lake Erie are:

- Projected water level changes in Lake Erie range from -14 to 45 cm, with little or no change in interannual variability (relative to recent past time-series) in the last 30-year of the century. However, the future water-levels time-series from 2070 to 2099 shows some important reduction in water levels, which indicates a larger year-to-year variability than typically observed during the reference period (1980–2009). These large long-term variations will likely favor the establishment of *Phragmites* at the expense of *Typha* by the end of the century, the latter being particularly sensitive to changes in mean interannual water levels.
- *Typha* population expansion is likely to be slowed down by the end of the century by either (1) high interannual variability in mean lake level (lower bound scenario), which limits vegetation propagation, or (2) high lake levels (upper-bound scenario), which greatly reduce suitable habitat.
- Under sustained lake level increase, *Phragmites* establishment and expansion in low (deep) wetland areas is likely to be limited due to unsuitable water depth. *Phragmites* will preferentially move inland, which should result in invasion of high wetland areas.
- Overall, the models predict more *Typha* than *Phragmites* in most sites of Lake Erie. However, a decrease in *Typha* distribution is projected by the lower-bound scenario around 2080, a decrease likely due to the expansion of *Phragmites* that tends to replace the former.

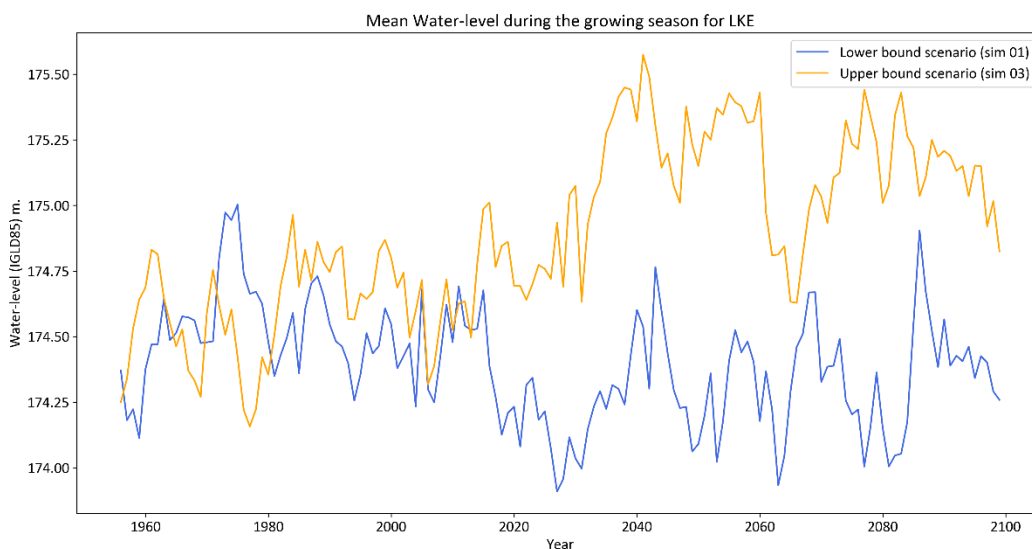


Figure 209: Projected water levels during the growing season for the lower and upper bound climate change scenarios in Lake Erie (LKE).

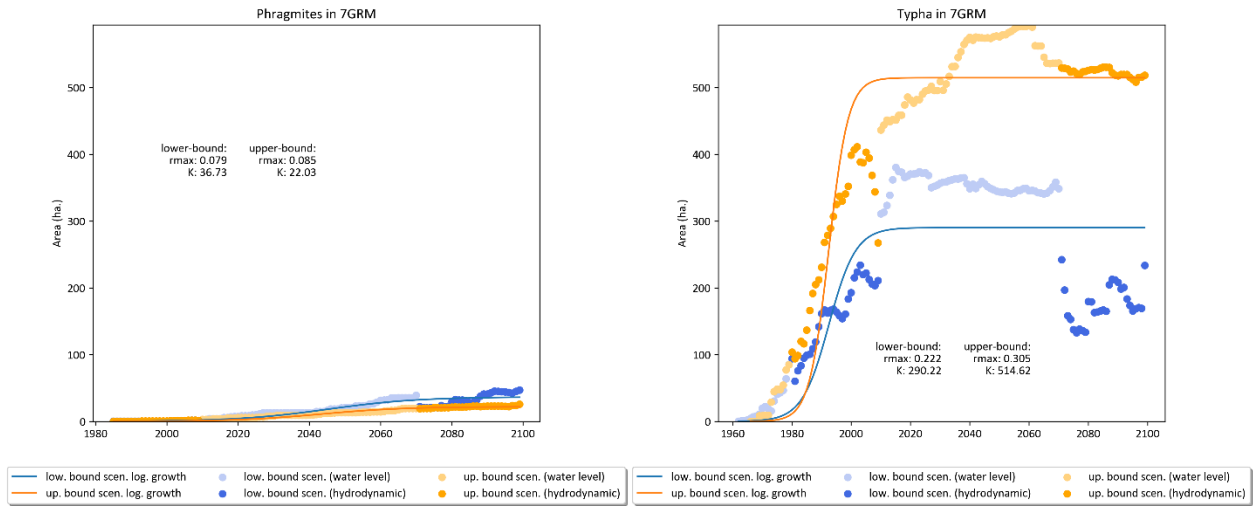


Figure 210: Phragmites (left) and Typha (right) evolution and logistic growth model in Grand River Mouth (7GRM) for lower (blue) and upper (orange) bound simulations.

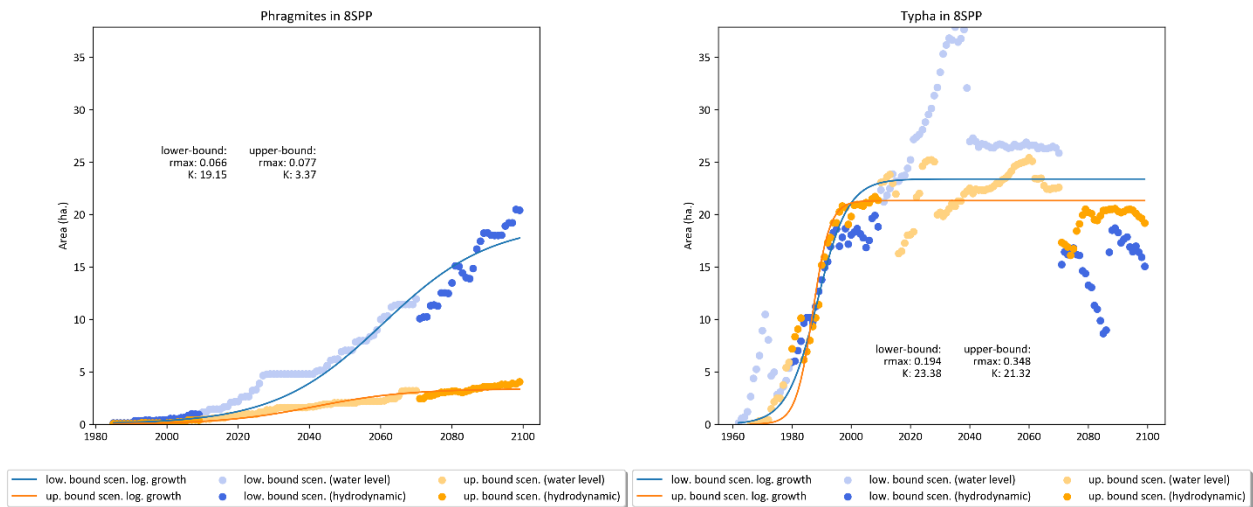


Figure 211: Phragmites (left) and Typha (right) evolution and logistic growth model in Selkirk Provincial Park (8SPP) for lower (blue) and upper (orange) bound simulations.

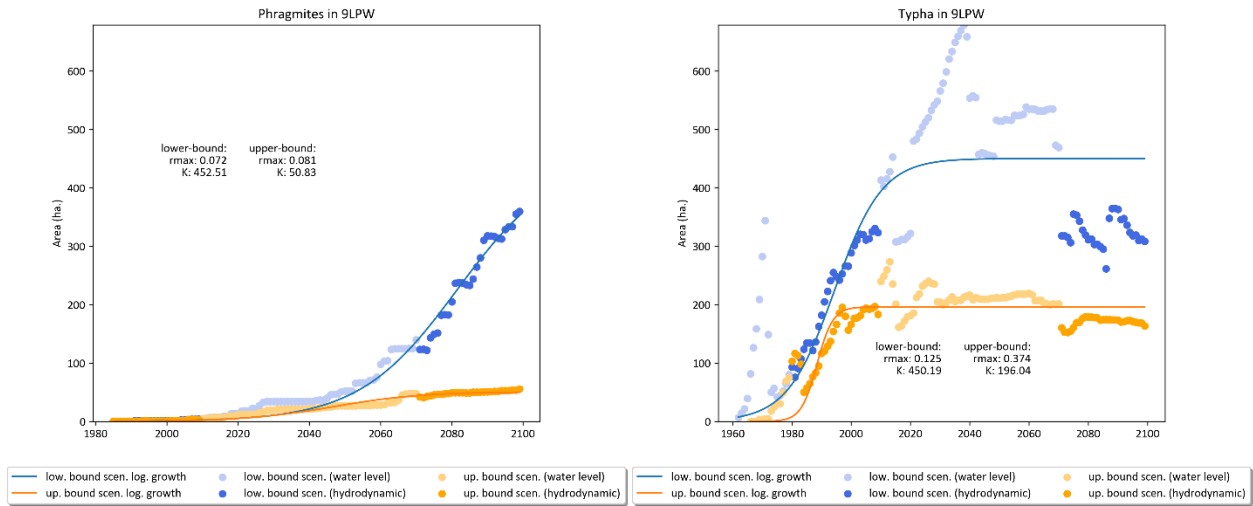


Figure 212: *Phragmites* (left) and *Typha* (right) evolution and logistic growth model in Long Point (9LPW) for lower (blue) and upper (orange) bound simulations.

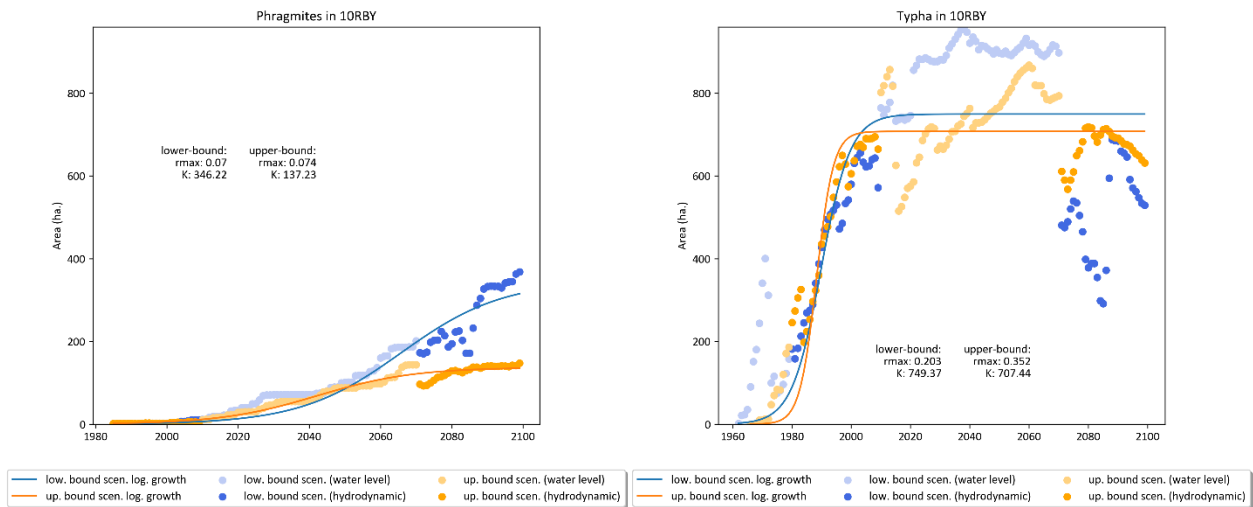


Figure 213: *Phragmites* (left) and *Typha* (right) evolution and logistic growth model Rondeau Bay (10RBY) for lower (blue) and upper (orange) bound simulations.

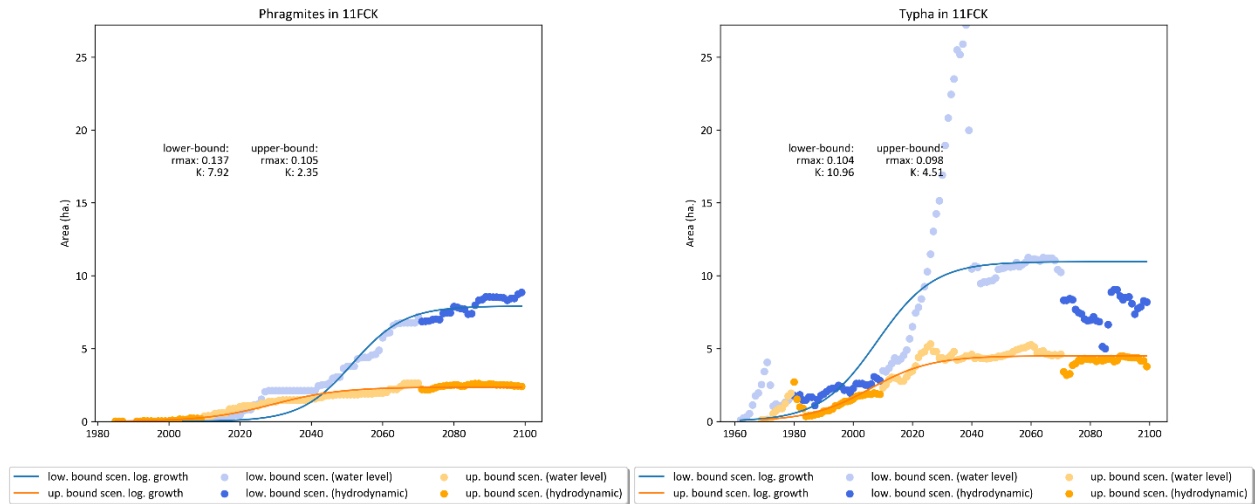


Figure 214: *Phragmites* (left) and *Typha* (right) evolution and logistic growth model in Fox Creek (11FCK) for lower (blue) and upper (orange) bound simulations.

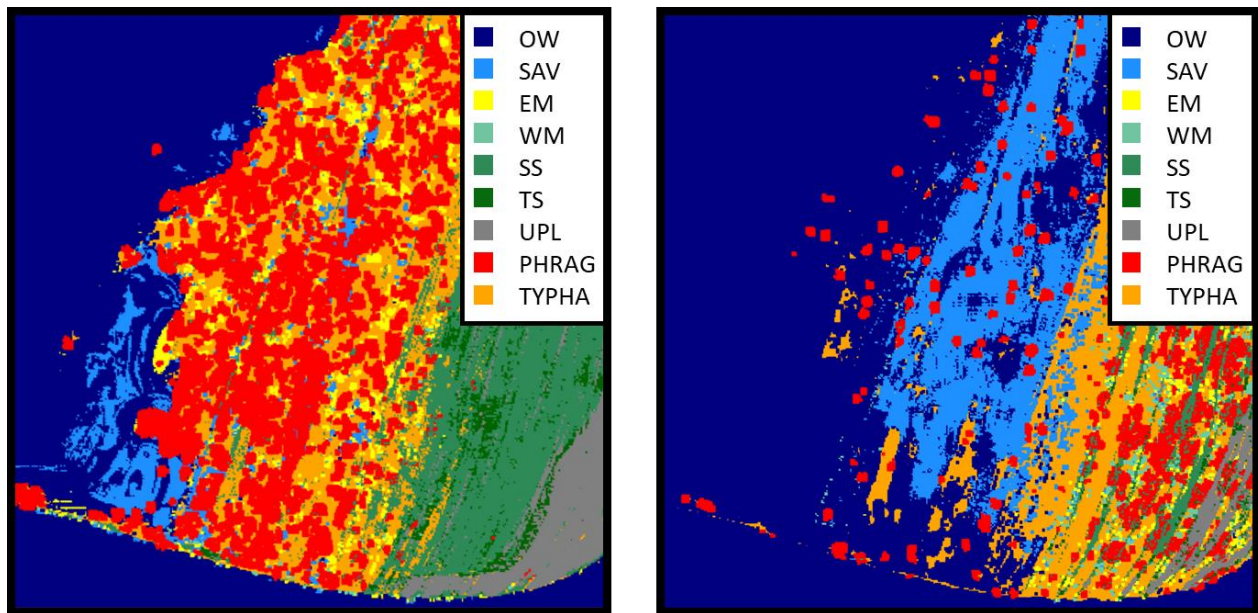


Figure 215: Invasive species (*Phragmites*: red, *Typha*: orange) spatial distribution at Rondeau Bay (10RBY) in 2099 under the lower (left) and upper (right) bound scenario.

6.3.2.2.3. Huron-Erie corridor

For both scenarios, water levels in the Lake St. Clair present a similar pattern to what is predicted by the model for Lake Erie (Figure 216). With the lower-bound scenario, *Phragmites* and *Typha* have higher carrying capacity since water depth is more suitable for those species than with the upper-bound scenario (Figure 217 to Figure 219). For 12DRM, the models predict more *Typha*

than *Phragmites* in the future period under both scenarios. The site is mostly dominated by *Typha* but *Phragmites* stands are slowly advancing (Figure 220). For 13LSC and 14SAM, there is a similar area of *Phragmites* and *Typha*. In both sites, *Typha* has reached its carrying capacity and starts declining because the *Phragmites* are expanding over *Typha* habitat. With the lower-bound scenario, around 2040 the rise in water levels causes a *Typha* die-off followed by a water level drawdown causing the *Phragmites* to thrive in the following years in all Huron-Erie corridor sites.

Under the upper-bound scenario, for 13LSC and 14SAM, the presence of dykes limits the migration of wetlands to higher elevations (Figure 221). *Typha* can establish in the higher elevation areas but occupy most of the niche and *Phragmites* hardly establishes because of the earlier *Typha* establishment and unsuitable water depths at lower elevations. For 12DRM, *Typha* establishes higher and small *Phragmites* stands establish among *Typha* and slowly advance.

The main Lake St. Clair conclusions are:

- The *Typha* expansion is likely to increase until the beginning of the 2020s and 2030s in wetlands of the Huron-Erie Corridor, after which projected distributions appear stable in all sites for both climate scenarios. Conversely, the projected *Phragmites* expansion is likely to continue beyond 2099, since growth curves obtained from the upper and lower-bound scenarios (Figure 219 to Figure 221) do not reach their stable equilibrium (i.e. carrying capacity).
- Large increases in lake levels (upper-bound scenario) promote conditions unsuitable for *Phragmites* establishment and expansion in the Huron-Erie Corridor.

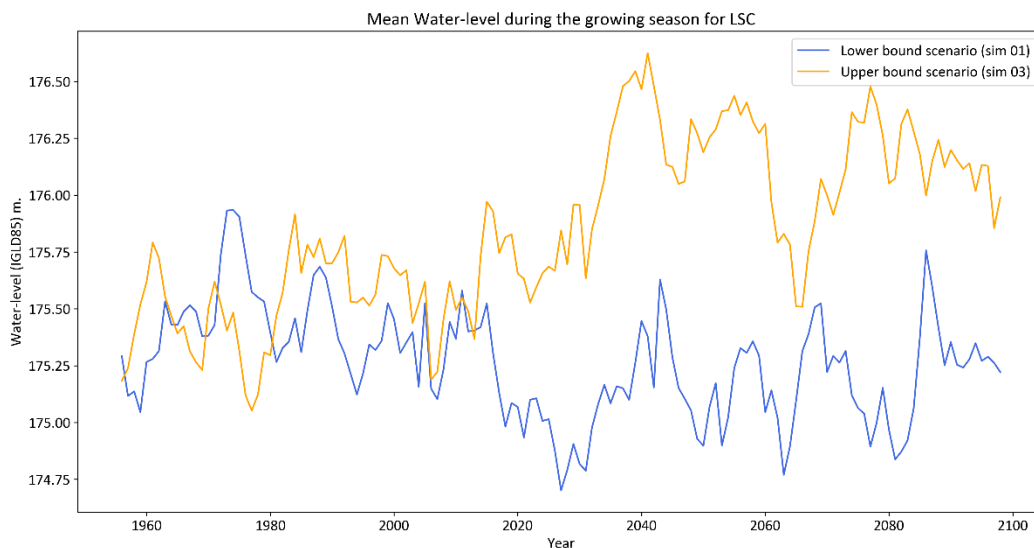


Figure 216: Projected water levels during the growing season for the lower and upper bound climate change scenarios in Lake St. Clair(LSC).

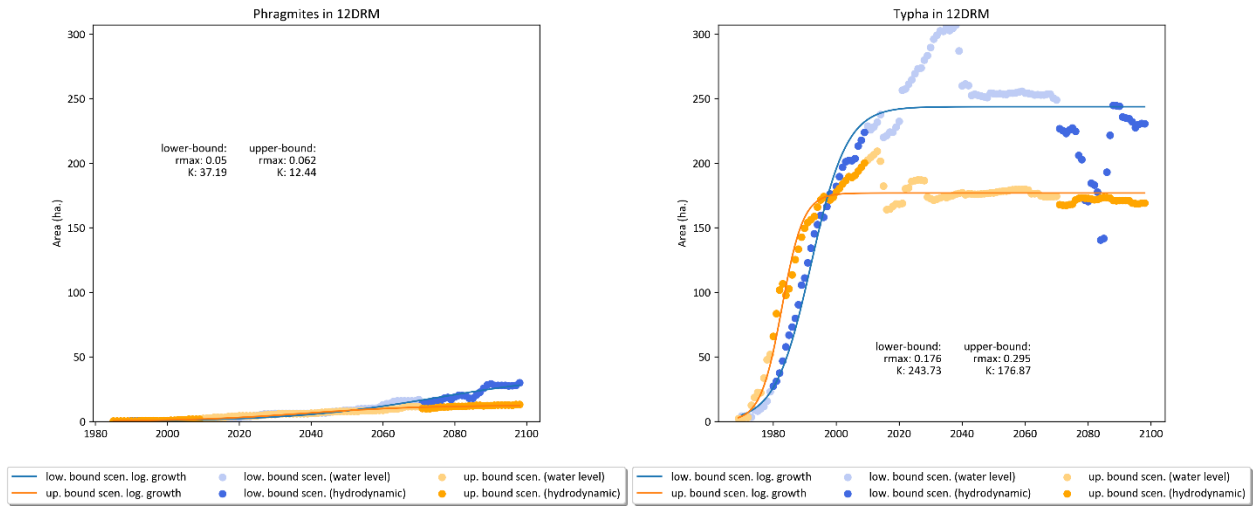


Figure 217: Phragmites (left) and Typha (right) evolution and logistic growth model in Detroit River Marsh (12DRM) for lower (blue) and upper (orange) bound simulations.

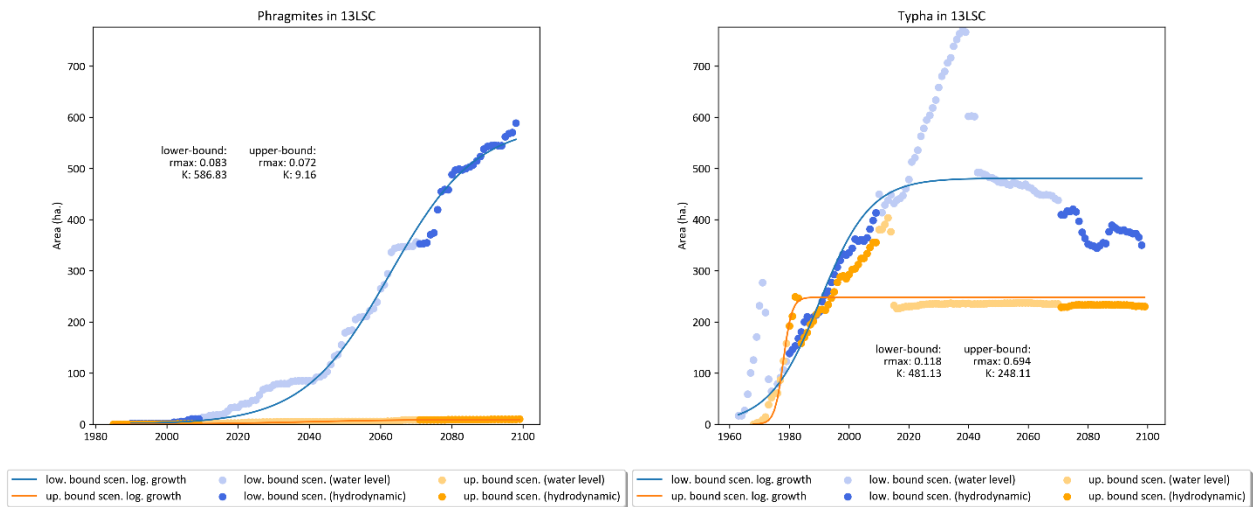


Figure 218: Phragmites (left) and Typha (right) evolution and logistic growth model in Lake St. Clair(13LSC) for lower (blue) and upper (orange) bound simulations.

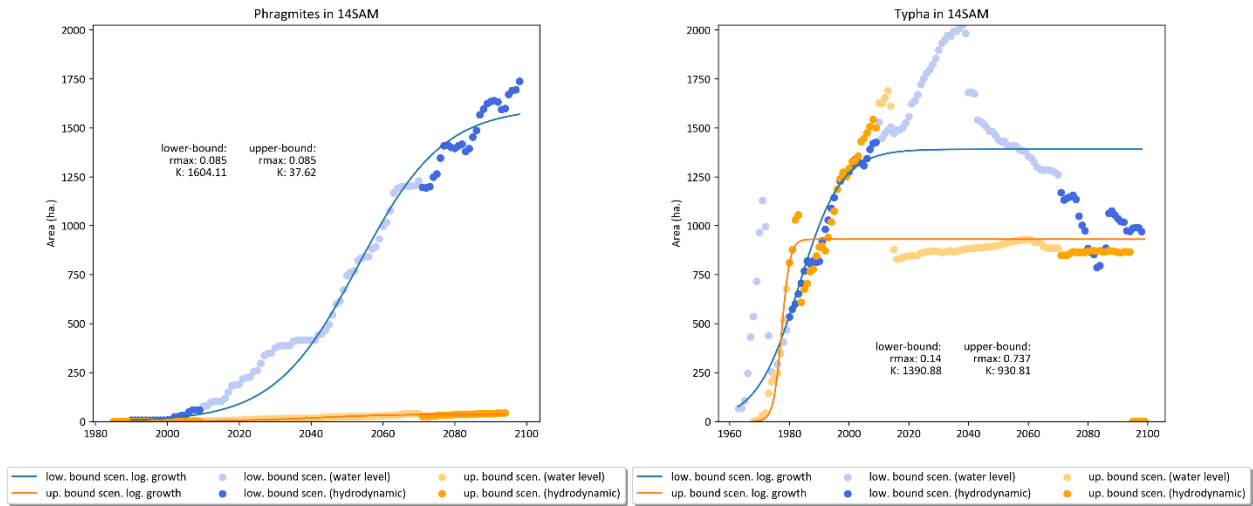


Figure 219: Phragmites (left) and Typha (right) evolution and logistic growth model in Johnston Bay (14SAM) for lower (blue) and upper (orange) bound simulations.

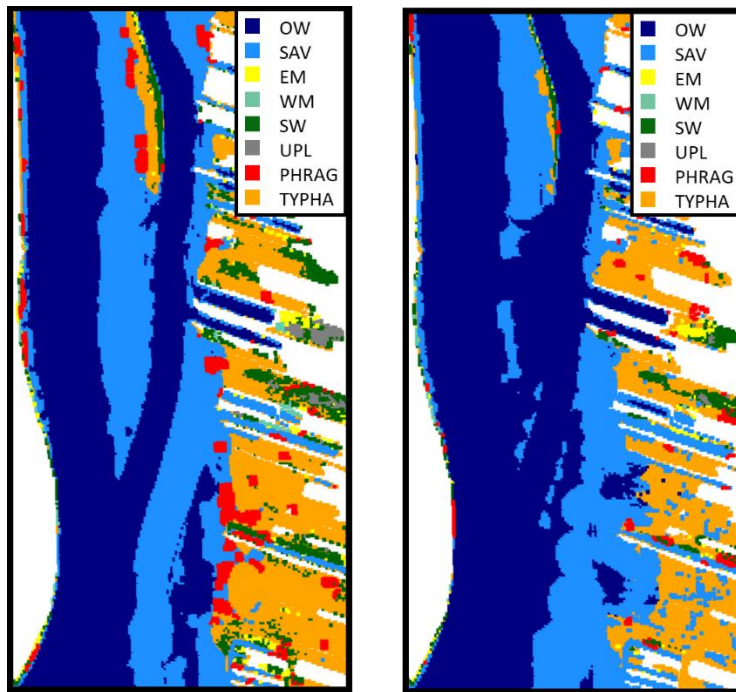


Figure 220: Invasive species (Phragmites: red, Typha: orange) spatial distribution at Detroit River Marsh (12DRM) in 2098 under the lower (left) and upper (right) bound scenario.

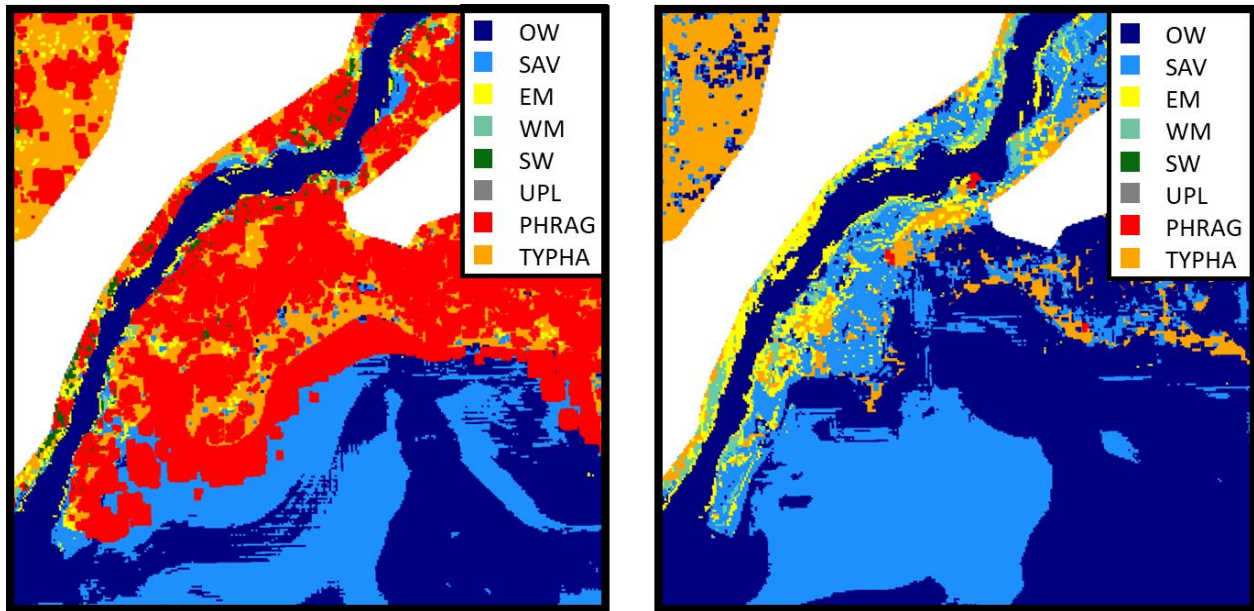


Figure 221: Invasive species (*Phragmites*: red, *Typha*: orange) spatial distribution at Johnston Bay (14SAM) in 2098 under the lower (left) and upper (right) bound scenario.

6.3.2.2.4. Lake Huron

Simulated water levels in Lake Huron present a similar trend to water levels in Lake Erie and Lake St. Clair (Figure 222). For Lake Huron sites, *Typha* is predicted to be more abundant than *Phragmites* in most sites, except for 15BDD (Figure 223 to Figure 229). It is hard to have a clear basin-wide conclusion for *Phragmites* invasion, as the results suggest varying responses to *Phragmites* invasion among sites. Site 15BDD is by far the most invaded site (Figure 223), since the invasion started early (1990s; Janice Gilbert, personal communication, 2021) and both climate change scenarios do not predict a better future. The lower-bound scenario predicts a more important *Phragmites* invasion in 18HGW, 19TBY, 22WHW and 27FPT sites. In 16HBW, *Phragmites* invasion is similar under both scenarios (Figure 224), while in 23ACK the invasion is more important under the upper-bound scenario (Figure 228).

For *Typha*, we see a major decline for both scenarios in 15BDD caused by the aggressive expansion of *Phragmites* (Figure 223). *Typha* invasion is similar in 16HBW (Figure 224), 18HGW (Figure 225), 19TBY (Figure 226) and 22WHW (Figure 227), under both scenario. For 23ACK, lower-bound scenario favors *Typha* expansion, whereas upper-bound scenario is more favorable for *Typha* expansion in 27FPT (Figure 229).

The main conclusions for Lake Huron are:

- *Typha* will likely be more abundant than *Phragmites* in all Lake Huron sites, except in Baie du Dorée. This site had an early *Phragmites* invasion, beginning in 1990s, and is therefore highly vulnerable to future expansion.
- Projected lake levels patterns determine the invasive species spatial distribution. They will establish in lower elevations with a decrease in water levels (lower-bound scenario) or, inversely, colonize higher ground if water level rises occur. Nevertheless, the greater the increase in mean water level, the more constrained the total expansion of *Phragmites* is in most sites due to the loss of habitat with suitable water depth.
- Since the simulations for Lake Huron were not validated, as the date when the invasion started in most sites is unknown for *Phragmites* and *Typha*, the results for this lake should be treated as hypothetical.

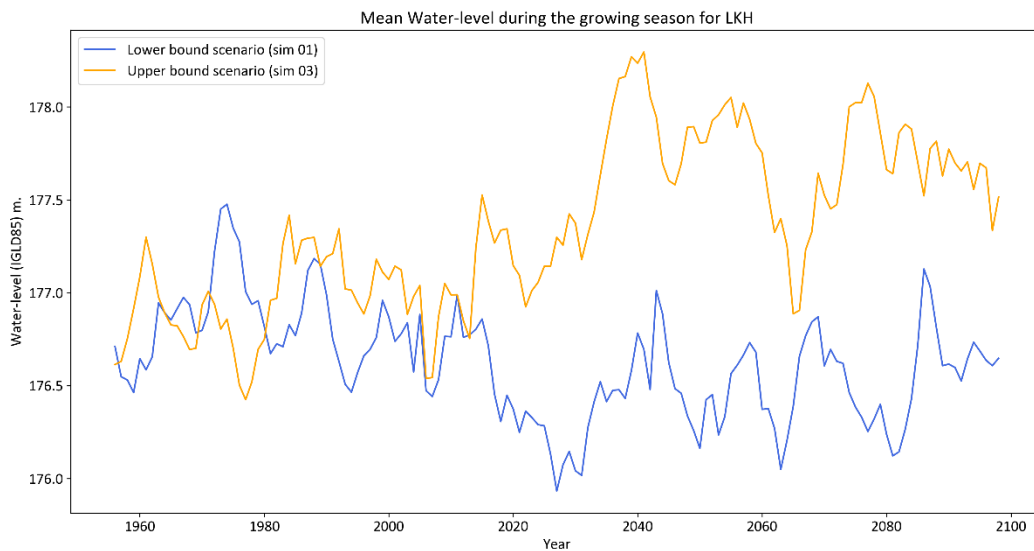


Figure 222: Projected water levels during the growing season for the lower and upper bound climate change scenarios in Lake Huron (LKH).

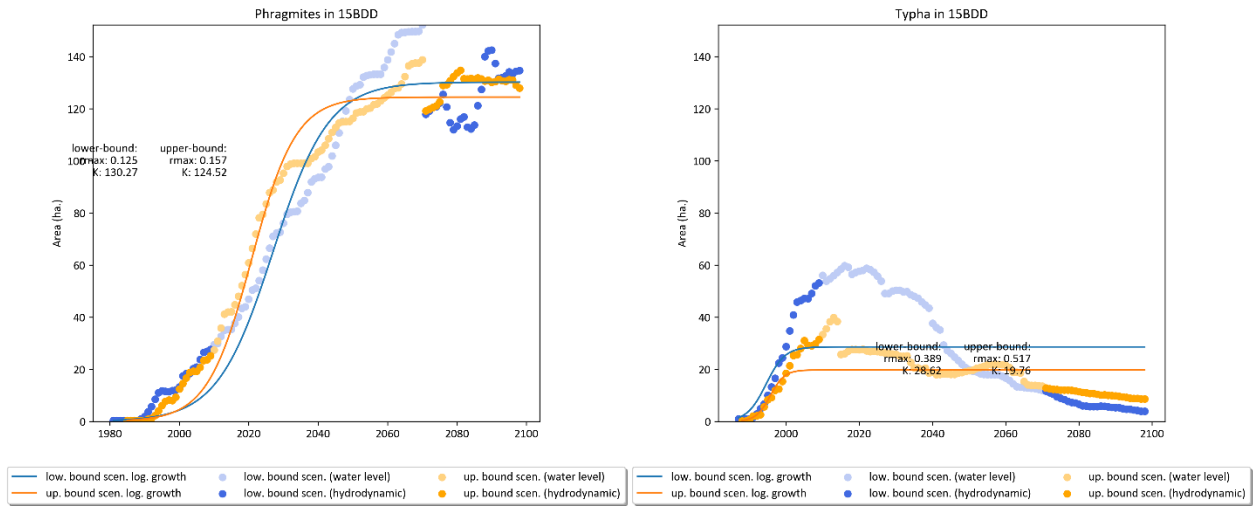


Figure 223: *Phragmites* (left) and *Typha* (right) evolution and logistic growth model in Baie du Doré (15BDD) for lower (blue) and upper (orange) bound simulations.

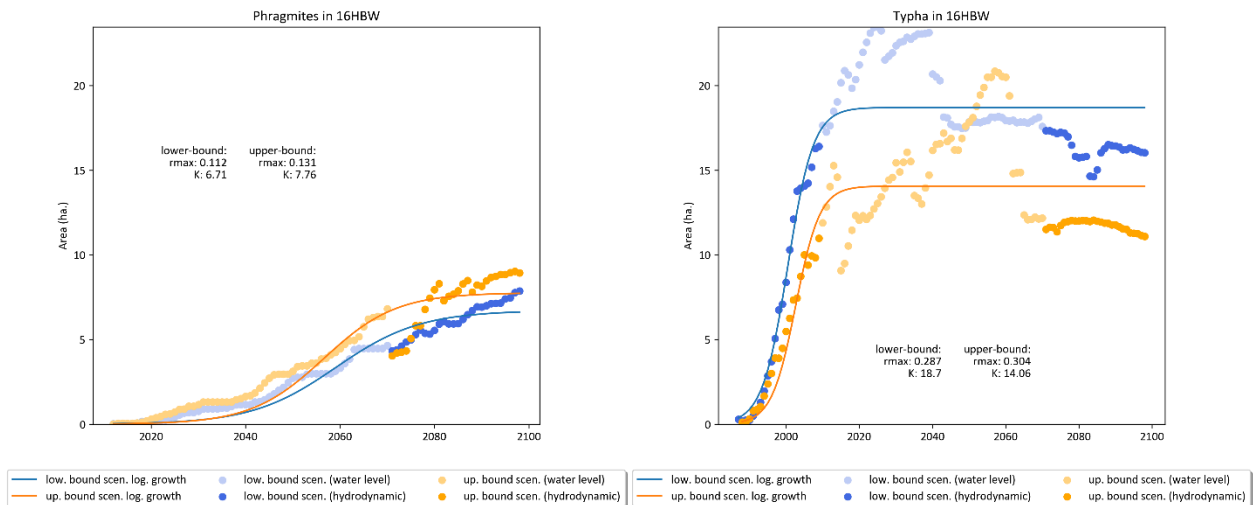


Figure 224: *Phragmites* (left) and *Typha* (right) evolution and logistic growth model in Hay Bay (16HBW) for lower (blue) and upper (orange) bound simulations.

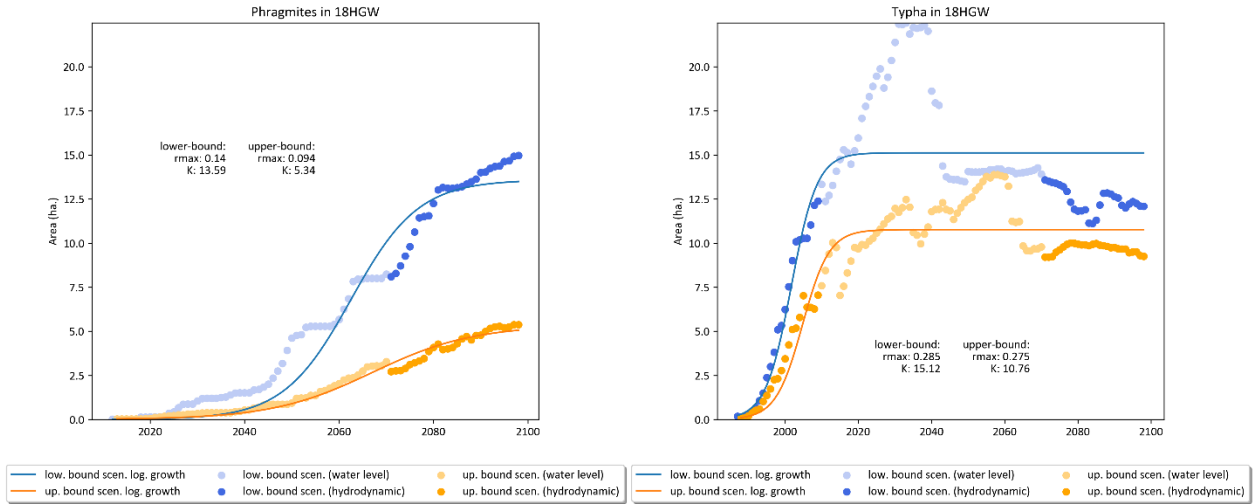


Figure 225: Phragmites (left) and Typha (right) evolution and logistic growth model in Hog Bay (18HGW) for lower (blue) and upper (orange) bound simulations.

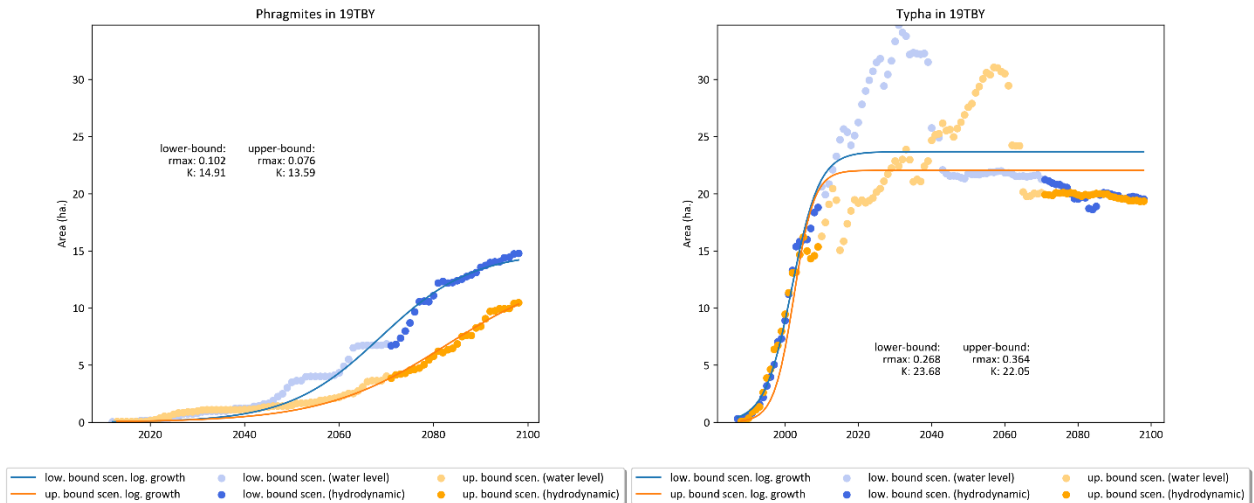


Figure 226: Phragmites (left) and Typha (right) evolution and logistic growth model in Treasure Bay (19TBY) for lower (blue) and upper (orange) bound simulations.

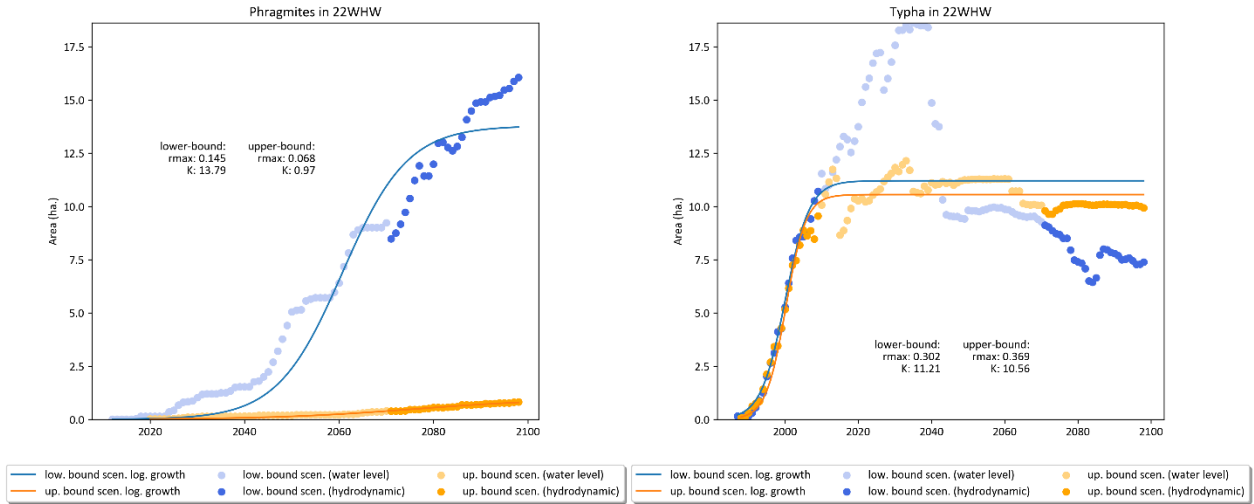


Figure 227: Phragmites (left) and Typha (right) evolution and logistic growth model in Whiskey Harbor (22WHW) for lower (blue) and upper (orange) bound simulations.

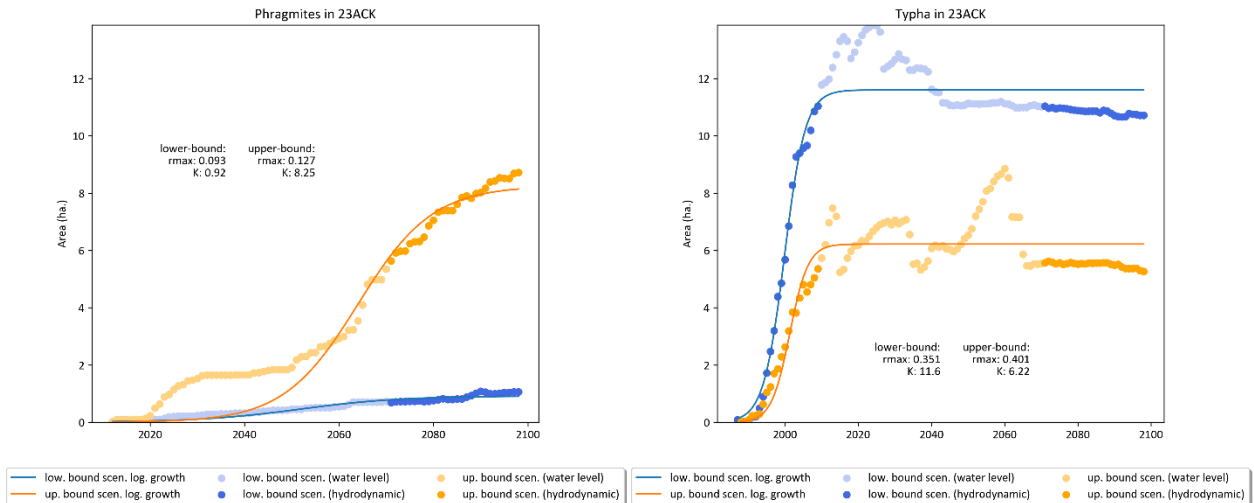


Figure 228: Phragmites (left) and Typha (right) evolution and logistic growth model in Anderson Creek (23ACK) for lower (blue) and upper (orange) bound simulations.

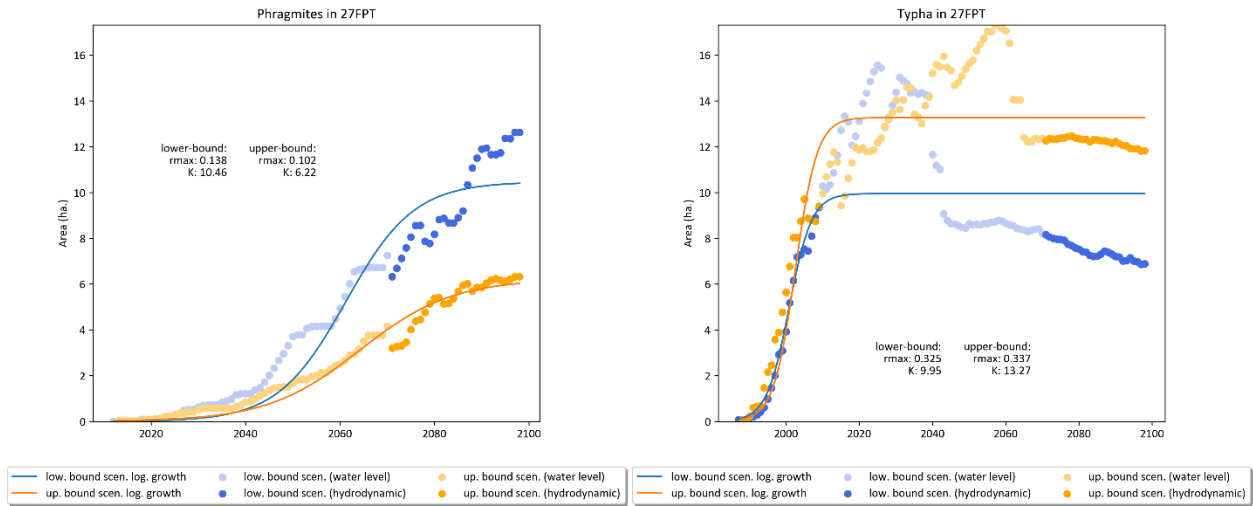


Figure 229: *Phragmites* (left) and *Typha* (right) evolution and logistic growth model in Frances Point (27FPT) for lower (blue) and upper (orange) bound simulations.

7. CONCLUSION

Great Lakes coastal wetlands are known to be highly dynamic ecosystems, rapidly responding and adapting to their physical environment. Although several climatic factors influence their structure and distribution, hydrologic conditions are recognized as the primary driver of changes that result in a marked shift in habitat location, extent, productivity and diversity. These conditions indirectly incorporate the effect of precipitation, evaporation, winds, and topography, which are essential components that shape the structure and composition of wetland plant communities. Any future changes in water level fluctuations will induce a change in the nominal conditions of these vulnerable ecosystems, which may be critical if the physical environment undergoes changes beyond what was observed in the past. As such, projected climate change in the Great Lakes basin may alter the annual and interannual variability of water levels in the various water bodies and the coastal wetlands that thrive there. Given the high vulnerability of these environments, global warming is a concern and should be studied to determine the potential impact on these habitats, as well as the measures that need to be taken to improve their resilience.

The Great Lakes Protection Initiative Project was created to identify and quantify the impact of climate change on coastal wetlands, and to assess their vulnerability. ECCC-NHS Hydrodynamic and Ecohydraulic Section has worked intensively to define the degree of climate stress to which coastal wetlands are exposed, and to examine to which extent wetland classes are going to be impacted by projected changes. These aspects, which define the exposure and sensitivity components of the vulnerability assessment, were evaluated through the use of a two-dimensional, integrated habitat-modelling platform that predicts the response of wetland classes to water-level changes: the Coastal Wetland Response Model (CWRM). To project future lake conditions, two climate scenarios were used, which are downscaled CMIP5 Atmosphere-Ocean General Circulation Model forced by a scenario of moderate anthropogenic CO₂ emissions (i.e. Representative Concentration Pathway 4.5). These two scenarios were selected to delineate the range of possible futures. This range covers, in the CMIP5 ensemble, the mid-range of projected changes in precipitation for the Midwest and Great Lakes region (i.e. positive change between ~9% and 16%), and the lower range of projected changes in surface air temperature (i.e. positive change between ~3.5°C to 6.1°C).

To model Great Lakes coastal wetland classes and their hydrological gradient from deep aquatic habitat to dry terrestrial areas, two main questions were answered using the CWRM:

1. What are the time scales and magnitude of natural disturbances within the wetland, which take the form of water depth variations and wave exposure?
2. How do plants (native and invasive) move along the hydrological gradient in response to environmental disturbances, with migration of wetland classes that follows their inherent dispersal capabilities?

The physical processes and conditions that modulate Great Lakes nearshore dynamics were modelled for the recent past (1980 to 2009) and future (2070 to 2099) under projected climatic conditions, and wetland response to key physical factors was evaluated for the selected range of possible climates.

7.1. Summary of methods

7.1.1. Physical modelling

Two different approaches were developed to model the water level and wave dynamics of the Great Lakes. The first one uses unsteady simulations and thus takes into account all the physical processes available, modelling the seiches and setups, which was applied for the shallower lakes of the system (Lakes Erie and St. Clair) and connecting channels (Huron-Erie corridor and Upper St. Lawrence River). The second approach is scenario-based and used steady-state simulations to model the water level and other physical variables in the deeper lakes (Lakes Ontario and Huron), modelling the wind setups. This approach, which does not allow the reproduction of transient processes like seiches, was used due to time constraints and significant difficulties associated with the first approach for bodies of water with large 3D effects (e.g. vertical stratification, barocline circulation, etc.). In the end, both approaches have been able to accurately model annual and sub-seasonal fluctuations in historical water levels, with an uncertainty ranging from 3 cm to 5 cm, and good temporal resolution (3-hour time step). The simulated data were then used to generate the variables used by CWRM to describe the disturbances that modulate shoreline dynamics in the wetland environment by using a wavelet analysis. The waves were also modelled in Lakes Erie and Ontario, but not in Lakes Huron and St. Clair due to time and computational resource constraints, leading to a slight degradation in wetland modelling performance in these lakes.

7.1.2. Digital Elevation Model

A collection of LIDAR point clouds and various bathymetric datasets was gathered to produce seamless DEMs that cover the land-water interface of all study sites. Since LIDAR tends to

overestimate elevation values in densely vegetated areas such as wetlands, a post-processing correction method, based on a statistical model using ground truth points and multispectral imagery, was applied to the terrestrial portion of all DEMs. This method uses a statistical model which, via empirical validation points and multispectral images, allows the correction of measurement errors. Then, various bathymetric data were combined, adjusted and interpolated to cover the lacustrine portion of each site which is impossible to estimate by conventional remote sensing. The final DEMs were obtained by merging the processed datasets and applying different filters to eliminate any artifacts or discontinuities. These models have a spatial resolution of 2 m and cover nearly 6000 ha.

7.1.3. Wetland class succession modelling

The wetland modelling aims to link the hydrology to wetland class spatial and temporal distribution. Different physical variables are therefore used to calibrate predictive models, which are used to reproduce observed historical conditions and the changes experienced by ecosystems in terms of extent and composition. This approach is based on the use of two distinct algorithms: a supervised machine learning (i.e. random forest) algorithm, which predicts wetland class based on environmental conditions, and a succession algorithm, which simulates the transition from one wetland class to another when the hydrology of the environment changes. The succession algorithm uses available empirical and theoretical knowledge of plant community biology to define tolerance thresholds for different wetland classes. It thus reproduces the sequence and latency of changes that control the transition from one state to another in a natural environment. In the end, five wetland classes can be predicted by the modelling, which also identifies open water and terrestrial areas: submerged aquatic vegetation, emergent marsh, wet meadow, shrub swamp and treed swamp. A variety of data sources were used to calibrate and validate these different algorithms, ranging from floristic inventories to cartographic classification sets, and allow the creation of models tailored to a lake or river reach.

The CWRM was also adapted to predict the habitat of two invasive plant species whose presence and abundance in the Great Lakes basin are already well documented: hybrid cattail (*Typha x glauca*) and invasive common reed (*Phragmites australis*). These species, which threaten the biodiversity of coastal wetlands, do not occupy their entire ecological niche in the environments studied and should continue to expand in the coming years. It is therefore difficult to model the growth of *Phragmites* and *Typha* while identifying the part of the invasion attributable to the species growth and the part attributable to climatic disturbances alone (regardless of the intrinsic

capacity of the species to expand). In order to separate these two aspects, two models were developed for each of these species, namely a suitable habitat model, which uses a random forest, and a population growth model, which is a strictly theoretical model. While the former allows us to determine the extent of habitat deemed favorable to the species and how it evolves with projected global warming, the latter attempts to simulate the phenological stages and mechanisms that control the growth of taxa. In both cases, only hydrological and topographical conditions are considered as explanatory variables. The population growth model, however, uses the predictions obtained for the wetland classes to determine which habitats are favorable for the establishment of *Phragmites* or *Typha*.

7.2. Summary of results and discussion

7.2.1. Climate scenarios: Lower and upper-bound projections

The two selected climate scenarios give the lower- and upper-bound of expected changes for the Great Lakes Basin. They define the climate change envelope projected for the last decades of the century, and can be considered as the low- and high-risk scenarios in terms of mean lake levels. These levels are directly linked to the conditions modelled by the AOGCMs, and the resulting amount of water supplied to the Great Lakes system under specific atmospheric regimes.

The **upper-bound scenario**, driven by the GFLD-ESM2M model, projects a significant increase in lake levels, with a net rise of up to ~0.70 m in Lake Ontario, including the upstream portion of the Upper St. Lawrence River, which will likely be the most affected lake.

The **lower-bound scenario**, driven by the CanESM2 GCM, rather projects a minor to moderate decrease in mean lake levels for the period 2070 to 2099 relative to baseline, with a maximum decline of -0.12 to -0.23 m in Lakes Erie, Huron, and the Huron-Erie Corridor, and no significant change in Lake Ontario and the Upper St. Lawrence River. Overall, the AOGCMs disagree on the signs of changes in the upper lakes, which include the Huron-Erie Corridor, revealing the large uncertainty in projections.

7.2.2. Changes in physical variables and vegetation

7.2.2.1. Natural variability, migration and submerged aquatic vegetation

The projected absolute change in mean level is 0.5 to more than 2.5 times the natural variability of the system, which can significantly influence the composition and positioning of wetland vegetation. A similar long-term change in water levels can force an up- or down-slope migration of plants that goes beyond the historical cycle, occasioning major changes in the wetland configuration. Existing anthropogenic stressors, such as urbanization, may therefore aggravate the situation by causing a decline in habitat quality. This situation is all the more realistic if the projected increase in lake levels is sustained and prolonged, as predicted in the upper-bound scenario, and if the topography limits any migration of plant classes. A decrease in total wetland area is therefore expected by the end of the century at sites where inland recovery is restricted.

The increase in mean (upper-bound scenario) water level by 2085 is expected to reduce the total area of wetlands in most lakes, with the exception of Lake Ontario, where the selected sites have topography that is predominantly conducive to the migration of vegetation classes. Sites in Lake Erie and Lake St. Clair are expected to be largely affected as the landward migration of wetland classes is particularly limited (by topography or land use). In Lake Huron, the increase could also reduce total wetland area, but this loss is less than in the southern lakes because of the natural state of the sites, which favors migration. At the opposite end of the spectrum (lower-bound scenario), if a decrease in mean levels occurs, wetland area is generally expected to increase.

In terms of wetland distribution, the projected changes are expected to result in either a gain (+) of wetlands or a loss (-) of submerged aquatic plants depending on whether levels are falling or rising, respectively. Other wetland classes are also expected to be disturbed, but their response is primarily site-specific. In general, the various wetland classes tend to move inland as the water level in the environment increases. This is particularly problematic for wetlands that are landlocked between the lake and habitat boundaries (i.e., agricultural land or urbanized areas).

The **projected loss of coastal wetland area** is of concern as this ecosystem type is one of the most productive on the planet. The loss of coastal wetlands could affect a variety of species at risk, as well as migratory birds, fish, amphibians and a variety of plants. These environments also provide a large number of ecological services essential to society, such as flood mitigation, low water support, groundwater recharge, sediment and pollutant filtration, nutrient retention, bank stabilization, erosion reduction and carbon sequestration. All of these benefits could be significantly impacted if the extent, distribution and composition of wetlands are negatively altered in the future.

Projected changes are also expected to alter the percentage of time during the growing season that habitats remain underwater if nominal conditions are significantly altered. This is expected to be the case for most sites on Lake Ontario and the Upper St. Lawrence River, which show an increase of +6% to +34% in their average strictly flooded area between 2070 and 2099 (relative to the baseline scenario). The river systems are also more likely to become inundated than any other site in the same basin, particularly under the upper-bound scenario. This flooding could affect the dominance of submerged aquatic vegetation (SAV), alter the overall deepmarsh habitat (i.e., aquatic habitat), and potentially the total area defined as open water if the flooding depth in the lacustrine boundary of coastal wetlands is substantially increased. In Lake Ontario, inundation of the low marshes is expected to result in an increase in the average area of SAV, which could undergo a relative change of up to +281% in the future period. In the remaining lakes, the water depth reached in the habitat area is often too deep below the upper limit of the projections to support SAVs, which decrease in area in favor of open water.

The **submerged aquatic plant** class generally responds very quickly to hydrological changes in its environment because of the high degree of adaptability of its component species. However, its habitat must meet a certain number of requirements to ensure the maintenance and survival of the plants that take root in the flooded part of the wetlands. Water quality is critical to the establishment and growth of submerged aquatic plants, which, when present, can help maintain a suitable environment for the low marsh by absorbing nutrients and binding suspended sediments (e.g. clay and silt). Increasing SAV extent is therefore beneficial to habitat values along the Great Lakes shoreline, as well as enhancing habitat structure for higher trophic levels, their biodiversity and, more broadly, the stability of lake ecosystems. A high biomass of submerged aquatic plants is generally associated with lower nutrient and phytoplankton concentrations, which promotes good clarity (i.e., light penetration) and overall water quality. A gain in SAV thus maintains properties essential to shallow aquatic ecosystems, whereas a loss may accelerate their deterioration. The overall consequences of increasing SAV at the expense of other wetland classes remain, however, difficult to quantify.

7.2.2.2. **Interannual Variability and invasive species**

Interannual variability in mean lake level is expected to increase by more than 25% in the upcoming decades for the Lower Great Lakes, which includes the Lower Detroit River. This change is particularly marked in Lake Ontario and the Upper St. Lawrence River, where the year-

to-year variation in mean lake levels will increase by up to 0.24 m, which represents a relative increase of +88% and +94% respectively.

No significant change in this aspect is projected in Lakes St. Clair (in the Huron-Erie Corridor), and Huron. Consequently, the extent of the strictly flooded area is expected to be more stable in these lakes by 2099, with a more pronounced effect in Lake St. Clair where a -79% to -89% decrease in interannual variability of the flooded area is expected. This suggests more stable conditions in the future, which can heighten the risk of perennial habitat loss in Lake St. Clair under the upper-bound projection. In Lake St. Clair, most wetland classes suffer important losses and the total wetland area is reduced by up to -40%. The agricultural lands and urbanized areas that surround the wetlands and prevent migration in this specific region of the Great Lakes are therefore expected to greatly impair the ability of the ecosystems to adapt to the projected changes.

More generally, **interannual fluctuations in water levels** can dramatically alter plant communities when periods of very high or very low water levels occur. While these types of fluctuations are necessary to maintain a high level of plant biodiversity, the occurrence of extremes encourages the establishment and expansion of invasive species, such as *Typha x glauca* and *Phragmites australis*. These plants, which take advantage of newly exposed mudflats to establish themselves, are already well established in the southern Great Lakes and threaten the ecological integrity of wetlands. Conversely, the absence of any variation in mean water levels is also detrimental to wetland biodiversity as it facilitates the expansion and invasion of *Typha x glauca*, which can quickly become dominant, a situation already observed in Lake Ontario.

Based on the modelling results, the increase in interannual variability of **Lake Ontario** levels by 2099 may be unfavorable to *Typha*, whose establishment has been facilitated by regulation during the historical period. However, this could benefit *Phragmites* and cause a reversal of invasion trends, with more *Phragmites* than *Typha* in the period 2070 to 2099. Thus, climate change should promote physical and ecological conditions more favorable to common reed if increased interannual variability takes place. Conversely, if climate change induces no change in variability by 2085, hybrid cattail should remain the most abundant invasive species in this portion of the Great Lakes. In both cases, the expansion of exotic species remains a concern for Lake Ontario wetland quality and should be monitored before establishment reaches a tipping point.

In **Lake Erie and Lake St. Clair**, climate change may increase or decrease the dominance of invasive species depending on the site and projections. Under lower average levels (lower-bound), potential *Phragmites* habitat is expected to increase in a majority of wetlands, while the range of *Typha* is expected to increase at only some sites. The spread of this taxon is expected to be disadvantaged by the high interannual variability projected between 2009 and 2070 (lower-bound scenario) or by high lake levels (upper-bound scenario). In the latter case, climate change is expected to be responsible for the decrease in the area of suitable areas for hybrid cattail growth. *Phragmites* is also expected to suffer from these conditions, as the water depth in the lake portion of the sites may become too deep for the species. However, reeds could migrate inland in the event of a sustained rise in mean lake levels in Lakes Erie and St. Clair and occupy habitat spared from flooding, resulting in a continued invasion.

In **Lake Huron**, climate change generally appears to be reducing the potential habitat for both invasive species. The steep topography of some of the environments in this water body appears to be generally unfavorable for invasion of *Phragmites* and *Typha* compared to what is observed elsewhere in the basin. However, these species are expected to invade the remaining untouched wetlands and thus alter the overall quality of these habitats by 2099. The Baie du Doré wetlands (15BDD), which are already heavily impacted by *Phragmites*, are expected to see the total area of invasion increase to 50% under any scenario. At the other sites studied, *Phragmites* could occupy up to 20% of the habitat and *Typha* up to 35%. Although Lake Huron wetlands are less vulnerable to exotic species, invasion monitoring should be encouraged. Control of invasive plants is essential for preserving biodiversity and protecting the integrity of these valuable ecosystems.

7.2.2.3. Transition zone and wetland composition

The transition zone, where daily and sub-seasonal fluctuations occur, is critical to the establishment and persistence of various wetland classes, especially wet meadow (WM) and emergent marshes (EM), where the greatest species richness is found. Results indicate that a clear positive change is likely to affect the extent of this zone in Lake Ontario sites, with changes up to +6% for the period 2070 to 2099, representing a relative increase of 24% to 103%. Projections obtained for Airport Creek Marshes, in the Bay of Quinte, show the largest shift, with a projected increase in absolute mean annual values of 3.3% to 5.5%, which is comparable to the observed historical variability of 6.3%. River systems in Lake Erie and some sites in Lake Huron show similar but less pronounced dynamics. Conversely, a significant decrease in the transition

zone is predicted for the connecting channel sites in the lower Detroit River and Upper St. Lawrence River.

This increase in the extent of the transition zone in Lake Ontario results in an overall increase in emergent marshes dominance. In the Airport Creek marshes, this change amounts to +44%. The area of wet meadows, on the other hand, is not favored by the projected physical changes. Thus, this class appears to be very sensitive to environmental conditions and unlikely to migrate to elevations where conditions are not optimal. Wet meadows essentially experience a loss of area in the future period.

Finally, a net reduction in the strictly flooded area is projected at sites in Lake Ontario and at some sites in Lake Erie, while the area of high marsh is projected to increase in Lake Huron. These changes could result in a decrease in terrestrial environments by the end of the century, with potential impact to high elevation vegetation classes such as swamps. However, several other factors may influence the establishment of woody species in the terrestrial portion of sites (e.g., water depth and the existence of fluctuations), making it difficult to generalize. This class also takes much longer to establish and can be quickly (i.e. within 3 years) replaced by forbs and grasses under unfavourable conditions.

7.2.2.4. Periodic events, storms and waves

Since short-term water level fluctuations that modulate the dry/wet cycles are driven by atmospheric forcing, the expected changes in lake surface dynamics follow those observed in surface winds. Based on the selected set of AOGCMs, no clear conclusion can be drawn for near-surface wind speeds, other than a more pronounced decrease in the mean annual daily intensity under the lower-bound scenario. Overall, there is great uncertainty about any change in intensity during the fall, while winds over Lake Huron, Lake Erie and Lake Ontario in summer and winter are expected to be less intense in the last decades of the century. A decrease in the climate of extreme winds is also predicted for all months except fall.

The modelled lake dynamics are found to be strongly influenced by the lower-bound of the projected changes by 2099, i.e. the more marked decrease in mean annual maximum wind speeds. Projections prescribe a decrease in the maximum monthly maximum set-ups amplitude in all lakes, although Lower Great Lakes, including the Lower Detroit River, will likely be the most affected basins. The relative changes, however, remain less than 10%, or less than 4 cm in Lake Erie and 1 cm in Lake Ontario. Such changes are unlikely to be critical to wetland classes, which

typically occupy large elevation ranges. With respect to site-scale physical processes, a general decrease in the mean annual duration of the wet/dry cycles is projected as a result of this change in winds and set-ups for a majority of sites in Lakes Ontario, Erie, and St. Clair, including the Lower Detroit River.

The projected future wave climate for Lakes Ontario and Erie stays similar to that observed during the baseline period. Relative changes in significant wave height and wave period were estimated to be less than 5%, with no agreement on bound values. Annual wind frequency and magnitude are not projected to change significantly by the horizon 2085, which is reflected in the modelled deep waves. Regarding near-bottom orbital velocities in the vicinity of wetlands, no clear signal of change is projected in Lake Ontario, although a more pronounced decrease is expected under the lower-bound scenario (up to -39% compared to a maximum relative change of +10%). Conversely, wave intensity is projected to increase by 2099 in Lake Erie wetlands, particularly in lacustrine sites like Long Point and Rondeau Bay where the projected changes range between +52% and +81%. This increase in wave exposure, which is ostensibly the result of a change in mean lake level and, hence, nearshore bathymetry rather than a change in deep wave climate, will likely limit aquatic species establishment in the outer fringe of the wetlands.

7.2.3. Lakes modelling: Long- and short-term fluctuations

Two modelling approaches were used to model long- and short-term lake level fluctuations: a non-stationary and a scenarios-based approaches. While the former gives a broad description of the physical processes that modulate the lake surface, including the seiches that characterize the Great Lakes Basin, the latter focuses only on the direct atmospheric influence, which is responsible for the wind set-ups. Both provided valuable information in terms of physical variables, but the non-stationary modelling proved to be significantly more demanding in terms of computational resources and storage. In such an approach, hourly and sub-hourly time series must be generated and stored, which covered 120 years of projections and 38 years of historical simulations for this specific project. Since the use of a restricted set of scenarios generated a large but manageable amount of data, using the conventional modelling technique would have been unrealistic with a larger number of possible climates. Climate change studies usually relies on several GCMs and RCPs to handle uncertainty in future projections. If further work is to provide a better understanding of the uncertainty related to future lake conditions, and more robust conclusions regarding the impacts of global warming for Great Lakes coastal wetlands, the scenario-based approach should be considered first.

7.2.4. Wetland modelling

The wetland modelling approach discriminated with relatively good accuracy up to five broad wetland classes, including two swamp classes in Lake Erie (i.e., shrub swamps and treed swamps). Although modelling more classes of emergent marshes would have been relevant (e.g., shallow, deep, and non-persistent emergent marshes), the tests conducted did not conclude that this was feasible. Modelling of non-persistent emergent marshes, which are abundant in Lake Huron, resulted in very confusing predictions, with non-persistent emergent marshes being confused with emergent marshes, wet meadows or submerged aquatic vegetation. This is due to a lack of empirical data, as non-persistent species are generally not differentiated in map classification sets and available floristic inventories rarely reported their presence in the wetlands visited. The model is also sensitive to the number of wetland classes used, as each of these classes must be well differentiated in terms of its ecological niche to enable good prediction. In order to promote more accurate distinction, the number of vegetation classes used was intentionally kept small. However, the succession algorithm for Lake Huron was modified to account for the presence of non-persistent species. The tolerance of emergent marshes to adverse conditions was lowered in this water body to reflect this.

The succession lag time are generally dependent on the species composition of a wetland class. The tolerance for most wetland classes were set identical for each lake, except for Lake Huron where the emergent marshes class time response was modified. The tolerance to dry conditions are a general approximation and may be different from site to site depending on soil type, nutrient supply, seed-bank and species composition. Conditions unfavorable to wetlands during prolonged high water levels are generally more consistent than those during low water levels, since these are less affected by external factors such as nutrient supply and soil type. Overall, the good performance of the succession models suggests that the thresholds chosen respect the ecological processes that control wetland ecosystems. The calibration of these thresholds was based on field observations.

7.2.5. Invasive species modelling

A simplified approach was used to model the growth of *Phragmites* and *Typha*, based on two distinct models: a population growth model and a suitable habitat model. The first one uses the knowledge acquired on the biology of the species to reproduce, in a simplified way, the mechanisms that govern the different stages of the plant, from seed to stand. This theoretical

model was calibrated with field observations, changes in satellite images and multiple years maps. Although the parameters used have been refined in order to ensure a reliable prediction of the invasion, in phase with the observations. A stochastic component was also integrated into the algorithm to control seed germination and reproduce the randomness of invasion, as well as the progressive establishment of taxa in wetlands. The suitable habitat model is complementary and allows us to determine to what extent climate change accelerates or hinders the invasion of the two species, independently of their intrinsic growth capacity. This model uses hydroperiod variables as explanatory variables (or predictors) and observations as response variables.

It is important to note that the results of invasive species modelling are highly dependent on the onset date of the invasion, which can be difficult to determine for a site or lake. Nevertheless, using available observations and knowledge from invasive species experts, we were able to replicate the historical invasion of the two most prevalent invasive species in the study area. With the CWRM, we modeled their habitat, incorporated the effect of water level changes on it, and determined the impact of long-term changes in the hydrologic regime on the potential expansion of the two invasive plants.

7.3. Model limitations

Like all modelling approaches, some simplifications had to be made for keeping computation requirements manageable. Those model limitations are discussed in the next paragraphs according to the climate and physical modelling, creation of DEM and vegetation modelling perspectives.

7.3.1. Climate modelling limitations

Climate projections have a variety of sources of uncertainty, ranging from the socio-economic perspectives used to generate emissions trajectories, to the mitigation measures implemented, to the inaccuracies in the mathematical models used to simulate climate, to downscaling, to the assumptions used to project Great Lakes levels under extreme scenarios. It is also important to note that the projections are not used to predict the water level of a lake at a given date, but rather the range of expected values for a future period, which depends on the changes circumscribed by the selected scenarios (e.g., in air temperature and precipitation). Due to the estimated computational time to produce the necessary data set for CWRM, a single emission scenario was used (i.e. RC4.5), which projects a moderate increase in CO₂ concentrations by the end of the century. The use of a more aggressive emission scenario, such as RCP8.5, would necessarily

have resulted in a different simulated wetland response and changed the conclusions of this study.

7.3.2. Physical modelling limitations

Various assumptions and/or simplifications had to be made in order to simplify the modelling of physical processes and be able to create water level time-series in such vast and heterogeneous wetland sites, located in four different lakes, each with its own particularities.

First, in the hydrodynamic models, the bathymetry is considered fixed through time for all lakes. Therefore, sediment transport and morphodynamics were not included in the present modelling effort. However, these processes are more important in the riverine reaches than in the Great Lakes, where most sites are located (with the exception of the Rondeau Bay spit, which is experiencing severe erosion). Although sediment transport models exist, their use in this project would have resulted in an excess cost-benefit ratio due to the computational resources required to use them. This omission may therefore influence the resulting projections, particularly at sites deemed sensitive (i.e., subject to severe erosion or heavily exposed to waves).

Second, ice conditions were not included as the simulations covered, essentially, the open water period (April to November), which corresponds to the plant growing season. The inclusion of ice would have required the parallel use of freeze-up projections and thus, the use of computationally heavy and time-consuming three-dimensional ocean models.

Third, the hydrodynamic simulations performed in Lakes Huron and Ontario use a scenario-based approach, which assumes stationary states that cannot allow for seiche reproduction, which is primarily transient. The omission of this component of lake dynamics has an impact on the magnitude of the simulated sub-seasonal shoreline variations. The use of this type of scenario nevertheless reduces the computational time otherwise required to create the time-series, which was necessary given the amount of work to be done in a short time frame (three lakes and two connecting channels, for a total of 158 years of simulations). Nevertheless, the use of the scenario-based approach allowed for adequate modelling of the wetlands involved, with the wetland succession models performing well overall. Lake Superior was also part of the project, but had to be excluded from the study due to time and computational constraints regarding hydrodynamic simulations. The two sites selected in this basin, i.e. Mission Marsh and Hurket Cove, nevertheless have DEMs ready for use should the project continue. The time required to

create and validate the hydrodynamic model for this large water body is estimated to be six to nine months.

Fourth, land use in the CWRM is another component that is considered fixed in time. Any potential disturbance to this land use, whether through cultivation, fallow, or urbanization, could therefore alter the value of the physical variables in the affected wetlands. As such, if the changes lead to the destruction or erection of a physical barrier that impedes the free flow of water, e.g., a dike, a change in water depth within the habitat boundary can be anticipated, invalidating any projections. Nevertheless, CWRM has demonstrated that the selected wetlands are threatened by climate change and thus, any anthropogenic development near these sites may increase the vulnerability of these habitats.

Fifth, the hydrodynamic models used simulate the action of lakes alone for the lacustrine sites, directly influenced by the water body. Sites protected by a natural barrier cannot be modeled by the current approach, as the water depth in this type of wetland also responds to the dynamics of the watershed to which it is attached. These sites would require an alternative modelling approach that would, for example, allow for the partial or sporadic opening of the barrier that cuts the link between the lake and the habitat, as well as non-lake influences (e.g., tributary, precipitation, evaporation, etc.).

Finally, there are other processes that do not directly influence water levels, but can still alter plant growth and establishment. This is the case for water clarity, nutrient inputs, or potential chemical exposure, which have not been incorporated into this iteration of CWRM.

7.3.3. DEM limitations

The AOI used to delineate DEMs is limited in spatial extent at a few sites by the coverage of available LIDAR data. This is particularly true for selected wetlands in Georgian Bay. The inland migration of vegetation classes is therefore restricted to this area and consequently cannot be adequately simulated when water levels tend to increase. In the context of this study, only the projections obtained for the Whiskey Harbor wetlands appear to be affected by this limitation in the upper bound scenario. It is important to note, however, that the coverage of the areas of interest and DEMs should be revisited if CWRM uses alternative climate change scenarios that project an even more drastic increase in mean lake levels.

In terms of DEMs, a median error of 16 cm characterizes the elevation of the corrected models. This error may seem high given the accuracy with which the CWRM attempts to predict changes in the physical environment of wetlands, including fluctuations of only a few centimeters. Nevertheless, and considering the particular nature of the soil in wetlands, the high vegetation density, and the accuracy of the GNSS receivers used to collect the validation points (i.e., about 5 cm), no numerical model can be completely free of uncertainty. Therefore, the accuracy obtained for all selected wetlands was considered adequate for CWRM purposes. In a future perspective, a detailed analysis of the error distribution and the use of various segmentation methods adapted to multispectral imagery could potentially improve the overall accuracy of the DEMs.

Finally, it is important to mention that the chosen correction technique has proven to be effective for the selected sites, but may be difficult to implement on a large-scale model. This method requires the use of a very large number of ground validation points in different areas of the wetlands in order to properly represent the error associated with a vegetation type in a given location. Spectral imagery coverage must also encompass the entire study area, which can greatly complicate the applicability of this type of correction to an area as large as, for example, the entire Great Lakes basin.

7.3.4. Vegetation modelling

The selection of the 20 sites for this study was challenging as the Great Lakes system covers not only thousands of hectares of wetlands, but also a variety of ecosystems. The sites selected were, however, large enough to demonstrate the impacts of long-term change in coastal dynamics (i.e., water levels and waves) on the distribution of wetland classes. However, this project's own effort has focused on the Canadian Great Lakes coast, which provides only part of the answer. In order to provide a holistic view of the impact of climate change for coastal wetlands in this broad basin, sites of interest identified along the U.S. coast should also be included in the CWRM.

With respect to invasive species modelling, the CWRM does not incorporate any form of past or future human intervention dedicated to exotic species management. The results of this study therefore demonstrate that the absence of any control of *Typha* and *Phragmites* in the wetland environment is, in itself, a worst-case scenario. The projected future distributions of these two species are alarming and demonstrate the very high vulnerability of wetlands to invasion. Incorporating management thresholds into the CWRM could allow comparison of the

effectiveness of different actions that can be implemented to counter or slow the invasion of these species in a climate change context.

7.3.5. Implications

The impact of these limitations or simplifications on the results of this study was considered insignificant or impossible to quantify. For example, sediment transport is not expected to play a major role in the projected changes as it only marginally affects the mean levels. Its overall effect on the wetland model results is also negligible. Water clarity and nutrient inputs can influence changes in wetland class distribution, but both require separate modelling and scenarios that are difficult to establish. The same is true for land use, where changes over time are subject to high uncertainty and depend on corporate governance and land-use choices.

The primary objective of CWRM was to compare the distribution of wetland classes between the recent past (1980 to 2009) and the future (2070 to 2099) using climate scenarios, which determine the disturbances caused by carbon emissions. The use of numerical modelling, which assumes the same biases in both periods considered, therefore allows the study to focus on this aspect alone, omitting or simplifying the so-called secondary influences. The present conclusions therefore remain valid within the framework of the changes circumscribed by the selected scenarios (i.e. in terms of air temperature and precipitation). They therefore present possible futures in a business-as-usual world, where only global warming is responsible for the observed changes in environmental conditions.

7.4. Key findings

The CWRM is a habitat response model that integrates all the components that regulate the spatiotemporal distribution of wetland classes and their succession. When coupled with climate change scenarios, this model can be used to create projections for the recent past and the future, and thus simulate the evolution of ecosystems in the event of continued greenhouse gas emissions. In this project, a so-called moderate emission trajectory was used to project the state of wetlands in the Great Lakes between 2070 and 2099 (i.e., RCP4.5), as well as to simulate the invasion of two invasive species: *Typha* and *Phragmites*. This trajectory foresees a peak in emissions around 2040, followed by a decrease with stabilization that allows to limit the radiative forcing at the end of the century. The two general circulation models employed to constrain the range of changes expected under this scenario are CanESM2 and GFLD-ESM2M, which provide the lower and upper bounds of possible futures, respectively. While CanESM2 projects slightly

lower or even stable average Great Lakes levels for the period 2070 to 2099 (relative to the period 1980 to 2009), GFLD-ESM2M projects a significant increase in Great Lakes levels by 2085.

In addition to providing a representation of the influence of climate change on wetland ecosystems, the CWRM has provided a state-of-the-art method for modelling physical (water levels and waves) and ecosystem conditions (wetland class succession and invasive species expansion) specific to the Great Lakes system. The model also clarifies the link between the large-scale processes that control climate and lake surface dynamics and the small-scale processes that explain the growth and establishment of plant species. These relationships are critical for studying the sensitivity of wetlands to climate change, and thus for assessing their vulnerability. A substantial number of results produced during this project will be made available to the public, which provide a representation of expected changes for the 20 selected sites and the two scenarios used. These results include high-resolution DEMs, floristic surveys, and projected spatiotemporal distributions for wetland classes in the form of annual maps.

The CWRM results demonstrate that Great Lakes coastal wetlands could be significantly disturbed by projected climate change and thus be significantly and adversely affected. In summary:

- Using the RCP 4.5 emission scenario, some models project that Lake Ontario may reach peak levels of around 77 m. Under the more extreme RCP 8.5 emission scenario, there are projections that result in even higher lake levels. However, there are various assumptions about the physical limitations and regulation of the system that would be violated with these extreme conditions. Thus further study is needed to assess the plausibility of these very high lake levels. The transition zone expands in the future under the studied climate change scenario on Lake Erie and Lake Ontario and some sites on Lake Huron but shrinks on connecting channels. Wetlands generally establish in this transition zone.
- There is a possible relative increase of wave activity between 52% to 81% on Lake Erie that will likely limit submerged aquatic and emergent plant species.
- Within the lower-bound scenario, a moderate increase of total wetland area (~7%) is expected across all sites, with changes ranging from -1% to +29%. Under the upper-bound scenario, results suggest an average decrease of 16% and up to 54% decrease of total wetland area with greater wetland loss expected in the southern Great Lakes. Rising water levels cause wetlands to migrate inland, which may be constrained by land use and topography.
- *Phragmites* will become established and more abundant than *Typha* in Lake Ontario by the end of the century. However, without significant water level change and interannual variability, *Typha* will likely remain dominant in Lake Ontario. In lakes Erie and St. Clair, *Phragmites* may expand under climate change. Higher water-level projections tend to reduce the growth of both invasive species but result in colonization and expansion at

higher elevations. For most sites in Lake Huron, CWRM predicts in the future a decrease in both invasive species habitat suitability.

7.5. Future developments

Although the integrated modelling approach used to simulate the state of wetlands may appear highly complex using different statistical analyses of data and many different models, it proved to be effective and even essential for this project. The processes that drive changes in the extent and composition of coastal wetlands need to be modeled with methods that take into account the variability of the system and the multi-variate relationship between the descriptive variables, especially in the context of climate change that is likely to significantly increase this variability. In other words, these processes cannot be simulated with simple methods that do not directly take into account the changes that affect their physical environment. Simulation of mechanisms involved is in fact essential to determine the impacts and, from there, to develop adaptive strategies that aim to ensure or enhance ecosystem resilience. Because the CWRM provides a robust analysis of the effects of projected climate change in a given location, the analyses produced are specific rather than global. This quality is valuable for any wetland protection or conservation intervention as it allows for differentiated action, tailored to an area or site.

Since the conclusions of the CWRM are dependent on the climate scenarios used and thus on the uncertainty surrounding natural climate variability, emission trajectories and the models themselves, imprecisions in the model outputs are inevitable. The results are still projections, which present the range of possible futures over the range of changes considered, to the best of current knowledge. They are therefore trends, not predictions. The conclusions reached should be used primarily to guide and plan conservation and protection actions for Great Lakes coastal wetlands, ecosystems threatened by climate change.

Nevertheless, a number of lessons have been learned from this project, both in terms of hydrodynamic modelling of lakes and waves, and in the use of physical variables for wetland modelling. This knowledge adds inestimable value to the scientific literature available today. In the near future, the use of stationary (i.e., scenario approach) or transient physical models for simulating shoreline water level dynamics should be compared. This effort would provide a better understanding, for the same lake, of the effect of sub-daily water level fluctuations (i.e., seiches) on the performance of wetland succession models. It would also ensure better planning of the modelling effort for any future studies.

In the future, the CWRM could be expanded and completed by adding a wider range of sites (e.g., Lake Superior, U.S. coastline, or barrier sites), more climate scenarios, or by developing wildlife habitat and population models. The CWRM could also be used to assess the effect of a non-climate change. For example, it could be used to determine the impact of a change in land use or the effect of active wetland management, whether it be conservation, restoration or invasive plant control. As the CWRM predicts the distribution of broad wetland classes, it can also be used to develop specific measures dedicated to a given wetland class. In this sense, it can support efforts to conserve key ecosystem services, such as nesting habitat for endangered birds. Finally, it is important to mention that the CWRM provides detailed projections for 20 Great Lakes wetlands. These projections should support a call to action to limit the potential impact of climate change on all wetlands in this broad basin. The results should help guide funding commitments for protection, conservation or restoration, and make them more effective and targeted.

8. APPENDICES

APPENDIX A: Ground-truth points, LIDAR and bathymetry datasets used for each site DEM

unique_ID	WETLAND_NA	LK_BASIN	Ground-truth points			Lidar dataset	Bathymetric datasets			
			RTK	Quadrats	N		Bathy1	Bathy2	Bathy3	Bathy4
1HIE	Hill island	LKO	CWS	CWS	365	LEAP	CWS	CHS (8039)		
2ACM	Airport Creek Marsh	LKO	CWS	CWS	264	LEAP	CWS	NOAA (L00066)		
3SBM	South Bay Marsh	LKO	BC2_1	Dillon	458	LEAP	CHS lidar (4013997)	BC2_1		
5LCM	Lynde Creek Marsh	LKO	BC2_1	Dillon	431	ECCC	CHS lidar (CE_M2-C_SDTP_5m)	BC2_1		
6JSM	Jordan Station Marsh	LKO	BC2_1	Dillon	372	ECCC	CHS lidar (CE_M2-E_SDTP_5m)	BC2_1	SHOALS_1	
7GRM	Grand River Mouth Wetlands	LKE	BC2_1	NRSI	387	LJO	CHS (8260, 8261, 8287, 8288)	BC2_1	CHS lidar (4014183_I)	NOAA (L00066)
8SPP	Selkirk Provincial Park	LKE	BC2_1	NRSI	397	LJO	CHS lidar (4014183_I)	BC2_1		
9LPW	Long Point Wetland	LKE	CWS	CWS	470	LJO	CHS lidar (4014183_E)	NOAA(L02268)	CHS(3782)	
10RBY	Rondeau Bay	LKE	BC2_1	Dillon	321	LJO	CHS lidar (4014183)	CHS(1200049)	BC2_1	NOAA (L00066)
11FCK	Fox Creek / Dolson's Creek	LKE	BC2_1	Dillon	373	LJO	BC2_1	NOAA (L00066)		
12DRM	Detroit River Marshes	HEC	BC2_1	Dillon	531	LJO	BC2_1	NOAA(D00132)	NOAA (L00066)	
13LSC	Lake St. Clair Marshes	HEC	BC2_1	Dillon	743	LJO	BC2_1	CWS	NOAA(L02360, L02123, L02122, H11912, H11913)	
15BDD	Baie Du Dore	LKH	BC2_2	NRSI	381	ECCC	CHS lidar (4014208)	BC2_2		
16HBW	Hay Bay Wetland	LKH	BC2_2	NRSI	383	ECCC	CHS lidar (4013584)	BC2_2		
18HGW	Hog Bay Wetland	LKH	BC2_2	NRSI	365	ECCC	BC2_2	RTK_pts		
19TBY	Treasure Bay	LKH	BC2_2	NRSI	447	ECCC	BC2_2	McMasterU	NRSI	
22WHW	Whiskey Harbour Wetland	LKH	CWS	CWS	345	ECCC	CWS	CHS(8273)		
23ACK	Anderson Creek	LKH	BC2_2	NRSI	393	ECCC	BC2_2	RTK_pts		
27FPT	Frances Point	LKH	CWS	CWS	434	N/A	CWS			

NRSI	Natural Ressource Solutions Inc. (2018)
BC2_1	BC2 (2019)
BC2_2	BC2 (2019)
LEAP	Government of Ontario. (2018)
LJO	Government of Ontario. (2019)
ECCC	KBM Ressources Group (2018)
CHS_lidar	IIC Technologies (2018)
CHS	https://inter-j01.dfo-mpo.gc.ca/registry-registre/orderMap-commanderCarte?lang=eng
NOAA	https://maps.ngdc.noaa.gov/viewers/bathymetry/
Dillon	Dillon Consulting (2018)
CWS	Canadian Wildlife Service

APPENDIX B: List of multispectral images used for DEM correction

unique_ID	WETLAND_NA	LK_BASIN	Multispectral image(s)
1HIE	Hill island	LKO	IKONOS_1_80cm_2008_09_03_20080903160808900000116054022000041210605THC
2ACM	Airport Creek Marsh	LKO	AirportCreek_19Apr2008_80cm_RGBN.tif (IKONOS)
3SBM	South Bay Marsh	LKO	GeoEye_1_50cm_2009_08_03_1050410001E0C500
4WMH	Wesleyville Marsh	LKO	WV02_20170818161528_1030010070737B00_17AUG18161528-M1BS-501576591010_01_P001
5LCM	Lynde Creek Marsh	LKO	WV02_20160721161856_103001005A815700_16JUL21161856-M1BS-501229954020_01_P002
6JSM	Jordan Station Marsh	LKO	WV03_20180905164334_10400100425DF000_18SEP05164334-M1BS-503120507020_01_P008
7GRM	Grand River Mouth Wetlands	LKE	IMG_PHR1B_MS_201809211620413_SEN_4488668101-2_R1C1 (Pleiades)
8SPP	Selkirk Provincial Park	LKE	WV03_20180804163257_1040010041315900_18AUG04163257-M1BS-503120506080_01_P001
9LPW	Long Point Wetland	LKE	WV02_20180809162521_1030010081C94F00_18AUG09162521-M2AS_R1C1-010447643020_01_P001, WV02_20180809162521_1030010081C94F00_18AUG09162521-M2AS_R1C2-010447643020_01_P001, WV02_20180809162537_1030010082864D00_18AUG09162537-M1BS-502529116010_01_P002, WV02_20180809162549_10300100820C7D00_18AUG09162549-M1BS-502529024090_01_P002
10RBY	Rondeau Bay	LKE	WV02_20161013161856_103001005E3AEB00_16OCT13161856-M1BS-503120501030_01_P013
11FCK	Fox Creek / Dolson's Creek	LKE	WV03_20170731163625_1040010031889400_17JUL31163625-M1BS-503120506060_01_P003
12DRM	Detroit River Marshes	HEC	WV03_20161007164711_1040010023D7EC00_16OCT07164711-M1BS-501145414010_01_P008
13LSC	Lake St. Clair Marshes	HEC	IMG_PHR1B_MS_201809261631506_SEN_4488682101-2_R1C1 (Pleiades), WV03_20170725164029_104001002E789100_17JUL25164029-M1BS-501583102100_01_P001, WV03_20170725164031_104001002E789100_17JUL25164031-M1BS-501583102100_01_P002
15BDD	Baie Du Dore	LKH	IMG_PHR1A_MS_201808131619291_ORT_3842320101-2_R1C1 (Pleiades)
16HBW	Hay Bay Wetland	LKH	WV02_20170924165130_10300100710A5900_17SEP24165130-M1BS-503120500050_01_P001
18HGW	Hog Bay Wetland	LKH	GE01_20160622161134_1050010005139300_16JUN22161134-M1BS-503164773090_01_P006
19TBY	Treasure Bay	LKH	GE01_20160622161137_1050010005139300_16JUN22161137-M1BS-503164773090_01_P007
22WHW	Whiskey Harbour Wetland	LKH	TRIPLESAT_1_PMS_20170503152136_000EADVI_019
23ACK	Anderson Creek	LKH	WV02_20170825165527_103001006CC28400_17AUG25165527-M1BS-501783541090_01_P007
27FPT	Frances Point	LKH	Multispectral spectral data extracted from UAV acquisition by Wildlife and Landscape Science Directorate on 2019-05-28

APPENDIX C: Statistical model terms for DEM correction

unique_ID	WETLAND_NA	Correction model resolution (m)	Elevation validity range (m)	Correction Model Terms						
				C	I	I**2	v	v**2	I*v	I*(v**2)
1HIE	Hill island	2	73.77 - 79.55	0.263	-0.021	-0.744	-1.222	-0.657	-17.327	0
2ACM	Airport Creek Marsh	2	74.06 - 76.16	1.442	5.884	1.799	0	0	0	0
3SBM	South Bay Marsh	2	73.85 - 76.73	0.598	-1.174	0.204	-2.359	1.058	15.773	6.326
5LCM	Lynde Creek Marsh	4	73.77 - 78.72	0.168	0	0	-1.247	0	0	12.985
6JSM	Jordan Station Marsh	2	73.87 - 86.42	0.343	0	0	0	0	0	0
7GRM	Grand River Mouth Wetlands	14	172.4 - 175.98	0.276	5.166	0.826	3.012	-2.22	105.688	-73.03
8SPP	Selkirk Provincial Park	2	172.72 - 177.83	0.301	-1.682	0.318	-1.324	0	0	0
9LPW	Long Point Wetland	2	172.79 - 176.84	0.631	-2.954	-1.715	0	-0.855	16.925	0
10RBY	Rondeau Bay	2	172.29 - 175.4	0.394	-0.649	0	-0.86	0	-2.463	0
11FCK	Fox Creek / Dolson's Creek	1	172.78 - 175.49	0.239	-0.557	0	0	0	0	0
12DRM	Detroit River Marshes	8	173.32 - 177.2	0.051	4.541	-8.814	5.231	-4.169	-108.462	50.69
13LSC	Lake St. Clair Marshes	2	173.19 - 176.71	0.553	-1.548	-0.948	-1.223	-0.882	0	0
15BDD	Baie Du Dore	4	175.21 - 177.37	0.317	-1.947	1.98	0	0.448	1.492	0
16HBW	Hay Bay Wetland	2	175.08 - 178.25	0.263	-1.33	1.372	1.083	0.996	-16.231	0
18HGW	Hog Bay Wetland	2	171.92 - 179.64	0.461	-1.268	0.063	-2.437	-0.593	0	3.987
19TBY	Treasure Bay	2	175.13 - 178.66	0.212	-1.011	0.585	-1.808	-0.162	0	15.57
22WHW	Whiskey Harbour Wetland	2	175.01 - 177.17	0.387	0	2.905	-2.39	-0.22	-27.465	19.87
23ACK	Anderson Creek	2	174.41 - 185.87	0.236	-2.677	0.894	-0.375	0.552	-3.575	7.854
27FPT	Frances Point	2	176.95-183.94	0.469	-0.166	0	0.78	0.247	0	2.815

C = Model's specific constant value

I = Uncorrected LIDAR DEM elevation

v =NDVI value

APPENDIX D: ASPRS Standard Lidar Point Classes

Classification Value	Meaning
0	Created, never classified
1	Unclassified ¹
2	Ground
3	Low Vegetation
4	Medium Vegetation
5	High Vegetation
6	Building
7	Low Point (“low noise”)
8	High Point (typically “high noise”). Note that this value was previously used for Model Key Points. Bit 1 of the Classification Flag must now be used to indicate Model Key Points. This allows the model key point class to be preserved.
9	Water
10	Rail
11	Road Surface
12	Bridge Deck
13	Wire - Guard
14	Wire – Conductor (Phase)
15	Transmission Tower
16	Wire-structure Connector (e.g. Insulator)
17	Reserved
18-63	Reserved
64-255	User definable – The specific use of these classes should be encoded in the Classification lookup VLR.

Source: ASPRS (2011): https://www.asprs.org/wp-content/uploads/2010/12/LAS_1-4_R6.pdf

APPENDIX E: Species frequency by water body

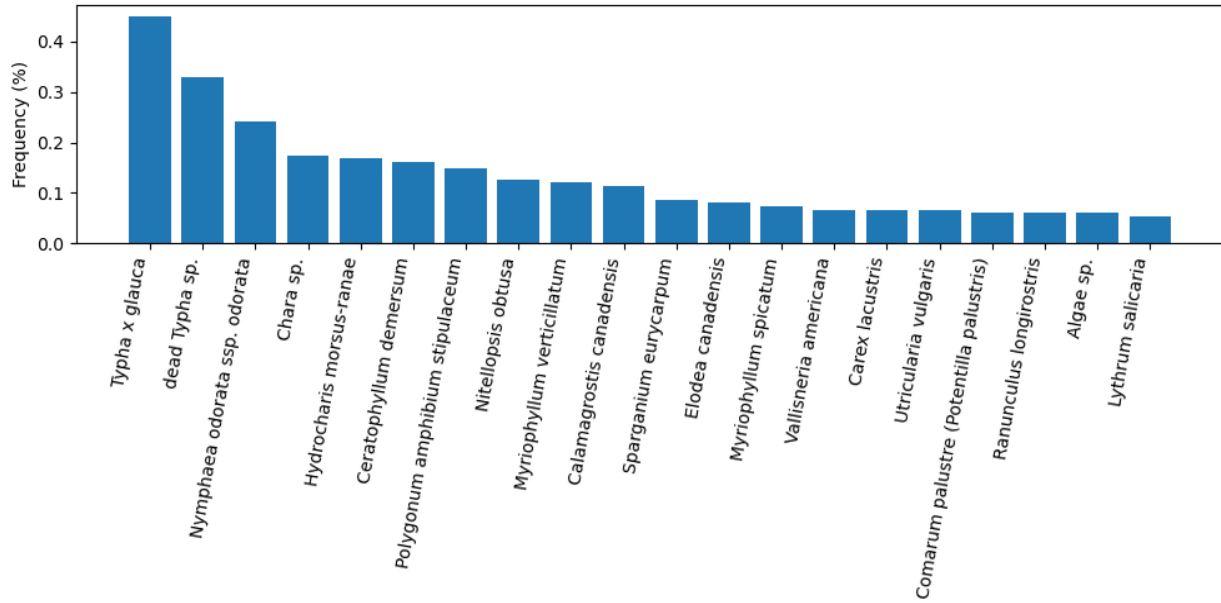


Figure E-1: Species frequency (%) for the 20 most frequent species in Upper Saint-Lawrence.

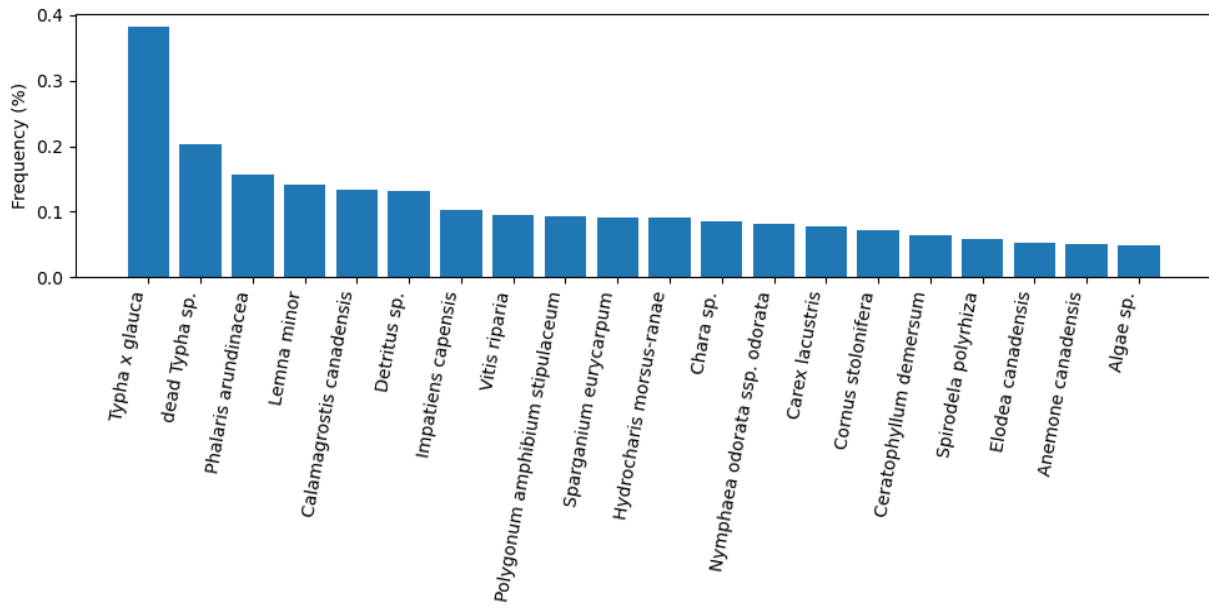


Figure E-2: Species frequency (%) for the 20 most frequent species in Lake Ontario.

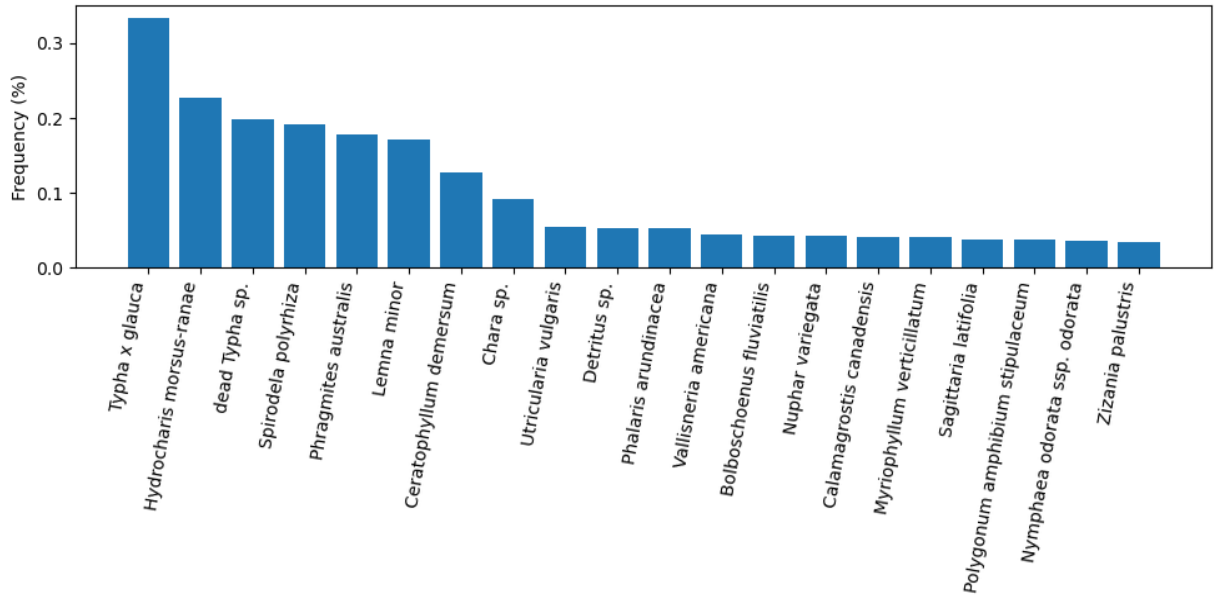


Figure E-3: Species frequency (%) for the 20 most frequent species in Lake Erie.

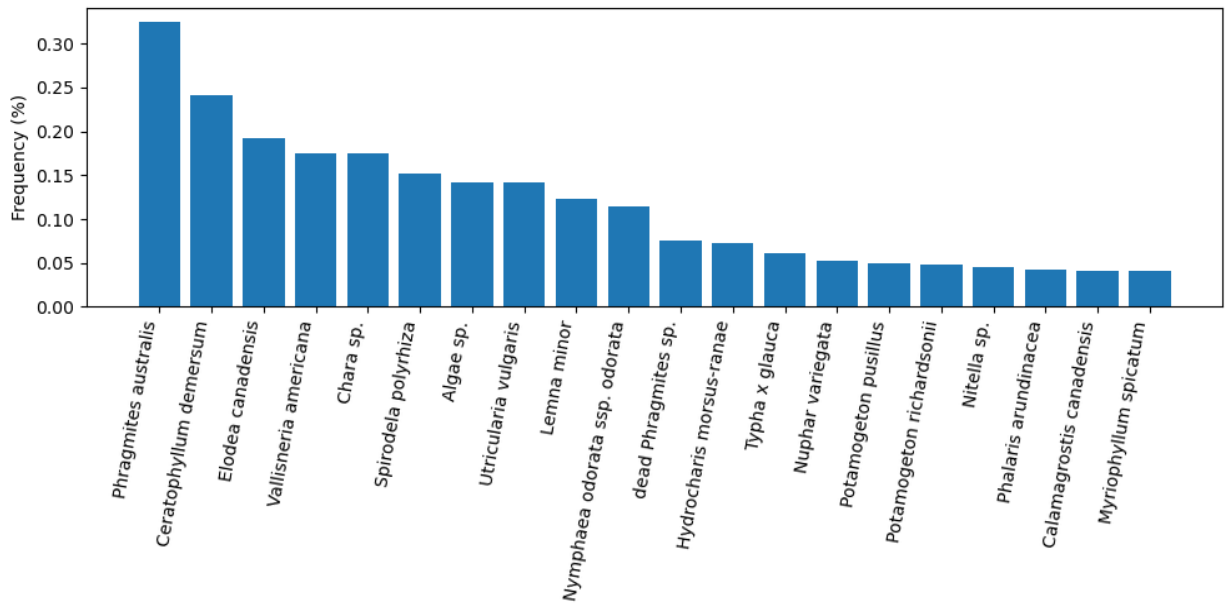


Figure E-4: Species frequency (%) for the 20 most frequent species in Lake St. Clair.

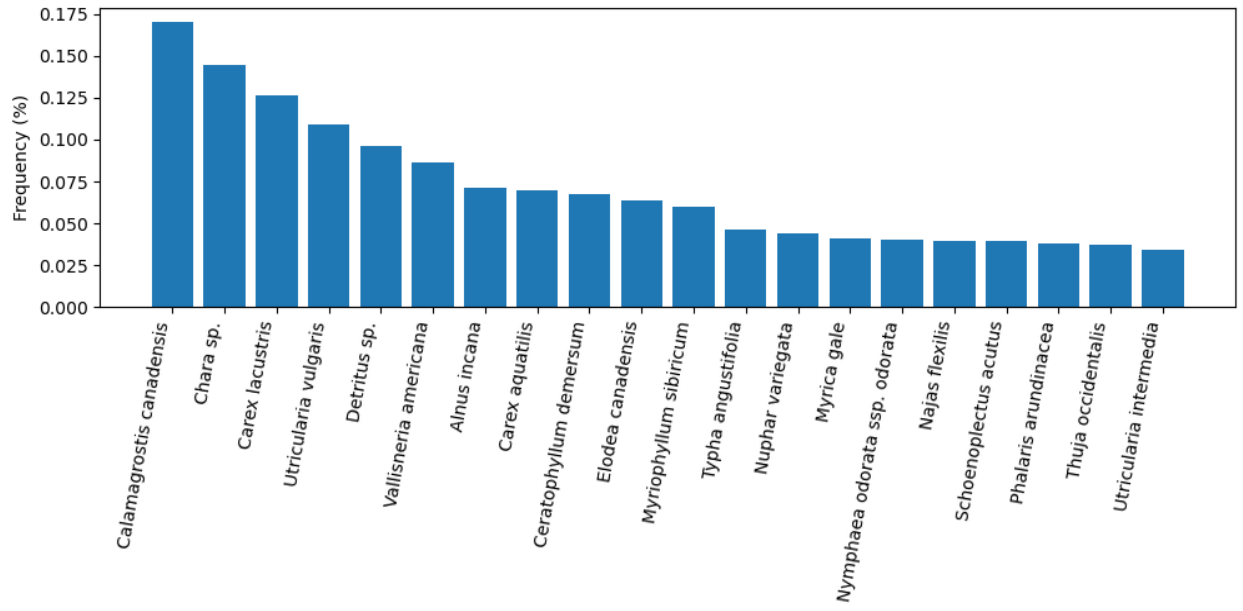


Figure E-5: Species frequency (%) for the 20 most frequent species in Lake Huron.

APPENDIX F: Observed species

Table F-1: List of observed species in the vegetation surveys for all wetland sites.

Species	Native status
<i>Abies balsamea</i>	Native
<i>Acer negundo</i>	Native
<i>Acer pensylvanicum</i>	Native
<i>Acer rubrum</i>	Native
<i>Acer saccharinum</i>	Native
<i>Acer saccharum</i>	Native
<i>Acer sp.</i>	Unspecified
<i>Achillea millefolium</i>	Native
<i>Acorus americanus</i>	Native
<i>Acorus calamus</i>	Exotic
<i>Actaea pachypoda</i>	Native
<i>Actaea sp.</i>	Unspecified
<i>Agalinis purpurea</i>	Native
<i>Agrimonia gryposepala</i>	Native
<i>Agrimonia sp.</i>	Unspecified
<i>Agrostis gigantea</i>	Exotic
<i>Agrostis hyemalis</i>	Native
<i>Agrostis scabra</i>	Native
<i>Agrostis stolonifera</i>	Exotic
<i>Algae sp.</i>	Unspecified
<i>Alisma plantago-aquatica</i>	Exotic
<i>Alliaria petiolata</i>	Exotic
<i>Alnus incana</i>	Native
<i>Alnus incana ssp. rugosa</i>	Native
<i>Alnus viridis ssp. Sinuata</i>	Native
<i>Ambrosia artemisiifolia</i>	Native
<i>Ambrosia trifida</i>	Native
<i>Amelanchier sp.</i>	Unspecified

<i>Amphicarpaea bracteata</i>	Native
<i>Andropogon gerardii</i>	Native
<i>Anemone canadensis</i>	Native
<i>Anemone cylindrica</i>	Native
<i>Anemone virginiana</i>	Native
<i>Angelica sylvestris</i>	Native
<i>Apios americana</i>	Native
<i>Apocynum androsaemifolium</i>	Native
<i>Apocynum cannabinum</i>	Native
<i>Apocynum</i> sp.	Native
<i>Aralia elata</i>	Native
<i>Aralia nudicaulis</i>	Native
<i>Arctium minus</i>	Exotic
<i>Arctostaphylos uva-ursi</i>	Native
<i>Argentina anserina</i> (<i>Potentilla anserina</i>)	Native
<i>Arisaema triphyllum</i>	Native
<i>Arrhenatherum elatius</i>	Native
<i>Artemisia campestris</i>	Native
<i>Artemisia</i> sp.	Unspecified
<i>Asclepias incarnata</i>	Native
<i>Asclepias syriaca</i>	Native
<i>Aster</i> sp.	Unspecified
<i>Astragalus</i> sp.	Unspecified
<i>Athyrium filix-femina</i>	Native
<i>Azolla caroliniana</i>	Native
<i>Azolla cristata</i>	Native
<i>Baptisia australis</i>	Native
<i>Betula alleghaniensis</i>	Native
<i>Betula papyrifera</i>	Native
<i>Bidens aristosa</i>	Native
<i>Bidens beckii</i>	Native
<i>Bidens cernua</i>	Native

<i>Bidens connata</i>	Native
<i>Bidens discoidea</i>	Native
<i>Bidens frondosa</i>	Native
<i>Bidens</i> sp.	Native
<i>Bidens tripartita</i>	Native
<i>Boehmeria cylindrica</i>	Native
<i>Bolboschoenus fluviatilis</i>	Native
<i>Brasenia schreberi</i>	Native
<i>Bromus inermis</i>	Exotic
Bryophyte sp.	Unspecified
<i>Butomus umbellatus</i>	Exotic
<i>Calamagrostis canadensis</i>	Native
<i>Calamagrostis</i> sp.	Native
<i>Calamagrostis stricta</i> subsp. <i>inexpansa</i>	Native
<i>Calla palustris</i>	Native
<i>Callitriche hermaphroditica</i>	Native
<i>Callitriche heterophylla</i> var. <i>heterophylla</i>	Native
<i>Callitriche palustris</i>	Native
<i>Caltha palustris</i>	Native
<i>Calystegia sepium</i>	Native
<i>Campanula aparinoides</i>	Native
<i>Campanula rotundifolia</i>	Native
<i>Campanula</i> sp.	Native
<i>Cardamine</i> sp.	Unspecified
<i>Carduus nutans</i> ssp. <i>nutans</i>	Exotic
<i>Carex aquatilis</i>	Native
<i>Carex atherodes</i>	Native
<i>Carex aurea</i>	Native
<i>Carex blanda</i>	Native
<i>Carex brunnescens</i>	Native
<i>Carex buxbaumii</i>	Native
<i>Carex canescens</i>	Native

Carex communis	Native
Carex comosa	Native
Carex crawei	Native
Carex crawfordii	Native
Carex crinita	Native
Carex diandra	Native
Carex disperma	Native
Carex eburnea	Native
Carex echinata	Native
Carex flava	Native
Carex gracillima	Native
Carex granularis	Native
Carex hystericina	Native
Carex intumescens	Native
Carex lacustris	Native
Carex laeviconica	Native
Carex lasiocarpa	Native
Carex leptalea	Native
Carex limosa	Native
Carex magellanica	Native
Carex pellita	Native
Carex pennsylvanica	Native
Carex prairea	Native
Carex projecta	Native
Carex pseudocyperus	Native
Carex retrorsa	Native
Carex rostrata	Native
Carex scoparia	Native
Carex sp.	Native
Carex stipata	Native
Carex stricta	Native
Carex tribuloides	Native

Carex trisperma	Native
Carex utriculata	Native
Carex vesicaria	Native
Carex vulpinoidea	Native
Carya cordiformis	Native
Carya ovata	Native
Celastrus scandens	Native
Celtis occidentalis	Native
Cephalanthus occidentalis	Native
Ceratophyllum demersum	Native
Chamaedaphne calyculata	Native
Chara sp.	Unspecified
Chelone glabra	Native
Chenopodium glaucum	Exotic
Cichorium intybus	Native
Cicuta bulbifera	Native
Cicuta maculata var. maculata	Native
Cicuta sp.	Native
Cinna arundinacea	Native
Circaea alpina	Native
Circaea canadensis	Native
Circaea lutetiana (C. quadrisulcata)	Native
Cirsium arvense	Exotic
Cirsium muticum	Native
Cirsium sp.	Unspecified
Cirsium vulgare	Exotic
Cladium mariscoides	Native
Clematis sp.	Unspecified
Clematis virginiana	Native
Clinopodium vulgare	Native
Clintonia borealis	Native
Comandra umbellata	Native

Comarum palustre (Potentilla palustris)	Native
Convallaria majalis	Exotic
Convolvulus arvensis	Exotic
Convolvulus sp.	Unspecified
Conyza canadensis (Erigeron canadensis)	Native
Cornus amomum	Native
Cornus foemina	Native
Cornus obliqua	Native
Cornus racemosa	Native
Cornus rugosa	Native
Cornus sp.	Native
Cornus stolonifera	Native
Crataegus sp.	Unspecified
Cuscuta gronovii	Native
Cyperus bipartitus	Native
Cyperus esculentus	Native
Dactylis glomerata	Exotic
Danthonia spicata	Native
Dasiphora fruticosa	Native
Daucus carota	Native
Decodon verticillatus	Native
Deschampsia cespitosa	Native
Deschampsia flexuosa	Native
Detritus sp.	Unspecified
Dichanthelium implicatum	Native
Dichanthelium sp.	Unspecified
Diervilla lonicera	Native
Digitaria sanguinalis	Native
Dipsacus fullonum	Native
Doellingeria umbellata	Native
Drosera linearis	Native
Drosera rotundifolia	Native

<i>Dryopteris carthusiana</i>	Native
<i>Dryopteris cristata</i>	Native
<i>Dryopteris intermedia</i>	Native
<i>Dryopteris marginalis</i>	Native
<i>Dulichium arundinaceum</i>	Native
<i>Echinochloa crus-galli</i>	Exotic
<i>Echinocystis lobata</i>	Native
<i>Elaeagnus umbellata</i>	Exotic
<i>Eleocharis acicularis</i>	Native
<i>Eleocharis compressa</i>	Native
<i>Eleocharis elliptica</i>	Native
<i>Eleocharis obtusa</i>	Native
<i>Eleocharis palustris</i>	Native
<i>Eleocharis quadrangulata</i>	Native
<i>Eleocharis quinqueflora</i>	Native
<i>Eleocharis rostellata</i>	Native
<i>Eleocharis smallii</i>	Native
<i>Eleocharis</i> sp.	Native
<i>Elodea canadensis</i>	Native
<i>Elodea nuttallii</i>	Native
<i>Elymus canadensis</i>	Native
<i>Elymus repens</i>	Exotic
<i>Elymus trachycaulus</i>	Native
<i>Epilobium ciliatum</i>	Native
<i>Epilobium coloratum</i>	Native
<i>Epilobium hirsutum</i>	Exotic
<i>Epilobium leptophyllum</i>	Native
<i>Epilobium parviflorum</i>	Exotic
<i>Epilobium</i> sp.	Unspecified
<i>Epipactis helleborine</i>	Exotic
<i>Equisetum arvense</i>	Native
<i>Equisetum fluviatile</i>	Native

<i>Equisetum hyemale</i>	Native
<i>Equisetum palustre</i>	Native
<i>Equisetum pratense</i>	Native
<i>Equisetum</i> sp.	Native
<i>Equisetum sylvaticum</i>	Native
<i>Equisetum variegatum</i>	Native
<i>Erechtites hieracifolia</i>	Native
<i>Eriocaulon aquaticum</i>	Native
<i>Euonymus alatus</i>	Exotic
<i>Eupatorium perfoliatum</i>	Native
<i>Eurybia macrophylla</i>	Native
<i>Euthamia graminifolia</i>	Native
<i>Eutrochium maculatum</i>	Native
<i>Fagus grandifolia</i>	Native
<i>Fallopia convolvulus</i>	Exotic
<i>Fallopia scandens</i>	Native
<i>Festuca</i> sp.	Unspecified
<i>Filipendula ulmaria</i> ssp. <i>ulmaria</i>	Exotic
<i>Fragaria</i> sp.	Unspecified
<i>Fragaria vesca</i>	Native
<i>Fragaria virginiana</i>	Native
<i>Frangula alnus</i>	Exotic
<i>Fraxinus americana</i>	Native
<i>Fraxinus nigra</i>	Native
<i>Fraxinus pennsylvanica</i>	Native
<i>Fraxinus</i> sp.	Native
<i>Galium aparine</i>	Exotic
<i>Galium asprellum</i>	Native
<i>Galium boreale</i>	Native
<i>Galium mollugo</i>	Exotic
<i>Galium palustre</i>	Native
<i>Galium</i> sp.	Unspecified

<i>Galium tinctorium</i>	Native
<i>Galium tricornutum</i>	Exotic
<i>Galium trifidum</i>	Native
<i>Gaultheria procumbens</i>	Native
<i>Gaylussacia baccata</i>	Native
<i>Gentiana andrewsii</i>	Native
<i>Geranium maculatum</i>	Native
<i>Geranium robertianum</i>	Native
<i>Geum aleppicum</i>	Native
<i>Geum canadense</i>	Native
<i>Geum rivale</i>	Native
<i>Geum sp.</i>	Native
<i>Glechoma hederacea</i>	Exotic
<i>Glyceria canadensis</i>	Native
<i>Glyceria grandis</i>	Native
<i>Glyceria sp.</i>	Native
<i>Glyceria striata</i>	Native
<i>Helianthus giganteus</i>	Native
<i>Helianthus tuberosus</i>	Native
<i>Heracleum maximum</i>	Native
<i>Hesperis matronalis</i>	Exotic
<i>Heteranthera dubia</i>	Native
<i>Hibiscus moscheutos</i>	Native
<i>Hieracium aurantiacum</i>	Exotic
<i>Hieracium caespitosum</i>	Exotic
<i>Hieracium sp.</i>	Unspecified
<i>Hydrocharis morsus-ranae</i>	Exotic
<i>Hydrodictyon sp.</i>	Unspecified
<i>Hypericum canadense</i>	Native
<i>Hypericum kalmianum</i>	Native
<i>Hypericum majus</i>	Native
<i>Hypericum perforatum</i>	Exotic

<i>Hypericum prolificum</i>	Native
<i>Hypericum</i> sp.	Unspecified
<i>Ilex mucronata</i>	Native
<i>Ilex verticillata</i>	Native
<i>Impatiens capensis</i>	Native
<i>Inula helenium</i>	Exotic
<i>Iris pseudacorus</i>	Exotic
<i>Iris</i> sp.	Unspecified
<i>Iris versicolor</i>	Native
<i>Isoetes lacustris</i>	Native
<i>Isoetes</i> sp.	Unspecified
<i>Juglans nigra</i>	Native
<i>Juncus acuminatus</i>	Native
<i>Juncus arcticus</i> ssp. <i>littoralis</i>	Native
<i>Juncus articulatus</i>	Native
<i>Juncus brachycephalus</i>	Native
<i>Juncus brevicaudatus</i>	Native
<i>Juncus canadensis</i>	Native
<i>Juncus compressus</i>	Exotic
<i>Juncus dudleyi</i>	Native
<i>Juncus effusus</i>	Native
<i>Juncus nodosus</i>	Native
<i>Juncus pelocarpus</i>	Native
<i>Juncus</i> sp.	Unspecified
<i>Juncus tenuis</i>	Native
<i>Juncus torreyi</i>	Native
<i>Juniperus communis</i>	Native
<i>Juniperus horizontalis</i>	Native
<i>Juniperus virginiana</i>	Native
<i>Justicia americana</i>	Native
<i>Kalmia polifolia</i>	Native
<i>Lactuca biennis</i>	Native

Lactuca sp.	Unspecified
Lamium purpureum	Exotic
Laportea canadensis	Native
Larix laricina	Native
Lathyrus japonicus	Native
Lathyrus latifolius	Exotic
Lathyrus palustris	Native
Leersia oryzoides	Native
Leersia virginica	Native
Lemna minor	Native
Lemna sp.	Native
Lemna trisulca	Native
Leucanthemum vulgare	Exotic
Lichen sp.	Unspecified
Linaria vulgaris	Exotic
Lindera benzoin	Native
Littorella americana	Native
Lobelia cardinalis	Native
Lobelia kalmii	Native
Lonicera canadensis	Native
Lonicera dioica	Native
Lonicera involucrata	Native
Lonicera morrowii	Exotic
Lonicera oblongifolia	Native
Lonicera sp.	Unspecified
Lonicera tatarica	Exotic
Lonicera villosa	Native
Lonicera x bella	Exotic
Lotus corniculatus	Exotic
Ludwigia palustris	Native
Lycopus americanus	Native
Lycopus europaeus	Exotic

Lycopus sp.	Unspecified
Lycopus uniflorus	Native
Lysimachia ciliata	Native
Lysimachia nummularia	Exotic
Lysimachia quadriflora	Native
Lysimachia quadrifolia	Native
Lysimachia sp.	Unspecified
Lysimachia terrestris	Native
Lysimachia thyrsoflora	Native
Lythrum salicaria	Exotic
Maianthemum canadense	Native
Maianthemum racemosum	Native
Maianthemum stellatum	Native
Maianthemum trifolium	Native
Malus sp.	Unspecified
Matteuccia struthiopteris	Native
Medicago lupulina	Exotic
Medicago sativa	Exotic
Melampyrum lineare	Native
Melilotus albus	Exotic
Mentha arvensis	Native
Mentha canadensis	Native
Mentha sp.	Unspecified
Mentha spicata	Exotic
Mentha x gracilis	Exotic
Menyanthes trifoliata	Native
Mimulus ringens	Native
Mitella nuda	Native
Moehringia lateriflora	Native
Monarda fistulosa	Native
Moss sp.	Unspecified
Muhlenbergia glomerata	Native

<i>Myosotis scorpioides</i>	Exotic
<i>Myrica gale</i>	Native
<i>Myriophyllum sibiricum</i>	Native
<i>Myriophyllum</i> sp.	Unspecified
<i>Myriophyllum spicatum</i>	Exotic
<i>Myriophyllum verticillatum</i>	Native
<i>Najas flexilis</i>	Native
<i>Najas gracillima</i>	Native
<i>Najas guadalupensis</i>	Native
<i>Najas minor</i>	Exotic
<i>Najas</i> sp.	Unspecified
<i>Nelumbo lutea</i>	Native
<i>Nitella</i> sp.	Unspecified
<i>Nitellopsis obtusa</i>	Exotic
<i>Nuphar variegata</i>	Native
<i>Nymphaea odorata</i> ssp. <i>odorata</i>	Native
<i>Nymphoides cordata</i>	Exotic
<i>Oenothera biennis</i>	Native
<i>Oligoneuron album</i> (<i>Solidago ptarmicoides</i>)	Native
<i>Onoclea sensibilis</i>	Native
<i>Osmunda claytoniana</i>	Native
<i>Osmunda regalis</i>	Exotic
<i>Ostrya virginiana</i>	Native
<i>Oxalis acetosella</i>	Exotic
<i>Oxalis</i> sp.	Unspecified
<i>Oxalis stricta</i>	Native
<i>Panicum capillare</i>	Native
<i>Panicum</i> sp.	Native
<i>Panicum virgatum</i>	Native
<i>Parnassia glauca</i>	Native
<i>Parnassia palustris</i>	Exotic
<i>Parthenocissus quinquefolia</i>	Native

<i>Parthenocissus vitacea</i>	Native
<i>Pastinaca sativa</i>	Exotic
<i>Penthorum sedoides</i>	Native
<i>Persicaria amphibia</i>	Native
<i>Persicaria</i> sp.	Unspecified
<i>Phalaris arundinacea</i>	Native
<i>Phleum pratense</i>	Exotic
<i>Phragmites americanus</i>	Native
<i>Phragmites australis</i>	Exotic
<i>Physalis</i> sp.	Unspecified
<i>Physocarpus opulifolius</i>	Native
<i>Physostegia virginiana</i>	Native
<i>Picea glauca</i>	Native
<i>Picea mariana</i>	Native
<i>Pilea fontana</i>	Native
<i>Pilea pumila</i>	Native
<i>Pinus strobus</i>	Native
<i>Plantago lanceolata</i>	Exotic
<i>Plantago major</i>	Exotic
<i>Pleurozium schreberi</i>	Native
<i>Poa compressa</i>	Exotic
<i>Poa palustris</i>	Native
<i>Poa pratensis</i>	Exotic
<i>Poa</i> sp.	Unspecified
Poaceae sp.	Unspecified
<i>Polygala senega</i>	Native
<i>Polygaloides paucifolia</i>	Native
<i>Polygonatum biflorum</i>	Native
<i>Polygonatum pubescens</i>	Native
<i>Polygonatum</i> sp.	Native
<i>Polygonum amphibium stipulaceum</i>	Native
<i>Polygonum cilinode</i>	Native

<i>Polygonum hydropiper</i>	Exotic
<i>Polygonum hydropiperoides</i>	Native
<i>Polygonum lapathifolium</i>	Native
<i>Polygonum persicaria</i>	Exotic
<i>Polygonum punctatum</i> var. <i>punctatum</i>	Native
<i>Polygonum sagittatum</i>	Native
<i>Polygonum</i> sp.	Unspecified
<i>Polygonum virginiana</i>	Native
<i>Polypodium virginianum</i>	Native
<i>Pontederia cordata</i>	Native
<i>Populus balsamifera</i>	Native
<i>Populus deltoides</i>	Native
<i>Populus grandidentata</i>	Native
<i>Populus</i> sp.	Unspecified
<i>Populus tremuloides</i>	Native
<i>Potamogeton alpinus</i>	Native
<i>Potamogeton amplifolius</i>	Native
<i>Potamogeton crispus</i>	Exotic
<i>Potamogeton foliosus</i>	Native
<i>Potamogeton friesii</i>	Native
<i>Potamogeton gramineus</i>	Native
<i>Potamogeton illinoensis</i>	Native
<i>Potamogeton natans</i>	Native
<i>Potamogeton nodosus</i>	Native
<i>Potamogeton obtusifolius</i>	Native
<i>Potamogeton pectinatus</i> (<i>Stuckenia pectinata</i>)	Native
<i>Potamogeton praelongus</i>	Native
<i>Potamogeton pusillus</i>	Native
<i>Potamogeton richardsonii</i>	Native
<i>Potamogeton robbinsii</i>	Native
<i>Potamogeton</i> sp.	Unspecified
<i>Potamogeton spirillus</i>	Native

Potamogeton strictifolius	Native
Potamogeton vaseyi	Native
Potamogeton zosteriformis	Native
Potentilla norvegica	Native
Potentilla sp.	Unspecified
Proserpinaca palustris	Native
Prunella vulgaris	Native
Prunus pensylvanica	Native
Prunus serotina	Native
Prunus sp.	Unspecified
Prunus virginiana	Native
Pteridium aquilinum	Native
Pyrola asarifolia	Native
Pyrola sp.	Unspecified
Quercus alba	Native
Quercus rubra	Native
Ranunculus acris	Exotic
Ranunculus aquatilis	Native
Ranunculus hispidus var. caricetorum	Native
Ranunculus longirostris	Native
Ranunculus recurvatus	Native
Ranunculus repens	Exotic
Ranunculus sceleratus	Native
Ranunculus sp.	Unspecified
Rhamnus alnifolia	Native
Rhamnus cathartica	Exotic
Rhamnus sp.	Unspecified
Rhus sp.	Unspecified
Rhus typhina	Native
Rhynchospora alba	Native
Rhynchospora capillacea	Native
Ribes americanum	Native

Ribes cynosbati	Native
Ribes hirtellum	Native
Ribes lacustre	Native
Ribes oxycanthoides var. oxycanthoides	Native
Ribes sp.	Unspecified
Ribes triste	Native
Riccia fluitans	Native
Ricciaceae sp.	Unspecified
Ricciocarpos natans	Native
Ricciocarpus sp.	Unspecified
Rorippa palustris	Native
Rosa blanda	Native
Rosa multiflora	Exotic
Rosa nitida	Native
Rosa palustris	Native
Rosa sp.	Unspecified
Rubus allegheniensis	Native
Rubus fruticosus	Exotic
Rubus hispidus	Native
Rubus idaeus	Exotic
Rubus idaeus ssp. idaeus	Exotic
Rubus occidentalis	Exotic
Rubus odoratus	Native
Rubus pubescens	Native
Rubus setosus	Native
Rubus sp.	Unspecified
Rumex acetosella	Exotic
Rumex crispus	Exotic
Rumex obtusifolius	Exotic
Rumex orbiculatus	Native
Rumex sp.	Unspecified
Rumex verticillatus	Native

Sagittaria cristata	Native
Sagittaria cuneata	Native
Sagittaria graminea	Native
Sagittaria latifolia	Native
Sagittaria rigida	Native
Sagittaria sp.	Unspecified
Salix alba	Exotic
Salix amygdaloides	Native
Salix bebbiana	Native
Salix candida	Native
Salix discolor	Native
Salix eriocephala	Native
Salix exigua	Native
Salix fragilis	Exotic
Salix lucida	Native
Salix nigra	Native
Salix pedicellaris	Native
Salix pellita	Native
Salix petiolaris	Native
Salix serissima	Native
Salix sp.	Unspecified
Salix x fragilis	Exotic
Sambucus nigra L. ssp. Canadensis	Native
Sanicula marilandica	Native
Saponaria officinalis	Exotic
Sarracenia purpurea	Native
Sassafras albidum	Native
Sassafras sp.	Unspecified
Schizachyrium scoparium	Native
Schoenoplectus acutus	Native
Schoenoplectus americanus	Native
Schoenoplectus pungens	Native

<i>Schoenoplectus subterminalis</i>	Native
<i>Schoenoplectus tabernaemontani</i>	Native
<i>Scirpus atrovirens</i>	Native
<i>Scirpus cyperinus</i>	Native
<i>Scirpus microcarpus</i>	Native
<i>Scirpus</i> sp.	Unspecified
<i>Scutellaria galericulata</i>	Native
<i>Scutellaria lateriflora</i>	Native
<i>Scutellaria</i> sp.	Unspecified
<i>Securigera varia</i>	Exotic
<i>Setaria pumila</i>	Exotic
<i>Setaria viridis</i>	Exotic
<i>Shepherdia canadensis</i>	Native
<i>Silene vulgaris</i>	Exotic
<i>Sisyrinchium montanum</i>	Native
<i>Sisyrinchium</i> sp.	Unspecified
<i>Sium suave</i>	Native
<i>Solanum dulcamara</i>	Exotic
<i>Solidago altissima</i>	Native
<i>Solidago caesia</i>	Native
<i>Solidago canadensis</i>	Native
<i>Solidago gigantea</i>	Native
<i>Solidago juncea</i>	Native
<i>Solidago nemoralis</i>	Native
<i>Solidago ohioensis</i>	Native
<i>Solidago rigida</i>	Native
<i>Solidago rugosa</i>	Native
<i>Solidago</i> sp.	Unspecified
<i>Solidago uliginosa</i>	Native
<i>Sonchus arvensis</i>	Exotic
<i>Sonchus</i> sp.	Unspecified
<i>Sorbaria sorbifolia</i>	Exotic

<i>Sorbus decora</i>	Native
<i>Sorghastrum nutans</i>	Native
<i>Sparganium americanum</i>	Native
<i>Sparganium angustifolium</i>	Native
<i>Sparganium emersum</i>	Native
<i>Sparganium eurycarpum</i>	Native
<i>Sparganium fluctuans</i>	Native
<i>Sparganium natans</i>	Native
<i>Sparganium</i> sp.	Unspecified
<i>Spartina pectinata</i>	Native
<i>Sphagnum</i> sp.	Unspecified
<i>Spiraea alba</i> var. <i>alba</i>	Native
<i>Spiraea alba</i> var. <i>latifolia</i>	Native
<i>Spiraea</i> sp.	Unspecified
<i>Spiraea tomentosa</i>	Native
<i>Spiranthes romanzoffiana</i>	Native
<i>Spirodela polyrhiza</i>	Native
<i>Spongilla</i> sp.	Unspecified
<i>Sporobolus cryptandrus</i>	Native
<i>Sporobolus vaginiflorus</i>	Native
<i>Stachys hispida</i>	Native
<i>Stachys palustris</i>	Exotic
<i>Stachys</i> sp.	Unspecified
<i>Stachys tenuifolia</i>	Native
<i>Stellaria</i> sp.	Unspecified
<i>Strophostyles helvola</i>	Native
<i>Stuckenia filiformis</i> subsp. <i>occidentalis</i>	Native
<i>Stuckenia pectinata</i>	Native
<i>Symphotrichum boreale</i>	Native
<i>Symphotrichum cordifolium</i>	Native
<i>Symphotrichum dumosum</i>	Native
<i>Symphotrichum ericoides</i>	Native

<i>Symphyotrichum laeve</i>	Native
<i>Symphyotrichum lanceolatum</i>	Native
<i>Symphyotrichum lateriflorum</i>	Native
<i>Symphyotrichum novae-angliae</i>	Native
<i>Symphyotrichum pilosum</i>	Native
<i>Symphyotrichum puniceum</i>	Native
<i>Symphyotrichum</i> sp.	Unspecified
<i>Symphyotrichum</i> x <i>amethystinum</i>	Native
<i>Tanacetum vulgare</i>	Exotic
<i>Taraxacum officinale</i>	Exotic
<i>Teucrium canadense</i>	Native
<i>Thalictrum dasycarpum</i>	Native
<i>Thalictrum dioicum</i>	Native
<i>Thalictrum pubescens</i>	Native
<i>Thalictrum</i> sp.	Unspecified
<i>Thelypteris palustris</i>	Native
<i>Thuja occidentalis</i>	Native
<i>Tilia americana</i>	Native
<i>Toxicodendron radicans</i>	Native
<i>Toxicodendron radicans</i> var. <i>rydbergii</i>	Native
<i>Tragopogon dubius</i>	Exotic
<i>Triadenum fraseri</i>	Native
<i>Triadenum virginicum</i>	Native
<i>Trientalis borealis</i>	Native
<i>Trifolium hybridum</i>	Exotic
<i>Trifolium pratense</i>	Exotic
<i>Trifolium repens</i>	Exotic
<i>Triglochin maritimum</i>	Native
<i>Tsuga canadensis</i>	Native
<i>Tussilago farfara</i>	Exotic
<i>Typha angustifolia</i>	Exotic
<i>Typha latifolia</i>	Native

Typha sp.	Unspecified
Typha x glauca	Exotic
Ulmus americana	Native
Ulmus sp.	Unspecified
Urtica dioica ssp. dioica	Exotic
USAV - uprooted SAV	Unspecified
Utricularia cornuta	Native
Utricularia gibba	Native
Utricularia intermedia	Native
Utricularia minor	Native
Utricularia sp.	Unspecified
Utricularia vulgaris	Native
Vaccinium angustifolium	Native
Vaccinium macrocarpon	Native
Vaccinium oxycoccos	Native
Vaccinium sp.	Unspecified
Vallisneria americana	Native
Verbascum thapsus	Exotic
Verbena hastata	Native
Veronica anagallis-aquatica	Native
Veronica officinalis	Exotic
Viburnum lantanoides	Native
Viburnum lentago	Native
Viburnum opulus ssp. opulus	Native
Viburnum opulus ssp. trilobum	Native
Viburnum opulus var. americanum	Native
Viburnum recognitum	Native
Viburnum sp.	Unspecified
Vicia cracca	Exotic
Vicia sp.	Unspecified
Vicia tetrasperma	Exotic
Viola sp.	Unspecified

Vitis aestivalis	Native
Vitis riparia	Native
Vitis sp.	Unspecified
Wolffia columbiana	Native
Wolffia sp.	Unspecified
Xanthium strumarium	Native
Zanthoxylum americanum	Native
Zizania palustris	Native

9. REFERENCES

Section 1: Introduction

Acreman, M. C., Blake, J. R., Booker, D. J., Harding, R. J., Reynard, N., Mountford, J. O. & Stratford, C.J. (2009). A simple framework for evaluating regional wetland ecohydrological response to climate change with case studies from Great Britain. *Ecohydrology*, 2(1), 1-17.

Brazner, J, Sierzen, M.E., Keough, J.R. & Tanner, DK (2001). Assessing the ecological importance of coastal wetlands in a large lake context. *Verhandlungen des Internationalen Verein Limnologie*, 26,1950-1961.

Charron, I. (2016). A Guidebook on Climate Scenarios: Using Climate Information to Guide Adaptation Research and Decisions, 2016 Edition. Ouranos, 94p.

Environment and Climate Change Canada & the U.S. Environmental Protection Agency (2021). *State of the Great Lakes 2019 Technical Report*. Cat No. En161-3/1E-PDF. EPA 905-R-20-044. Available at binational.net.

Great Lakes Coastal Wetland Consortium (2004). Great Lakes Coastal Wetland Inventory. A geospatial dataset published on behalf of the Great Lakes Commission. Ann Arbor, MI.

Host, G. E., Kovalenko, K. E., Brown, T. N., Ciborowski, J. J. & Johnson, L. B. (2019). Risk-based classification and interactive map of watersheds contributing anthropogenic stress to Laurentian Great Lakes coastal ecosystems. *Journal of Great Lakes Research*, 45(3), 609-618.

Mortsch, L., J. Ingram, A. Hebb & Doka, S. (eds) (2006). Great Lakes Coastal Wetland Communities: Vulnerability to Climate Change and Response to Adaptation Strategies. Final report submitted to the Climate Change Impacts and Adaptation Program, Natural Resources Canada. Environment Canada and and Department of Fisheries and Oceans, Toronto, Ontario. 251 pp. + appendices.

Sierszen, M. E., Morrice, J. A., Trebitz, A. S. & Hoffman, J.C (2012). A review of selected ecosystem services provided by coastal wetlands of the Laurentian Great Lakes. *Aquat Ecosystem tHealth Management*, 15(1), 92-106.

Seglenieks, F. & Temgoua, A. (2022). *Future hydroclimate variables and lake levels for the Great Lakes using data from the Coupled Model Intercomparison Project Phase 5*, Environment and Climate Change Canada. [In preparation]

Talbot, A. editor (2006). *Water Availability Issues for the St. Lawrence River: An Environmental Synthesis*. Environment Canada, Montréal. 204 pages.

Taylor, K. E., Stouffer, R. J. & Meehl, G. A. (2012). An overview of CMIP5 and the experiment design. *Bulletin of the American meteorological Society*, 93(4), 485-498.

Wei, A, Chow-Fraser, P & Albert, D (2004). Influence of shoreline features on fish distribution in the Laurentian Great Lakes, *Canadian Journal of Fisheries and Aquatic Sciences*, 61(7):1113–1123.

Section 2: Climate Modelling

Agbazo, M. N. & Grenier, P. (2020). Characterizing and avoiding physical inconsistency generated by the application of univariate quantile mapping on daily minimum and maximum temperatures over Hudson Bay. *International Journal of Climatology*, 40(8), 3868-3884.

Ahmed, K. F., Wang, G., Silander, J., Wilson, A. M., Allen, J. M., Horton, R. & Anyah, R. (2013). Statistical downscaling and bias correction of climate model outputs for climate change impact assessment in the US northeast. *Global and Planetary Change*, 100, 320-332.

Breslow, P. B. & Sailor, D. J. (2002). Vulnerability of wind power resources to climate change in the continental United States. *Renewable Energy*, 27(4), 585-598.

Briley, L. J., Rood, R. B. & Notaro, M. (2021). Large lakes in climate models: A Great Lakes case study on the usability of CMIP5. *Journal of Great Lakes Research*, 47(2), 405-418.

Byun, K. & Hamlet, A. F. (2018). Projected changes in future climate over the Midwest and Great Lakes region using downscaled CMIP5 ensembles. *International Journal of Climatology*, 38, e531-e553.

Carvalho, D. (2019). An assessment of NASA's GMAO MERRA-2 reanalysis surface winds. *Journal of Climate*, 32(23), 8261-8281.

Chen, L. (2020). Impacts of climate change on wind resources over North America based on NA-CORDEX. *Renewable Energy*, 153, 1428-1438.

Costa, A. C. & Soares, A. (2009). Homogenization of climate data: review and new perspectives using geostatistics. *Mathematical geosciences*, 41(3), 291-305.

Cunderlik, J. M. & Burn, D. H. (2004). Linkages between regional trends in monthly maximum flows and selected climatic variables. *Journal of Hydrologic Engineering*, 9(4), 246-256.

Deardorff, J. W. (1968). Dependence of air-sea transfer coefficients on bulk stability. *Journal of geophysical research*, 73(8), 2549-2557.

Decremer, D., Chung, C. E., Ekman, A. M. & Brandefelt, J. (2014). Which significance test performs the best in climate simulations? *Tellus A: Dynamic Meteorology and Oceanography*, 66(1), 231239.

Dee, D.P., with 35 co-authors (2011). The ERA-Interim reanalysis: Configuration and performance of the data assimilation system. *Quarterly Journal of the royal meteorological society*, 137(656), 553-597.

Dullaart, J. C., Muis, S., Bloemendaal, N. & Aerts, J. C. (2020). Advancing global storm surge modelling using the new ERA5 climate reanalysis. *Climate Dynamics*, 54(1), 1007-1021.

Eichenlaub, V. L. (1978). Weather and climate of the Great Lakes region [USA].

Flato, G. M. (2011). Earth system models: an overview. *Wiley Interdisciplinary Reviews: Climate Change*, 2(6), 783-800.

Fletcher, Steven J. Data assimilation for the geosciences: From theory to application. Elsevier, 2017.

Friedlingstein, P., Jones, M. W., O'sullivan, M., Andrew, R. M., Hauck, J., Peters, G. P., ... & Zaehle, S. (2019). Global carbon budget 2019. *Earth System Science Data*, 11(4), 1783-1838.

Gasset, N., Fortin, V., Dimitrijevic, M., Carrera, M., Bilodeau, B., Muncaster, R., ... & Khedhaouiria, D. (2021). A 10 km North American Precipitation and Land Surface Reanalysis Based on the GEM Atmospheric Model. *Hydrology and Earth System Sciences Discussions*, 1-50.

Grenier, P. & Music, B. (2020). *Great Lakes Coastal Wetland Climate Change Vulnerability Assessment: Wind Scenarios Analyses*. Report submitted to Environment and Climate Change Canada, Montréal. 50 p. + 3 Appendices.

Gronewold, A. D., Fortin, V., Lofgren, B., Clites, A., Stow, C. A. & Quinn, F. (2013). Coasts, water levels, and climate change: A Great Lakes perspective. *Climatic Change*, 120(4), 697-711.

Guo, Q., Chen, J., Zhang, X., Shen, M., Chen, H. & Guo, S. (2019). A new two-stage multivariate quantile mapping method for bias correcting climate model outputs. *Climate Dynamics*, 53(5), 3603-3623.

Hansen, J. & Sato, M. (2016). Regional climate change and national responsibilities. *Environmental Research Letters*, 11(3), 034009.

Hausfather, Z. & Peters, G. P. (2020). Emissions—the 'business as usual' story is misleading.

- Hnilica, J., Hanel, M. & Puš, V. (2017). Multisite bias correction of precipitation data from regional climate models. *International Journal of Climatology*, 37(6), 2934-2946.
- Ho, E., Budescu, D. V., Bosetti, V., van Vuuren, D. P. & Keller, K. (2019). Not all carbon dioxide emission scenarios are equally likely: a subjective expert assessment. *Climatic Change*, 155(4), 545-561.
- Jung, C. & Schindler, D. (2019). Changing wind speed distributions under future global climate. *Energy Conversion and Management*, 198, 111841.
- Karnauskas, K. B., Lundquist, J. K. & Zhang, L. (2018). Southward shift of the global wind energy resource under high carbon dioxide emissions. *Nature Geoscience*, 11(1), 38-43.
- Klink, K. (2007). Atmospheric circulation effects on wind speed variability at turbine height. *Journal of applied meteorology and climatology*, 46(4), 445-456.
- Kuiper, N. H. (1960, January). Tests concerning random points on a circle. *Koninklijke Nederlandse Akademie van Wetenschappen Proceedings. Series A*, 63(1), 38-47.
- Kumar, D., Mishra, V. & Ganguly, A. R. (2015). Evaluating wind extremes in CMIP5 climate models. *Climate Dynamics*, 45(1), 441-453.
- Large, W. G. & Crawford, G. B. (1995). Observations and simulations of upper-ocean response to wind events during the ocean storms experiment. *Journal of physical Oceanography*, 25(11), 2831-2852.
- Large, W. G., Morzel, J. & Crawford, G. B. (1995). Accounting for surface wave distortion of the marine wind profile in low-level ocean storms wind measurements. *Journal of Physical Oceanography*, 25(11), 2959-2971.
- Large, W. G. & Pond, S. (1981). Open ocean momentum flux measurements in moderate to strong winds. *Journal of physical oceanography*, 11(3), 324-336.
- Leduc, M., Mailhot, A., Frigon, A., Martel, J. L., Ludwig, R., Brietzke, G. B., ... & Scinocca, J. (2019). The ClimEx project: a 50-member ensemble of climate change projections at 12-km resolution over Europe and northeastern North America with the Canadian Regional Climate Model (CRCM5). *Journal of Applied Meteorology and Climatology*, 58(4), 663-693.

Levene, H. (1960). Contributions to probability and statistics. Essays in honor of Harold Hotelling, 278-292.

Li, X., Zhong, S., Bian, X. & Heilman, W. E. (2010). Climate and climate variability of the wind power resources in the Great Lakes region of the United States. *Journal of Geophysical Research: Atmospheres*, 115(D18).

Lucas-Picher P, Wulff-Nielsen M, Christensen J, Adalgeirsdottir G, Mottram R, Simonsen S (2012) Very high resolution regional climate model simulations over Greenland: Identifying added value. *J Geophys Res Atmos*, 117: D02108.

Mailhot, E., Music, B., Nadeau, D. F., Frigon, A. & Turcotte, R. (2019). Assessment of the Laurentian Great Lakes' hydrological conditions in a changing climate. *Climatic Change*, 157(2), 243-259.

Mann, H. B. & Whitney, D. R. (1947). On a test of whether one of two random variables is stochastically larger than the other. *The annals of mathematical statistics*, 50-60.

Martynov, A., Laprise, R., Sushama, L., Winger, K., Šeparović, L. & Dugas, B. (2013). Reanalysis-driven climate simulation over CORDEX North America domain using the Canadian Regional Climate Model, version 5: model performance evaluation. *Climate Dynamics*, 41(11), 2973-3005.

Mastrandrea, M. D., Mach, K. J., Plattner, G. K., Edenhofer, O., Stocker, T. F., Field, C. B., ... & Matschoss, P. R. (2011). The IPCC AR5 guidance note on consistent treatment of uncertainties: a common approach across the working groups. *Climatic Change*, 108(4), 675-691.

Mearns, L. O., McGinnis, S., Korytina, D., Arritt, R., Biner, S., Bukovsky, M., ...& Gutowski, W. (2017). The NA-CORDEX dataset, version 1.0. *NCAR Climate Data Gateway. Boulder (CO): The North American CORDEX Program*, 10, D6SJ1JCH.

Moeini, M. H., Etemad-Shahidi, A. & Chegini, V. (2010). Wave modelling and extreme value analysis off the northern coast of the Persian Gulf. *Applied Ocean Research*, 32(2), 209-218.

Ozturk, T., Ceber, Z. P., Türkeş, M. & Kurnaz, M. L. (2015). Projections of climate change in the Mediterranean Basin by using downscaled global climate model outputs. *International Journal of Climatology*, 35(14), 4276-4292.

Perkins, S. E., Pitman, A. J., Holbrook, N. J. & McAneney, J. (2007). Evaluation of the AR4 climate models' simulated daily maximum temperature, minimum temperature, and precipitation over Australia using probability density functions. *Journal of climate*, 20(17), 4356-4376.

Pettitt, A. N. & Siskind, V. (1981). Effect of within-sample dependence on the Mann–Whitney–Wilcoxon statistic. *Biometrika*, 68(2), 437-441.

Piani, C. & Haerter, J. O. (2012). Two dimensional bias correction of temperature and precipitation copulas in climate models. *Geophysical Research Letters*, 39(20).

Räisänen, J. (2002), CO₂-induced changes in interannual temperature and precipitation variability in 19 CMIP2 experiments, *Journal of Climate*, 15, 2395–2411.

Riette, S. & Caya, D. (2002). Sensitivity of short simulations to the various parameters in the new CRCM spectral nudging. *Research activities in atmospheric and oceanic modelling*, 39, 40.

Rodionov, S.N. (2005): A brief overview of the regime shift detection methods. In: Large-Scale Disturbances (Regime Shifts) and Recovery in Aquatic Ecosystems: Challenges for Management Toward Sustainability, V. Velikova and N. Chipev (Eds.), UNESCO-ROSTE/BAS Workshop on Regime Shifts, 14-16 June 2005, Varna, Bulgaria, 17-24.

Rusu, L., Bernardino, M. & Soares, C. G. (2009). Influence of wind resolution on the prediction of waves generated in an estuary. *Journal of Coastal Research*, 56(56), 1419-1423.

Saha, S., and Coauthors (2010). The NCEP climate forecast system reanalysis. *Bulletin of the American Meteorological Society*, 91(8), 1015-1058.

Schaaf, B., von Storch, H. & Feser, F. (2017). Does spectral nudging have an effect on dynamical downscaling applied in small regional model domains? *Monthly Weather Review*, 145(10), 4303-4311.

Schaeffer, A., Garreau, P., Molcard, A., Fraunié, P. & Seity, Y. (2011). Influence of high-resolution wind forcing on hydrodynamic modelling of the Gulf of Lions. *Ocean Dynamics*, 61(11), 1823-1844.

Schoof, J. T. & Pryor, S. C. (2014). Assessing the fidelity of AOGCM-simulated relationships between large-scale modes of climate variability and wind speeds. *Journal of Geophysical Research: Atmospheres*, 119(16), 9719-9734.

Separovic, L., de Elía, R. & Laprise, R. (2012). Impact of spectral nudging and domain size in studies of RCM response to parameter modification. *Climate dynamics*, 38(7), 1325-1343.

Shabbar, A., Bonsal, B. & Khandekar, M. (1997). Canadian precipitation patterns associated with the Southern Oscillation. *Journal of Climate*, 10(12), 3016-3027.

Smith, A., Lott, N. & Vose, R. (2011). The integrated surface database: Recent developments and partnerships. *Bulletin of the American Meteorological Society*, 92(6), 704-708.

Solaun, K. & Cerdá, E. (2019). Climate change impacts on renewable energy generation. A review of quantitative projections. *Renewable and Sustainable Energy Reviews*, 116, 109415.

Taylor, K. E., Stouffer, R. J. & Meehl, G. A. (2012). An overview of CMIP5 and the experiment design. *Bulletin of the American meteorological Society*, 93(4), 485-498.

Van Vuuren, D. P., Edmonds, J., Kainuma, M., Riahi, K., Thomson, A., Hibbard, K., ... & Rose, S. K. (2011). The representative concentration pathways: an overview. *Climatic change*, 109(1), 5-31.

Vrac, M. (2018). Multivariate bias adjustment of high-dimensional climate simulations: the Rank Resampling for Distributions and Dependences (R2D2) bias correction. *Hydrology and Earth System Sciences*, 22(6), 3175-3196.

Wang, X. L. (2008). Accounting for autocorrelation in detecting mean shifts in climate data series using the penalized maximal t or F test. *Journal of Applied Meteorology and Climatology*, 47(9), 2423-2444.

Watson, S. (2014). Quantifying the variability of wind energy. *Wiley Interdisciplinary Reviews: Energy and Environment*, 3(4), 330-342.

Weiss C. C. & Sousounis, P. J. (1999) A climatology of collective lake disturbances. *Monthly Weather Review*, 127: 565-574.

Wilcoxon, F. (1945). Individual comparisons by ranking methods. *Biometrics. Bulletin*, 1, 80-83.

WMO (2018): Guide to Instruments and Methods of Observation. Volume I – Measurement of Meteorological Variables. *World Meteorological Organization No.8*, 573p., https://library.wmo.int/doc_num.php?explnum_id=10179

Zwiers, F. W. & Von Storch, H. (1995). Taking serial correlation into account in tests of the mean. *Journal of Climate*, 8(2), 336-351.

Section 3: Great Lakes Physical Modelling

Albert, D. A., Wilcox, D. A., Ingram, J. W. & Thompson, T. A. (2005). Hydrogeomorphic classification for Great Lakes coastal wetlands. *Journal of Great Lakes Research*, 31, 129-146.

Alves, J. H. G., Chawla, A., Tolman, H. L., Schwab, D. J., Lang, G. & Mann, G. (2011, October). *The great lakes wave model at NOAA/NCEP: challenges and future developments*. In 12th International Workshop on Wave Hindcasting and Forecasting, Hawaii.

Alves, J. H. G., Chawla, A., Tolman, H. L., Schwab, D., Lang, G. & Mann, G. (2014). The operational implementation of a Great Lakes wave forecasting system at NOAA/NCEP. *Weather and Forecasting*, 29(6), 1473-1497.

Anderson, E. J. & Schwab, D. J. (2013). Predicting the oscillating bi-directional exchange flow in the Straits of Mackinac. *Journal of Great Lakes Research*, 39(4), 663-671.

Anderson, M. E. & Smith, J. M. (2014). Wave attenuation by flexible, idealized salt marsh vegetation. *Coastal Engineering*, 83, 82-92.

Angel, J. R. (1995). Large-scale storm damage on the US shores of the Great Lakes. *Journal of Great Lakes Research*, 21(3), 287-293.

Angradi, T. R., Pearson, M. S., Bolgrien, D. W., Bellinger, B. J., Starry, M. A. & Reschke, C. (2013). Predicting submerged aquatic vegetation cover and occurrence in a Lake Superior estuary. *Journal of Great Lakes Research*, 39(4), 536-546.

Ardhuin, F., Rogers, E., Babanin, A. V., Filipot, J. F., Magne, R., Roland, A. & Collard, F. (2010). Semiempirical dissipation source functions for ocean waves. Part I: Definition, calibration, and validation. *Journal of Physical Oceanography*, 40(9), 1917-1941.

Assani, A. A., Azouaoui, O., Pothier-Champagne, A. & Quessy, J. F. (2016). Relationship between Water Levels in the North American Great Lakes and Climate Indices. *Lake Sciences and Climate Change*, 25.

Austin, J. A., & Allen, J. (2011). Sensitivity of summer Lake Superior thermal structure to meteorological forcing. *Limnology and Oceanography*, 56(3), 1141-1154.

- Babanin, A. V., Young, I. R. & Banner, M. L. (2001). Breaking probabilities for dominant surface waves on water of finite constant depth. *Journal of Geophysical Research: Oceans*, 106(C6), 11659-11676.
- Bachand, M., Martin, S., Guénard, G., Champoux, O., Callapi, T., Bruxer, J. & Morin, J. (2017). *Scientific Report–SR-113 Ecohydraulic modelling of St. Marys Rapids: Evaluating the impact of gate opening scenarios on the spawning habitat suitability of four species.*
- Badulin, S. I., Pushkarev, A. N., Resio, D. & Zakharov, V. E. (2005). Self-similarity of wind-driven seas. *Nonlinear Processes in Geophysics*, 12(6), 891-945.
- Bai, X., Wang, J., Schwab, D. J., Yang, Y., Luo, L., Leshkevich, G. A. & Liu, S. (2013). Modeling 1993–2008 climatology of seasonal general circulation and thermal structure in the Great Lakes using FVCOM. *Ocean Modelling*, 65, 40-63.
- Bai, P., Wang, J., Chu, P., Hawley, N., Fujisaki-Manome, A., Kessler, J. & Li, Y. (2020). Modeling the ice-attenuated waves in the Great Lakes. *Ocean Dynamics*, 70, 991-1003.
- Battjes, J. A. & Janssen, J. P. F. M. (1978). Energy loss and set-up due to breaking of random waves. In *Coastal engineering 1978*, 569-587.
- Battjes, J. A. (1994). *Shallow water wave modelling*. In the Proceedings of International Symposium: Waves physical and numerical modelling, Vancouver, 1-23.
- Bechle, A. J., Wu, C. H., Kristovich, D. A., Anderson, E. J., Schwab, D. J. & Rabinovich, A. B. (2016). Meteotsunamis in the Laurentian Great Lakes. *Scientific reports*, 6(1), 1-8.
- Beck, H. E., Van Dijk, A. I., Levizzani, V., Schellekens, J., Miralles, D. G., Martens, B. & Roo, A. D. (2017). MSWEP: 3-hourly 0.25 global gridded precipitation (1979–2015) by merging gauge, satellite, and reanalysis data. *Hydrology and Earth System Sciences*, 21(1), 589-615.
- Beletsky, D., Hawley, N., Rao, Y. R., Vanderploeg, H. A., Beletsky, R., Schwab, D. J., & Ruberg, S. A. (2012). Summer thermal structure and anticyclonic circulation of Lake Erie. *Geophysical Research Letters*, 39(6).
- Beletsky, D., Hawley, N., & Rao, Y. R. (2013). Modeling summer circulation and thermal structure of Lake Erie. *Journal of Geophysical Research: Oceans*, 118(11), 6238-6252.

- Blackmon, M. L., Wallace, J. M., Lau, N. C. & Mullen, S. L. (1977). An observational study of the Northern Hemisphere wintertime circulation. *Journal of the Atmospheric Sciences*, 34(7), 1040-1053.
- Bocaniov, S. A., Ullmann, C., Rinke, K., Lamb, K. G., & Boehrer, B. (2014). Internal waves and mixing in a stratified reservoir: Insights from three-dimensional modeling. *Limnologica*, 49, 52-67.
- Boegman, L., Loewen, M. R., Hamblin, P. F., & Culver, D. A. (2001). Application of a two-dimensional hydrodynamic reservoir model to Lake Erie. *Canadian Journal of Fisheries and Aquatic Sciences*, 58(5), 858-869
- Bolsenga, S. J. & Herdendorf, C. E. (Eds.). (1993). *Lake Erie and Lake St. Clair Handbook*. Wayne State University Press.
- Booij, N. R. R. C., Ris, R. C. & Holthuijsen, L. H. (1999). A third-generation wave model for coastal regions: 1. Model description and validation. *Journal of geophysical research: Oceans*, 104(C4), 7649-7666.
- Bouffard, D., Boegman, L., & Rao, Y. R. (2012). Poincaré wave–induced mixing in a large lake. *Limnology and oceanography*, 57(4), 1201-1216.
- Boyce, F. M., Donelan, M. A., Hamblin, P. F., Murthy, C. R. & Simons, T. J. (1989). Thermal structure and circulation in the Great Lakes. *Atmosphere-ocean*, 27(4), 607-642.
- Brant, R. A. & Herdendorf, C. E. (1972). *Delineation of Great Lakes estuaries*. Ohio State University. Center for Lake Erie Area Research.
- Brissette, F. P., Tsanis, I. K. & Wu, J. (1993). Wave directional spectra and wave-current interaction in Lake St. Clair. *Journal of Great Lakes Research*, 19(3), 553-568.
- Bruxer, J., ENG, B. & ENG, P. (2010). *Uncertainty analysis of Lake Erie net basin supplies as computed using the residual method* (Doctoral dissertation, MS thesis, Dept. of Civil Engineering, McMaster University, 238 pp. [Available online at <http://digitalcommons.mcmaster.ca/opendissertations/4987>]).
- Byun, K., Chiu, C. M. & Hamlet, A. F. (2019). Effects of 21st century climate change on seasonal flow regimes and hydrologic extremes over the Midwest and Great Lakes region of the US. *Science of the Total Environment*, 650, 1261-1277.

- Caron, J. F., Milewski, T., Buehner, M., Fillion, L., Reszka, M., Macpherson, S. & St-James, J. (2015). Implementation of deterministic weather forecasting systems based on ensemble–variational data assimilation at Environment Canada. Part II: The regional system. *Monthly Weather Review*, 143(7), 2560-2580.
- Cavaleri, L. (1994). Wave models and input wind. *Wave Dynamics and Modelling of Ocean Waves*, 259, 378.
- Cavaleri, L., Alves, J. H., Ardhuin, F., Babanin, A., Banner, M., Belibassakis, K. & WISE Group. (2007). Wave modelling—the state of the art. *Progress in oceanography*, 75(4), 603-674.
- Cavaleri, L. (2009). Wave modeling—Missing the peaks. *Journal of Physical Oceanography*, 39(11), 2757-2778.
- Chang EK (2013) CMIP5 projection of significant reduction in extratropical cyclone activity over North America. *J Clim* 26:9903–9922. Again, black (white) shaded areas indicated permanently dried (flooded) zones.
- CHC, Canadian Hydraulics Centre, National Research Council (2009). *Preparation of a Hydrodynamic model of Detroit River- St. Clair River waterways with Telemac-2D, CHC-CTR-085*. Ottawa, Ontario.
- Chu, P. Y., Kelley, J. G., Mott, G. V., Zhang, A. & Lang, G. A. (2011). Development, implementation, and skill assessment of the NOAA/NOS Great Lakes Operational Forecast System. *Ocean Dynamics*, 61(9), 1305-1316.
- Clifton, A. & Lundquist, J. K. (2012). Data clustering reveals climate impacts on local wind phenomena. *Journal of Applied Meteorology and Climatology*, 51(8), 1547-1557.
- Colucci, S. J. (1976). winter cyclone frequencies over the eastern United States and adjacent western Atlantic, 1964–1973: Student paper—First place winner of The Father James B. Macelwane Annual Award in Meteorology, announced at the Annual Meeting of the AMS, Philadelphia, Pa., 21 January 1976. *Bulletin of the American Meteorological Society*, 57(5), 548-553.

- Cook, N. J. (2019). The OEN mixture model for the joint distribution of wind speed and direction: A globally applicable model with physical justification. *Energy Conversion and Management*, 191, 141-158.
- Croft, M. V. & Chow-Fraser, P. (2007). Use and development of the wetland macrophyte index to detect water quality impairment in fish habitat of Great Lakes coastal marshes. *Journal of Great Lakes Research*, 33, 172-197.
- Croley, T. E. (1989). Verifiable evaporation modelling on the Laurentian Great Lakes. *Water Resources Research*, 25(5), 781-792.
- Croley, T. E. (1992). Long-term heat storage in the Great Lakes. *Water Resources Research*, 28(1), 69-81.
- Croley, T. E. & Assel, R. A. (1994). A one-dimensional ice thermodynamics model for the Laurentian Great Lakes. *Water Resources Research*, 30(3), 625-639.
- Croley, T. E. (2005). Recent Great Lakes evaporation model estimates. In *Impacts of Global Climate Change* (pp. 1-11).
- Csanady, G. T. (1968). Motions in a model Great Lake due to a suddenly imposed wind. *Journal of Geophysical Research*, 73(20), 6435-6447.
- Csanady, G. T. (1981). Circulation in the coastal ocean. *Advances in Geophysics*, 23, 101-183.
- Cueva, D. A., Monzón, C. O., Filonov, A., Tereshchenko, I., Covarrubias, P. L. & González, J. R. G. (2019). Natural frequencies of seiches in Lake Chapala. *Scientific reports*, 9(1), 1-11.
- Cushman-Roisin, B., Willmott, A. J. & Biggs, N. R. (2005). Influence of stratification on decaying surface seiche modes. *Continental shelf research*, 25(2), 227-242.
- Cushman-Roisin, B. & Beckers, J. M. (2011). The Ekman layer. In *International Geophysics* (Vol. 101, pp. 239-270). Academic Press.
- Dally, W. R. (2019). *Surf zone processes*. In *Encyclopedia of coastal science*, 1654-1663. Springer, Cham.

- Derecki, J. A. & Quinn, F. H. (1990). Comparison of measured and simulated flows during the 15 December 1987 Detroit River flow reversal. *Journal of Great Lakes Research*, 16(3), 426-435.
- DeRoy, E. M. & MacIsaac, H. J. (2020). Impacts of invasive species in the Laurentian Great Lakes. *Contaminants of the Great Lakes*, 135-156.
- Dhatt, G., Touzot, G. & Lefrançois, E. (2005). *Méthode des éléments finis*. Lavoisier.
- Dibling, D. R. (2012). *Development and validation of a high-resolution, nearshore model for Lake Erie (Doctoral dissertation, The Ohio State University)*.
- Dingman, J. S. & Bedford, K. W. (1986). Skill tests and parametric statistics for model evaluation. *Journal of Hydraulic Engineering*, 112(2), 124-140.
- Dodet, G., X. Bertin, N. Bruneau, A. B. Fortunato, A. Nahon, and A. Roland (2013), Wave–current interactions in a wave-dominated tidal inlet, *Journal of Geophysical Research: Oceans*, 118, 1587–1605, doi:10.1002/jgrc.20146.
- Donelan, M. A. (1982). *The dependence of the aerodynamic drag coefficient on wave parameters*. In Proceedings First International Conference on Meteorological and Air-Sea Interaction of the Coastal Zone. American Meteorological Society, 381-387.
- Donelan, M. A. (1990), *Air-sea interaction, in The Sea, vol. 9, Ocean Engineering Science*, edited by B. LeMehaute, and D. M. Hanes, Wiley-Interscience, Hoboken, N. J., 239–292
- Donelan, M. A., Babanin, A. V., Young, I. R. & Banner, M. L. (2006). Wave-follower field measurements of the wind-input spectral function. Part II: Parameterization of the wind input. *Journal of physical oceanography*, 36(8), 1672-1689.
- Donn, W. L. (1959). The Great Lakes storm surge of May 5, 1952. *Journal of Geophysical Research*, 64(2), 191-198.
- Douglass, S. L. (1990). Influence of wind on breaking waves. *Journal of waterway, port, coastal, and ocean engineering*, 116(6), 651-663.
- Dupont, F., Chittibabu, P., Fortin, V., Rao, Y. R. & Lu, Y. (2012). Assessment of a NEMO-based hydrodynamic modelling system for the Great Lakes. *Water Quality Research Journal of Canada*, 47(3-4), 198-214.

ECCC and OMECC (2018). *Canada-Ontario Lake Erie action plan, partnering on achieving phosphorus loading reductions to Lake Erie from Canadian sources*. 2018. In: Environment and climate change Canada and Ontario Ministry of the Environment and climate change, Queen's Printer for Ontario, 84 pp.

Eldeberky, Y. (1995). *Parameterization of triad interaction in wave energy model*. In Proceedings of Coastal Dynamics Conference. Gdansk, Poland, 1995.

Elsayed, M. (2010). An overview of wavelet analysis and its application to ocean wind waves. *Journal of Coastal Research*, 26(3), 535-540.

Farhadzadeh, A. (2017). A study of Lake Erie seiche and low frequency water level fluctuations in the presence of surface ice. *Ocean Engineering*, 135, 117-136.

Fay, D. & Kerlake, H. (2009). *Development of New Stage-Fall-Discharge Equations for The St. Clair and Detroit Rivers*. International Upper Great Lakes Study.

Fernández, L., Calvino, C. & Dias, F. (2021). Sensitivity analysis of wind input parametrizations in the WAVEWATCH III spectral wave model using the ST6 source term package for Ireland. *Applied Ocean Research*, 115, 102826.

Filazzola, A., Blagrove, K., Imrit, M. A. & Sharma, S. (2020). Climate change drives increases in extreme events for lake ice in the Northern Hemisphere. *Geophysical Research Letters*, 47(18), e2020GL089608.

Fletcher, S. J. (2017). *Data assimilation for the geosciences: From theory to application*. Elsevier.

Frieswyk, C. B. & Zedler, J. B. (2007). Vegetation change in Great Lakes coastal wetlands: deviation from the historical cycle. *Journal of Great Lakes Research*, 33(2), 366-380.

Fu, W. & Steinschneider, S. (2019). A diagnostic-predictive assessment of winter precipitation over the Laurentian Great Lakes: Effects of ENSO and other teleconnections. *Journal of Hydrometeorology*, 20(1), 117-137.

Garrison, T. S. (2012). *Oceanography: an invitation to marine science*. Cengage Learning.

- Gasset, N., Fortin, V., Dimitrijevic, M., Carrera, M., Bilodeau, B., Muncaster, R. & Khedhaouiria, D. (2021). A 10 km North American Precipitation and Land Surface Reanalysis Based on the GEM Atmospheric Model. *Hydrology and Earth System Sciences Discussions*, 1-50.
- Gathman, J. P., Albert, D. A. & Burton, T. M. (2005). Rapid plant community response to a water level peak in northern Lake Huron coastal wetlands. *Journal of Great Lakes Research*, 31, 160-170.
- Ghanbari, R. N. & Bravo, H. R. (2008). Coherence between atmospheric teleconnections, Great Lakes water levels, and regional climate. *Advances in Water Resources*, 31(10), 1284-1298.
- Gottgens, J. F., Swartz, B. P., Kroll, R. W. & Eboch, M. (1998). Long-term GIS-based records of habitat changes in a Lake Erie coastal marsh. *Wetlands Ecology and Management*, 6(1), 5-17.
- Grabas, G. P. & Rokitnicki-Wojcik, D. (2015). Characterizing daily water-level fluctuation intensity and water quality relationships with plant communities in Lake Ontario coastal wetlands. *Journal of Great Lakes Research*, 41(1), 136-144.
- Grieco, M. B. & DeGaetano, A. T. (2019). A climatology of extreme wave height events impacting Eastern Lake Ontario shorelines. *Theoretical and Applied Climatology*, 136(1), 543-552.
- Gronewold, A. D., Clites, A. H., Hunter, T. S. & Stow, C. A. (2011). An appraisal of the Great Lakes advanced hydrologic prediction system. *Journal of Great Lakes Research*, 37(3), 577-583.
- Gronewold, A. D., Fortin, V., Lofgren, B. M., Clites, A. H., Stow, C. A. & Quinn, F. H. (2013). Coasts, water levels, and climate change: A Great Lakes perspective. *Climatic Change*, 120(4), 697–711.
- Gronewold, A. D., Anderson, E. J. & Smith, J. (2019). Evaluating operational hydrodynamic models for real-time simulation of evaporation from large lakes. *Geophysical Research Letters*, 46(6), 3263-3269.
- Günther, H., Rosenthal, W. & Dunckel, M. (1981). The response of surface gravity waves to changing wind direction. *Journal of Physical Oceanography*, 11(5), 718-728.
- Harris, R. I. & Cook, N. J. (2014). The parent wind speed distribution: Why Weibull?. *Journal of wind engineering and industrial aerodynamics*, 131, 72-87.

Heniche, M., Secretan, Y., Boudreau, P. & Leclerc, M. (2000). A two-dimensional finite element drying-wetting shallow water model for rivers and estuaries. *Advances in water resources*, 23(4), 359-372.

Hess, K. W., Gross, T. F., Schmalz, R. A., Kelley, J. G. W., Aikman, F., Wei, E. & Vincent, M. S. (2003). *NOS standards for evaluating operational nowcast and forecast hydrodynamic model systems*.

Hands, E. B. (2018). *The Great Lakes as a test model for profile responses to sea-level changes* (pp. 167-190). CRC press.

Hanrahan, J. L., Kravtsov, S. V. & Roebber, P. J. (2010). Connecting past and present climate variability to the water levels of Lakes Michigan and Huron. *Geophysical Research Letters*, 37(1).

Harris, D. L. (1953). Wind tide and seiches in the Great Lakes. *Coastal Engineering Proceedings*, (4), 3-3.

Hasselmann, S., Hasselmann, K., Allender, J. & Barnett, T. P. (1985). Computations and parameterizations of the nonlinear energy transfer in a gravity-wave spectrum. Part II: Parameterizations of the nonlinear energy transfer for application in wave models. *Journal of Physical Oceanography*, 15(11), 1378-1391.

Hasselmann, S. & Hasselmann, K. (1985). Computations and parameterizations of the nonlinear energy transfer in a gravity-wave spectrum. Part I: A new method for efficient computations of the exact nonlinear transfer integral. *Journal of Physical Oceanography*, 15(11), 1369-1377.

Hawley, N. & Niester, J. (1993). Measurement of horizontal sediment transport in Green Bay, May-October, 1989. *Journal of Great Lakes Research*, 19(2), 368-378.

Herdendorf, C. E. (1987). *The ecology of the coastal marshes of western Lake Erie: a community profile*. Ohio State University Columbus.

Hlevca, B., Wells, M. G. & Parker, S. (2015). Amplification of long-period waves in shallow coastal embayments of the Great Lakes. *Environmental Fluid Mechanics*, 15(6), 1181-1213.

Holthuijsen, L. H. (2010). *Waves in oceanic and coastal waters*. Cambridge university press.

Holtschlag, D. J., & Koschik, J. A. (2002). Two-dimensional hydrodynamic model of the St. Clair-Detroit River Waterway in the Great Lakes basin (No. 1). US Department of the Interior, US Geological Survey.

Holtschlag, D. J. & Koschik, J. A. (2005). *Augmenting two-dimensional hydrodynamic simulations with measured velocity data to identify flow paths as a function of depth on Upper St. Clair River in the Great Lakes Basin: Date Posted: June 15, 2005*. US Geological Survey Scientific-Investigations Report, 5081.

Hu, H., van der Westhuysen, A. J., Chu, P. & Fujisaki-Manome, A. (2021). Predicting Lake Erie wave heights using XGBoost and LSTM. *Ocean Modelling*, 101832.

Huang, A., Rao, Y. R., & Zhang, W. (2012). On recent trends in atmospheric and limnological variables in Lake Ontario. *Journal of climate*, 25(17), 5807-5816.

Hudon, C., Gagnon, P., Amyot, J. P., Létourneau, G., Jean, M., Plante, C., ... & Deschênes, M. (2005). Historical changes in herbaceous wetland distribution induced by hydrological conditions in Lake Saint-Pierre (St. Lawrence River, Quebec, Canada). *Hydrobiologia*, 539(1), 205-224.

International Joint Commission (2014). *Lake Ontario St. Lawrence River Plan 2014: Protecting against extreme water levels, restoring wetlands and preparing for climate change*.

Jackson, P. R. (2016). *Seiche-induced unsteady flows in the Huron-Erie Corridor: Spectral analysis of oscillations in stage and discharge in the St. Clair and Detroit Rivers*. River Flow 2016: Iowa City, USA, July 11-14, 2016, 235.

Johnston, C. A., Bedford, B. L., Bourdaghs, M., Brown, T., Frieswyk, C., Tulbure, M., ... & Zedler, J. B. (2007). Plant species indicators of physical environment in Great Lakes coastal wetlands. *Journal of Great Lakes Research*, 33, 106-124.

Jonsson, I. G. & Carlsen, N. A. (1976). Experimental and theoretical investigations in an oscillatory turbulent boundary layer. *Journal of Hydraulic Research*, 14(1), 45-60.

Kantha, L. (2006). A note on the decay rate of swell. *Ocean Modelling*, 11(1-2), 167-173.

Kazor, K. & Hering, A. S. (2015). Assessing the performance of model-based clustering methods in multivariate time series with application to identifying regional wind regimes. *Journal of Agricultural, Biological, and Environmental Statistics*, 20(2), 192-217.

- Keddy, P. A. (1982). Quantifying within-lake gradients of wave energy: interrelationships of wave energy, substrate particle size and shoreline plants in Axe Lake, Ontario. *Aquatic Botany*, 14, 41-58.
- Keddy, P. A. (1983). Shoreline vegetation in Axe Lake, Ontario: effects of exposure on zonation patterns. *Ecology*, 64(2), 331-344.
- Keddy, P. A. & Reznicek, A. A. (1986). Great Lakes vegetation dynamics: the role of fluctuating water levels and buried seeds. *Journal of Great Lakes Research*, 12(1), 25-36.
- Kelley, J. G. W., Chen, Y., Anderson, E. J., Lang, G. A. & Xu, J. (2018). *Upgrade of NOS Lake Erie Operational Forecast System (LEOFS) to FVCOM: Model development and hindcast skill assessment*.
- Keough, J. R., Thompson, T. A., Guntenspergen, G. R. & Wilcox, D. A. (1999). Hydrogeomorphic factors and ecosystem responses in coastal wetlands of the Great Lakes. *Wetlands*, 19(4), 821-834.
- Kumar, R. R., Kumar, B. P., Satyanarayana, A. N. V., Subrahmanyam, D. B., Rao, A. D. & Dube, S. K. (2009). Parameterization of sea surface drag under varying sea state and its dependence on wave age. *Natural hazards*, 49(2), 187-197.
- Lavidas, G. & Polinder, H. (2019, September). *Wind effects in the parametrisation of physical characteristics for a nearshore wave model*. In Proceedings of the 13th European Wave and Tidal Energy Conference (pp. 1-6).
- Lehmann J, Coumou D, Frieler K, Eliseev AV, Levermann A (2014) Future changes in extratropical cyclone tracks and baroclinicity under climate change. *Environmental Research Letters* 9:084002.
- Lemein, T., Albert, D. A. & Tuttle, E. D. G. (2017). Coastal wetland vegetation community classification and distribution across environmental gradients throughout the Laurentian Great Lakes. *Journal of Great Lakes Research*, 43(4), 658-669.
- Lespinas, F., Fortin, V., Roy, G., Rasmussen, P. & Stadnyk, T. (2015). Performance evaluation of the Canadian precipitation analysis (CaPA). *Journal of Hydrometeorology*, 16(5), 2045-2064.

- Li, X., Zhong, S., Bian, X. & Heilman, W. E. (2010). Climate and climate variability of the wind power resources in the Great Lakes region of the United States. *Journal of Geophysical Research: Atmospheres*, 115(D18).
- Lin, S., Boegman, L., & Rao, Y. R. (2021). Characterizing spatial and temporal distributions of turbulent mixing and dissipation in Lake Erie. *Journal of Great Lakes Research*, 47(1), 168-179.
- Lishawa, S. C., Albert, D. A. & Tuchman, N. C. (2010). Water level decline promotes *Typha X glauca* establishment and vegetation change in Great Lakes coastal wetlands. *Wetlands*, 30(6), 1085-1096.
- Liu, W., Bocaniov, S. A., Lamb, K. G., & Smith, R. E. (2014). Three-dimensional modeling of the effects of changes in meteorological forcing on the thermal structure of Lake Erie. *Journal of Great Lakes Research*, 40(4), 827-840.
- Ma, Y., Dong, G., Perlin, M., Liu, S., Zang, J. & Sun, Y. (2009). Higher-harmonic focused-wave forces on a vertical cylinder. *Ocean Engineering*, 36(8), 595-604.
- MackKey, B. G., McKenney, D. W., Yang, Y. Q., McMahon, J. P. & Hutchinson, M. F. (1996). Site regions revisited: a climatic analysis of Hills' site regions for the province of Ontario using a parametric method. *Canadian Journal of Forest Research*, 26(3), 333-354.
- Mao, M., Van Der Westhuysen, A. J., Xia, M., Schwab, D. J. & Chawla, A. (2016). Modeling wind waves from deep to shallow waters in Lake Michigan using unstructured SWAN. *Journal of Geophysical Research: Oceans*, 121(6), 3836-3865.
- Mason, L. A., Riseng, C. M., Layman, A. J. & Jensen, R. (2018). Effective fetch and relative exposure index maps for the Laurentian Great Lakes. *Scientific Data*, 5(1), 1-7.
- Meadows, G. A., Meadows, L. A., Wood, W. L., Hubertz, J. M. & Perlin, M. (1997). The relationship between Great Lakes water levels, wave energies, and shoreline damage. *Bulletin of the American Meteorological Society*, 78(4), 675-684.
- Möller, I., Kudella, M., Rupprecht, F., Spencer, T., Paul, M., Van Wesenbeeck, B. K., ... & Schimmels, S. (2014). Wave attenuation over coastal salt marshes under storm surge conditions. *Nature Geoscience*, 7(10), 727-731.

- Monbaliu, J., Padilla-Hernandez, R., Hargreaves, J. C., Albiach, J. C. C., Luo, W., Sclavo, M. & Guenther, H. (2000). The spectral wave model, WAM, adapted for applications with high spatial resolution. *Coastal Engineering*, 41(1-3), 41-62.
- Monbaliu, J. (2003). Spectral wave models in coastal areas. Elsevier *Oceanography Series*, 67, 133-158.
- Monismith, S. G. (1985). Wind-forced motions in stratified lakes and their effect on mixed-layer shear. *Limnology and Oceanography*, 30(4), 771-783.
- Mortsch, L. D. (1998). Assessing the impact of climate change on the Great Lakes shoreline wetlands. *Climatic Change*, 40(2), 391-416.
- Nekouee, N., Ataie-Ashtiani, B. & Hamidi, S. A. (2016). Uncertainty analysis of wind-wave predictions in Lake Michigan. *China Ocean Engineering*, 30(5), 811-820.
- Niu, Q. & Xia, M. (2016). Wave climatology of Lake Erie based on an unstructured-grid wave model. *Ocean Dynamics*, 66(10), 1271-1284.
- Oort, A. H. & Taylor, A. (1969). On the kinetic energy spectrum near the ground. *Monthly Weather Review*, 97(9), 623-636.
- Paturi, S., Boegman, L. & Rao, Y. R. (2012). Hydrodynamics of eastern Lake Ontario and the upper St. Lawrence River. *Journal of Great Lakes Research*, 38, 194-204.
- Pond, S. & Pickard, G. L. (1983). Introductory dynamical oceanography. Gulf Professional Publishing.
- Price, J. F. & Sundermeyer, M. A. (1999). Stratified ekman layers. *Journal of Geophysical Research: Oceans*, 104(C9), 20467-20494.
- Quinn, F. H. (1977). Annual and seasonal flow variations through the Straits of Mackinac. *Water Resources Research*, 13(1), 137-144.
- Quinn, F. H. (2002). Secular changes in Great Lakes water level seasonal cycles. *Journal of Great Lakes Research*, 28(3), 451-465.

Rabinovich, A. B. (2010). *Seiches and harbour oscillations*. In Handbook of coastal and ocean engineering, 193-236.

Rao, D. B., Schwab, D. J. & Mortimer, C. H. (1976). Surface normal modes of Lake Michigan: Calculations compared with spectra of observed water level fluctuations. *Journal of Physical Oceanography*, 6(4), 575-588.

Rao, D. B. & Schwab, D. J. (1976). Two dimensional normal modes in arbitrary enclosed basins on a rotating earth: application to lakes ontario and superiror. Philosophical Transactions of the Royal Society of London. Series A, *Mathematical and Physical Sciences*, 281(1299), 63-96.

Raubenheimer, B. (2002). Observations and predictions of fluid velocities in the surf and swash zones. *Journal of Geophysical Research: Oceans*, 107(C11), 11-1.

Razali, A. M. & Al-Wakeel, A. A. (2013). Mixture Weibull distributions for fitting failure times data. *Applied Mathematics and Computation*, 219(24), 11358-11364.

Razavi, S., Asadzadeh, M., Tolson, B., Fay, D., Moin, S., Bruxer, J. & Fan, Y. (2014). Evaluation of new control structures for regulating the Great Lakes system: Multiscenario, multireservoir optimization approach. *Journal of Water Resources Planning and Management*, 140(8), 04014018.

Richards, T. L., Dragert, H. & McIntyre, D. R. (1966). Influence of atmospheric stability and over-water fetch on winds over the lower Great Lakes. *Monthly Weather Review*, 94(7), 448-453.

Roberts, D. C., Sprague, H. M., Forrest, A. L., Sornborger, A. T. & Schladow, S. G. (2019). Observations and modeling of the surface seiches of Lake Tahoe, USA. *Aquatic sciences*, 81(3), 1-17.

Robertson, D. M., & Ragotzkie, R. A. (1990). Changes in the thermal structure of moderate to large sized lakes in response to changes in air temperature. *Aquatic Sciences*, 52(4), 360-380.

Roelvink, D., Reniers A, van Dongeren, A., van Thiel de Vries, J., McCall, R. & Lescinski, J. (2009) Modelling storm impacts on beaches, dunes and barrier islands. *Coastal Engineering* 56(11-12):1133-1152. doi:10.1016/j.coastaleng.2009.08.006

Roelvink, D., Reniers, A. J. H. M., Van Dongeren, A., Van Thiel de Vries, J., Lescinski, J. & McCall, R. (2010). XBeach model description and manual. Unesco-IHE Institute for Water Education, Deltares and Delft University of Technology. Report June, 21, 2010.

Roelvink, D. & Reniers, A. (2011). A guide to modeling coastal morphology (Vol. 12). World Scientific. 292 p. DOI: <https://doi.org/10.1142/7712>.

Rogers, W. E., Babanin, A. V. & Wang, D. W. (2012). Observation-Consistent Input and Whitecapping Dissipation in a Model for Wind-Generated Surface Waves: Description and Simple Calculations, *Journal of Atmospheric and Oceanic Technology*, 29(9), 1329-1346. Retrieved Aug 11, 2021, from https://journals.ametsoc.org/view/journals/atot/29/9/jtech-d-11-00092_1.xml

Saylor, J. H. & Danek, L. J. (1977). Wind-driven circulation of Saginaw Bay. *Coastal Engineering*, 1976, 3262-3275.

Schertzer, W. M., Saylor, J. H., Boyce, F. M., Robertson, D. G. & Rosa, F. (1987). Seasonal thermal cycle of Lake Erie. *Journal of Great Lakes Research*, 13(4), 468-486.

Schwab, D. J. & Rao, D. B. (1977). Gravitational oscillations of Lake Huron, Saginaw Bay, Georgian Bay, and the North Channel. *Journal of Geophysical Research*, 82(15), 2105-2116.

Secretan, Y. (2013). H2D2 Software [Online]. Available: <http://www.gre-ehn.ete.inrs.ca/H2D2>.

Seglenieks, F. & Temgoua, A. (2022). *Future hydroclimate variables and lake levels for the Great Lakes using data from the Coupled Model Intercomparison Project Phase 5*, Environment and Climate Change Canada. [In preparation]

Simons, T.J., 1971. Development of numerical models of Lake Ontario. In: Proc. 14th Conf. Great Lakes Res., Intern. Assoc. Great Lakes Res., Ann Arbor, Mich., pp. 654–669.

Smith, J. M., Resio, D. T. & Zundel, A. K. (1999). *STWAVE: Steady-state spectral wave model. Report 1. User's Manual for STWAVE Version 2.0*. Army Engineer Waterways Experiment Station Vicksburg MS Coastal and Hydraulics Lab.

Spence, C., Blanken, P. D., Lenters, J. D. & Hedstrom, N. (2013). The importance of spring and autumn atmospheric conditions for the evaporation regime of Lake Superior. *Journal of Hydrometeorology*, 14(5), 1647-1658.

Steinschneider, S. (2021). A hierarchical Bayesian model of storm surge and total water levels across the Great Lakes shoreline–Lake Ontario. *Journal of Great Lakes Research*, 47(3), 829-843.

Stevens, C. L. & Lawrence, G. A. (1997). Estimation of wind-forced internal seiche amplitudes in lakes and reservoirs, with data from British Columbia, Canada. *Aquatic Sciences*, 59(2), 115-134.

Suzuki, N., Endoh, S., Kawashima, M., Itakura, Y., McNabb, C. D., D'Itri, F. M. & Batterson, T. R. (1995). Discontinuity bar in a wetland on Lake Huron's Saginaw Bay. *Journal of Freshwater Ecology*, 10(2), 111-123.

Tan, X., Gan, T. Y. & Shao, D. (2016). Wavelet analysis of precipitation extremes over Canadian ecoregions and teleconnections to large-scale climate anomalies. *Journal of Geophysical Research: Atmospheres*, 121(24), 14-469.

Thomas, R. L., Christensen, M. D., Szalinska, E. & Scarlat, M. (2006). Formation of the St. Clair river delta in the Laurentian Great Lakes system. *Journal of Great Lakes Research*, 32(4), 738-748.

Thompson, A. F. & Moin, S. M. (2003). *Hydrodynamic modelling of the Upper St. Lawrence River, Kingston/Cape Vincent to Cornwall Reach*. Proceedings, 16th Canadian Hydrotechnical Conference by the Canadian Society for Civil Engineering, Montreal.

Thompson, A. F. (2006). Uncertainty analysis of a two-dimensional hydrodynamic model. MSc Thesis, McMaster University.

Thompson, E. F., Energy spectra in shallow U.S. coastal waters. U.S. Army Coastal Eng. Res. Cent. Tech Pap, TP 80-2. 1980.

Tolman, H. L., Balasubramanian, B., Burroughs, L. D., Chalikov, D. V., Chao, Y. Y., Chen, H. S. & Gerald, V. M. (2002). Development and implementation of wind-generated ocean surface wave Modelsat NCEP. *Weather and forecasting*, 17(2), 311-333.

Torrence, C. & Compo, G. P. (1998). A practical guide to wavelet analysis. *Bulletin of the American Meteorological society*, 79(1), 61-78.

Trebitz, A. S. (2006). Characterizing seiche and tide-driven daily water level fluctuations affecting coastal ecosystems of the Great Lakes. *Journal of Great Lakes Research*, 32(1), 102-116.

- Trigo, I. F., Davies, T. D., & Bigg, G. R. (1999). Objective climatology of cyclones in the Mediterranean region. *Journal of Climate*, *12*(6), 1685-1696.
- Tsanis, I. K. & Brissette, F. P. (1992). Wave directional spectra measurements by small arrays in Lake Ontario. *Journal of Great Lakes Research*, *18*(3), 489-506.
- Tulbure, M. G. & Johnston, C. A. (2010). Environmental conditions promoting non-native *Phragmites australis* expansion in Great Lakes coastal wetlands. *Wetlands*, *30*(3), 577-587.
- Tuomi, L., Kahma, K. K. & Fortelius, C. (2012). Modelling fetch-limited wave growth from an irregular shoreline. *Journal of Marine Systems*, *105*, 96-105.
- Turner, A. J., Fiore, A. M., Horowitz, L. W. & Bauer, M. (2013). Summertime cyclones over the Great Lakes Storm Track from 1860–2100: variability, trends, and association with ozone pollution. *Atmospheric Chemistry and Physics*, *13*(2), 565-578.
- Uzarski, D. G., Brady, V. J., Cooper, M. J., Wilcox, D. A., Albert, D. A., Axler, R. P., ... & Schneider, J. P. (2017). Standardized measures of coastal wetland condition: implementation at a Laurentian Great Lakes basin-wide scale. *Wetlands*, *37*(1), 15-32.
- Valipour, R., Rao, Y. R., León, L. F. & Depew, D. (2019). Nearshore-offshore exchanges in multi-basin coastal waters: Observations and three-dimensional modeling in Lake Erie. *Journal of Great Lakes Research*, *45*(1), 50-60.
- WAMDI Group (1988). The WAM model—A third generation ocean wave prediction model. *Journal of Physical Oceanography*, *18*(12), 1775-1810.
- Wang, J., Bai, X., Hu, H., Clites, A., Colton, M. & Lofgren, B. (2012). Temporal and spatial variability of Great Lakes ice cover, 1973–2010. *Journal of Climate*, *25*(4), 1318-1329.
- Watras, C. J., Read, J. S., Holman, K. D., Liu, Z., Song, Y. Y., Watras, A. J., ... & Stanley, E. H. (2014). Decadal oscillation of lakes and aquifers in the upper Great Lakes region of North America: Hydroclimatic implications. *Geophysical Research Letters*, *41*(2), 456-462.
- Weber, R. O. & Kaufmann, P. (1995). Automated classification scheme for wind fields. *Journal of Applied Meteorology and Climatology*, *34*(5), 1133-1141.

- Weller, J. D. & Chow-Fraser, P. (2019a). Simulated changes in extent of Georgian Bay low-marsh habitat under multiple lake levels. *Wetlands Ecology and Management*, 27(4), 483-495.
- Weller, J. D. & Chow-Fraser, P. (2019b). Hydrogeomorphic modelling of low-marsh habitat in coastal Georgian Bay, Lake Huron. *Wetlands Ecology and Management*, 27(2), 207-221.
- Wilcox, D. A., Ingram, J. W., Kowalski, K. P., Meeker, J. E., Carlson, M. L., Xie, Y., ... & Patterson, N. J. (2005). Evaluation of water level regulation influences on Lake Ontario and upper St. Lawrence River coastal wetland plant communities. Final Project Report.
- Wilcox, D. A. & Nichols, S. J. (2008). The effects of water-level fluctuations on vegetation in a Lake Huron wetland. *Wetlands*, 28(2), 487-501.
- Wilcox, D. A. (2012). Response of wetland vegetation to the post-1986 decrease in Lake St. Clair water levels: seed-bank emergence and beginnings of the *Phragmites australis* invasion. *Journal of Great Lakes Research*, 38(2), 270-277.
- Willmott, C. J. (1982). Some comments on the evaluation of model performance. *Bulletin of the American Meteorological Society*, 63(11), 1309-1313.
- Wilson, B. W. (1972). *Seiches*. In *Advances in Hydroscience* (Vol. 8). Elsevier, pp. 1-94.
- Wu, H. B. & Zheng, B. H. (2020). Wetland area identification and waterbird protection management in consideration of lake topography and water level change. *Global Ecology and Conservation*, 23, e01056.
- Wuebbles, D., Cardinale, B., Cherkauer, K., Davidson-Arnott, R., Hellmann, J., Infante, D. & Ballinger, A. (2019). *An assessment of the impacts of climate change on the Great Lakes*. Environmental Law & Policy Center. 71p.
- Xu, J., Zhang, A., Anderson, E. J., Lang, G. A., Kelley, J. G. W. & Chen, Y. (2018). Implementation of the upgraded Lake Erie Operational Forecast System (LEOFS) and the semi-operational nowcast/forecast skill assessment. DOI:10.7289/V5/TR-NOS-COOPS-087.
- Young, I. R. & Babanin, A. V. (2006). Spectral distribution of energy dissipation of wind-generated waves due to dominant wave breaking. *Journal of Physical Oceanography*, 36(3), 376-394.

Zacharias, I. & Ferentinos, G. (1997). A numerical model for the winter circulation in Lake Trichonis, Greece. *Environmental Modelling & Software*, 12(4), 311-321.

Zijlema M, Stelling G, Smit P (2011) SWASH: an operational public domain code for simulating wave fields and rapidly varied flows in coastal waters. *Coastal Engineering*, 58(10), 992-1012. doi:10.1016/j.coastaleng.2011.05.015.

Zyryanov, V. N. (2011). Under-ice seiches. *Water Resources*, 38(3), 261-273.

Section 4: Selected Sites

Albert, D. A., Wilcox, D. A., Ingram, J. W. & Thompson, T. A. (2005). Hydrogeomorphic classification for Great Lakes coastal wetlands. *Journal of Great Lakes Research*, 31, 129-146.

Beckford, C. L., Jacobs, C., Williams, N. & Nahdee, R. (2010). Aboriginal Environmental Wisdom, Stewardship, and Sustainability: Lessons From the Walpole Island First Nations, Ontario, Canada. *The Journal of Environmental Education*, 41(4), 239-248.
<https://doi.org/10.1080/00958961003676314>

Birds Canada (2018). The Great Lakes Marsh Monitoring Program.

Bruce Power (2019). Sustainability Report. URL: https://www.brucepower.com/wp-content/uploads/2019/12/190200_SustainabilityReport_Book_R000_DIGITAL.pdf

Canadian Wildlife Service - Ontario Region (2001). Canada 16: St. Clair National Wildlife Area, Ontario. Information Sheet on Ramsar Wetlands.

Central Michigan University, 2018. Great Lakes Coastal Wetland Monitoring Program (CWMP) Site Mapping Tool. URL: <https://www.greatlakeswetlands.org/Map.vbhtml>

Chip Weseloh, D. V., Pekarik, C., Havelka, T., Barrett, G. & Reid, J. (2002). Population Trends and Colony Locations of Double-crested Cormorants in the Canadian Great Lakes and Immediately Adjacent Areas, 1990–2000: A Manager's Guide. *Journal of Great Lakes Research*, 28(2), 125-144. [https://doi.org/10.1016/S0380-1330\(02\)70571-6](https://doi.org/10.1016/S0380-1330(02)70571-6)

Cvetkovic, M. & Chow-Fraser, P. (2011). Use of ecological indicators to assess the quality of Great Lakes coastal wetlands. *Ecological Indicators*, 11(6), 1609-1622.

Cvetkovic, M., Wei, A. & Chow-Fraser, P. (2010). Relative importance of macrophyte community versus water quality variables for predicting fish assemblages in coastal wetlands of the Laurentian Great Lakes. *Journal of Great Lakes Research*, 36(1), 64-73.
<https://doi.org/10.1016/j.jglr.2009.10.003>

DeCatanzaro, R., Cvetkovic, M. & Chow-Fraser, P. (2009). The relative importance of road density and physical watershed features in determining coastal marsh water quality in Georgian Bay. *Environmental Management*, 44(3), 456-467.

Environment Canada - Canadian Wildlife Service (2007). Bay of Quinte Area of Concern: Coastal Wetland Status and Remedial Action Plan Delisting Target Recommendations.

Environment Canada and Central Lake Ontario Conservation Authority (2007). Durham Region Coastal Wetland Monitoring Project: Methodology Handbook. Oshawa, ON: Central Lake Ontario Conservation Authority. March 2007-08.

Environment and Climate Change Canada (2016). St. Marys River: Area of Concern. URL: <https://www.canada.ca/en/environment-climate-change/services/great-lakes-protection/areas-concern/st-marys-river.html>

Environment Canada - Canadian Wildlife Service (2016). St. Clair National Wildlife Area Management Plan.

Environment and Climate Change Canada (2017). Detroit River: Area of Concern. URL: <https://www.canada.ca/en/environment-climate-change/services/great-lakes-protection/areas-concern/detroit-river.html>

Essex Region Conservation Authority (2020). Petite Côte. URL: <https://essexregionconservation.ca/location/petite-cote/>

Fracz, A. & Chow-Fraser, P. (2013). Impacts of declining water levels on the quantity of fish habitat in coastal wetlands of eastern Georgian Bay, Lake Huron. *Hydrobiologia*, 702(1), 151-169.

Friends of Rondeau (2016). About Rondeau Park. URL: <http://rondeauprovincialpark.ca/about-rondeau-park/>

Georgian Bay Biosphere Reserve (2020). About the Georgian Bay Biosphere. URL: <https://www.stateofthebay.ca/about-us/>

Grabas, G. P., Blukacz-Richards, E. A. & Pernanen, S. (2012). Development of a submerged aquatic vegetation community index of biotic integrity for use in Lake Ontario coastal wetlands. *Journal of Great Lakes Research*, 38(2), 243-250. <https://doi.org/10.1016/j.jglr.2012.02.014>

Grabas, G. P., Fiorino, G. E. & Reinert, A. (2019). Vegetation species richness is associated with daily water-level fluctuations in Lake Ontario coastal wetlands. *Journal of Great Lakes Research*, 45(4), 805-810. <https://doi.org/10.1016/j.jglr.2019.05.008>

Grabas, G. P. & Rokitnicki-Wojcik, D. (2015). Characterizing daily water-level fluctuation intensity and water quality relationships with plant communities in Lake Ontario coastal wetlands. *Journal of Great Lakes Research*, 41(1), 136-144. <https://doi.org/10.1016/j.jglr.2014.12.019>

Grand River Conservation Authority (2018). Our Watershed. URL: <https://www.grandriver.ca/en/our-watershed/Our-Watershed.aspx>

Georgian Bay Biosphere Reserve (2020). About the Georgian Bay Biosphere. URL: <https://www.stateofthebay.ca/about-us/>

Government of Canada (2020). St-Clair National Wildlife Area. URL: <https://www.canada.ca/en/environment-climate-change/services/national-wildlife-areas/locations/st-clair.html>

Ingram, *et al.* (2004). Development of a Coastal Wetlands Database for the Great Lakes Canadian Shoreline. Final Report to: The Great Lakes Commission. Report no. WETLANDS2-EPA-03.

Keddy, P. A. & Reznicek, A. A. (1986). Great Lakes Vegetation Dynamics: The Role of Fluctuating Water Levels and Buried Seeds. *Journal of Great Lakes Research*, 12(1), 25-36. [https://doi.org/10.1016/S0380-1330\(86\)71697-3](https://doi.org/10.1016/S0380-1330(86)71697-3)

Keough, J. R., Thompson, T. A., Guntenspergen, G. R. & Wilcox, D. A. (1999). Hydrogeomorphic factors and ecosystem responses in coastal wetlands of the Great Lakes. *Wetlands*, 19(4), 821-834. <https://doi.org/10.1007/BF03161786>

Kraus, D., Henson, B. & Ewert, D. (2009). Biodiversity and conservation of Lake Huron's islands. *Aquatic Ecosystem Health & Management*, 12(1), 90-100. <https://doi.org/10.1080/14634980802715225>

Midwood, J. D. & Chow-Fraser, P. (2010). Mapping floating and emergent aquatic vegetation in coastal wetlands of Eastern Georgian Bay, Lake Huron, Canada. *Wetlands*, 30(6), 1141-1152.

Midwood, J. D. & Chow-Fraser, P. (2012). Changes in aquatic vegetation and fish communities following 5 years of sustained low water levels in coastal marshes of eastern Georgian Bay, Lake Huron. *Global Change Biology*, 18(1), 93-105.

Midwood, J., Rokitnicki-Wojcik, D. & Chow-Fraser, P. (2012). Development of an inventory of coastal wetlands for eastern Georgian Bay, Lake Huron. *International Scholarly Research Notices*, 2012.

Parks Canada Agency (2016a). Fathom Five National Marine Park. URL: <https://www.pc.gc.ca/en/amnc-nmca/on/fathomfive>

Parks Canada Agency (2019). Thousand Islands National Park Management Plan.

Rokitnicki-Wojcik, D., Wei, A. & Chow-Fraser, P. (2011). Transferability of object-based rule sets for mapping coastal high marsh habitat among different regions in Georgian Bay, Canada. *Wetlands Ecology and Management*, 19(3), 223-236. <https://doi.org/10.1007/s11273-011-9213-7>

Thomas, R. L., Christensen, M. D., Szalinska, E. & Scarlat, M. (2006). Formation of the St. Clair river delta in the Laurentian Great Lakes system. *Journal of Great Lakes Research*, 32(4), 738-748.

Uzarski, D. G., Brady, V. J., Cooper, M. J., Wilcox, D. A., Albert, D. A., Axler, R. P., Bostwick, P., Brown, T. N., Ciborowski, J. J. & Danz, N. P. (2017). Standardized measures of coastal wetland condition : Implementation at a Laurentian Great Lakes basin-wide scale. *Wetlands*, 37(1), 15-32.

Wei, A. & Chow-Fraser, P. (2007). Use of IKONOS imagery to map coastal wetlands of Georgian Bay. *Fisheries*, 32(4), 167-173.

Weller, J. D. & Chow-Fraser, P. (2019). Hydrogeomorphic modeling of low-marsh habitat in coastal Georgian Bay, Lake Huron. *Wetlands Ecology and Management*, 27(2), 207-221.

Wilcox, D. (2012). Response of wetland vegetation to the post-1986 decrease in Lake St. Clair water levels : Seed-bank emergence and beginnings of the *Phragmites australis* invasion. *Journal of Great Lakes Research*, 38, 270–277. <https://doi.org/10.1016/j.jglr.2012.02.007>

Wilcox, D. A., Ingram, J. W., Kowalski, K. P., Meeker, J. E., Carlson, M., Xie, Y., Grabas, G., Holmes, K. & Patterson, N. (2005). Evaluation of water level regulation influences on Lake Ontario and upper St. Lawrence River coastal wetland plant communities. *Final Project Report*.

Wilcox, D. A. & Meeker, J. E. (1991). Disturbance effects on aquatic vegetation in regulated and unregulated lakes in northern Minnesota. *Canadian Journal of Botany*, 69(7), 1542-1551.

Wilcox, D. A., Meeker, J. E., Hudson, P. L., Armitage, B. J., Black, M. G. & Uzarski, D. G. (2002). Hydrologic variability and the application of index of biotic integrity metrics to wetlands : A Great Lakes evaluation. *Wetlands*, 22(3), 588-615.

Section 5: High-Resolution Digital Elevation Models of Coastal Wetlands

Amidror, I. (2002). Scattered data interpolation methods for electronic imaging systems: a survey, *Journal of Electronic Imaging*, April 2002, 11(2).

Anselin, L. (1995). Local indicators of spatial association –LISA, *Geographical Analysis*, 27, 93–115;

Anselin, L., Ibnu S. & Youngihn K. (2006). GeoDa: An Introduction to Spatial Data Analysis, *Geographical Analysis*, 38 (1), 5-22.

Arvais, M. & Demers, A. (2011). *Guide de normalisation des inventaires bathymétriques*, Ministère des Ressources naturelles et de la Faune, Service de la faune aquatique .

BC2 (2018). Collecte et livraison de données topographiques et bathymétriques provenant de neuf milieux humides côtiers situés du côté canadien de la portion nord du bassin des grands lacs, Prepared for Environment and Climate Change Canada, 26 p..

BC2 (2019). Collecte et livraison de données topographiques et bathymétriques provenant de dix milieux humides côtiers situés du côté canadien de la portion sud du bassin des grands lacs, Prepared for Environment and Climate Change Canada, 26 p.

Buffington, K.J., Dugger, B.D., Thorne, K.M. & Takekawa, J. Y. (2016). Statistical correction of LIDAR-derived digital elevation models with multispectral airborne imagery in tidal marshes, *Remote Sensing of Environment*, 186 (2016) 616–625.

Dillon Consulting (2018). *Final Summary Report - Great Lakes Coastal Wetland Vegetation Data Collection (South)*, Prepared for Environment and Climate Change Canada (ECCC), 14 p.

Dunn, M. & Hickey, R., (1998). The Effect of Slope Algorithms on Slope Estimates within a GIS, *Cartography*, 27, 9-15.

Frank B. (2019). Pyfor, Tools for analyzing aerial point clouds of forest data, URL <https://github.com/brycefrank/pyfor>.

Friedman, J., Hastie, T. & Tibshirani, R. (2010). Regularization Paths for Generalized Linear Models via Coordinate Descent. *Journal of Statistical Software*, 33(1), 1–22. <http://www.jstatsoft.org/v33/i01/>

Gallant, J. C. & J. P. Wilson, (2000). *Primary topographic attributes, in Terrain Analysis: Principles and Applications*, edited by J. P. Wilson and J. C. Gallant, 51-86.

GDAL/OGR contributors (2019). GDAL/OGR Geospatial Data Abstraction software Library, *Open Source Geospatial Foundation*, URL <https://gdal.org>

Gillies *et al.* (2019). Rasterio: geospatial raster I/O for {Python} programmers, url = <https://github.com/mapbox/rasterio>

Gonga-Saholiariliva, N., Gunnell, Y., Petit C. & Mering C. (2011). Techniques for quantifying the accuracy of gridded elevation models and for mapping uncertainty in digital terrain analysis, *Progress in Physical Geography*, 35(6), 739-764.

Government of Ontario. (2016). *South Central Ontario Orthophotography Project (SCOOP) 2013 Classified LAS, User Guide*, Provincial Mapping Unit, Mapping and Information Resources Branch, Corporate Management and Information Division, Ministry of Natural Resources and Forestry, 15 p.

Government of Ontario. (2017). *Central Ontario Orthophotography Project (COOP) 2016 Digital Elevation Model, User Guide*, Provincial Mapping Unit, Mapping and Information Resources Branch, Corporate Management and Information Division, Ministry of Natural Resources and Forestry, 23 p.

Government of Ontario. (2018). *User Guide for LiDAR Eastern Acquisition Project Classified Point Cloud (2009) LIO Dataset*, Provincial Mapping Unit, Mapping and Information Resources Branch, Corporate Management and Information Division, Ministry of Natural Resources and Forestry, 54 p.

Government of Ontario. (2018). *User Guide for LiDAR Eastern Acquisition Project Digital Terrain Model (2009) LIO Dataset*, Provincial Mapping Unit, Mapping and Information Resources Branch, Corporate Management and Information Division, Ministry of Natural Resources and Forestry, 34 p.

Government of Ontario. (2019). *User Guide LIDAR Point Cloud (2016-18) LIO Dataset*, Provincial Mapping Unit, Mapping and Information Resources Branch, Corporate Management and Information Division, Ministry of Natural Resources and Forestry, 50 p.

Government of Ontario. (2019). *User Guide Ontario Digital Terrain Model (LIDAR-Derived) LIO Dataset*, Provincial Mapping Unit, Mapping and Information Resources Branch, Corporate Management and Information Division, Ministry of Natural Resources and Forestry, 69 p.

Hladik, C., Schalles, J., Alber, M. (2013). Salt marsh elevation and habitat mapping using hyperspectral and LIDAR data, *Remote Sensing of Environment*, 139, 318–330.

Horn, B.K.P. (1981). Hill shading and the reflectance map, *Proceedings of the IEEE*, 69(1), 14-47.

IIC Technologies (2018). Report of Survey: CHS Central Region Bathymetric and Topographic Airborne LiDAR Acquisition, Prepared for the Canadian Hydrographic Service, 53p.

Jones, E., Oliphant, T., Peterson, P., & others. (2001). *SciPy: Open source scientific tools for Python*, Retrieved from <http://www.scipy.org/>

KBM Ressources Group (2018). Acquisition and classification of airborne LiDAR data –Great Lakes Area, Deliverable Report, NRCan-Contract No. 3000668790, 11p.

Kraus, K. & Pfeifer, N. (1998). Determination of terrain models in wooded areas with airborne laser scanner data, *Journal of Photogrammetry and Remote Sensing*, 53, 193–203.

Lee, H., Bakowsky, W., Riley, J., Bowles, J., Puddister, M., Uhlig, P. & McMurray, S. (1998). *Ecological Land Classification for Southern Ontario: First Approximation and Its Application*, North Bay, Ontario: Ontario Ministry of Natural Resources.

Lindsay, J.B. (2018). A new method for the removal of off-terrain objects from LiDAR-derived raster surface models, Available online, DOI: 10.13140/RG.2.2.21226.62401

Lindsay, J.B. (2014). The Whitebox Geospatial Analysis Tools project and open-access GIS, *Proceedings of the GIS Research UK 22nd Annual Conference*, The University of Glasgow, 16-18 April.

Lucas, G. (2011). Introduction to Natural Neighbour Interpolation, URL <https://github.com/gwlucastrig/Tinfour/wiki/Introduction-to-Natural-Neighbour-Interpolation>

Morin, J., M. Mingelbier, J. A. Bechara, O. Champoux, Y. Secretan, M. Jean & J.-J. Frenette (2003). Emergence of new explanatory variable for 2D habitat modelling in large rivers: the St. Lawrence experience. *Canadian Water Resources Journal*. 28: 249-272.

Montané, J.M. & Torres, R. (2006). Accuracy assessment of LIDAR saltmarsh topographic data using RTK GPS, *Photogrammetric Engineering and Remote Sensing*, 961–967.

Murphy S. & the Pykrige Developers (2015-2018). Kriging toolkit for Python, URL <https://github.com/bsmurphy/PyKrige>

Natural Resources Canada. (2020, 04 06). *Geodetic Tools and Applications*. Retrieved from Canada.ca: <https://www.nrcan.gc.ca/maps-tools-publications/tools/geodetic-reference-systems-tools/tools-applications/10>

Natural Resource Solutions Inc. (2018). *Great Lakes Coastal Wetland Vegetation Data Collection*, Prepared for Environment and Climate Change Canada, 16 p.

ORFEO ToolBox - Open Source Processing of Remote Sensing Images. <https://www.orfeo-toolbox.org/>. Accessed April 2019

Rosso, P.H., Ustin, S.L. & Hastings, A. (2005). Mapping marshland vegetation of San Francisco Bay, California, using hyperspectral data, *International Journal of Remote Sensing*, 26, 5169–5191.

Sadro, S., Gastil-Buhl, M. & Melack, J. (2007). Characterizing patterns of plant distribution in a southern California salt marsh using remotely sensed topographic and hyperspectral data and local tidal fluctuations. *Remote Sensing of Environment*, 110, 226–239.

Schmid, K.A., Hadley, B.C. & Wijekoon, N. (2011). Vertical accuracy and use of topographic, LIDAR data in coastal marshes. *Journal of Coastal Research*, 275, 116–132.

Véronneau, M. (s.d.). *Height Reference Systems in North America and Gravity*, Document from Geodetic Survey Division, CCRS, Natural Resources Canada, 9p.

Wilson, J.P. (2012). Digital terrain modelling, *Geomorphology*, 137, 107–121.

Zhang K., Chen, S-C., Whitman, D., Shyu, M-L., Yan, J. & Zhang, C. (2003). A progressive morphological filter for removing non-ground measurements from airborne LIDAR data, *IEEE Transactions on Geoscience and Remote Sensing*, 41(4):872–882.

Section 6: Great Lakes Coastal Wetland Modelling

- Alvarez, M., Tron, F., & Mauchamp, A. (2005). Sexual Versus Asexual Colonization by *Phragmites australis* : 25-Year Reed Dynamics in a Mediterranean Marsh, Southern France. *Wetlands*, 25, 639-647. [https://doi.org/10.1672/0277-5212\(2005\)025\[0639:SVACBP\]2.0.CO;2](https://doi.org/10.1672/0277-5212(2005)025[0639:SVACBP]2.0.CO;2)
- Amsberry, L., Baker, M., Ewanchuk, P., & Bertness, M. (2000). Clonal Integration and the Expansion of *Phragmites australis*. *Ecological Applications*, 10, 1110-1118. [https://doi.org/10.1890/1051-0761\(2000\)010\[1110:CIATEO\]2.0.CO;2](https://doi.org/10.1890/1051-0761(2000)010[1110:CIATEO]2.0.CO;2)
- Antonia H. B. M. Wijte, & Gallagher, J. L. (1996). Effect of Oxygen Availability and Salinity on Early Life History Stages of Salt Marsh Plants. I. Different Germination Strategies of *Spartina alterniflora* and *Phragmites australis* (Poaceae). *American Journal of Botany*, 83(10), 1337-1342. JSTOR. <https://doi.org/10.2307/2446119>
- Apfelbaum, S. I. (1985). Cattail (*Typha* spp.) management. *Natural Areas Journal*, 9-17.
- Armstrong, J., Afreen-Zobayed, F., Blyth, S., & Armstrong, W. (1999). *Phragmites australis*: Effects of shoot submergence on seedling growth and survival and radial oxygen loss from roots. *Aquatic Botany*, 64(3-4), 275-289.
- Asamoah, S. A., & Bork, E. W. (2010). Drought tolerance thresholds in cattail (*Typha latifolia*): A test using controlled hydrologic treatments. *Wetlands*, 30(1), 99-110.
- Baldwin, A. H., Kettenring, K. M., & Whigham, D. F. (2010). Seed banks of *Phragmites australis*-dominated brackish wetlands : Relationships to seed viability, inundation, and land cover. *Aquatic Botany*, 93(3), 163-169.
- Banks, S., White, L., Behnamian, A., Chen, Z., Montpetit, B., Brisco, B., Pasher, J., & Duffe, J. (2019). Wetland Classification with Multi-Angle/Temporal SAR Using Random Forests. *Remote Sensing*, 11(6), 670. <https://doi.org/10.3390/rs11060670>
- Bansal, S., Lishawa, S. C., Newman, S., Tangen, B. A., Wilcox, D., Albert, D., Anteau, M. J., Chimney, M. J., Cressey, R. L., & DeKeyser, E. (2019). *Typha* (Cattail) invasion in North American wetlands : Biology, regional problems, impacts, ecosystem services, and management. *Wetlands*, 39(4), 645-684.

Battaglia, M. J., Banks, S., Behnamian, A., Bourgeau-Chavez, L., Brisco, B., Corcoran, J., Chen, Z., Huberty, B., Klassen, J., Knight, J., Morin, P., Murnaghan, K., Pelletier, K., & White, L. (2021). Multi-Source EO for Dynamic Wetland Mapping and Monitoring in the Great Lakes Basin. *Remote Sensing*, 13(4), 599. <https://doi.org/10.3390/rs13040599>

Bazoge, A., D. Lachance et C. Villeneuve. (2014). *Identification et délimitation des milieux humides du Québec méridional*, Ministère du Développement durable, de l'Environnement et de la Lutte contre les changements climatiques, Direction de l'écologie et de la conservation et Direction des politiques de l'eau, 64 p

Beaumont, L. J., Gallagher, R. V., Thuiller, W., Downey, P. O., Leishman, M. R., & Hughes, L. (2009). Different climatic envelopes among invasive populations may lead to underestimations of current and future biological invasions. *Diversity and Distributions*, 15(3), 409-420. <https://doi.org/10.1111/j.1472-4642.2008.00547.x>

Bedish, J. W. (1967). Cattail Moisture Requirements and their Significance to Marsh Management. *American Midland Naturalist*, 288-300.

Beule, J. D. (1979). Control and management of cattails in southeastern Wisconsin wetlands. *Department of Natural Resources, Technical Bulletin no. 112*.

Boers, A. M., & Zedler, J. B. (2008). Stabilized water levels and Typha invasiveness. *Wetlands*, 28(3), 676-685.

Bosley, T. R., & TR, B. (1978). *Loss of wetlands on the west shore of Green Bay*.

Bourgeau-Chavez, L. L., Endres, S., Powell, R., Battaglia, M. J., Benscoter, B., Turetsky, M., Kasischke, E. S., & Banda, E. (2017). Mapping boreal peatland ecosystem types from multitemporal radar and optical satellite imagery. *Canadian Journal of Forest Research*, 47(4), 545-559. <https://doi.org/10.1139/cjfr-2016-0192>

Bourgeois, B., Hugron, S., & Poulin, M. (2012). Establishing a moss cover inhibits the germination of Typha latifolia, an invasive species, in restored peatlands. *Aquatic botany*, 100, 76-79.

Breiman, L. (2001). Random Forests. *Machine Learning*, 45(1), 5-32. <https://doi.org/10.1023/A:1010933404324>

Brock, G., Pihur, V., Datta, S., & Datta, S. (2008). cValid : An R package for cluster validation. *Journal of Statistical Software*, 25, 1-22.

Brown, M. B., & Forsythe, A. B. (1974). Robust Tests for the Equality of Variances. *Journal of the American Statistical Association*, 69(346), 364-367.
<https://doi.org/10.1080/01621459.1974.10482955>

Bunbury-Blanchette, A. L., Freeland, J. R., & Dorken, M. E. (2015). Hybrid *Typhax glauca* outperforms native *T. latifolia* under contrasting water depths in a common garden. *Basic and applied ecology*, 16(5), 394-402.

Byun, C., Blois, S., & Brisson, J. (2014). Interactions between abiotic constraint, propagule pressure, and biotic resistance regulate plant invasion. *Oecologia*, 178.
<https://doi.org/10.1007/s00442-014-3188-z>

Chambers, R. M., Meyerson, L. A., & Saltonstall, K. (1999). Expansion of *Phragmites australis* into tidal wetlands of North America. *Aquatic botany*, 64(3-4), 261-273.

Chun, Y.-M., & Choi, Y. (2009). Expansion of *Phragmites australis* (Cav.) Trin. Ex Steud. (Common Reed) into *Typha* spp. (Cattail) Wetlands in Northwestern Indiana, USA. *Journal of Plant Biology*, 52, 220-228. <https://doi.org/10.1007/s12374-009-9024-z>

Clevering, O. A., & Lissner, J. (1999). Taxonomy, chromosome numbers, clonal diversity and population dynamics of *Phragmites australis*. *Aquatic Botany*, 64(3-4), 185-208.

Cohen, J. (1960). A coefficient of agreement for nominal scales. *Educational and psychological measurement*, 20(1), 37-46.

Coops, H., & van der Velde, G. (1995). Seed dispersal, germination and seedling growth of six helophyte species in relation to water-level zonation. *Freshwater biology*, 34(1), 13-20.

Coops, H., Vulink, J. T., & Van Nes, E. H. (2004). Managed water levels and the expansion of emergent vegetation along a lakeshore. *Limnologica*, 34(1-2), 57-64.

Couillard, L., & Grondin, P. (1986). *La végétation des milieux humides du Québec*. Gouvernement du Québec, Ministère de l'environnement. <https://books.google.ca/books?id=Q9RqAAAACAAJ>

Duncan, J., Rozum, R., Powell, J., & Kettenring, K. (2017). Multi-scale methods predict invasion speeds in variable landscapes : Case study : *Phragmites australis*. *Theoretical Ecology*, 10. <https://doi.org/10.1007/s12080-017-0329-0>

Dvorák, J., Imhof, G., Day Jr, J., Hacker, R., Holíček, J., Hudec, K., Pelikan, J., & Opatrný, E. (1998). The role of animals and animal communities in wetlands. *The Production Ecology of Wetlands*. Cambridge University Press, New York, NY, USA, 211-318.

Ellison, A. M., & Bedford, B. L. (1995). Response of a Wetland Vascular Plant Community to Disturbance : A Simulation Study. *Ecological Applications*, 5(1), 109-123. JSTOR. <https://doi.org/10.2307/1942056>

Ernst, K. A., & Brooks, J. R. (2003). Prolonged flooding decreased stem density, tree size and shifted composition towards clonal species in a central Florida hardwood swamp. *Forest Ecology and Management*, 173(1-3), 261-279.

Farrer, E., & Goldberg, D. (2009). Litter drives ecosystem and plant community changes in cattail invasion. *Ecological applications : a publication of the Ecological Society of America*, 19, 398-412. <https://doi.org/10.1890/08-0485.1>

Fitzpatrick, M. C., & Weltzin, J. F. (2005). Ecological niche models and the geography of biological invasions : A review and a novel application. In Inderjit (Éd.), *Invasive Plants : Ecological and Agricultural Aspects* (p. 45-60). Birkhäuser Basel. https://doi.org/10.1007/3-7643-7380-6_3

Fortin, V., & Gronewold, A. D. (2012). Water Balance of the Laurentian Great Lakes. In L. Bengtsson, R. W. Herschy, & R. W. Fairbridge (Éds.), *Encyclopedia of Lakes and Reservoirs* (p. 864-869). Springer Netherlands. https://doi.org/10.1007/978-1-4020-4410-6_268

Frieswyk, C. B., & Zedler, J. B. (2007). Vegetation change in Great Lakes coastal wetlands : Deviation from the historical cycle. *Journal of Great Lakes Research*, 33(2), 366-380.

Galatowitsch, S. M., Anderson, N. O., & Ascher, P. D. (1999). Invasiveness in wetland plants in temperate North America. *Wetlands*, 19(4), 733-755.

Gathman, J. P., Albert, D. A., & Burton, T. M. (2005). Rapid plant community response to a water level peak in northern Lake Huron coastal wetlands. *Journal of Great Lakes Research*, 31, 160-170.

Georgian Bay Forever. (2020). *Submerged Rock Shoal Mapping of Lake Huron Wetlands*.

Grabas, G. P., Blukacz-Richards, E. A., & Pernanen, S. (2012). Development of a submerged aquatic vegetation community index of biotic integrity for use in Lake Ontario coastal wetlands. *Journal of Great Lakes Research*, 38(2), 243-250. <https://doi.org/10.1016/j.jglr.2012.02.014>

Grace, J. B., & Harrison, J. S. (1986). The biology of Canadian weeds. : 73. *Typha latifolia* L., *Typha angustifolia* L. and *Typha xglauca* Godr. *Canadian Journal of Plant Science*, 66(2), 361-379.

Grace, J. B., & Wetzel, R. G. (1981). Effects of size and growth rate on vegetative reproduction in *Typha*. *Oecologia*, 50(2), 158-161. <https://doi.org/10.1007/BF00348030>

Grace, J. B., & Wetzel, R. G. (1982). Niche differentiation between two rhizomatous plant species: *Typha latifolia* and *Typha angustifolia*. *Canadian Journal of Botany*, 60(1), 46-57.

Gucker, C. L. (2008). *Typha latifolia*. *Fire Effects Information System*, [Online]. US Department of Agriculture, Forest Service, Rocky Mountain Research Station, Fire Sciences Laboratory (Producer). Available: <http://www.fs.fed.us/database/feis/>[2009, January 15].

H. B. Mann, & D. R. Whitney. (1947). On a Test of Whether one of Two Random Variables is Stochastically Larger than the Other. *The Annals of Mathematical Statistics*, 18(1), 50-60. <https://doi.org/10.1214/aoms/1177730491>

Hall, T., & Smith, G. (1955). Effects of flooding on woody plants, West Sandy dewatering project, Kentucky Reservoir. *Journal of Forestry*, 53(4), 281-285.

Harris, H. J., Bosley, T. R., & Roznik, F. D. (1978). *Green Bay's Coastal Wetlands—A Picture of Dynamic Change*. Wetlands: Ecology, Values, and Impacts, Proceedings of the Waubesa Conference on Wetlands June 2-5, 1977, Madison, Wisconsin, p 337-358, 1978. 7 fig, 6 tab, 14 ref.

Harris, S. W., & Marshall, W. H. (1963). Ecology of water-level manipulations on a northern marsh. *Ecology*, 44(2), 331-343.

Haslam, S. M. (1971). The development and establishment of young plants of *Phragmites communis* Trin. *Annals of Botany*, 35(5), 1059-1072.

Haslam, S. M. (1972). Phragmites Communis Trin. (ArundoPhragmites L., ? Phragmites Australis (Cav.) Trin. Ex Steudel). *Journal of Ecology*, 60(2), 585-610. JSTOR. <https://doi.org/10.2307/2258363>

Hastie, T., Tibshirani, R., & Friedman, J. (2009). Random forests. In *The elements of statistical learning* (p. 587-604). Springer.

Hazelton, E., Mozdzer, T., Burdick, D., Kettenring, K., & Whigham, D. (2014). Phragmites australis management in the United States: 40 years of methods and outcomes. *AoB plants*, 6. <https://doi.org/10.1093/aobpla/plu001>

Hellings, S. E., & Gallagher, J. L. (1992). The Effects of Salinity and Flooding on Phragmites australis. *Journal of Applied Ecology*, 29(1), 41-49. JSTOR. <https://doi.org/10.2307/2404345>

Hong Han, Xiaoling Guo, & Hua Yu. (2016). Variable selection using Mean Decrease Accuracy and Mean Decrease Gini based on Random Forest. *2016 7th IEEE International Conference on Software Engineering and Service Science (ICSESS)*, 219-224. <https://doi.org/10.1109/ICSESS.2016.7883053>

Hudon, C., Gagnon, P., & Jean, M. (2005). Hydrological factors controlling the spread of common reed (Phragmites australis) in the St. Lawrence River (Québec, Canada). *Ecoscience*, 12(3), 347-357.

Hudon, C., Gagnon, P., Jean, M., Jetté, I., Létourneau, G., & Deschênes, M. (2004). La progression du Phragmite commun (Phragmites australis) dans le fleuve Saint-Laurent. *Rapport scientifique et technique DT-30, Environnement Canada, Centre Saint-Laurent, Conservation de l'environnement, Montréal, Québec.*

Jung, J. A., Rokitnicki-Wojcik, D., & Midwood, J. D. (2017). Characterizing past and modelling future spread of Phragmites australis ssp. Australis at Long Point Peninsula, Ontario, Canada. *Wetlands*, 37(5), 961-973.

Jutras, S., Plamondon, A. P., Hökkä, H., & Bégin, J. (2006). Water table changes following precommercial thinning on post-harvest drained wetlands. *Forest Ecology and Management*, 235(1), 252-259. <https://doi.org/10.1016/j.foreco.2006.08.335>

- Keddy, P. A., & Reznicek, A. A. (1986). Great Lakes Vegetation Dynamics: The Role of Fluctuating Water Levels and Buried Seeds. *Journal of Great Lakes Research*, 12(1), 25-36. [https://doi.org/10.1016/S0380-1330\(86\)71697-3](https://doi.org/10.1016/S0380-1330(86)71697-3)
- Kettenring, K. M., McCormick, M. K., Baron, H. M., & Whigham, D. F. (2011). Mechanisms of *Phragmites australis* invasion: Feedbacks among genetic diversity, nutrients, and sexual reproduction. *Journal of Applied Ecology*, 48(5), 1305-1313.
- Kozlowski, T. (1997). Responses of woody plants to flooding and salinity. *Tree physiology*, 17(7), 490-490.
- Krusi, B. O., & Wein, R. W. (1988). Experimental studies on the resiliency of floating *Typha* mats in a freshwater marsh. *The Journal of Ecology*, 60-72.
- Lavoie, C. (2007). Envahissement du roseau commun le long des corridors autoroutiers : État de situation, causes et gestion. *Centre de recherche en aménagement et développement, Université Laval, Québec*.
- Lavoie, C. (2008). *Le roseau commun (Phragmites australis) : Une menace pour les milieux humides du Québec*.
- Lavoie, C. (2019). *50 plantes envahissantes. Protéger la nature et l'agriculture*. Les Publications du Québec.
- Lavoie, C., Jean, M., Delisle, F., & Létourneau, G. (2003). Exotic plant species of the St Lawrence River wetlands: A spatial and historical analysis. *Journal of Biogeography*, 30(4), 537-549. <https://doi.org/10.1046/j.1365-2699.2003.00854.x>
- Legendre, P., & Legendre, L. (1998). Numerical ecology: Developments in environmental modelling. *Developments in Environmental Modelling*, 20(1).
- Lishawa, S., Albert, D., & Tuchman, N. (2010). Water Level Decline Promotes *Typha X glauca* Establishment and Vegetation Change in Great Lakes Coastal Wetlands. *Wetlands*, 30, 1085-1096. <https://doi.org/10.1007/s13157-010-0113-z>

- Lishawa, S. C., Treering, D. J., Vail, L. M., McKenna, O., Grimm, E. C., & Tuchman, N. C. (2013). Reconstructing plant invasions using historical aerial imagery and pollen core analysis : Typha in the Laurentian Great Lakes. *Diversity and Distributions*, 19(1), 14-28.
- Liu, H., Bu, R., Liu, J., Leng, W., Hu, Y., Yang, L., & Liu, H. (2011). Predicting the wetland distributions under climate warming in the Great Xing'an Mountains, northeastern China. *Ecological Research*, 26(3), 605-613. <https://doi.org/10.1007/s11284-011-0819-2>
- Lorenzen, B., Brix, H., McKee, K. L., Mendelssohn, I. A., & Miao, S. (2000). Seed germination of two Everglades species, Cladium jamaicense and Typha domingensis. *Aquatic Botany*, 66(3), 169-180.
- Ludwig, D. F., Iannuzzi, T. J., & Esposito, A. N. (2003). Phragmites and environmental management : A question of values. *Estuaries*, 26(2), 624-630.
- Madsen, J. D., Chambers, P. A., James, W. F., Koch, E. W., & Westlake, D. F. (2001). The interaction between water movement, sediment dynamics and submersed macrophytes. *Hydrobiologia*, 444(1), 71-84. <https://doi.org/10.1023/A:1017520800568>
- Mahdianpari, M., Granger, J. E., Mohammadimanesh, F., Salehi, B., Brisco, B., Homayouni, S., Gill, E., Huberty, B., & Lang, M. (2020). Meta-Analysis of Wetland Classification Using Remote Sensing : A Systematic Review of a 40-Year Trend in North America. *Remote Sensing*, 12(11), 1882. <https://doi.org/10.3390/rs12111882>
- Mal, T. K., & Narine, L. (2004). The biology of Canadian weeds. 129. Phragmites australis (Cav.) Trin. Ex Steud. *Canadian Journal of Plant Science*, 84(1), 365-396.
- Marks, M., Lapin, B., & Randall, J. (1994). Phragmites australis (P. communis) : Threats, management and monitoring. *Natural Areas Journal*, 14(4), 285-294.
- Martin, L., & Blossey, B. (2013). The Runaway Weed : Costs and Failures of Phragmites australis Management in the USA. *Estuaries and Coasts*, 36. <https://doi.org/10.1007/s12237-013-9593-4>
- Mauchamp, A., Blanch, S., & Grillas, P. (2001). Effects of submergence on the growth of Phragmites australis seedlings. *Aquatic botany*, 69(2-4), 147-164.

- Mazur, M., Kowalski, K., & Galbraith, D. (2014). Assessment of suitable habitat for *Phragmites australis* (common reed) in the Great Lakes coastal zone. *Aquatic Invasions*, 9, 1-19. <https://doi.org/10.3391/ai.2014.9.1.01>
- Meng, H., Wang, X., Tong, S., Lu, X., Hao, M., An, Y., & Zhang, Z. (2016a). Seed germination environments of *Typha latifolia* and *Phragmites australis* in wetland restoration. *Ecological Engineering*, 96, 194-199.
- Meng, H., Wang, X., Tong, S., Lu, X., Hao, M., An, Y., & Zhang, Z. (2016b). Seed germination environments of *Typha latifolia* and *Phragmites australis* in wetland restoration. *Ecological Engineering*, 96, 194-199.
- Meyer, D. L., Johnson, J. M., & Gill, J. W. (2001). Comparison of nekton use of *Phragmites australis* and *Spartina alterniflora* marshes in the Chesapeake Bay, USA. *Marine Ecology Progress Series*, 209, 71-83.
- Meyer, S. W., Badzinski, S. S., Petrie, S. A., & Ankney, C. D. (2010). Seasonal Abundance and Species Richness of Birds in Common Reed Habitats in Lake Erie. *The Journal of Wildlife Management*, 74(7), 1559-1566. <https://doi.org/10.1111/j.1937-2817.2010.tb01284.x>
- Meyerson, L., Saltonstall, K., Windham, L., Kiviat, E., & Findlay, S. (2000). A Comparison of *Phragmites australis* in Freshwater and Brackish Marsh Environments in North America. *Wetlands Ecology and Management*, 8, 89-103. <https://doi.org/10.1023/A:1008432200133>
- Millar, J. B. (1973). Vegetation changes in shallow marsh wetlands under improving moisture regime. *Canadian Journal of Botany*, 51(8), 1443-1457. <https://doi.org/10.1139/b73-184>
- Mitchell, M. E., Lishawa, S. C., Geddes, P., Larkin, D. J., Treering, D., & Tuchman, N. C. (2011). Time-dependent impacts of cattail invasion in a Great Lakes coastal wetland complex. *Wetlands*, 31(6), 1143-1149.
- Mitsch, W. J., & Gosselink, J. G. (2000). The value of wetlands : Importance of scale and landscape setting. *Ecological Economics*, 35(1), 25-33. [https://doi.org/10.1016/S0921-8009\(00\)00165-8](https://doi.org/10.1016/S0921-8009(00)00165-8)

Morin, J., Bachand, M., H. Richard, J., & Martin, S. (2016). *Modeling the Rainy Lake and Namakan Reservoir ecosystem response to water level regulation*. <https://doi.org/10.13140/RG.2.1.4738.0087>

Morin, J., Champoux, O., Mingelbier, M., Bechara, J. A., Secretan, Y., Jean, M., & Frenette, J.-J. (2005). Modélisation intégrée de la réponse de l'écosystème dans le fleuve Saint-Laurent: Rapport final des activités entreprises dans le cadre du Plan d'étude sur la régularisation du lac Ontario et du fleuve Saint-Laurent. *SMC Québec - section hydrologie, Environnement Canada, Sainte-Foy*.

Mortsch, L., Ingram, J., Hebb, A., & Doka, S. (2006). *Great Lakes Coastal Wetland Communities: Vulnerability to Climate Change and Response to Adaptation Strategies*. (p. 251). Final report submitted to the Climate Change Impacts and Adaptation Program, Natural Resources Canada. Environment Canada and the Department of Fisheries and Oceans.

Mozdzer, T. J., Zieman, J. C., & McGlathery, K. J. (2010). Nitrogen Uptake by Native and Invasive Temperate Coastal Macrophytes: Importance of Dissolved Organic Nitrogen. *Estuaries and Coasts*, 33(3), 784-797. JSTOR.

Nilsson, C., & Keddy, P. (2011). Predictability of Change in Shoreline Vegetation in a Hydroelectric Reservoir, Northern Sweden. *Canadian Journal of Fisheries and Aquatic Sciences*, 45, 1896-1904. <https://doi.org/10.1139/f88-221>

Odland, A., & Del Moral, R. (2002). Thirteen years of wetland vegetation succession following a permanent drawdown, Myrkdalen Lake, Norway. *Plant Ecology*, 162(2), 185-198.

Ontario Ministry of Natural Resources and Forestry. (2010). *Ontario Hydro Network (OHN)—Watercourse*. <https://geohub.lio.gov.on.ca/datasets/mnrf::ontario-hydro-network-ohn-watercourse>

Ontario Ministry of Natural Resources and Forestry. (2018). *Ontario Hydro Network (OHN)—Waterbody*. <https://geohub.lio.gov.on.ca/datasets/mnrf::ontario-hydro-network-ohn-waterbody/explore?location=49.261208%2C-84.732487%2C5.83>

Ontario Ministry of Natural Resources and Forestry. (2019a). *Southern Ontario Land Resource Information System (SOLRIS) 3.0*. <https://geohub.lio.gov.on.ca/documents/lio::southern-ontario-land-resource-information-system-solris-3-0/about>

Ontario Ministry of Natural Resources and Forestry. (2019b). *Ecological Land Classification (ELC) of Ontario*. <https://geohub.lio.gov.on.ca/documents/f8c790e0408f4c5e90d259c5e305e45b/about>

Ontario Ministry of Natural Resources and Forestry. (2019c). *Great Lakes Shoreline Ecosystem Inventory V 1.0: Lake Erie*. <https://geohub.lio.gov.on.ca/documents/fb6cb57e75ba4040ae74d1e0fd9a724a/about>

Ontario Ministry of Natural Resources and Forestry. (2021). *Great Lakes Shoreline Ecosystem Inventory V 2.0*. <https://geohub.lio.gov.on.ca/documents/f1fe178a57504baf8a7f529899210e56/about>

Ontario Ministry of Natural Resources and Forestry, Ministry of Environment, Conservation and Parks, & Canadian Wildlife Service. (2019). *Invasive Phragmites Control at Long Point Region and Rondeau Provincial Park Implementation Plan*.

Packer, J. G., Meyerson, L. A., Skalova, H., Pyšek, P., & Kueffer, C. (2017). Biological flora of the British Isles : *Phragmites australis*. *Journal of Ecology*, 105(4), 1123-1162.

Pagter, M., Bragato, C., & Brix, H. (2005). Tolerance and physiological responses of *Phragmites australis* to water deficit. *Aquatic Botany*, 81, 285-299. <https://doi.org/10.1016/j.aquabot.2005.01.002>

Pedregosa, F., Varoquaux, G., Gramfort, A., Michel, V., Thirion, B., Grisel, O., Blondel, M., Prettenhofer, P., Weiss, R., & Dubourg, V. (2011). Scikit-learn : Machine learning in Python. *the Journal of machine Learning research*, 12, 2825-2830.

Peng, K., Jiang, W., Deng, Y., Liu, Y., Wu, Z., & Chen, Z. (2020). Simulating wetland changes under different scenarios based on integrating the random forest and CLUE-S models : A case study of Wuhan Urban Agglomeration. *Ecological Indicators*, 117, 106671. <https://doi.org/10.1016/j.ecolind.2020.106671>

Perrier, A. (2015). *Feature importance in Random Forests*. <https://alexisperrier.com/datascience/2015/08/27/feature-importance-random-forests-gini-accuracy.html>

Peters, J., Baets, B. D., Verhoest, N. E. C., Samson, R., Degroeve, S., Becker, P. D., & Huybrechts, W. (2007). Random forests as a tool for ecohydrological distribution modelling. *Ecological Modelling*, 207(2-4), 304-318. <https://doi.org/10.1016/j.ecolmodel.2007.05.011>

Peterson, A. T., Monica Papes, & Daniel A. Kluza. (2003). Predicting the Potential Invasive Distributions of Four Alien Plant Species in North America. *Weed Science*, 51(6), 863-868. JSTOR.

Powers, D. (2008). Evaluation : From Precision, Recall and F-Factor to ROC, Informedness, Markedness & Correlation. *Mach. Learn. Technol.*, 2.

Reed Jr, P. B. (1997). *Revision of the national list of plant species that occur in wetlands*. US Department of the Interior, Fish and Wildlife Service. Washington DC. 470 p.

Reed, P. B. (1988). *National list of plant species that occur in wetlands : National summary*. US Government Printing Office.

Rice, D., Rooth, J., & Stevenson, J. (2000). Colonization and expansion of *Phragmites australis* in upper Chesapeake Bay tidal marshes. *Wetlands*, 20(2), 280-299.

Ricketson, J. (2001). Typhaceae Cattail Family. *Journal of the Arizona-Nevada Academy of Science*, 69-72.

Rooth, J. E., Stevenson, J. C., & Cornwell, J. C. (2003). Increased Sediment Accretion Rates Following Invasion by *Phragmites australis* : The Role of Litter. *Estuaries*, 26(2), 475-483. JSTOR.

Rubec, C. (2018). The Canadian Wetland Classification System. In C. M. Finlayson, M. Everard, K. Irvine, R. J. McInnes, B. A. Middleton, A. A. van Dam, & N. C. Davidson (Éds.), *The Wetland Book : I: Structure and Function, Management, and Methods* (p. 1577-1581). Springer Netherlands. https://doi.org/10.1007/978-90-481-9659-3_340

Rudrappa, T., Bonsall, J., Gallagher, J. L., Seliskar, D. M., & Bais, H. P. (2007). Root-secreted allelochemical in the noxious weed *Phragmites australis* deploys a reactive oxygen species response and microtubule assembly disruption to execute rhizotoxicity. *Journal of chemical ecology*, 33(10), 1898-1918.

Seabloom, E. W., Moloney, K. A., & Van der Valk, A. G. (2001). Constraints on the establishment of plants along a fluctuating water-depth gradient. *Ecology*, 82(8), 2216-2232.

Sharp, J. L. L. (2002). *Managing cattail (Typha latifolia) growth in wetland systems*. University of North Texas.

Shay, J. M., de Geus, P. M. J., & Kapinga, M. R. M. (1999). Changes in shoreline vegetation over a 50-year period in the delta marsh, manitoba in response to water levels. *The Society of Wetland Scientists*, 19(2), 413-425.

Shih, J. G., & Finkelstein, S. A. (2008). Range dynamics and invasive tendencies in *Typha latifolia* and *Typha angustifolia* in eastern North America derived from herbarium and pollen records. *Wetlands*, 28(1), 1-16.

Smith, I. M., Fiorino, G. E., Grabas, G. P., & Wilcox, D. A. (2021). Wetland vegetation response to record-high Lake Ontario water levels. *Journal of Great Lakes Research*, 47(1), 160-167. <https://doi.org/10.1016/j.jglr.2020.10.013>

Snell and Cecile Environmental Research. (2001). *Wetland Trends Through Time : Long Point, Four Lake Huron Wetlands and Additional to Seven Previously Mapped Wetlands*. Environment Canada, Toronto, Ontario.

Snyder, R. L. (1985). *EVALUATION OF THE IMPACT OF TWO COMMON AQUATIC PLANTS, TYPHA LATIFOLIA AND EICHHORNIA CRASSIPES, ON WATER LOSS FROM FRESHWATER PONDS*. Auburn University.

Sojda, R., & Solberg, K. (1993). *Management and control of cattails. Fish and Wildlife Leaflet 13.4. 13.*

Squires, L., & Valk, A. G. V. der. (1992). Water-depth tolerances of the dominant emergent macrophytes of the Delta Marsh, Manitoba. *Canadian Journal of Botany*, 70(9), 1860-1867. <https://doi.org/10.1139/b92-230>

Stuckey, R. L., & Salamon, D. P. (1987). *Typha-Angustifolia in North-America-a foreigner masquerading as a native. 87, 4-4.*

Swarzenski, C. M., Swenson, E. M., Sasser, C. E., & Gosselink, J. G. (1991). Marsh mat flotation in the Louisiana delta plain. *The Journal of Ecology*, 999-1011.

Tabacchi, E., Correll, D. L., Hauer, R., Pinay, G., Planty-Tabacchi, A., & Wissmar, R. C. (1998). Development, maintenance and role of riparian vegetation in the river landscape. *Freshwater biology*, 40(3), 497-516.

Tessier, C., Maire, A., & Aubin, A. (1981). Étude de la végétation des zones riveraines de l'archipel des Cent-îles du fleuve Saint-Laurent, Québec. *Canadian Journal of Botany*, 59(8), 1526-1536. <https://doi.org/10.1139/b81-209>

Tom van den Broek, van Diggelen, R., & Bobbink, R. (2005). Variation in Seed Buoyancy of Species in Wetland Ecosystems with Different Flooding Dynamics. *Journal of Vegetation Science*, 16(5), 579-586. JSTOR.

Toner, M., & Keddy, P. (1997). River Hydrology and Riparian Wetlands : A Predictive Model for Ecological Assembly. *Ecological Applications*, 7(1), 236-246. JSTOR. <https://doi.org/10.2307/2269420>

Tougas-Tellier, M., Morin, J., Hatin, D., & Lavoie, C. (2015). Freshwater wetlands : Fertile grounds for the invasive *Phragmites australis* in a climate change context. *Ecology and Evolution*, 5. <https://doi.org/10.1002/ece3.1576>

Townsend, P. A. (2001). Mapping seasonal flooding in forested wetlands using multi-temporal Radarsat SAR. *Photogrammetric engineering and remote sensing*, 67(7), 857-864.

Travis, S. E., Marburger, J. E., Windels, S., & Kubátová, B. (2010). Hybridization dynamics of invasive cattail (Typhaceae) stands in the Western Great Lakes Region of North America : A molecular analysis. *Journal of Ecology*, 98(1), 7-16.

Trebitz, A. S. (2006). Characterizing seiche and tide-driven daily water level fluctuations affecting coastal ecosystems of the Great Lakes. *Journal of Great Lakes Research*, 32(1), 102-116.

Tulbure, M. G., Johnston, C. A., & Auger, D. L. (2007). Rapid Invasion of a Great Lakes Coastal Wetland by Non-native *Phragmites australis* and *Typha*. *Coastal Indicators*, 33, 269-279. [https://doi.org/10.3394/0380-1330\(2007\)33\[269:RIOAGL\]2.0.CO;2](https://doi.org/10.3394/0380-1330(2007)33[269:RIOAGL]2.0.CO;2)

Tulbure, M., & Johnston, C. (2010). Environmental Conditions Promoting Non-native *Phragmites australis* Expansion in Great Lakes Coastal Wetlands. *Wetlands*, 30, 577-587. <https://doi.org/10.1007/s13157-010-0054-6>

Turgeon, K., Champoux, O., Martin, S., & Morin, J. (2004). Modélisation des milieux humides de la plaine inondable du Saint-Laurant, du lac Saint-Pierre au lac Saint-Louis. *SMC Québec - section hydrologie, Environnement Canada*.

Turgeon, K., & Morin, J. (2005). Modelling submerged macrophytes distribution : Evaluation of models transferability in three St. Lawrence River sections scientific report MSC Québec–Hydrology Section RS-105. *Environment Canada, Sainte-Foy*, 61.

Van der Valk, A. G. (1981). Succession in Wetlands : A Gleasonian Approach. *Ecology*, 62(3), 688-696. JSTOR. <https://doi.org/10.2307/1937737>

Van der Valk, A. G., & Davis, C. B. (1978). The Role of Seed Banks in the Vegetation Dynamics of Prairie Glacial Marshes. *Ecology*, 59(2), 322-335. JSTOR. <https://doi.org/10.2307/1936377>

Van der Valk, A. G., Squires, L., & Welling, C. H. (1994). Assessing the Impacts of an Increase in Water Level on Wetland Vegetation. *Ecological Applications*, 4(3), 525-534. <https://doi.org/10.2307/1941954>

Warren, R. S., Fell, P. E., Grimsby, J. L., Buck, E. L., Rilling, G. C., & Fertik, R. A. (2001). Rates, patterns, and impacts of *Phragmites australis* expansion and effects of experimental *Phragmites* control on vegetation, macroinvertebrates, and fish within tidelands of the lower Connecticut River. *Estuaries*, 24(1), 90-107.

Waters, I., & Shay, J. (1990). A field study of the morphometric response of *Typha glauca* shoots to a water depth gradient. *Canadian Journal of Botany*, 68(11), 2339-2343.

Weisner, S., Graneli, W., & Ekstam, B. (1993). Influence of submergence on growth of seedlings of *Scirpus lacustris* and *Phragmites australis*. *Freshwater Biology*, 29, 371-375. <https://doi.org/10.1111/j.1365-2427.1993.tb00771.x>

Weisner, S., & Strand, J. (1996). Rhizome Architecture in *Phragmites Australis* in Relation to Water Depth : Implications for Within-Plant Oxygen Transport Distances. *Folia Geobotanica*, 31, 91-97. <https://doi.org/10.1007/BF02803998>

Weller, M. W. (1975). Studies of cattail in relation to management for marsh wildlife. *Iowa State Journal of Research*.

White, J., Chambers, L., Sees, M., & Corstanje, R. (2008). The Short-Term Effects of Prescribed Burning on Biomass Removal and the Release of Nitrogen and Phosphorus in a Treatment Wetland. *Journal of environmental quality*, 37, 2386-2391. <https://doi.org/10.2134/jeq2008.0019>

Wilcox, D. (2012). Response of wetland vegetation to the post-1986 decrease in Lake St. Clair water levels : Seed-bank emergence and beginnings of the *Phragmites australis* invasion. *Journal of Great Lakes Research*, 38, 270–277. <https://doi.org/10.1016/j.jglr.2012.02.007>

Wilcox, D. A., Kowalski, K. P., Hoare, H. L., Carlson, M. L., & Morgan, H. N. (2008). Cattail Invasion of Sedge/Grass Meadows in Lake Ontario : Photointerpretation Analysis of Sixteen Wetlands over Five Decades. *Journal of Great Lakes Research*, 34(2), 301-323. [https://doi.org/10.3394/0380-1330\(2008\)34\[301:CIOGMI\]2.0.CO;2](https://doi.org/10.3394/0380-1330(2008)34[301:CIOGMI]2.0.CO;2)

Wilcox, D. A., & Xie, Y. (2007). Predicting wetland plant community responses to proposed water-level-regulation plans for Lake Ontario : GIS-based modeling. *Journal of Great Lakes Research*, 33(4), 751-773.

Wilcox, K. L., Petrie, S. A., Maynard, L. A., & Meyer, S. W. (2003). Historical Distribution and Abundance of *Phragmites australis* at Long Point, Lake Erie, Ontario. *Journal of Great Lakes Research*, 29(4), 664-680. [https://doi.org/10.1016/S0380-1330\(03\)70469-9](https://doi.org/10.1016/S0380-1330(03)70469-9)

Windham, L., & Lathrop, R. G. (1999). Effects of *Phragmites australis* (Common Reed) Invasion on Aboveground Biomass and Soil Properties in Brackish Tidal Marsh of the Mullica River, New Jersey. *Estuaries*, 22(4), 927-935. JSTOR. <https://doi.org/10.2307/1353072>

Yu, J., Wang, X., Ning, K., Li, Y., Wu, H., Fu, Y., Zhou, D., Guan, B., & Lin, Q. (2012). Effects of salinity and water depth on germination of *Phragmites australis* in coastal wetland of the Yellow River Delta. *CLEAN–Soil, Air, Water*, 40(10), 1154-1158.

Zedler, J. B., & Kercher, S. (2004). Causes and consequences of invasive plants in wetlands : Opportunities, opportunists, and outcomes. *critical Reviews in Plant sciences*, 23(5), 431-452.

Zoltai, S. (1988). *Wetland environments and classification Environment Canada. 0.*

